Measurement of the Underlying Event using track-based event shapes in $Z \to \ell^+\ell^-$ events with ATLAS

D i s s e r t a t i o n
zur Erlangung des akademischen Grades
d o c t o r r e r u m n a t u r a l i u m
(Dr. rer. nat.)
im Fach Physik
eingereicht an der

Mathematisch-Naturwissenschaftlichen Fakultät
der Humboldt-Universität zu Berlin

von

Diplom-Physiker Holger Schulz

Präsident der Humboldt-Universität zu Berlin
Prof. Dr. Jan-Hendrik Olbertz

Dekan der Mathematisch-Naturwissenschaftlichen Fakultät
Prof. Dr. Elmar Kulke

Gutachter/innen:
1. Prof. Dr. Heiko Lacker
2. Prof. Dr. Arno Straessner
3. Dr. Klaus Moenig

eingereicht am: 17. April 2014
Tag der mündlichen Prüfung: 11. September 2014

Abstract

This thesis describes a measurement of hadron-collider event shapes in proton-proton collisions at a centre of momentum energy of 7 TeV at the Large Hadron Collider (LHC) at CERN (Conseil Européenne pour la Recherche Nucléaire) located near Geneva (Switzerland). The analysed data (integrated luminosity: 1.1 fb^{-1}) was recorded in 2011 with the ATLAS-experiment. Events where a Z-boson was produced in the hard sub-process which subsequently decays into an electron-positron or muon-antimuon pair were selected for this analysis. The observables are calculated using all reconstructed tracks of charged particles within the acceptance of the inner detector of ATLAS except those of the leptons of the Z-decay. Thus, this is the first measurement of its kind. The observables were corrected for background processes using data-driven methods. For the correction of so-called "pile-up" (multiple overlapping proton-proton collisions) a novel technique was developed and successfully applied. The data was further unfolded to correct for remaining detector effects. The obtained distributions are especially sensitive to the so-called "Underlying Event" and can be compared with predictions of Monte-Carlo event-generators directly, i.e. without the necessity of running time-consuming simulations of the ATLAS-detector. Finally, it was tried to improve the predictions of the event generators Pythia8 and Sherpa by finding an optimised setting of relevant model parameters in a technique called "Tuning". It became apparent, however, that the underlying Sjöstrand-Zijl model is unable to give a good description of the measured event-shape distributions.

Zusammenfassung

Diese Dissertation beschreibt eine Messung von hadronischen Ereignisformvariablen ("event shapes") in Protonkollisionen mit einer Schwerpunktsenergie von 7 TeV am Large Hadron Collider (LHC) am CERN (Conseil Européenne pour la Recherche Nucléaire) bei Genf (Schweiz). Die analysierten Daten mit einer integrierten Luminosität von 1.1 fb^{-1} wurden im Jahr 2011 mit dem ATLAS Experiment aufgenommen. Für die Analyse wurden solche Ereignisse ausgewählt, in deren harten Streuprozessen ein Z-Boson produziert wurde, welches entweder in ein Elektron-Positron-Paar oder ein Muon-Antimuon-Paar zerfällt. Die Observablen wurden mit sämtlichen rekonstruierten Spuren innerhalb der Akzeptanz des inneren Spurdetektors (Inner Detector) von ATLAS außer denen der Leptonen des Zerfalls des Z-Bosons berechnet. Somit handelt es sich hierbei um die erste Messung dieser Art. Anschließend wurden die Observablen auf Untergrundprozesse mit auf Daten basierenden Methoden korrigiert wobei ein neues Verfahren für die Korrektur des sogenannten "Pile-up" (Überlagerung mehrerer Proton-Proton Wechselwirkungen) entwickelt und erfolgreich zur Anwedung gebracht wurde. Schließlich wurden die gemessenen Verteilungen entfaltet. Die so erhaltenen Daten sind insbesondere sensitiv auf das sogenannte "Underlying Event" und können direkt mit Monte-Carlo-Ereignisgeneratoren ohne aufwändige Simulation des ATLAS-Detektors verglichen werden. Abschließend wurde versucht die Modellparameter in den Simulationsprogrammen Pythia8 und Sherpa mithilfe der gewonnenen Daten durch eine bessere Abstimmung ("Tuning") zu verbessern. Hierbei zeigte sich, dass das zugrunde liegende Sjöstrand-Zijl Modell nicht ausreicht, um eine adäquate Beschreibung der gemessenen Verteilungen zu erreichen.

Contents

Chapter 1.

Introduction

This thesis describes the first measurement of hadron collider event shapes with the ATLAS (A Torroidal Lhc ApparatuS, Chapter 4) detector at the LHC (Large Hadron Collider, Chapter 3) in events where a leptonically decaying Z-boson was produced in the hard sub-process. The observables (event shapes) measured are chosen because of their sensitivity to multiple parton interactions (MPI), one compenent of the so-called "Underlying Event", an irreducible background to all hadron collisions, comprised of all event avtivity not related to the hardest (largest momentum transfer) parton-parton interaction. The phenomenon of MPI is an immediate consequence of the compound nature of hadrons, i.e. colour-singlet particles that consist of coloured quarks, anti-quarks and gluons, such as protons that are collided at the LHC. In such a collision, the constituents of both protons (called partons) undergo interactions where typically the hardest parton-parton interaction is the (hard) sub-process of interest for a measurement, e.g. production of a Higgs boson. In the measurement conducted in this analysis events with a hard sub-process are selected that allows for itself to be removed from the overall event activity, i.e. the production of a Z-boson that decays into an electron-positron or a muon anti-muon pair. These leptons can easily be identified with the ATLAS detector and thus removed from the event, leaving particles that predominantly should have been produced in subsequently softer parton-parton interactions, that occur in addition to the hard sub-process.

The properties of charged particles (except the decay products of the Z-bosons) reconstructed using the inner detector of ATLAS only (called tracks) are used in this measurement to calculate event shapes (Chapter 7). The measurement thus requires reconstructed properties of

- electrons and positrons

- muons and anti-muons
- other charged particles

Further, this measurement uses the transverse momentum of the Z-boson ($p_\perp(\mathrm{Z})$) to define five phases-space regions the event shapes are measured in:

- $p_\perp(\mathrm{Z}) \in [0, 6)$ GeV
- $p_\perp(\mathrm{Z}) \in [6, 12)$ GeV
- $p_\perp(\mathrm{Z}) \in [12, 25)$ GeV
- $p_\perp(\mathrm{Z}) \in [25, \infty)$ GeV
- $p_\perp(\mathrm{Z}) \in [0, \infty)$ GeV

The first $p_\perp(\mathrm{Z})$ phase-space region is considered most sensitive to MPI activity as the transverse momentum of the Z-boson is very small, meaning it is likely that it was produced without a recoiling jet (a cascade of hadrons). Thus after removal of the leptons, all particles should have been produced in additional parton-parton interactions. As $p_\perp(\mathrm{Z})$ increases, the event shapes change dramatically, thus allowing to gain insight even into the interplay of MPI and jets produced in the hard sub-process.

The reconstruction of the objects mentioned above is never perfect, in fact it is only possible with a certain efficiency smaller than 100%. Reasons for this deficiency are interactions of the to be identified particles with the detector material and the algorithms used. The latter are all based on statistical hypothesis tests bearing the principal property of leading to incorrect results. One example would be the misidentification of e.g. jets as electrons. The ATLAS experiment has measured the efficiencies relevant for this analysis using several different techniques, all associated with uncertainties, which give rise to systematic uncertainties (Chapter 9) on the observables measured in this analysis.

The LHC programme is primarily set out to search for physics beyond the standard model of particle physics (Chapter 2) which are very rare processes (small cross-sections). In order to have a chance to produce these kind of physics, the beams of the LHC are designed to produce a very high number of proton-proton collisions, which is achieved by a dense packing of protons within the beams which, however, leads to another phenomenon, the multiple proton-proton interaction within one proton bunch-crossing of the beams. These interactions take place simultaneously in the sense that the ATLAS detector records all proton-proton interactions happening during a single bunch-crossing as a

single event. This effect is called "pile-up" and needs to be corrected for which this analysis does using a novel technique solely based on data (Chapter 10), instead of using Monte-Carlo simulations (Chapter 8).

Further, many more processes can produce the same signature used in the selection of events in this analysis (two oppositely charged electrons or muons with an invariant mass comparable to the mass of the Z-boson). This can for instance happen due to a process yielding more than two leptons but only two of them falling into the acceptance of the lepton selection. Further, the wrongly reconstruction of a jet as a lepton (fake) as well as processes in which heavy quarks are produced that subsequently decay into leptons can lead to a non-signal event being selected in this analysis. The latter two possibilities are facilitated by QCD processes which turn out to be the largest background to this analysis (Chapter 11). They too are corrected for using a technique solely relying on data.

A final step that is applied to obtain data distributions that can be compared with Monte-Carlo simulation without the necessity to apply a simulation of the interaction of particles with the detector is called unfolding (Chapter 12) which corrects the measured distributions for all distorting detector effects.

The ultimate aim of this measurement is to provide deeper insight into the physics of the underlying event which is so far impossible to derive from first principles. Instead, phenomenological models (Chapter 8) are needed to describe data, where agreement of the simulations with the latter is achieved by an optimisation of the parameters these models introduce (Chapter 13).

Chapter 2.

The standard model of particle physics

The standard model of particle physics is a theory framework that describes matter in form of point-like particles with spin $\frac{1}{2}$ (fermions) and their interaction mediated by spin 1 particles (bosons). It is thus able to give a unified description of phenomena encountered due to electro-magnetism, weak and strong interactions. It is a quantum field theory that is strongly based on the concept of (gauge) symmetry. The reason being that NOETHER's theorem [1] provides a link between symmetries and conserved quantities. In the standard model of particle physics, those conserved quantities are the charges that permit interactions of fields and the symmetries are local gauge-symmetries of the fields. If a particle carries such a charge then it takes part in the corresponding interaction, e.g. if a particle carries an electric charge different from zero then it is subject to electromagnetic phenomena.

In its most compact formulation, the standard model of particle physics is described via the gauge group

$$SU(3)_C \times SU(2)_L \times U(1)_Y \tag{2.1}$$

wherein the special unitary group $SU(3)_C$ is used to describe the charges of the strong force (C for colour). $SU(2)_L \times U(1)_Y$ is the basis for the unified description of the electromagnetic and weak interactions developed by WEINBERG and SALAM [2]. The index L indicates a coupling to left-handed fermions only and the index Y denotes the generator of the U(1) group to be the weak hypercharge. The theory was developed as a YANG-MILLS gauge theory [3] as it is based on symmetry groups $SU(N)$. The reason for

the usage of unitary groups is the requirement for conversation of the norm and therefore invariance of probability of a state $|\Psi\rangle$ under a local (gauge) transformation $\mathcal{M}|\Psi\rangle$:

$$\langle\Psi \mid \Psi\rangle \stackrel{!}{=} \langle\Psi|\,\mathcal{M}^\dagger\mathcal{M}\,|\Psi\rangle \quad \Longrightarrow \quad \mathcal{M}^\dagger \stackrel{!}{=} \mathcal{M}^{-1} \tag{2.2}$$

An important aspect of the theory is its re-normalisability which allows a treatment of singularities that arise in the calculations of observable quantities that lead to finite results. The re-normalisability of any Yang-Mills theory with massless gauge bosons was proven in 1971 by 't Hooft [4] and Veltman.

It is a fact, however, that the observable particles described by the standard model indeed are massive (with the exception of the gluon and the photon). This apparent contradiction is resolved by the introduction of the concept of electroweak symmetry breaking, independently developed in 1962 by Brout and Englert [5], Higgs [6] and Guralnik as well as Hagen and Kibble [7]. The general idea is that the massive exchange bosons in the theory gain their mass due to spontaneous symmetry breaking ("Higgs mechanism") and coupling to an omnipresent "Higgs" field. The massive fermions acquire mass due to Yukawa interactions with the same scalar "Higgs" field.

The excitations of the latter are massive spin 0 bosons that should be observable in high-energy physics experiments. It took until 2012 that a particle consistent with the standard model "Higgs"boson, was found by the ATLAS and CMS experiments at the LHC, thus seemingly confirming the mechanism [8, 9].

2.1. Building blocks of nature

The building blocks of the standard model are elementary point-like particles that can be grouped into particles of spin $\frac{1}{2}$ (fermions) which themselves are further split into quarks and leptons, depending on whether they carry colour (charge of the strong force) or not.

The exchange particles which are called gauge bosons (spin 1) mediate the forces between particles carrying a charge (in brackets):

- photon, γ (electric charge, Q)
- gluon, g (colour, r, g, b)

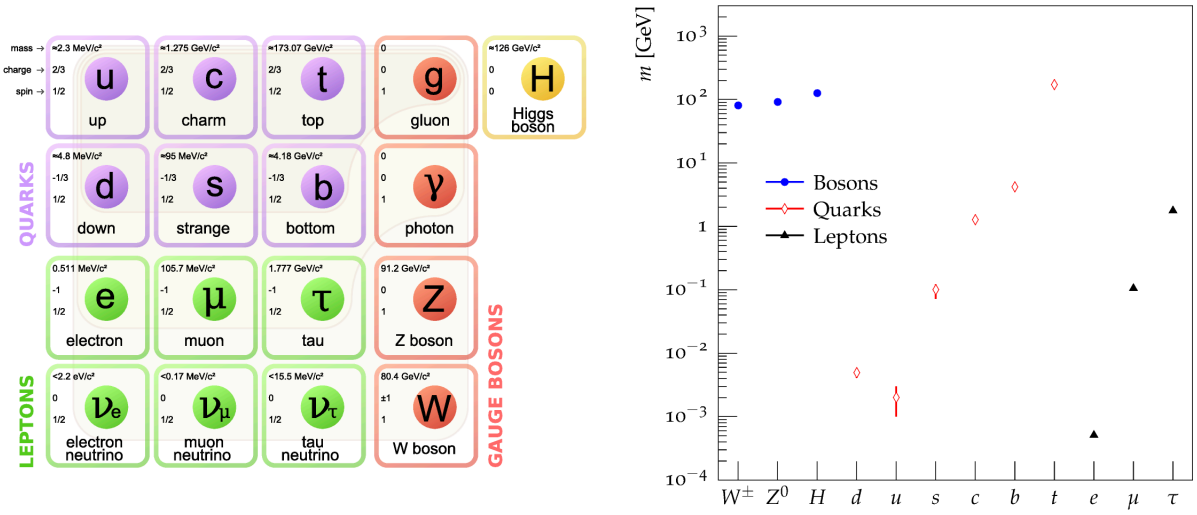

(a) Standard model particles **(b)** Masses

Figure 2.1.: Fundamental particles. (a) gives an overview of the classification of fundamental particles in the standard model and their properties (mass, electrical charge, spin) [10]. The first three columns each represent a "family" of gradually heavier fermions which constitute matter. The fourth column summarises the gauge bosons that mediate the strong (gluon), electromagnetic (photon) and electroweak forces (W, Z). Finally, the "Higgs" boson is shown which is needed to explain the masses of the W and Z bosons. The plot (made with data taken from [11]) in (b) summarises the masses of all massive fundamental particles. The reason for the apparent ordering of lepton and quark masses is not known.

- W (weak isospin, T_3) and Z bosons (no defined weak isospin but couples to T_3)

Figure 2.1 gives an overview of the fundamental particles of the standard model of particle physics.

2.1.1. Gauge Bosons

Photons: The mediator of electromagnetic interactions is the photon, γ. It is e.g. responsible for atoms being bound object. All particles that carry an electric charge, Q, can undergo interactions with it. It is a massless ($m_\gamma < 10^{-18}$ eV), stable particle without electric charge ($Q_\gamma < 10^{-15}\ e$). A photon does not interact with another photon as it does not carry an electric charge. In the standard model interaction of electrically charged

fermions (described by "Dirac" spinor fields) with (vector) photon fields are described by the $U(1)$ symmetry in equation (2.1).

Gluons: Strong interactions are also mediated by massless spin 1 particles, called gluons. In contrast to photons, gluons carry the charge of the strong force (colour) meaning that gluons can interact with other gluons which gives rise to a very rich phenomenology of strong interactions. Colour charges come in three different types, red (r), green (g) and blue (b). Gluons always carry a combination of a colour and an anti-colour charge, e.g. $r\bar{g}$. As the theory describing the gluon field is based on an $SU(3)$ group (equation (2.1)), eight different gluon states exist that carry a non-vanishing net-colour charge. Gluons do not exist as free particles and can only be studied indirectly.

W and Z bosons: Weak interactions on the other hand are mediated by massive particles. Two charged W-bosons exist with electric charge $Q = \pm 1$, the W^+ and its anti-particle, the W^-. They allow for transitions between different "flavours" of leptons or quarks. They are responsible for radioactive decays of nucleons, e.g. the β-decay where an electron and an anti-neutrino are emitted from a nucleon while changing a d-flavoured quark into a u-flavoured quark and hence a neutron into a proton.

$\mathrm{W}^\pm$ and Z^0 bosons are very short-lived, the average lifetimes are of the order $\tau_{\mathrm{W,Z}} \sim 3 \cdot 10^{-25}\ s$. They were predicted by Glashow, Weinberg, Salam based on an $SU(2) \times U(1)$ symmetry [2]. Their discoveries by UA1 [12] and UA2 [13] at CERN are widely seen as major breakthroughs for the acceptance of the standard model. Together with the photon they are used to give a unified description of electromagnetic and weak interactions in what has come to be known as electroweak interactions ($SU(2)_L \times U(1)_Y$ in equation (2.1)).

The electrically neutral Z^0-boson couples to electric and weak charges but in contrast to the $W^\pm$ does not allow flavour changes. The Z^0-boson will be discussed in more detail as it is central for the event selection of the data-analysis presented in this thesis.

2.1.2. Leptons

Within the standard model, three "families" or flavours of leptons (derived from the ancient-greek word $\lambda\epsilon\pi\tau o\varsigma$, meaning slim or light-weight) are known to exist. All leptons are carriers of a weak charge, T_3, the third component of the weak isospin, meaning they take part in weak interactions. Each family consists of a particle, ℓ that carries an electric charge of $Q = -1$, its antiparticle, $\bar{\ell}$ with electric charge $Q = +1$, a neutrino

($Q = 0$), ν_ℓ and the corresponding anti-neutrino, $\bar{\nu_\ell}$. Thus electrically charged leptons can undergo electromagnetic interactions (coupling to photons) while neutrinos only interact weakly. The known charged leptons within the standard model are the electron, e (the only stable lepton), the muon μ with a life-time of about two microseconds and the tau with a life-time of 290 femtoseconds.

2.1.3. Quarks

Those fermions also carrying a colour charge are called quarks. They are grouped together with the fermions as generations or families, e.g. the up (u) and down (d) quark together with the electron and electron neutrino, as well as the corresponding anti-particles, form the first fermion generation (Figure 2.1). Up and down quarks are the fundamental building blocks of protons (uud) and neutrons (udd), held together by gluons. Thus, the first generation of leptons, together with photons and gluons forms the ordinary matter encountered in everyday life as atoms. All other quarks, i.e. the 2^{nd} generation (strange (s) and charm (c) quarks) and the 3^{rd} generation (bottom (b) and top (t) quarks) need to be produced in a laboratory or as result of cosmic radiation impacts in order to be studied. Quarks carry charges of all fundamental forces present in the standard model (electrical and colour charge, weak isospin) and hence take part in all standard model interactions.

Quarks do not exist as free particles. In a low energy limit (large distances, $r \approx \mathcal{O}(1\text{ fm})$) they form colour-neutral objects called hadrons. If quarks are produced with high energies (small distances), they exist as (non-observable) asymptotically free particles. This behaviour is due to the potential between colour-charged objects which is of the form [14]

$$V(r) \sim \underbrace{-\frac{C_1}{r}}_{\text{asymptotically free part}} + \underbrace{C_2 \cdot r}_{\text{confining part}} \tag{2.3}$$

where the constant C_1 is dependent on the energy (Section 2.2.2).

The hadrons formed by quarks and antiquarks exist in two different classes. A quark and an anti-quark form so-called mesons of which the charged pions (π, constituted from u and d quarks) constitute the bulk of the charged particles measured in this analysis.

The other class of particles is called (anti-) baryons (derived from $\beta\alpha\rho\upsilon\varsigma$, meaning heavy) which are formed from combinations of three quarks and anti-quarks. The most prominent specimen of those are protons (uud) which are used as beam particles in the LHC (Chapter 3). It should be noted that the quarks mentioned as forming hadrons are called valence quarks. Hadrons also consist of an infinite number of gluons as well as so-called "sea-quarks" which are the result of these gluons splitting into virtual quark anti-quark pairs. Hence quarks and corresponding anti-quarks exist in e.g. a proton and can therefore take part in interactions. In this context the term "parton" is a common expression for valence and sea-quarks as wells as for gluons that form a hadron.

2.1.4. Z-Boson production in pp-collisions

When two protons are brought to collision at the LHC, the production of a Z-boson as result of the hard scattering process can to first order be achieved by two processes (Figure 2.2):

1. $gq \rightarrow \mathrm{Z}q$ (t-channel)
2. $q\overline{q} \rightarrow \mathrm{Z}$ (s-channel)

where the t-channel process produces a Z-boson accompanied by a jet. The total inclusive cross-section for Z-boson production was measured in [15] to be $\sigma_{\mathrm{Z}} = (27.8 \pm 1.1)$ nb at the LHC at $\sqrt{s} = 7$ TeV in good agreement with theoretical next-to-next-to leading order (NNLO) predictions of $\sigma_{\mathrm{Z,NNLO}} = 29.0^{+1.1}_{-0.5}$ nb [15]. The total cross-section at the LHC at $\sqrt{s} = 7$ TeV was measured by TOTEM to be $\sigma_{\mathrm{tot}} = 98.3 \pm 2.8$ mb [16], thus only a seemingly tiny fraction of $3 \cdot 10^{-7}$ of the collisions happening at the LHC produce a Z-boson. With the nominal interaction rate at the LHC of 40 million bunch collisions per second (Chapter 3) roughly 11 Z-bosons were produced every second. The recorded and analysed number of events containing Z-bosons is however greatly reduced due to detector effects (Chapter 4, 5).

The average life-time of a Z-boson, which is a resonance, is very short such that produced Z-bosons almost immediately decay to first order into pairs of a particle and the corresponding anti-particle. The relative probability of a decay into a pair of a certain species is called "branching-fraction". The largest branching fraction of Z-bosons is into hadronic final states, i.e. decay into $q\ \overline{q}$ pairs of 70% [11]. In 20% of all cases, a Z-boson decays into neutrinos. These two decay modes are hard to access experimentally, leaving the

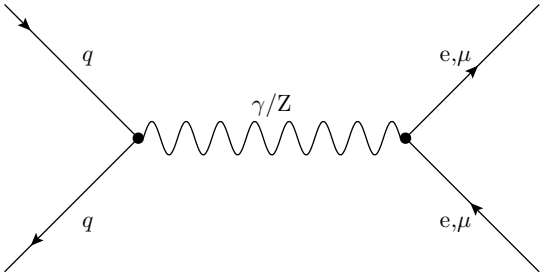

(a) s-channel

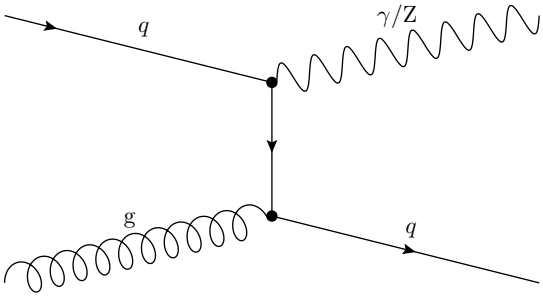

(b) t-channel

Figure 2.2.: Tree-level FEYNMAN diagrams of processes relevant for this analysis. (a) shows the s-channel production with subsequent decay into a pair of charged leptons. This process also happens via the exchange of a photon which is experimentally indistinguishable from Z-boson exchange (DRELL-YAN process). (b) shows the t-channel production of a Z-boson with an associated jet (quark).

remaining $\approx 10\%$ of decays into e^+e^-, $\mu^+\mu^-$ and $\tau^+\tau^-$ pairs for analysis. The decays into these lepton pairs occur with the same probability of 3.36% [11]. In this analysis only the decay modes e^+e^- and $\mu^+\mu^-$ are measured as the reconstruction of tau leptons is very difficult. An example tree-level FEYNMAN-diagram of an s-channel Z-boson decaying into a pair of charged leptons is shown in Figure 2.2a.

2.2. Quantum-Chromo-Dynamics (QCD)

The strong force that describes the interaction of elementary particles that carry a colour charge is one of the fundamental forces. The quantum field theory of strong interactions developed by David Gross, David Politzer, Frank Wilczek, Gerardus 't Hooft, Martinus J.G. Veltman, Murray Gell-Mann, Harald Fritzsch and Heinrich Leutwyler is called Quantum chromodynamics (QCD). The name is derived from the greek word for colour, $\chi\rho\omega\mu\alpha$.

In contrast to QED, where the Lagrangian is invariant under local U(1) gauge transformations (one conserved charge, ABELian group), the fundamental symmetry group in QCD is SU(3) due to the three conserved charges (colour) of the quarks. Quarks carry colour charge r, g, b while anti-quarks carry anti-colour $\bar{r}$, $\bar{g}$, $\bar{b}$ and the symmetry requires strong interactions to be invariant under colour transformations. Furthermore, SU(3) is a non-ABELian group. The consequences of that will be explained in more detail below. Quarks are considered to be in the fundamental representation of SU(3):

$$r = \begin{pmatrix} 1 \\ 0 \\ 0 \end{pmatrix} \quad g = \begin{pmatrix} 0 \\ 1 \\ 0 \end{pmatrix} \quad b = \begin{pmatrix} 0 \\ 0 \\ 1 \end{pmatrix} \tag{2.4}$$

The interaction of quarks is mediated by gluons which themself carry colour charge. In fact, they are required to carry both colour- and anti-colour in order to have colour conserved at fundamental vertices. This gives rise to 9 possible combinations of colour and anti-colour to be carried by gluons. In group-theory language this is often written as $\mathbf{3} \otimes \bar{\mathbf{3}} = \mathbf{8} \oplus \mathbf{1}$ meaning that the combinations of the fundamental SU(3), $\mathbf{3}$, representation with its adjoint representation, $\bar{\mathbf{3}}$, yields an octet $\mathbf{8}$ and a singlet $\mathbf{1}$. The octet states carry net-colour charge, while the singlet state, $\frac{1}{\sqrt{3}}\left(r\bar{r} + g\bar{g} + b\bar{b}\right)$, is colour-neutral and hence does not take part in strong interactions. A pictorial representation of the fundamental representations and octet states of $\mathrm{SU}(3)_{\mathrm{colour}}$ can be found in Figure 2.3.

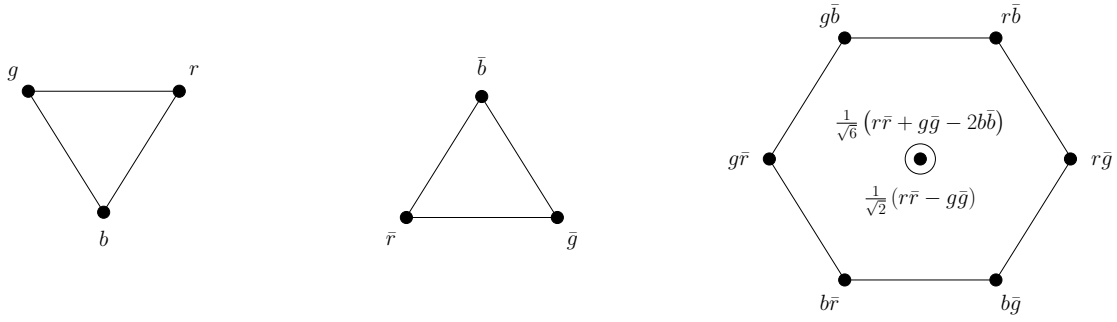

(a) 3 **(b) $\bar{\mathbf{3}}$** **(c) 8**

Figure 2.3.: Pictorial representation of the fundamental representation of $\mathrm{SU}(3)_{\mathrm{colour}}$, $\mathbf{3}$, its adjoint, $\bar{\mathbf{3}}$ and the colour-octet of the gluon colour wave-functions.

2.2.1. Lagrangian

The gauge-invariant Lagrangian of QCD can be written as [14]

$$\mathcal{L}_{\mathrm{QCD}} = \bar{q}\left(i\gamma^{\mu}\partial_{\mu} - m\right)q - g\left(\bar{q}\gamma^{\mu}T_{A}q\right)F_{\mu}^{A} - \frac{1}{4}F_{\mu\nu}^{A}F_{A}^{\mu\nu} \tag{2.5}$$

The term $\bar{q}\left(i\gamma^{\mu}\partial_{\mu} - m\right)q$ describes the propagation of quarks in absence of an external field. In fact, application of the Euler-Lagrange equation yields the Dirac-equation that was formulated by Paul Dirac in 1928 to describe the propagation of spin-$\frac{1}{2}$ particles.

The second term, $g\left(\bar{q}\gamma^{\mu}T_{A}q\right)F_{\mu}^{A}$, describes the interaction of quarks and gluons while the last term, $-\frac{1}{4}F_{\mu\nu}^{A}F_{A}^{\mu\nu}$ is required to assure SU(3) local gauge-invariance of $\mathcal{L}_{\mathrm{QCD}}$. While the first two terms have analogous counterparts in QED, the last term is unique in QCD and gives rise to a much larger phenomenology as it introduces self-interaction terms of the gauge bosons of QCD, the gluons.

The field strength tensor of QCD, $F_{A}^{\mu\nu}$, that comes into the theory due to the gauge field of the gluons, $\mathcal{A}_{\mu}^{A}$, can be written as:

$$F_{A}^{\mu\nu} = \partial_{\mu}\mathcal{A}_{\nu}^{A} - \partial_{\nu}\mathcal{A}_{\mu}^{A} - gf^{ABC}\mathcal{A}_{\mu}^{B}\mathcal{A}_{\nu}^{C} \tag{2.6}$$

where f^{ABC} denote the structure constants of SU(3) and the indices A,B,C run over colour combinations of the gluons and g is the strong coupling-strength. It is the last part in equation (2.6) that contains the gluon self-interactions. This is in contrast to QED where such a term does not exist. The reason for that is that in QED the Lagrangian has to be symmetrical under local U(1) transformations as there is only one gauge field, namely that of the photon, while the QCD Lagrangian is required to be symmetrical under local SU(3) transformations which is non-Abelian.

$\mathcal{L}_{\mathrm{QCD}}$ (equation (2.5)) can symbolically be rewritten [14] as:

$$\mathcal{L}_{\mathrm{QCD}} = \underbrace{\text{"}\bar{q}q\text{"}}_{\text{quark propagator}} + \underbrace{\text{"}F^{2}\text{"}}_{\text{gluon propagator}} + \underbrace{g\text{"}\bar{q}qF\text{"}}_{\text{quark-gluon interaction}} + \underbrace{g\text{"}F^{3}\text{"} + g^{2}\text{"}F^{4}\text{"}}_{\text{gluon self-interactions}} \tag{2.7}$$

This allows us to identify the possible interactions in QCD. In contrast to QED we find two self-interaction terms of the gauge-fields, represented by the 3-gluon vertex and the 4-gluon vertex (Figure 2.4).

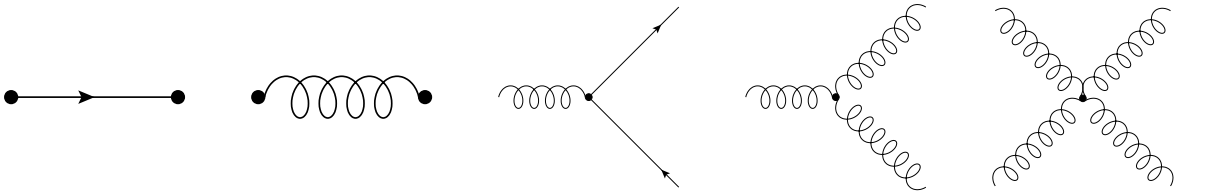

(a) Propagator of the (anti-) quark field **(b)** Propagator of the gluon field **(c)** Quark-gluon interaction **(d)** Self-interaction of three gluons **(e)** Self-interaction of four gluons

Figure 2.4.: Pictorial representation of terms in the Lagrangian of QCD equation (2.5).

2.2.2. Coupling α_S

Another fundamental difference of QCD compared to QED is the running of the coupling "constant" α_S. While the electromagnetic coupling increases with energy (or scale μ), $\alpha_S(\mu)$ decreases logarithmically as μ grows:

$$\alpha_S(\mu) \approx \frac{1}{\beta_0 \ln \frac{\mu^2}{\Lambda^2_{\mathrm{QCD}}}} \tag{2.8}$$

The expression β_0 is the first term of the β-function of QCD. β-functions are properties of re-normalisable quantum field theories such as QED and QCD. They allow to calculate the dependence of the coupling with energy and are obtained through pertubative calculations. The first term of the QCD β-function can be written as

$$\beta_0 = \frac{33 - 2n_f}{12\pi} \tag{2.9}$$

where n_f is the number of quark flavours considered in the calculation. As long as $n_f < 16$, which is valid with the known number of quark flavours $n_f = 6$, β_0 remains

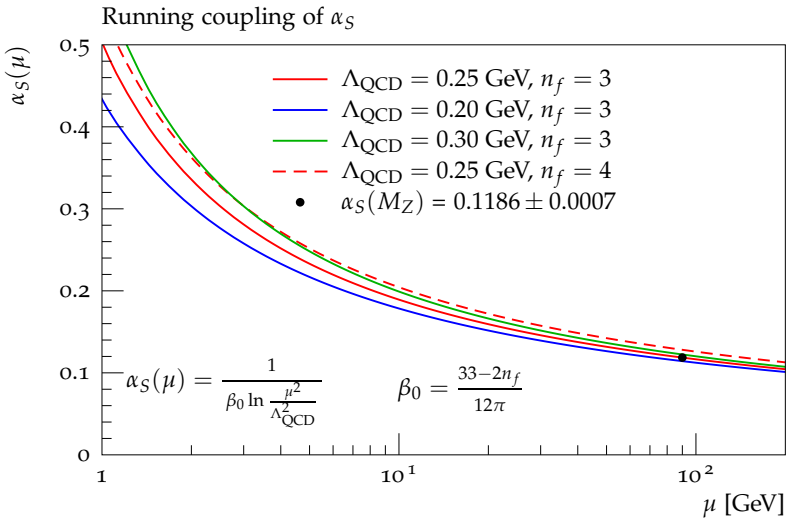

Figure 2.5.: Running of the coupling of the strong force, α_S, with energy for different choices of Λ_{QCD} and the number of participating flavours. The graphs show the leading order predictions and a comparison with the 2013 world average of measurements of α_S at the mass of the Z-boson [17].

positive thus resulting in an ever decreasing coupling (equation (2.8)) as the energy grows. This behaviour is known as asymptotic freedom.

The pole Λ_{QCD} is a scale necessarily introduced in order to make QCD a re-normalisable theory. It's value defines the energy regime where the perturbative calculation breaks down as the resulting coupling constant becomes large which is in agreement with experimental non-observation of free quarks (confinement).

Figure 2.5 shows the running of $\alpha_S(\mu)$ with the scale (or energy) μ for a number of different choices of Λ_{QCD} and n_f. A comparison with a measurement of $\alpha_S(m_{\text{Z}})$ [17] shows very good agreement. It further shows that independent from the choice of the aforementioned parameters α_S rapidly grows as μ approaches 1 GeV thus illustrating the inevitable break-down of perturbative methods.

2.3. Limitations of the standard model

Although the standard model of particles is considered the best theory ever developed in the sense that no contradicting or falsifying observations have been made as of today there are several short comings. For instance, gravity is not explained by the standard model as is the reason for the weak force being 10^{32} stronger than gravity ("hierarchy

problem"). In that sense, it is believed that the standard model of particles physics is an effective theory in a low energy limit where gravity is not important for the understanding of fundamental processes. Further, neutrinos are massless in the standard model, however the observation of neutrino oscillations [18] are evidence of neutrino masses different from zero.

Also the low mass of the discovered particle compatible with the standard model "Higgs" boson leads to strong problems of the standard model of particle physics as a very precise setting ("fine-tuning") of parameters would be required by nature in order to obtain finite results due to the structure of the divergencies in the theory. Further, astrophysical observations suggest that the "ordinary" matter described by the standard model only accounts for 5% of the energy-matter content of the universe. A further 27% of the matter in the universe is of unknown origin, dubbed "dark matter" [19], and the remaining 68% of this budget is attributed to "dark energy". For both the standard model does not have an explanation for.

Finally, the baryon-antibaryon asymmetry in the universe is much too large to be explained by known CP-violating standard model processes.

Chapter 3.

The Large Hadron Collider (LHC)

3.1. Overview

The Large Hadron Collider is a particle accelerator facility based at CERN, Geneva, Switzerland. It delivers the highest energetic particle beams produced in laboratory conditions to date. Several pre-accelerators, most of which hosted previous experiments, are used in order to boost proton beams to an energy of 450 GeV (per proton) at which they are injected into the 27 km circumference LHC.

The LHC itself is housed in the tunnel of a former electron-positron collider (LEP), that operated at centre-of-momentum-energies of up to $\sqrt{s} = 209$ GeV. Higher energies where not efficiently possible to facilitate due to bremsstrahlungs-losses (i.e. synchrotron radiation). With proton beams it is possible to significantly increase the beam energies in the same underground structure since the power of bremsstrahlung is inversely proportional to the fourth power of the mass of (accelerated) charged particles [20].

3.2. Pre-accelerators

Gaseous hydrogen is ionised to produce protons that can be accelerated by means of electromagnetic fields. The first stage is a linear accelerator, LINAC2, that delivers proton beams of 50 MeV. These are injected into the Proton Synchroton Booster (PSB) which further accelerates the protons to 1.4 GeV before they are injected into the Proton Synchroton (PS). The PS is currently the oldest still running accelerator structure at CERN. Protons leave it with an energy of 28 GeV. The final pre-accelerator is called the

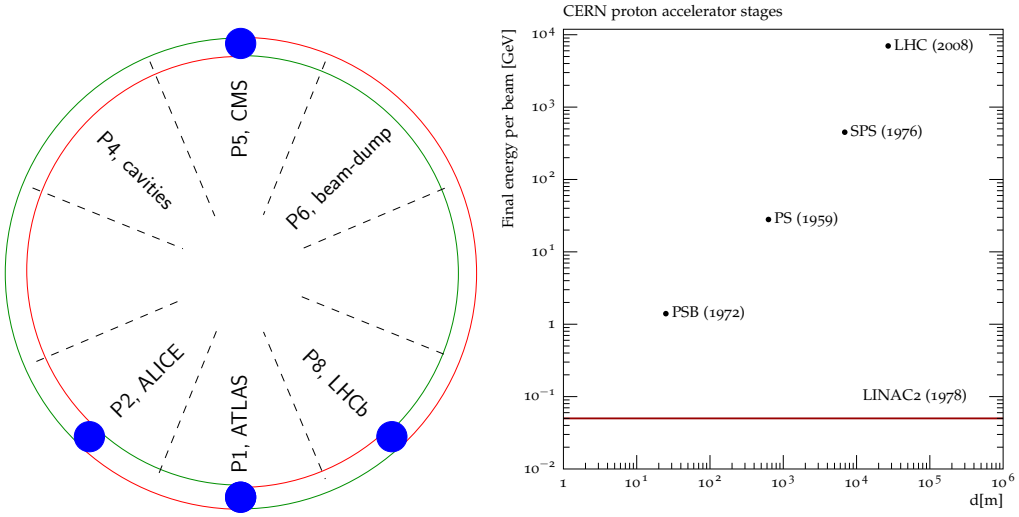

(a) Schematic view of the LHC **(b)** LHC and pre-accelerators

Figure 3.1.: (a): Schematic view of the LHC. The experiments where crossings of the two oppositely circulating beams (red and green arcs) occur are indicated in blue. (b): Overview of the circumference, d, and maximum beam energy of the LHC and its pre-accelerators used for proton acceleration in 2011. The number in brackets gives the first year of operation (not necessarily at the maximum energy). LINAC2 is a linear accelerator and hence does not have a circumference.

Super Proton Synchroton (SPS) which is an upgraded version of the former Intersection Storage Ring (ISR) that hosted such famous experiments as UA1, UA2, UA5. The SPS brings the proton beams to the LHC injection energy of 450 GeV. An overview of all pre-accelerators in terms of energy delivered and circumference (where applicable) can be found and compared to the LHC in Figure 3.1b.

3.3. LHC magnets

Protons are guided through the LHC tunnel by means of dipole magnets and the beams are focussed using quadrupole magnets. The construction of the magnets is done such that both beam-pipes, each housing one of the oppositely circulating beams, are placed in the same magnet. Thus only one magnet system is needed for two beams. In order to reduce energy losses to to resistivity the magnets are built using superconducting materials, requiring a cooling of the magnet system with liquid helium, constantly keeping the temperature at 1.9 K.

	Dipole	Quadrupole
Number deployed	1232	392
Magnetic field strength (design value)	8.3 T	311 T/m
Current [kA] (design value)	12	13
Operating temperature [K]	1.9	1.9

Table 3.1.: Overview of most relevant parameters of magnets deployed at the LHC.

An overview of important technical parameters of the dipole and quadrupole magnets for the design beam-energy of 7 TeV can be found in Table 3.1. Due to faulty wiring between magnets an accident happened in the early stage of LHC operation in 2008. An electrical arc caused the rapid transformation of liquid helium into its gaseous state resulting in a leak of the liquid helium system and successive expansion of six tonnes of helium, accompanied by a shock-wave that damaged more than thousand magnets. Following extensive repairs it was chosen as a precautionary measure to limit the current applied to the dipoles to 6 kA to allow operation of the LHC with an energy of 3.5 TeV per beam.

Operations in 2012 allowed to raise the beam energy to 4 TeV. The LHC is currently undergoing planned maintenance work including the installation of a protection system against the sort of accident that happened in 2008. It is planned to resume LHC operation in late 2014 with an energy of 6.5 TeV per beam.

3.4. Cavities

The accelerating structures at the LHC are called cavities. A single instalment of eight super-conduction cavities at Point 4 (Figure 3.1a) is sufficient to accelerate both beams from the injection energy (450 GeV) up to 7 TeV. The LHC cavities operate with a voltage of 2 MV leading to a field gradient of 5 MV/m. Per revolution, the energy of protons increases by 485 keV. This procedure took about 35 minutes in 2011 where both beams were operated at $E_{\text{beam}} = 3.5$ TeV when taking the data used in this analysis.

3.5. Beams

The proton beams in the LHC are arranged in so-called bunches that are separated from one another. Each bunch consists of about 10^{11} protons, the design parameters of the LHC project a maximum of 2808 bunches per beam that are 25 ns apart, leading to a maximum energy stored in the beams alone of about 700 MJ. The theoretical limit of 3556 bunches is not fully exploited in order to allow for the possibility to dump the beams. This is achieved by a 900 m long gap in each beam.

The rate R_P at which a certain process, P, occurs at the LHC is dependent on the process' cross-section, σ_P and a machine parameter, the luminosity which is calculated as follows:

$$\mathcal{L} = \nu_{\text{collisions}} \frac{N_1 N_2}{4\pi\sigma_x\sigma_y}, \tag{3.1}$$

where $\nu_{\text{collisions}}$ denotes the frequency of bunch-crossings at an interaction point. $N_{1/2}$ stands for the number of protons in either of the colliding bunches which to first first order can be described as GAUSSian wave packets with $\sigma_{x/y}$ being the standard deviations of these density functions.

The rate can be calculated as such:

$$R_P = \sigma_P \cdot \mathcal{L} \tag{3.2}$$

Obviously, in order to obtain large statistics for rare processes (small σ_P) it is desirable to increase the luminosity as much as possible. The number of particles per bunch can not be easily increased well beyond the design value, leaving the frequency of collisions and the beam profiles. The frequency of collisions can be increased by a denser packing of bunches. The LHC design distance of bunches in a beam is 25 ns while the configuration during data taking of this analysis was twice as much.

The beam sizes can also be expressed in terms of the transverse emittance, ε, and a beam amplitude function, β [11]

$$\varepsilon_{x/y} = \sigma_{x/y}^2 / \beta_{x/y} \tag{3.3}$$

The emittance is a measure for the quality of a beam defined via the phase-space volume of the particles in a beam. It is important for the focussing of particle beams and depends on the whole acceleration process and cannot be decreased easily.

Using equation (3.3), equation (3.1) can be written as

$$\mathcal{L} = \nu_{\text{collisions}} \frac{N_1 N_2}{\sqrt{\varepsilon_x \beta_x^* \cdot \varepsilon_y \beta_y^*}}. \tag{3.4}$$

Where $\beta_{x,y}^*$ is the beam amplitude function at the interaction point. The LHC experiments use magnets to squeeze the beams at the points where the beams are brought to collision in order to increase the luminosity and thus the chance of collision and thus the rate of rare processes.

An important side-effect of a high luminosity is that more than one proton-proton interactions occur during a single beam-crossing. In fact, the mean number, $\langle \mu \rangle$ of simultaneous interactions was $\langle \mu \rangle = 5$. Implications of this effect (pile-up) on data analysis are described in detail in Chapter 10.

An overview of important beam parameters can be found in Table 3.2.

During data taking, the luminosity decreases as the beam quality deteriorates when interactions happen. A typical run during data taking for this analysis lasted about 14 hours. Eventually, kicker magnets are activated that deflect both beams into carbon structures called beam dumps at P6 (Figure 3.1a).

3.6. Experiments

Several experiments are located at four interaction points where the two beams are deflected such that they are brought to collision. Most notably, the CMS (Compact Muon Solenoid, P5, Figure 3.1a) and ATLAS (A Toroidal Lhc ApparatuS, P1, Figure 3.1a)

Parameter	This analysis	LHC design
$\hat{\mathcal{L}}$ $[\frac{1}{cm^2 s}]$	$1.5 \cdot 10^{33}$	10^{34}
N_{bunches}	1380	2808
β^*[m] at ATLAS	1.5	0.55
Bunch spacing [ns]	50	25
E_{beam} [TeV]	3.5	7
$\langle\mu\rangle$	5	40

Table 3.2.: Key parameters of the LHC. Comparison of design values and those present during data taking of this analysis.

were designed as 4π multi purpose detectors to study the electroweak symmetry breaking and to look for physics beyond the standard model accessible at the scale of the collision energies. The ATLAS experiment will be described in more detail in the next chapter.

The largest success of the LHC so far is the discovery of a bosonic particle with a mass of about 125 GeV [8, 9] the properties of which being in agreement with the standard model Higgs boson. Further, the parameters of a large number of models beyond the standard model of particle physics could be limited strongly, e.g. the most simple super-symmetric extensions of the standard model [21].

The LHC-b experiment located at P7 (Figure 3.1a) seeks for CP-violating processes in B_s- and D-meson systems. The fourth big experiment is called ALICE (P2, Figure 3.1a). It specialises in experiments with lead-lead collisions to study the phase-transition to a quark-gluon plasma.

Chapter 4.

The ATLAS experiment

The ATLAS ("**A** **T**orroidal **L**HC **A**pparatu**S**") experiment is a multi-purpose detector for particle physics at the Large Hadron Collider (LHC) accelerator at CERN. It is located in a cavern about 100 m below surface at Point 1 of the LHC (Chapter 3, Figure 3.1a).

At the very centre of the detector the particle beams are brought to collision at the so-called interaction point. The detector is designed such that all four sub-systems are roughly cylindrically symmetric around the beam-pipe. The sub-system closest to the beam-pipe is the inner detector (Section 4.4.1), followed by the calorimeters (Section 4.4.4), the magnet system (Section 4.4.3) and the muon spectrometer (Section 4.4.5) as the outermost sub-detector.

Further, a three-stage trigger system (Section 4.5) has been set up, utilising multiple sub-detectors and software reconstruction to bring down the data-rate to a level manageable by the available data acquisition resources such that analysis of the recorded data becomes feasible.

For the sake of simplicity, electrons and positrons are both called electrons in the following. Similarly, the word muon is used as synonym for muons and anti-muons.

4.1. Introduction, history

The primary motivation for the ATLAS experiment is the studying of the electroweak symmetry break. First ideas of retrofitting the still under-construction LEP accelerator with hadron beams were made in the early 1980s and the proposal for construction of the ATLAS detector was made in 1994 [22] and officially funded in 1995. The technical design

report [23] was published in 1999 and assembly of the individual detector components in the cavern lasted from 2003 to 2008. LHC operation was interrupted for more than a year due to a magnetic quench in the accelerator destroying several magnets, necessitating extensive repairs and limitation of the beam energies to 3.5 TeV in 2011 and 4 TeV in 2012/13. The first publication of a measurement of minimum-bias physics [24] was made shortly after data-taking resumed in autumn 2009 at $\sqrt{s} = 900$ GeV.

Down to the present day ATLAS has released more than 240 publications with the most prominent one likely to be the discovery of a 126 GeV particle consistent with the Higgs boson of the standard model [8].

4.2. Coordinate system

The ATLAS experiment uses a right-handed Cartesian coordinate system with the positive x-axis pointing from the interaction point towards the centre of the LHC. The positive y-axis points upwards from the interaction point (IP). Thus, the z-axis is parallel to the beams with the positive z-axis coinciding with the direction of the counter-clockwise beam. The x- and y-axes span the transverse plane.

Furthermore, the cylindrical symmetry of the detector allows the usage of a cylindrical coordinate system with the symmetry axis being the beam axis. The azimuthal angle, Φ, is measured from the x-axis in the x-y plane and the polar angle, Θ, is defined as the angle between the beam axis and the line from the point of origin (IP) to a point (x, y, z).

A very useful quantity is the so-called pseudo-rapidity, η, which is identical to the rapidity in case of massless particles. It is defined as

$$\eta = -\ln \tan\left(\frac{\Theta}{2}\right) \tag{4.1}$$

A pictorial representation can be found in Figure 4.1.

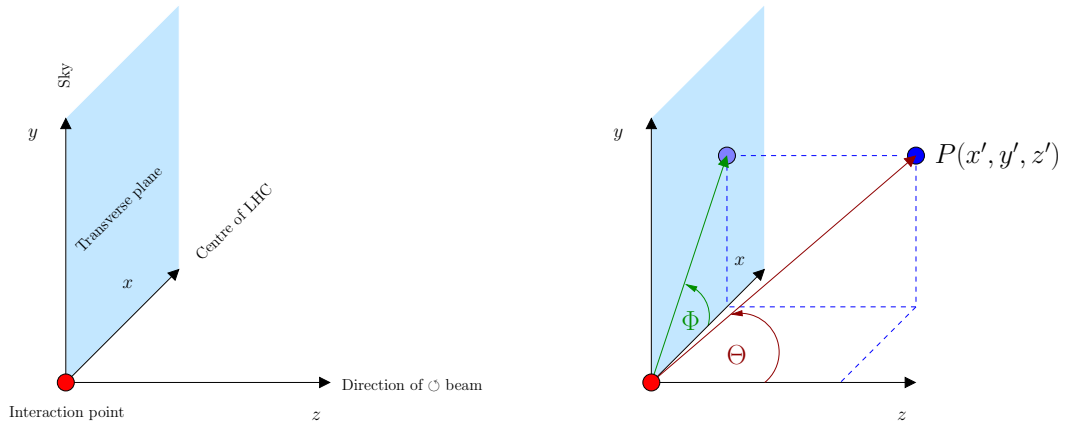

(a) Cartesian coordinates **(b)** Cylindrical coordinates

Figure 4.1.: Illustration of the coordinates system of the ATLAS experiment. The interaction point serves as point of origin.

4.3. General overview

The ATLAS detector is a multi-purpose detector in a 4π geometry comprised of an inner detector (ID) placed in a solenoid magnetic field used for the precision measurement of trajectories of charged particles, called "tracks". The ID is surrounded by two calorimeter systems, an electro-magnetic calorimeter (ECAL), designed for the measurement of electron/positron and photon energies, and a hadronic calorimeter (HCAL) set out to measure the energy of jets. The outer shell of the detector is formed by a large muon spectrometer that is placed in a toroidal magnetic field. Figure 4.2 shows a to scale overview of all sub-detector systems as well as the coils used to create the magnetic fields.

4.4. Detector components relevant for this analysis

4.4.1. Inner detector

The inner detector [23] of the ATLAS experiment is composed of three sub-detectors that have cylindrical symmetry around the beam-pipe. They all have components parallel to the beam in a portion called "barrel" and perpendicular to the beam in what is called the

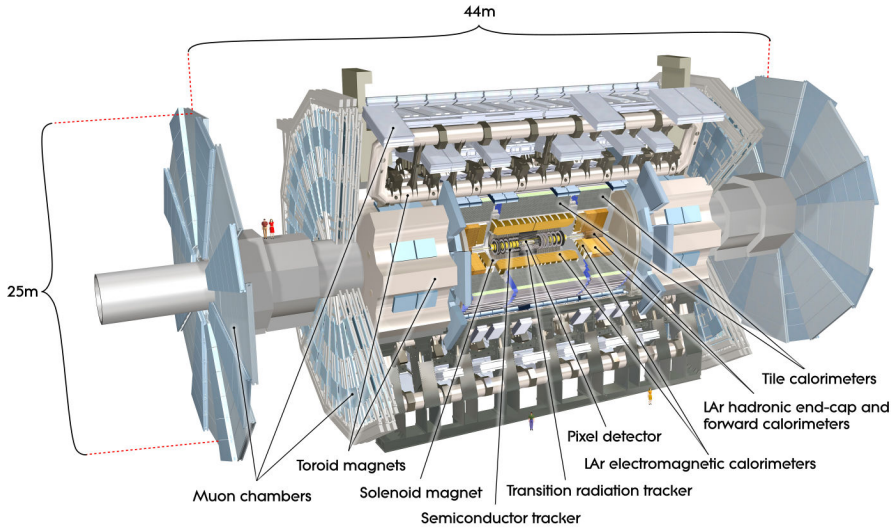

Figure 4.2.: Computer generated image of the ATLAS detector. The interaction point is located in the very centre of the detector. The cylindrical detector subsystems (from smallest to largest) are aligned with the beam-pipe: Inner detector, calorimeters, magnet system, muon spectrometer. (Copyright CERN).

"end-cap" region of the sub-detector. Figure 4.3 gives a general overview of the detector components while Figure 4.4 shows how the individual layers and wheels are positioned within the inner detector. It is designed to have very good track reconstruction capability within $|\eta| < 2.5$ as can be seen from the layout.

Closest to the beam-pipe, the pixel detector is located, followed by the SCT (Semiconductor tracker). They both rely on p-n junctions present in the intrinsic semi-conductor material silicon. The general principle is that the application of high-voltage distorts the band-structure of the active material in such a away that the band-gap is enlarged, effectively leading to a space-charge region. If a charged particle travels through that region, electron-hole pairs are created that are absorbed due the high-voltage, leading to a measurable current. If the generated current and the related voltage pass a threshold a "hit" is recorded. The density of active nodes in the pixel modules is required to be much more fine (and therefore more expensive) due to it being so close to the interaction point. The technology chosen for the SCT is a bit more coarse for reasons of cost.

The outermost part of the inner detector is called TRT (transition radiation tracker) which, as the name implies, relies on the effect of transition radiation.

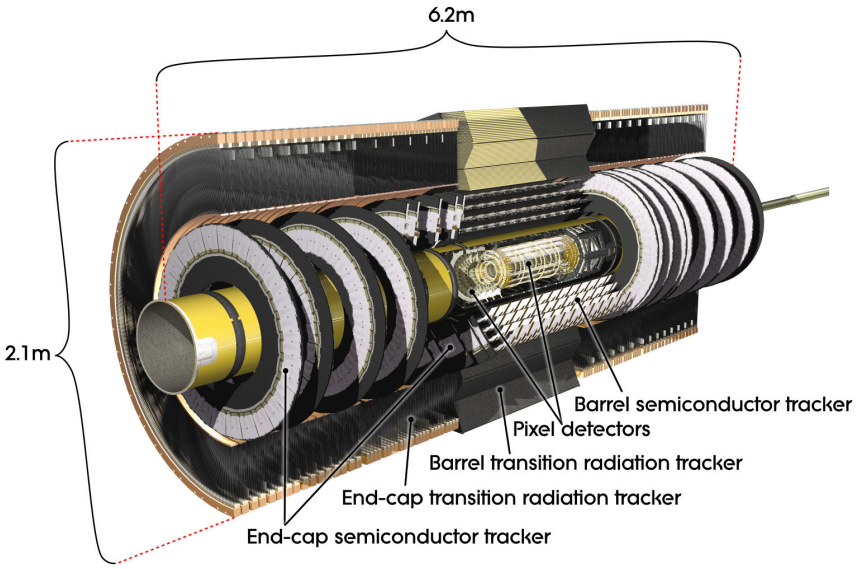

Figure 4.3.: Computer generated image of the inner detector of the ATLAS experiment. (Copyright CERN).

Pixel detector

The pixel detector consists of 1744 identical modules with high-purity silicon as active material that form a cylindrical shape in three layers around the beams, which is called the barrel part, and three disks perpendicular to the beams at each side of the pixel, forming the end-cap parts. The modules are grouped together in so-called staves in the barrel region and so-called sectors in the end-caps. The pixel components closest to the beam-pipe are called 'b-layer'. Table 4.1 gives a summary of the overall layout of the pixel modules and the number of pixels/channels.

Being so close to the beams and interaction point, the pixel detector is subject to large doses of radiation. The technology chosen for the sensors allows to have good efficiency even after radiation damage since it turns the ab initio n-type sensors into p-type sensors over time. The effective sensitive area of a single module is 19 mm $\times$ 63 mm while a single pixel has the dimensions 50 μm $\times$ 400 μm. Each pixel is bump-bonded using a conductive glue to the readout electronics of a module. The voltage applied to each pixel is of the order of 300 V. The modules are operated at temperatures between -5°C and -10°C to keep leakage currents low.

Barrel	r [mm]	# Staves	# Modules	# Pixels
Layer 1	50.5	22	286	$13.2 \cdot 10^6$
Layer 2	88.5	38	494	$22.8 \cdot 10^6$
Layer 3	122.5	52	676	$31.2 \cdot 10^6$
End-cap	$\|z\|$ [mm]	# Sectors	# Modules	# Pixels
Disk 1	495	8	48	$2.2 \cdot 10^6$
Disk 2	580	8	48	$2.2 \cdot 10^6$
Disk 3	650	8	48	$2.2 \cdot 10^6$

Table 4.1.: Summary of module organisation in the pixel detector of the ATLAS experiment where r and z denote the radial and axial coordinates of the ATLAS coordinate system. Numbers are taken from [25].

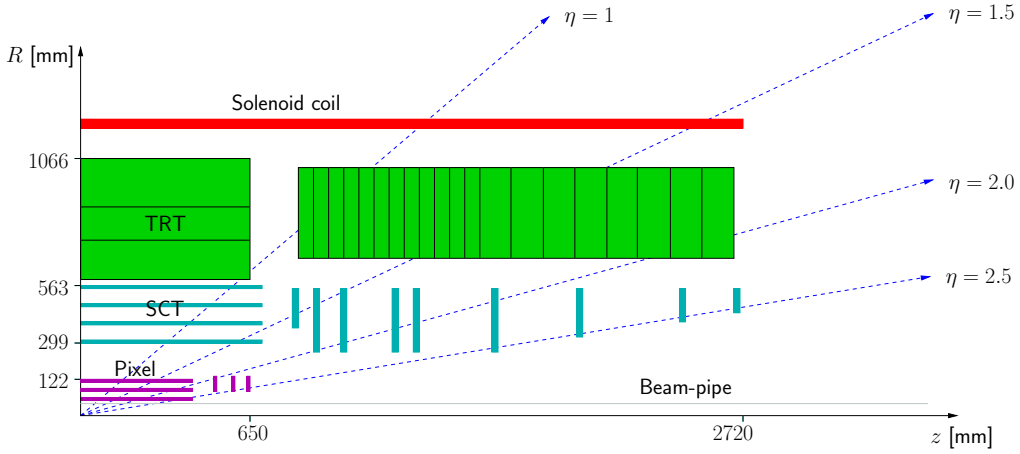

Figure 4.4.: Schematic overview of the positions and pseudorapidity coverage of the main detector components of the inner detector relative to the solenoid magnet and beam-pipe. Modules of the pixel detector are drawn in pink, those of the SCT in blue and TRT components in green. Pixel, SCT and TRT all have components parallel ("barrel") and perpendicular ("end-cap") to the beam. Only a quarter-section of the actual detector is drawn. The original image with more details can be found in [25].

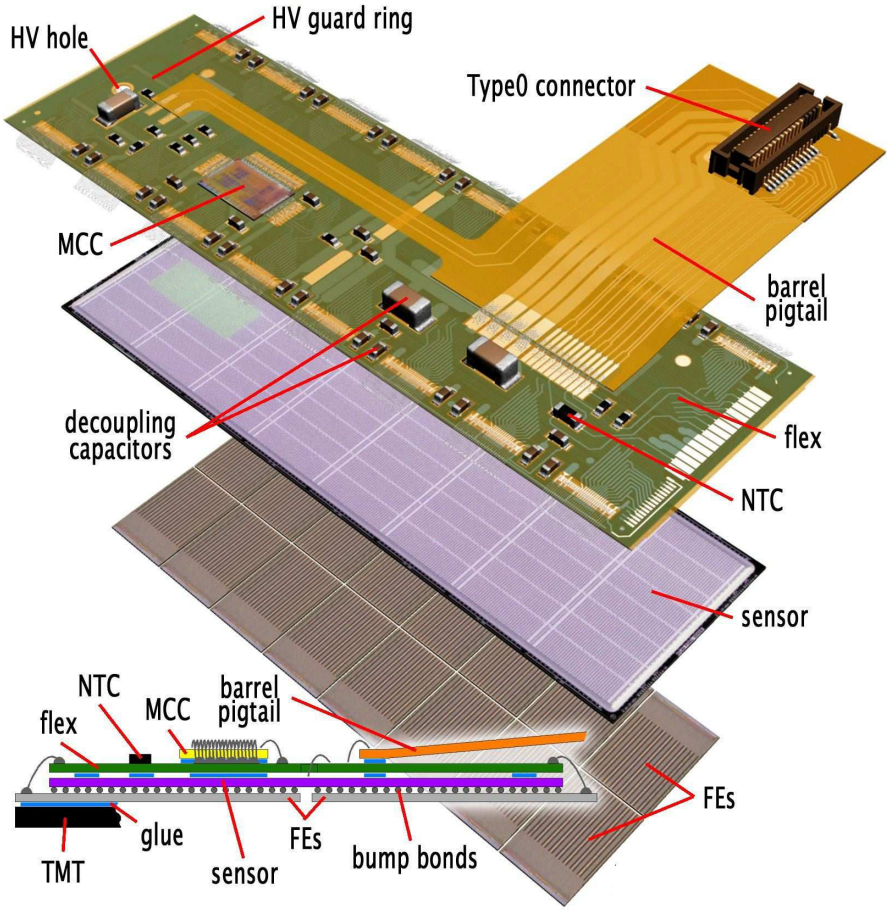

Figure 4.5.: Technical drawing of a pixel module. The actual sensor has an effective area of 19 mm × 63 mm and a thickness of 250 μm. The sensors are bump-bonded to the front-end chips (FE) from one side and glued to the circuit board (flex) from the other side. There are 16 FEs on one module, each with 2880 read-out channels. The circuit board also hosts the read-out connector and a control chip (MCC). The image is taken from [25]

SCT

The SCT consists of 4088 modules plugged into four layers in the barrel region and 9 disks in each end-cap regions that cover a total surface of 63 m^2 of silicon. The SCT modules use a silicon-strip technology. In the barrel part, a module consists of a supporting structure onto which four silicon strip sensors are glued, two on its front and two on its back. The individual strips are slightly tilted against one-another to improve spatial resolution. A single module contains $2 \cdot 768$ active silicon strip sensors. A summary of the number of modules and their positions is given in Table 4.2.

In each end-cap region, a total of 9 SCT wheels of varying size and numbers of modules are located. The wheels 2 to 6 are identical, they consist of a three sets of modules, outer, middle and inner modules. Detailed numbers are given in Table 4.4.

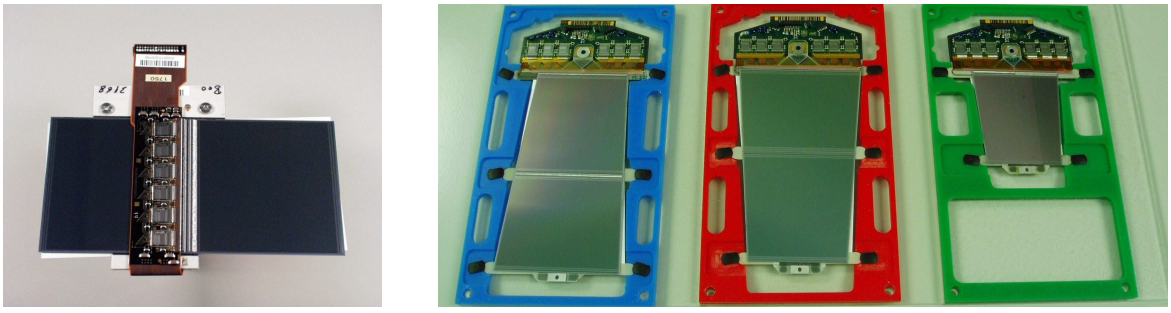

(a) Barrel **(b)** End-cap

Figure 4.6.: Photographs of SCT modules [25]. The barrel modules consist of 4 sensors, glued onto a supporting structure. Each module contains $2 \cdot 768$ strip sensors. The end-cap modules in(from left to right: outer, middle, inner) consist of two layers, too. Detailed specifications of the modules can be found in Table 4.4. The typical powering of the sensors is 450 V.

4.4.2. TRT

The transition radiation tracker (TRT) is the final and outermost component of the inner detector. It exploits the effect of electromagnetic emissions of charged particles passing through the boundary of two materials with different dielectric properties at relativistic speeds. The intensity of the radiation is hereby proportional to the Lorentz-factor

Barrel	r [mm]	Tilt-angle [°]	# Modules
Layer 1	284	11.00	384
Layer 2	355	11.00	480
Layer 3	427	11.25	576
Layer 4	498	11.25	672

Table 4.2.: Summary of module organisation in the barrel part of the SCT of the ATLAS experiment. Numbers are taken from [25].

Disk	1	2	3	4	5	6	7	8	9
$\|z\|$ [mm]	853.8	934.0	1091.5	1299.9	1399.7	1771.4	2115.2	2505.0	2720.2
# outer modules	52								
# middle modules	40								—
# inner modules	—	40						—	

Table 4.3.: Summary of module organisation in end-cap region of the SCT of the ATLAS experiment. Numbers taken from [25].

Barrel	Length = 126.09 mm	
End-cap	Length [mm]	Radius [mm]
Outer	119.14	438.77 - 560.00
Middle	115.61	337.60 - 455.30
Inner	59.1	275.00 - 344.10

Table 4.4.: Summary of SCT module parameters. Numbers are taken from [25].

$\gamma = \frac{E}{m}$ [11] giving rise to particle identification in terms of the particle's mass, m, if the three-momentum vector, $\vec{p}$, was measured. The TRT can be used to distinguish pions from electrons. Due to the release of transition radiation being inversely proportional to a charged particle's mass, it can easily be seen that electrons will loose 200 times as much energy as muons with the same momentum would. This is the reason why the TRT is also used in the reconstruction of muons as their energy loss due to transition radiation is negligible.

The TRT of the ATLAS experiment is constructed using proportional drift-tubes ("straws") [26] as detecting components interleaved with polypropylene foils as radiators, meaning that the two dielectric media are air $\varepsilon_r \sim 1$ and polypropylene ($\varepsilon_r = 2.2$). The tubes are manufactured with 4 mm inner diameter, filled with a gas composition of 70% Xe + 27% CO_2 + 3% O_2. Xenon serves as ionisable medium while the other components are used as quenching gas. The very centre of each straw is a 30 μm thick gold-plated tungsten wire that serves as anode (at ground potential). The outer structure, which serves as cathode, is made from a composition of aluminium, Kapton, polyurethane and carbon-fibres.

The barrel part contains a total of 52444 straws of 150 cm length, parallel to the beam-pipe. They are organised in three nested hollow cylinder structures with radii between 56 and 107 cm that each contain 32 modules. Each module is embedded in a matrix made of 19 μm thick polypropylene fibres that are used as radiative material in the barrel. The barrel TRT's span along the beam-pipe is $|z| < 72$ cm which is equivalent to a pseudorapidity coverage of $|\eta| < 0.7$.

Both end-caps of the TRT contain 159744 straws each that are split into 18 separate wheels (cf. Figure 4.4) that cover the region $63 < r < 103$ cm and $83 < |z| < 340$ cm, equivalent to a pseudorapidity coverage of $0.7 < |\eta| < 2.5$. The alignment of the straws in the wheels is radial. Each wheel contains 8 layers of straw-tubes with 15 μm thick polypropylene foils in between. The 12 wheels closest to the interaction point have a spacing of 8 mm between individual straw-tube layers while the outer 8 wheels have a spacing of 15 mm.

4.4.3. Magnet system

The purpose of magnetic fields in a particle detector is to bend trajectories of charged particles due to Lorentz force, $\vec{F}_L = q \cdot \vec{v} \times \vec{B}$. Since $\vec{F}_L$ depends on the velocity, $\vec{v}$ of

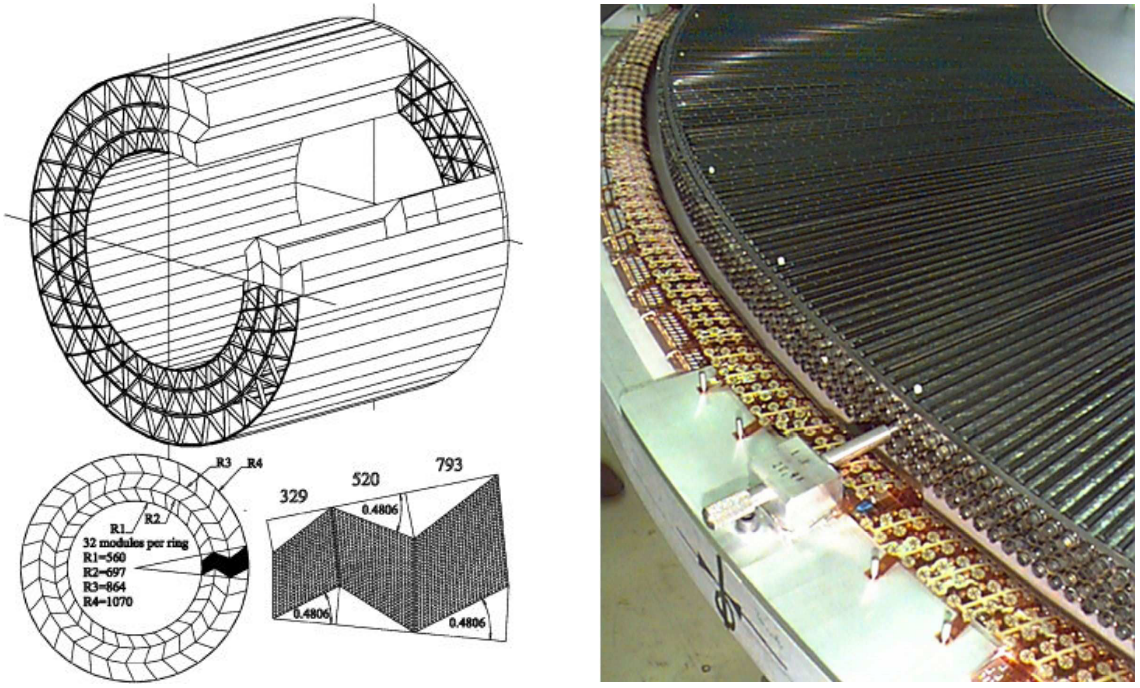

(a) Barrel **(b)** End-cap

Figure 4.7.: Pictures of TRT components. (a) shows a technical drawing of the barrel part with its distinctive geometry. (b) shows a photograph of an end-cap wheel. The layered structure is visible.

the particle carrying an electric charge q, a momentum measurement is possible due to the curvature of reconstructed tracks.

The magnet system of the ATLAS detector consists of a 2 T super-conducting solenoid into which the inner detector is immersed. It produces a magnetic field that is roughly parallel to the beam-pipe. Thus, trajectories of charged particles are bent in the $x - y$ plane.

Further a toroid magnet system is placed just outside the calorimeters and inside the muon spectrometer. The produced field is asymmetric with field strength varying between 2 and 8 T. It is perpendicular to the field created by the solenoid, thus muons are bent away from the $x - y$ plane [23].

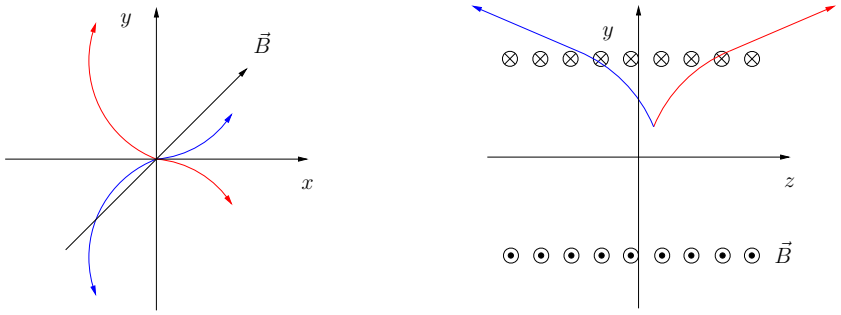

(a) Solenoid **(b)** Toroid

Figure 4.8.: Pictorial representation of curvatures of particle trajectories entering the solenoidal and toroidal magnetic fields of the ATLAS detector. Trajectories of positively charged particles are drawn red, negatively charged ones in blue.

4.4.4. Electromagnetic calorimeter (ECAL)

Just outside the magnet coil of the solenoid, the electromagnetic calorimeter (ECAL) of the ATLAS detector is located dedicated to identify electrons (and photons) and to measure their energy. This is done by exploiting the fact that high energy electrons (and photons) will initiate intense interaction cascades when hitting material with a high atomic number, Z, subsequently producing electron-positron pairs which themselves will radiate photons due to the deflection enforced by the electric fields of the nuclei in such materials ("Bremsstrahlung"). This cascade is stopped as soon as ionisation of atomes becomes the dominant mechanism for energy loss. Ionisation of atoms results in the creation of an ion-electron pair which, after application of high voltage, can be read out electronically.

The technology used in the ATLAS experiment to achieve both, a quickly developing particle cascade ideally with full dissipation of the electron (or photon) energy in a small volume and a fast readout of ionised atoms is called "sampling calorimeter". Two different materials are arranged in an alternating way. Lead ($Z = 82$) is chosen as the passive material that will initiate the particle cascades while the active material used for the measurement of energy deposits is liquid argon (LAr), a noble gas at standard conditions, which is monatomic and hence lacks the requirement for vibrational and

rotary excitations which makes ionisation the dominant effect of interaction with electrons and photons [27].

The design of the ECAL further exploits the different stopping powers, $-\langle\frac{\mathrm{d}E}{\mathrm{d}x}\rangle$, of electrons and muons. Figure 4.12 shows the stopping power of lead and iron for electron and muons as function of the incident energy. For energies relevant for physics analyses with ATLAS ($10 \cdots 100$ GeV) electrons loose significantly more energy than muons in both materials.

Although the choice of lead as passive material arranges for a very rapid development of the particle shower in a small volume, full coverage of the ECAL in ϕ (around the beam pipe) with a high chance of having showers initiated by photons and electrons fully developing in the ECAL, i.e. low leakage into the adjacent hadronic calorimeter, is achieved by a shape of the calorimeter cells similar to bellows of an accordion.

Radiation length:

Materials can be classified by the radiation length, X_0, which describes the distance over which electrons typically loose a fraction of $1 - \frac{1}{e}$ of its incident energy through bremsstrahlung . An approximate expression is given by [11]:

$$X_0 = \frac{1432.8 \cdot A}{Z(Z+1)(11.319 - \ln Z)} = \begin{cases} 6.33 \ \frac{\mathrm{g}}{\mathrm{cm}^2} & \text{for } {}^{208}_{82}\mathrm{Pb} \\ 14.18 \ \frac{\mathrm{g}}{\mathrm{cm}^2} & \text{for } {}^{56}_{26}\mathrm{Fe} \end{cases} \tag{4.2}$$

The ECAL is made of two end-cap wheels, covering $1.375 < |\eta| < 3.2$, and a barrel module, covering $|\eta| < 1.475$. The radiation length are at least $22 \cdot X_0$ for the barrel part and at least $24 \cdot X_0$ for the end-cap parts. Each of these components is segmented in four parts, a presampler, a front part, a middle part and a back part. All of them consist of calorimeter cells of varying granularity and radiation length. The presampler modules only contain active material (LAr) as they are intended to correct for energy losses suffered by electrons and photons due to interaction with material on front of the ECAL. Figure 4.10 shows the granularity ($\Delta\eta \times \Delta\phi$) of cells in all parts of the ECAL as function of the pseudorapidity and a schematic view of a central barrel module is shown in Figure 4.11.

The energy resolution of the ECAL was measured in [28] using an electron test-beam at CERN. The following result was obtained from a fit of test-beam data :

$$\frac{\sigma_E}{E} = \underbrace{\frac{a}{\sqrt{E}}}_{\text{Fit-function}} \oplus b, \text{ with } a = 10.1 \pm 0.1\% \cdot \sqrt{\text{GeV}} \text{ and } b = 0.17 \pm 0.04\% \tag{4.3}$$

The uncertainties are purely statistical and the $\oplus$ symbol stands for addition in quadrature. In Figure 4.9, this resolution is drawn as function of the electron energy. It shows that for the resolution improves with the electron energy, reaching values of 1% for $E > 100$ GeV while the resolution worsens by more than a factor of two as the electron energy approaches 20 GeV with values $> 2\%$.

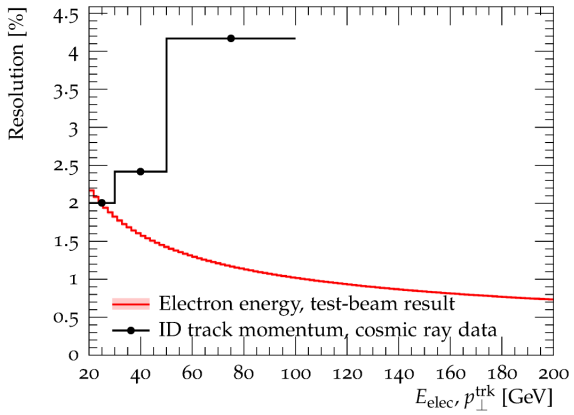

Figure 4.9.: Test-beam results of an energy resolution measurement (red line) of a central ($\eta = 0.687, \phi = 0.28$) barrel module [28]. The error band displays the statistical uncertainties of equation (4.3). For comparison, the transverse momentum resolution of cosmic rays measured with the inner detector [29] is also shown, demonstrating the preference of an energy measurement over a $p_\perp$ measurement for energies above ~ 30 GeV.

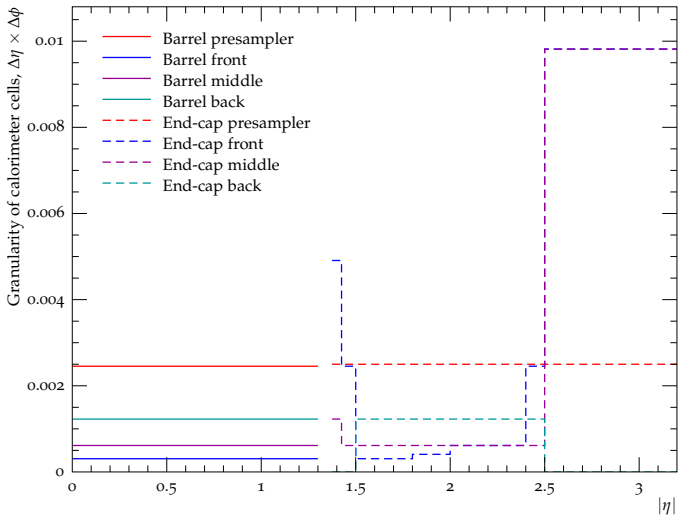

Figure 4.10.: Granularity of calorimeter cells in the ECAL of ATLAS. This plot was made using tabulated information presented in [30] and [31].

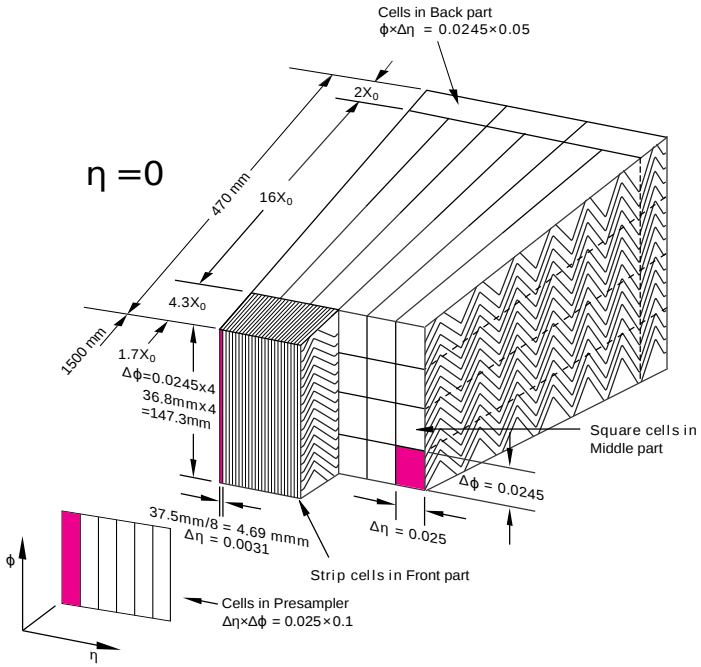

Figure 4.11.: Schematic view of a barrel module of ECAL, showing the size of the calorimeter cells for the three main layers as well as the presampler. The image is taken from [23] with slight modifications to the text displayed to match the naming convention used here.

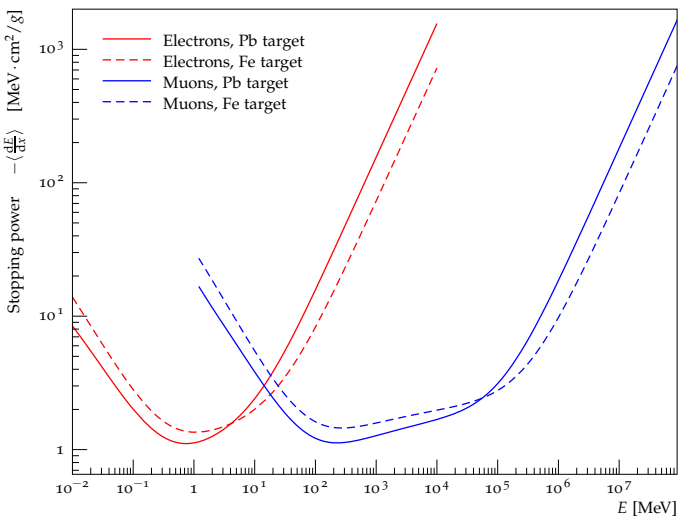

Figure 4.12.: Stopping power of electrons and muons in lead (Pb) and iron (Fe), the passive materials in the electromagnetic and hadronic calorimeter of the ATLAS detector as function of the incident energy. Calculations published in [32] and [33] have been used to make the graphs.

4.4.5. Muon spectrometer

As mentioned before, the stopping power of the materials used in the calorimeters passed by a muon (Figure 4.12) is very low, meaning that muons pass the ATLAS detector with very low energy loss due to bremsstrahlung and also ionisation. In order to measure the momentum of muons, a large muon spectrometer (MS) forms the outer shell of the ATLAS detector [23].

The MS consists of a barrel part and two end-cap wheels. Muons traversing the MS are deflected from the $x - y$ plane by the magnetic field created by the toroid magnet (Figure 4.8b) allowing for the reconstruction of their trajectory by means of tracking chambers found in all parts of the MS.

The barrel part consists of three layers of tracking chambers that, similar to the ECAL barrel modules, are constructed as concentric hollow cylinders around the beam-pipe. The end-cap wheels also consists of three layers of tracking chambers but forming discs perpendicular to the beam-axis.

Two slightly different tracking chamber technologies are used for the measurement of muon trajectories. This is required by the position dependent expected rate of muons entering the MS. Further, very fast resistive plate chambers (RPC) and thin gap chambers

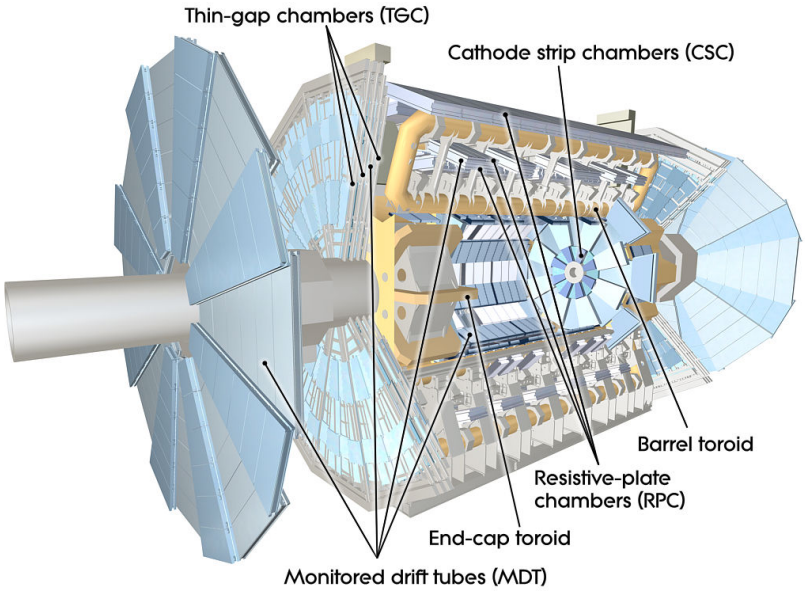

Figure 4.13.: Computer generated image of the ATLAS muon system, showing the end-cap wheels and the barrel part.

(TGC) are built into the MS. They are used for triggering the data recording of events containing muons. Figure 4.14 shows the arrangement of all these four technologies in a segment of the MS. An overview of technical specifications of these four module types is given in Table 4.5.

Monitored drift tube chambers (MDT): MDT chambers constitute the most precise instrument for the measurement of muon trajectories. They are constructed as multiple layers of individual aluminium tubes with a diameter of 3 cm and a length varying between one and six meters. The tubes are filled with a gas mixture of 93% Argon and 7% CO_2 where Argon is the active material that gets ionised. Along the centre of each tube a tungsten-rhenium alloy wire which is very stable against long-time exposure to electrons with a 50 μm diameter is located which is used as the detecting anode (high-voltage: 3080 V). It collects the electrons produced when argon atoms are ionised, thus yielding a signal that can be read out electronically. However, the drift-time which is needed for an electron to reach the anode wire of up to 700 ns as well as the signal processing time limits the MDT modules to counting rates of 150 $\frac{1}{s \cdot cm^2}$, which is not sufficient for regions of $|\eta| > 2.0$ which is why the MDT are accompanied by cathode strip chambers (CSC) in the innermost part of the MS in the high pseudorapidity region [34].

Cathode strip champers (CSC): The cathode strip chambers are multi-wire proportional chambers with a technology also based on the ionisation of argon. The construction is such that multiple anode wires are oriented radially. The detecting elements are called cathode strips and are aligned perpendicular to the anode wires. A muon traversing a CSC will ionise argon atoms (the gas mixture is 80% argon, 20% CO_2) producing a charge cloud that induces a signal in the cathode strips made out of copper [35].

Resistive plate chambers (RPC): RPCs are very fast gaseous detectors located in the barrel part of the MS. The achievable spatial resolution is very low compared to that of CSCs and MDTs which is why they are used in the trigger system of the ATLAS detector. They are constructed using a gas mixture of $C_2H_2F_4$ 94.7% , C_4H_{10} 5%, SF_6 0.3% as active material [35]. A high-voltage of 9.6 kV is applied to the electrodes which are only 2 mm apart. They are made of the highly resistive material bakelite. Each electrode is coated with a thin layer of linseed oil which arranges for a very smooth surface required for the stability of this extreme electrical field. Muons traversing an RPC will ionise the gas atoms and the high voltage provides the basis for a subsequent avalanche of ionisations and thus an electron cloud is created that will drift through the gas. The read-out of this signal is performed using two layers of orthogonal strips into which

Module	Coverage	Spatial resolution	Time resolution	High-Voltage [V]
		Trajectory measurement		
MDT	$\|\eta\| < 2.7$	35 μm	$\mathcal{O}(100$ ns)	3080
CSC	$2.0 < \|\eta\| < 2.7$	40 μm	7 ns	3080
		Trigger system		
RPC	$\|\eta\| < 1.05$	10 mm	1.5 ns	9600
TGC	$1.05 < \|\eta\| < 2.7$	2...7 cm	4 ns	2900

Table 4.5.: Technical specifications of the four different technologies used in the ATLAS MS. Numbers are taken from [34]

signals are induced. The combination of the signal of both layers can then be transformed into information about one point (η, ϕ) of a muon trajectory.

Thin gap chambers (TGC): The trigger system is fed with information of the end-cap region of the MS using another multi-wire proportional chamber technology, called thin gap chambers [36]. A very small wire-spacing of 1.8 mm and a distance of the wires to the graphite cathodes of just 1.6 mm (hence thin gap) allow for a very high time-resolution of successive signals. The anode wire is made of a tungsten-gold alloy. The high-voltage applied amounts to 2.9 kV and the gas-mixture consists of 55% CO_2 and 45% C_5H_{12}. Read-out of the signal produced is again performed using cathode strips.

The resolution of the measurement of the transverse momentum of muons was performed by analysing cosmic muon events [37] as:

$$\frac{\sigma(p_\perp)}{p_\perp} = \frac{0.29}{p_\perp\ [\text{GeV}]} \oplus 4.3\% \oplus 0.0004 \cdot p_\perp[\text{GeV}] \tag{4.4}$$

where the symbol $\oplus$ stands for addition in quadrature.

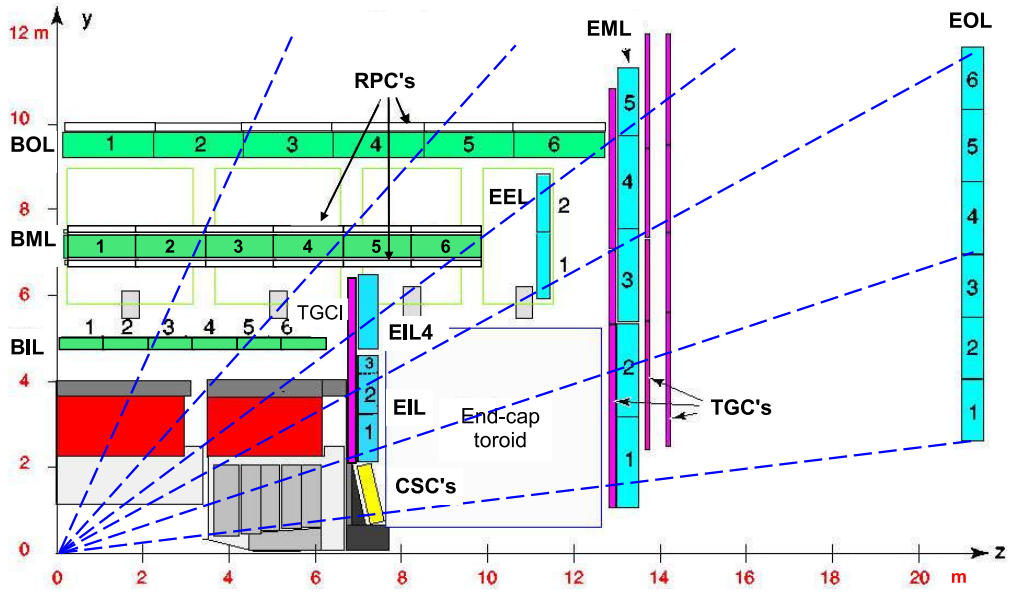

Figure 4.14.: Cut-away view along the beam axis (z) of a section of the ATLAS muon system in the bending plane of a muon trajectory (dashed lines show hypothetical trajectories of muons with infinite momentum) due to the toroid showing the arrangement of different technologies in the barrel and end-cap parts of the muon system. The measurement of muon trajectories is performed using information obtained from the cathode strip chambers (CSC, yellow) and monitored drift tube chambers, labelled in this sketch as BXL (barrel, green) and EXL (end-cap, blue) (X $\in$ [I,M,O] for inner, middle and outer layer). Further, the location of the resistive plate chambers (RPC) as well as the thin gap chambers (TGC) used for triggering data recording are shown. The image is taken from [38],

4.5. Trigger system

The general objective of the trigger of the ATLAS experiment is to reduce the amount of data to be stored permanently. This is necessary, firstly, due to the fact that the overwhelming amount of the collisions are considered to be non-interesting background to the ATLAS physics programme of comparably low momentum-transfer. Secondly, the available bandwidth of 450 MB/s limits the rate of events to be stored to a few hundred Hz in contrast to the rate of collisions of 40 MHz which would be equivalent to a bandwidth of 1 PB/s. Figure 4.15 shows an overview of the individual components of the trigger system that will be discussed in the following,

4.5.1. Level-1 trigger (LVL1)

The level-1 trigger of the ATLAS experiment is a pure hardware-trigger, meaning that the selection whether to discard an event at this stage is executed by fast electronics that coarsely read out calorimeter and muon information from the TGPs and RPCs. If an event passes the level-1 trigger, so-called regions-of-interest (ROI) are calculated that are likely to contain objects of interest. The ROI information is passed on to the next stage of the trigger for a fine-grained assessment. The typical the rate of events passing LVL1 is of the order of 75 kHz, i.e. a reduction by more than a factor of 500.

4.5.2. High-level trigger (HLT)

The level-2 trigger (LVL2) and the event filter form the software based high-level trigger. LVL2 only reads out regions of the detector seeded by the ROIs defined by the LVL1 trigger. It does so with the full granularity, i.e. all modules (Inner detector, calorimeters and muon system) present in that particular ROI. This step reduces the data rate to about 3 kHz. If an event passes the LVL2 trigger, the full reconstruction of the event is done using the event builder. This information is then passed on to the event filter. The event filter has access to all modules of the detector and is thus able to allow for a very precise decision making process on whether to write an event to disk or not. The final event rate is of the order of 300 Hz.

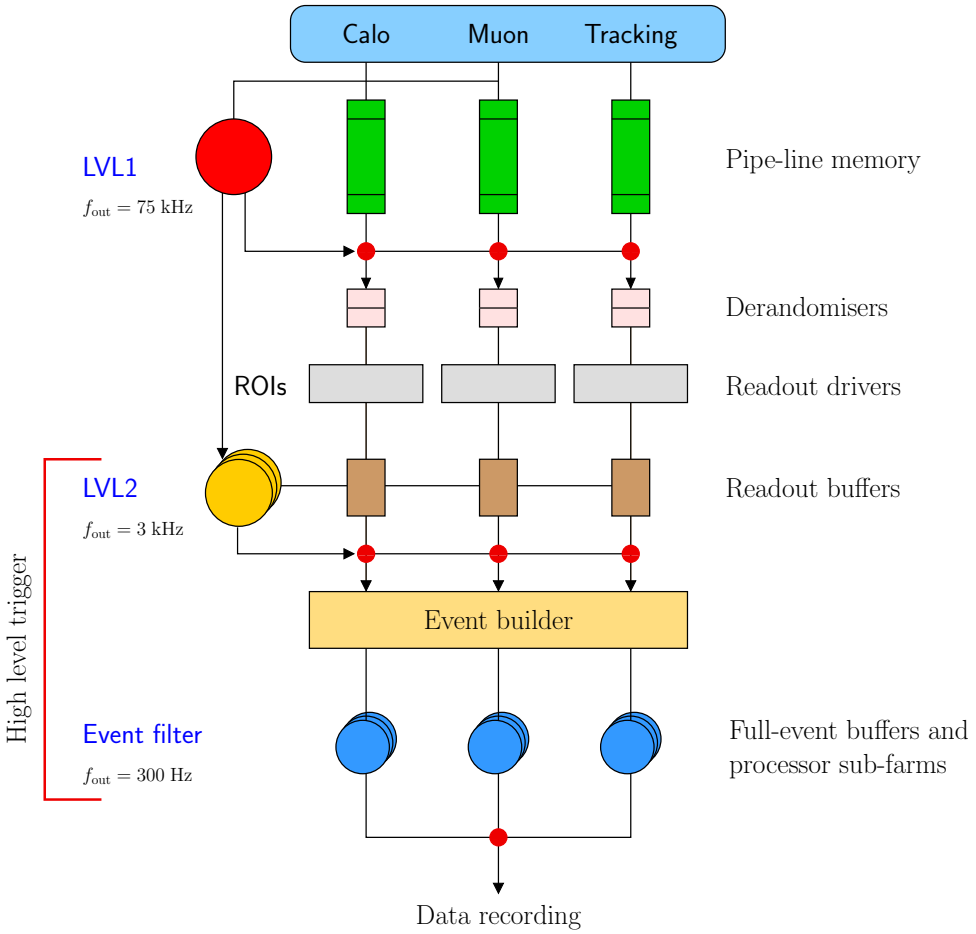

Figure 4.15.: Technical sketch of the ATLAS trigger system (original image in [23]). The data of each event is temporarily stored in buffers while hardware information (LVL1) is processed leading to a decision on whether to keep an event. In that case, the buffered data is read out in more and more detail based on software reconstruction (LVL2, event filter), ultimately leading to a data rate of 300 Hz which is sufficiently small to be stored on disks.

4.6. Luminosity in 2011

Luminosity, L, is a measure for both, the amount of data taken by a high-energy physics experiment, and the amount of hypothetically recordable data delivered by the accelerator. It is connected to the number of events to be expected for a specific process, N_P, by that process's cross-section σ_P and the time-integrated luminosity $\mathcal{L} = \int \mathrm{d}t L$: $N_P = \sigma_P \cdot \mathcal{L}$.

The machine luminosity depends on the configuration of the beams brought to collision (Chapter 3), while the detector luminosity makes a statement how efficient the detector operates. Figure 4.16 gives an overview of the luminosity delivered by the LHC and recorded with ATLAS in 2011. Further, the amount of data used in this analysis is indicated. A phenomenon of high-luminosity experiments, which ATLAS can be considered as, is the effect of simultaneous proton-proton interactions (pile-up) that will be discussed in detail in Chapter 10. The maximum number of such simultaneous interactions recorded in each data taking period ("lumi block"), $\mu^{\max}$, is given in Figure 4.16 as well.

The data taking with the ATLAS detector is subdivided into periods. In this analysis data collected of the data taking periods D-H with a mean number of simultaneous interactions of $\mu = 5$ was analysed, amounting to an integrated luminosity of $\int \text{Ł} \mathrm{d}t = 1.1\ \text{fb}^{-1}$. A summary of the datasets used can be found in Table A.1.

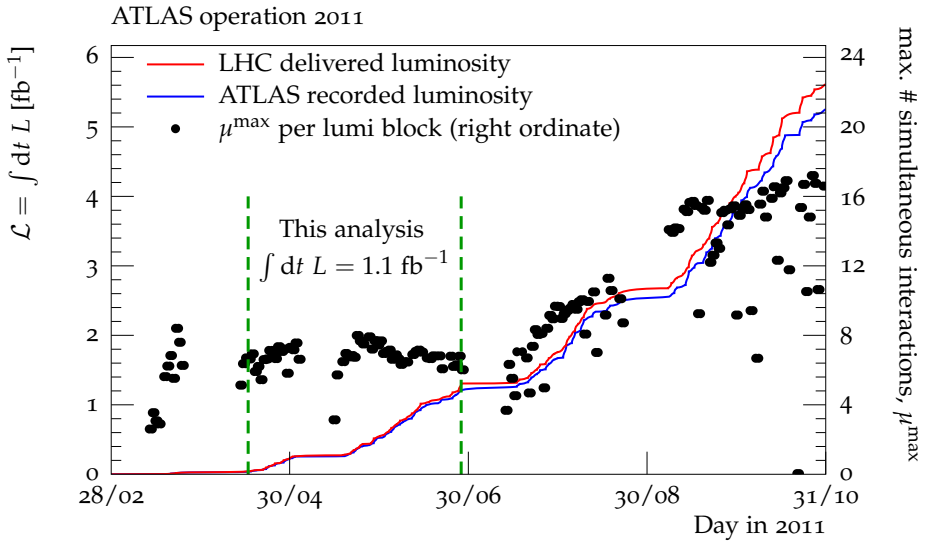

Figure 4.16.: Integrated luminosity delivered by the LHC (red line) and recorded with ATLAS (blue line) as function of time, showing a highly efficient data taking of the ATLAS detector. Further, the pile-up conditions (maximum number of simultaneous interactions recorded per "lumi-block") are shown, which are almost constant in the data used in this analysis (indicated by the vertical green lines).

Chapter 5.

Reconstruction and selection of physical objects

In this chapter, the reconstruction of objects used in the data analysis is discussed. This includes the reconstruction of electrons and muons, tracks of charged particles and vertices. The reconstruction and selection of tracks and vertices is identical in the muon and electron channel of this analysis.

5.1. Tracks of charged particles

The reconstructed properties of charged particles are essential to this analysis. They are used for the measurement of the event-shape observables but also tracks of charged leptons (electron, muons) are used in the reconstruction of the latter. Further, the reconstruction of vertices, i.e. the actual interaction points from which the primary interactions originate from are based on reconstructed trajectories of charged particles.

The reconstruction algorithm for tracks used processes information from the entire inner detector of the ATLAS experiment (Pixel, SCT, TRT) and is based on the curvature of charged particles due to the solenoid magnetic field the inner detector is immersed in. In short, so-called hits (electronic signals registered by the various modules) are tried to be assigned to charged particle trajectories while the curvature of the latter is used to measure the transverse momentum of those tracks.

The algorithm used in the reconstruction of tracks is called "inside-out" and is implemented in a software called NEWT (NEW Tracking) [39]. The procedure has in principle

two steps that go hand in hand, however, and can not clearly be separated. It consists of a pattern recognition, which is performed once trying to identify signals from different modules to a single particle in order to get a rough estimate on a charged particles trajectory but also for further refining of particle trajectories. The actual track-fitting that extracts the parameters necessary to fully define a particle trajectory is performed several times as well. [40].

When processing an event that passed the LVL1 trigger, three-dimensional space-points are formed from Pixel and SCT hits, incorporating both the spatial coordinates of the hits as well as that of the module. While single Pixel hits suffice and the spatial coordinates of the pixel module suffice for the formation of a space-point, the formation of space-points from SCT information requires two hits on an SCT module, one from the front and one from the back of the same module (as well as the spatial coordinates of the module).

Combinations of three such space-points are then used to define a circle in the transverse plane ($z = 0$) which is called "seed". The transverse momentum of the seed is measured and the seed is tried to be geometrically associated with a collision. If the latter is found to be the case and the transverse momentum measured is above the threshold[1] of the track-fitting algorithm, a so-called "track candidate" is formed. Space-points are no longer used, instead the more precise hits are used. The identification of a track candidate is performed using a KALMAN filter algorithm [41] that tries to associate all compatible hits with the initial track seed while iteratively updating the likely trajectory of the charged particle.

In this process, ambiguities arise, leading to a very high number of track candidates. The ambiguities arise from incomplete tracks or fakes (majority of hits not originating from a single particle). Further, more than one track candidate may share hits [39]. These ambiguities are resolved by assigning "track scores", similar to likelihoods, based on a refitting of each track candidate with the KALMAN filter using a finer geometry. Only those track candidates with the highest scores are accepted. Figure 5.1 shows an illustration how such ambiguities arise.

The next step of the pattern recognition is an extension of the accepted track candidates that pass the transverse momentum threshold of the track-fitter to the TRT. The components of a track candidate from the Pixel and SCT are not touched any more. Instead, fitting algorithms are used to find TRT hits compatible with the initial track

[1] The track reconstruction algorithm used for the data analysed in this thesis had a threshold of $p_\perp = 400$ MeV

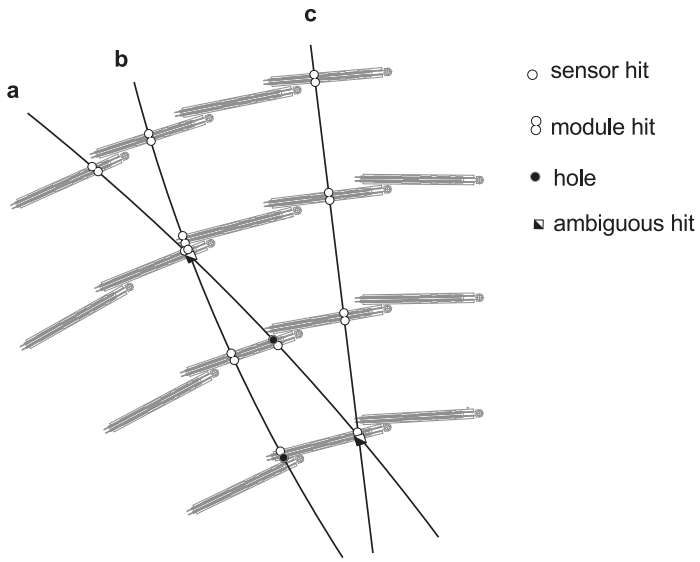

Figure 5.1.: Illustration of the solving of ambiguities during track reconstruction in the barrel part of the SCT. The tracks-candidates a,b and c where found in the seeding process. Module hits (one hit in front and one in back part of same module) result in a higher score than two single hits, i.e. hits on one side of the panel without the trajectory expecting a hit on the other side. If such a hit would be expected but is not found ("hole") the track score receives a penalty. Hits in two overlapping modules (candidate b) receive a very high score. In this illustration, candidate b has the highest score. The picture is taken from [39].

candidate. Finally, a last application of the KALMAN filter to the extended track candidate is used to determine whether the extended or the initial (silicon based) track candidate will be used as the final track and the obtained parameters are used to define the charged particle trajectory.

5.1.1. Track parameters

Since the solenoid magnetic field of the ATLAS experiment is at first order uniform along the z-axis, the LORENTZ force only has an influence in the transverse plane ($z = 0$) thus making the transverse momentum of a charged particle a constant of motion. Having measured the radius of the curvature of a track in the transverse plane, ρ, its transverse momentum can be calculated according to [40] as

$$p_\perp = cB\rho \quad \rightarrow \quad p_\perp \text{ [GeV]} = 0.3 \; B\text{[T]} \; \rho\text{[m]} \tag{5.1}$$

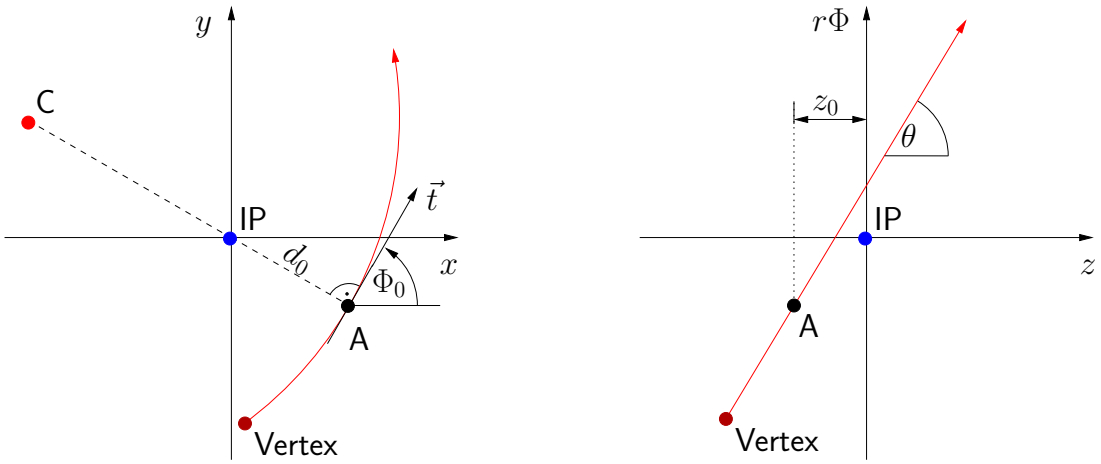

Figure 5.2.: Definition of track-helix parameters. The transverse and longitudinal impact parameters d_0 and z_0 are determined using projections of the point of closest approach, A, of a track helix to the nominal interaction point into the $x-y$ and $r\Phi - z$ plane respectively. The point C in the left hand plot represents the centre of a circle in the xy-plane. The radius of which is constraint by d_0 and the curvature of the track in the xy-plane. The vector $\vec{t}$ illustrates the tangent to the track curvature at the point of closest approach, needed to define the angle Φ_0.

The motion of a charged particle in a solenoid magnetic field can be parametrised using a helix. The ATLAS convention is to use a parametrisation based on constants of motion present in the inner detector and the muon spectrometer and on the point of closest approach, (x_0, y_0, z_0), of the trajectory to the beam-axis (perigee). The parameters chosen by ATLAS to describe a charged particle trajectory are

- $\Phi_0 = \arctan\left(\frac{y_0}{x_0}\right)$, azimuthal angle of the track direction, i.e. angle with respect to the x-axis in the $x-y$ plane
- θ, polar angle of the track direction, i.e. angle with the z-axis in the $r\Phi - z$ plane
- $d_0 = \sqrt{x_0^2 + y_0^2}$, signed distance to beam-axis $\begin{cases} d_0 > 0 & \text{if } \Phi - \Phi_0 = \frac{\pi}{2} \mod (2\pi) \\ d_0 < 0 & \text{else} \end{cases}$
  with Φ being the angle to the perigee in the $x-y$ plane
- z_0, z-coordinate of the track at the point of closest approach
- $\frac{q}{p}$, charge of particle divided by its momentum

An illustration of the track parameters can be found in Figure 5.2.

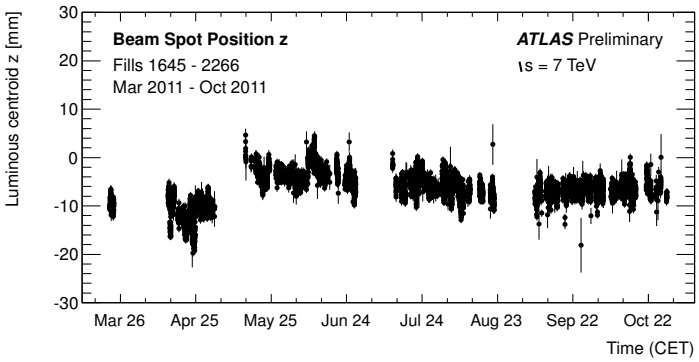

Figure 5.3.: Beam-spot position (z-coordinate) measured by ATLAS as function of time in 2011. The variation is of the order of a few mm between fills used in this analysis (beginning of April - end of June). The picture is taken from https://twiki.cern.ch/twiki/bin/view/AtlasPublic/BeamSpotPublicResults.

5.1.2. Vertex reconstruction

The reconstruction of vertices is performed using an iterative algorithm on all reconstructed tracks of an event that contains at least two tracks fulfilling $p_\perp > 400$ MeV. Further, their transverse distance of closest approach w.r.t. the beam-spot (luminous region in the detector [42], Figure 5.3) position, $|d_0^{\mathrm{BS}}|$, is required to be smaller than 4 mm.

The global maximum of the distribution of the z-coordinates of all these tracks is used as seed for the vertex finding as are the tracks in the vicinity of the found maximum. The "adaptive vertex fitting" algorithm [43] which is based on a χ^2 minimisation is then used iteratively to determine the (primary) vertex position. The algorithm assigns tracks to vertices based on the distance (z-coordinate) of the track and the found vertex position. Tracks that are not assigned to a vertex are used as seeds for further vertices. The procedure is repeated until all tracks are associated with vertices.

Vertices and their properties are further discussed in Chapter 10.

5.1.3. Track selection

The track reconstruction algorithm is not perfect. There are effects such as tracks from secondary interactions with the detector material and the already mentioned fakes that lead to a reconstruction efficiency $\varepsilon < 1$ for real tracks which will be discussed in

Property	Cut
$p_{\perp}^{\mathrm{trk}}$	> 500 MeV
$\lvert\eta^{\mathrm{trk}}\rvert$	< 2.5
$\lvert d_0\rvert$	< 1.5 mm
$\lvert z_0 \cdot \sin\theta\rvert$	< 1.5 mm

Table 5.1.: Kinematic track requirements for the selection of tracks for this analysis.

Chapter 9. The efficiency strongly depends on quality criteria imposed when selecting tracks [44, 45].

The following quality requirements[2] which are identical to the ones used in the $\sqrt{s} = 7$ TeV measurement of charged particles with ATLAS [44] must be met for a track to be considered in this analysis:

- a b-layer hit if the reconstructed trajectory would have passed an active b-layer module
- at least one hit in the Pixel sub-detector
- at least six SCT hits

The requirements on the b-layer and Pixel hits greatly reduce the number of secondary tracks. Further, charged particles with a low transverse momentum give a shorter track thus making the measurement less precise, which is why an indirect requirement on the track length is imposed by requiring at least six SCT hits, which translates to at least three SCT modules being traversed by the charged particle.

The kinematic cuts imposed on the track selection (Table 5.1) are driven by the acceptance of the inner detector (η), the reconstruction efficiency ($p_{\perp}$, plateau of reconstruction efficiency) and the aim to suppress tracks not originating from the primary vertex of the event (cuts on d_0 and z_0).

Lepton track removal

As this analysis tries to be sensitive to the underlying event, the decay products of the Z-boson produced in the hard sub-process need to be removed. Since all observables

[2] These cuts where optimised based on simulations.

are calculated from reconstructed tracks the tracks produced by the leptons need to be removed from the collection of tracks in each event. As the majority of electrons is reconstructed using not only information from the tracking system but also the ECAL, ambiguities arise when trying to identify electron tracks. Hence a conservative approach based on a cone around the reconstructed electrons is chosen. In order to treat the electron and muon channel analyses as similar as possible, this approach is also done for the removal of muon tracks. For each reconstructed lepton (Section 5.2, 5.3) a cone of $\Delta R = 0.1$ around the three-momentum vector of the reconstructed lepton as symmetry axis is defined. Each track passing the selection cuts listed in Table 5.1 is probed whether it falls into the cone by calculating the $\tilde{\Delta R}$ measure between the lepton and track three-momentum vectors:

$$\tilde{\Delta R} = \sqrt{(\eta_{\text{trk}} - \eta_{\text{lepton}})^2 + (\Phi_{\text{trk}} - \Phi_{\text{lepton}})^2} \tag{5.2}$$

All tracks with $\tilde{\Delta R} < 0.1$ are removed from the event, i.e. they are not used in the calculation of the event shape observables.

As the choice of the cone size of $\Delta R = 0.1$ is ad hoc, the stability of obtained results under variation of ΔR needs to be studied. This is important as the data is eventually unfolded using Monte-Carlo information (Chapter 12). The test is performed by measuring the event-shape distributions using reconstructed tracks in data and Monte-Carlo events passing the full event-selection (Chapter 6) with an additional cut on the transverse momentum of the reconstructed Z-boson, requiring $p_\perp(\text{Z}) < 6$ GeV.

The observables are once measured using $\Delta R = 0.05$ and once with $\Delta R = 0.2$, i.e. a variation of the nominal value of ΔR by a factor of two up and down. The ratio $\frac{f(\Delta R=0.2)}{f(\Delta R=0.05)}$ of the distributions is then calculated. The observables are considered stable under these variations if the observed shape of the ratios $\frac{f(\Delta R=0.2)}{f(\Delta R=0.05)}$ is similar in data and Monte-Carlo meaning that the Monte-Carlo information of reconstructed properties can be trusted when unfolding data.

The corresponding plots of this test are shown in the ratio-plots of Figure 5.4. Within the statistical uncertainties, the ratios $\frac{f(\Delta R=0.2)}{f(\Delta R=0.05)}$ are compatible with one for data and Monte-Carlo, demonstrating that the cone-based removal of lepton tracks is stable under variations of ΔR. It should be noted that only results for the electron channel are shown.

The corresponding plots for the muon channel look very similar. This is also true for the observables not shown (F-Parameter, transverse minor, Spherocity).

Distributions of reconstructed tracks

Figure 5.5 compares properties of reconstructed non-lepton tracks present in events passing the full event selection (Chapter 6) in data and Monte-Carlo, showing differences in the $p_\perp$ spectrum that can be explained by imperfect modelling of charged particles kinematics in the Monte-Carlo generators used.

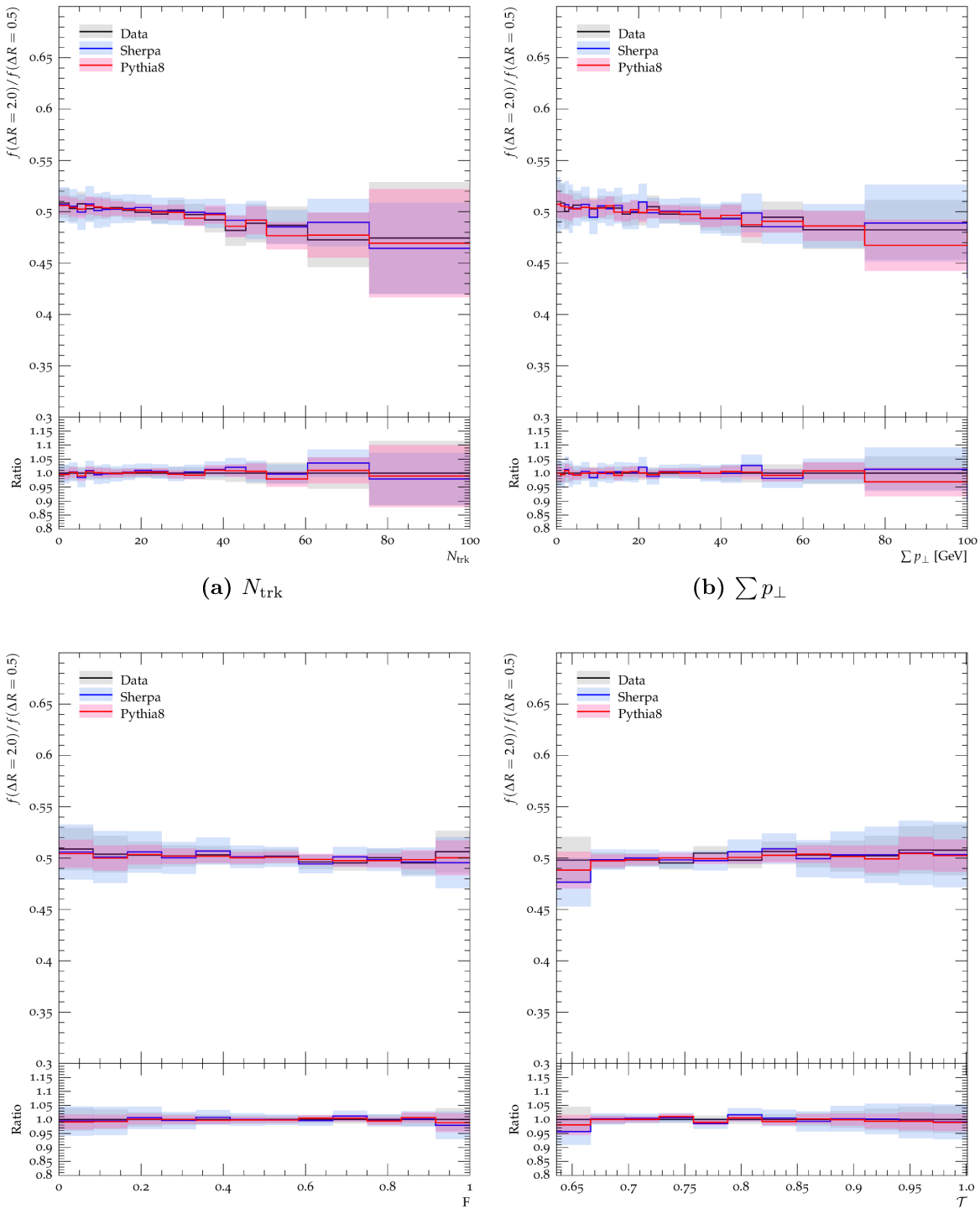

(a) N_{trk} **(b)** $\sum p_\perp$

(c) F-parameter **(d)** Transverse thrust

Figure 5.4.: Stability test for the cone size ΔR used to remove tracks from the event originating from the leptons that are the decay products of the Z-boson. Shown are the ratios of a selection of event shape observables when calculated with $\Delta R = 0.2$ and those calculated using $\Delta R = 0.05$. The actual test of the stability is visible in the ratio plots that show that within (statistical) errors the behaviour is identical for data and Monte-Carlo (Pythia8, Sherpa). The observables are calculated for events passing the full event selection (Chapter 6) and $p_\perp(\mathrm{Z}) < 6$ GeV.

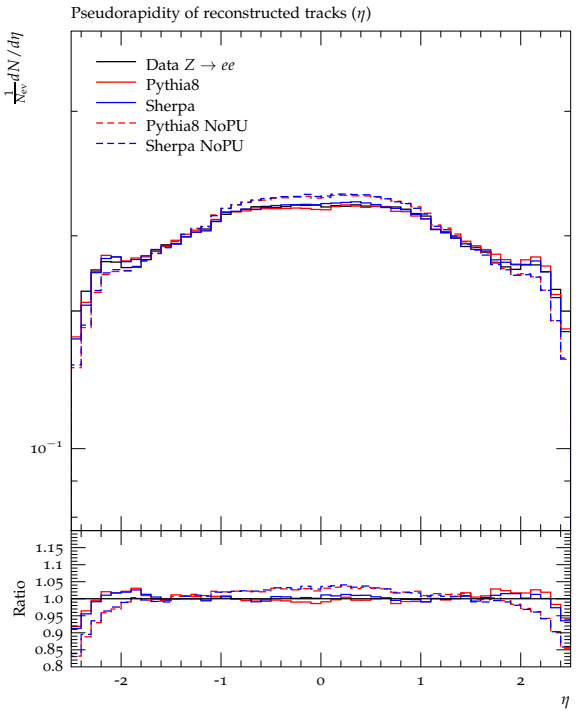

(a) Pseudorapidity, electron channel

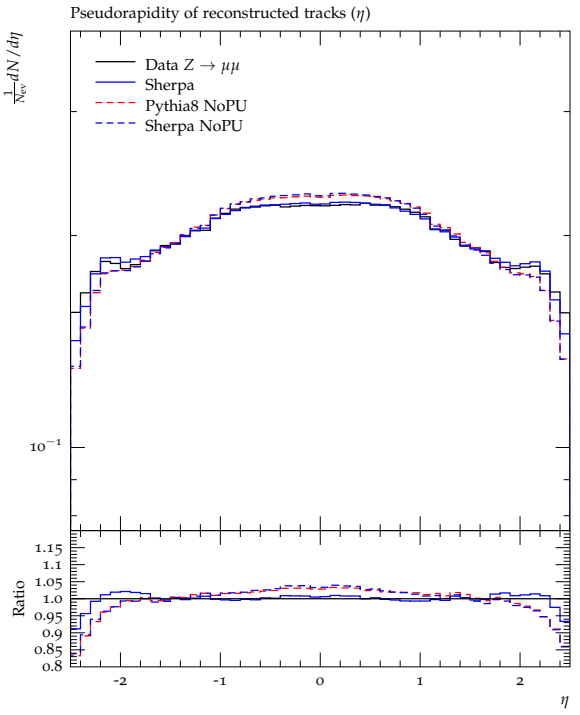

(b) Pseudorapidity, muon channel

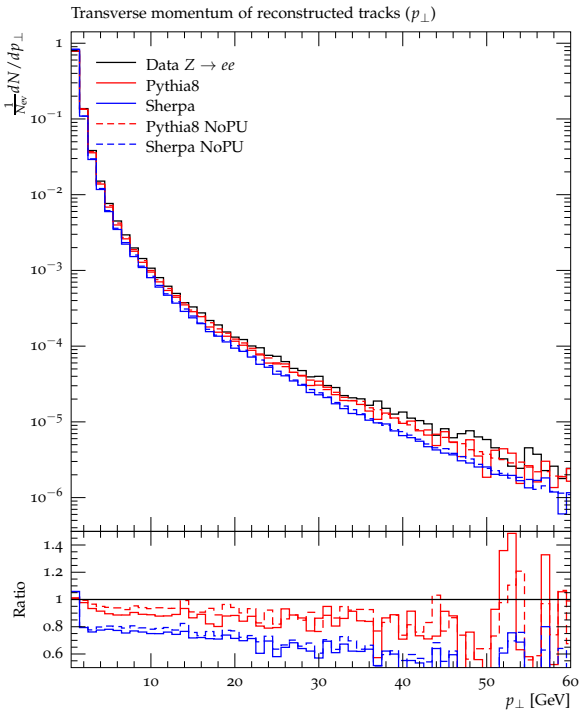

(c) Transverse momentum, electron channel

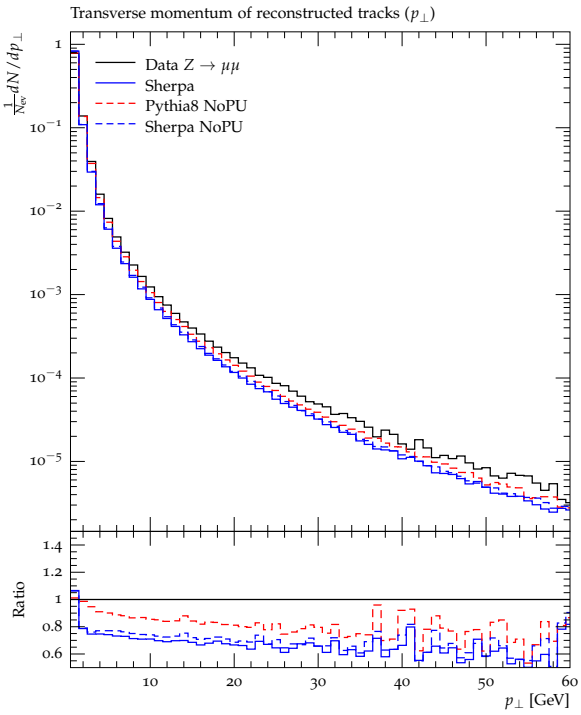

(d) Transverse momentum, muon channel

Figure 5.5.: Reconstructed properties of selected tracks after lepton removal. Shown are the pseudorapidity and transverse momentum distributions for both channels and all signal Monte-Carlo samples (Chapter 8) with and without pile-up, highlighting both, the impact of tracks from pile-up interactions and the model imperfections present in Sherpa and Pythia8.

5.2. Electron reconstruction

The reconstruction of electrons utilises information of the inner detector (track) as well as the ECAL (energy). A so-called "sliding window" algorithm [46] forms seed clusters of deposits in the ECAL with an energy of at least 2.5 GeV. The size of the window is thereby chosen to be 3×5 in units of the middle layer granularity of the ECAL (Chapter 4). Further, a seed cluster is required to be matched with one or more tracks reconstructed in the inner detector. The matching is done in a window of size $\Delta\eta \times \Delta\Phi = 0.05 \times 0.10$. If more than one track is matched to a seed cluster, the track yielding the smallest $\Delta R = \sqrt{\Delta\eta^2 + \Delta\Phi^2}$, calculated from a track's impact parameter with the ECAL and the seed cluster, is taken as the matched track. The track momentum, p, further needs to be compatible with the energy deposit, E, in the seed cluster: $\frac{E}{p} < 10$.[3] The final cluster energy is calculated from the energy in the seed cluster as well as from the energy deposit in the presampler corrected for the estimated leakages. The actual pattern of the energy deposits in the calorimeter cells (called "shower") is used to define electrons of different quality.

5.2.1. Electron selection

During the reconstruction step, also a track-based electron reconstruction algorithms is executed, which is more precise for the reconstruction of low energy electrons.

So called "bad electrons" which were reconstructed with clusters containing a dead module are filtered out ("Bitmask `OQ` = 1446").

Further, so-called noise bursts (short but large signals of distorted shape related to bunches of low quality) in the liquid argon (LAr) system severely affect the performance of the ECAL. These bursts are detected however and the information on whether such a burst was present or not is accessible in each data event. In this analysis, events that are flagged to have suffered a LAr noise burst are rejected.

In this analysis, only electrons are selected that were successfully reconstructed using the aforementioned calorimeter based algorithm as the electrons are required to have a relatively high transverse momentum of at least 20 GeV where the track momentum resolution is rapidly worsening w.r.t. the energy resolution of the ECAL (Figure 4.9).

[3] "<" since electrons loose energy due to Bremsstrahlung prior to entering the ECAL. The photonic energies are deposited in the ECAL and therefore contribute to E.

This cut is applied after several corrections related to the calibration of the ECAL are applied.

Information on the electron's transverse momentum $p_{\perp,e}^{\text{cluster}}$, its energy E_e^{cluster}, its pseudorapidity η_e^{cluster} and its azimuthal angle, Φ_e^{cluster} are, in a first step, taken from the measured values in the calorimeter clusters. The electron's transverse energy, $E_{\perp,e}$, is used for the correction of electrons measured in data and in Monte-Carlo. Its measurement also uses information of the matched track in case it is measured with high precision (based on the number of Pixel and SCT hits, $n_e^{\text{SCT hits}}$, $n_e^{\text{Pixel hits}}$), in all other cases it only uses information of the ECAL clusters:

$$E_{\perp,e} = \begin{cases} E_e^{\text{cluster}} / \cosh(\eta_e^{\text{trk}}) & \text{if} \quad n_e^{\text{SCT hits}} + n_e^{\text{Pixel hits}} \geq 4 \\ E_e^{\text{cluster}} / \cosh(\eta_e^{\text{cluster}}) & \text{else} \end{cases} \tag{5.3}$$

The corrections (calibrations in case of data) of electron energies and resolutions (Monte-Carlo only) were obtained by the ATLAS EGamma working group using tag and probe methods in $Z \to e^- e^+$ events and are described in more detail in [47].

Correction for the crack region:

The ECAL has a so-called "crack-region" at $|\eta| \in [1.37, 1.52]$ where support structures and cables are located. Electrons reconstructed in the crack-region are not selected in this analysis. For those electrons reconstructed to be in the region $|\eta| \in [1.52, 1.55]$ the reconstructed energy is underestimated due to leakage into the crack-region. Hence, an additional calibration for those electrons is required, which is applied for both data and MC. In Figure 5.6 the correction factors for several electron energies are shown. The correction factors, $f^{\text{crack}}(E_{\perp,e}^{\text{cluster}}, \eta_e^{\text{cluster}})$, are of the order of 8 % for $E_e^{\text{cluster}} = 20$ GeV in and near the crack region, while it is one outside of $|\eta| \in [1.42, 1.55]$, meaning that for those electrons no additional calibration due to the crack is applied. This is the first correction to cluster information applied, meaning that

$$\begin{aligned} E_e^{\text{cluster}} &\to f^{\text{crack}}(E_{\perp,e}^{\text{cluster}}, \eta_e^{\text{cluster}}) \cdot E_e^{\text{cluster}} \\ p_{\perp,e}^{\text{cluster}} &\to f^{\text{crack}}(E_{\perp,e}^{\text{cluster}}, \eta_e^{\text{cluster}}) \cdot p_{\perp,e}^{\text{cluster}} \\ E_{\perp,e} &\to f^{\text{crack}}(E_{\perp,e}^{\text{cluster}}, \eta_e^{\text{cluster}}) \cdot E_{\perp,e} \end{aligned}$$

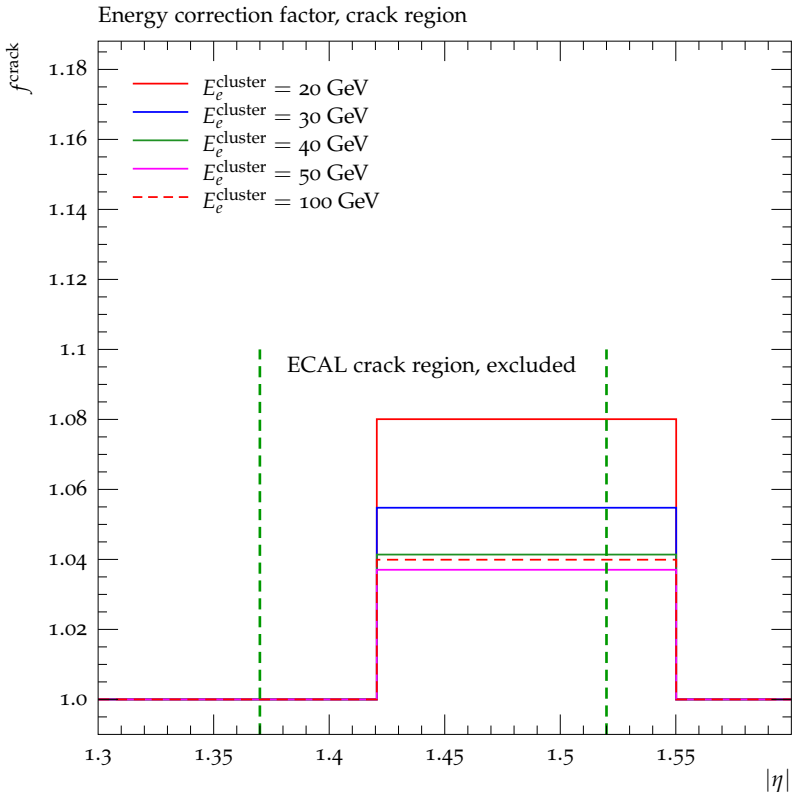

Figure 5.6.: Energy correction factors, f^{crack}, for regions in and close to the crack-region in the ECAL for various electron energies, E_e^{cluster} [48]. The vertical dashed lines indicate the crack-region $|\eta| \in [1.37, 1.52]$. Electrons reconstructed in it are not considered in this analysis.

Correction and smearing for all electrons:

Reconstructed energies and transverse momenta of electrons in data as measured by the ECAL need to be scaled to account for residual energy scale corrections. The corresponding information in MC events in addition requires a smearing to reproduce the resolution present in data. The scaling of electron energy and transverse momenta in data is performed using a tool that requires information on E_e^{cluster}, $p_{\perp,e}^{\text{cluster}}$, $E_{\perp,e}$ and Φ_e^{cluster} and returns multiplicative correction factors f^{scale}:

$$p_{\perp,e}^{\text{cluster}} \rightarrow f^{\text{scale}}(\eta_e^{\text{cluster}}, \Phi_e^{\text{cluster}}, p_{\perp,e}^{\text{cluster}}, E_{\perp,e}) \cdot p_{\perp,e}^{\text{cluster}} \tag{5.4}$$

$$E_e^{\text{cluster}} \rightarrow f^{\text{scale}}(\eta_e^{\text{cluster}}, \Phi_e^{\text{cluster}}, E_e^{\text{cluster}}, E_{\perp,e}) \cdot E_e^{\text{cluster}} \tag{5.5}$$

The treatment of MC information is handled similarly, introducing multiplicative factors $f^{\text{scale, MC}}$. The scaling and smearing of energies and transverse momenta requires information on $\eta_e^{\text{cluster, MC}}$ and $E_e^{\text{cluster, MC}}$ such that:

$$p_{\perp,e}^{\text{cluster, MC}} \rightarrow f^{\text{scale, MC}}(\eta_e^{\text{cluster, MC}}, E_e^{\text{cluster, MC}}) \cdot p_{\perp,e}^{\text{cluster, MC}} \tag{5.6}$$

$$E_e^{\text{cluster, MC}} \rightarrow f^{\text{scale, MC}}(\eta_e^{\text{cluster, MC}}, E_e^{\text{cluster, MC}}) \cdot E_e^{\text{cluster, MC}} \tag{5.7}$$

Systematic uncertainties of the correction and smearing factors are discussed in Chapter 9.

5.2.2. Medium and loose electrons

The electron candidates selected in this analysis are required to fulfil a set of quality cuts, summarised as `medium++`. For the estimation of QCD background events (Chapter 11) a second set with less strict criteria is used (`loose++`). The `medium++` selection contains all the selections made for `loose++` electrons. A summary of these quality criteria can be found in Table 5.2. Definitions are taken from [49].

`loose++`

Hadronic leakage: Electrons deposit most of their energy in the ECAL with little leakage into the adjacent hadronic calorimeter (HCAL). For electrons reconstructed with $0.8 < |\eta|$ and $|\eta| > 1.37$, the measure R_{had1} is defined as the ratio of the transverse energy deposit in the first layer of the HCAL over the total cluster transverse energy in the ECAL. For $0.8 > |\eta|$ and $|\eta| < 1.37$ the hadronic leakage, R_{had}, is calculated as the ratio of the total transverse energy deposit in the HCAL and the total transverse energy deposit in the ECAL. The cuts applied to these variables are dependent on the transverse energy and pseudorapidity of the electron. For the typical transverse energies of electrons selected in this analysis the values R_{had1} and R_{had} are typically required to be smaller than two percent. These cuts are designed to reject the selection of jets which will deposit larger amounts of energy in the HCAL (Figure 5.7a).

Shower-shapes: Further, the shape of the shower is used to refine the electron selection. The variable R_η is defined as the ratio of uncalibrated measured energy depositions

in the middle layer of the ECAL, obtained from a fine and a coarser segmentation of cells ($\Delta\eta \times \Delta\Phi = 3 \times 7$ over $\Delta\eta \times \Delta\Phi = 7 \times 7$). For electrons, this variable results in a strongly peaked distribution (Figure 5.7b) with the peak around $R_\eta = 0.85 \cdots 0.95$ and a broad tail towards smaller R_η values due to the narrow shower produced by electrons. For hadrons, a broad distribution is found that intercepts that of the electrons left of the peak. The actual cut used again depends on the transverse energy and pseudorapidity of the electron.

Also the width of the shower in the middle layer of the ECAL, w_2, which is defined as the standard deviation of an energy-weighted distribution of the pseudorapidity of calorimeter cells (Figure 5.7c) is used to judge the quality of electrons:

$$w_2 = \sqrt{\frac{\sum_i E_i \cdot \eta_i^2}{\sum_i E_i} - \left(\frac{\sum_i E_i \cdot \eta_i}{\sum_i E_i}\right)^2} \tag{5.8}$$

where E_i is the energy of a calorimeter cell and η_i its pseudorapidity. The transverse energy and pseudorapidty dependent cuts typically require $w_2 < 0.02$.

The width of the shower in the first layer of the ECAL (strips), $w_{s,tot}$ is also used to purify the electron selection. It is defined as

$$w_{s,tot} = \sqrt{\frac{\sum_i E_i \cdot (i - i_{\max})}{\sum_i E_i}} \tag{5.9}$$

where the sums run over all calorimeter strips i of energy E_i. The index $i_{\max}$ refers to the strip with the largest energy deposit. This distributions peaks for electrons at values between 2 and 4 while hadrons tend to give a much broader distribution (Figure 5.7d), therefore allowing another separation of electrons and hadrons. The cuts are dependent on the transverse energy and pseudorapidty of the electron and typically require $w_{s,tot} < 3$.

Further, a requirement on the energy of the two highest energy depositions in the first layer of the ECAL, $E_{\max 1}$ and $E_{\max 2}$, is imposed, requiring the property E_{ratio}, defined as

$$E_{\text{ratio}} = \frac{E_{\max 1} - E_{\max 2}}{E_{\max 1} + E_{\max 2}} \tag{5.10}$$

to be close to one (typically > 0.7) as jets are usually found to have more than one particle being associated with energy deposited in a cluster. The distribution of E_{ratio} is very peaked close to one while the corresponding distribution obtained from hadrons can

be described as linearly falling and then abruptly going to zero as E_{ratio} approaches one (Figure 5.7e).

Track quality: A track-cluster match is required for an electron to pass the `loose++` selection, allowing a mismatch of only $\Delta\eta < 0.015$. Further, the associated track is required to have at least one Pixel hit or at least one Pixel outlier, which is a hit with unresolvable ambiguity and similarly the sum of SCT hits and SCT outliers is required to be greater than six.

`medium++`

The standard electron selection used in this analysis, `medium++`, consists of all of the `loose++` criteria. Some of them have to fulfil tighter cuts and a few more selection criteria are applied.

Shower-shapes and hadronic leakage: The same variables as in `loose++` are used (R_η, R_{had}, R_{had1}, w_2, w_s, tot and E_{ratio}) but with slightly tighter cut values.

Track quality: The track-cluster match is now required to be tighter by a factor of three: $\Delta\eta < 0.005$. In addition to the hit criteria present in `loose++` an electron track is further required to have at least one b-layer hit. The sum of Pixel hits and Pixel outliers is now required to be at least equal to two. Finally, a cut on the transverse impact parameter of the electron track of $|d_0| < 5$ mm is imposed (Figure 5.7f). Events with heavy flavour decays tend to have larger values of d_0 due to the comparably large life-time of b-quarks and can be suppressed to some degree with this cut. However, mainly electrons stemming from conversion processes are affected by this cut.

Criterion	Description	Symbol
	`loose++`	
Acceptance	$\|\eta\| < 2.47$	
Leakage into HCAL	Electrons with $0.8 < \|\eta\|$ and $\|\eta\| > 1.37$	R_{had1}
	Electrons with $0.8 > \|\eta\|$ and $\|\eta\| < 1.37$	R_{had}
Shower shapes	Narrowness of shower	R_{η}
	Shower-width in middle layer	w_2
	Shower-width in first layer	$w_{s,tot}$
	Shower concentration in first layer	E_{ratio}
Track quality	track-cluster match with $\Delta\eta < 0.015$	
	Pixel hits + Pixel outliers > 0	
	SCT hits + SCT outliers > 6	
	`medium++`	
Leakage into HCAL	Same variables as in `loose++` but tighter cuts	
Shower shapes	Same variables as in `loose++` but tighter cuts	
Track quality	track-cluster match with $\Delta\eta < 0.005$	
	Pixel hits + Pixel outliers > 1	
	SCT hits + SCT outliers > 6	
	b-layer hits > 0	
	tranverse impact parameter cut $\|d_0\| < 5$ mm	

Table 5.2.: Overview of the selection criteria for `loose++` and `medium++` electrons. The `loose++` cuts are all fulfilled if an electron passed the `medium++` selection.

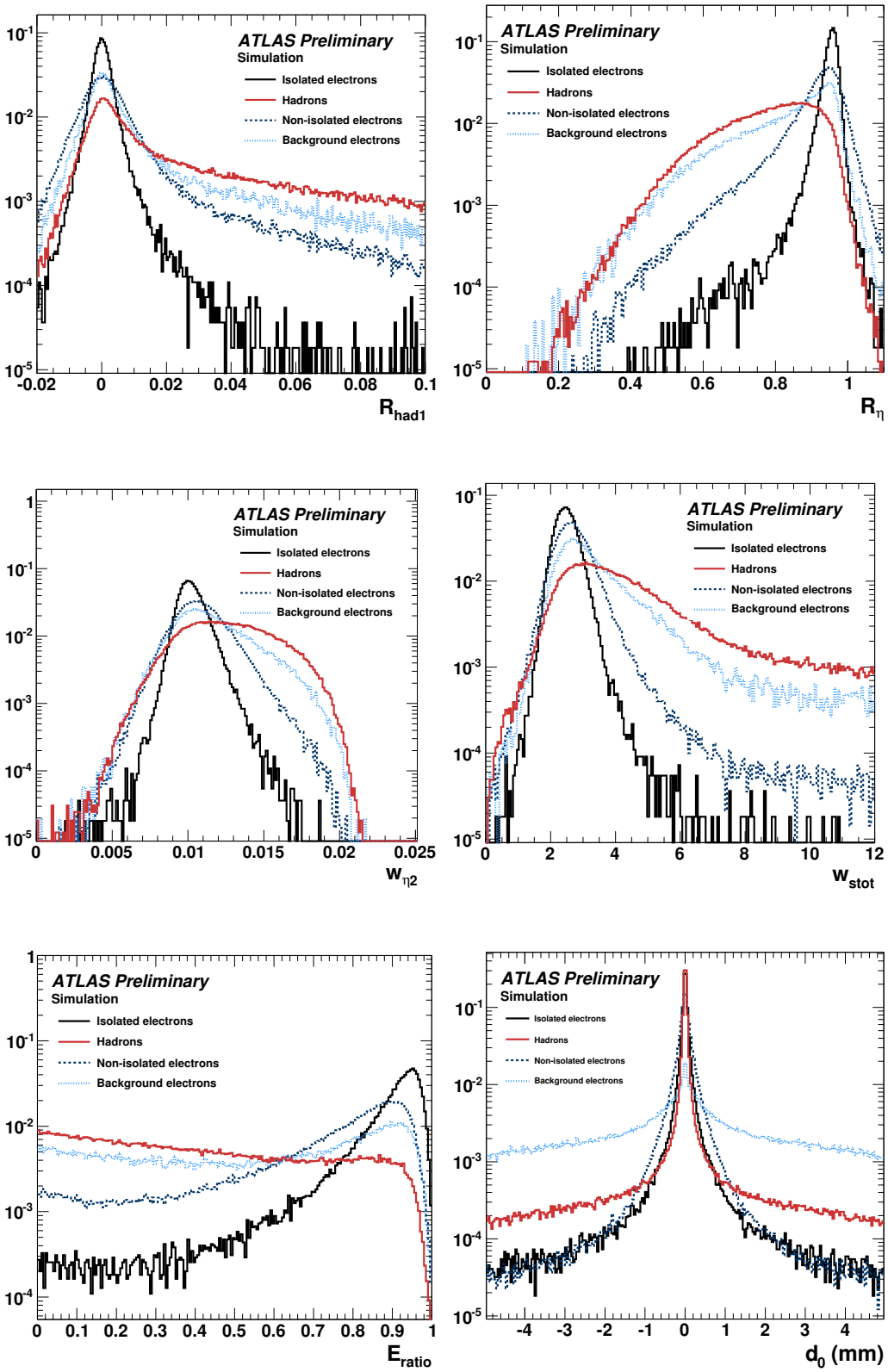

Figure 5.7.: Example distributions of some of the variables used in the `loose++` and `medium++` electron criteria. The relevant curves for this analysis are the "Non-isolated electrons". Plots have been taken from [27].

5.2.3. Kinematic cuts

The corrected `medium++` electrons are required to fulfil further kinematic requirements that have to do with efficiencies and acceptances of the detector. The reconstruction efficiency of electrons with the ATLAS detector in 2011 was measured in data ($Z \to e^- e^+$, $J/\Psi \to e^- e^+$ and $W \to e\nu$ events) and published in [50]. The selection criteria are not identical to the ones used in this analysis but similar to the `medium++` requirements. The plots in Figure 5.8 nonetheless show a reconstruction efficiency of mostly $> 90\%$. The following cut on the pseudorapidity is applied when selecting electrons: $|\eta_e^{\text{cluster}}| \in [0, 2.4]$ except the crack region ($[1.37, 1.52]$). This is done in order to exclude the crack-region and to ensure good coverage of the `ECAL`. Although the electromagnetic calorimeter covers the pseudorapidity of up to $|\eta| < 2.47$, it was chosen to limit the acceptance in the selection to $|\eta| = 2.4$ in order to be closer to the muon selection. Another requirement exists for the transverse momenta of electrons. Depending on how well the electron track has been measured it is defined (similarly to equation (5.3)) as:

$$p_{\perp,e} = \begin{cases} E_e^{\text{cluster}} \cdot \sin(\theta_e^{\text{trk}}) & \text{if} \quad n_e^{\text{SCT hits}} + n_e^{\text{Pixel hits}} \geq 4 \\ p_{\perp,e}^{\text{cluster}} & \text{else} \end{cases} \tag{5.11}$$

Electrons passing the selection are required to fulfil $p_{\perp,e} > 20$ GeV thus they are selected with high efficiency (Figure 5.8a).

In Figure 5.9 kinematic distributions of reconstructed electrons passing the selection criteria for events passing the full event selection (Chapter 6) are shown, comparing distributions obtained from data events with those obtained from Monte-Carlo samples. The agreement is 10% or better. The results are in agreement with other ATLAS measurements of $Z \to e^- e^+$ events in 2011.

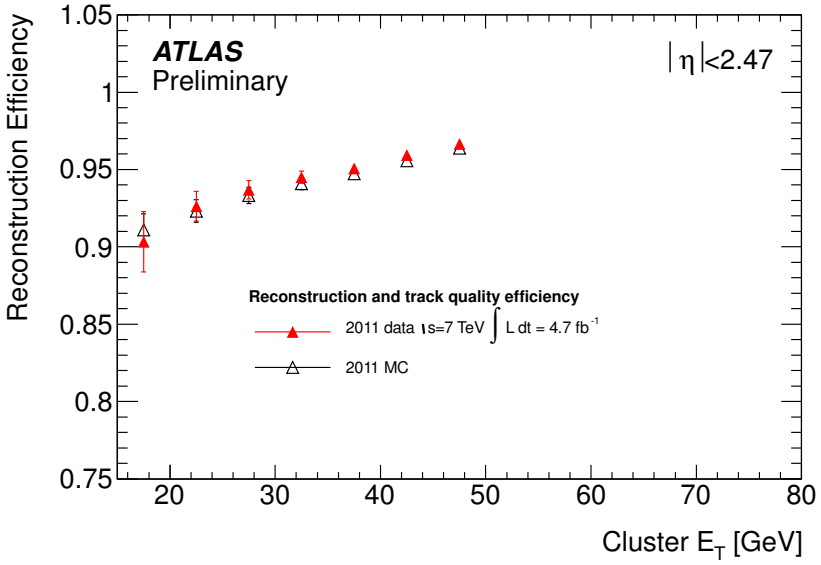

(a) ε vs. $E_{\perp}^{\text{cluster}}$

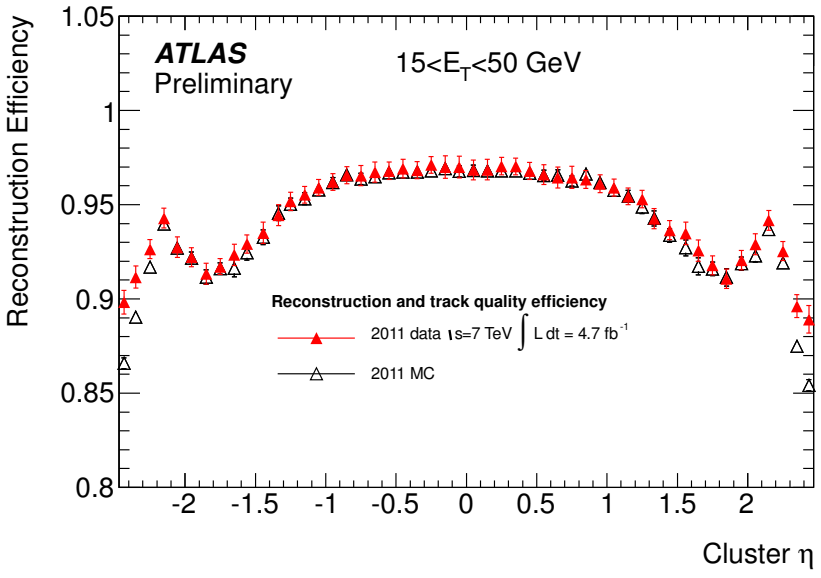

(b) ε vs. η^{cluster}

Figure 5.8.: Electron reconstruction efficiency, ε, measured in 2011 as function of the transverse energy (a) and pseudorapidity (b) of the electron [50], comparing results obtained from data (red filled triangles) and Monte-Carlo events (black non-filled triangles). The original image also contained corresponding points for 2012 data which were omitted from these plots for clarity.

5.3. Muons

The reconstruction algorithm used in this analysis utilises information from the inner detector as well as from the muon system (Chapter 4), which is why the thus reconstructed muons are called "combined" muons [51], or "STACO combined" muons. The great benefit of it is the rejection of muons produced in hadron decays that are part of a jet as well as an improved momentum resolution compared to muons reconstructed using only the muon spectrometer. Muon tracks are first reconstructed using only the muon chambers using a technique called "HOUGH transformation" [52] after which they are corrected for energy losses suffered by the transition of all previous sub-detectors and eventually extrapolated to the beam-spot. Each resulting muon track can be parametrised using the same constants of motion that are chosen for the track reconstruction in the inner detector (Section 5.1.1) resulting in a set of helix parameters, $\mathbf{T}_{MS}$. Reconstructed tracks (parametrised as $\mathbf{T}_{ID}$) in the inner detector of an event can thus be attempted to match a muon track by constructing a χ^2 measure:

$$\chi^2_{\text{match}} = (\mathbf{T}_{MS} - \mathbf{T}_{ID})^{\top}(C_{MS} + C_{ID})^{-1}(\mathbf{T}_{MS} - \mathbf{T}_{ID}) \tag{5.12}$$

where C_{MS} and C_{ID} denote the covariance matrices of the track measurement in the muon spectrometer and inner detector, respectively.

Hits

A series of quality cuts concerning hits in the inner detector segments used in the reconstruction are applied on the reconstructed muon

- If there was a b-layer hit to be expected (i.e. if the corresponding module was not flagged as dead): require at least one hit in the b-layer
- The sum of hits in the pixel detector and the number of dead pixel sensors passed by the muon-candidate has to be at least 1
- The sum of hits in the SCT and the number of dead SCT sensors passed by the muon-candidate has to be greater than 5

- The sum of modules of the pixel detector and the SCT in the trajectory of the muon-candidate not detecting a charged particle must be smaller than three

TRT: The reconstruction algorithm processing TRT information (pseudorapidity coverage $|\eta| < 2.0$) at times is unable to unambiguously assign a certain number of hits to a muon track candidate. These hits are called "outliers" in the sense of not necessarily attributable to the muon track in question. For all muon candidates, the fraction of outliers is calculated as such:

$$f_{\text{outliers}} = \frac{N_{\text{outliers}}^{\text{TRT}}}{N_{\text{hits}}^{\text{TRT}} + N_{\text{outliers}}^{\text{TRT}}} \tag{5.13}$$

where $N_{\text{outliers}}^{\text{TRT}}$ denotes the number of outliers and $N_{\text{hits}}^{\text{TRT}}$ the number of TRT hits identified for the muon candidate in question. The requirements to be met by the muon candidate are based on its pseudorapidity, $\eta(\mu)$, if $\eta(\mu) < 1.9$:

$$\begin{cases} N_{\text{hits}}^{\text{TRT}} + N_{\text{outliers}}^{\text{TRT}} > 5 \text{ and } f_{\text{outliers}} < 0.9 & \text{if } |\eta(\mu)| < 1.9 \\ N_{\text{hits}}^{\text{TRT}} + N_{\text{outliers}}^{\text{TRT}} < 6 \text{ or } f_{\text{outliers}} < 0.9 & \text{else} \end{cases} \tag{5.14}$$

Impact parameter

In order to select muon candidates that were very likely produced in the primary vertex a requirement on the longitudinal impact parameter with respect to the latter, z_0^{PV}, is applied:

- $z_0^{\text{PV}}(\mu) < 10$ mm

Kinematic cuts

The reconstruction efficiency of muons is dependent on its transverse momentum, $p_\perp(\mu)$ (and its pseudorapidity, $\eta(\mu)$).

Transverse momentum:

In order to select muons as inclusive as possible the cut on $p_\perp(\mu)$ is chosen such that it is as low as possible with respect to a saturated reconstruction efficiency (Figure 9.11). For the datasets used in this analysis this happens to be

- $p_\perp(\mu) > 20$ GeV

This value allows a muon selection with high efficiency of at least 95% (Figure 9.11).

Pseudorapidity: The reconstruction efficiency is comparably flat in terms of the muon's pseudorapidity and the cut on it is driven by the acceptance of the muon system:

- $|\eta(\mu)| < 2.4$

Comparing this value with Figure 9.11 it shows that muons are selected with an efficiency of at least 95%, except for the very central region ($|\eta| < 0.3$) where the number of MDT modules (Chapter 4) is relatively small.

In Figure 5.9 kinematic distributions of reconstructed muons passing the selection criteria for events passing the full event selection (Chapter 6) are shown, comparing distributions obtained from data events with those obtained from Monte-Carlo samples. The agreement is 10% or better. The results are in agreement with other ATLAS measurements of $\mathrm{Z} \to \mu^-\mu^+$ events in 2011 [53].

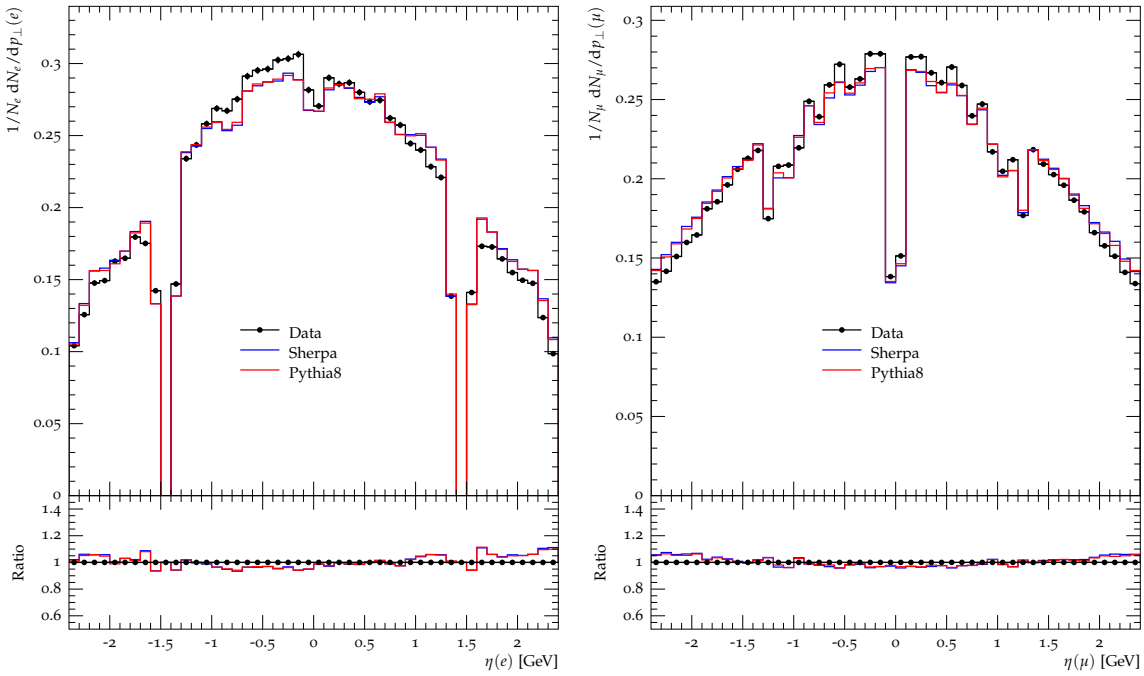

(a) Pseudorapidity

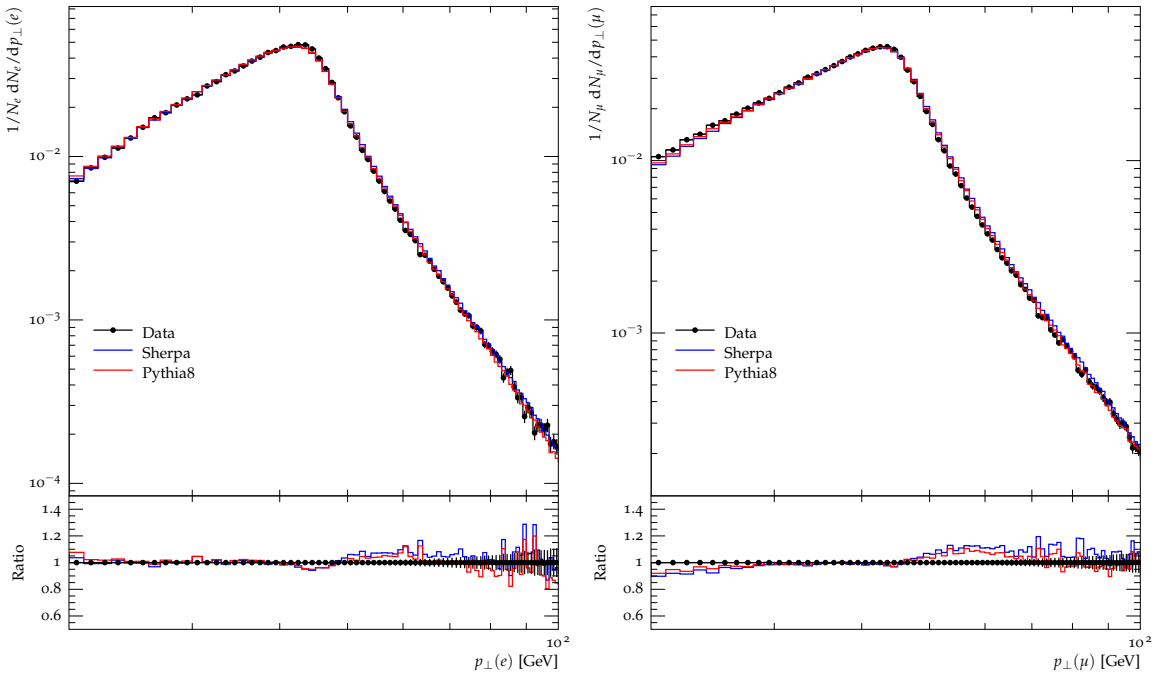

(b) Transverse momentum

Figure 5.9.: Reconstructed lepton properties comparing the pseudorapidity (a) and transverse momentum (b) distributions obtained from data (black dots) with those obtained from Monte-Carlo. The electron distributions are to be found on the left-hand side, the corresponding muon distributions on the right-hand side.

Chapter 6.

Event selection

In this chapter the event selections performed for the electron and muon channel analyses are described. The selection comprises the selection of lepton- and track-candidates. The latter is common for both channels. All selection criteria concerning physical objects are based on reconstructed objects and are hence common for simulated and actual data events.

The general flow of selecting an event for either channel consists of the following steps:

1. data quality selection
2. trigger selection
3. lepton selection, including kinematic cuts and object quality (Chapter 5)
4. di-lepton selection, including kinematic cuts and requirement for opposite charges

The data-taking with the ATLAS detector is at times hampered by partially inoperative sub-detectors, high-voltage failures and human error which is why a data quality working group collects information on the quality of recorded data. A fine segmentation of recorded data is done by defining so-called "lumi blocks" which are periods with stable data taking conditions. If a lumi block is considered of a quality good enough for physics analysis it is entered into a database, called "good run list" (GRL). Each recorded event is linked to exactly one lumi block which allows for the selection of "good" events using the unique combination of the run and event number assigned to each event and comparison of it with the information stored in the GRL. The good run list used in this analysis is `data11_7TeV.periodDtoH_DetStatus-v36-pro10_CoolRunQuery-00-04-08_WZjets_allchannels.xml` It includes good runs from `179710` to `184169` and is valid for the electron and the muon channel of this analysis. A graphical representation of the integrated luminosity and

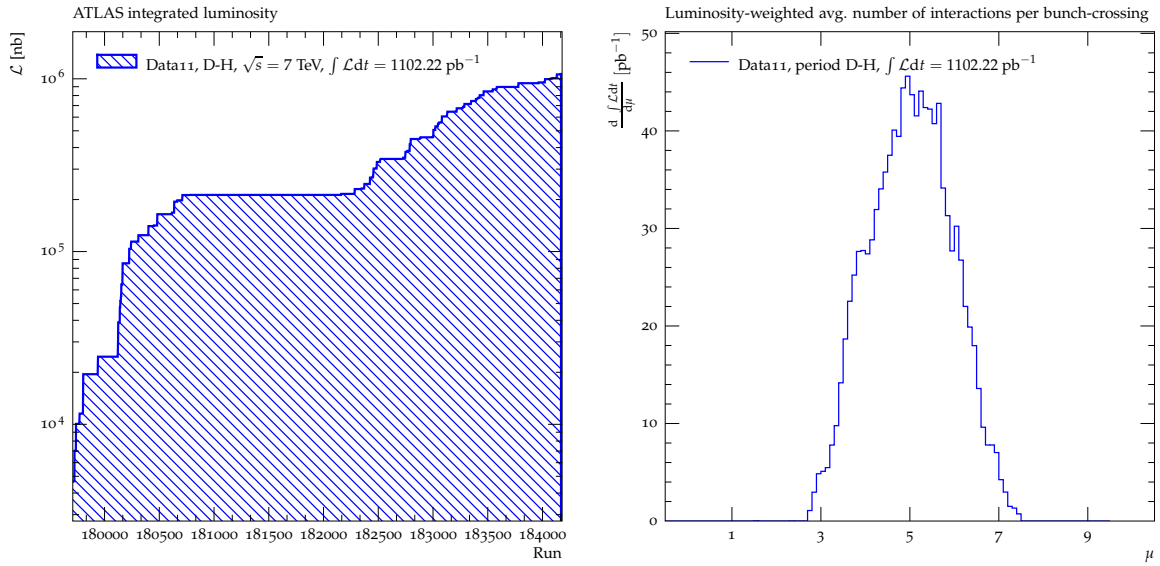

(a) Integrated luminosity as function of run-numbers.

(b) Integrated luminosity vs. μ

Figure 6.1.: Integrated luminosity and average number of interactions, μ, for the data period used in this analysis.

the mean number of interactions can be found in Figure 6.1. All further selections are specific to the electron and muon channel.

6.1. Electron channel selection

Events that passed the GRL but were recorded while there was a fault in the liquid-argon calorimeter (noise burst, Chapter 5) are rejected.

6.1.1. Trigger

The LVL1 trigger requires the registration of a bunch-crossing and two depositions of at least 7 GeV in the `ECAL` ("`L1EM7`"). The LVL2 trigger passes an event to the event filter if it finds at least one reconstructed electron with `medium` quality (explanation further down) in a region of interest (`L2_e12_medium`). The event filter itself accepts an event if the reconstruction algorithm suffices the trigger conditions summarised as `EF_2e12_medium` which require:

- two electron candidates (opposite- or same-sign)

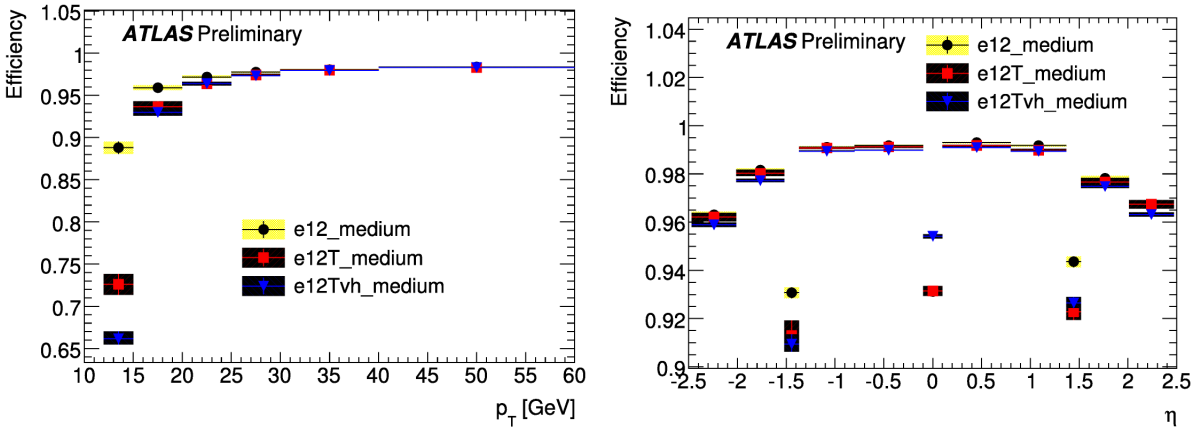

(a) (b)

Figure 6.2.: Electron trigger efficiencies [54] of the LVL2 single electron trigger items (`L2_e12_medium`) used by the di-electron trigger used in this analysis (`EF_2e12_medium`) as function of the reconstructed electron's transverse momentum (a) and pseudorapidity (b).

- with an energy deposition in the `ECAL` of at least 12 GeV each
- that satisfy the `medium` quality criteria

It should be noted that `EF_2e12_medium` is the lowest multi-electron trigger without prescaling available for 2011 data used in this analysis. The requirements for medium quality in the event filter are slightly more loose than the `medium++` requirements used for the actual electron selection in this analysis. The efficiency of the selection of single electrons (`L2_e12_medium`) used in the event filter was measured in [54]. The values obtained are above 95% for electrons with a transverse momentum of 20 GeV (Figure 6.2a) which is the reason for this analysis to require this cut also in the electron selection. The efficiency drops slightly for central electrons ($\eta \sim 0$) and those found in the crack region of the ECAL (Figure 6.2b). No publicly accessible plots for the HTL trigger efficiency of `EF_2e12_medium` are available. It can be stated though that the `EF_2e12_medium` efficiencies are very similar to those of `L2_e12_medium` shown in Figure 6.2.

6.1.2. Selection of reconstructed electrons

The selection criteria for electrons applied in this analysis were explained in detail in Section 5.2. They are briefly repeated in their logical order here:

1. Remove electron/positron candidates not reconstructed with the calorimeter based algorithm ("author")
2. Remove electron/positron candidates not passing the pseudorapidity selection ($|\eta(\mathrm{e})| \in [0, 2.4]/[1.37, 1.52]$)
3. Remove electron/positron candidates not passing the transverse momentum selection ($p_\perp(\mathrm{e}) > 20$ GeV)
4. Remove all electron/positron candidates flagged as "bad" (`OQ`=1446)

6.1.3. Final event selection

The final electron selection requires that the remaining number of electron candidates is exactly two, that they both fulfil the `medium++` criteria and that they are oppositely charged. For each event that not filtered out yet, the invariant di-electron mass, $M_{\mathrm{e^+e^-}}$, is calculated from the reconstructed e^+ and e^- four-vectors. If the event satisfies $M_{\mathrm{e^+e^-}} \in [66, 116]$ GeV, i.e. if it is likely to contain a Z-boson decay into an electron and a positron it is selected for this analysis and the event shapes are calculated from the selected tracks (Section 5.1.3).

A graph summarising the loss of events after each selection step ("cut-flow") can be found in Figure 6.3. It shows that the number of initially available data events ($N_{\mathrm{events}} = 1.42 \cdot 10^8$) dramatically drops by a factor of ~ 100 to 1.1 million events after the HLT selection (`EF_2_e12_medium`). The successive cuts reduce the number of events for further analysis to a total of 255593 events with the opposite charge requirement being the second most selective cut.

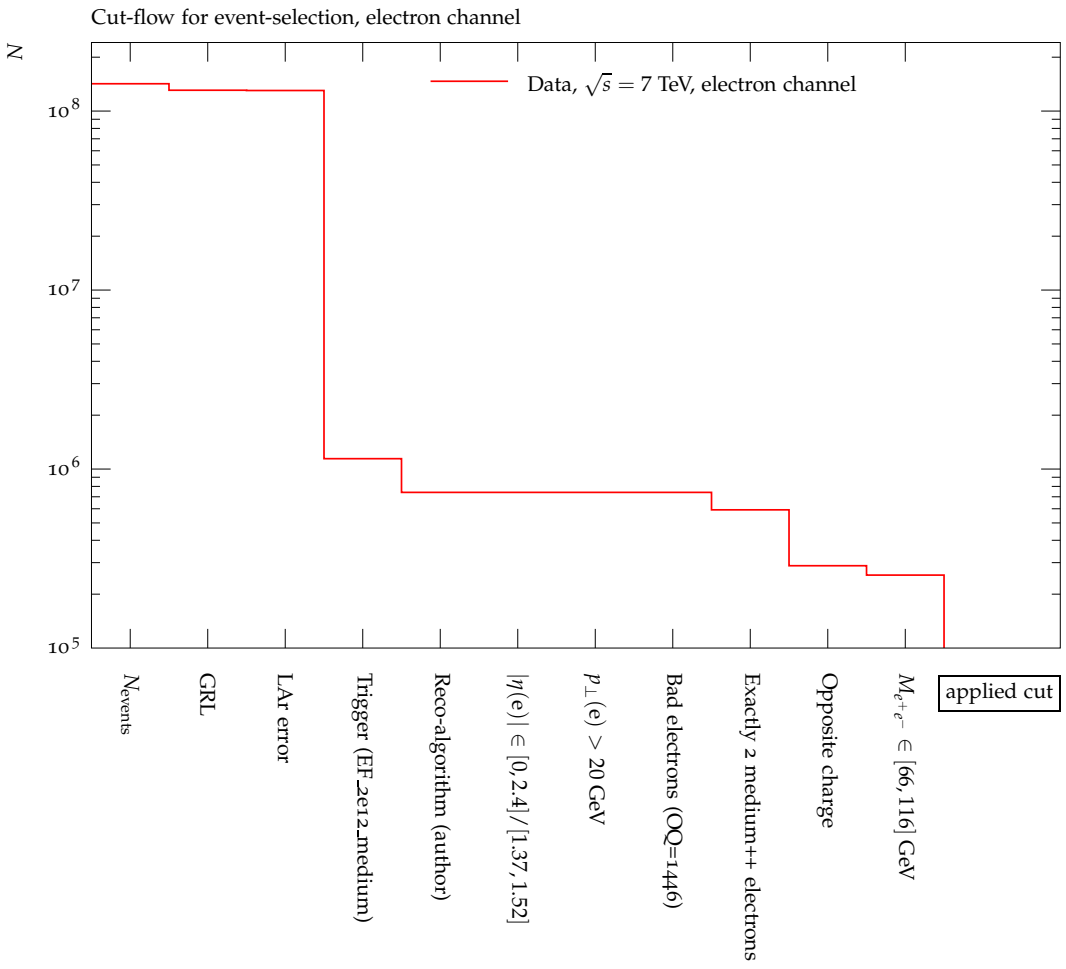

Figure 6.3.: Cut-flow of the event-selection in data for the electron channel.

6.2. Muon channel selection

6.2.1. Trigger

The chosen HLT, `EF_mu18_MG_medium`, for reconstructed muons follows the recommendation made and studies conducted by the muon trigger sub-group within the ATLAS experiment [55] and is at the very end of a trigger-chain seeded by the level-1 trigger `L1_MU11`. It has a threshold of 18 GeV, and is the lowest available unprescaled muon-trigger that uses combined information of the muon spectrometer and the inner detector. Thus the kinematic selection of muons of $p_\perp > 20$ GeV is within its efficiency-plateau (Figure 6.4). The trigger efficiency is of the order of 70% for central muons ($|\eta| < 1.05$) and of the order of 90% for all other muons ($1.05 < |\eta| < 2.4$). The trigger is a single-muon trigger and hence for an event to pass this selection criterion, two muons need to be in the event individually passing the requirements of `EF_mu18_MG_medium`.

6.2.2. Selection of reconstructed muons

The selection criteria for muons applied in this analysis is explained in detail in Section 5.3. They are briefly repeated in their logical order here:

1. Remove muon candidates not reconstructed as combined muons
2. Remove muon candidates not passing the hit requirements of the inner detector part of the muon track
3. Remove muon candidates not passing the impact parameter requirement ($z_0^{\mathrm{PV}}(\mu) <$ 10 mm)
4. Remove muon candidates not passing the transverse momentum selection ($p_\perp(\mu) >$ 20 GeV)
5. Remove muon candidates not passing the pseudorapidity selection ($|\eta| < 2.4$)

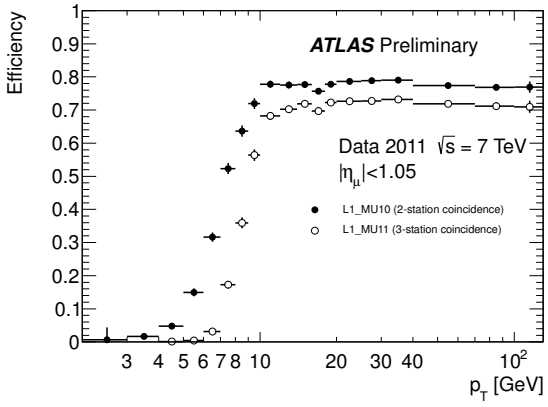

(a) LVL1, $\eta(\mu) < 1.05$

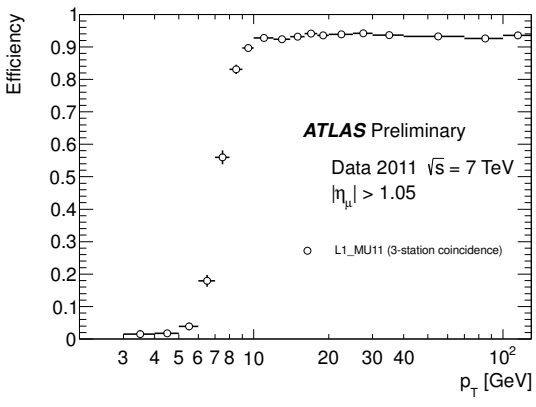

(b) LVL1, $\eta(\mu) > 1.05$

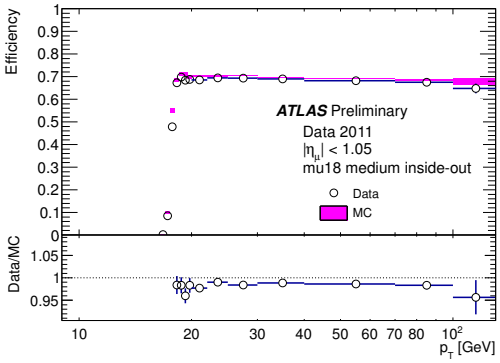

(c) EF, $\eta(\mu) < 1.05$

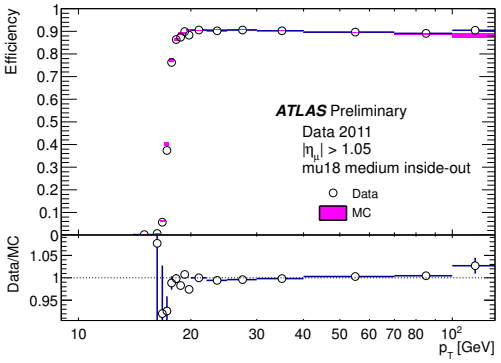

(d) EF, $\eta(\mu) > 1.05$

Figure 6.4.: Efficiencies of the Level-1 (`L1_MU11`) and event-filter (EF) single-muon triggers used in this analysis. Plots are taken from [55]

6.2.3. Final event selection

For events to pass the final Z-selection, it is required that exactly two muon candidates passing the aforementioned cuts but with opposite charges are present in the event and that their invariant mass, $M_{\mu^-\mu^+}$, suffices $M_{\mu^-\mu^+} \in [66, 116]$ GeV,

A graph summarising the loss of events after each selection step ("cut-flow") can be found in Figure 6.5. The number of initially available data events ($N_{\text{events}} = 1.3 \cdot 10^8$) is reduced by two-thirds after the (single muon) trigger selection. The reconstruction algorithm requirement further reduces the number of events by more than one order of magnitude to four million events. The next significant reduction is produced by the transverse momentum cut (518000 events). The following cuts gradually reduce the number of events to the final number of 411032 events available for this analysis.

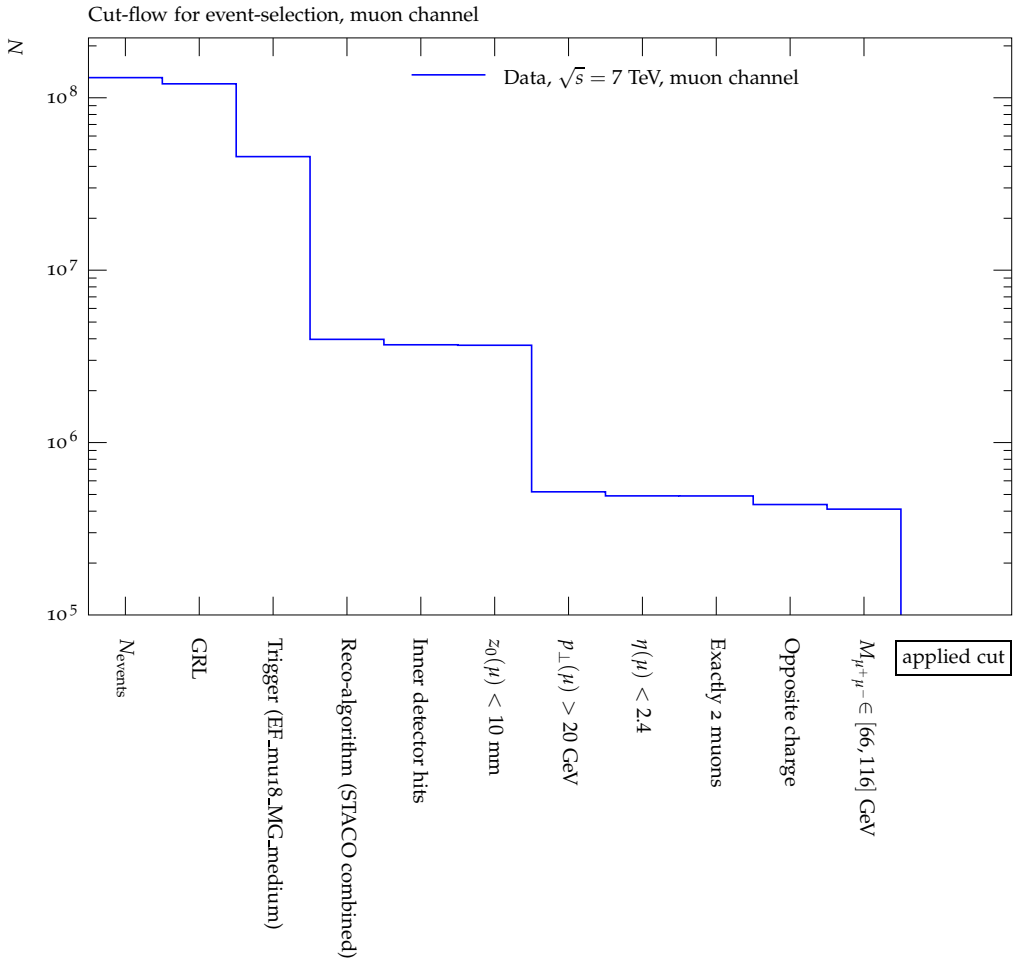

Figure 6.5.: Cut-flow of the event-selection in data for the muon channel.

Chapter 7.

Event shapes

In this chapter the measured observables are defined and motivated.

Historically, event shapes were proposed in order to measure the overall structure of particle collisions resulting in hadronic final states without the necessity to introduce computationally expensive and model-dependent jet algorithms and to extract the value of the strong coupling constant, α_S. The advantage of event shapes is that unlike jets they are model-independent observables. A large class of jet algorithms exists utilising different clustering strategies of hadrons involving arbitrary cut-off parameters. Thus a reconstructed jet object is depending on several assumptions.

Event shapes, however, represent well-defined event properties. Instead of trying to identify events that have e.g. a two-jet back-to-back signature by reconstructing and counting the QCD jets produced by emitted quarks or gluons, geometrical or topological properties of an event are measured that can e.g. be used to quantify the "jetiness" of an event.

7.1. Event shapes at electron-positron colliders

The first measurement of event shapes in e^-e^+ collisions was performed at the Mark1 experiment at the SPEAR storage ring in 1975 yielding evidence for the existence of quarks [56].

Further measurements of event shapes were carried out by experiments at the PETRA [57, 58], PEP [59], TRISTAN [60–62], SLC [63] and LEP(I/II) [64–66] experiments yielding valuable data at centre-of-momentum energies ranging from $\sqrt{s} = 8$ GeV to 208 GeV that were used

in fits of the strong coupling constant [67] exploiting the infra-red safety (computational robustness against very low energetic emissions) of event shapes.

7.2. Hadron collider event shapes

The principal problem when trying to define event shapes at hadron colliders is that due to the unknown fractional momentum of partons inside the colliding the hadronic beam-particles the longitudinal momenta of the objects undergoing interactions are unknown. Hence hadron-collider event shapes are defined only on the basis of transverse momenta.

7.2.1. Event shapes measured in this analysis

A large collection of observables were proposed by `Banfi`, `Salam` and `Zanderighi` in [68]. Since the purpose of the measurements described in this thesis is to provide input to the improvement of multiple-parton-interaction models in Monte-Carlo generators, it was chosen to measure only those event shapes that are most sensitive to changes of parameters of the models in question. The relevant study is described in [69]. The chosen observables will be discussed in the following paragraphs.

Charged particle multiplicity

The observable charged particle multiplicity, n_{ch}, essentially counts the number of selected tracks present in an event after removal of the lepton tracks. Especially the low-multiplicity region contains valuable information for tuning as will become evident when looking at comparisons with present models (Chapter 12).

Scalar sum of transverse momenta

This observable, $\sum_i p_{\perp,i} \equiv \sum p_{\perp}$, measures the scalar sum of transverse momenta of selected charged particles in an event after removal of the electrons. Thus, compared with n_{ch}, it also contains information on the kinematic configuration of an event, i.e. the produced amount of transverse momentum. Again, the low $\sum p_{\perp}$ bins contain valuable

information for tuning, especially about the interplay between MPI and beam-remnant activity.

Beamthrust

Beamthrust is an observable proposed by Stewart, Tackmann and Waalewijn [70]. Its definition is similar to that of $\sum p_\perp$ except that the transverse momenta of particles are weighted using their pseudorapidity, η:

$$\mathcal{B} = \sum_{i=1}^{n_{\text{ch}}} p_{\perp,i} \cdot e^{\,-|\eta_i|} \tag{7.1}$$

This means that contributions from particles in a forward and backward direction (large values of $|\eta|$) are suppressed with respect to particles emitted at central rapidities ($\eta \approx 0$).

Transverse thrust

Historically, Thrust has been among the first observables used to study the topology of events, particularly with regard to the presence of jets — without the necessity to run a jet-finding algorithm and with the benefit of being infra-red and collinear safe as contributions from soft particles with momenta $\to 0$ do not contribute and collinear splittings do not change the value of Thrust. The idea is that in each event an axis, $\vec{n}_T$ exists for which the projection of the momenta of particles becomes minimal. At electron-positron collider experiments, such as LEP, the three-momentum vectors can be used as the full kinematics of the incoming beam-particles are well known. At a hadron-collider such as the LHC, however, the longitudinal momenta of colliding partons are not known, thus only transverse momenta can be used in the definition of the transverse thrust, $\mathcal{T}$, as proposed by Banfi, Salam and Zanderighi [68]:

$$\mathcal{T} = \max_{\vec{n}_T} \frac{\sum_{i=1}^{n_{\text{ch}}} |\vec{p}_{\perp,i} \cdot \vec{n}_T|}{\sum_{i=1}^{n_{\text{ch}}} p_{\perp,i}} \tag{7.2}$$

The thrust axis, $\vec{n}_T$, is determined numerically using the algorithm described in [71].

In the limit of pencil-like events, i.e., if all particle momenta in the transverse plane are parallel or anti-parallel, (7.2) simply becomes

$$\mathcal{T} = \sum_{i=1}^{n_{\text{ch}}} \frac{|\vec{p}_{\perp,i}|}{p_{\perp,i}} = 1 \tag{7.3}$$

In the other extreme of a perfectly spherical event, i.e. an isotropic distribution of particles in an event ($|\vec{p}_{\perp,i}| = |\vec{p}_{\perp,i}| \; \forall \; i,j$), (7.2) turns into

$$\mathcal{T} = \frac{\int_0^{\pi} \cos\phi \, \mathrm{d}\phi}{\int_0^{\pi} \mathrm{d}\phi} = \frac{2}{\pi} \tag{7.4}$$

with ϕ being the angle between the thrust axis and a particle's momentum vector in the transverse plane. Hence, for all events, $\mathcal{T} \in [\frac{2}{\pi}, 1]$, holds, which allows to classify the topology of an event purely on the basis of its Thrust value.

Transverse minor

Minor is closely related to thrust. Once the thrust-axis of an event has been determined, the projections on the axis perpendicular to $\vec{n}_T$ can be calculated as well:

$$m_{\perp} = \frac{\sum_{i=1}^{n_{\text{ch}}} |\vec{p}_{\perp,i} \times \vec{n}_T|}{\sum_{i=1}^{n_{\text{ch}}} p_{\perp,i}} \tag{7.5}$$

The thrust axis $\vec{n}_T = (n_x, n_y, 0)$ and the beam direction $\vec{e}_z = (0,0,1)$ form the so-called "event-plane", $\vec{\Phi}$:

$$\vec{\Phi} = \vec{n}_T \times \vec{e}_z = (-n_y, n_x, 0) \tag{7.6}$$

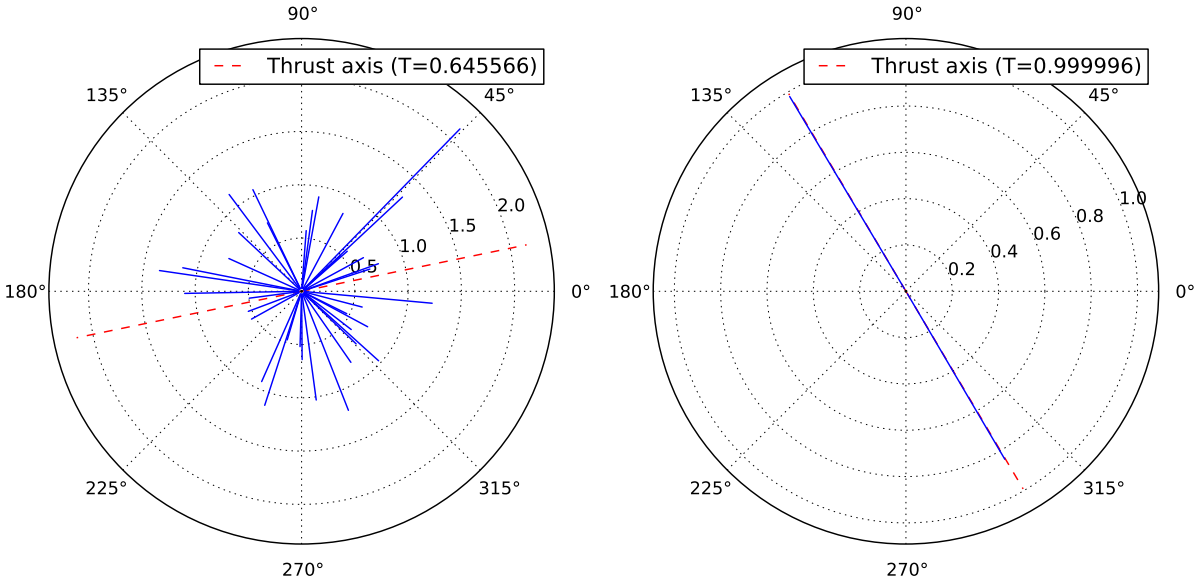

(a) Spherical event: $\mathcal{T} = 2/\pi$ **(b)** Pencil-like event: $\mathcal{T} = 1$

Figure 7.1.: Graphical representation of the spatial orientation in the transverse plane of selected charged particles (blue lines) for spherical (a) and pencil-like (b) events, demonstrating the usefulness of the event-shape variable transverse thrust in terms of classifying an event's overall topology. The length of the blue lines is proportional to the corresponding particles transverse momentum. The iteratively determined thrust-axis is depicted as dashed line.

the third component of which is zero. Since the third (longitudinal, z) component of the $\vec{p}_{\perp,i}$ and $\vec{n}_T$ is zero by construction as well, the cross-product in equation (7.5) only contains terms of the form $(0, 0, n_x p_y - p_x n_y)$. Thus transverse minor measures the amount of activity outside of the event-plane defined by $\vec{\Phi}$. Hence the value of $m_\perp$ is 0 for perfectly pencil-like events ($\mathcal{T}$ =1) and reaches its maximum of $\frac{2}{\pi}$ for perfectly spherical events ($\mathcal{T} = \frac{2}{\pi}$).

F-Parameter

The F-Parameter of an event is the hadron-collider equivalent to the C- and D-parameters often measured at e^-e^+ colliders. The calculation requires to first build the transverse momentum tensor M^{lin} of the (charged) particles in an event:

$$M^{\text{lin}} = \sum_i \frac{1}{p_{\perp,i}} \begin{pmatrix} p_{x,i}^2 & p_{x,i}p_{y,i} \\ p_{x,i}p_{y,i} & p_{y,i}^2 \end{pmatrix} \tag{7.7}$$

which is solved for it's eigenvalues $\Lambda_{1,2}$. The F-Parameter of an event is calculated from the ratio of the smaller and the larger eigenvalue:

$$F = \frac{\Lambda_2}{\Lambda_1} \quad \text{with} \quad \Lambda_1 \geq \Lambda_2 \tag{7.8}$$

In an extreme case of a perfectly pencil-like event with two particles $(p, 0, 0)$ and $(-p, 0, 0)$, M^{lin} becomes

$$\begin{pmatrix} 2p & 0 \\ 0 & 0 \end{pmatrix} \tag{7.9}$$

resulting in the eigenvalues $\lambda_1 = 2p$ and $\lambda_2 = 0$ and thus an F-Parameter of $F = \frac{\lambda_2}{\lambda_1} = 0$ which defines the lower boundary of possible values of F.

If there are for example two multiple-parton interactions overlapping in an event, each of which yielding a perfectly balanced di-jet structure ($\vec{p}_1 = -\vec{p}_2$), the possible values of F-Parameter can be studied as function of the angle between the two di-jet axes, Φ. Choosing one of the systems to have particles with transverse momentum vectors $(p_1, 0)$ and $(-p_1, 0)$, the other can be parametrised as $(p_2 \cos\Phi, p_2 \sin\Phi)$ and $(-p_2 \cos\Phi, -p_2 \sin\Phi)$. Thus, equation (7.7) becomes:

$$M^{\text{lin}} = 2 \begin{pmatrix} p_1 + p_2 \cos^2\Phi & p_2 \sin\Phi \cos\Phi \\ p_2 \sin\Phi \cos\Phi & p_2 \sin^2\Phi \end{pmatrix} \tag{7.10}$$

Exploiting the symmetry of M^{lin}, the eigenvalues (after some simplifications) can be written as

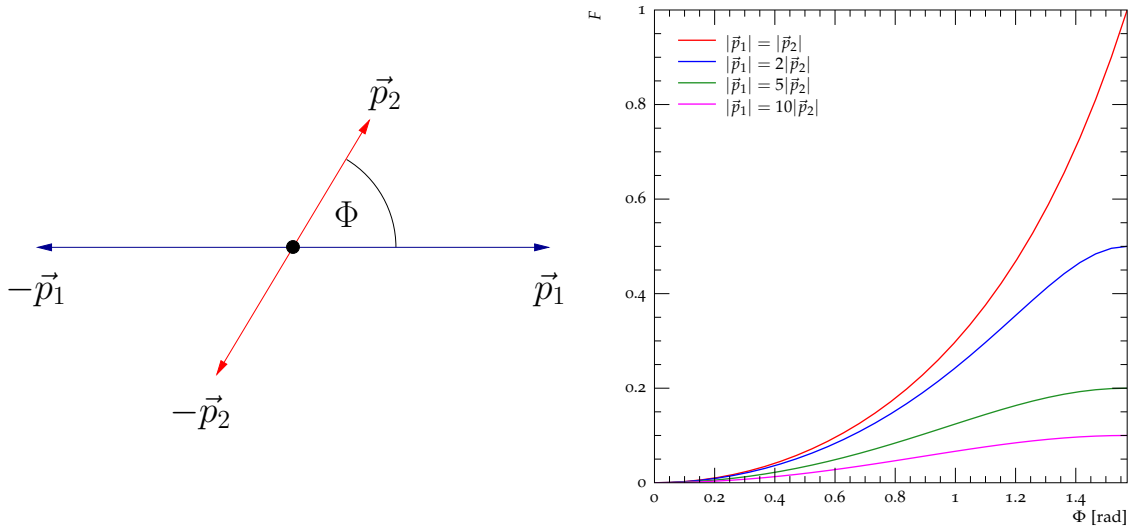

Figure 7.2.: Illustration of F-Parameter for two exactly balanced pairs of particles overlapping in an event (left hand side). The figure on the right hand side shows the dependence of F-Parameter as function of the angle between the dijet systems, Φ, for several scenarios concerning the ratio of the absolute values of $\vec{p}_1$ and $\vec{p}_2$. The larger the F-Parameter of an event the more spherical it is, while pencil-like events are found in the vicinity of 0.

$$\lambda_{1,2} = \frac{p_1 + p_2}{2} \pm \sqrt{\frac{(p_1 + p_2)^2}{4} - p_1 p_2 \sin^2 \Phi} \tag{7.11}$$

which in the case of $\Phi = \frac{\pi}{2}$ and $|\vec{p}_1| = |\vec{p}_2| \equiv p$, i.e. two orthogonal di-jet pairs of same momentum, yields $\lambda_{1,2} = p$, thus giving $F = 1$.

Setting $\Phi = 0$ in equation (7.11) always results in $F = 0$, regardless of the absolute values of the transverse momenta.

The F-Parameter values derived from equation (7.11) are shown as function of Φ for four different scenarios, demonstrating that the F-Parameter of an event allows a classification in terms of it being spherical or pencil-like but without the necessity to introduce/calculate a particular axis.

Spherocity

The spherocity of an event is closely related to the Sphericity [68, 72] but does not require a minimisation algorithm. It is formally defined as

$$S = \frac{\pi^2}{4} \min_{\vec{n}=(n_x,n_y,0)^\top} \left(\frac{\sum_i |\vec{p}_{\perp,i} \times \vec{n}|}{\sum_i p_{\perp,i}} \right)^2 \tag{7.12}$$

trying to find the spherocity axis, $\vec{n}$, that minimises the above expression. The calculation is dramatically simplified do to the observation that $\vec{n}$ always coincides with one of the transverse momentum vectors $\vec{p}_{\perp,i}$ [68]. Hence it is sufficient to iterate over the charged particles to find the axis that minimises the expression in equation (7.12). It is thus computationally less expensive and more robust than Thrust, which spherocity is highly anti-correlated with. Figure 7.3 shows the thrust- and spherocity axes of some Monte-Carlo events. In the case of pencil-like events, the two axes almost coincide, while this is not necessarily the case for spherical events.

The correlation between different event-shape variables is explored in more detail in the following.

7.2.2. Correlation of event shapes

As mentioned earlier, the event shapes transverse thrust, transverse minor, Spherocity and F-Parameter are highly (anit-) correlated. In Figure 7.2((a)-(f)) scatter plots of all possible combinations of these observables are shown in three equidistant and disjoint Thrust ($\Delta\mathcal{T} = \frac{2-\pi}{3\pi}$) intervals obtained from the Pythia8 $\mathrm{Z} \to \mathrm{e}^+\mathrm{e}^-$ signal sample ($p_\perp(\mathrm{Z}) < 6\ GeV$, i.e. high sensitivity to MPI). In addition, the correlation coefficient for the studied sample of events is given in the corresponding legends. The absolute value of the latter is generally found to increase with the Thrust value of events, almost reaching -1 for the correlation of the F-Parameter and (transverse) thrust.

The other observables (N_{trk}, $\sum p_\perp$, Beamthrust) measured in this analysis are highly correlated with one another by construction, reaching a positive correlation of almost 100% in all cases.

More interesting is the correlation of those observables with e.g. thrust. Whilst for events with relatively small thrust values (spherical events) the correlation is very weak (order of 10%), it rises to -44% in the case of the correlation between thrust and N_{trk} (Figure 7.3g). This indicates that a high thrust value is likely due to di-jet-like events.

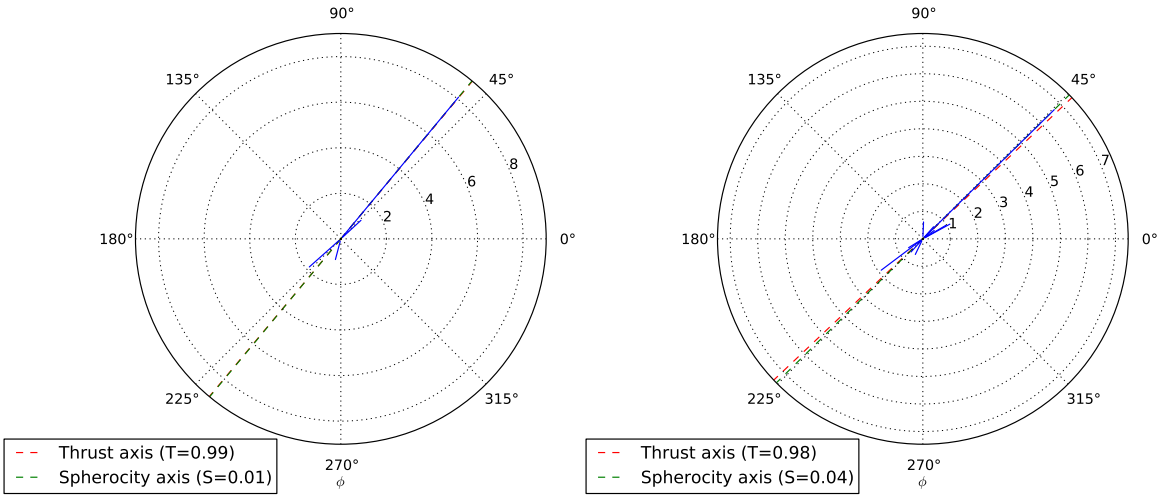

(a) Pencil-like events

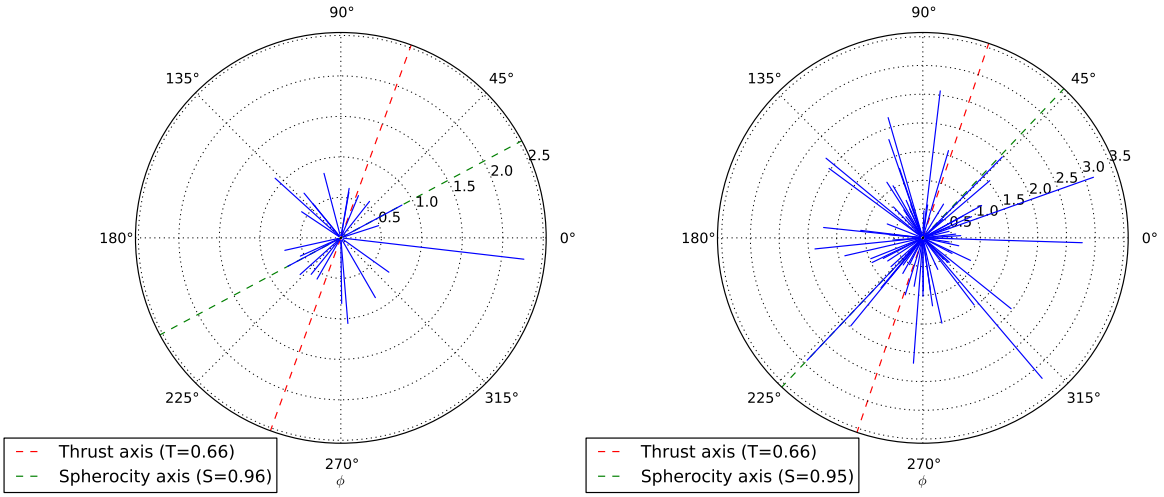

(b) Spherical events

Figure 7.3.: Event-displays of Monte-Carlo events in the transverse plane ($z = 0$). The transverse momentum vectors of charged particles is shown as blue lines, the length of which indicate the $p_\perp$ of the corresponding particle in GeV. For pencil-like events (a) the thrust (red) and spherocity (green) axes (dashed lines) are almost identical. In the case of spherical events this is not necessarily the case (a).

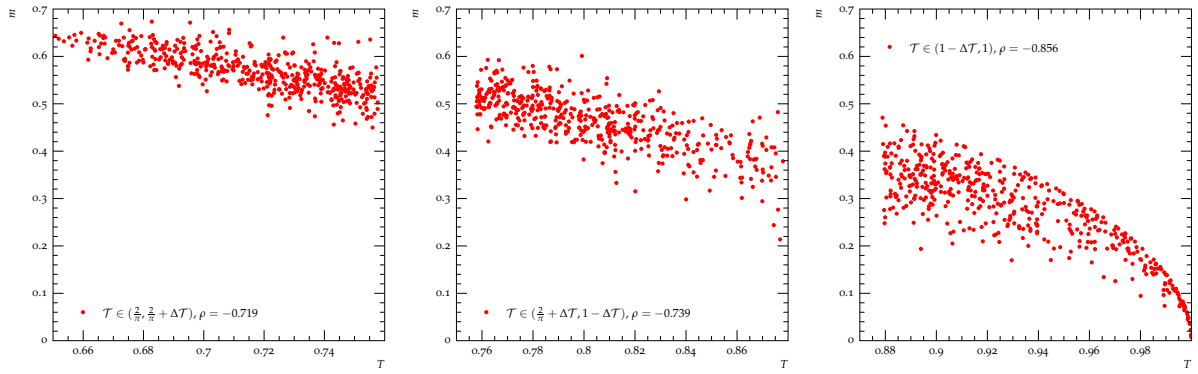

(a) Minor vs. Thrust

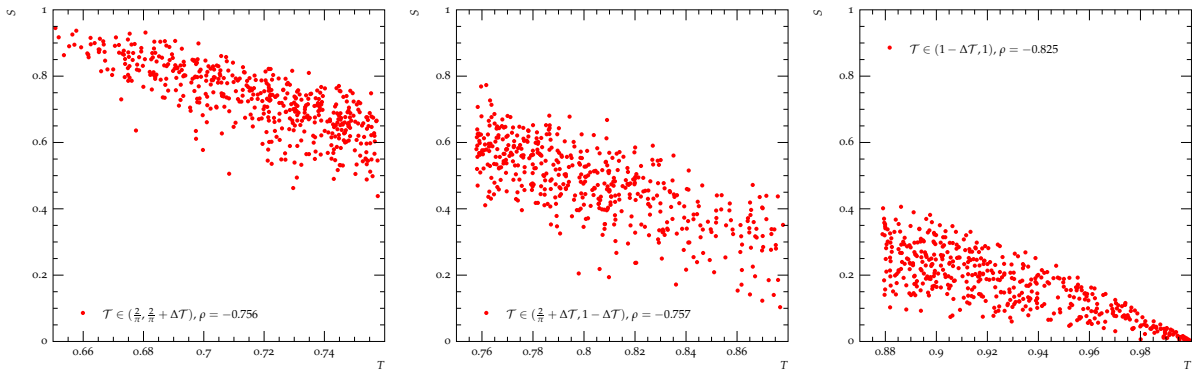

(b) Spherocity vs. Thrust

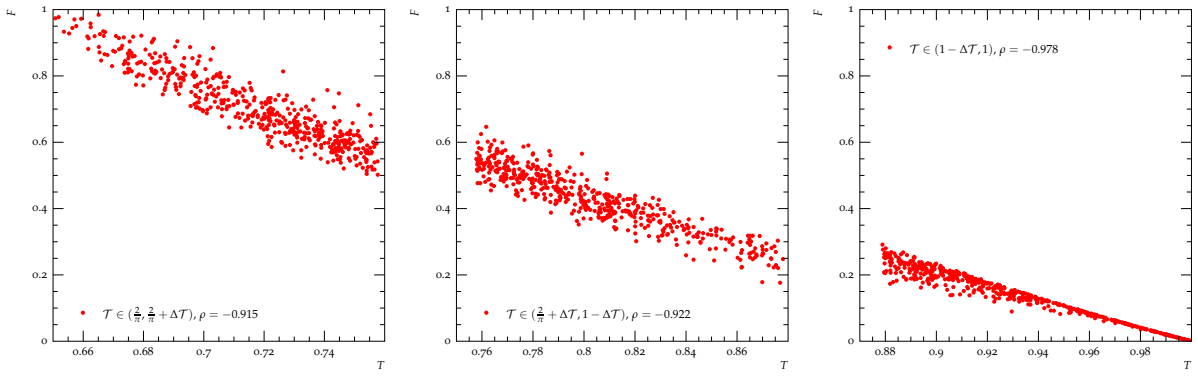

(c) F-Parameter vs. Thrust

Figure 7.4.: Correlation of event shapes. Left column: small Thrust values. Central column: intermediate Thrust values. Right column: large Thrust values. $\Delta\mathcal{T} = \frac{2-\pi}{3\pi}$. 500 randomly chosen Monte-Carlo (Pythia signal sample of the electron channel) events fulfilling $p_\perp(\mathrm{Z}) < 6$ GeV as well as individual Thrust requirement have been used for each plot (red dots). The correlation coefficient, ρ, was calculated using 100000 events each.

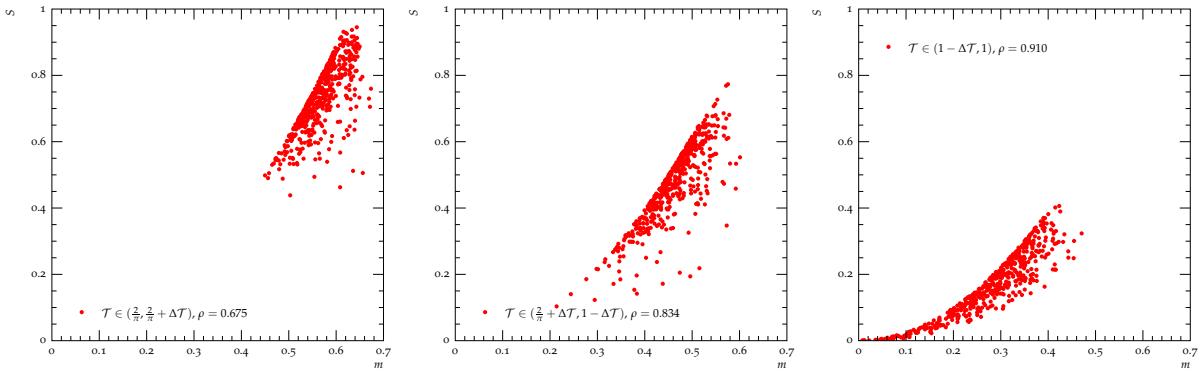

(d) Spherocity vs. Minor

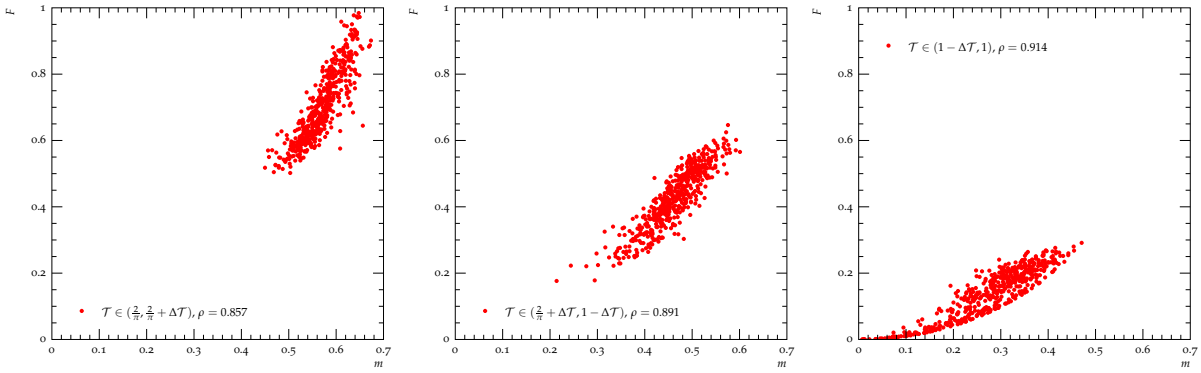

(e) F-Parameter vs. Minor

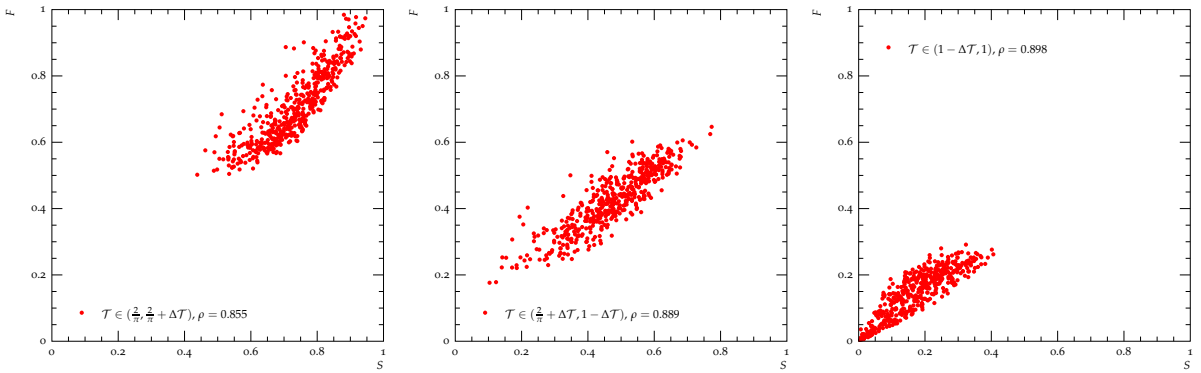

(f) F-Parameter vs. Spherocity

Figure 7.3.: Correlation of event shapes. Left column: small Thrust values. Central column: intermediate Thrust values. Right column: large Thrust values. $\Delta\mathcal{T} = \frac{2-\pi}{3\pi}$. 500 randomly chosen Monte-Carlo (Pythia signal sample of the electron channel) events fulfilling $p_\perp(\mathrm{Z}) < 6$ GeV as well as individual Thrust requirement have been used for each plot (red dots). The correlation coefficient, ρ, was calculated using 100000 events each.

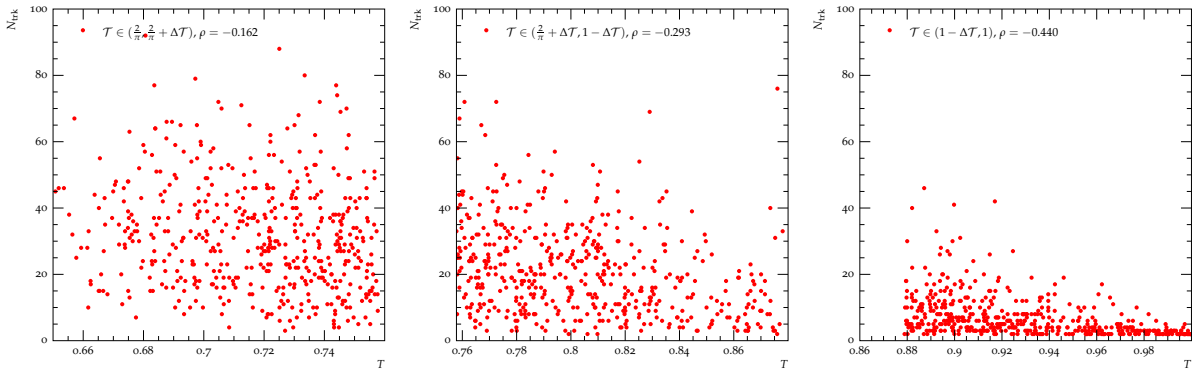

(g) N_{trk} vs. Thrust

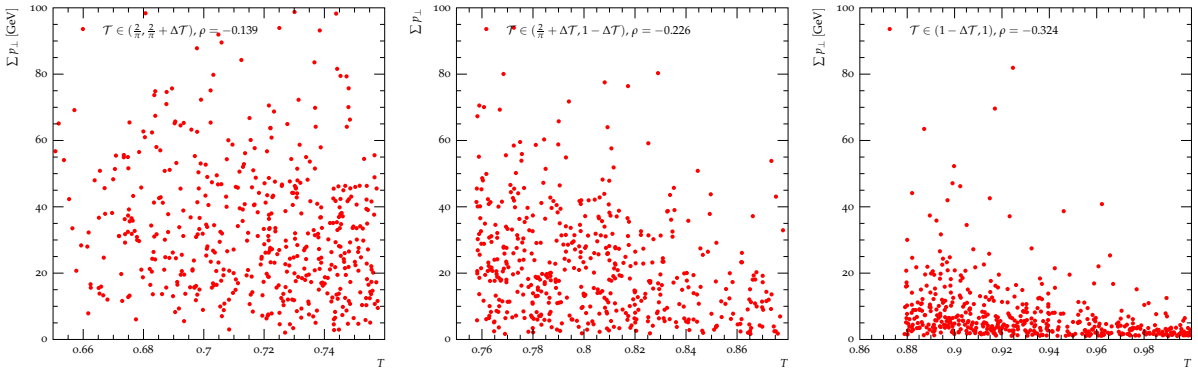

(h) $\sum p_\perp$ vs. Thrust

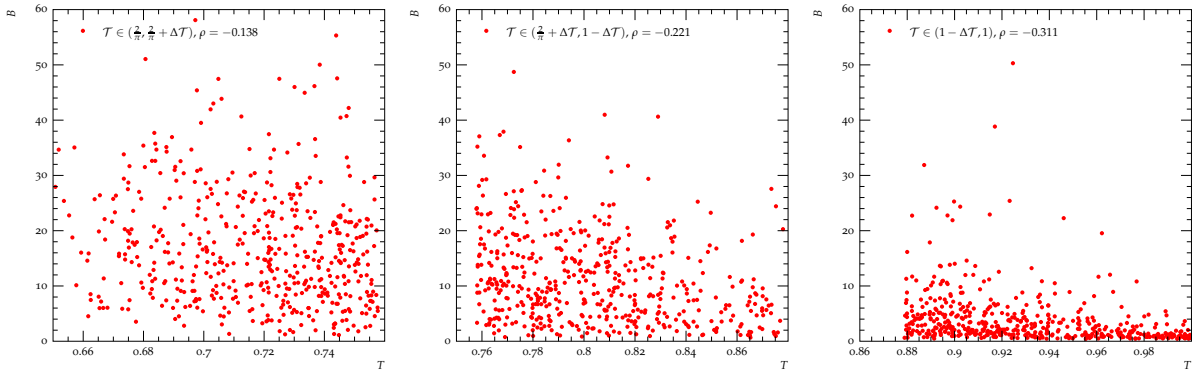

(i) Beamthrust vs. Thrust

Figure 7.2.: Correlation of event shapes. Left column: small Thrust values. Central column: intermediate Thrust values. Right column: large Thrust values. $\Delta\mathcal{T} = \frac{2-\pi}{3\pi}$. 500 randomly chosen Monte-Carlo (Pythia signal sample of the electron channel) events fulfilling $p_\perp(\text{Z}) < 6$ GeV as well as individual Thrust requirement have been used for each plot (red dots). The correlation coefficient, ρ, was calculated using 100000 events each.

7.2.3. Event shapes and the number of parton-parton interactions

It has been argued earlier, that the measured observables in this analysis will yield valuable input for the improvement of MPI models. Using MC generator information it is possible to count the number of MPI scatters, which are implemented as $2 \to 2$ interactions in the present models (Sherpa, Pythia8). The plots of Figure 7.3 show some of the event shapes differential in the number of MPI scatters, N_{MPI}. They were obtained using a `Rivet` [73] implementation of the event shapes measured in this analysis, capable of counting the MPI scatters in the Pythia8 signal samples ($\mathrm{Z} \to \mathrm{e}^{+}\mathrm{e}^{-}$ was used here). Figure 7.3 demonstrates that especially observables like transverse thrust allow to distinguish between events with more or less parton-parton scatters. The measured and unfolded event-shape distributions should allow to improve the composition of simulated events in terms of the number and orientation of multiple parton interactions to improve agreement of MC with data.

7.2.4. Previous measurements

Up to this point event shapes have not been extensively measured at hadron colliders. So far, one measurement from ATLAS [74] has been published that also investigates event shapes measured from tracks but in so-called Minimum Bias events, i.e. an environment where the hard sub-process does not decouple in terms of colour from multiple parton interactions (Chapterchap:introduction).

Further, a CMS measurement of the Thrust distribution calculated explicitly from the Z-boson and jets for events containing at least one jet ($p_{\perp}(\mathrm{jet}) > 50$ GeV) and a Z-boson [75] has been published. Another CMS measurement studies event shapes in multi-jet topologies with $p_{\perp}\mathrm{jet} > 90$ GeV [76]. Lastly, another high-$p_{\perp}$ measurement has been performed using jets ($p_{\perp}(\mathrm{jet}) > 250$ GeV) [77]. The scope of the high-$p_{\perp}$ measurements is to gain insight into the hard sub-process which is orthogonal to the aim of this analysis, thus showing the versatility of event shapes at hadron colliders.

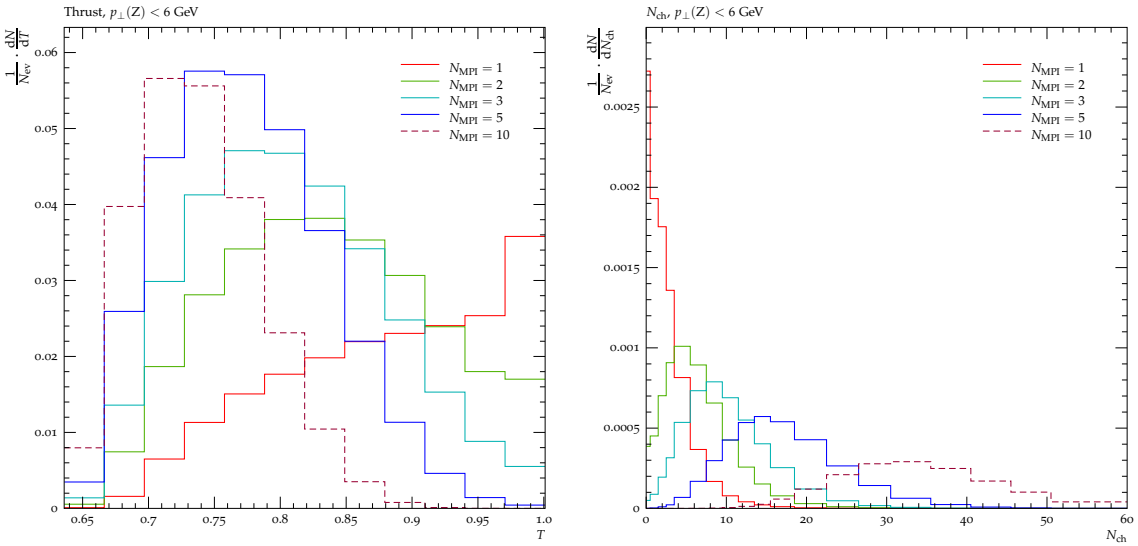

(a) $p_\perp(Z) < 6$ GeV

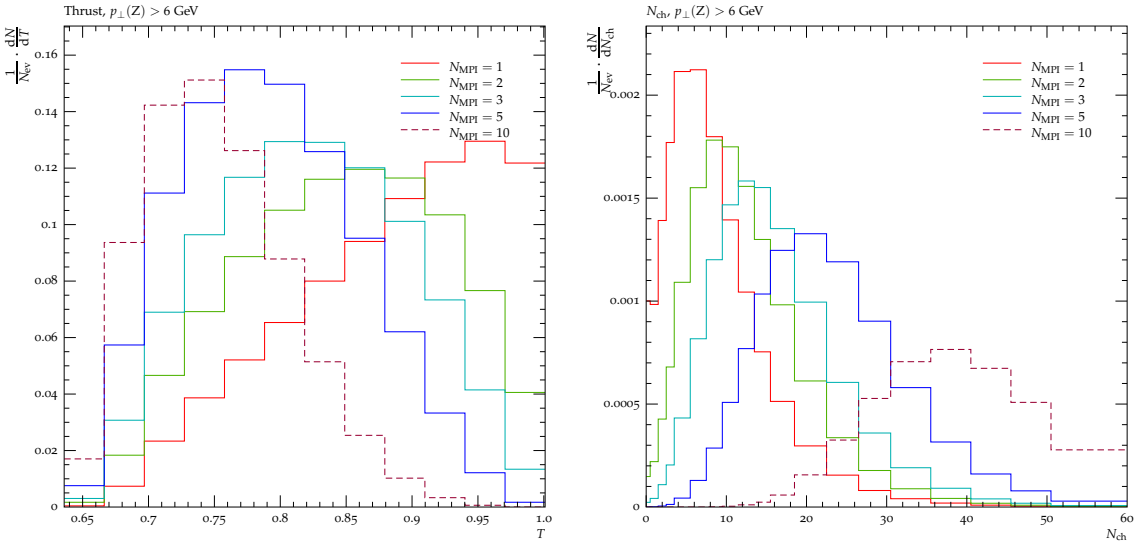

(b) $p_\perp(Z) > 6$ GeV

Figure 7.3.: Comparison of event shapes obtained from (Pythia8 $Z \to e^+e^-$) events with a specific number of multiple parton interactions (MPI), N_{MPI}, in a low $p_\perp(Z)$ phase-space region (a) and the disjoint counterpart $p_\perp(Z) > 6$ GeV. The plots on the left hand side demonstrate the usefulness of the observable Thrust when it comes to the distinction of spherical and pencil-like events. The latter are found in bins of $\mathcal{T}$ close to one, which dominate the distribution of events with $N_{MPI} = 1$.

Chapter 8.

Monte Carlo generators

Monte-Carlo (MC) generators are very important tools in particle-physics analyses. Among other tasks, they are used to predict background contributions, quantify detector efficiencies and resolutions. As such, they play a crucial role in the correction for detector effects (unfolding).

In order to obtain simulated events precise enough for the LHC physics programme general-purpose Monte-Carlo generators are used. These programs are able to simulate proton-proton collisions with up to several thousand particles in the final state. The starting point are perturbative (mostly leading order) calculations of the hard sub-process that are implemented as processes with two incoming partons, further requiring the sampling of parton distribution functions (PDF). The number of outgoing particles in the hard sub-process in the production of Z-bosons (signal process in this analysis) differs between the generators used. While Pythia8 does not produce any additional partons, Sherpa generates up to five. The high-multiplicity final states present in data are obtained using various parton shower approximations (QED and QCD) as well as phenomenological models for multiple parton interactions and eventually the transitions of systems generated by the previous steps into final state hadrons (fragmentation, hadronisation). Table 8.1 gives an overview of components typically found in general-purpose MC generators with a classification as to their physical motivation/precision. The key to successful computation of high-energy physics collisions is the factorisation [78] theorem[1]. It allows to write the most general formula for the calculation of the cross-section of an interaction of the type $ab \to n$ [79]:

[1] It is a theorem that has been proven for the Drell-Yan process.

	preturbative calculation	approximation	phenomenology
Hard cross-section	○		
Primordial $k_\perp$		○	
ISR shower		○	
FSR shower		○	
QED shower		○	
MPI			○
Hadronisation			○

Table 8.1.: Overview of Monte-Carlo generator components. Only the hard cross-section calculation is perturbatively calculated (fixed order). All other components are based on approximations or phenomenological model assumptions that introduce parameters.

$$\sigma_{ab\to n} = \sum_{a,b} \int_0^1 \mathrm{d}x_a \mathrm{d}x_b f_{a/A}(x_a, \mu_F^2) f_{b/B}(x_b, \mu_F^2) \hat{\sigma}_{ab\to n}(\hat{s}, \mu_F^2, \mu_R^2) \tag{8.1}$$

where x_a and x_b are the momenta of partons a and b relative to the momenta of the incoming protons A and B in the infinite momentum frame. With s being the square of the centre-of-mass energy of the colliding proton-proton system, $\hat{s}$ can be written as

$$\hat{s} = x_a x_b s \tag{8.2}$$

The partonic cross-section $\hat{\sigma}_{ab\to n}(\hat{s}, \mu_F^2, \mu_R^2)$ is in addition to $\hat{s}$ also depdendent on the renormalisation (Chapter 2) scale μ_R and the factorisation scale μ_F. The latter will be explained in more detail in the next section.

8.1. Factorisation

Factorisation allows to split perturbative and non-perturbative parts of the simulation of e.g. a proton-proton collision by introduction of a factorisation scale, μ_F, which the calculation of $\hat{\sigma}$ and is dependent on. The dependence is, however, the smaller the higher

the perturbative order is. The present day situation is that the most commonly used MC generators are using leading order (LO) calculations such that the factorisation scale dependence of $\hat{\sigma}$ and therefore of σ is important. The value of μ_F itself can not be chosen from first principles, it is usually set to a value that has proven to yield results of the full simulation that describe experimental data.

In a typical hadron-hadron collision at the LHC where the hard sub-process (largest momentum transfer parton-parton scattering) produces an object such as a Z-boson, one is confronted with physics happening at two different scales. The initial partons, decribed by a PDF, live at a scale of the proton mass, m_P, while the hard-matrix element is at a much higher scale, in this case the mass of the Z-boson, m_Z.

The low-scale part of the process introduces calculatory problems due to the large values of α_S that arise from the running coupling of the latter, effectively preventing the application of perturbative methods. The currently only known technique to circumvent this is the application of the factorisation theorem which allows to split (factorise) the calculation of the cross-section into a perturbative part (partonic cross-section, $\hat{\sigma}$) at the scale m_Z and a non-perturbative part, the PDFs, $f_{a/b}(x, \mu_F)$ at the proton mass, m_P, in the example of a Z-boson production at the LHC. For instance a very soft (low energy) and/or collinear radiation of a gluon off of a quark taking part in the hard sub-process leads to divergences that can either be counted in the matrix element of as part of the proton. By defining it as part of the proton the divergent part of the calculation can be absorbed in the non-perturbative parton distribution functions (PDF).

Factorisation requires the introduction of an a-priori arbitrary factorisation scale, μ_F, which determines at what scale the calculation is split into the perturbative and the non-perturbative part. The left hand side of equation (8.1) must be independent from μ_F. The arbitrariness of the choice of μ_F is diminished by the fact that the partonic cross-section is calculated at fixed order in perturbation and the logarithmic terms in $\hat{\sigma}$ are of the structure $\log\left(\frac{m_Z}{\mu_F}\right)$. These logarithms appear in all order of the perturbation series and are hence required to be small such that the validity of the fixed order result does not suffer from large higher-order corrections. Thus μ_F is prudently chosen close to the scale of the hard process, $Q^2 = -q^2 = m_Z^2$ with q being the (four-) momentum transfer of the hard process.

The resulting $\hat{\sigma}$ thus describes the physics of all the matrix elements for a particular process happening at the fixed order chosen between the factorisation scale and the scale of the hard process. The connection of the partons at (μ_F, x) to the non-perturbative physics

at the scale of the PDFs is made using the DGLAP evolution equation (Dokshitzer-Gribov-Lipatov-Altarelli-Parisi).

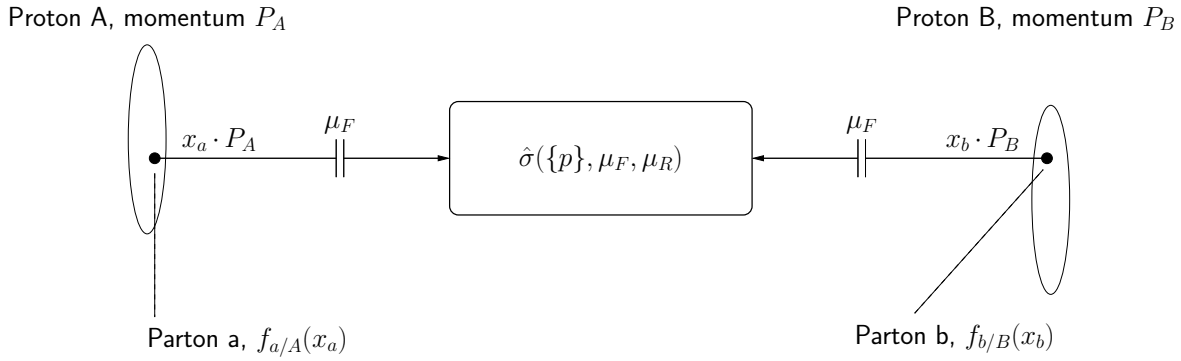

Although the latter is perturbatively calculable, further input from measurements ,namely the PDFs, $f(x)$, is needed. At both scales, QCD is the underlying theory and QCD tells us how to connect the evolution of a parton from a non-perturbative scale (proton mass) to the scale of the scattering process, Q^2, that is perturbatively calculated via the hard matrix-element.

8.2. Parton distribution functions (PDF)

The choice of parton distribution functions has been shown to be non-significant in terms of the description of observables sensitive to MPI. In an extensive tuning study performed by ATLAS [80] testing 9 different PDFs it was found that although changing the PDF always requires a proper retuning of the MPI parameters, the obtained agreement with data is of comparable quality.

Both MC generators used in this analyis utilise the (leading order) PDF set 6L1 obtained by CTEQ [81]. Figure 8.1 shows the corresponding parton distribution for $Q^2 = 91$ GeV and demonstrates the dominance of the gluon distribution function for low values of x.

8.3. Matrix element

When running a Monte-Carlo generator, the user has to define the specific hard process which is of the type $2 \to n$ where n corresponds to the number of (tree-level) legs (outgoing parton lines) of the matrix elements to be used. The first step in the simulation of a $2 \to n$ process is the randomly chosen point in the phase-space, $\Phi_{2 \to n}$, which has the

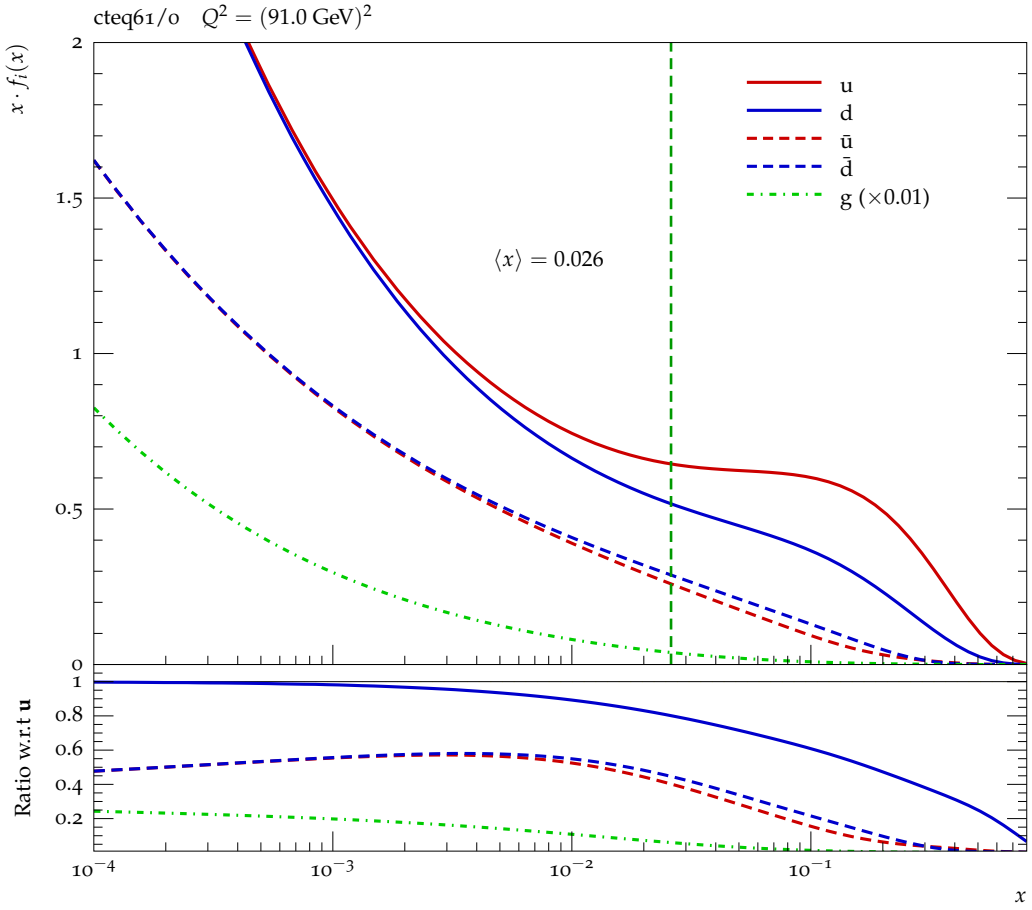

Figure 8.1.: Parton distributions functions (PDF) relevant for the production of a Z-boson, $Q^2 = (91\text{GeV})^2$, in proton-proton collision at $\sqrt{s} = 7$ TeV. The graphs show the central values of $x \cdot f_i(x)$ for $i = u, d, \bar{u}, \bar{d}, g$ of PDFs extracted by the CTEQ group in the PDF-set CTEQ6L1 [81] which was used in the Monte-Carlo samples described in this analysis. The mean value of x, $\langle x \rangle$, was extracted from those samples and found to be 0.026, leading to a mean $\hat{s}$ of $(91\ \text{GeV})^2$, consistent with predominant s-channel production of Z-bosons ($Q^2 = xy\hat{s}$).

dimension $3n + 2$ made up of the n momentum vectors of the outgoing legs (masses are not considered random) and the incoming BJÖRKEN variables x_1 and x_2 of the incident partons. The matrix element is then evaluated for $\Phi_{2\to n}$.

In the case of the Pythia8 Monte-Carlo samples only the matrix element for Z plus up to one parton is implemented. Sherpa on the other hand offers two tree-level matrix element generators of which the module COMIX [82] was used for the samples in this analysis. It was set up to generate matrix elements of Z plus up to five partons. The advantage of matrix elements have over parton showers is the better description of hard (wide angle) emissions and interference effects.

8.4. Parton showers

The hard matrix element calculations alone do no yield physical (in the sense of observable) final states. At the LHC, multiplicities of the order of a thousand observable particles in the final state are quite common, which makes it impossible to exactly calculate cross-sections and kinematics with Monte-Carlo methods. However, an approximate solution for all higher orders of the perturbation series is available that goes by the name of parton showers (PS) leading to an intermediate state with a comparably large number of partons. The final multiplicity of stable (colour-singlet) of an event is reached after several non-perturbative steps in the simulation (Section 8.5, 8.7).

The general idea is to independently evolve the legs of the hard matrix element from the scale of the hard interaction down to a scale set by a cut-off parameter where evolution means that recursively probabilities for a parton to split into two new partons are calculated. The cut-off is typically chosen at a scale of ~ 1 GeV where confinement of partons is deemed to be dominating. The evolution scale is usually chosen to be the transverse momentum of partons meaning that emissions are ordered in $p_\perp$ with the first emission being the hardest. The two main ingredients to this evolution are parton splitting functions and so-called SUDAKOV form factors explained in the following.

8.4.1. Splitting functions

Let σ_0 be the perturbatively calculated fixed-order cross-section of a process generating partons of flavour i, then the cross-section for the next-order, i.e. additional production of parton j with momentum fraction z, can be written as [79]

$$d\sigma \approx \sigma_0 \sum_i \frac{\alpha_S}{2\pi} \frac{\mathrm{d}\theta^2}{\theta^2} P_{ji}(z,\phi)\mathrm{d}\phi \tag{8.3}$$

where the P_{ji} are so-called splitting functions which in their spin-averaged form are defined as [79]:

$$
\begin{aligned}
P_{qq}(z) &= C_F \cdot \frac{1+z^2}{1-z} && \text{for } q \to qg \\
P_{gq}(z) &= C_F \cdot \frac{1+(1-z)^2}{z} && \text{for } q \to gq \\
P_{gg}(z) &= C_A \cdot \frac{z^4+1+(1-z)^4}{z(1-z)} && \text{for } g \to gg \\
P_{qg}(z) &= \frac{1}{2} \cdot (z^2+(1-z)^2) && \text{for } g \to q\bar{q}
\end{aligned} \tag{8.4}
$$

where $C_F = \frac{N_c^2-1}{2N_c}$ and $C_A = N_c$ with N_c being the number of colours and z being the momentum fraction of the newly generated parton with respect to its mother parton. θ is the opening angle of the cone between the two. By recursively treating each state after a splitting has occured as new final-state, splitting cascades can be generated.

In Figure 8.2 the spin-averaged splitting functions are shown as function of z. It shows that in the case of gluon-radiation (P_{qq}, P_{gq} and P_{gg}) the following divergences arise:

- P_{qq} diverges as $z \to 1$, i.e. radiated gluon has $z \sim 0$
- P_{gq} diverges as $z \to 0$, i.e. radiated gluon has $z \sim 0$
- P_{gg} diverges as $z \to 0$ and $z \to 1$, i.e. one of the gluons is created with $z \sim 0$

Apparently all these divergences occur as one of the gluons after the splitting is soft ($z \sim 0$) which is why these divergences are called "soft" divergences.

The equation (8.3) contains a further divergence as $\theta \to 0, \pi$. This is called a collinear divergence. In the process of e.g. $q\bar{q} \to q\bar{q}g$ it occurs if the radiated gluon is collinear with its mother parton (the quark or anti-quark) or if both are back-to-back and thus the gluon collinear with the anti-quark or quark.

All divergencies mentioned above constitute non-observably distinguishable circumstances, be it the emissions of a gluon without energy or the emission of a gluon collinear to another parton. In order to achieve a formalism that generates physical quantities, a resolution criterion is introduced based on the relative transverse momentum of two partons that is required to be larger than a certain parameter Q_{cut} in order to consider the two partons as resolvable.

In order to calculate a finite probability for resolvable emissions a trick is used based on SUDAKOV form-factors.

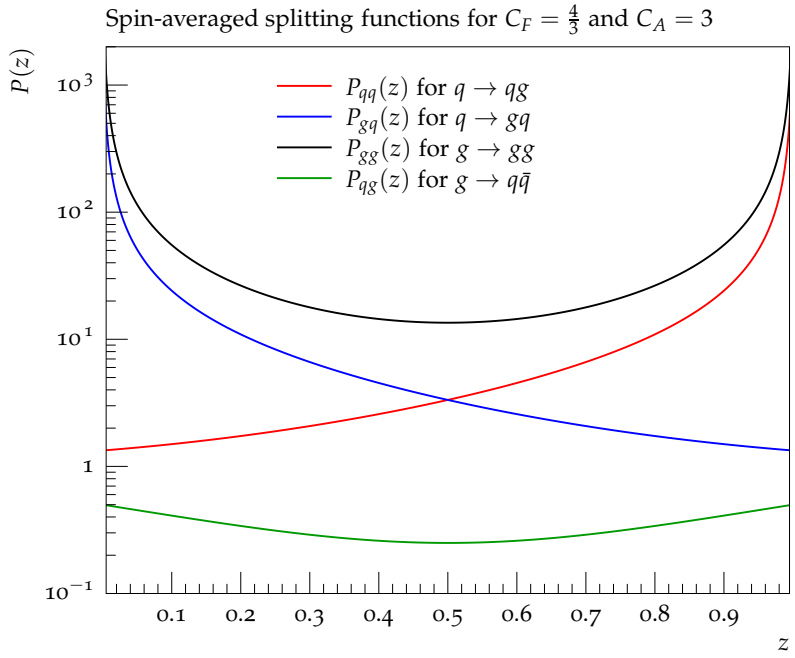

Figure 8.2.: The spin averaged splitting functions used in QCD parton showers.

8.4.2. Sudakov form-factors

By introducing an ordering variable q (typically $p_\perp$ is used, as e.g. in Sherpa and Pythia8) that has a maximum value of Q ($q < Q$) it is possible to calculate a probability for the most energetic (hardest) branching by calculating the probability $\Delta_i(Q^2, q^2)$ not to have any emissions between q and Q [79]:

$$\Delta_i(Q^2, q^2) = \exp\left[-\int_{q^2}^{Q^2} \frac{\mathrm{d}k^2}{k^2} \frac{\alpha_S}{2\pi} \int_{Q_0^2/k^2}^{1-Q_0^2/k^2} \mathrm{d}z P_{ji}(z)\right] \tag{8.5}$$

The probability not to have *any* emission is obtained when calculating $\Delta_i(Q^2, Q_0^2)$. Where Q^0 is a cut-off parameter that needs to be adjusted to data. This is called the Sudakov form-factor which is used to generate Parton-showers in Monte-Carlo generators.

The probability for a first branching is calculated from the differential equation [79]:

$$p_{\text{branch}} = \Delta_i(Q^2, q^2) \frac{\mathrm{d}P_i}{\mathrm{d}q^2} \tag{8.6}$$

where P_i describes the total branching of a parton [79], calculated from the spin-averaged splitting-function (equation (8.4)):

$$\mathrm{d}P_i = \frac{\alpha_S}{2\pi}\frac{\mathrm{d}q^2}{q^2}\int_{Q_0^2/q^2}^{1-Q_0^2/q^2}\mathrm{d}z P_{ji}(z) \tag{8.7}$$

In the Monte-Carlo programs, a uniform random number $\rho \in [0,1]$ is chosen and equation (8.6) is solved for q. If q happens to be above Q_0, a branching at scale q is generated with z being picked according to P_{ji}(z). As mentioned earlier, all systems produced as the result of splitting are treated as new initial states for further branchings. The parton shower algorithm comes to a stop as soon as none of the generated q is above Q_0.

The procedure described above applies to a parton shower that is applied to final state partons (final state radiation, FSR). However, partons are found to radiate also prior to the hard interaction (initial state radiation, ISR). For those, the same mechanism could be used, starting from a parton picked from the proton, evolving it in terms of a parton shower with one of the produced partons eventually undergoing the hard interaction. However, this would be very inefficient as the correct kinematics for the sought after hard sub-process would have to be generated by the parton shower by chance. Instead, a modified algorithm is used for ISR actually starting from the hard sub-process and evolving the parton shower backwards [79] to the PDF.

The non-emission probability for ISR showers is [79]:

$$\Delta_i(Q^2,q^2,x) = \exp\left[-\int_{q^2}^{Q^2}\frac{\mathrm{d}k}{k^2}\frac{\alpha_S}{2\pi}\int_{Q_0^2/k^2}^{1-Q_0^2/k^2}\mathrm{d}z P_{ij}(z)\cdot\frac{\frac{x}{z}f_j(\frac{x}{z},k^2)}{x f_i(x,k^2)}\right] \tag{8.8}$$

where f is the parton distribution function used. The additional term in equation (8.8) w.r.t. equation (8.5), $\frac{\frac{x}{z}f_j(\frac{x}{z},k^2)}{x f_i(x,k^2)}$ is the ratio of PDF at the backward evolution ($\frac{x}{z}$) and the current value (x).

It should be noted that the actual procedure involves many more details such as final state parton showers applied to particles generated from ISR (IFSR). Further, implementations differ between the codes of Sherpa and Pythia8. For instance, Pythia8 introduces quite a

number of parameters, such as different values of α_s and cut-offs Q_0 in different showers (ISR, FSR, IFSR), while Sherpa modifies the radiation pattern by substituting the hardest emissions with matrix elements (Section 8.4.4).

8.4.3. Logarithmic accuracy

A very strong feature of parton-showers is the so-called logarithmic accuracy which exploits the fact that in the perturbation series certain terms occur at all orders and that the emissions are ordered by hardness ($p_\perp$). Those terms have a logarithmic structure that are known to be large (and therefore dominating the terms at a particular order) in at least some regions of phase space. This gives rise to the fact that neglecting all other terms from the perturbation series except the logarithms gives a very small error. This technique is often referred to as "resummation".

8.4.4. Merging

The approximation made in parton showers is called "soft-collinear approximation" which implies that a parton shower algorithm is good/exact only if no wide-angle emissions happen. The underlying reason is that the individual emissions are treated independent from each other. The situation can be improved by a so-called merging of parton-showers and the matrix element which is a method to correct the first (hardest and therefore most wide-angle) parton-shower emission after the full parton-shower sequence of an event by means of replacement of the first parton-shower emissions at scale "t_i" with a tree-level matrix-element.

The procedure requires the introduction of a merging-scale, `QCUT`, that needs to be chosen properly as it tells the Monte-Carlo generator at what scale in the evolution variable the parton shower should take over.

The general idea of merging is a reclustering of the $2 \to n$ kinematics in order to find the scales t_i where the parton shower algorithm would have produced the emission (or branching) corresponding to the legs found in the matrix element calculated. The procedure needs to be carefully designed in order to avoid double-counting of emissions.

In the example shown in Figure 8.3 a matrix elements with 4 legs was generated, two of which are leptons and hence do not participate in strong interations. The reclustering first tries to "undo" the last splitting and finds that the parton shower would have split

the gluon into two gluons at a scale t_2. The next step in the procedure is to find the scale t_1 where the parton shower algorithm would have radiated the gluon off of the outgoing quark leg.

In summary, four scales are known, the starting scale of the parton shower evolution, t_0, identical to the known scale of the hard process, further, the merging gives us the end-scales of the first and second branchings, t_1 and t_2 as well as the merging scale `QCUT`. With those scales at hand it is possible to calculate the corresponding SUDAKOV form-factors $\mathcal{S}(t_0, t_1)$, $\mathcal{S}(t_1, t_2)$ $\mathcal{S}(t_2, \texttt{QCUT})$ which allow to correct the parton shower in the sense that it does not generate emissions between the scales t_0 and `QCUT`.

As of today, two such methods are available. The CKKW [83, 84] (CATANI-KUHN-KRAUSS-WEBBER) approach which is an exact inversion of a parton-shower and the MLM [85] (MANGANO) merging which is a not as effective approximation using a cone-jet clustering algorithm. CKKW is implemented and used in the Sherpa samples used in this analysis.

The result of these methods is a more correct description of the first and therefore hardest emissions.

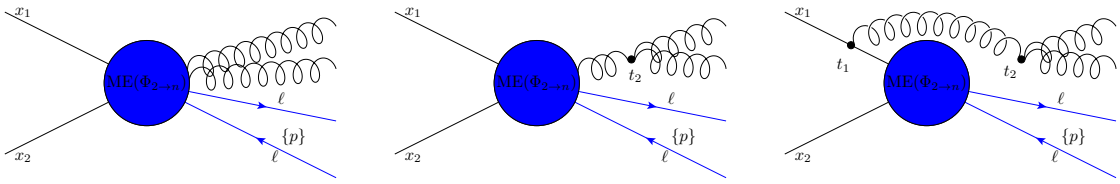

(a) Specified $2 \to 4$ process **(b)** First reclustering **(c)** Second reclustering

Figure 8.3.: Illustration of the merging procedure of a parton shower and a matrix element.

8.5. The Sjöstrand-Zijl MPI model

As this measurement specifically aims to be sensitive to multiple parton interactions, a brief summary of the models present in the Monte-Carlo simulations used is given in this section.

The MPI model implemented in both generators used in this analysis is the SJÖSTRAND-ZIJL model proposed in 1987 that attempts to describe the charged particle multiplicity distribution measured at the UA5 experiment [86]. The starting point is the interpretation of the hard cross-section (equation (8.1)) exceeding the total cross-section being a manifestation that more than one pair of partons can undergo a hard interaction as two protons collide. Thus, the extended and composite nature of protons is paid attention to. Simply put, the MPI model generates additional $2 \to 2$ scatters that yield partons which are again subject to ISR and FSR thus adding to the overall event activity.

The model assumption is that the mean number of parton-parton interactions is proportional to $\frac{\sigma_{2\to 2}}{\sigma_{\mathrm{ND}}}$ with σ_{ND} being the inelastic, non-diffractive part of the total proton-proton cross-section, σ_{tot}[2]:

$$\langle n \rangle \sim \frac{\sigma_{2\to 2}}{\sigma_{\mathrm{ND}}} \tag{8.9}$$

with σ_{ND} calculated according to [87] as the difference of σ_{tot}, diffractive and elastic cross-section:

$$\sigma_{\mathrm{ND}} = \sigma_{\mathrm{tot}} - (\sigma_{el} + \sigma_{\mathrm{DD}} + \sigma_{\mathrm{SD}}) \tag{8.10}$$

where σ_{tot}, σ_{DD}, σ_{SD} and σ_{el} are obtained from fits of Reggeon trajectories to data.

The perturbative QCD cross-section (equation (8.1)) in its differential form can be written as function of $p_\perp$ [86]:

[2] Elastic and diffractive processes are characterised by the exchange of colour-neutral objects (Pomeron, Reggeon...), contrary to inelastic non-diffractive processes. Single and double diffractive (SD, DD) processes lead to one and both protons breaking up while elastic processes keep the protons intact.

$$\frac{d\sigma_{2\to 2}}{dp_\perp^2} = \sum_{a,b,k} \int \mathrm{d}x_a \mathrm{d}x_b \mathrm{d}\hat{t} f_{a/A}(x_a, Q^2) f_{b/B}(x_b, Q^2) \hat{\sigma}_{ij}^k(\hat{s}, \hat{t}, \hat{u}) \; \delta\left[p_\perp^2 - \frac{\hat{t}\hat{u}}{\hat{s}}\right] \tag{8.11}$$

where the scale Q^2 has been set to $p_\perp^2 = \frac{\hat{t}\hat{u}}{\hat{s}}$ using the perturbative MANDELSTAM variables, $\hat{t}$, $\hat{u}$ and $\hat{s}$. The partonic hard-scattering cross-section $\hat{\sigma}_{ij}^k$ now describes the k-th possible hard interaction between incoming parton i and j.

When integrated, the expression in equation (8.11) above a certain scale $p_{\perp,min}$, is given by [86]:

$$\sigma_{2\to 2}(p_{\perp,min}) = \int_{p_{\perp,min}}^{s/4} \frac{d\sigma_{2\to 2}}{dp_\perp^2} dp_\perp^2 \tag{8.12}$$

which is divergent with $p_{\perp,min} \to 0$. In order to retain a finite result, the model introduces $p_{\perp,min}$ as a cut-off that is considered as a tuneable parameter.

In Figure 8.4 the hard cross-section is shown as function of $\sqrt{s}$ for several values of $p_{\perp,min}$ and for different parton distribution functions. In addition, the total cross-section, calculated by DONNACHIE-LANDSHOFF [88] is drawn, showing that the hard partonic cross-section quickly exceeds not only the non-diffractive but also the total cross-section.

8.5.1. Impact parameter dependence

Further, the model introduces an impact parameter dependence, based on assumptions about the overlap of hadronic matter as two protons collide. By doing so, the mean number of interactions, $\langle n \rangle$ (equation (8.9)), becomes dependent on the impact parameter, b (See Figure 8.5)i, i.e. $\langle n \rangle \to \langle \tilde{n}(b) \rangle$. Typically, some variation of GAUSSian distributions is chosen to model the aforementioned matter distribution inside hadrons. The free parameters of this model are usually related to the widths of the GAUSSian distribution chosen. Agreement with data is obtained by tuning these parameters to data. The general idea is that the smaller the impact parameter is, the larger the overlap of the matter distributions of the incoming protons and thus the higher the probability of additional parton-parton interactions gets.

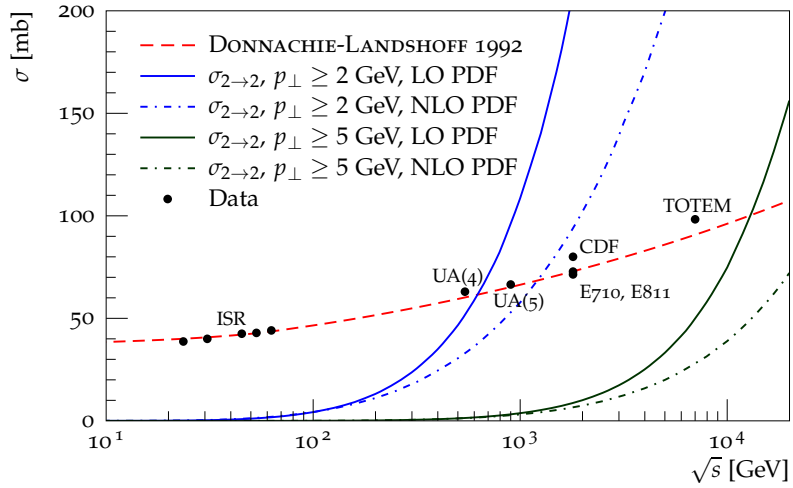

Figure 8.4.: The total proton-proton cross-section (red line [88]) and the hard parton-parton cross-section (calculated with Pythia8) for several MSTW08 parton distribution functions [89] and cross-section cut-offs, $p_{\perp,min}$, as function of $\sqrt{s}$. The data points show corresponding measurements of the total-cross-sections from ISR [90], UA(4) [91], UA(5) [92], E711/811 [93, 94], CDF [95] and TOTEM [96].

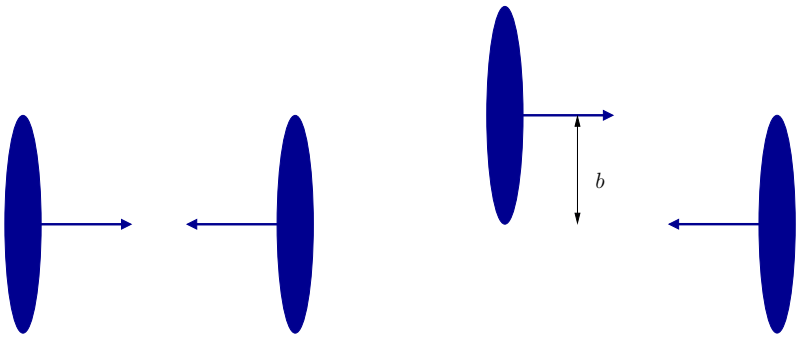

(a) Small impact parameter **(b)** Large impact parameter

Figure 8.5.: Illustration of the impact parameter dependence of Multitple Parton Interactions (MPI). A small impact parameter, b, leads to a large overlap of hadronic matter and thus increases the probability of MPI, while a large impact parameter (grazing collision) has a low probability to generated MPI.

The impact parameter dependent expectation value of the number of all parton-parton interactions is assumed to be linearly related to the matter overlap, $\tilde{\mathcal{O}}(b)$:

$$\langle \tilde{n}(b) \rangle = k \, \tilde{\mathcal{O}}(b) = f(b) \langle k \tilde{\mathcal{O}} \rangle \tag{8.13}$$

The last equality in equation (8.13) represents the aim of the model, which is to formulate an impact parameter dependent enhancement factor, $f(b)$, that drives the number of parton-parton interactions, $\tilde{n}$, while absorbing the linear constant, k, into the matter overlap. By doing so, the mean matter overlap, $\langle\tilde{\mathcal{O}}\rangle$ (integrated over all impact parameters), is introduced. Since k is constant, $f(b)$ can be written as

$$f(b) = \frac{\tilde{\mathcal{O}}(b)}{\langle\tilde{\mathcal{O}}\rangle} \tag{8.14}$$

which is thus independent from the actual normalisation of the matter overlap, $\tilde{\mathcal{O}}(b)$.

Some care must be taken requiring that a first (hard) interaction has taken place already. Assuming that parton-parton interactions occur independently from one another the probability that two protons with impact parameter b will interact can be calculated according to Poissonian statistics as

$$P(b) = 1 - \underbrace{\exp\left[-\langle\tilde{n}(b)\rangle\right]}_{\text{Probability for no interaction}} \underset{(8.13)}{=} 1 - \exp\left[-k\ \tilde{\mathcal{O}}(b)\right] \tag{8.15}$$

Using equation (8.15), $\langle\tilde{\mathcal{O}}\rangle$ can be defined such that for events with $\tilde{n} > 0$, the average enhancement factor $\langle f(b)\rangle$ is equal to one [86]:

$$\langle\tilde{\mathcal{O}}\rangle = \frac{\int \tilde{\mathcal{O}}(b)\ P(b)\ \mathrm{d}^2b}{\int P(b)\ \mathrm{d}^2b} \tag{8.16}$$

Putting it all together, the mean number of parton-parton interactions is given by

$$\langle\tilde{n}(b)\rangle = c \cdot f(b)\frac{\sigma_{2\to 2}(p_{\perp,min})}{\sigma_{ND}} \tag{8.17}$$

with c being the impact parameter independent quantity $c = (\int \tilde{\mathcal{O}}(b)\ P(b)\ \mathrm{d}^2b)/(\int \tilde{\mathcal{O}}(b)\ \mathrm{d}^2b)$.

In the event generation, the non-diffractive cross-section is calculated according to [87] and $\sigma_{2\to 2}(p_{\perp,min})$ is calculated perturbatively according to equation (8.12). An impact parameter b is randomly chosen according to $f(b)$, yielding the *average* number of parton-parton interactions for this event from which Poissonian distribution is constructed which is used to randomly pick the *actual* number of MPI for this event.

8.5.2. Double Gaussian matter distribution

A common option to model the matter distribution inside protons is a double Gaussian distribution, $\rho_{DG}(r)$. In this picture, the proton consists of a core region that contains the fraction $\beta \in [0,1]$ of the overall hadronic matter. The relative size of this core (w.r.t. the proton size) is steered with the parameter $a_2 \in [0,1]$. The remaining matter fraction $1-\beta$ resides outside the core:

$$\rho_{DG}(r) \quad = \quad \underbrace{\frac{\beta}{a_2^3}\ \exp\left[\frac{-r^2}{a_2^2}\right]}_{\text{core}} \quad + \quad (1-\beta)\ \exp\left[-r^2\right] \tag{8.18}$$

The corresponding matter overlap, $\tilde{\mathcal{O}}(b)$, as function of the impact parameter, b, and z being the beam direction, is obtained by solving the integral ([86], eq. (21)):

$$\tilde{\mathcal{O}}(b) \propto \int \mathrm{d}t \int \mathrm{d}^3x\ \rho(x,y,z)\rho(x,y,z-\sqrt{b^2+t^2})$$

which in the case of equation (8.18) leads to

$$\tilde{\mathcal{O}}_{DG}(b) = \frac{\beta^2}{2a_2^2}\ \exp\left[\frac{-b^2}{2a_2^2}\right] + \frac{2\beta(1-\beta)}{1+a_2^2}\exp\left[\frac{-b^2}{1+a_2^2}\right] + \frac{(1-\beta)^2}{2}\exp\left[\frac{-b^2}{2}\right] \tag{8.19}$$

Examples of the resulting matter overlap distribution used in Sherpa are given for several parameter sets a_2, β in Figure 8.6a. The default of the Sherpa version used in this analysis ($a_2 = 0.437$, $\beta = 0.842$, black line) is very close to a single Gaussian distribution. Further, the plots show that for small core regions ($a_2 = 0.1$) the matter fraction parameter β has a large influence on the overall shape of $\tilde{\mathcal{O}}$. For values of

$a_2 > 0.5$ the matter distribution essentially becomes a single GAUSSIAN distribution, i.e. the last term in equation (8.19) dominates.

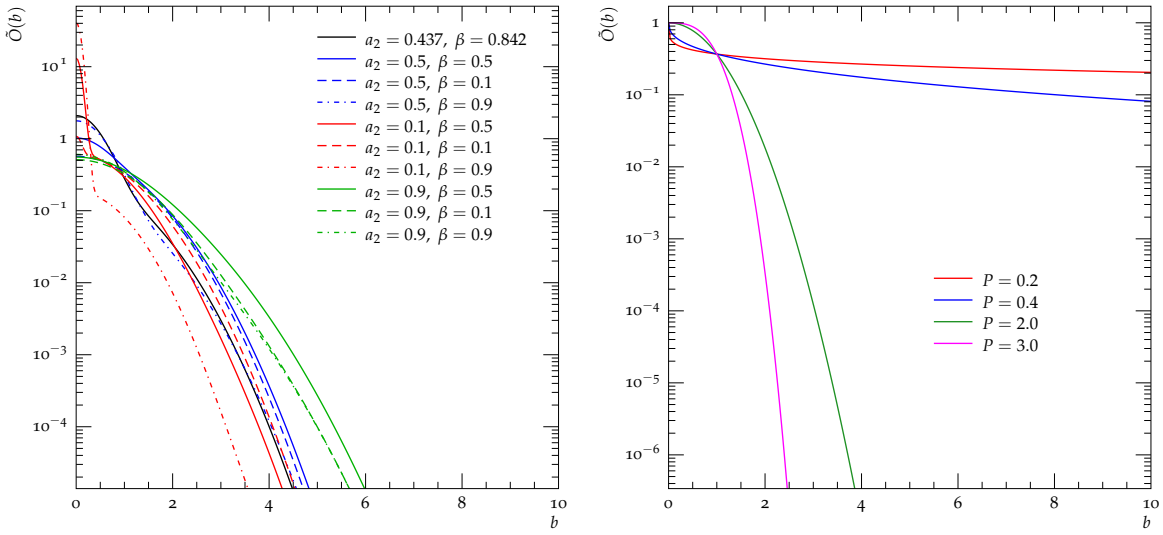

(a) Double-GAUSS **(b)** Exponential

Figure 8.6.: Matter overlap distributions used in the MPI models in Sherpa (a) and Pythia8 (b) to determine the mean number of parton-parton interactions per event.

8.5.3. Implementation differences between Pythia8 and Sherpa

Although, both MC generators used in this analysis use the SJÖSTRAND-ZIJL MPI model, some details between the implementations differ between Sherpa and Pythia8. Table 8.2 gives a quick overview of these differences which will be explained in the following.

Pythia8 specifics

Exponential matter distribution:

The Pythia8 samples used in this analysis (Tune 4C, introduced in Pythia8.145) were generated using an exponential matter overlap of the form

$$\tilde{\mathcal{O}}_{exp}(b, P) = \exp\left[-b^P\right] \tag{8.20}$$

which introduces a new tuning parameter, $P \in [0, 10]$, that steers the functional form of the matter overlap. The matter overlap according to equation (8.20) is shown in Figure 8.6b for several values of P. It shows a strong sensitivity to P. The value used in Tune 4C is $P = 2.0$ which yields a simple GAUSSian matter overlap. In the limit of $P \to \infty$, the impact parameter dependence vanishes. Recent tunings [97] show that the data prefer values P at about 0.2, which results in a comparably spiked behaviour at b close to zero, and which is significantly different from the value used in Tune 4C (version 8.145 of [98]).

Colour reconnection:

The mechanism of colour reconnection was introduced in order to describe measurements of the mean transverse momentum of charged particles as function of an event's charged multiplicity ($\langle p_\perp \rangle$ vs. N_{ch}). It is an ad-hoc procedure to merge separate subsystems n the event-generation process that are the result of multiple parton interactions. The colour-field is modelled in Pythia8 using (Lund) strings. Colour-reconnection aims at a reduction of the total length of all strings than span between various subsystems, prior to the fragmentation (Section 8.7.1). All such subsystems are ordered in $p_\perp$, allowing for the calculation of the probability of merging the system of lowest scale $p_\perp$ with the next lowest one in order to reduce the total (Lund) string length and eventually to manipulate the number and hardness of produced hadrons:

$$P_{CR} = \frac{1}{1 + (\frac{p_\perp}{\kappa \cdot p_{\perp,min}})} \tag{8.21}$$

The parameter $\kappa \in [0, 10]$ is another tuning parameter that needs to be adjusted to data.

Figure 8.7 shows corresponding graphs for several values of κ at a typical reference scale of $p_{\perp,min} = 2$ GeV. Independent of κ it can be stated that the probability is generally higher for low-$p_\perp$ systems, i.e. it is harder in the algorithm to merge two high-$p_\perp$ systems. This behaviour is exactly what is needed in order to describe the aforementioned data ($\langle p_\perp \rangle$ vs. N_{ch}). The authors admit [99] that

"The true origin of this behaviour and the correct mechanism to reproduce it remains one of the big unsolved issues at the borderline between perturbative and nonperturbative QCD."

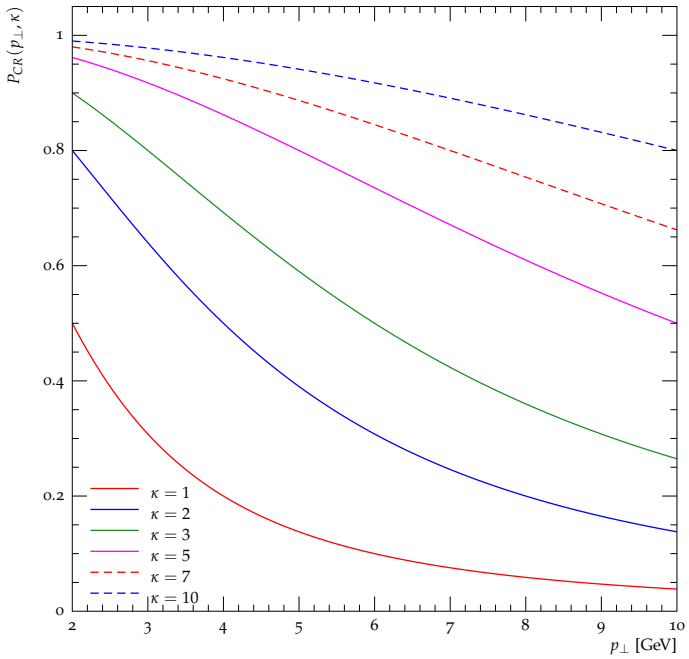

Figure 8.7.: Pythia8's colour reconnection probability to merge a system generated at scale $p_\perp$ with the next highest $p_\perp$ system (equation (8.21)) for several values of the tuning parameter κ. The reference scale $p_{\perp,min}$ is set to 2 GeV in these plots.

Sherpa specifics

In contrast to Pythia8, Sherpa does not have a mechanism for colour reconnections. Further, it introduces another tuning parameter `SIGMA_ND_FAC`$\in [0, 1]$ that is multiplied with σ_{ND} in equation (8.17) and thus manipulates the mean number of parton-parton interactions.

	Sherpa	Pythia8
Matter overlap	double Gauss	exponential
Colour reconnection	—	■
`SIGMA_ND_FACTOR`	■	—

Table 8.2.: Overview of most important differences of the Sjöstrand-Zijl MPI model between Sherpa and Pythia8.

8.5.4. PDF considerations

The parton distribution functions are rescaled after each parton-parton collision in an event, reserving the nominal PDF (evaluated at the scale of the hardest interaction) for the hard sub-process. All subsequent scatterings are iteratively evaluated at

$$x_a^{(n)\prime} = \frac{x_a^{(n)}}{1 - \sum_{i=1}^{n-1} x_a^{(i)}} \tag{8.22}$$

instead of $x_a^{(n)}$, thus the amount of energy already taken out of the colliding protons is taken into consideration for all subsequent scatterings.

8.5.5. Model limitations

When first proposed, the Sjöstrand-Zijl MPI model also introduced an energy dependence of the cut-off parameter $p_{\perp,min}$ which was motivated by the scaling of the total cross-section with the centre-of-momentum energy [88] with the unfortunately cancelled Superconducting Super Collider in mind ($\sqrt{s} = 40$ TeV). Thus, the model was expected to be accurate to energies up to 40 TeV using the following energy evolution:

$$p_{\perp_0}(\sqrt{s}) = p_{\perp 0,\text{ ref}} \cdot \left(\frac{\sqrt{s}}{\text{Reference scale}} \right)^{\text{Exponent}} \tag{8.23}$$

where $p_{\perp 0,\text{ref}}$ is the tuning parameter that is equivalent to $p_{\perp_0}(\sqrt{s})$ at a reference scale (typically chosen to be 1.8 TeV) and Exponent is another tuning parameter which is supposed to determine the energy scaling of $p_{\perp_0}$.

However, extensive tuning studies performed at the advent of the first LHC data at $\sqrt{s} = 7$ TeV showed that a common description of experimental data with the scaling in equation (8.23) is only possible if the model parameters are tuned to data from two different $\sqrt{s}$. Adding data of a third or more scales breaks agreement with data [97].

8.6. Primordial $k_\perp$

Most of the transverse momentum of partons inside the protons prior to an interaction are generated by ISR showers. However, discrepancies of model predictions with data (mostly the transverse momentum of Z-bosons produced at the Tevatron collider [100]) led to the introduction of a mechanism that accounts for any other source of transverse parton momentum not considered by ISR. This includes the FERMI-motion [101] of partons of $\mathcal{O}(300)$ MeV, unresolved ISR shower activity below a cut-off scale and any other shortcomings of the parton-shower. The mechanism to generate additional transverse parton momentum is called "primordial $k_\perp$".

In the model implementations of both, Sherpa and Pythia8, the primordial transverse momenta of particles are randomly chosen according to a positive GAUSSian distribution with a cut-off (required for computational reasons) at a scale of the order of 10 GeV. The latter is treated as a phenomenological parameter that is subject to tuning to experimental data as is the width of the GAUSSian.

An example distribution with $\langle k_\perp \rangle = 2$ GeV can be found in Figure 8.8.

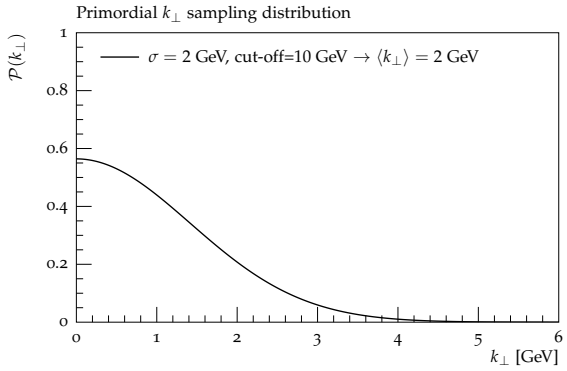

Figure 8.8.: Example distribution for the sampling of primordial $k_\perp$ in MC generators with typical values of the tuning parameters σ (width of GAUSSian) and the cut-off needed for computational reasons.

8.7. Hadronisation and decay

The result of the description so far are partons, either produced directly by the hard sub-process or MPI or as the result of parton shower activity. However, these object need to be transformed into physical object, i.e. hadrons. The transition, which is called

hadronisation, is performed using models. While Pythia8 implements the "Lund string model", Sherpa's hadronisation is based on a cluster model. The result of each model are hadrons that are further decayed, based on the lifetime and branching ratios implemented. Thus, a fully exclusive final state with observable hadrons is generated.

8.7.1. Lund string model

The principle idea of the Lund string model [102] is that colour dipoles, e.q. a quark-anti-quark pair move away from one another thus increasing the potential energy between the two (described as semi-classical strings) until the string breaks into smaller pieces, forming colour singlet objects (hadrons). Such a sub-system may break further, if the invariant mass is large enough to potentially allow for the production of two lighter hadrons. The whole procedure introduces a plethora of parameters that steer flavour, spin and angular momentum of produced hadrons.

8.7.2. Cluster model

The cluster model of hadronisation implemented in Sherpa relies on the pre-confinement property of parton-showers [103] if all gluons have split into $q\bar{q}$ pairs. In that case, each quark is colour-connected to exactly one anti-quark. These systems are called clusters and they are further evolved by splitting into hadrons. The algorithm forces each gluon to split just after the parton shower evolution has come to a stop. Thus, the initial clusters are potentially at a large scale. Several tuning parameters determine the fate of the high mass cluster, it may decay into two lighter clusters, or if its mass and quantum numbers are suitable, transform into a hadron. It should be noted that the cluster model in Sherpa, in contrast to Pythia8, requires full hadron-multiplets in order to achieve the transition of clusters to hadrons, which is why the variety of hadrons produced by Sherpa is much larger than that by Pythia8.

8.8. QED radiation

The Monte-Carlo generators used in this analysis use different ways to emit photons of electrically charged objects. Pythia8 uses the same parton shower algorithm that was also used for QCD radiation. Thus, photon emissions are ordered in $p_\perp$. Further, the

QED shower exhibits the same soft-collinear approximation present in the QCD shower, thus yielding accurate descriptions if the emission of photons is collinear.

Sherpa on the other hand uses an implementation of the YFS (Yennie, Frautschi, Suura) model [104] that allows for higher-order corrections of the QED radiation. The main difference in the results w.r.t. a parton shower is that also the wide-angle emission of soft photons is described correctly [105]. In the signal events used in this analysis, YFS is applied to the charged leptons as well as electrically charged hadrons after they were produced in the hadronisation step.

A consequence of the two different approaches will become important in the definition of leptons used when unfolding data (Chapter 12).

8.9. Detector simulation

In order to obtain Monte-Carlo datasets that are comparable with reconstructed data it is necessary to firstly process the simulated events as described above ("hadron-level") with a software that simulates the interaction of the generated particles with matter, i.e. the ATLAS detector itself and secondly to simulate the response of the electronics to interaction with the simulated particles, thus yielding simulated data ("detector-level") that can be reconstructed just like real data events.

Since the ATLAS detector is a very complex machine, the position and alignment of its components is not known with infinite precision. Moreover, the condition of detector modules deteriorates with time depending on how much they are exposed to radiation. This is why databases of the geometry and the condition of subsystems of the detector are constantly updated. These databases serve as another input to the detector simulation, which is performed using the software `Geant4` [106].

As the simulation of the interaction of particles especially with the calorimeters (lots of material) is very time consuming, a fast simulation was used for the detector simulation of the signal samples used in this analysis. The software is called `ATLFAST2` [107] and replaces the full simulation of the calorimeters with parametrisations obtained through full simulations of single particle interactions with the calorimeters. Studies [108] have shown very good agreement of the fast with the full simulation with differences of up to 1% for electron spectra and less than 0.1% for muon spectra.

Chapter 9.

Systematic uncertainties of reconstructed tracks and leptons

In this chapter, systematic effects on reconstructed distributions due to the reconstruction of charged particle tracks and leptons are presented. The propagation onto the final results is described in 12.5.

9.1. Track reconstruction efficiency

The event-shape variables used in this analysis are calculated from reconstructed tracks. The latter can only be reconstructed with a certain efficiency ε, which has been determined with Monte-Carlo samples. For each Monte-Carlo event, information prior to the detector simulation ("truth") and information after the detector simulation and reconstruction is available. Thus, efficiencies can be obtained by matching reconstructed tracks with corresponding truth information [109].

The efficiency, ε, is a function of $p_\perp$ and η of reconstructed tracks that has a systematic uncertainty, $\Delta\varepsilon(\eta, p_\perp)$, associated with it. The tracking efficiency and its systematic uncertainties were determined in [109]. Figure 9.2a shows the dependency of $\varepsilon(\eta, p_\perp)$ on η and $p_\perp$ of reconstructed tracks. Four sources of systematic uncertainties are quantified therein. They will be explained in the following paragraphs. A summary of numerical values of relative systematic uncertainties, $\frac{\Delta\varepsilon}{\varepsilon}$, can be found in Table 9.1 and a graphical representation in Figure 9.2b.

9.1.1. Material systematics, $\Delta\varepsilon_{\text{mat}}(\eta)$

The simulation of the ATLAS detector is very complex. Especially the material distribution and its interaction with particles is not precisely known. Hence data-driven tests were developed in order to estimate the uncertainty of the track reconstruction due to the material modelling in the detector simulation. In [109] two methods are used. One is based on the decay of $K^0_S \to \pi^+\pi^-$ and the precisely known invariant mass of the K^0_S. The other compares the length of reconstructed tracks in data with the length of tracks reconstructed from simulated events. Both methods compare the results obtained from data with several different material distributions in the detector simulation. The estimated uncertainty was found to be independent on the transverse momentum of tracks with $p_\perp > 500$ MeV as they are used in this analysis. The η-dependence shows that the uncertainties are small for the barrel part of the inner detector but grow in the end-caps (Figure 9.2b, Table 9.1). This shows a significant miss-modelling of the detector-material in the vicinity of service structures and cooling pipes.

9.1.2. Track selection, $\Delta\varepsilon_{\text{sel}}$

The track selection (Chapter 5.1.3) itself introduces a systematic uncertainty of the track reconstruction efficiency. The transverse impact parameter cut and the cut on b-layer hits, both introduced to reduce the contamination with tracks from secondary interactions (with detector material), are varied to estimate $\Delta\varepsilon_{\text{sel}}(\eta)$. A comparison of the resulting cut efficiencies in MC and data led to an estimate of $\frac{\Delta\varepsilon_{\text{sel}}(\eta)}{\varepsilon} = 0.01$, independent of η and $p_\perp$ for tracks with $p_\perp > 500$ MeV as they are used in this analysis.

9.1.3. Badly measured tracks with $p_\perp^{\text{trk}} > 10$ GeV, $\Delta\varepsilon_{\text{highpT}}(\eta, p_\perp)$

Badly measured (MC) tracks are defined as tracks reconstructed with a transverse momentum $p_\perp^{\text{reco}} \geq 10$ GeV with a corresponding matched generated particle transverse momentum $p_\perp^{\text{gen}} < 5$ GeV. Such large discrepancies arise primarily due to interactions of comparably low-$p_\perp$ charged particles with detector material. An illustration of this process can be found in Figure 9.1. This effect was found to happen most likely at large values of $|\eta|$. The fraction of badly measured tracks was determined in Monte-Carlo and data using various techniques. However, the high $|\eta|$ region suffers from low statistics, thus making it complicated to calculate correction factors for Monte-Carlos. Instead, a

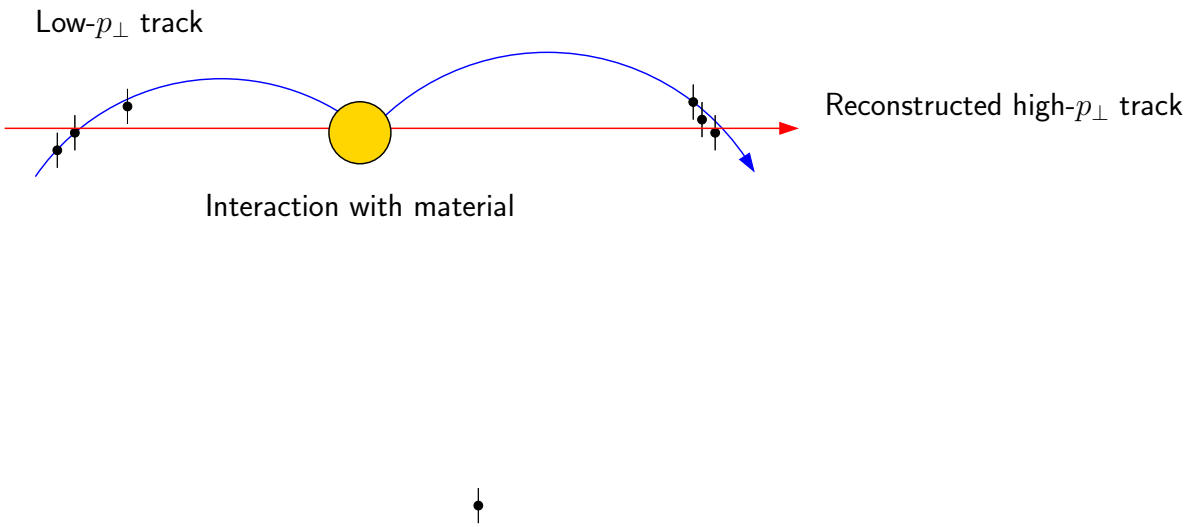

Figure 9.1.: Illustration of a badly measured track. In this example, a comparably low-$p_\perp$ charged particle (blue line) coming from the left produces hits in the inner detector (black dots). Then it interacts with detector material (yellow circle) resulting in it being scattered and producing a second set of hits. The reconstruction algorithm may reconstruct these hits as coming from a very high-$p_\perp$ track (red line). The original image can be found in [109].

conservative approach was chosen by using the fraction of badly measured tracks in data as additional source of systematic uncertainty of the tracking efficiency. The fraction was measured in four bins of $p_\perp$ and three bins of η. $\Delta\varepsilon_{\mathrm{highpT}}(\eta, p_\perp)$ is shown in Figure 9.2b. Apparently, $\frac{\Delta\varepsilon_{\mathrm{highpT}}(\eta,p_\perp)}{\varepsilon}$ is of the order of 2% in the central part of the inner detector (4% for track with $p_\perp > 30$ GeV) but rises dramatically to values of up to 80% for $|\eta| > 2.25$. The asymmetry is due to the large statistical uncertainties in the data in this η region.

9.1.4. Goodness-of-fit cut for badly measured tracks, $\Delta\varepsilon_{\mathrm{GoF}}(p_\perp)$

A cut on the goodness-of-fit measure of tracks with $p_\perp > 10$ GeV was used in the determination of the tracking efficiency with the aim to reduce the fraction of badly measured tracks. A flat conservative systematic uncertainty of $\frac{\Delta\varepsilon_{\mathrm{GoF}}}{\varepsilon} = 10\%$ is introduced to cover differences in the cut efficiency when comparing MC with data.

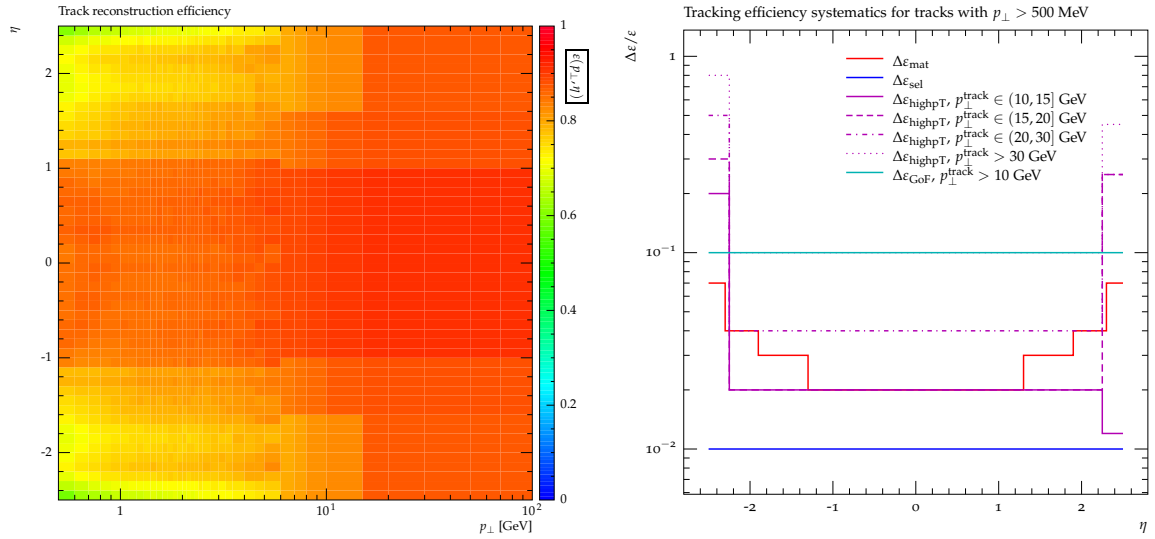

(a) Track reconstruction efficiency **(b)** Relative systematic uncertainties

Figure 9.2.: Track reconstruction efficiency, ε, as estimated in [109]. The central values are shown in (a) as function of the track-$p_\perp$ and η. (b) shows a summary of the corresponding relative systematic uncertainties as function of a track's pseudorapidity η.

$\lvert\eta\rvert$	< 1.3	$\in [1.3, 1.9)$	$\in [1.9, 2.1)$	$\in [2.1, 2.3)$	$\in [2.3, 2.5)$
$\frac{\Delta\varepsilon_{\text{mat}}}{\varepsilon}$	0.02	0.03	0.04	0.04	0.07
$\frac{\Delta\varepsilon_{\text{sel}}}{\varepsilon}$	0.01	0.01	0.01	0.01	0.01
$\frac{\Delta\varepsilon_{\text{GoF}}}{\varepsilon}$ $(p_\perp^{\text{trk}} > 10$ GeV)	0.1 for all values of η				
η	< -2.25	$\in [-2.25, 2.25]$	> 2.25		
$\frac{\Delta\varepsilon_{\text{highpT}}}{\varepsilon}$ $(p_\perp^{\text{trk}} \in (10, 15]$ GeV)	0.2	0.02	0.012		
$\frac{\Delta\varepsilon_{\text{highpT}}}{\varepsilon}$ $(p_\perp^{\text{trk}} \in (15, 20]$ GeV)	0.3	0.02	0.25		
$\frac{\Delta\varepsilon_{\text{highpT}}}{\varepsilon}$ $(p_\perp^{\text{trk}} \in (20, 30]$ GeV)	0.5	0.04	0.25		
$\frac{\Delta\varepsilon_{\text{highpT}}}{\varepsilon}$ $(p_\perp^{\text{trk}} > 30$ GeV)	0.8	0.1	0.45		

Table 9.1.: Relative systematic uncertainties on the track reconstruction efficiency for tracks with $p_\perp^{\text{track}} > 500$ MeV. The values are taken from [109].

9.1.5. Track "killing"

The general idea to account for $\Delta\varepsilon(\eta, p_\perp)$ is to randomly remove reconstructed tracks from simulated events thus producing reconstructed observables corresponding to a smaller than nominal tracking efficiency $\varepsilon(\eta, p_\perp) - \Delta\varepsilon$ ("killing" technique). $\Delta\varepsilon(\eta, p_\perp)$ is calculated using the systematic uncertainties described above, adding them in quadrature:

$$\Delta\varepsilon(\eta, p_\perp) = \sqrt{\Delta\varepsilon_{\text{mat}}(\eta)^2 + \Delta\varepsilon_{\text{sel}}^2 + \Delta\varepsilon_{\text{GoF}}(p_\perp)^2 + \Delta\varepsilon_{\text{highpT}}(\eta, p_\perp)^2} \tag{9.1}$$

Since it is impossible to add tracks of non-reconstructed particles, the method is asymmetric. However it is assumed that the effect *is* symmetric. The removal works as follows.

For each reconstructed track $\varepsilon(\eta, p_\perp)$ and $\Delta\varepsilon(\eta, p_\perp)$ are determined. Then a binomially distributed random number ($p = \varepsilon - \Delta\varepsilon$), $\mathcal{B}$, is used to decide whether to keep this track or to remove it from the event:

$$\mathcal{B} = \begin{cases} 0 & \rightarrow \text{remove track} \\ 1 & \rightarrow \text{keep track} \end{cases} \tag{9.2}$$

This results in observables calculated from fewer tracks than nominal, corresponding to a modified (smaller) track-reconstruction efficiency.

In Figure 9.3 the ratio plots of observables measured using the nominal and the modified tracking efficiencies are shown. It can be seen that those observables where the number of tracks enters the definition (N_{trk}, Beamthrust, $\sum p_\perp$) are a lot more susceptible to this effect than event shapes like transverse thrust. For the former, differences of up to 20% can be observed while the latter show an effect of up to 3% only. Further, the plots show that the effects observed are fairly independent from the specific Monte-Carlo sample used.

The propagation of $\Delta\varepsilon$ onto final results is discussed in Chapter 12.

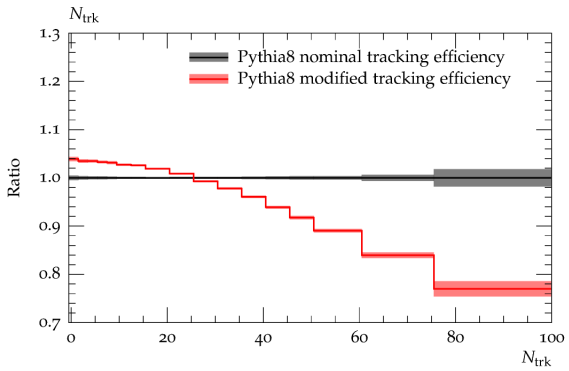

(a) N_{trk}, Pythia8

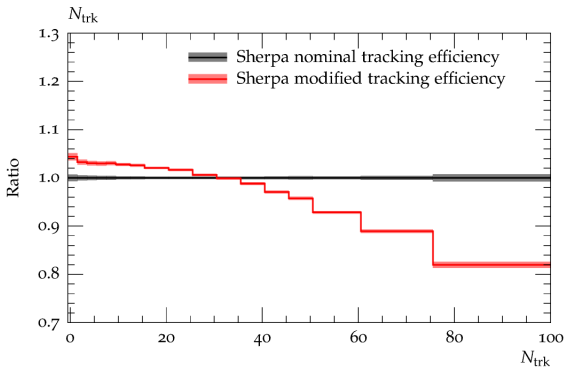

(b) N_{trk}, Sherpa

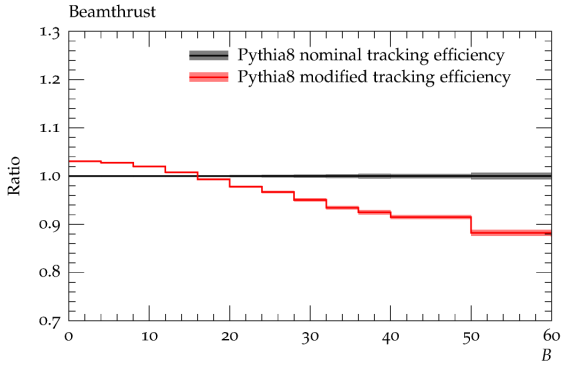

(c) Beamthrust, Pythia8

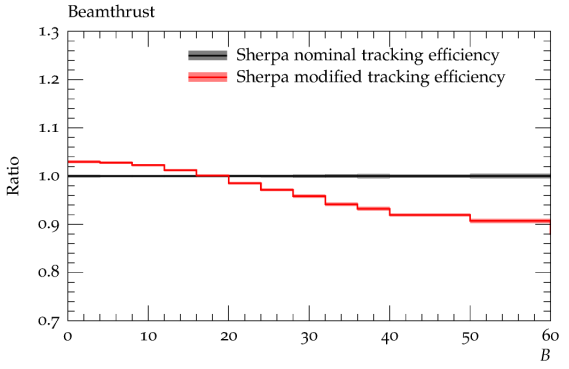

(d) Beamthrust, Sherpa

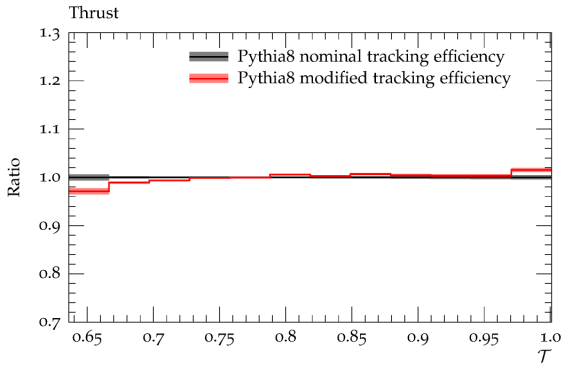

(e) Transverse thrust, Pythia8

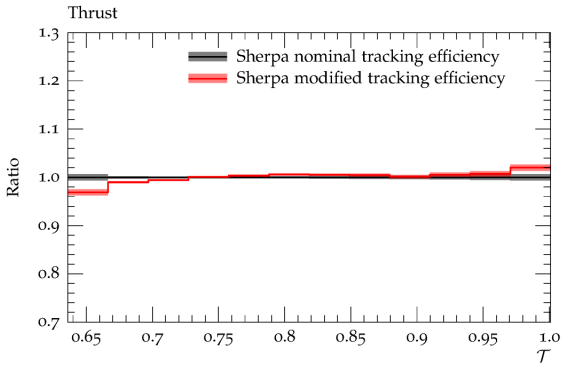

(f) Transverse thrust, Sherpa

Figure 9.3.: Effects on event shapes from uncertainties on the track reconstruction efficiency. Ratio plots of normalised observables corresponding to the nominal (black) and the systematically varied tracking efficiency (red) are shown. Plots on the left-hand side show the results for Pythia8, plots on the right-hand side show the Sherpa counterpart. All observables shown use the fully inclusive $p_{\perp}(\text{Z})$ phase-space region. The bands represent the statistical error only. Observables where the number of tracks enters the definition (N_{trk}, BeamThrust, $\sum p_{\perp}$) are much more susceptible to the variation than observables like transverse thrust.

9.2. Lepton systematics

In this section, the systematic effects related to the reconstruction of leptons are explained. Although the leptons are removed from the final selection tracks when calculating observables, the lepton systematics affect the reconstructed Z-boson transverse momentum in data and MC. This is especially important for the final correction step of this analysis, the unfolding (Chapter 12) where the subdivision of the data into $p_\perp(\mathrm{Z})$ phase-space regions is performed based on the reconstructed $p_\perp(\mathrm{Z})$.

9.2.1. Electron systematics

The treatment of reconstructed electrons requires several consecutive corrections that have to be applied in the following order

1. Correct the energy resolution (MC only)
2. Correct the energy (data and MC)
3. Correct electron efficiencies (MC only)

Electron energy resolution, $\delta E_{\mathrm{smear}}$

The electrons reconstructed from Monte-Carlo samples have previously run through the detector simulation. Remaining differences between the obtained energy resolutions with respect to data are corrected for by multiplying the reconstructed electron energies with a dimensionless smearing factor, σ_{res}:

$$E_{\mathrm{smear}} = E_{\mathrm{reco}} + \Delta E_{\mathrm{reco}}(\eta_{\mathrm{e}}) = E_{\mathrm{reco}} + \mathcal{G}(0, \sigma_{\mathrm{res}}\left(\eta_{\mathrm{e}}\right) \cdot E_{\mathrm{reco}}\right) \tag{9.3}$$

The resolution correction ΔE_{reco} is obtained by pulling a random number from a GAUSSian distribution $\mathcal{G}$ with a mean of 0 and width $\sigma_{\mathrm{res}}(\eta_{\mathrm{e}}) \cdot E_{\mathrm{reco}}$. The resolution σ_{res} itself is dependent on the electron pseudorapidity, η_{e}, and has been measured in data [110] (Figure 9.4).

The statistical uncertainties of σ_{res} are propagated as systematic uncertainties on E_{smear} by varying σ_{res} within its errors $\delta\sigma_{\mathrm{res}}$:

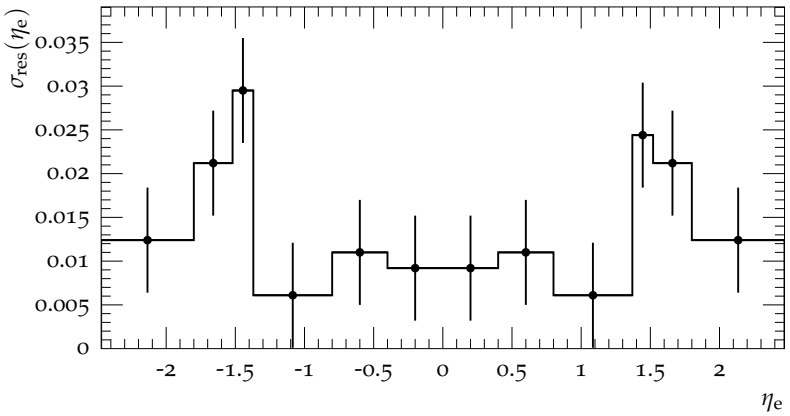

Figure 9.4.: The data resolution [48] used to smear the reconstructed electron energies reconstructed from Monte-Carlo samples processed with the ATLAS detector simulation (equation (9.4)).

$$\delta E_{\text{smear}} = E_{\text{reco}} + \mathcal{G}\left(0, [\sigma_{\text{res}}(\eta_e) \pm \delta\sigma_{\text{res}}(\eta_e)] \cdot E_{\text{reco}}\right) \tag{9.4}$$

The resulting systematic uncertainty on the event-shape distributions of this analysis is negligible, it rarely exceeds the statistical uncertainties (Figure 9.10).

Electron energy correction

Differences between the line shapes (ratio of the normalised $M_{e^-e^+}$ distributions in MC and data) of the reconstructed invariant di-electron mass, $M_{e^-e^+}$, are ab initio present when comparing data and Monte-Carlo. To correct for this, an energy correction is performed by applying a correction factor that is dependent on the electron energy and pseudorapidity to the (smeared in case of MC) reconstructed electron energy [110]:

$$E_{\text{corr}} = \frac{E_{\text{reco/smear}}}{1 + \alpha(E_{\text{reco}}, \eta_e)} \tag{9.5}$$

$\alpha(E_{\text{reco}}, \eta_e)$ has several components that have different uncertainties associated with them:

$$\alpha = \alpha_{\text{Zee}}(\eta_e) + \alpha_{\text{PS}}(\eta_e, E_{\text{reco}}) + \alpha_{\text{material}}(\eta_e, E_{\text{reco}}) \tag{9.6}$$

The individual α_i will briefly be explained in the following.

$\boldsymbol{\alpha_{\text{Zee}}(\eta_e)}$: This describes the nominal correction when comparing reconstructed data and fully reconstructed Monte-Carlo properties. Three sources of systematic uncertainties have been evaluated:

1. Statistical uncertainties in the Monte-Carlo sample used, $\Delta\alpha_{\text{ZeeStat}}$
2. Systematic uncertainty due to usage of different Monte-Carlo simulations, $\Delta\alpha_{\text{ZeeGen}}$
3. Systematic uncertainty due to the extraction method of α, $\Delta\alpha_{\text{ZeeMethod}}$

The central values of $\frac{1}{1+\alpha_{\text{Zee}}}$ as well as the corresponding uncertainties are shown in Figure 9.5. It shows that the uncertainties on $\frac{1}{1+\alpha_{\text{Zee}}}$ are rather small ($< 1\%$). These uncertainties are propagated in this analysis by individually varying α_{Zee} within those errors and thus obtaining slightly different correction factors $\frac{1}{1+\alpha}$:

$$\begin{aligned} \delta E_{\text{ZeeStat}} &: \alpha_{\text{Zee}} \pm \Delta\alpha_{\text{ZeeStat}} \\ \delta E_{\text{ZeeGen}} &: \alpha_{\text{Zee}} \pm \Delta\alpha_{\text{ZeeGen}} \\ \delta E_{\text{ZeeMethod}} &: \alpha_{\text{Zee}} \pm \Delta\alpha_{\text{ZeeMethod}} \end{aligned} \tag{9.7}$$

The effect of these systematic uncertainties is visible in the ratio plots of the reconstructed N_{trk} and $p_{\perp}(\text{Z})$ distributions (Figure 9.10). The individual contributions are of the order of a few percent.

$\boldsymbol{\alpha_{\text{material}}(E_{\text{reco}}, \eta_{\text{e}})}$: In addition to the purely Monte-Carlo related contribution to α described above, systematic studies have been performed in order to estimate the effect of more or less material in the ECAL description of the detector simulation [110].

The values of $\frac{1}{1+\alpha_{\text{material}}}$ as well as the corresponding systematic uncertainties obtained in [110] are displayed for some typical electron energies in Figure 9.6.

When propagated in this analysis, the nominal correction factor is varied up and down corresponding to the systematic uncertainties of α_{material}:

$$\delta E_{\text{material}} : \alpha_{\text{material}} \pm \Delta\alpha_{\text{material}} \tag{9.8}$$

The effect of these systematic uncertainties on the $p_{\perp}(\text{Z})$ distribution is shown in Figure 9.10. It reaches up to 3%.

$\boldsymbol{\alpha_{\text{PS}}(E_{\text{reco}}, \eta_{\text{e}})}$: A similar study of adding or removing material has been performed for the pre-sampler as well [110].

The propagation of the corresponding systematic uncertainties (Figure 9.7) is again performed by varying the nominal correction factor up and down:

$$\delta E_{\text{presampler}} : \alpha_{PS} \pm \Delta\alpha_{PS} \tag{9.9}$$

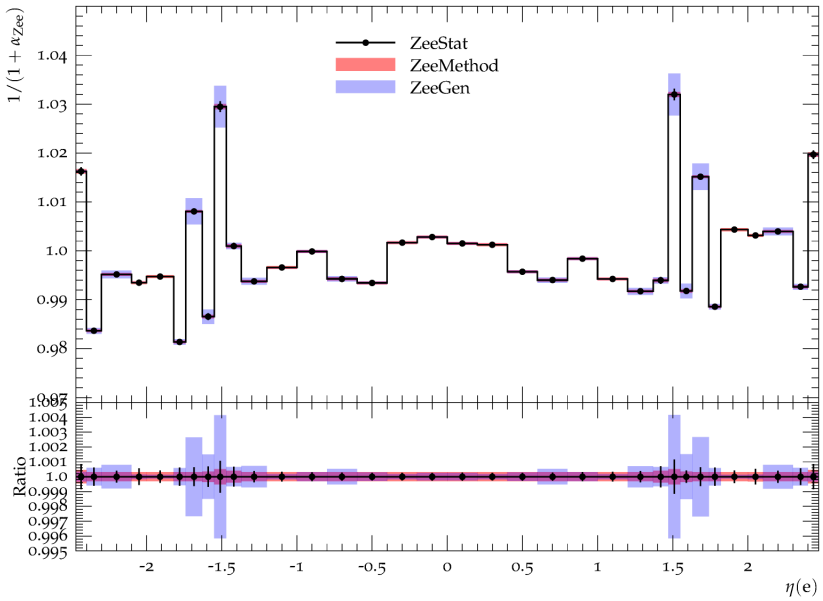

Figure 9.5.: Electron energy correction factors [48] for reconstructed Monte-Carlo events reflecting the differences of measured $Z \to e^- e^+$ events and the modelling of the latter in a Monte-Carlo simulation (equation (9.6) and 9.8). The error bars reflect the systematic uncertainties of the indiviual contributions explained in Section 9.2.1.

leading to an effect of up to 5% if propagated onto the $p_\perp(Z)$ distribution (Figure 9.10).

Figure 9.8 shows the central values as well as the total combined systematic uncertainties of the energy correction factors $\frac{1}{1+\alpha}$ for several typical electron energies. It shows that there is an average energy uncertainty of 0.1% that rises with decreasing electron energy.

Electron efficiency corrections

The identification efficiency for electrons passing the `medium` requirements is different in Monte-Carlo and data, thus scale factors are applied to the Monte-Carlo event weights. The scale-factors, ε_{ID} were obtained as function of the reconstructed electron's transverse momentum and pseudorapidity from data using a tag-and-probe (B.1) method [111].

Further, the electron track reconstruction efficiency differs between data and reconstructed Monte-Carlo events. Again, $p_\perp$- and η-dependent scale factors, $\varepsilon_{\text{reco}}$, are used to correct for the aforementioned differences.

Since exactly two reconstructed electrons (e_1, e_2) are selected in this analysis, the Monte-Carlo event-weight is multiplied with ε_{ID} and $\varepsilon_{\text{reco}}$ corresponding to both electrons:

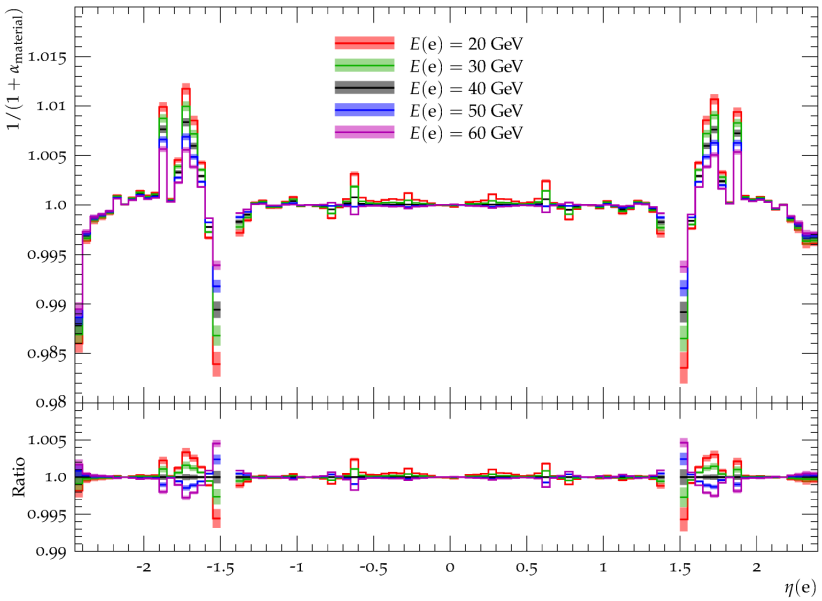

Figure 9.6.: Electron energy correction factors [48] $\frac{1}{1+\alpha_{\text{material}}(\eta_{\text{e}},E_{\text{e}})}$ for reconstructed Monte-Carlo events taking into account the lack of knowledge of the amount of material in the ECAL. The error bars show the systematic uncertainties explained in Section 9.2.1.

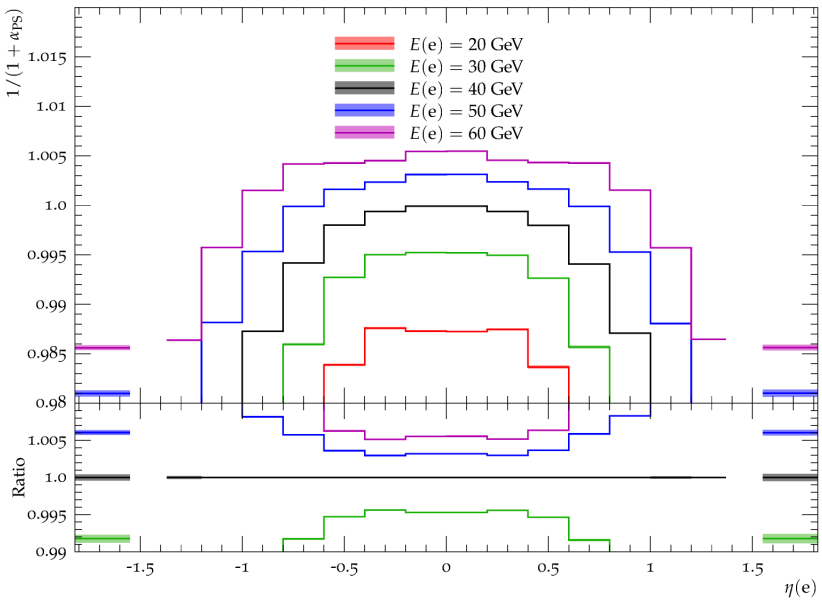

Figure 9.7.: Electron energy correction factors [48] for reconstructed Monte-Carlo events taking into account the lack of knowledge of the amount of material in the presampler (equation (9.10)). The error bars show the systematic uncertainties explained in Section 9.2.1.

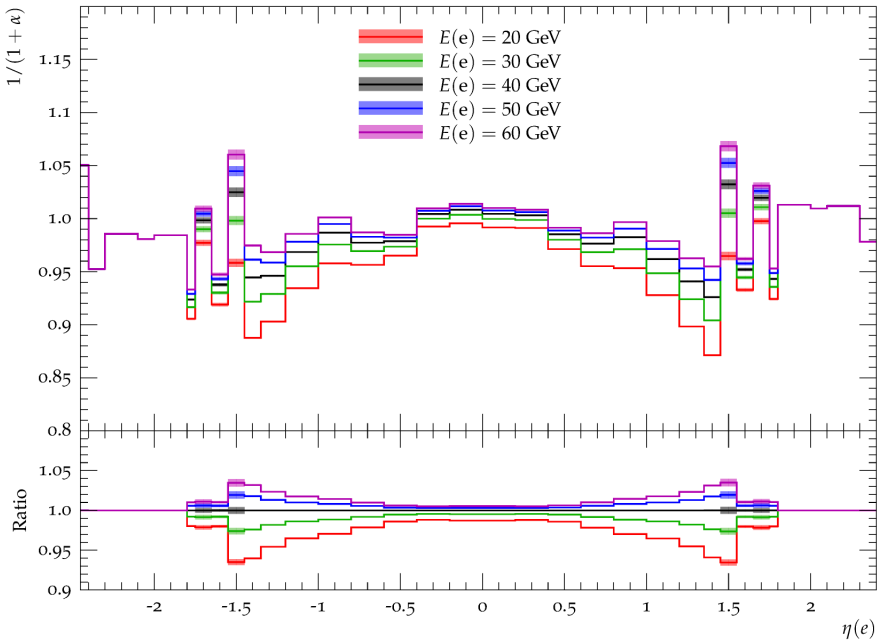

(a) $\frac{1}{1+\alpha}$

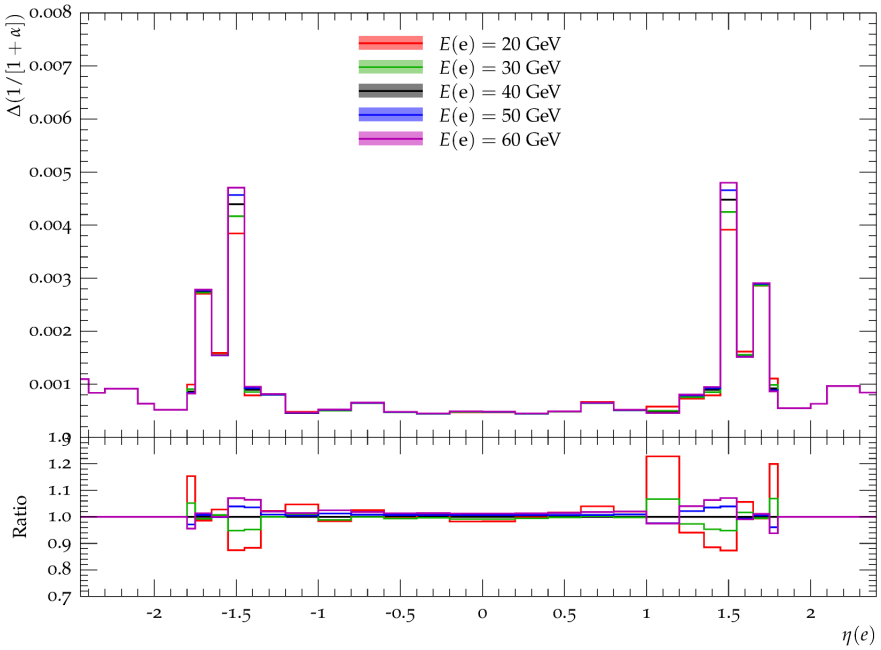

(b) $\Delta(\frac{1}{1+\alpha})$

Figure 9.8.: The total energy correction factors [48] (equation (9.6)) (top) and the propagated systematic uncertainties (bottom) for several typical electron energies.

$$\tilde{w}_{\mathrm{MC}} = w_{\mathrm{MC}} \cdot \varepsilon_{\mathrm{ID}}(\mathrm{e}_1) \cdot \varepsilon_{\mathrm{ID}}(\mathrm{e}_2) \cdot \varepsilon_{\mathrm{reco}}(\mathrm{e}_1) \cdot \varepsilon_{\mathrm{reco}}(\mathrm{e}_2) \tag{9.10}$$

Figure 9.9 shows the scale-factors for some typical electron energies as function of the electron's pseudorapidity. It shows that the values of $\varepsilon_{\mathrm{reco}}$ are not sensitive to the electron's transverse momentum. On the other hand, $\varepsilon_{\mathrm{ID}}$ is the closer to 1 (i.e. no effect) the higher the electron's $p_\perp$. Also, its systematic uncertainties shrink with growing $p_\perp$.

These systematic uncertainties are propagated through the analysis by varying the individual scale factors within its uncertainties, leading to modified total scale factors $\delta\varepsilon$, thus obtaining slightly different MC event weights, $\delta\tilde{w}_{\mathrm{MC}} = w_{\mathrm{MC}} \cdot \delta\varepsilon$:

$$\delta\varepsilon_{\mathrm{ID}} = \begin{cases} [\varepsilon_{\mathrm{ID}}(\mathrm{e}_1) + \Delta\varepsilon_{\mathrm{ID}}(\mathrm{e}_1)] \cdot [\varepsilon_{\mathrm{ID}}(\mathrm{e}_2) + \Delta\varepsilon_{\mathrm{ID}}(\mathrm{e}_2)] \cdot \varepsilon_{\mathrm{reco}}(\mathrm{e}_1) \cdot \varepsilon_{\mathrm{reco}}(\mathrm{e}_2) \\ [\varepsilon_{\mathrm{ID}}(\mathrm{e}_1) - \Delta\varepsilon_{\mathrm{ID}}(\mathrm{e}_1)] \cdot [\varepsilon_{\mathrm{ID}}(\mathrm{e}_2) - \Delta\varepsilon_{\mathrm{ID}}(\mathrm{e}_2)] \cdot \varepsilon_{\mathrm{reco}}(\mathrm{e}_1) \cdot \varepsilon_{\mathrm{reco}}(\mathrm{e}_2) \\ [\varepsilon_{\mathrm{ID}}(\mathrm{e}_1) + \Delta\varepsilon_{\mathrm{ID}}(\mathrm{e}_1)] \cdot [\varepsilon_{\mathrm{ID}}(\mathrm{e}_2) - \Delta\varepsilon_{\mathrm{ID}}(\mathrm{e}_2)] \cdot \varepsilon_{\mathrm{reco}}(\mathrm{e}_1) \cdot \varepsilon_{\mathrm{reco}}(\mathrm{e}_2) \\ [\varepsilon_{\mathrm{ID}}(\mathrm{e}_1) - \Delta\varepsilon_{\mathrm{ID}}(\mathrm{e}_1)] \cdot [\varepsilon_{\mathrm{ID}}(\mathrm{e}_2) + \Delta\varepsilon_{\mathrm{ID}}(\mathrm{e}_2)] \cdot \varepsilon_{\mathrm{reco}}(\mathrm{e}_1) \cdot \varepsilon_{\mathrm{reco}}(\mathrm{e}_2) \end{cases} \tag{9.11}$$

$$\delta\varepsilon_{\mathrm{reco}} = \begin{cases} \varepsilon_{\mathrm{ID}}(\mathrm{e}_1) \cdot \varepsilon_{\mathrm{ID}}(\mathrm{e}_2) \cdot [\varepsilon_{\mathrm{reco}}(\mathrm{e}_1) + \Delta\varepsilon_{\mathrm{reco}}(\mathrm{e}_1)] \cdot [\varepsilon_{\mathrm{reco}}(\mathrm{e}_2) + \Delta\varepsilon_{\mathrm{reco}}(\mathrm{e}_2)] \\ \varepsilon_{\mathrm{ID}}(\mathrm{e}_1) \cdot \varepsilon_{\mathrm{ID}}(\mathrm{e}_2) \cdot [\varepsilon_{\mathrm{reco}}(\mathrm{e}_1) - \Delta\varepsilon_{\mathrm{reco}}(\mathrm{e}_1)] \cdot [\varepsilon_{\mathrm{reco}}(\mathrm{e}_2) - \Delta\varepsilon_{\mathrm{reco}}(\mathrm{e}_2)] \\ \varepsilon_{\mathrm{ID}}(\mathrm{e}_1) \cdot \varepsilon_{\mathrm{ID}}(\mathrm{e}_2) \cdot [\varepsilon_{\mathrm{reco}}(\mathrm{e}_1) - \Delta\varepsilon_{\mathrm{reco}}(\mathrm{e}_1)] \cdot [\varepsilon_{\mathrm{reco}}(\mathrm{e}_2) + \Delta\varepsilon_{\mathrm{reco}}(\mathrm{e}_2)] \\ \varepsilon_{\mathrm{ID}}(\mathrm{e}_1) \cdot \varepsilon_{\mathrm{ID}}(\mathrm{e}_2) \cdot [\varepsilon_{\mathrm{reco}}(\mathrm{e}_1) + \Delta\varepsilon_{\mathrm{reco}}(\mathrm{e}_1)] \cdot [\varepsilon_{\mathrm{reco}}(\mathrm{e}_2) - \Delta\varepsilon_{\mathrm{reco}}(\mathrm{e}_2)] \end{cases} \tag{9.12}$$

The effect of these systematic variations on reconstructed observables is negligible. As can be seen in Figure 9.10, the variations never exceed the statistical uncertainties.

Summary of electron systematics

The effects of the systematic variations explained in the previous paragraphs is shown in Figure 9.10, where ratio plots of the variations w.r.t. the nominal reconstructed N_{trk} and $p_\perp(\mathrm{Z})$ distributions are shown for Pythia8 and Sherpa. For N_{trk} (fully inclusive in $p_\perp(\mathrm{Z})$) the effect of the systematic variations is of the same order of magnitude as the statistical

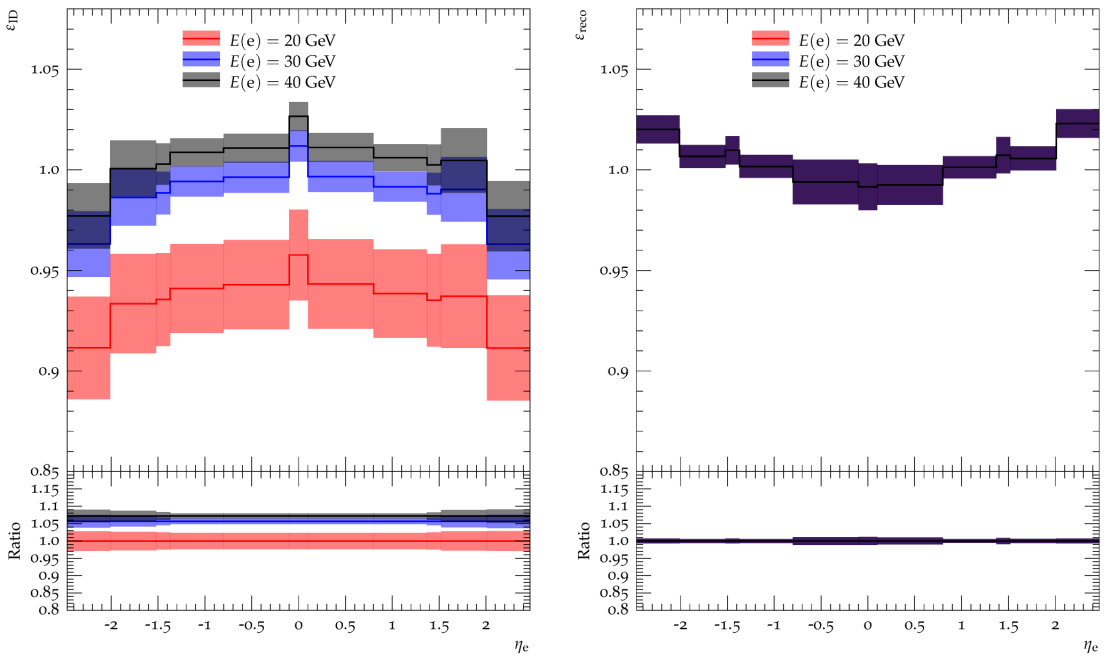

(a) $\varepsilon_{\mathrm{ID}}$ **(b)** $\varepsilon_{\mathrm{reco}}$

Figure 9.9.: Electron scale factors [48] and uncertainties for some typical electron energies.

uncertainties, except for the first bin. This means that the lepton systematics do not have a large impact on the event shapes in the fully inclusive $p_{\perp}(\mathrm{Z})$ phase-space region, which is not surprising as the lepton tracks are removed from the events. However do to the removal being based on a cone method (Chapter 5.1.3), a small dependence can be expected that seems to affect low multiplicity events.

The effect on $p_{\perp}(\mathrm{Z})$ is larger and reaches values of 5% (3%) for Pythia8 (Sherpa). The scale-factor variations are found to be negligible as are the electron resolution variations. The largest effect have the electron energy correction systematics which are all of the same order of magnitude for both Pythia8 and Sherpa.

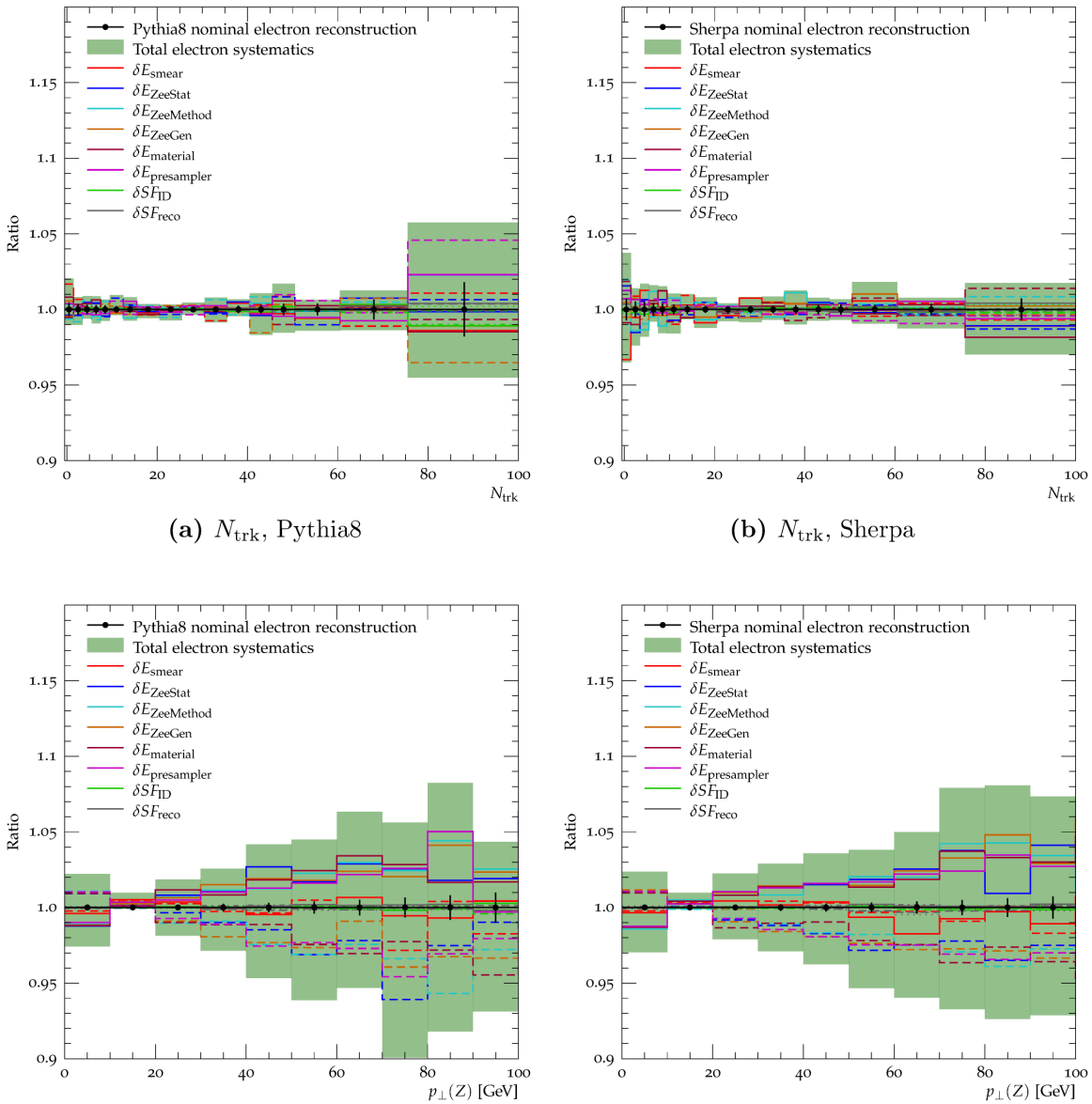

(a) N_{trk}, Pythia8 **(b)** N_{trk}, Sherpa

(c) $p_{\perp}(\text{Z})$, Pythia8 **(d)** $p_{\perp}(\text{Z})$, Sherpa

Figure 9.10.: Electron systematics and their effect on N_{trk} and $p_{\perp}(\text{Z})$. Shown are ratios of systematic variations with respect to the nominal reconstructed distributions as well as the total electron systematic uncertainty (added in quadrature, green band). The statistical uncertainties of the nominal reconstructed observables is shown as black error-bars. The $p_{\perp}(\text{Z})$ phase-space is fully inclusive. Significant effects are visible in the $p_{\perp}(\text{Z})$ distribution for all but the energy resolution systematic δE_{smear} and the scale-factor variations. The "up"-variations are drawn as solid lines while the "down"-variations are drawn as dashed lines. The only exception are the scale-factor variations where there are four variations each, displayed as solid, dashed, dotted and dash-dotted lines.

9.2.2. Muon systematics

The reconstruction of muons introduces several sources of systematic uncertainty which are all propagated through the analysis. The sources include efficiencies (reconstruction and trigger) as well as corrections on the reconstructed muon transverse momentum.

Muon efficiency corrections

Similar to the electrons, the efficiency of the muon reconstruction but also that of the trigger present in Monte-Carlo differs from that measured in data. Hence, again, scale factors are applied to the Monte-Carlo event weights in order to correct for this effect.

Muon reconstruction efficiency, δSF_{reco}: The muon reconstruction efficiencies were obtained in Monte-Carlo and (2010) data events using a tag-and-probe method ([112], B.1). As the algorithm and the conditions of the detector components relevant for the reconstruction of muons did not change significantly in 2011, these efficiencies can be applied to this analysis as well. The determined efficiencies as well as the corresponding scale-factors are shown as function of the reconstructed muon $p_\perp$ and η in Figure 9.11. The latter are compatible with 1 within the uncertainties, $\Delta SF_{\text{reco}}(\mu)$, which amount up to 2%.

These uncertainties are used in this analysis to estimate systematic uncertainties on observables by varying the nominal values of the scale factors within their uncertainties. The scale factors are applied to the reconstructed Monte-Carlo event weight, w_{MC}, thus the systematic variations are carried out as follows:

$$\tilde{w}_{\text{MC}} = w_{\text{MC}} \cdot \begin{cases} [SF_{\text{reco}}(\mu_1) + \Delta SF_{\text{reco}}(\mu_1)] \cdot [SF_{\text{reco}}(\mu_2) + \Delta SF_{\text{reco}}(\mu_2)] \\ [SF_{\text{reco}}(\mu_1) - \Delta SF_{\text{reco}}(\mu_1)] \cdot [SF_{\text{reco}}(\mu_2) - \Delta SF_{\text{reco}}(\mu_2)] \end{cases} \tag{9.13}$$

The effect of these variations on reconstructed distributions is so small, that it never exceeds the statistical uncertainties. Concerning the $p_\perp(\text{Z})$ distribution, it has a slightly larger effect on the observable obtained from the Sherpa sample than that obtained from the Pythia8 sample (Figure 9.14), leading to slightly larger systematic uncertainties when unfolding the data with the Sherpa samples (Chapter 12).

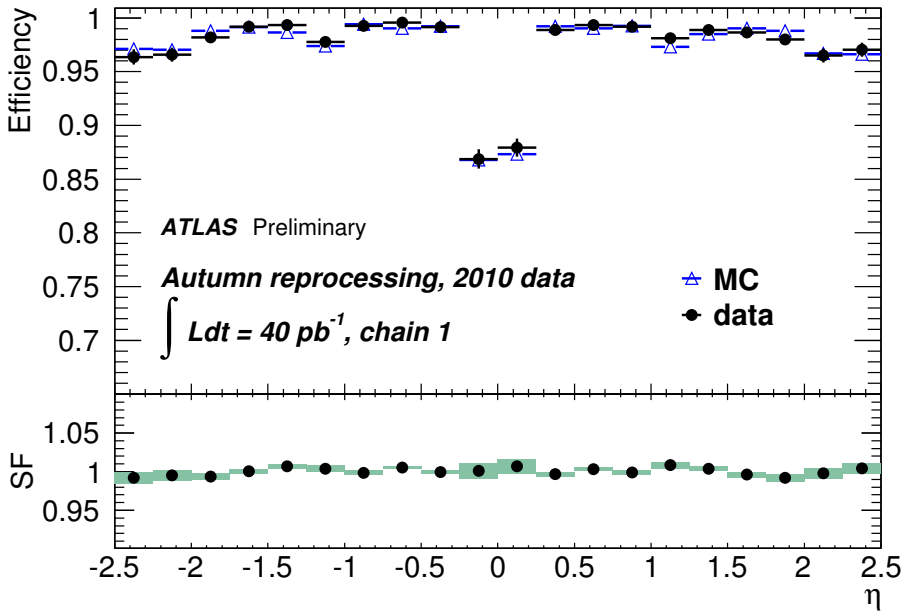

(a) $\varepsilon_{\mathrm{reco}}(\eta)$

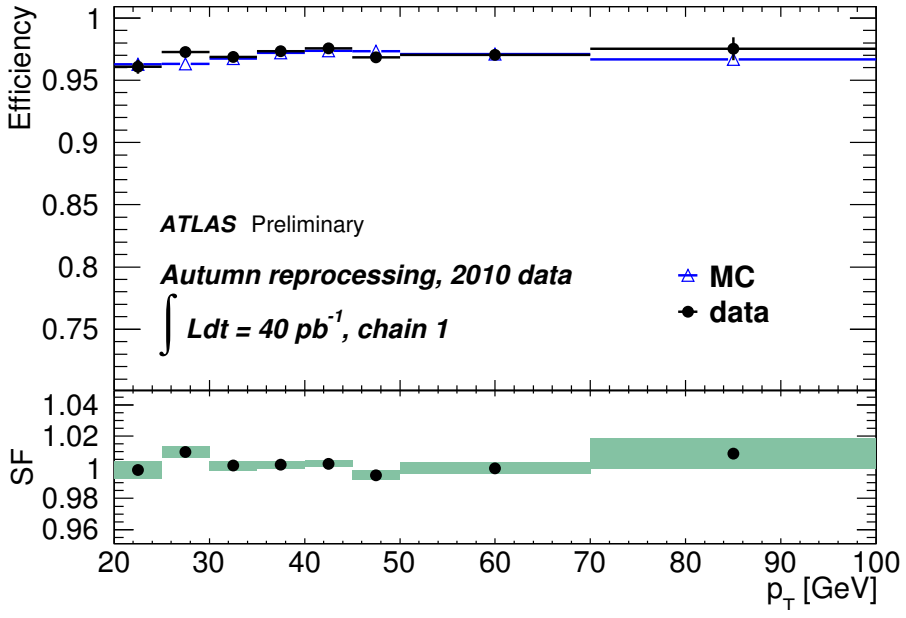

(b) $\varepsilon_{\mathrm{reco}}(p_{\perp})$

Figure 9.11.: Muon reconstruction efficiencies and resulting scale-factors, SF_{reco}, (ratio plot) determined using reprocessed 2010 data [112] as function of the reconstructed muon pseudorapidity (top) and transverse momentum (bottom). Chain 1 corresponds to combined muons. The uncertainty bands show the systematic errors.

Muon trigger efficiency, $\delta SF_{\text{trigger}}$: The muon trigger efficiencies (for `mu_18_MG`) have been determined for Monte-Carlo and data in [55]. The scale factors are simply the (η_μ) and ϕ_μ dependent) ratios of the efficiency in data and in Monte-Carlo:

$$SF_{\text{trigger}}(\eta_\mu, \phi_\mu) = \frac{\varepsilon_{\text{data}}(\eta_\mu, \phi_\mu)}{\varepsilon_{\text{MC}}(\eta_\mu, \phi_\mu)} \tag{9.14}$$

The ϕ-averaged values as well as the uncertainties estimated in [55] are shown in Figure 9.12. The uncertainties are of the order of 2 %.

Since the correction for this data-MC discrepancy is performed by multiplying the Monte-Carlo event weight, w_{MC}, with the trigger scale factors of both muons, systematic uncertainties due to the uncertainties on $SF_{\text{trigger}}(\eta_\mu, \phi_\mu)$ are estimated by varying both scale factors up and down within these uncertainties:

$$\tilde{w}_{\text{MC}} = w_{\text{MC}} \cdot \begin{cases} [SF_{\text{trigger}}(\mu_1) + \Delta SF_{\text{trigger}}(\mu_1)] \cdot [SF_{\text{trigger}}(\mu_2) + \Delta SF_{\text{trigger}}(\mu_2)] \\ [SF_{\text{trigger}}(\mu_1) - \Delta SF_{\text{trigger}}(\mu_1)] \cdot [SF_{\text{trigger}}(\mu_2) - \Delta SF_{\text{trigger}}(\mu_2)] \end{cases} \tag{9.15}$$

The effect of these variations on reconstructed distributions reaches up to 1% in the $p_\perp$(Z) distribution and is negligible in the fully inclusive event shape distributions (Figure 9.14 shows only N_{trk} which is representative for all other event shapes).

Muon transverse momentum corrections

The reconstruction algorithm applies corrections to Monte-Carlo muons in order to match their transverse momenta according to the resolution measured in data. The corrections have been determined in [113] from the di-muon invariant mass distribution present in data and in reconstructed Monte-Carlo events. These uncertainties are treated as systematic uncertainties on the reconstructed muon $p_\perp$ in this analysis.

The nominal correction is obtained from fits for combined muons (inner detector and muon system information). Systematic variations are estimated by varying the correction

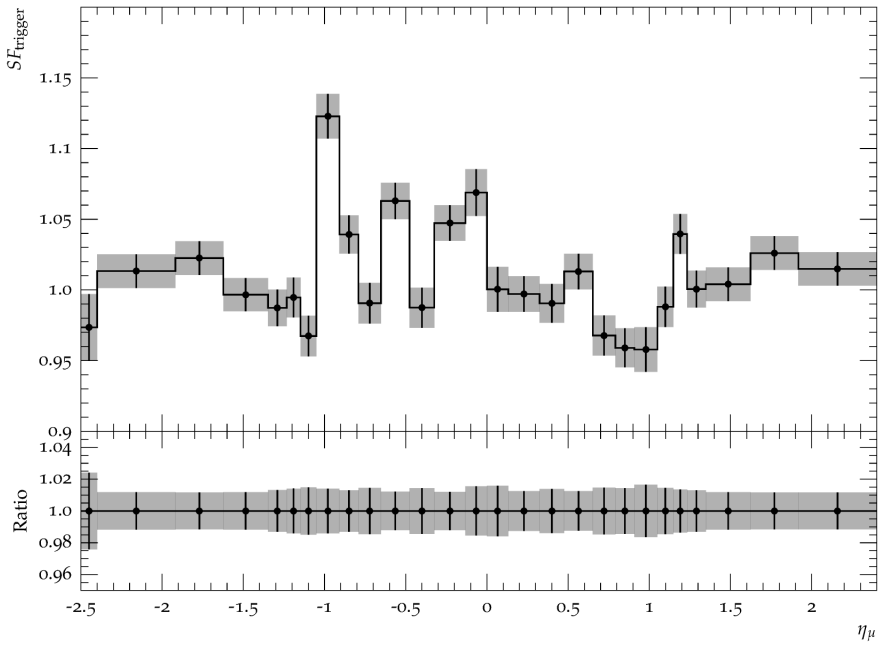

Figure 9.12.: ϕ-averaged muon scale factors [55] for the trigger `mu_18_MG` used in this analysis.

within uncertainties obtained for the inner detector and muon spectrometer information separately.

Inner detector (IS), $\delta p_\perp(\mu)_{\text{ID}}$:

Two variations are performed:

1. varying the correction upwards for both muons
2. varying the correction downwards for both muons

As Figure 9.14 shows that the effect is always smaller than the statistical uncertainties, it rarely exceeds 0.5%.

Muon system (MS), $\delta p_\perp(\mu)_{\text{MS}}$: Again, two variations are performed:

1. varying the correction upwards for both muons
2. varying the correction downwards for both muons

The effect on reconstructed observables is generally small (Figure 9.14). Only for very high values of $p_\perp(\text{Z}) > 80$ GeV does it exceed the statistical uncertainties.

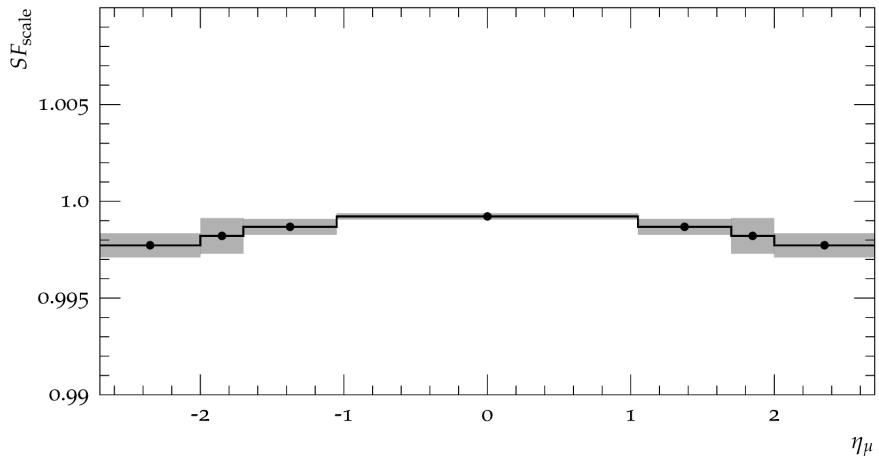

Figure 9.13.: Scale factors SF_{scale} [55] used to match the (combined) reconstructed $p_\perp$ resolution of simulated muons to the one present in data. A systematic uncertainty is estimated by omitting the application of these scale factors ($\delta p_\perp(\mu)_{\text{noscale}}$).

Combined (CB), $\delta p_\perp(\mu)_{\text{noscale}}$:

The nominal combined muons used in this analysis are scaled using the scale-factors, SF_{scale}, shown in Figure 9.13. The systematic uncertainty attributed to this scaling is simply obtained by not applying these scale factors. This procedure is a pragmatic approach to come up with a conservative estimate. The effect on reconstructed distributions is most important for the $p_\perp$(Z) distribution where it reaches values of up to 1% (Figure 9.14), making it the most important source of systematic uncertainties specific to the reconstruction of muons.

Summary of muon systematics

All systematic variations are covered by the statistical uncertainties present in the Sherpa and Pythia8 samples (Figure 9.14) with the total systematic uncertainty rarely exceeding 2%.

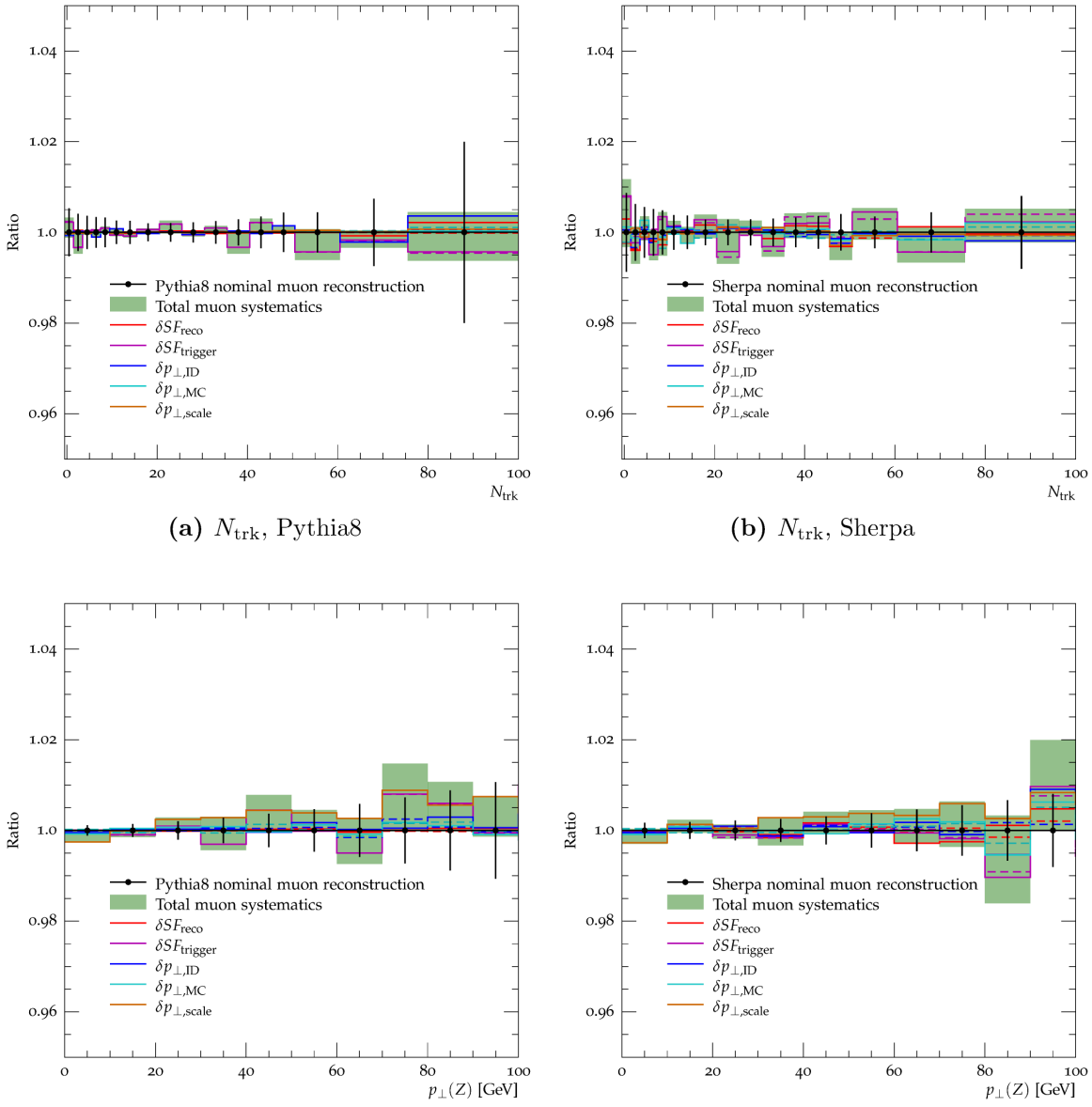

(a) N_{trk}, Pythia8 **(b)** N_{trk}, Sherpa

(c) $p_{\perp}$(Z), Pythia8 **(d)** $p_{\perp}$(Z), Sherpa

Figure 9.14.: Muon systematics and their effect on N_{trk} and $p_{\perp}$(Z). Shown are ratios of systematic variations with respect to the nominal reconstructed distributions as well as the total muon systematic uncertainty (added in quadrature, green band). The statistical uncertainties of the nominal reconstructed observables is shown as black error-bars which always cover the systematic variation. The "up"-variations are drawn as solid lines while the "down"-variations are drawn as dashed lines.

Chapter 10.

Pile-up

10.1. Phenomenology

Since the LHC physics programme is set out primarily to measure the electroweak symmetry breaking and to discover physics beyond the standard model, the processes of interest typically have tiny cross sections, σ_p, compared to typical standard model processes. As the number of events, N_p, of a certain process, p, is connected with σ_p via the luminosity ($N_p = \sigma_p \mathcal{L}$), the design of the LHC is such that the luminosity is as large as technically possible, both in terms of the colliding beams, and the computing resources available required for processing and storing collected data.

Thus, a high spatial density of protons within bunches brought to collision at the LHC and their frequency can give rise to the phenomenon of more than one simultaneous proton-proton interaction being overlaid in a reconstructed event. This effect is commonly known as pile-up and is an inevitable consequence at any high luminosity collider experiment, such as ATLAS. The readout electronics are simply too slow to resolve multiple proton-proton interactions happening during a single bunch-crossing.

The probability for one particular proton to undergo an interaction with a proton from the crossing bunch is extremely small, leading to the necessity to have $\sim 10^{11}$ protons packed in a single bunch in order to have collisions at all. Since the interactions can also be considered independent of one another, the actual number of simultaneous interactions (in a fixed beam setup) is distributed according to a POISSONian with a mean $\langle\mu\rangle$.

While the average number of simultaneous interactions, $\langle\mu\rangle$, at the Tevatron never exceeded 2.5, the ATLAS detector is designed to cope with $\langle\mu\rangle \sim 40$. The data used

in this analysis is from a period with $\langle\mu\rangle = 5$. The type of interactions happening in these additional proton-proton collisions is of course also depending on the cross-sections of processes possible at the LHC with the dominant one being so-called Minimum-Bias events, which includes diffractive proton-proton interactions as well as soft QCD scattering events. What they have in common is the production of charged hadrons and therefore tracks in the reconstruction that overlay the tracks used in this measurement to calculate event shapes. The latter were explicitly chosen because of their high sensitivity to additional tracks coming from multiple parton interactions. Thus they are also highly sensitive to additional charged particles coming from pile-up interactions.

In the following, the effects on the observables of this measurement from and a data-driven correction strategy for pil-up is explained.

10.2. Influence of pile-up on event shape distributions

In Figure 10.1, the effect of pile-up contributions on some of the event shapes measured in this analysis is demonstrated by comparing distributions obtained from reconstructed properties of Pythia8 samples with and without pile-up. The plots show distributions of the electron channel in the fully inclusive $p_{\perp}(\mathrm{Z})$ phase-space. Results for Sherpa and other $p_{\perp}(\mathrm{Z})$ phase-space regions are similar. Obviously, the effect is of non-trivial nature, i.e. it is not a simple constant shift but rather a bin- and observable-dependent variation of up to 15% with the effect being even larger for N_{trk} (Figure 10.1a). Thus, an observable wise correction strategy needs to be applied.

10.3. Pile-up correction

For the data recorded at $\sqrt{s}$ =7 TeV used in this analysis Monte-Carlo samples were produced with pile-up interactions overlaid trying to match the pile-up conditions present in data. This is achieved by merging reconstructed properties of simulated signal events with simulated minimum-bias events with $\langle\mu\rangle$ according to the one present in data[1].

However, the description of predictions obtained from minimum-bias simulations with data is not perfect. In fact, the disagreement is on the order of up to 20% for distributions

[1] Currently, attempts are being made to replace simulated Minimum-Bias events with measured ones in the production of Monte-Carlo samples

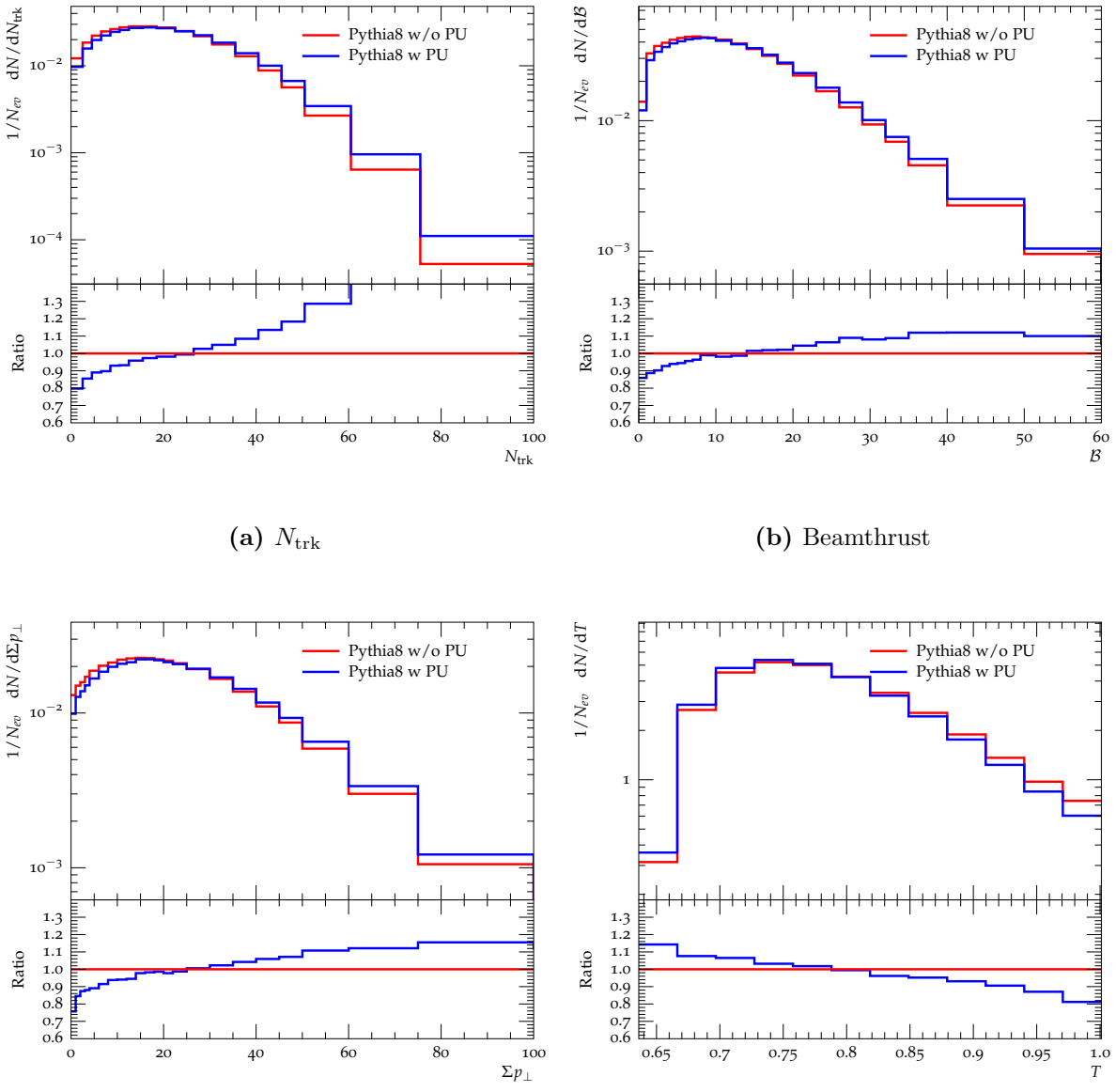

(a) N_{trk} **(b)** Beamthrust

(c) $\sum p_\perp$ **(d)** Transverse Thrust

Figure 10.1.: Comparison of event-shape distributions obtained from the `Pythia8` $Z \to ee$ sample without pile-up (red line) with event shapes obtained from the corresponding `Pythia8` $Z \to ee$ sample with pile-up (blue line) in the fully inclusive $p_\perp(\mathrm{Z})$ phase-space. The observed effect is dependent on the observable under study and partially exceeds 20%.

like the transverse momentum of charged particles [80] in spite of the fact that the Monte-Carlo simulations have been tuned very extensively. Thus, a correction strategy using those Monte-Carlo samples would be very difficult to defend. Nonetheless, the Monte-

Carlo samples with pile-up will prove to be an important test-bed for the data driven pile-up correction procedure explained in the following paragraphs.

The pile-up correction used in this analysis is based on the "Hit Backspace Once More" (HBOM [114]) approach which relies on recursive application of a (detector) effect on to be measured distributions, the parametrisation of these distribution as function of how often the effect was applied and subsequent extrapolation to zero-effect in order to correct for the effect.

In the following, a detailed description is given of how the effect of pile-up contamination on the event-shape distributions is modelled in a data-driven way and how the detector-level correction-factors are obtained and applied. Further, tests of the method based on Monte-Carlo samples will be presented as well as an explanation on how the systematic uncertainties of the method are estimated.

10.4. The HBOM approach

HBOM tries to correct for effects of an imperfect detector (in our case pile-up) by recursive parametrisation of that effect on data distributions and extrapolation of that effect to zero. It then relies on the ability to mimic this effect which of course requires quite some effort as one needs to understand the nature of its source. With this at hand one can start from the distribution one would like to correct for pile-up, D_1. It can be thought of as the bare distribution with a one-time application of the detector effect.

If one knows how to mimic pile-up for a given dataset, its application on on D_1 yields a distribution D_2 which corresponds to the bare distribution but recursively overlaid with pile-up *twice*. One can repeat this procedure a number of times to get a set of histograms $\{D_i\}$ that can be used to calculate a parametrisation of the observables as function of the number of how often the bare distribution was recursively overlaid with pile-up, N_{cont}. The final step (the actual correction) is then to extrapolate to D_0.

The parametrisations are carried out bin-wise without accounting for bin-bin correlations. We use the Professor[115] [2] tool-kit to calculate the parametrisations and extrapolations. In Fig. 10.2) the application of the HBOM method for the correction of pile-up is exemplary illustrated for the transverse thrust distribution obtained from the electron channel Pythia8 sample with pile-up for a single bin (a) and the whole observable (b). The very

[2] The parametrisation is achieved by means of a singular value decomposition (SVD) [116]

involved method to mimic the pile-up contamination applied there is explained in the next paragraph.

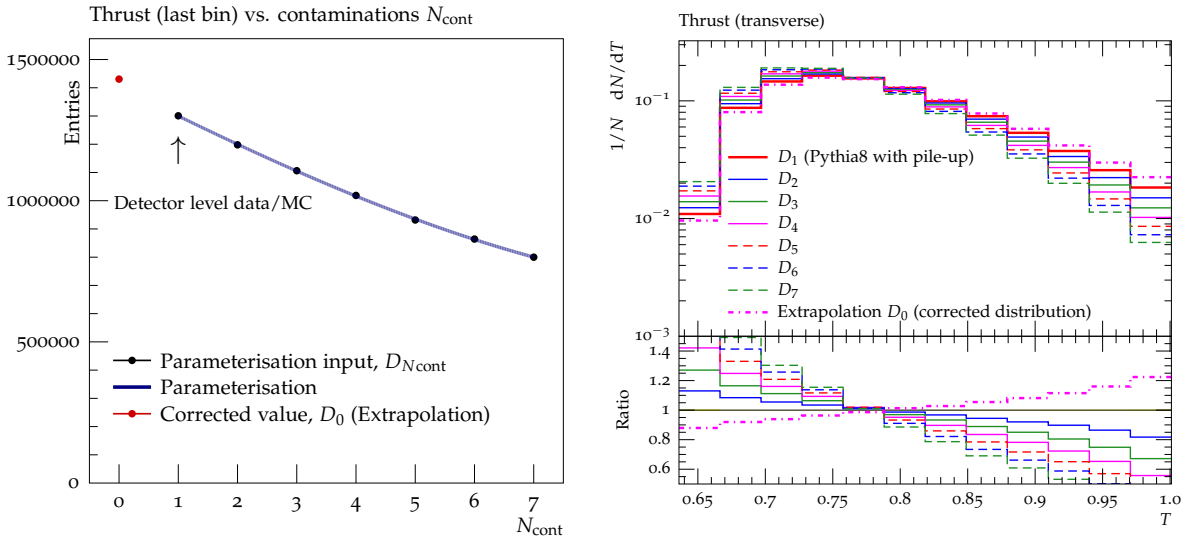

(a) Parametrisation, 1-bin example **(b)** Parametrisation inputs and corrected distribution

Figure 10.2.: Illustration of the HBOM correction-procedure for transverse thrust obtained from a Pythia8 sample. In (a) the dependence of the content of the highest bin of the transverse thrust distribution on the number of recursively added pile-up contaminations, N_{cont}, is shown (black dots). These serve as input for the parametrisation, shown as blue line. The red dot is the extrapolation to the null-effect, i.e. the bin content corrected for pile-up. In (b) the parametrisation inputs are shown as well but for all bins of the observable. The distribution corrected for pile-up (D_0, null-effect extrapolation) is shown as pink, dash-dotted line.

10.4.1. HBOM for pile-up correction

In order to be able to apply the HBOM method for a pile-up correction it is necessary to be able to reproduce pile-up contaminations as realistically as possible, i.e. the effect of a track coming from a pile-up interaction entering the signal track selection (Figure 10.3) needs to be understood and reproduced. This is necessary as the reconstruction software is no able to perfectly distinguish between tracks coming from the primary vertex and tracks coming from pile-up vertices. Thus, the correction procedure will not attempt to remove pile-up tracks on an event-by-event basis but correct for the collective effect of pile-up on observables as a whole. While the exact procedure is described in Section 10.6 it is first necessary to define the inputs needed.

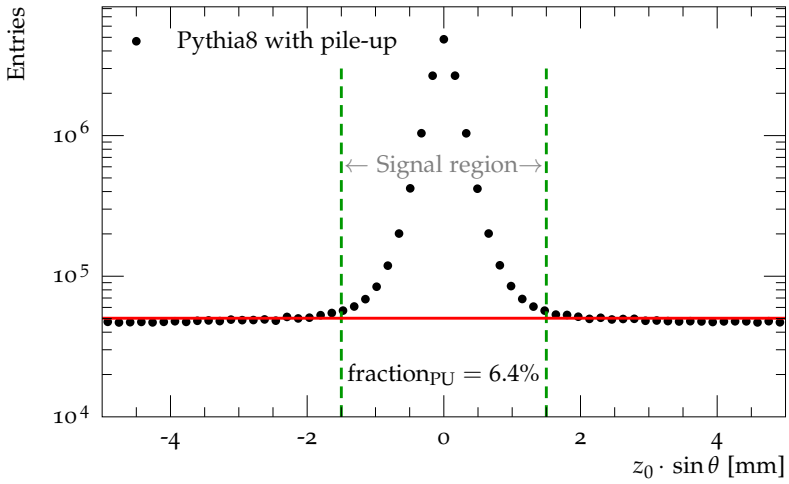

Figure 10.3.: Distribution of $z_0 \cdot \sin\theta$ of tracks used to define the signal selection window of tracks in this analysis ($|z_0 \cdot \sin\theta| < 1.5$ mm, Chapter 5). The narrow peak of signal tracks sits on top of a flat pedestal attributed to tracks coming from pile-up interactions. The distribution is obtained from the Pythia8 $Z \to e^+e^-$ sample with pile-up. The fraction of pile-up tracks in $|z_0 \cdot \sin\theta| < 1.5$ mm was determined for this sample to be 6.4%.

As has been explained in Chapter 5 the reconstruction software used in ATLAS is capable of classifying vertices in an event as primary (`type 1`) and pile-up vertices (`type 3`). This allows to determine the distribution of the number of pile-up vertices per event by simply counting the `type-3` vertices per event. Although a data-period with an approximately constant number of simultaneous interactions ($\langle\mu\rangle \sim 5$) was analysed in this measurement, this does not necessarily limit the applicability of the `HBOM` method as the distribution of the number of additional proton-proton interactions is directly taken from the actual distribution of the per-event number of `type-3` vertices present in the sample one wishes to correct for pile-up (Figure 10.4a). By doing do, the vertex reconstruction efficiency is automatically taken into consideration.

Finally, and most important, the reconstruction algorithm is capable of associating tracks to `type 3` vertices, however only if such a vertex is well separated from another vertex. This turned out to be crucial in the development of the correction method, since the (as became clear) naive approach to simply remove those tracks associated to `type-3` vertices was found to fail exactly due to `type-3` vertices being too close to one another in z, since it can happen that a single vertex is falsely reconstructed as two vertices close in z (so-called split vertices). Thus, a method was developed that accounts for split vertices by the construction of a library of pseudo-vertices using tracks in the vicinity of well

isolated `type 3` vertices instead of relying on the association of tracks to vertices made by the reconstruction. Since the probability to find a pile-up vertex at a given position along the beam-line, z, is non-constant (Figure 10.4b) it is necessary to store the pile-up pseudo-vertices in such a way that the information of its z-position is kept.

It is important to stress that all input to the method are extracted from the same sample that is to be corrected for pile-up. On one hand, this gives rise to the application of closure-tests based on Monte-Carlo samples. The successful outcome of the latter (Section 10.7) is the basis for the application of the method to data. On the other hand, this is the reason why the method is purely data-driven when applied to distributions obtained from reconstructed data events.

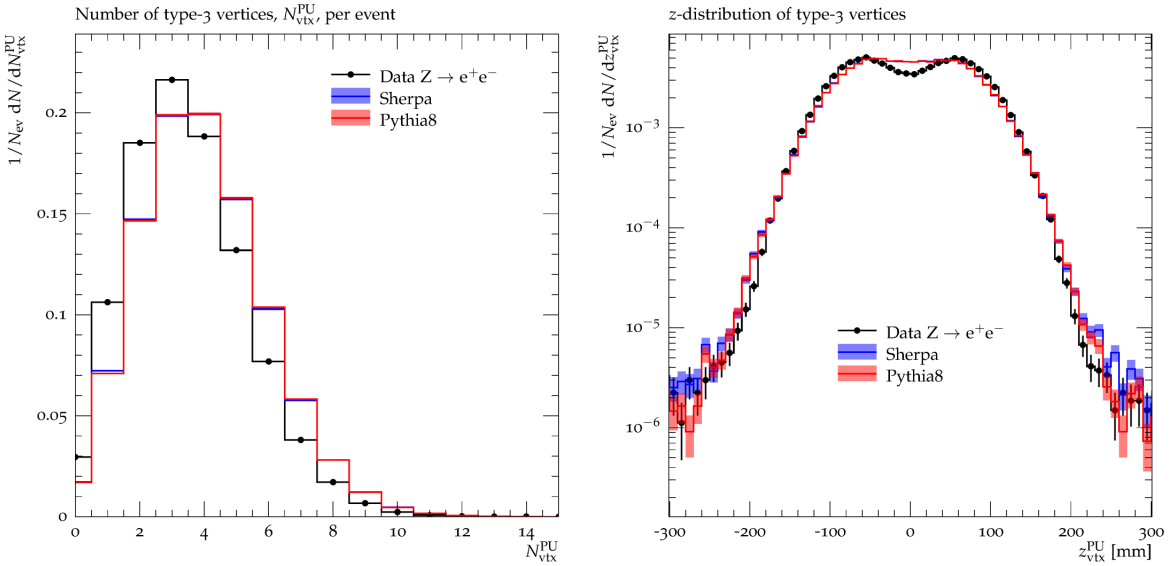

(a) Number of `type-3` vertices per event

(b) z-distribution of `type-3` vertices per event

Figure 10.4.: Histograms used as input for the pile-up correction. (a) shows the distribution of the number of reconstructed `type 3` vertices per event (electron channel) as obtained from the sample to be corrected for pile-up. (b) shows the z-distribution of `type 3` vertices as present in the sample to be corrected for pile-up. The histograms are used to get random numbers N_{rdm} and $z_{\text{rdm},i}$ used as input for the recursive pollution of events with pile-up. Only electron channel results are shown since the corresponding muon channel distributions are almost identical.

10.5. The pile-up library

The pile-up library stores tracks in the vicinity of `type-3` separately for each event processed (called "pseudo-vertex" in the following) and also keeps track of the position of the corresponding vertices along the beam-pipe, z_{vtx}. The procedure is done separately for each sample one wishes to correct for pile-up. *In praxi* this means separate libraries for data and each Monte-Carlo sample with pile-up are created. Further and although not necessarily important, the procedure is done separately for electron and muon channel samples.

All `type-3` vertices of events passing the nominal event selection of a sample are potential candidates for the library, however, to safeguard against the effect of split vertices mentioned earlier it is required that `type-3` vertices have a minimum distance along the beam line, $\Delta z^{\text{vtx}}_{\text{min}}$, from any other vertex (primary and pile-up) of 60 mm in order to be selected for the pile-up library. An illustration of the vertex-selection procedure can be found in Figure 10.5a.

The selection of tracks when constructing a pseudo-vertex at z_{vtx} requires the tracks to fall into a track selection window in the vicinity of z_{vtx}. In order to select these tracks similar to the signal tracks (Figure 10.3) a longitudinal impact parameter of each track w.r.t. z_{vtx} needs to be constructed. Its calculation requires the longitudinal impact parameter of a track w.r.t. the primary vertex, $z_{0,\text{trk}}$, which is a property of the track reqconstruction algorithm as is the track's polar angle θ_{trk}. Finally, the (`type-3`) vertex position, $z^{\text{PU}}_{\text{vtx}}$ is required:

$$\left|z_0^{\text{PU}} \cdot \sin\theta_{\text{trk}}\right| := \left|(z^{\text{PU}}_{\text{vtx}} - z_{0,\text{trk}}) \cdot \sin\theta_{\text{trk}}\right| < 3 \text{ mm} \tag{10.1}$$

Note that this selection window is larger than the nominal track selection window w.r.t. the primary vertex when selecting signal tracks. This is necessary to be able to account for a strafing superposition of the primary vertex with a pile-up pseudo vertex (Figure 10.5b).

For each track fulfilling the requirements above, the following properties are stored to form the pseudo-vertex in order to allow the calculation of the longitudinal impact parameter of a pile-up track w.r.t. a to be overlaid primary vertex, to decide whether a track falls into the signal track selection when overlaid and to add the track three-vector to the event:

Sample	# pseudo-vertices, electron channel	# pseudo-vertices, muon channel
Data	268164	419550
Pythia8	547864	865653
Sherpa	516398	838443

Table 10.1.: Overview of the available statistics of pseudo-vertices extracted from data and Monte-Carlo samples available in the corresponding pile-up libraries.

- longitudinal distance to the `type-3` vertex, $z_0^{\mathrm{PU}} = z_{\mathrm{vtx}}^{\mathrm{PU}} - z_{0,\mathrm{trk}}$
- angle between $\vec{p}_{\mathrm{trk}}$ and the beam-line, θ_{trk}
- three momentum vector $\vec{p}_{\mathrm{trk}} = (p_x, p_y, p_z)$

Table 10.1 gives an overview of the extracted numbers of pseudo-vertices for all data and Monte-Carlo samples used in this analysis.

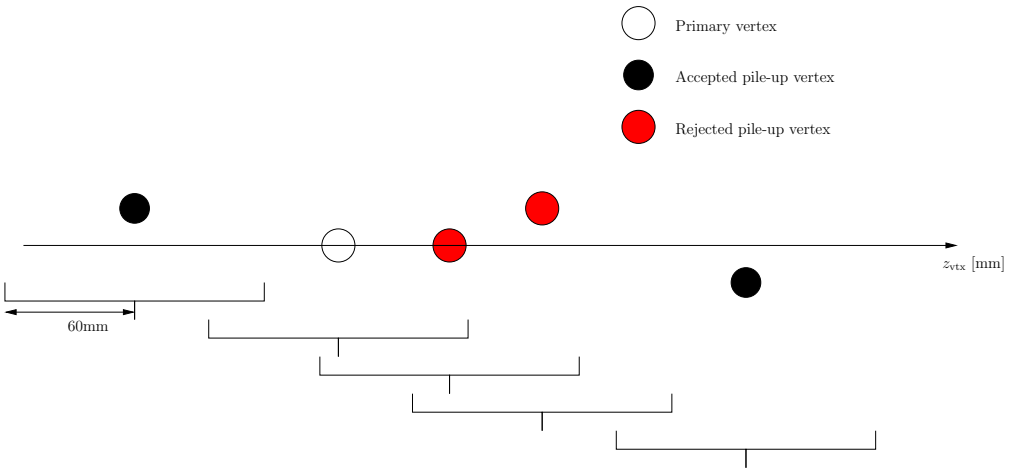

(a) Vertex selection. Only the black vertices fulfil the isolation criterion of being 60 mm apart from the primary and any other vertex and are thus selected when building the pile-up library.

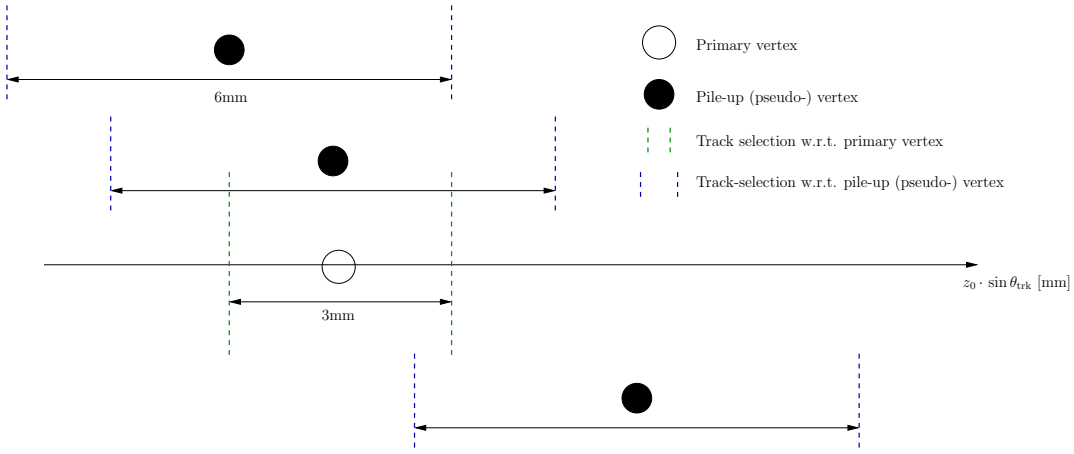

(b) Sketch of overlapping vertices, illustrating the principal idea of how to add pile-up tracks to an event, i.e. the track selection w.r.t. the primary vertex (white). Each track of a randomly added pile-up vertex is probed whether it falls into the signal track selection window. In order to allow for non-exactly overlapping scenarios (e.g. black vertex at the bottom), the track selection window when constructing pile-up (pseudo-) vertices (black) needs to be chosen twice as wide as the actual track selection window w.r.t. the primary vertex of $|z_0 \cdot \sin\theta_{\text{trk}}| < 1.5$ mm.

Figure 10.5.: Schematic description of vertex and track selection for the pile-up library. The y-coordinate is irrelevant here. In (a) only those vertices are considered that suffice a minimum distance requirement to any other vertex in the event. In (b) the selection window $|(z_{\text{vtx}}^{\text{PU}} - z_{0,\text{trk}}) \cdot \sin\theta_{\text{trk}}|$ is chosen wide enough to allow for modelling of non-exactly overlapping vertices. The nominal values for the cuts entering the selection of tracks are summarised in Table 10.2. Note that only events passing the nominal event selection are used.

10.6. Mimicking the pile-up contamination

With the pile-up library and the distributions shown in Figure 10.4 at hand the pile-up contamination can be mimicked on an event-by-event basis. To obtain the nominal distribution (one-time pile-up polluted, i.e. data), D_1 (Figure 10.2b), no additional pile-up tracks are added. The recursive contamination of D_1 with the aim to obtain the two-times contaminated distribution, D_2, the following steps are performed for each event:

1. Pull a random number of pseudo-vertices, N_{rdm}, from the distribution of the number of `type-3` vertices per event corresponding to the data or MC sample to be corrected for pile-up (Figure 10.4a). This number is used to determine how many pile-up vertices are present in addition to the primary vertex in this event.

2. Pull N_{rdm} random vertex positions, $z_{\mathrm{rdm},i}$, from the corresponding histogram (Figure 10.4b). For each of those, pick a random pile-up vertex from the library entry corresponding to $z_{\mathrm{rdm},i}$. Each of these vertices will contain a different number of tracks. At this point, also the position of the N_{rdm} pseudo-vertices is known, as well as the number of tracks associated to each of those.

3. For each of those tracks it is probed whether it falls into the signal track selection window $|(z_{\mathrm{PV}} - z_{\mathrm{trk}}) \cdot \sin\theta_{\mathrm{trk}}| < 1.5$ mm (see Section 10.5). To do that, the distance along the beamline of a track to the event's primary vertex position, z_{PV}, is calculated. A track fulfilling

$$\left| \left(z_{\mathrm{PV}} + z_{\mathrm{rdm},i} + \underbrace{z_{0,ij}^{\mathrm{PU}}}_{\text{Distance of track and pile-up vertex}} \right) \cdot \sin\theta_{\mathrm{trk}}^{ij} \right| < 1.5 \text{ mm}$$

   is then added to the list of an event's signal tracks. The index i corresponds to a certain pseudo-vertex and j to a track from its vicinity (Section 10.5).

In order to obtain the more-than-once HBOM contaminated distributions, $D_{3\ldots N}$, all steps are repeated recursively N times.

10.6.1. Forward closure

The validity of the method can be test using Monte-Carlo samples. The test described here checks if it is possible to derive the one-time pile-up contaminated distributions

D_1 obtained from the Monte-Carlo sample without pile-up by applying the procedure explained above once to each event when processing the corresponding Monte-Carlo sample without pile-up.

Since the number of observables is very large in this analysis, it was chosen to only present results for two observables for the low $p_\perp(\mathrm{Z})$ phase-space region, namely N_{trk} (Figure 10.6) and transverse thrust (Figure 10.7). The non-closure (difference between D_1 obtained from pile-up sample and D_1 obtained from sample without pile-up) is very small (a few percent in some bins). It was found that observable where the number of tracks does not enter the definition (transverse thrust and major, F-Parameter, spherocity) yield a closure that is almost perfect in all bins in all $p_\perp(\mathrm{Z})$ phase-space regions. For all other observables, bins with low statistics tend to show some deviation. No dependence of that behaviour on the $p_\perp(\mathrm{Z})$ phase-space region was found. Further, results for the electron and muon channel are very similar. The same is true when comparing Pythia8 and Sherpa which gives confidence that the method will also work when recursively repeated in order to obtain the parametrisations and eventually extrapolations to null-effect, i.e. correction for pile-up.

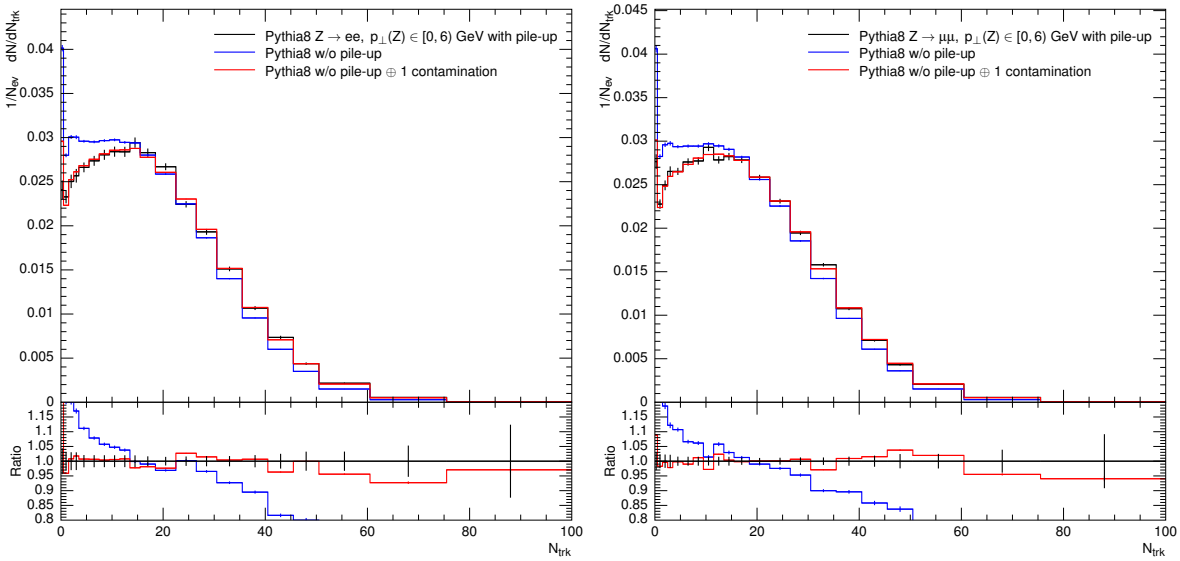

(a) Pythia8

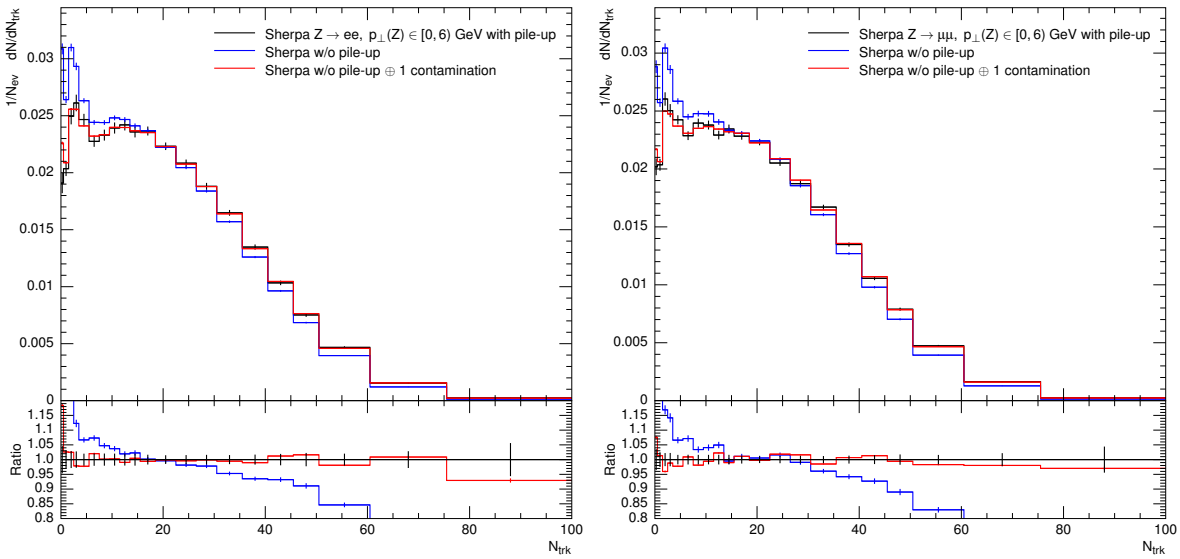

(b) Sherpa

Figure 10.6.: Forward closure tests for the `HBOM` procedure to contaminate distributions with pile-up in case of N_{trk}. A comparison of the distribution obtained from the Monte-Carlo sample with pile-up (black line) and the distribution obtained from the corresponding Monte-Carlo sample without pile-up before (blue line) and after one application of the procedure described in Section 10.6 (red line) is shown for Pythia8 (top) and Sherpa (bottom). Results of the electron channel are shown in the plots on the left hand side, those for the muon channel on the right hand side. All plots show results for the $p_{\perp}(\text{Z}) < 6$ GeV phase-space region. The closure (black and red line) was found to be of the order of $1 \ldots 2\%$ for most bins with the difference being covered by the (statistical) error-bars.

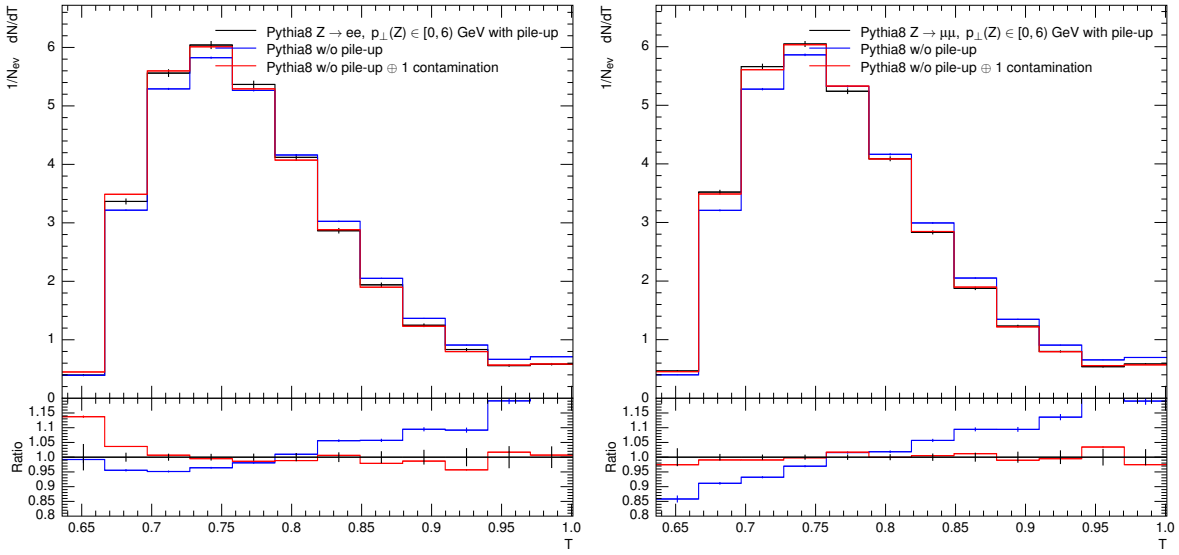

(a) Pythia8

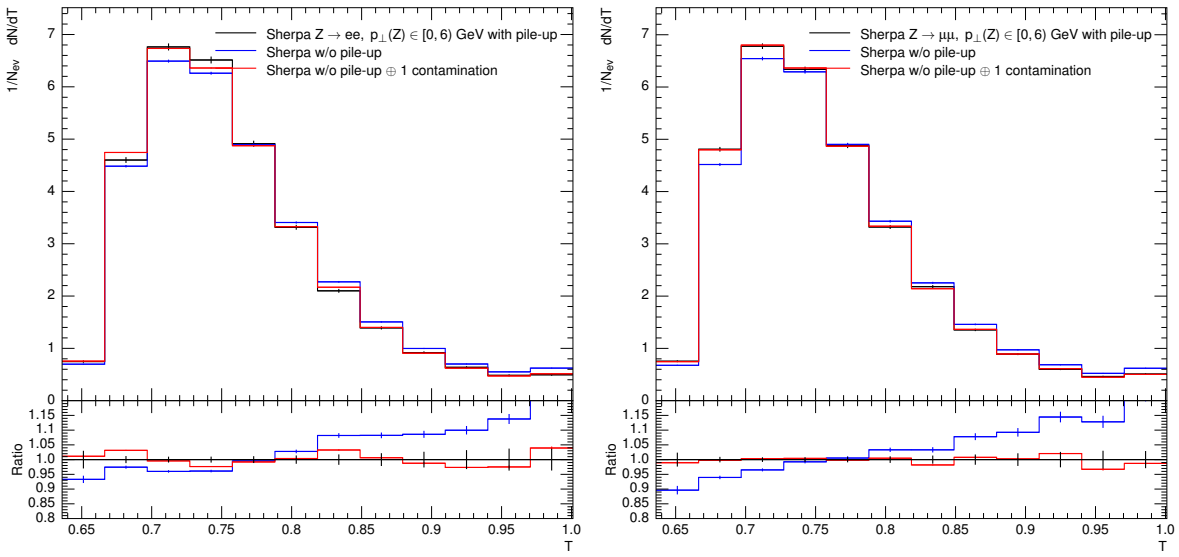

(b) Sherpa

Figure 10.7.: Forward closure tests of the HBOM procedure to contaminate distributions with pile-up in case of transverse thrust. A comparison of the distribution obtained from the Monte-Carlo sample with pile-up (black line) and the distribution obtained from the corresponding Monte-Carlo sample without pile-up before (blue line) and after one application of the procedure described in Section 10.6 (red line) is shown for Pythia8 (top) and Sherpa (bottom). Results of the electron channel are shown in the plots on the left hand side, those for the muon channel on the right hand side. All plots show results for the $p_\perp(\mathrm{Z}) < 6$ GeV phase-space region. The closure (black and red line) was found to be of the order of 1% for most bins with the difference being covered by the (statistical) error-bars.

10.7. Correction closure tests and systematics

The results of the previous section allow to proceed with the HBOM procedure, i.e. the production of more than twice contaminated distributions, the parametrisation of the shape change as function of the number of pile-up contaminations and the extrapolation to the null-effect. The ultimate test of the validity of the pile-up correction method is a comparison of distributions free of pile-up, D_0, obtained from the sample without pile-up and obtained from the sample *with* pile-up after the pile-up correction. Obviously, these tests are performed using Monte-Carlo samples. For a realistic comparison, the systematic uncertainties of the method and their effect on the pile-up corrected distributions need to be quantified first. All systematic uncertainties considered are related to the parametrisation and thus affect the result of the extrapolation:

- Variation of the degree of polynomials used (Section 10.7.1)
- Smearing of parametrisation inputs within their statistical uncertainties (Section 10.7.2)
- Omission of anchor points of the parametrisations (Section 10.7.3)

To obtain the total uncertainty of the method, these systematic uncertainties are added in quadrature. The individual components are explained in the following.

10.7.1. Degree of polynomials

The extrapolations used to obtain the distributions corrected for pile-up will depend to some degree on the functional form of the parametrisation used which is based on polynomials. The limiting factor for the order of the polynomials, n, used is the computational cost which increases linearly with n, since the pile-up pollution is applied recursively.

Further, the minimal number of anchor points required to calculate a parametrisation using a one-dimensional polynomial of order n is $N_n = n + 1$. N_n however does not yield a sufficiently good parametrisation (in terms of closure tests), as the system of equations used to obtain the latter is not over-constrained. A good quality of the parametrisation requires N_n being at least $2 \cdot n$ (See [115] for a discussion). For all Monte-Carlo and data samples, $n = 11$ anchor points were produced.

2^{nd} order polynomials were found to be insufficient while 3^{rd} order polynomials vastly improve the performance of the HBOM method. Only small qualitative improvements

are found when using 4^{th} order polynomials. 5^{th} order polynomials were deemed too computationally expensive with only marginal improvements, which is why 4^{th} order polynomials are used to obtain the nominal extrapolations used to correct for pile-up.

It was thus chosen to be pragmatic about the estimation of a systematic uncertainty due to the choice of the order of the polynomials, i.e. the symmetrised difference of the extrapolations obtained using 3^{rd} and 4^{th} order polynomials is used as systematic uncertainty.

Results for a selection of observables can be found in Figure 10.8 and 10.9. The uncertainty rarely exceeds 2% except for bins with low statistics, e.g. $N_{\text{trk}} > 60$.

10.7.2. Smearing of input data

The method used for the parametrisation (singular value decomposition, SVD) does not take statistical uncertainties of the input data into account. In order to quantify the effect on the extrapolations due to these nonetheless, the input distributions $D_1 \cdots D_{11}$ are smeared within their statistical uncertainties, thus creating slightly different inputs for the parametrisations. The smearing is done using random numbers pulled from a GAUSSIAN distribution, $\mathcal{G}_{\text{bin}}(\mu, \sigma_{\text{bin}})$ with mean $\mu = 0$ and standard deviation σ_{bin}, being a bin's statistical uncertainty.

Each input distribution is smeared 1000 times allowing for the calculation of 1000 slightly different parametrisations and thus 1000 slightly different sets of extrapolations, $\{\tilde{D}_0\}$. For each bin of an observable the distribution of differences of the $\{\tilde{D}_0\}$ and the nominal corrected histograms D_0 is fitted with a GAUSSIAN. The standard deviation of the fit is then taken as the systematic uncertainty of that particular bin due to statistical uncertainties present in the parametrisation inputs.

The estimated uncertainty is the dominant source of systematic uncertainties in most bins (Figure 10.8 and 10.9) with values up to a few percent. In bins with low statistics and thus large statistical uncertainties, the systematic uncertainty estimates rises significantly.

10.7.3. Variation of parametrisation inputs

Another systematic uncertainty estimate is obtained by omitting an anchor-point when calculating the parametrisations so that the stability of the interpolation can be tested.

It was chosen to never skip D_1 such that the extrapolation is not too far away from the interpolation. Thus $n-1$ different parametrisations are calculated, omitting a single anchor-point D_n, $n \in [2, 11]$. The largest deviations of these extrapolations in a particular bin to the nominal extrapolation (using all D_n) is taken as systematic uncertainty of that bin. The effect was found to rarely exceed 1% and being negligible in most bins (Figure 10.8 and 10.9).

10.7.4. Closure-tests of the correction

To convince oneself that the HBOM pile-up correction works as expected, further closure tests are performed, called "backward closure-tests" in contrast to the "forward closure-tests" in Section 10.6.1.

This time, distributions free of pile-up, D_0, obtained once from the sample without pile-up and once obtained from the sample *with* pile-up after being corrected for pile-up are compared.

When taking the total systematic uncertainty of the extrapolation into account, the closure is found to be perfect for most bins of most observables. Especially transverse thrust and minor as well as F-Parameter and Spherocity yield very convincing results. However, a large difference in the first bin of the N_{trk} distribution is not covered by the uncertainties estimated.

The closure was found to be of similar quality for both Monte-Carlo samples in all $p_\perp(\text{Z})$ phase-space regions in the electron as well as the muon channel (Figure 10.8 and 10.9).

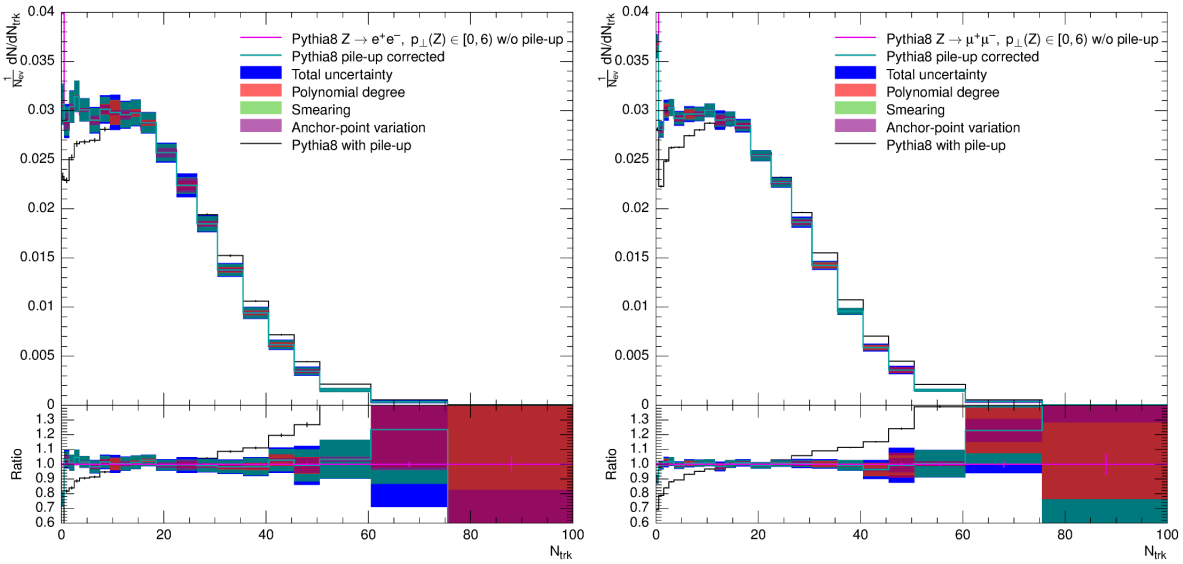

(a) Pythia8

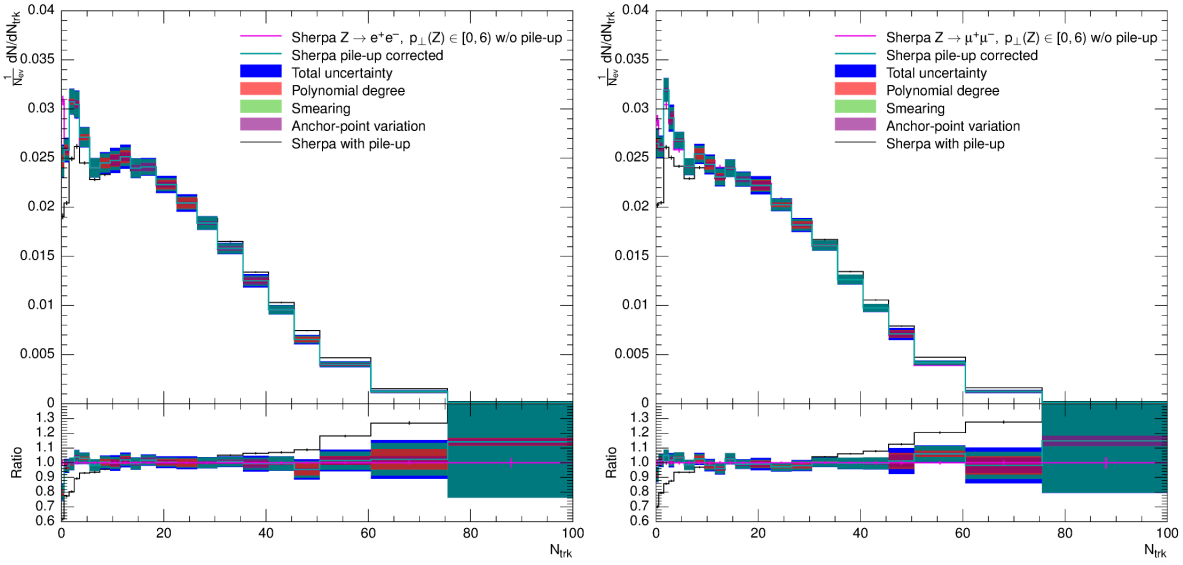

(b) Sherpa

Figure 10.8.: Backward closure tests for the HBOM pile-up correction for N_{trk}. A comparison of the distribution obtained from the Monte-Carlo sample without pile-up (magenta line) and the distribution obtained from the corresponding Monte-Carlo sample with pile-up before (black line) and after pile-up correction (cyan line) is shown for Pythia8 (top) and Sherpa (bottom). Results of the electron channel are shown in the plots on the left-hand side, those for the muon channel on the right-hand side. All plots show results for the $p_\perp(\text{Z}) < 6$ GeV phase-space region. The closure (cyan and magenta line) is perfect for most bins when taking the total systematic uncertainty into account (blue band).

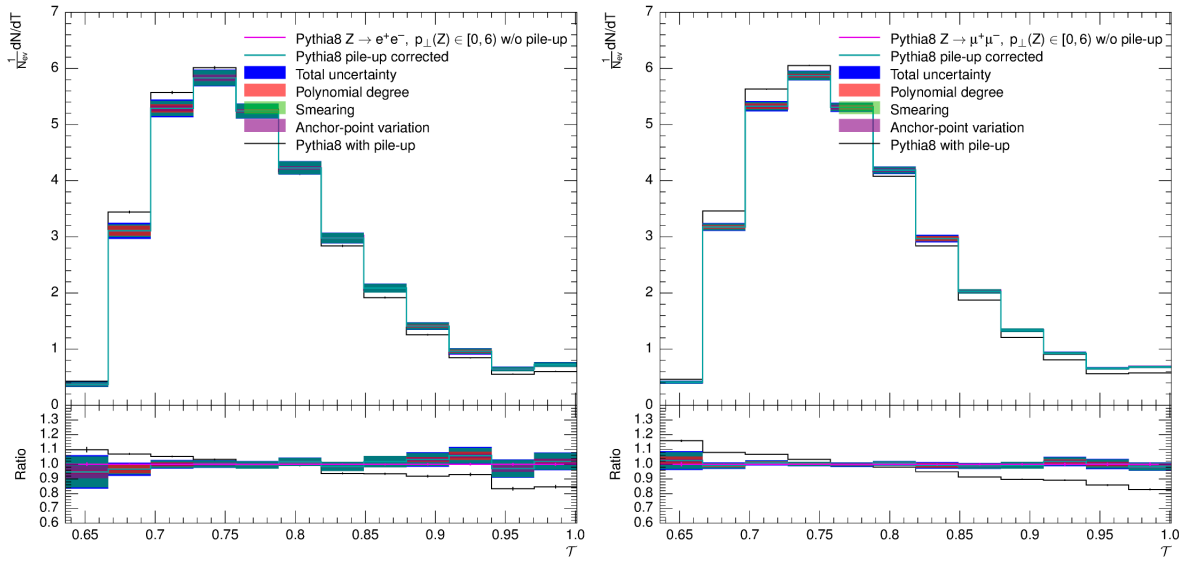

(a) Pythia8

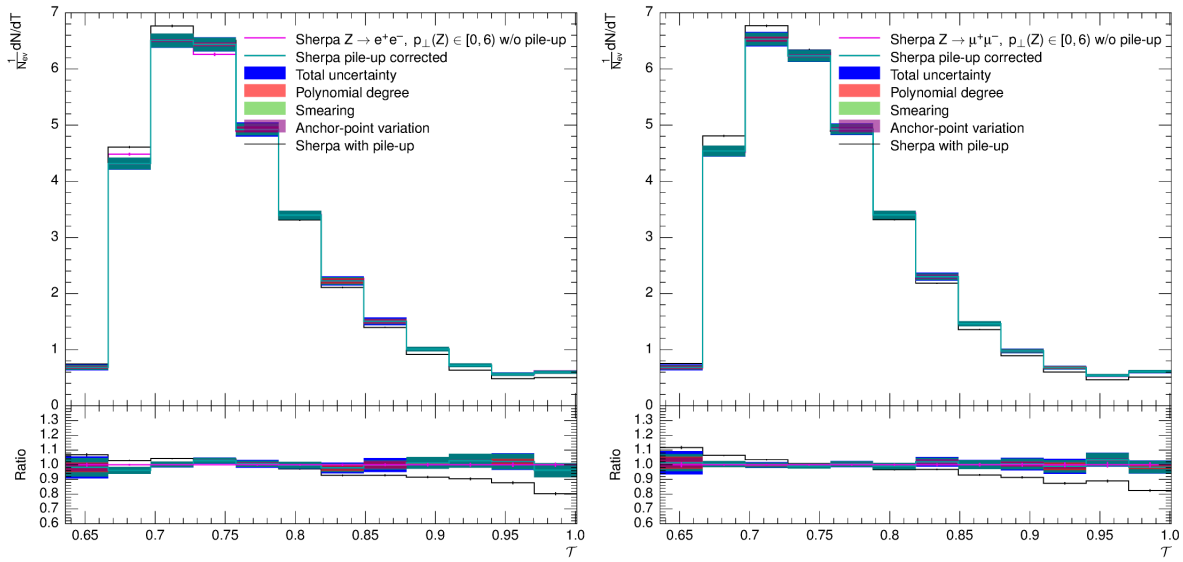

(b) Sherpa

Figure 10.9.: Backward closure tests for the HBOM pile-up correction for transverse thrust. A comparison of the distribution obtained from the Monte-Carlo sample without pile-up (magenta line) and the distribution obtained from the corresponding Monte-Carlo sample with pile-up before (black line) and after pile-up correction (cyan line) is shown for Pythia8 (top) and Sherpa (bottom). Results of the electron channel are shown in the plots on the left-hand side, those for the muon channel on the right-hand side. All plots show results for the $p_\perp(\mathrm{Z}) < 6$ GeV phase-space region. The closure (cyan and magenta line) is perfect when taking the total systematic uncertainty into account (blue band).

10.8. Stability test of the pile-up library

A final test of the pile-up correction method investigates the stability under changes of the two parameters driving the vertex and the track selection for the pile-up library, i.e. the minimum distance of vertices, $\Delta z_{\text{min}}^{\text{vtx}}$, and the track selection window, $\left|z_0^{\text{PU}} \cdot \sin\theta_{\text{trk}}\right|$. In the following, the results of a study are presented where these parameters were varied in a correlated way of $\pm 10\,\%$ from their nominal values (see Table 10.2). By doing so, four different pile-up libraries are generated (V1...V4) that, depending on the variation, contain more or less isolated pseudo-vertices as well as more or less tracks associated with them compared with the nominal pile-up library[3].

Each of these libraries is used to redo the extrapolation to the null-effect, yielding four sets of slightly different distributions corrected for pile-up. Given the previous findings on the universality of the successful application of the method regarding the applicability to Monte-Carlo samples and to both lepton channels in all $p_\perp(\text{Z})$ phase-space regions, it was chosen to conduct this study using the electron channel Pythia8 sample in the fully inclusive $p_\perp(\text{Z})$ phase-space only. In order to describe the maximal deviations from the nominally obtained corrected distributions, the envelope of the corrected distributions obtained with $\text{V1}\cdots\text{V4}$ is calculated and compared with the total systematic uncertainties of the nominal pile-up corrected distributions.

The results are shown for a selection of observables in Figure 10.10. The variations obtained through the usage of different selection criteria when building the pile-up library is found to be compatible with the total systematic uncertainty of the pile-up correction. The variation has the largest effect on low statistics bins of N_{trk}. In summary, the pile-up correction procedure is found to be stable against variations of the track selection cuts used to build the pile-up library.

Parameter	Nominal value	V1	V2	V3	V4
$\Delta z_{\text{min}}^{\text{vtx}}$ [mm]	60	54	54	66	66
$\left\|z_0^{\text{PU}} \cdot \sin\theta_{\text{trk}}\right\|$ [mm]	3.0	2.7	3.3	2.7	3.3

Table 10.2.: Parameters for the selection of vertices and tracks when constructing pile-up libraries.

[3] It should be noted that the same random seeds were used when building the nominal pile-up libaries and the libraries $\text{V1}\cdots\text{V4}$.

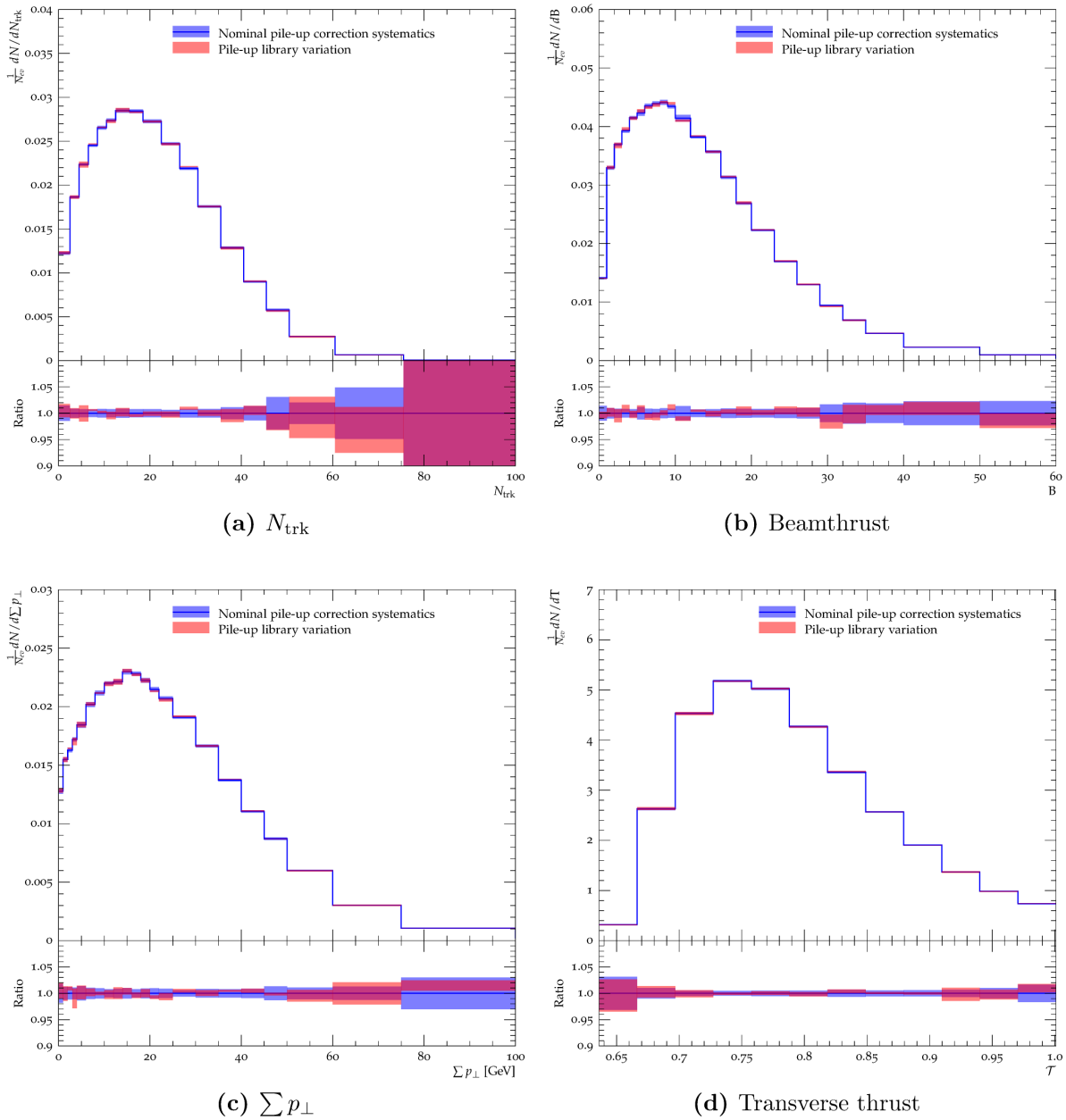

(a) N_{trk} **(b)** Beamthrust

(c) $\sum p_\perp$ **(d)** Transverse thrust

Figure 10.10.: Stability test of the pile-up correction. The vertex isolation cut and the track selection window used when building the pile-up library were varied in a correlated way by $\pm 10\,\%$ of their nominal values. The red band shows the total envelope of these variations. A comparison with the total systematic uncertainty of the nominal pile-up correction (blue band) shows compatibility for most bins of most observables. The plots show results for the electron channel Pythia8 sample in the fully inclusive $p_\perp(\text{Z})$ phase-space region.

10.9. Pile-up correction factors

As will be explained in Chapter 12 the correction strategy of this analysis requires to correct detector-level distributions for pile-up prior to the final correction step, i.e. unfolding. The software used requires the pile-up correction to be formulated in a multiplicative way, i.e. the calculation of pile-up correction factors, $c_{\mathcal{O}}^{\mathrm{PU}}(b)$, for each bin, b, of each observable $\mathcal{O}$:

$$c_{\mathcal{O}}^{\mathrm{PU}}(b) = 1 - \frac{f_{\mathcal{O}}^{\text{PU corrected}}(b)}{f_{\mathcal{O}}^{\text{nominal}}(b)} \tag{10.2}$$

where $f_{\mathcal{O}}^{\text{PU corrected}}(b)$ is the pile-up corrected content of bin b of observable $\mathcal{O}$ (identical to D_0) and $f_{\mathcal{O}}^{\text{nominal}}$ denotes the corresponding detector-level distribution contaminated with pile-up (identical to D_1).

Figure 10.11 shows the N_{trk} and transverse thrust distributions of the so obtained pile-up correction factors to be applied on data for both lepton channels and all $p_{\perp}(\mathrm{Z})$ phase-space regions. The corresponding plots for all other observables can be found in the appendix (Section C.1). Although in general the correction factors are rather similar for all $p_{\perp}(\mathrm{Z})$ phase-space regions, a mild dependence on the latter with differences up to 10% can be observed. This shows that observables change dramatically as soon as a recoiling jet emerges, which is taken into account with the pile-up correction method chosen.

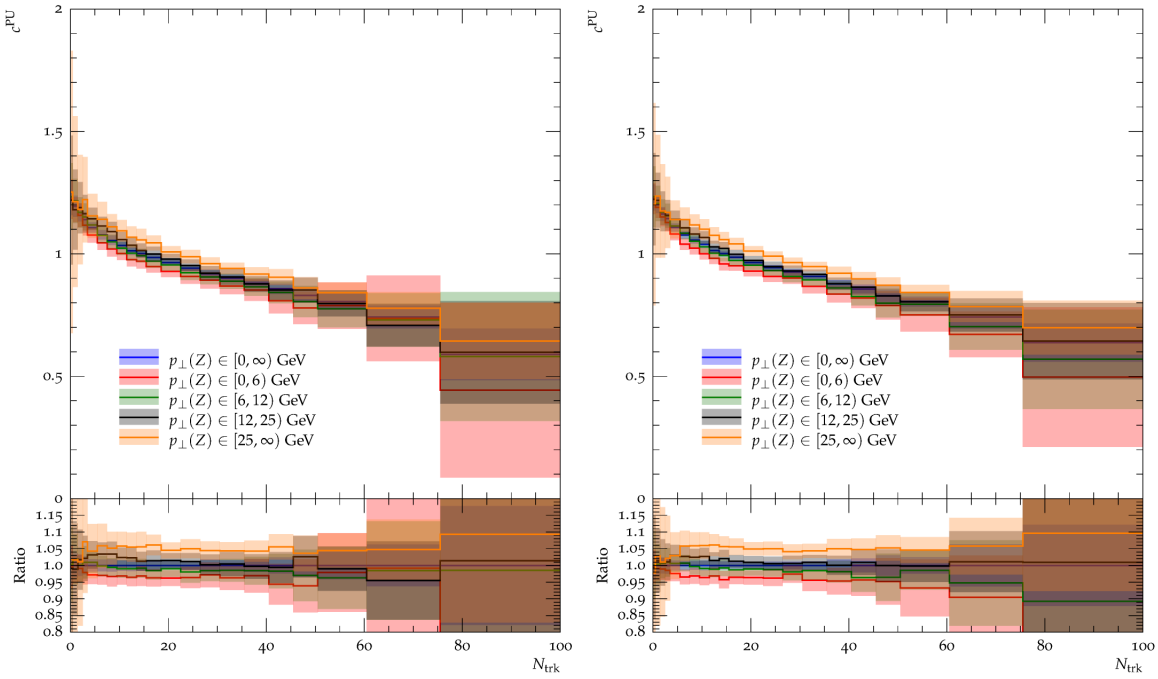

(a) N_{trk}

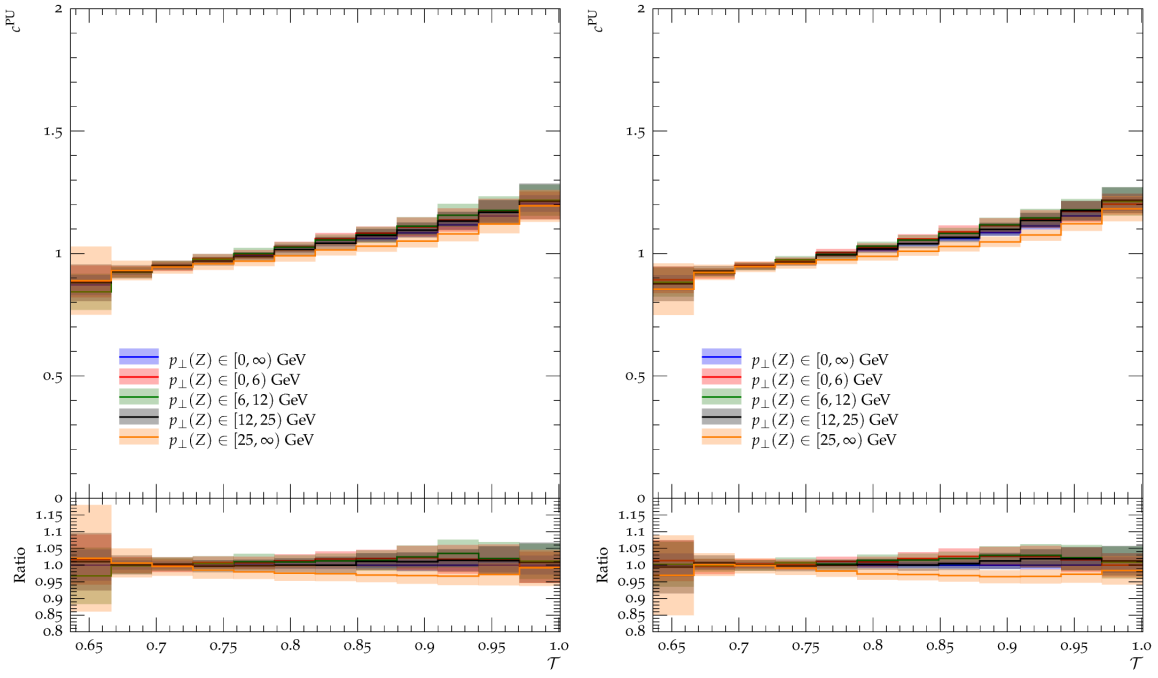

(b) Transverse thrust

Figure 10.11.: Pile-up correction factors obtained using the HBOM technique from the data samples to be corrected for pile-up. Plots on the left-hand side show results for the electron channel, plots on the right-hand side those of the muon channel. The error-bands show the total systematic uncertainty of the pile-up correction.

Chapter 11.

Background subtraction

In this section, the treatment of background processes entering the event-selection is explained. The dominating source in both channels are contributions from QCD processes. They are corrected for in a data-driven way. Combinatorial backgrounds from standard model processes other than the signal process are at least one order of magnitude smaller than QCD contributions and are thus not estimated.

11.1. QCD background

In both lepton channels, the relative amount of and the event shapes of QCD background are estimated from data. Modified event selections are used to obtain the dilepton invariant mass distributions, $M_{\ell\ell}^{\mathrm{QCD}}$. The latter is fitted using a linear function, $f^{\mathrm{QCD}}(M_{\ell\ell})$, omitting the peak region. The integral, I^{QCD}, of the fit function over the whole signal window ($M_{\ell\ell}^{\mathrm{QCD}} \in [66, 116]$ GeV) estimates the amount of QCD entering the signal region, while the event shapes obtained with the modified selections are used as a prediction of the corresponding QCD background shape. These histograms are then scaled as to match the total amount of QCD background, I^{QCD}. This procedure is performed for all $p_{\perp}(\mathrm{Z})$ phase-space regions separately since the amount of QCD background is found to be dependent on the $p_{\perp}(\mathrm{Z})$ phase-space and generally rises with increasing $p_{\perp}(\mathrm{Z})$. For the fully inclusive distributions it amounts to 0.7% in the electron channel (Table 11.1) and to 2.1% in the muon channel (Table 11.4). This finding is well in agreement with other ATLAS measurements, e.g. [117], a measurement of the Z-boson production cross-section at $\sqrt{s} = 7$ TeV, which cites a QCD background varying from $(0.65 \pm 0.23\%)$ to $(1.20 \pm 0.44\%)$ depending on the jet multiplicity in the electron channel. The corre-

sponding numbers of the muon channel cannot directly be compared due to an additional muon isolation cut applied. They quote a QCD background between (0.25 ± 0.04) and $(2.2 \pm 2.2\%)$.

11.1.1. Electron channel

The selection of events for this analysis, requiring exactly two oppositely charged electrons is not only passed by signal events. Also QCD events may produce a signal like signature. This may occur due to heavy flavour decays into electrons/positrons, the chances of which are however greatly reduced due to the `medium++` selection criterion of electrons and positrons (Chapter 5) which constitutes an implicit isolation criterion. A much more important source are decays of pions produced in jets. Neutral pions decay to almost 99% into a pair of photons which, due to interactions with the detector material, may convert into electron-positron pairs. Charged pions (and all other charged hadrons in a jet) may radiate photons due to bremsstrahlung which may also decay into electron-positron pairs.

In the following, a data-driven technique will be explained that tries to estimate QCD background fraction passing the signal selection. Further, a correction for this effect will be developed.

The approach chosen is based on a modified event selection that changes only one cut, namely that instead of exactly two oppositely charged electrons a same-sign selection (two electrons or two positrons) is performed when processing the data. As the probability for standard-model processes to yield same-sign final states is very low, mostly QCD events will be selected but also actual signal events where either the charge of the electron or the charge of the positron was misidentified. The reason for this is the emission of a hard photon (bremsstrahlung) off an electron and subsequent interaction of the photon with detector material leading to conversion into an electron-positron pair and eventually a misidentification of the charge of the original electron (Figure 11.1a). The misidentification can happen since the reconstruction algorithm assigns the charge of the most energetic of the resulting three tracks to the electron object. These events also yield a signal-like peak in the M_{ee} distribution but with the peak-position slightly shifted to lower values of M_{ee} due to the energy loss accompanied with the photon radiation (Figure 11.1b).

In the following, the assumption is made that the same-sign and opposite-sign selection select equal amounts of QCD events. Further, it is assumed that the QCD events in the

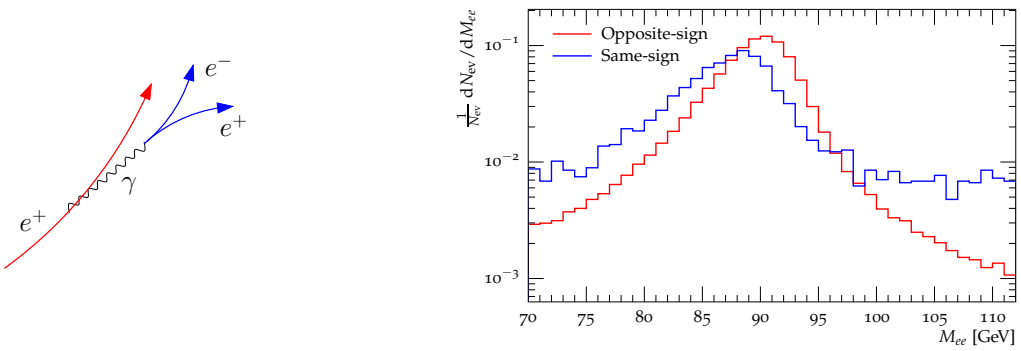

(a) **(b)**

Figure 11.1.: Same-sign electron selection. (a): Sketch of an example scenario in which the reconstruction algorithm may assign the wrong charge to an actual signal electron or positron after emission of a hard bremsstrahlung photon inside the detector material with subsequent conversion also inside the detector material. (b): The resulting M_{ee} normalised spectrum of the same-sign selection compared to the opposite-sign selection, showing the shift of the peak-position of (wrongly reconstructed) signal events due to the photon emission.

same-sign and opposite-sign selection yield the same event-shape distributions (a cross-check is presented in Section 11.1.1). By doing so, the QCD background contribution in the same-sign selection can be quantified. The final step is to obtain a QCD background prediction for the signal selection based on event-shapes obtained in the same-sign selection.

Fit of M_{ee}

The shape observed when calculating the same-sign M_{ee} distribution, omitting the signal peak (Figure 11.1b), is compatible with a linear function, which is hence used to fit the corresponding histograms outside the peak region:

$$f^{\mathrm{QCD}}(M_{\mathrm{ee}}) = a \cdot M_{\mathrm{ee}} + b \tag{11.1}$$

$p_\perp(Z)$	a [GeV^{-1}]	b	I^{QCD}	κ^{QCD} [%]
< 6 GeV	-0.08 ± 0.01	11 ± 1	220.3 ± 9.6	0.3
$\in (6, 12)$ GeV	-0.16 ± 0.01	21 ± 1	341.3 ± 9.3	0.4
$\in (12, 25)$ GeV	-0.19 ± 0.01	27 ± 1	475.7 ± 9.2	0.6
> 25 GeV	0.18 ± 0.01	1 ± 1	880.8 ± 9.2	1.6
$\in (0, \infty]$ GeV	-0.20 ± 0.01	54 ± 1	1785.5 ± 9.2	0.7

Table 11.1.: Fit results for the estimates of the amount of QCD events in the electron channel. A linear fit using $f^{\mathrm{QCD}}(M_{\mathrm{ee}})$ (equation (11.1)) is performed on the di-electron (same-sign) invariant mass distributions omitting the peak ($M_{\mathrm{ee}} \in [77, 97]$ GeV). The integral of $f^{\mathrm{QCD}}(M_{\mathrm{ee}})$ for $M_{\mathrm{ee}} \in [66, 116]$ GeV is given in the fourth column (I^{QCD}). The fifth column contains the relative amount of QCD background events in the opposite-sign selection (equation (11.2)). Plots of all fit results are shown in Figure 11.2.

The fit is performed for all $p_\perp$(Z) phase-space regions. The fit results along with the obtained integrals, I^{QCD} (integral of the fit function over the whole signal window, $M_{\mathrm{ee}} \in [66, 116]$ GeV), are given in Table 11.1. The errors quoted therein are the fit uncertainties. A graphical representation of both the (nominal) opposite-sign and the same-sign selection as well as the linear fits are shown in Figure 11.2. Further, the relative amount of QCD events, κ^{QCD}, w.r.t. the total number of events entering the nominal opposite-sign signal selection ($N_{\mathrm{ee}}^{\mathrm{OS}}$) is given by:

$$\kappa^{\mathrm{QCD}} = \frac{\int_{66\ \mathrm{GeV}}^{116\ \mathrm{GeV}} \mathrm{d}M_{\mathrm{ee}}\, f^{\mathrm{QCD}}(M_{\mathrm{ee}})}{N_{\mathrm{ee}}^{\mathrm{OS}}} \tag{11.2}$$

The relative amount of QCD contributions rises with $p_\perp$(Z) which is not astonishing since the main cause of $p_\perp$(Z) larger than a few GeV where primordial $k_\perp$ becomes a sub-dominant effect are recoiling jets.

The events of the same-sign selection can also be used to calculate corresponding event-shape distributions. A few of those QCD event-shape distributions are shown in Figure 11.3. Differences between those and the nominal data distributions are dependent on the observable and the $p_\perp$(Z) phase-space in question. The remaining distributions can be found in the analysis support note [118].

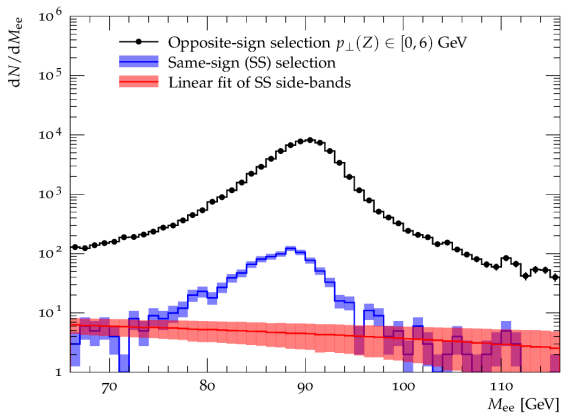

(a) $p_\perp(\mathrm{Z}) < 6$ GeV

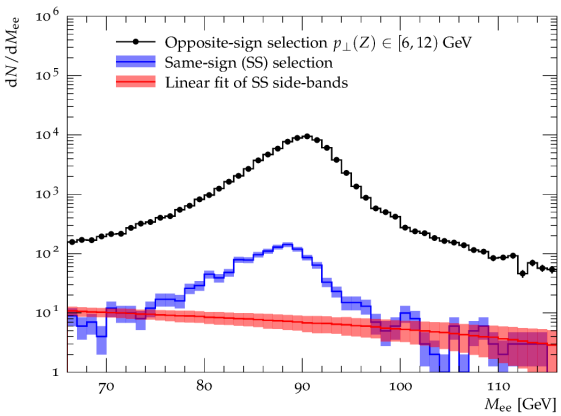

(b) $p_\perp(\mathrm{Z}) \in (6, 12]$ GeV

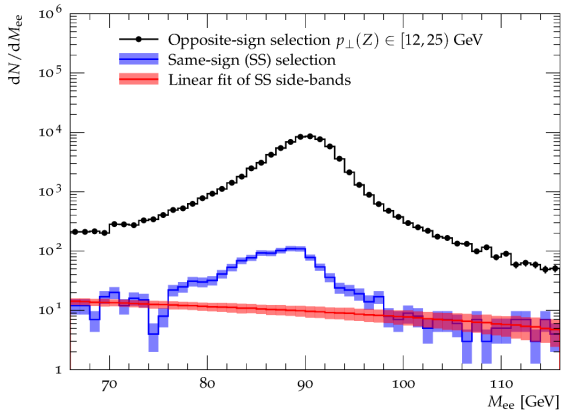

(c) $p_\perp(\mathrm{Z}) \in (12, 25]$ GeV

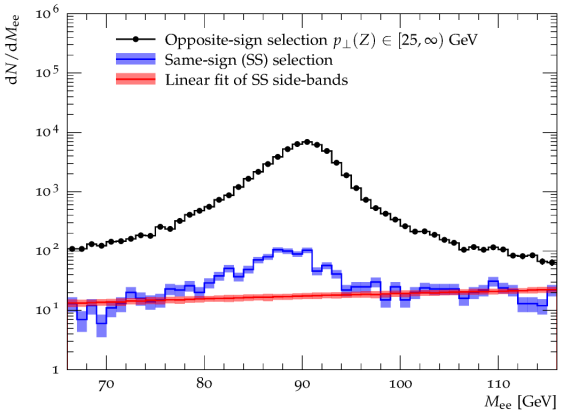

(d) $p_\perp(\mathrm{Z}) > 25$ GeV

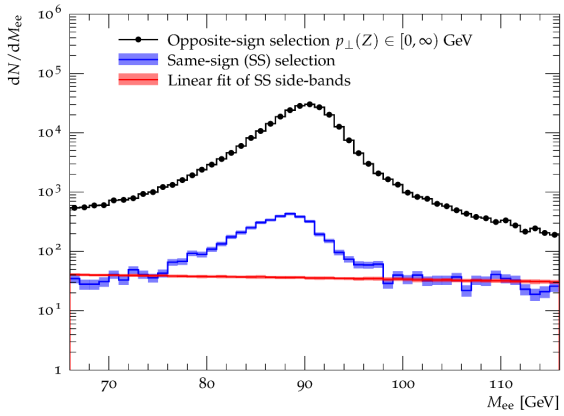

(e) $p_\perp(\mathrm{Z}) \in (0, \infty]$ GeV

Figure 11.2.: Comparison of the M_{ee} spectra between opposite-sign and same-sign selections on data events and the linear fits (equation (11.1)) used to estimate the amount of QCD events entering the signal selection in the electron channel. The fit omits the peak region ($M_{\mathrm{ee}} \in [77, 97]$ GeV). The fit results can be found in Table 11.1. The blue error-band is statistical only while the red error-band (linear fit) shows the fit uncertainties.

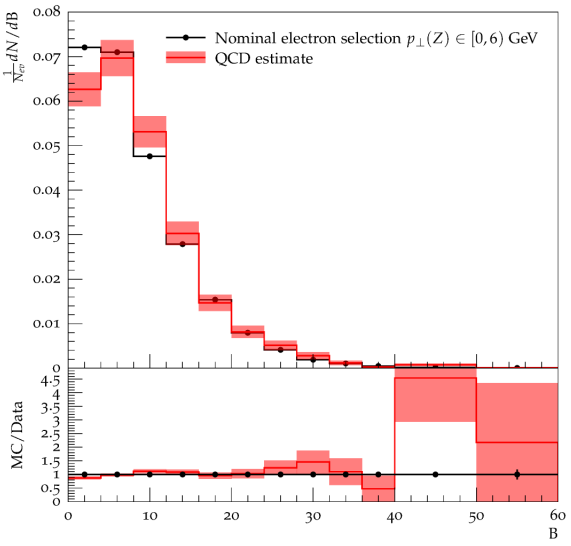

(a) Beamthrust, $p_\perp(Z) < 6$ GeV

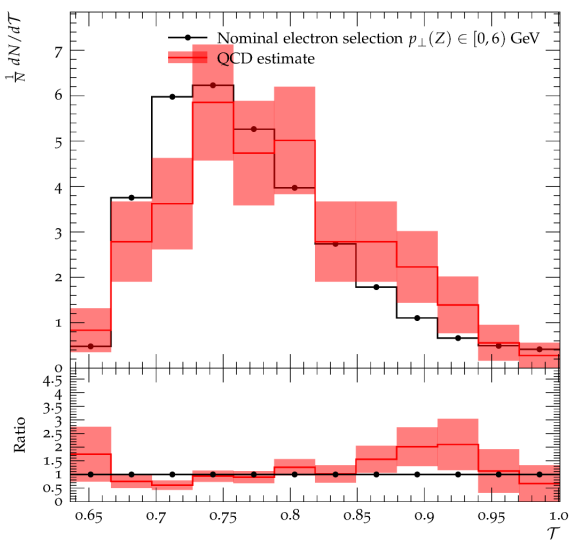

(b) Transverse thrust $p_\perp(Z) < 6$ GeV

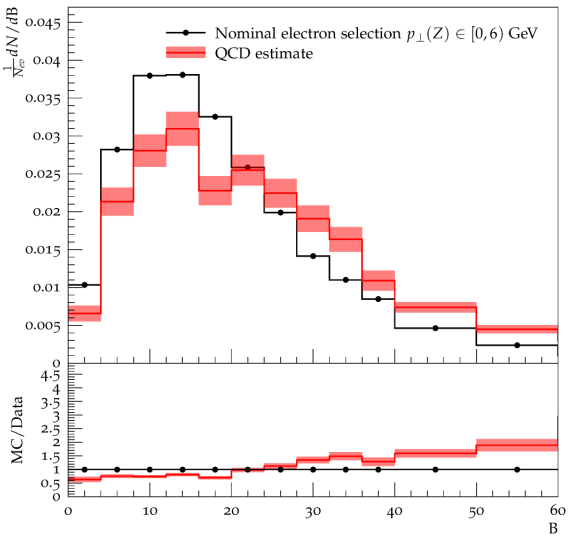

(c) Beamthrust, $p_\perp(Z) > 25$ GeV

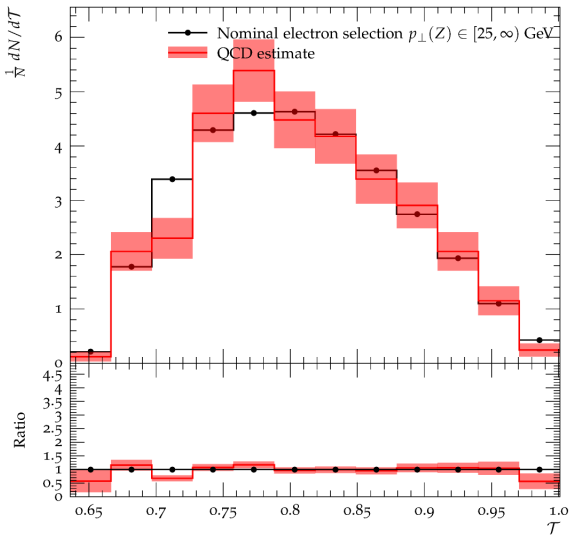

(d) Transverse thrust $p_\perp(Z) > 25$ GeV

Figure 11.3.: Normalised electron channel QCD event-shape estimates ($f_{\mathcal{O}}^{\text{QCD}}$) from the same-sign selection used for the QCD correction compared to normalised nominal event-shape distributions. The top-row shows distributions of the low $p_\perp(Z)$ region and the bottom row the corresponding ones for the high $p_\perp(Z)$ region. The error-bands are statistical only.

Comparison of same-sign (SS) and opposite-sign (OS) QCD shapes

An important check to prove the consistency of using same-sign distributions as QCD estimates for an opposite-sign signal selection is to show that QCD enriched distributions of the SS selection are compatible with their counterparts of the OS selection. In order to do so, the medium quality criterion in the electron selection is replaced by a loose quality cut which enhancing the relative amount of QCD events in the SS and OS selections.

It is possible to subtract the signal contribution to the loose selection on a statistical basis by subtracting the events passing the medium selection. However, the selection efficiencies of signal events differ for the loose and medium selections. The ratio of these two efficiencies can be determined from the height of the corresponding Z-peaks over the background:

$$\varepsilon_{\text{signal,lm}} = \frac{\hat{M}_{\ell\ell}^{\text{medium}}}{\hat{M}_{\ell\ell}^{\text{loose}}} \tag{11.3}$$

It is further assumed that this efficiency ratio is constant over the whole M_{ee} region under consideration. Table 11.2 contains the values of $\varepsilon_{\text{signal,lm}}$ for all $p_{\perp}(Z)$ phase-space regions. They are all of the order of 85%.

The subtraction of the medium signal selection from the loose signal selection can thus be carried out bin-wise (b), resulting in QCD estimates of the event-shape distributions, $\mathcal{O}^{\text{qcd}}$:

$$f_{\mathcal{O}}^{\text{QCD, OS-SS}}(b) = \varepsilon_{\text{signal,lm}} \cdot f_{\mathcal{O}}^{\text{signal, loose}}(b) - f_{\mathcal{O}}^{\text{signal, medium}}(b) \tag{11.4}$$

The distributions $f_{\mathcal{O}}^{\text{QCD, OS-SS}}$ consist mainly of loose same-sign QCD events since the QCD selection efficiency in the loose selection is much larger than the counterpart of the medium selection.

$p_{\perp}(Z)$ [GeV]	$\in [0, 6)$	$\in [6, 12)$	$\in [12, 25)$	$\in [25, \infty)$	$\in [0, \infty)$
	0.8494	0.8551	0.8481	0.8517	0.8551

Table 11.2.: Relative selection efficiencies of the loose and medium electron selections, $\varepsilon_{\text{signal,lm}}$, corresponding to equation (11.3)

The thus obtained QCD estimates are found to be compatible within (statistical) errors for the OS and SS selections in all $p_{\perp}(Z)$ phase-spaces, meaning that the usage of QCD estimates of a same-sign selection can be used to correct for QCD background in the opposite-sign signal selection. A few plots comparing the obtained QCD estimates of both selections can be found in Figure 11.4. The remaining plots which are of similar agreement can be found in the ATLAS note of this analysis [118].

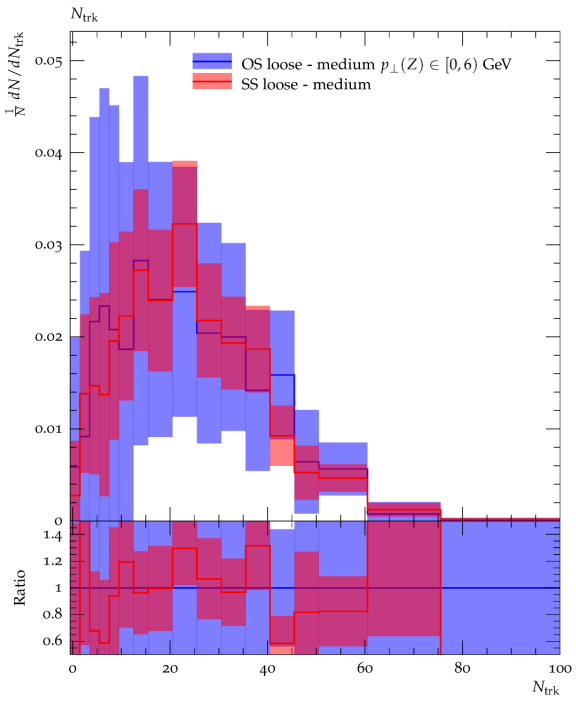

(a) $N_{\text{trk}}, p_\perp(Z) < 6$ GeV

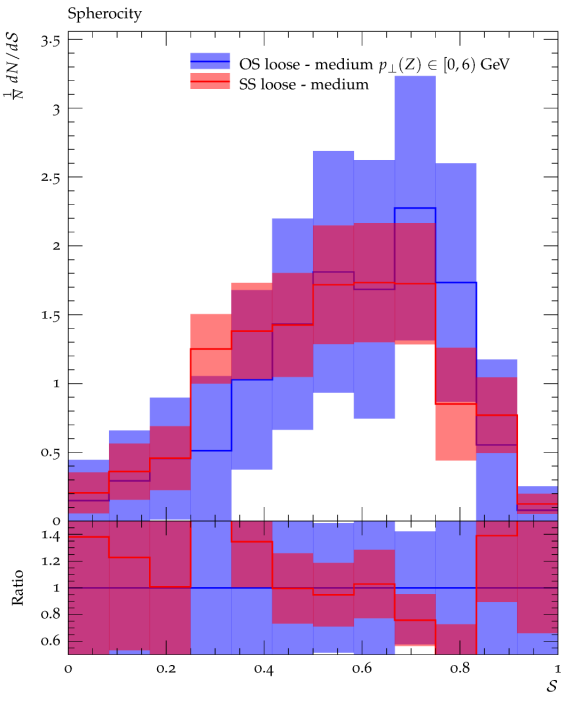

(b) Spherocity $p_\perp(Z) < 6$ GeV

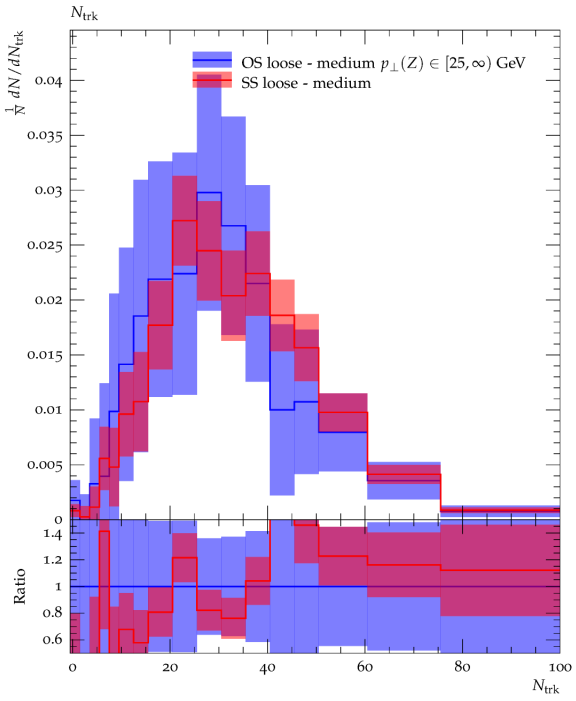

(c) $N_{\text{trk}}, p_\perp(Z) > 25$ GeV

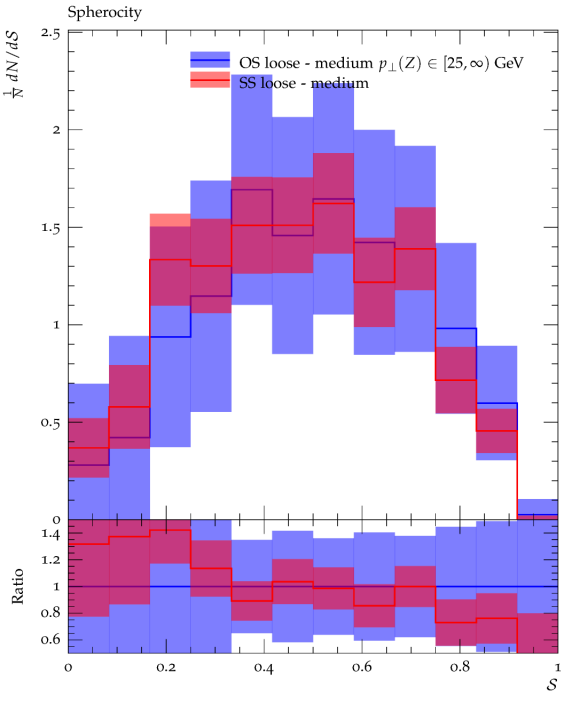

(d) Spherocity $p_\perp(Z) > 25$ GeV

Figure 11.4.: Comparison of (normalised) electron channel QCD shape estimates, $f_{\mathcal{O}}^{\text{QCD, OS-SS}}$, obtained by subtracting the medium selection from the (scaled) loose selection for opposite-sign (OS) and same-sign (SS) selections showing agreement within the shown statistical uncertainties. The top-row shows distributions of the low $p_\perp(Z)$ region and the bottom row the corresponding ones for the high $p_\perp(Z)$ region.

QCD correction

Since the unfolding procedure requires a multiplicative correction, the following correction factors are calculated for every bin, b, of an observable, $\mathcal{O}$:

$$c_{\mathcal{O}}^{\mathrm{QCD}}(b) = 1 - \frac{f_{\mathcal{O}}^{\mathrm{QCD}}(b)}{f_{\mathcal{O}}^{\mathrm{nominal}}(b)} \tag{11.5}$$

where $f_{\mathcal{O}}^{\mathrm{QCD}}$ represents the QCD event-shape distribution (same-sign medium selection away from Z-peak plus linear fit) and $f_{\mathcal{O}}^{\mathrm{nominal}}$ the nominal (signal + background) event-shape distribution of an observable, $\mathcal{O}$.

Systematic uncertainty:

A systematic uncertainty is assigned to the shape of the QCD event-shapes by taking into account the difference between distributions obtained with the same-sign side-band approach (Section 11.1.1), $f_{\mathcal{O}}^{\mathrm{QCD}}$, and the difference of the loose and medium selection in the same-sign selection (Section 11.1.1), $f_{\mathcal{O}}^{\mathrm{QCD,\ OS\text{-}SS}}$.

The distributions of the latter are scaled as to match the integral of the former, I^{QCD}. The systematic uncertainty is then calculated as follows:

$$\Delta c_{\mathcal{O}}^{\mathrm{QCD}}(b) = \frac{\left| f_{\mathcal{O}}^{\mathrm{QCD}}(b) - f_{\mathcal{O}}^{\mathrm{QCD,\ OS\text{-}SS}}(b) \right|}{f_{\mathcal{O}}^{\mathrm{nominal}}(b)} \tag{11.6}$$

The distributions corresponding to equation (11.5) and equation (11.6) can be found in Figure 11.4. The correction factors are very close to one 1 and are mostly flat, with the exception of N_{trk} and Beamthrust. The largest impact is visible for the phase-space region $p_{\perp}(\mathrm{Z}) > 25$ GeV.

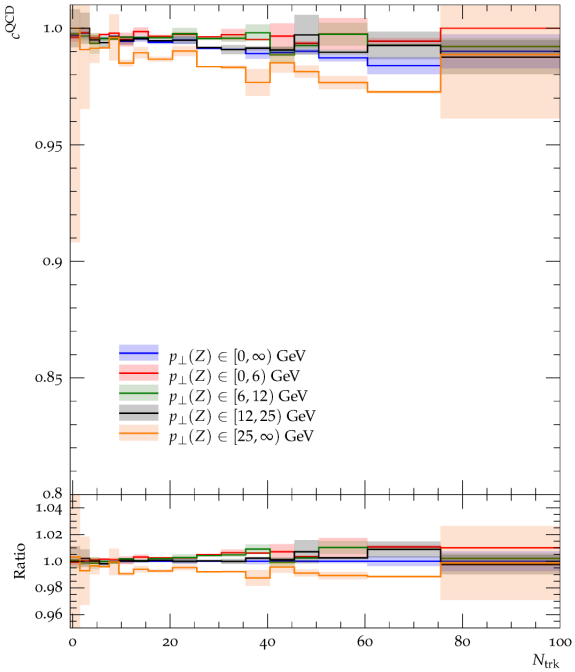

(a) N_{trk}

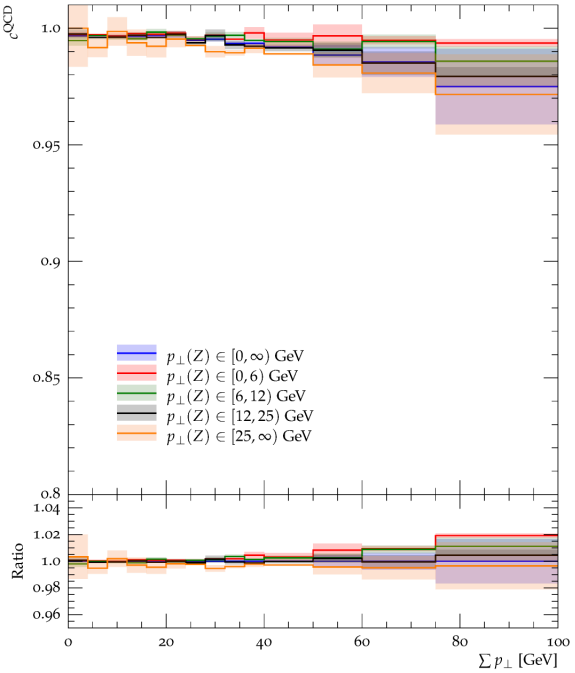

(b) $\sum p_\perp$

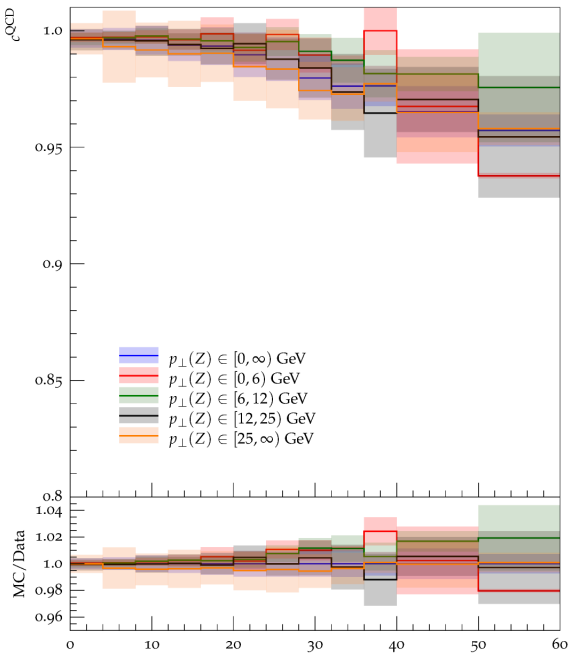

(c) Beamthrust

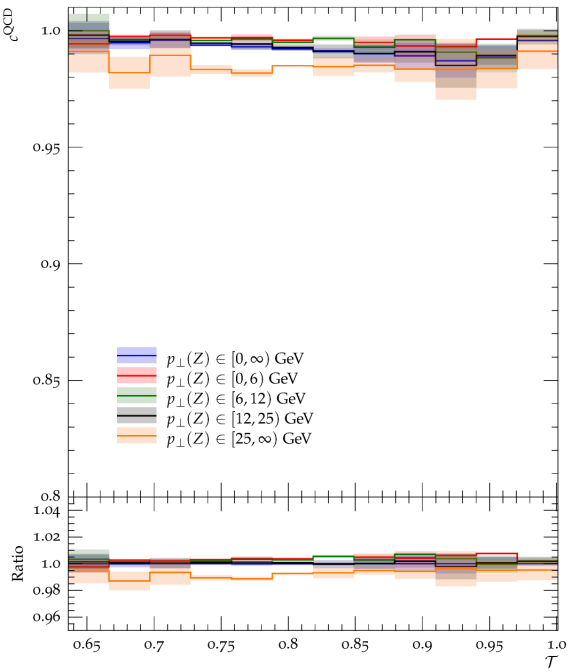

(d) Thrust

Figure 11.5.

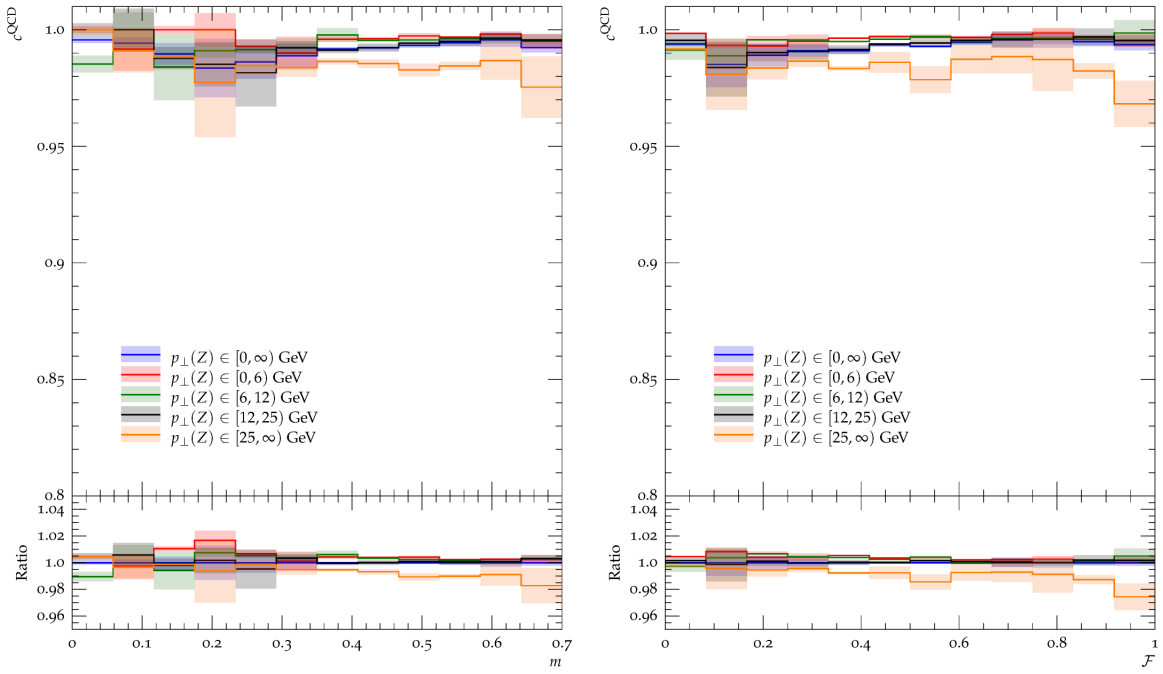

(e) Minor **(f)** F-Parameter

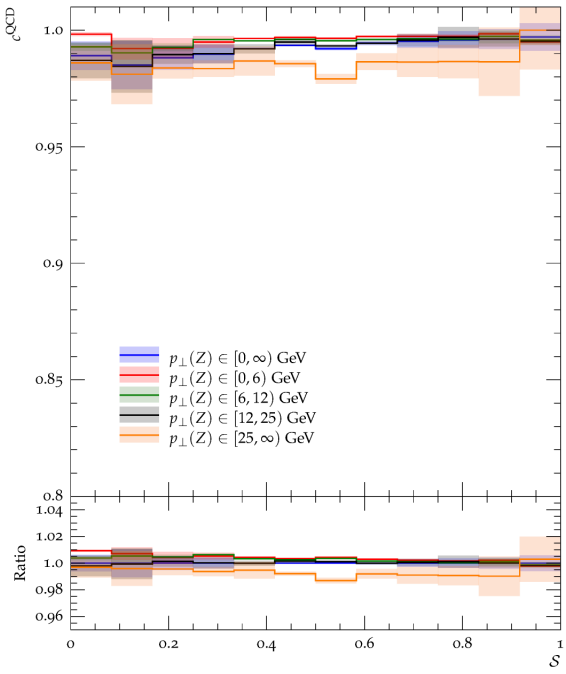

(g) Spherocity

Figure 11.4.: Electron channel QCD correction factors, $c_{\mathcal{O}}^{\mathrm{QCD}}$ (equation (11.5)). The error-bands shown correspond to the systematic uncertainties, $\Delta c_{\mathcal{O}}^{\mathrm{QCD}}$, estimated according to equation (11.6). The $p_\perp(Z)$ inclusive distributions ($p_\perp(\mathrm{Z}) \in [0,\infty)$) are taken as reference for the ratio plots.

11.1.2. Muon channel

Also in the muon-channel analysis, QCD events can pass the signal event selection. For instance, muons may be produced in decays of heavy-flavour particles present in jets which is the main source for QCD background in this analysis as no isolation criterion is applied when selecting muons. Further, pion and Kaon-decays produce muons in flight.

To obtain a QCD background estimate in the muon-channel analysis, an isolation criterion is introduced. The working assumption for this procedure is that requiring muons to be isolated greatly suppresses contributions from such events where, e.g. a b-jet with subsequent weak-decay of the b-quark into a c-quark, resulting in a muon (and corresponding neutrino) likely to be accompanied by activity from the b-jet.

The isolation criterion is based on the scalar sum of transverse momenta found in a cone of size ΔR^{iso} around the muon. The absolute values of the transverse momenta $p_\perp(t) > p_\perp^{\text{iso}}$, of tracks of charged particles, t, that fulfil $\Delta R(\mu, t) \leq \Delta R^{\text{iso}}$ are added to form the quantity $P(\mu)^{\text{iso}}$. The decision if a muon is considered isolated or not is then made based on the ratio of $P(\mu)^{\text{iso}}$ and the reconstructed muon transverse momentum, $p_\perp(\mu)$. A muon is considered non-isolated, if the following condition is met:

$$P(\mu)^{\text{iso}}/p_\perp(\mu) > \phi^{\text{iso}}, \qquad \text{with} \qquad P(\mu)^{\text{iso}} = \sum_{\substack{\Delta R(\mu,t)\leq\Delta R^{\text{iso}} \\ p_\perp(t)>p_\perp^{\text{iso}}}}^{N_{\text{tracks}}} p_\perp(t) \tag{11.7}$$

where the sum runs over all selected tracks, t, in an event and ϕ^{iso}, ΔR^{iso} and $p_\perp^{\text{iso}}$ being parameters. The central values of those are chosen in accordance to [53]. They are given in Table 11.3 as are systematic variations (UP/DOWN) of these parameters. The variations are comparably large and are considered conservative. Combinatorics in principle allow for eight different points in the parameter space (ϕ^{iso}, ΔR^{iso}, $p_\perp^{\text{iso}}$). It was found, however, that strong (anti-) correlations between the parameters exist in terms of the achievable deviation from the central isolation. It was possible to cover maximal deviations from the central isolation by using two points in the parameter space only which are labelled as UP and down in Table 11.3.

A selection of observables demonstrating the effect of the isolation criteria in Table 11.3 is shown in Figure 11.5. The strength of the effect is dependent on the observable and the

$p_\perp$(Z) phase-space. Plots for all other observables can be found in the analysis support note [118].

Parameter set	ϕ^{iso}	ΔR^{iso}	$p_\perp^{\text{iso}}$
Central isolation	0.1	0.2	1.0
Variation UP	0.08	0.23	2.0
Variation DOWN	0.12	0.17	0.5

Table 11.3.: Isolation parameters used (equation (11.7)) in the event selection for the construction of QCD-depleted event-shapes.

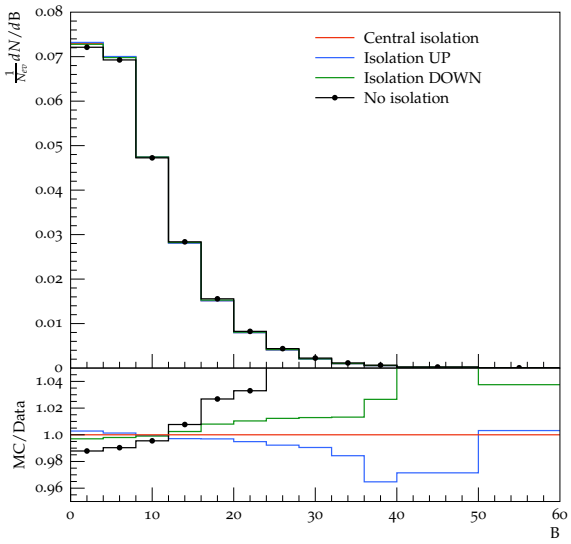

(a) Beamthrust, $p_\perp(Z) < 6$ GeV

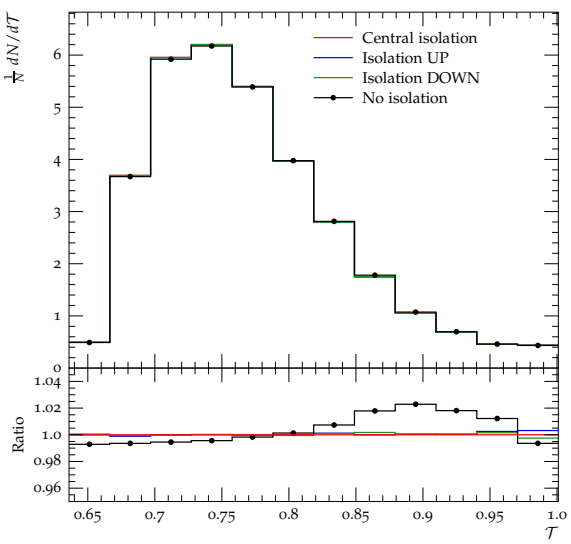

(b) Thrust $p_\perp(Z) < 6$ GeV

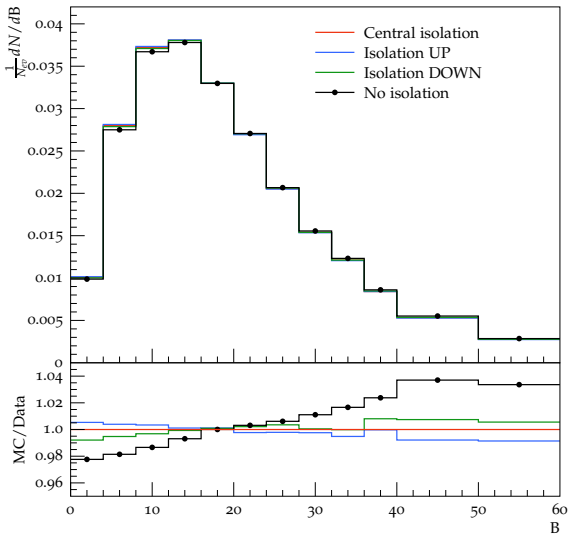

(c) Beamthrust, $p_\perp(Z) > 25$ GeV

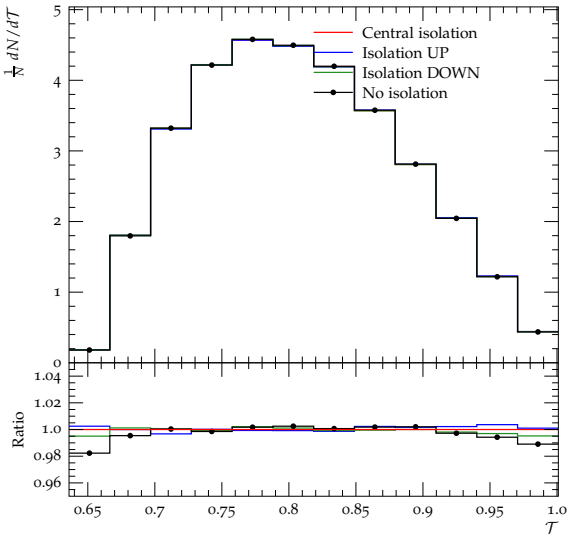

(d) Thrust $p_\perp(Z) > 25$ GeV

Figure 11.5.: Effect of isolation criteria (Table 11.3) on event shape distributions. The top-row shows distributions of the low $p_\perp(Z)$ region and the bottom row the corresponding ones for the high $p_\perp(Z)$ region.

Fit of $M_{\mu\mu}$

The amount of QCD background in the muon-channel analysis on data can now be estimated by statistically subtracting the di-muon invariant mass distribution obtained with the isolation criterion of equation (11.7) applied ($M_{\mu\mu}^{iso}$) from the nominal muon channel event selection ($M_{\mu\mu}^{\text{noiso}}$). The resulting distribution $M_{\mu\mu}^{\text{QCD}}$ outside the Z-peak is assumed to be dominated by QCD events. The subtraction is carried out bin-wise (b):

$$M_{\mu\mu}^{\text{QCD}}(b) = M_{\mu\mu}^{\text{noiso}}(b) - M_{\mu\mu}^{iso}(b) \tag{11.8}$$

The amount of QCD events, I^{QCD}, is obtained similar to the electron-channel analysis by fitting $M_{\mu\mu}^{\text{QCD}}$ with a linear function (equation (11.1)) and integrating the fit function over $M_{\mu\mu} \in [66, 116]$ GeV. The fits are carried separately for each $p_{\perp}(\text{Z})$ phase-space region, excluding the Z-peak ($M_{\mu\mu} \in [80, 100]$ GeV). Resulting fit parameters can be found in Table 11.4. Further, the absolute (I^{QCD}) and relative (κ^{QCD}, equation (11.2)) QCD contributions are given in Table 11.4.

The construction of the corresponding QCD event-shapes then simply uses events from the non-peak region of $M_{\mu\mu}^{\text{QCD}} \notin [80, 100]$ GeV. The QCD event-shapes are scaled to I^{QCD} (Table 11.4).

Some resulting QCD event-shape distributions are shown in Figure 11.3. Differences between those and the nominal data distributions are dependent on the observable and the $p_{\perp}(\text{Z})$ phase-space in question. All other distributions can be found in the analysis support note [118].

$p_\perp(Z)$	a [GeV^{-1}]	b	I^{QCD}	κ^{QCD} [%]
< 6 GeV	-1.13 ± 0.01	128.9 ± 0.9	1310.9 ± 9.1	1.2
$\in (6, 12)$ GeV	-1.67 ± 0.01	194.3 ± 0.9	2119.0 ± 9.1	1.7
$\in (12, 25)$ GeV	-1.94 ± 0.01	232.0 ± 0.9	2786.2 ± 9.1	2.3
> 25 GeV	-0.83 ± 0.01	111.8 ± 0.9	1799.4 ± 9.1	1.9
$\in (0, \infty]$ GeV	-5.07 ± 0.01	607.7 ± 0.9	8620.6 ± 9.1	2.1

Table 11.4.: Fit results for the estimates of the amount of QCD events in the muon channel. A linear fit of the form $a \cdot x + b$ is performed on the di-muon (opposite-sign) invariant mass distributions omitting the peak ($M_{\mu\mu} \in [80, 100]$ GeV). Corresponding plots are shown in Figure 11.6.

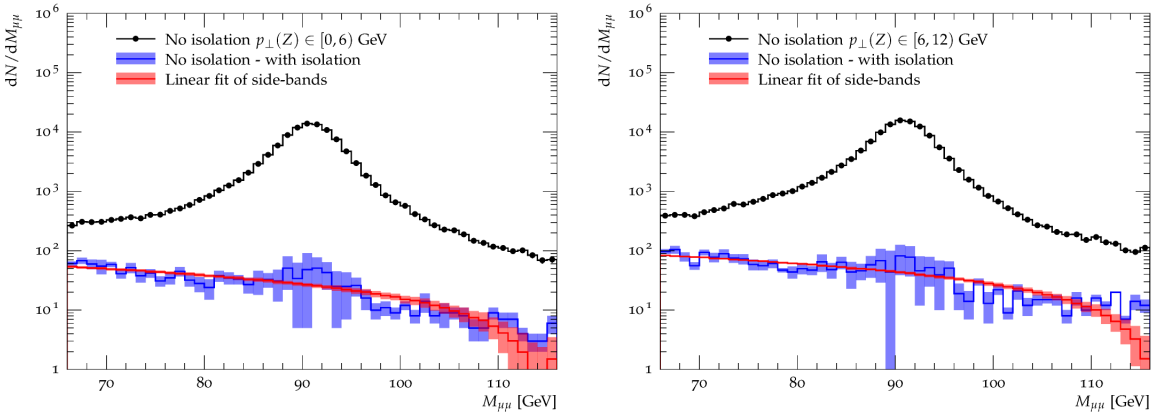

(a) $p_\perp(\mathrm{Z}) < 6$ GeV

(b) $p_\perp(\mathrm{Z}) \in (6, 12]$ GeV

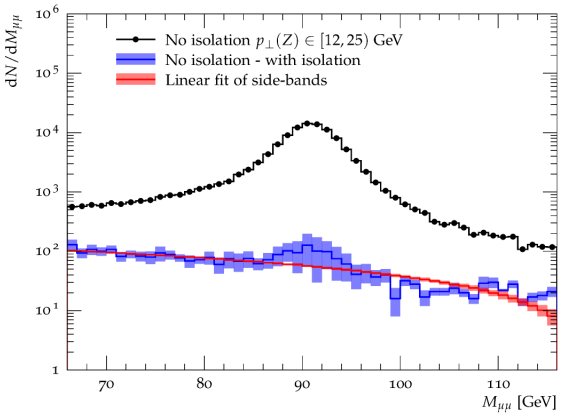

(c) $p_\perp(\mathrm{Z}) \in (12, 25]$ GeV

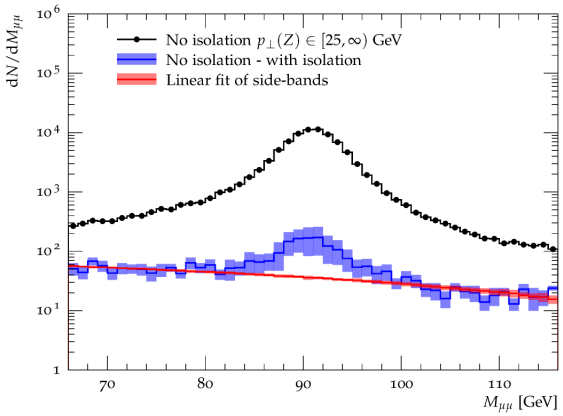

(d) $p_\perp(\mathrm{Z}) > 25$ GeV

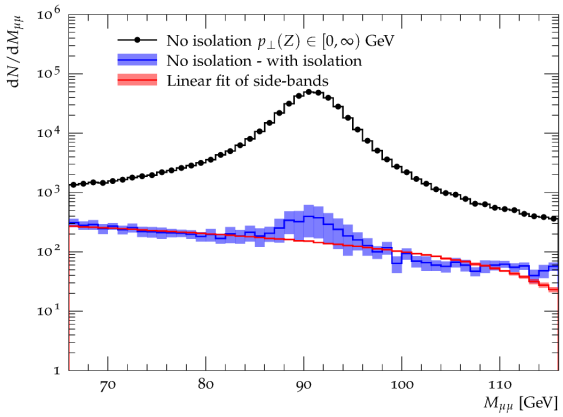

(e) $p_\perp(\mathrm{Z}) \in [0, \infty)$ GeV

Figure 11.6.: Comparison of the nominal signal event-selection and the QCD enriched difference of the latter and the same selection but with an isolation criterion imposed according to equation (11.7) for data events. Further, the linear fits (equation (11.1)) used to estimate the amount of QCD events entering the signal selection in the muon-channel analysis are shown. The fit omits the peak region ($M_{\mu\mu} \in [80, 100]$ GeV). The fit results can be found in Table 11.4. The blue error-band represents the systematic variations of the isolation criterion while the red error-band (linear fit) shows the fit uncertainties.

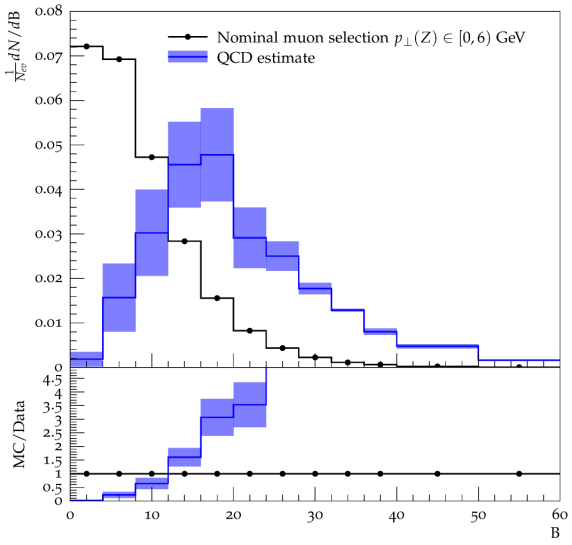

(a) Beamthrust, $p_\perp(Z) < 6$ GeV

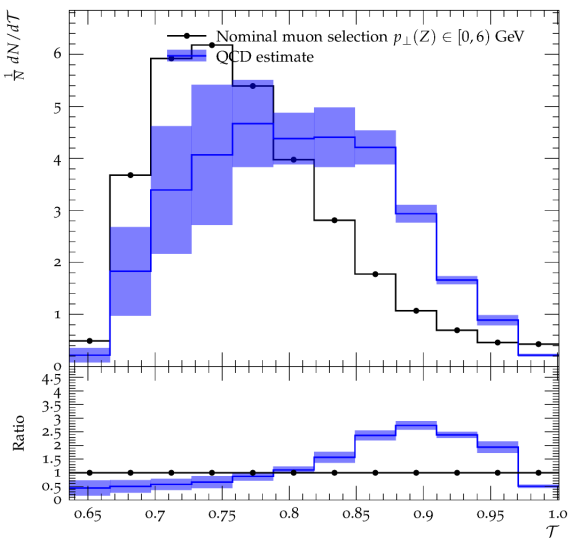

(b) Thrust $p_\perp(Z) < 6$ GeV

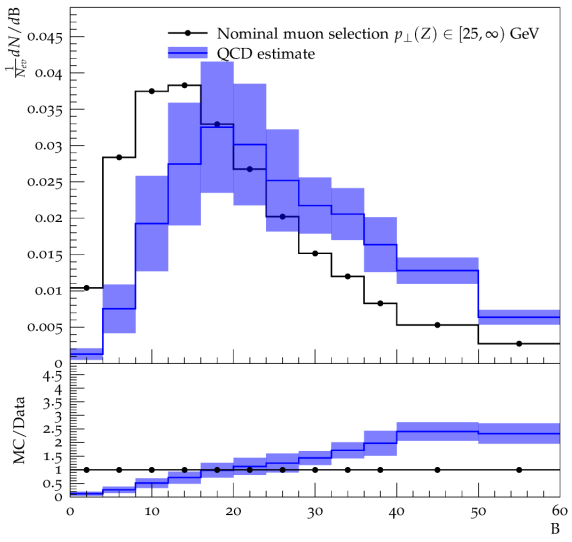

(c) Beamthrust, $p_\perp(Z) > 25$ GeV

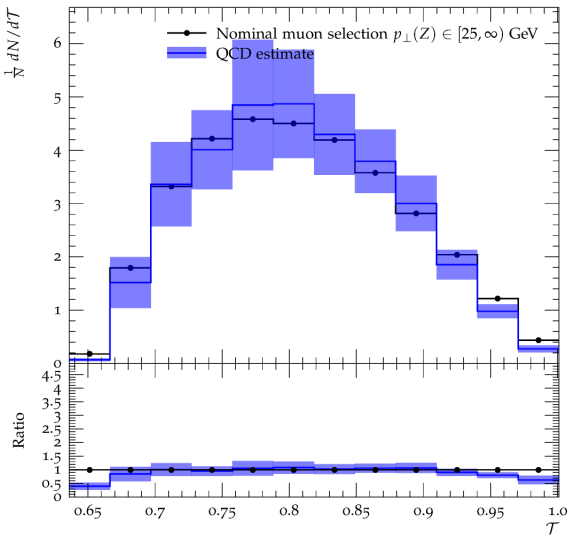

(d) Thrust $p_\perp(Z) > 25$ GeV

Figure 11.7.: Comparison of QCD shape estimates (muon channel), $f_{\mathcal{O}}^{\mathrm{QCD}}$, used for the QCD correction with the nominal event shape distributions, $f_{\mathcal{O}}^{\mathrm{nominal}}$. The top-row shows distributions of the low $p_\perp(Z)$ region and the bottom row the corresponding ones for the high $p_\perp(Z)$ region. The error-bands are statistical only.

QCD correction

The calculation of the QCD correction factors for the muon channel distributions exactly follows equation (11.5).

Systematic uncertainty:

In order to estimate the systematic uncertainty of the correction factors, the calculation of the latter is repeated using the systematic variations of the isolation criteria (Table 11.3). The largest difference per bin to the central isolation is taken as systematic uncertainty:

$$\Delta c_{\mathcal{O}}^{\mathrm{QCD}\mu}(b) = \frac{\max\left[\left|f_{\mathcal{O}}^{\mathrm{QCD}}(b) - f_{\mathcal{O}}^{\mathrm{QCD,\ Isolation\ UP/DOWN}}(b)\right|\right]}{f_{\mathcal{O}}^{\mathrm{nominal}}(b)} \tag{11.9}$$

The resulting correction factors are shown for all $p_{\perp}(\mathrm{Z})$ phase-space and all distributions in Figure 11.7. The systematic uncertainties are shown as error-bands. The $c_{\mathcal{O}}^{\mathrm{QCD}}(b)$ of the muon channel are substantially larger and have more structure than the electron channel equivalents (Figure 11.4).

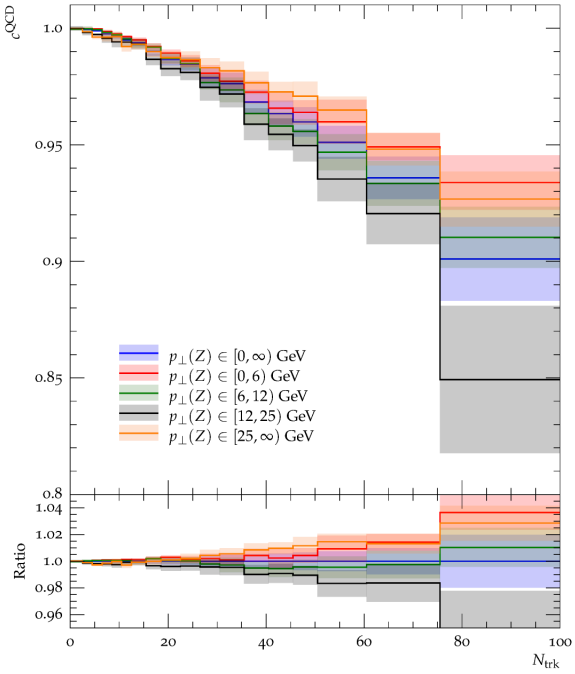

(a) N_{trk}

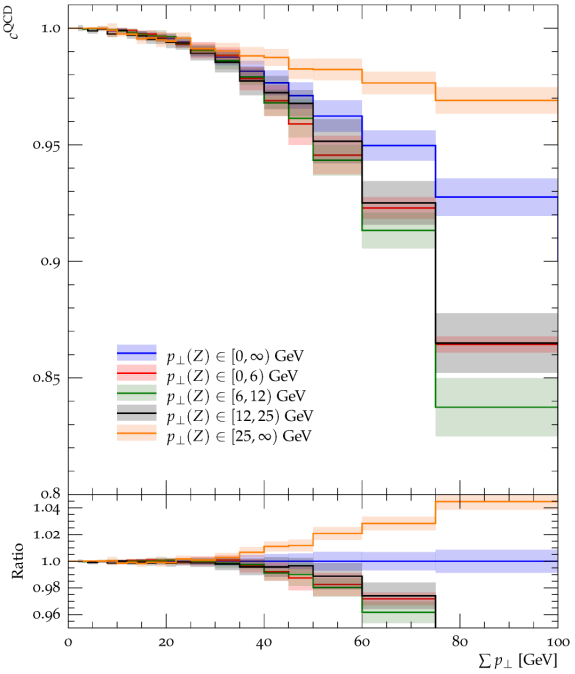

(b) $\sum p_\perp$

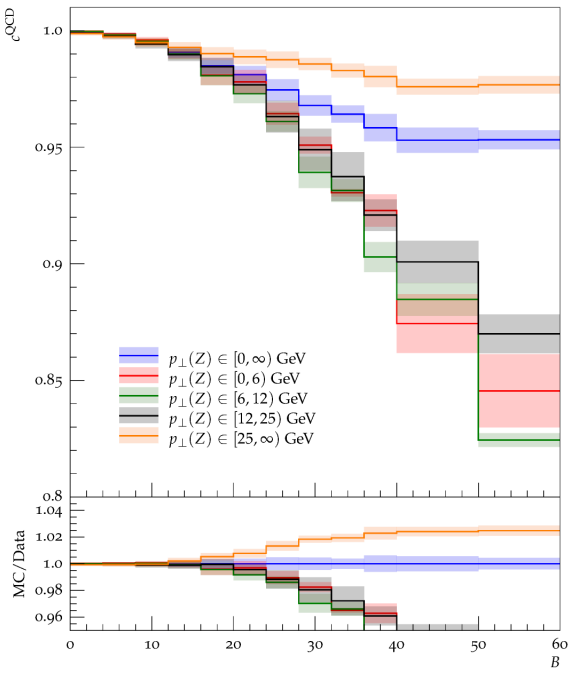

(c) Beamthrust

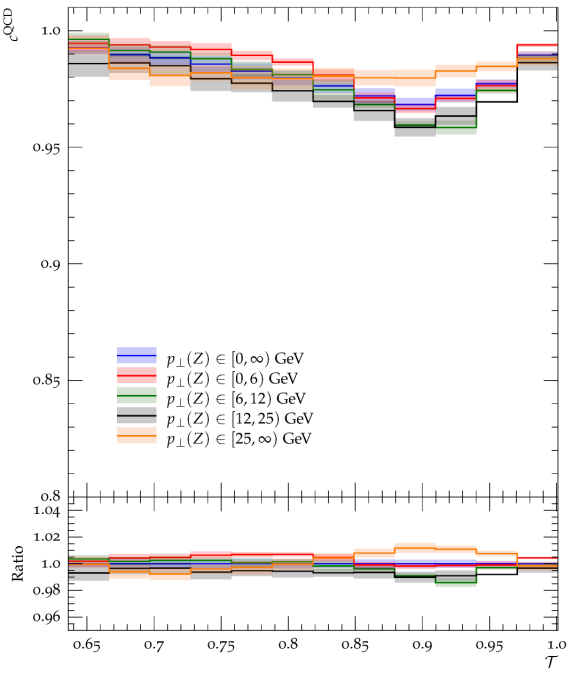

(d) Transverse thrust

Figure 11.8.

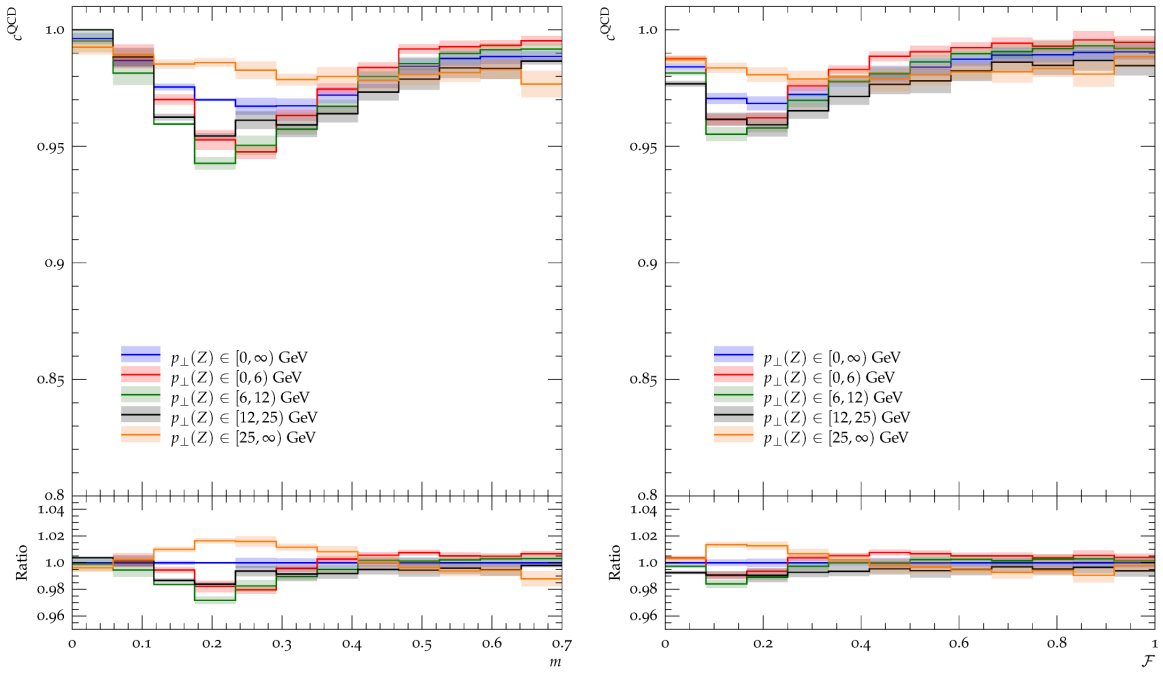

(e) Minor **(f)** F-Parameter

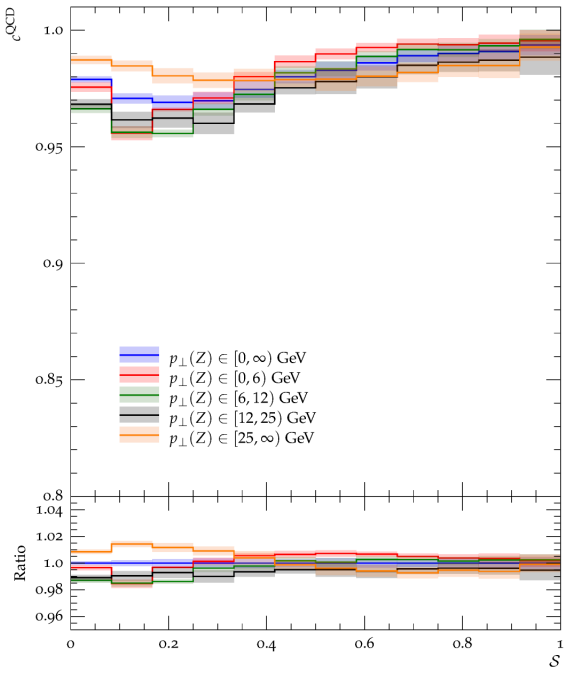

(g) Spherocity

Figure 11.7.: Muon channel QCD correction factors, $c_{\mathcal{O}}^{\mathrm{QCD}}$ (equation (11.5)). The error-bands shown correspond to the systematic uncertainties, $\Delta c_{\mathcal{O}}^{\mathrm{QCD}}$, estimated according to equation (11.9). The $p_\perp(Z)$ inclusive distributions ($p_\perp(\mathrm{Z}) \in [0,\infty)$) are taken as reference for the ratio plots.

11.2. Electroweak backgrounds

In this section, the electroweak backgrounds (EWBG) are briefly discussed. To be upfront with it, EWBG contributions are not corrected for in this analysis. This can be justified by the small number of EWBG events in the MC simulation passing the signal selections in both channels when compared to the QCD estimate of background events. Further, it will be shown that (on a Monte-Carlo level) about two-thirds of the expected EWBG events yield event-shape distributions very similar to the ones obtained with a signal Monte-Carlo.

11.2.1. Scaling to luminosity

When comparing with data, the EWBG and signal Monte-Carlo predictions need to be scaled to the luminosity present in data, $\mathcal{L}^{\text{Data}}$ (Chapter 4). All available EWBG (and signal) samples are based on leading-order calculations and are hence required to take into account so-called K-factors (Section B.2). Further, branching ratios (BR) into the exclusive di-lepton final-states need to be considered. This information is summarised in Table 11.5.

The histograms corresponding to the signal and background samples are each scaled to

$$A = \frac{\sigma^{\text{MC}} \cdot \text{BR} \cdot K \cdot \mathcal{L}^{\text{Data}}}{\sum_{i=1}^{N_{\text{evt}}} w_i} \tag{11.10}$$

with the sum in the denominator being the total sum of (Monte-Carlo) event weights present in a sample before any selection is imposed.

11.2.2. Electroweak background processes

$Z \to \tau^+\tau^-$: Lepton universality dictates that Z-bosons decay into lepton pairs of the three families with equal proportions. Hence one third of all leptonically decaying Z-bosons will decay into a τ^- τ^+ pair. The τ^- itself being unstable and sufficiently short-lived ($c\tau = 87\mu$m) to decay into a muon or electron and corresponding neutrino with a branching ratio of roughly 18% before escaping the detector can potentially lead

to the situation that a Z $\rightarrow \tau^-\ \tau^+$ is selected in the muon or electron channel analysis. However, since the hard process is identical to the one in the selected events in this analysis (i.e. decoupled from MPI in terms of colour), the event-shapes cannot be significantly different from those of Z $\rightarrow \mathrm{e}^-\ \mathrm{e}^+$ or Z $\rightarrow \mu^-\ \mu^+$ events. Indeed, Figure 11.9 shows the resulting event-shape distributions of Z $\rightarrow \tau^-\ \tau^+$ events being compatible (within errors) with or very close to the actual signal.

Diboson (Z Z): The comparably rare standard model processes resulting in a diboson production can potentially also be selected as signal process in this analyses. In the case of Z Z production with four leptons in the final state, combinatorics, together with misidentification of lepton charges (and τ^- decays) allows for a number of scenarios where this can happen. It is most likely to have one of the produced Z-bosons to decay into the corresponding lepton pair of the electron- or muon-channel analysis with the decay products of the other Z simply being outside of the lepton selection acceptance ($|\eta^\ell < 2.4|$, $p_\perp^\ell > 20$ GeV). The finding from a Monte-Carlo based study is that also for the Z Z production, resulting event-shapes are compatible with the ones from the actual signal process (Figure 11.9). This process has the largest yield of all electro-weak backgrounds considered (Table 11.6). The s-channel process is suppressed in the standard model as it contains a vertex with three Z-bosons. Thus the dominating Z Z production is the t-channel process shown in Figure 11.8c.

Diboson (W Z): The situation is different for diboson production if in addition to a Z a W is produced. As can be seen in Figure 11.9 the resulting event-shapes are significantly different from the ones obtained from a signal sample. However, the cross-section is rather small and only a few events are expected to pass the event-selection (Table 11.6). In both channels, the amount of W Z background events passing the signal selection is about two orders of magnitude smaller than the amount of QCD. The dominating s-channel tree-level diagram is shown in Figure 11.8b.

t $\bar{\mathrm{t}}$: Top quarks decay to almost 100% weakly into a b-quark and a W. Lepton universality (and taking tau decays into consideration) lead to a probability of about 12% that a top-decay ultimately generates a muon or an electron. Thus a small chance of about 1% percent exists that a t $\bar{\mathrm{t}}$ event produces a $\mu^-\mu^+$- or $\mathrm{e}^-\mathrm{e}^+$-pair. However, the kinematic requirements on the leptons and the di-lepton invariant mass in this analysis lead to an expectation of only 45 such events in the electron and 74 events in the muon channel analysis, which is again very small compared to the number of estimated QCD background events (Table 11.6). With this in mind, the fact that the resulting

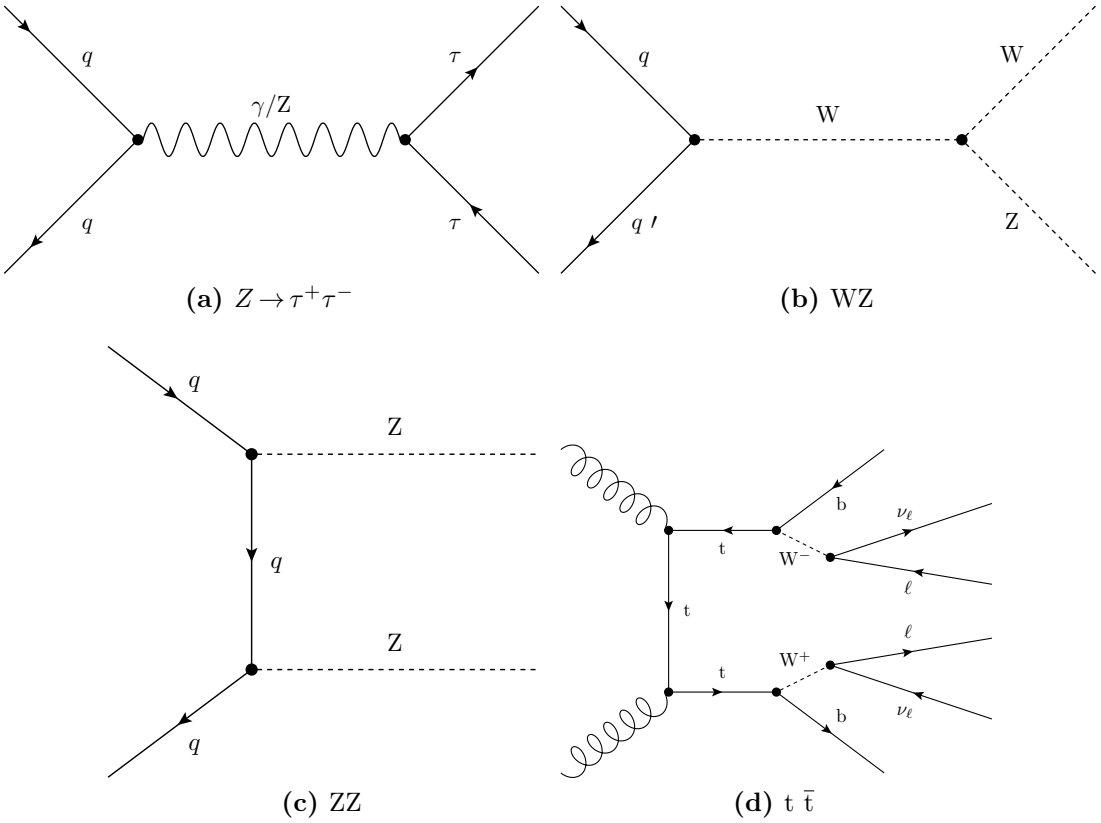

Figure 11.8.: Tree-level Feynman diagrams of EWBG processes that have the potential to produce a opposite-sign lepton pair that passes the lepton and di-lepton selection.

event-shape distributions are very different from those of the signal process, becomes negligible.

Summary: To summarise, a total of 203 EWBG events are expected to pass the electron channel analysis and 303 the muon channel analysis. About two-thirds (Z Z, $Z \to \tau^+\tau^-$) of which yield event-shape distributions very similar to the ones of the signal process, leading to fractions of $\frac{48}{250.000} \approx 0.02\%$ in the electron and $\frac{106}{400.000} \approx 0.03\%$ of events that yield significantly different event-shapes compared with the signal process that are not corrected for.

Plots of the di-lepton invariant mass distributions of the electron and the muon channel are shown in Figure 11.10 for the $p_\perp$(Z)-inclusive phase-space with signal and background contributions stacked onto one another such as to be comparable with data. Considering that leading order cross-section uncertainties are typically of the order of 10% [79], the

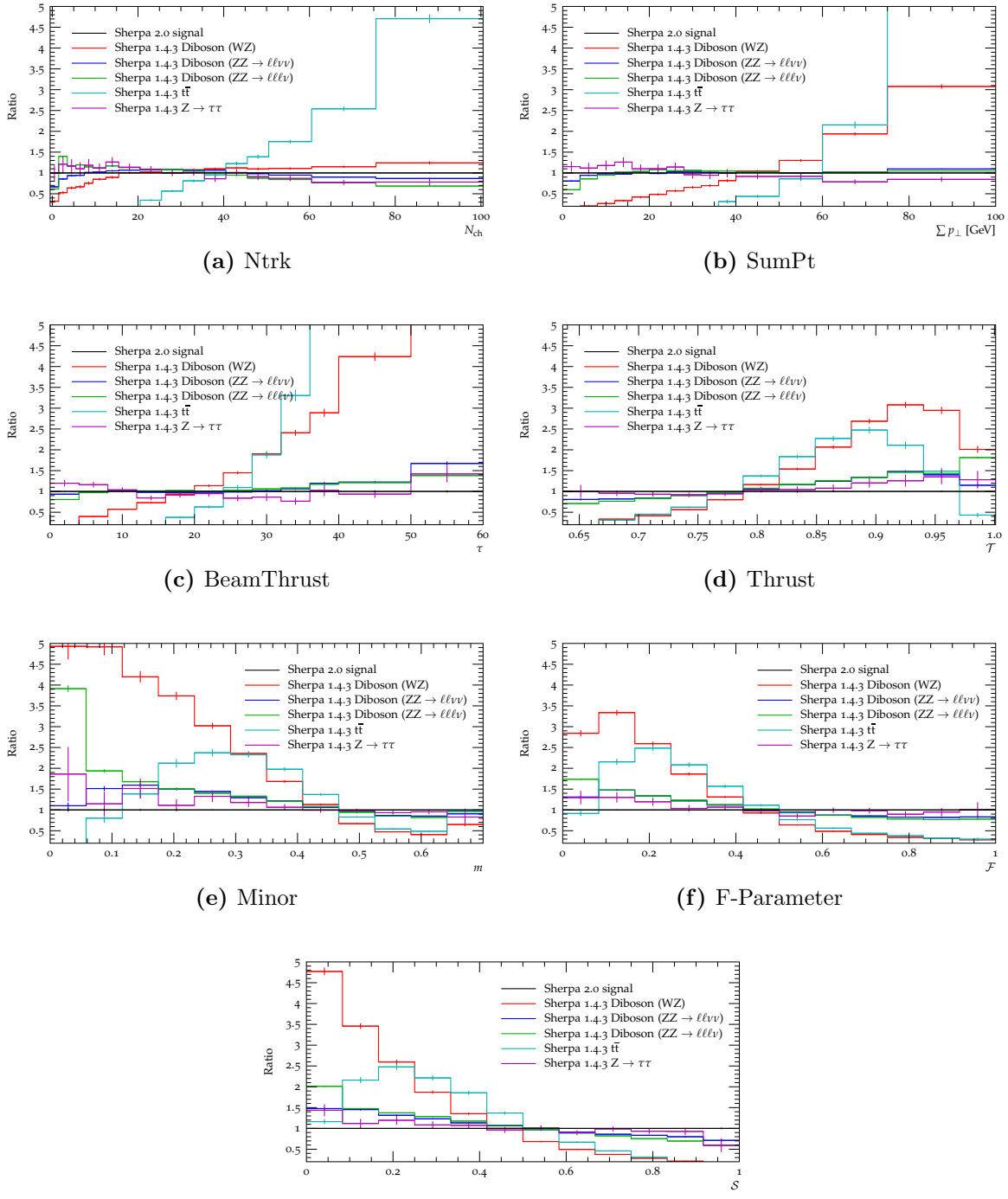

(a) Ntrk **(b)** SumPt

(c) BeamThrust **(d)** Thrust

(e) Minor **(f)** F-Parameter

(g) Spherocity

Figure 11.9.: Comparison of event-shapes obtained from electroweak background samples with a signal sample.

achieved agreement is satisfying and demonstrates that all relevant backgrounds are under control and especially that the amount of QCD background is estimated properly.

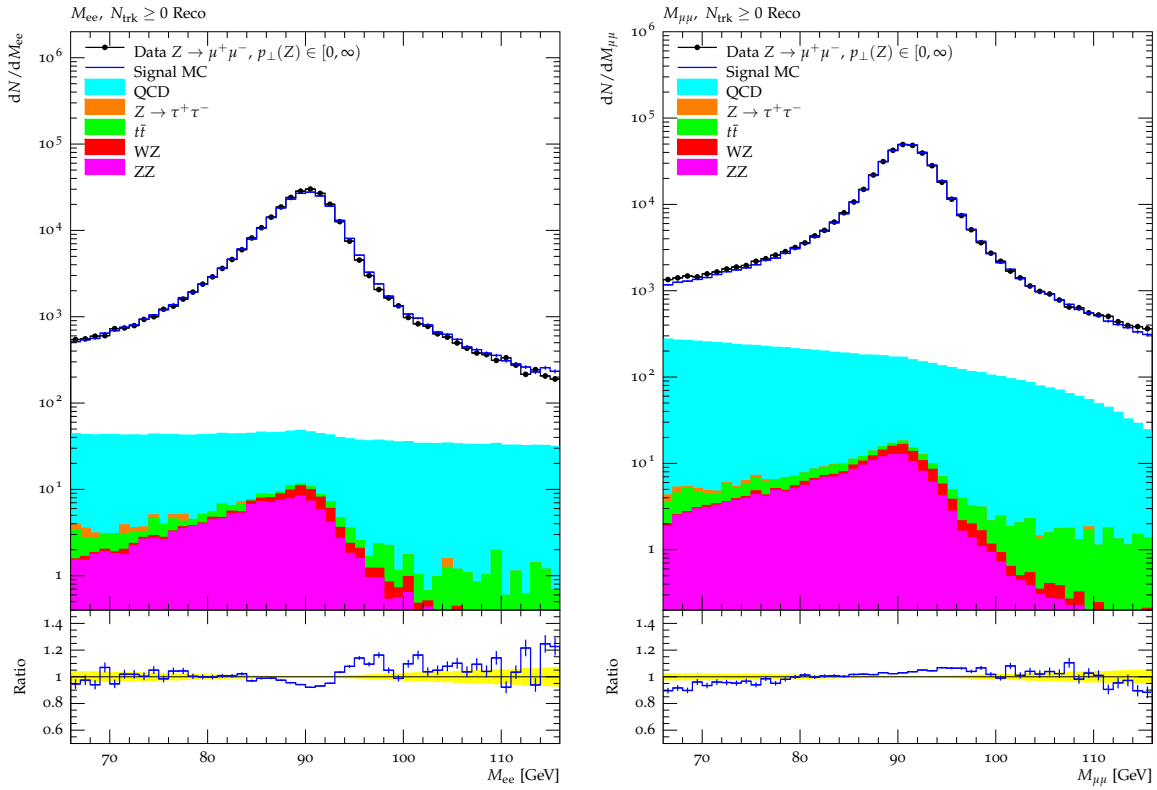

(a) Electron channel **(b)** Muon channel

Figure 11.10.: Comparison of reconstructed data with signal and background processes stacked onto one another showing satisfying agreement with the former. Signal and EWBG distributions are taken from Monte-Carlo predictions and are scaled to data luminosity (Section 11.2.1). The QCD background estimates are determined in a data-driven way (Section 11.1).

Generator	Sample	σ [nb]	K	BR
Sherpa	Signal	0.89972	1.2	1.0
Sherpa	ZZ($\ell\ell\ell\ell$)	$4.6244 \cdot 10^{-3}$	1.2	0.3
Sherpa	ZZ($\ell\ell\nu\nu$)	$3.3788 \cdot 10^{-4}$	1.2	0.3
Sherpa	WZ	$6.2579 \cdot 10^{-3}$	1.2	0.3
Sherpa	$t\bar{t}$	$3.4085 \cdot 10^{-3}$	1.2	0.3
Sherpa	$Z \to \tau^+\tau^-$	1.0459	1.2	0.3

Table 11.5.: Cross sections and K-factors of Monte-Carlo samples used for the construction of Figure 11.10. The actual samples can be found in Table A.3. The cross sections, σ, are leading-order cross sections calculated by Sherpa.

Sample	N_{BG} (electron channel)	N_{BG} (muon channel)
ZZ	129	191
WZ	23	32
$\mathrm{t\bar{t}}$	45	74
$Z \to \tau^+\tau^-$	6	6
QCD	1780	8621

Table 11.6.: Background yields for the fully inclusive $p_\perp$(Z) phase-space.

Chapter 12.

Unfolding

12.1. Introduction

The measurement of distributions with a highly complex detector such as ATLAS always suffers from effects like migration (due to finite resolution) and limited acceptance. Unfolding is a general term for techniques to correct for such effects. The key idea is to create a mapping of true event quantities and corresponding reconstructed quantities which contain all the imperfections mentioned above, e.g. the actual number of charged particles in a single event, N_{ch}, and the counterpart given by the return value of the detector simulation and reconstruction through which the very same event was processed, yielding the number of reconstructed tracks N_{trk}. For example, this analysis defines its phase-space for charged particles as $|\eta| < 2.5$, $p_{\perp} > 500$ MeV. Several reconstruction effects can now lead to the fact that e.g. one of the charged particles is reconstructed with a transverse momentum just below 500 MeV although the actual simulation created this particle with more than 500 MeV. The opposite effect is also possible, meaning that a particle generated with a transverse momentum lower than 500 MeV is reconstructed to have more than 500 MeV thus passing the cut. Both situations lead to differences between the true and reconstructed properties, i.e. $N_{\mathrm{ch}} \neq N_{\mathrm{trk}}$.

Once such a map, M, is at hand, the effect of the detector on true distributions can be written as a matrix equation:

$$\vec{R} = \mathbf{M}\vec{T} \tag{12.1}$$

Naively, the true values $\vec{T}$ could now be obtained from the reconstructed values $\vec{R}$ by inverting $\mathbf{M}$ as such:

$$\vec{T} = \mathbf{M}^{-1}\vec{R} \tag{12.2}$$

However it is not clear if $\mathbf{M}$ is actually invertible [119]. Further, $\mathbf{M}$ is only known with finite statistics, leading to statistical fluctuations present in $\vec{R}$ of being identified with actual structures in the data which leads to oscillations in the unfolded data. Hence a procedure is required that dampens these oscillations.

Two principal approaches for unfolding exist, either based on Frequentist statistics or Bayes theorem. In this analysis, a Bayesian apporach is chosen, proposed by D'Agostini [120] that relies on Bayes' theorem which states

$$P(A|B) = \frac{P(B|A) \cdot P(A)}{P(B)} \tag{12.3}$$

i.e. it connects the hypothesis A with the result B in terms of the probability that A is correct given a result B. In the context of unfolding, A corresponds to a certain bin of the true distribution, T_i, and B corresponds to a certain bin of the reconstructed distribution, R_j. The map M (equation (12.1)) which is also referred to as "smearing matrix" then allows to calculate for all pairs i, j ($i, j \in [1 \cdots N]$, N being the number of bins of the distribution in question) the probability of the hypothesis $P(T_i|R_j)$

$$P(T_i|R_j) = \frac{M_{ij} \cdot P(T_i)}{P(R_j)} = \frac{P(R_j|T_i) \cdot P(T_i)}{P(R_j)} \tag{12.4}$$

It is important to stress that initially assumptions on $P(T_i)$ need to be made (prior). The identification of M_{ij} with $P(R_j|T_i)$ allows to calculate the quantity $P(R_j)$ restating equation (12.1):

$$P(R_j) = \sum_i^N M_{ij} \cdot P(T_i) = \sum_i^N P(R_j|T_i) \cdot P(T_i) \tag{12.5}$$

Misses and Fakes:

It is generally possible that a true event property does not have a reconstructed counterpart. This may happen due to acceptance cuts in the event selection leading to a situation where the true part passes the event selection while the reconstructed does not. Such events are called "misses" and they are treated by introducing an efficiency ε_i:

$$\varepsilon_i = \sum_j P(R_j|T_i) \tag{12.6}$$

Thus ε_i gives the probability that for a certain observable the true property in bin i of an event has a reconstructed partner in any bin of the reconstructed property.

The opposite effect, i.e. that a reconstructed property does not have a counterpart in any of the bins of the true distribution is also accounted for. This effect is called a "fake" and comes into the procedure at the point where the Monte-Carlo and data distributions are subdivided in $p_\perp$(Z) phase-space regions. Technically this is accounted for in `Imagiro` by adding another column to the smearing matrix that contains the probability of a reconstructed event being a fake. This column thus contains information on the probability of fake events migrating into the measured distribution. Further, the prior distributions are also extended by one bin into which all the fake events are filled. The prior distribution is normalised after adding the fake bin. Thus, the prior distribution covers all possible outcomes and even contains information on the expected number of fakes.

The equivalent of an inverted smearing matrix $\mathbf{M}^{-1}$ in a BAYESian unfolding is now fully given by known quantities:

$$\mathbf{M}^{-1} \widehat{=} P(T_i|R_j) \underset{(12.4),(12.5)}{=} \frac{P(R_j|T_i) \cdot P(T_i)}{\varepsilon_i \sum_{l}^{N} [P(R_j|T_l) \cdot P(T_l)]} \equiv U_{ij} \tag{12.7}$$

In total there are two requirements for this method to calculate the unfolding matrix $P(T_i|R_j)$, the smearing matrix $P(R_j|T_i)$ and a prior distribution $P(T_i)$, both are known only from simulated events. Originally, D'Agostini argued that a flat distribution should be used as prior. However, the prior dependence has been found to be very small for one-dimensional distributions compared to other uncertainties, which is why the prior distribution is usually taken from a true distribution of a Monte-Carlo sample [121].

With this at hand, the correction of e.g. the bin j of the distribution of the charged number of tracks mentioned above to the number of charged particles (bin i) can be written as:

$$N_{\mathrm{ch}}(i) \underset{(12.2)}{=} \sum_{j}^{N} P(T_i|R_j) \cdot N_{\mathrm{trk}}(j) = \sum_{j}^{N} U_{\mathrm{ij}} \cdot N_{\mathrm{trk}}(j) \tag{12.8}$$

or more generally

$$\vec{C} = \mathbf{U} \cdot \vec{R} \tag{12.9}$$

where C stands for the unfolded distribution of R.

The result will depend on the prior distribution $P(T_i)$ which is why D'Agostini proposed to iteratively repeat the procedure using the result of the n-th application of equation (12.8) as new prior for the (n+1)-th step, thus altering the unfolding matrix somewhat each step.

After a certain number of iterations, the result should converge to the true data distribution, eliminating the dependence on the prior. Several technical features are available in the implementation used in this analysis that assert the validity of the method. The im-

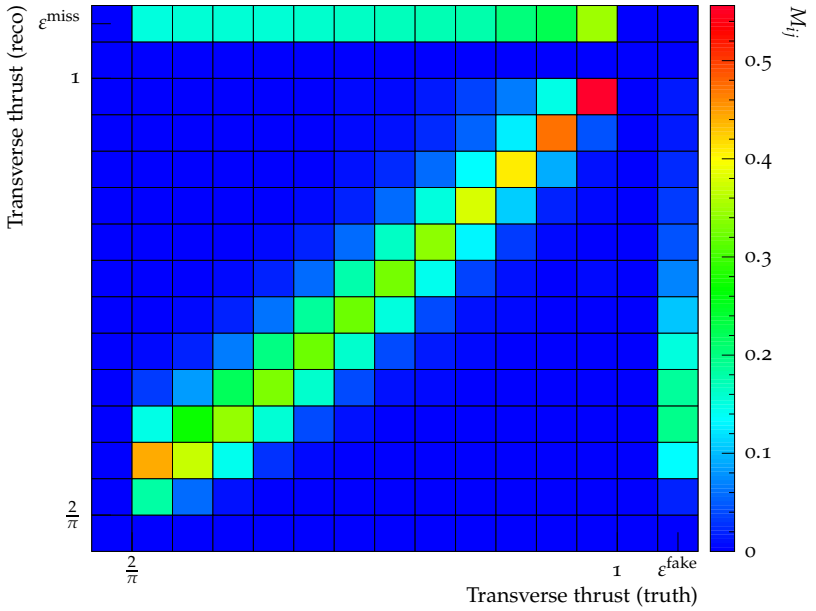

Figure 12.1.: Example of a smearing matrix constructed by `Imagiro`. The majority of events can be found in the main diagonal where reconstructed properties (in this case transverse Thrust) are correctly matched to the corresponding true properties of an event. All of-diagonal elements show the smearing effect of the detector. The column, labelled in this plot as $\varepsilon^{\text{fake}}$, is constructed by `Imagiro` to account for events where reconstructed properties do not have a truth partner. Similarly, the column, labelled in this plot as $\varepsilon^{\text{miss}}$, is constructed by `Imagiro` to account for events where true properties do not have a reconstructed partner.

plementation of iterative BAYESian unfolding used is the one provided by WYNNE, called `Imagiro` [121] with improvements to the error calculation as suggested by AYDE [122].

In Figure 12.1 a typical example of a smearing matrix used when unfolding data is given.

12.1.1. Unfolding strategy in this analysis

One of the crucial problems this analysis has to deal with are charged particles coming from pile-up interactions (Chapter 10). In principle one could rely on simulated events to correctly describe this effect but by doing so several problems arise. Firstly, the available statistics of samples generated with pile-up simulation is very low compared to the equivalent sample generated without pile-up. Secondly, the dominant effect leading to pile-up interactions, i.e. Minimum-Bias events, are not well described by the simulations, even though a lot was invested in tuning the phenomenological parameters

of the underlying models. Lastly, it is unclear how to realistically estimate systematic uncertainties due to the model imperfections. The Monte-Carlo samples generated with pile-up are thus not used in the unfolding of data. However, they serve as valuable test-bed in the evaluation of the validity of the unfolding mechanism itself (Section 12.6.2). When unfolding with information taken from the samples with pile-up, equation (12.8) remains unchanged.

In all other cases, one (MC only) or even two correction factors (data) are applied to the reconstructed properties prior to unfolding. Thus, the unfolding equation has to be altered:

$$N_{\mathrm{ch}}(i) = \sum_{j}^{N} P(T_i|R_j) \cdot \prod_{k} c_j^k \cdot N_{\mathrm{trk}}(j) = \sum_{j}^{N} U_{\mathrm{ij}} \cdot \prod_{k} c_j^k \cdot N_{\mathrm{trk}}(j) \tag{12.10}$$

where the bin-wise correction factors c_j^k are those for pile-up (Chapter 10) and those for the QCD background (Chapter 11). The latter only applies when unfolding data:

$$\prod_{k} c_k^j = \begin{cases} c_j^{\mathrm{PU}} & \text{when unfolding Monte-Carlo} \\ c_j^{\mathrm{PU}} \cdot c_j^{\mathrm{QCD}} & \text{when unfolding data} \end{cases} \tag{12.11}$$

This procedure is necessary since the unfolding matrix does not "know" about pile-up and QCD background when the smearing matrix as well as the initial priors are constructed using Monte-Carlo simulations for signal without pile-up.

12.1.2. Definition of true properties

When constructing the unfolding matrix, care needs to be taken concerning the definition of the objects. In the simulation, reconstructed tracks of charged particles are mapped to stable charged hadrons ($c\tau > 10$ cm) requiring $p_\perp > 500$ MeV and $|\eta| < 2.5$ thus applying the same kinematic cuts as they are applied for the reconstructed tracks.

Concerning the leptons, there are three commonly used definitions of what a final state lepton is. The definitions are related to ambiguities that arise due to photon radiation off of leptons:

1. BORN-level leptons
2. bare leptons
3. dressed leptons

BORN level leptons are simply the objects taken from the Monte-Carlo event record before any photon radiation. This approach is typically chosen in experiments where data statistics are low since this definition allows to simply combine electron and muon channels of an analysis. However, this approach has a slight problem in terms of interpretation of the result as BORN level leptons cannot be "seen" in data, some QED radiation will always be present, i.e. it is experimentally impossible to state whether a lepton has radiated off a photon or not.

Bare leptons on the other hand are final state objects that are present after all QED emissions have been evaluated. Thus, bare leptons have an implicit dependency on the algorithms and models implemented in a particular Monte-Carlo simulation.

Dressed leptons represent an approach to defining final state leptons in some analogy to jets. It is an attempt to get as close to experimental conditions as possible. A bare lepton is taken as seed for the dressed lepton counterpart by defining a cone of size ΔR using the bare lepton as axis. ΔR is generally calculated for pairs of particles from their azimuthal angles, $\Phi_{1,2}$, and their pseudorapidities, $\eta_{1,2}$:

$$\Delta R(p_1, p_2) = \sqrt{(\Phi_1 - \Phi_2)^2 + (\eta_1 - \eta_2)^2} \tag{12.12}$$

The four-vectors of all photons radiated off of leptons that happen to fall into this cone are added to the four-vector of the bare lepton, resulting in the four-vector of the dressed lepton:

$$p_{\text{dressed}}(\ell) = p_{\text{bare}}(\ell) + \sum_{\Delta R(p_{\text{bare}}(\ell), p_\gamma) < 0.1} p_\gamma \tag{12.13}$$

The sum in equation (12.13) runs over all photons that are not the result of hadron or τ decays or final-state of FSR radiation of charged hadrons and τ-particles. The size of the dressing cone, ΔR, is a somewhat arbitrary compromise chosen to collect as much lepton

Truth level property	cut
Lepton dressing cone size $\Delta R(\ell^{\text{Born}}, \gamma)$	0.1
Photons origin	no τ or hadron-decays
Dressed lepton $p_\perp$	> 20 GeV
Dressed lepton $\lvert\eta\rvert$	< 2.4
Invariant mass of dressed di-leptons, $M_{\ell\ell}$	$\in (66, 116)$ GeV
Charged particle $p_\perp$	> 500 MeV
Charged particle $\lvert\eta\rvert$	< 2.5

Table 12.1.: Truth-level object definitions used in the unfolding.

FSR as possible but not collecting too much ISR photons. The value $\Delta R = 0.1$ follows the definitions for dressed leptons used in [123] and is based on unpublished studies of the effect of different cone-sizes made for that analysis.

An illustration of the dressing procedure as well as the definition of bare and BORN leptons can be found in Figure 12.3.

An important consequence of this approach is that the resulting truth level distributions of the observables measured in this analysis will be different for the electron and the muon channel since the QED radiation is much stronger in the case of electrons than in the case of muons as the QED radiation is proportional to $\frac{1}{m_\ell^2}$ with m_ℓ being the mass of the leptons. Since the four-vectors of the dressed leptons are used to calculate the truth-level $p_\perp(\text{Z})$, this difference is propagated to the selection of events for specific $p_\perp(\text{Z})$ phase-space regions. Moreover, the modelling of QED radiation (Chapter 8) is done differently in the two Monte-Carlo simulations used in the unfolding, leading to slightly different priors (up to a few percent, see Figure 12.2) and smearing matrices and thus to slightly different unfolded distributions. Thus, a combination of the results of this analysis of the electron and the muon channel does not make sense.

The radiation of photons off of leptons is different in Sherpa and Pythia8 with sherpa generally radiating more soft collinear as well as wide-angle photons than Pythia8 does (Chapter 8.8). The difference is very strong in the case of electrons, which ultimately leads to larger differences between electron and muon channel observables in Sherpa compared to Pythia8.

A summary of the truth-level objects unfolded to can be found in Table 12.1.

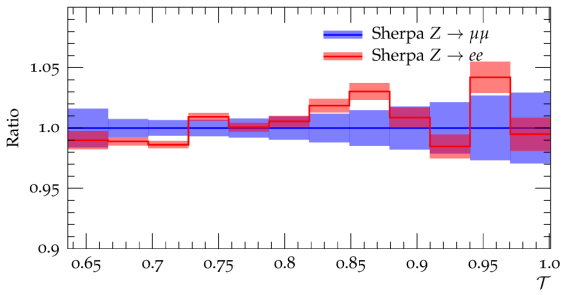

(a) Thrust, $p_\perp(\mathrm{Z}) \in [6, 12)$ GeV

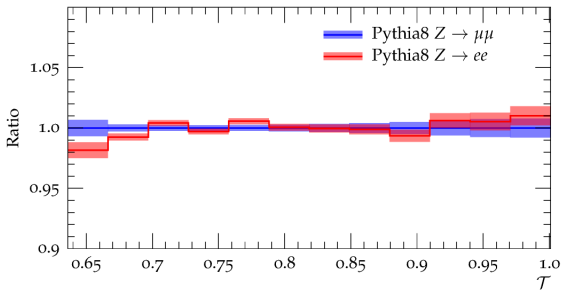

(b) Thrust, $p_\perp(\mathrm{Z}) \in [6, 12)$ GeV

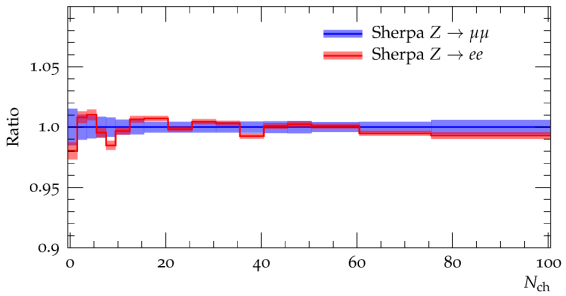

(c) N_{ch}, $p_\perp(\mathrm{Z}) \in [0, \infty)$ GeV

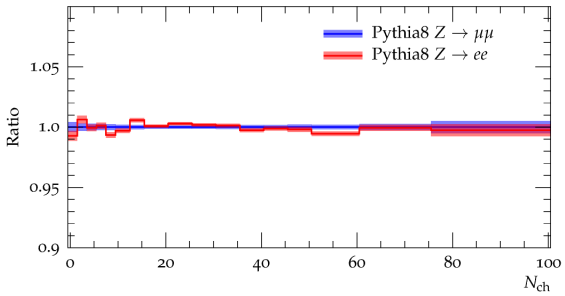

(d) N_{ch}, $p_\perp(\mathrm{Z}) \in [0, \infty)$ GeV

Figure 12.2.: Example ratio plots of muon and electron channel truth level observables using dressed leptons. The differences are observable and generator specific. The error bands shown represent the statistical uncertainties of the Monte-Carlo simulations. Results for Sherpa are shown on the left-hand side, the right-hand side plots show the equivalent result obtained with Pythia8. If instead of the dressed lepton definition BORN-level leptons are used, the ratio is exactly 1 in all cases.

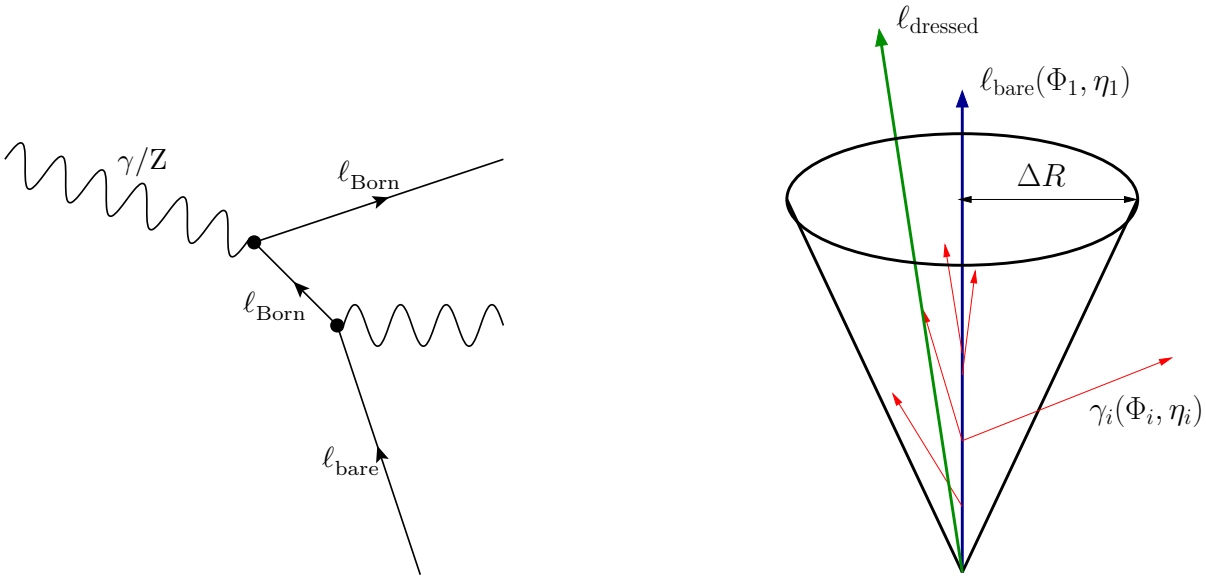

(a) BORN and bare leptons **(b)** Dressed leptons

Figure 12.3.: Illustration of truth level lepton definitions. In (a) the BORN level leptons ℓ_{Born} are defined as outgoing particles from the hard subprocess (Z-production). The bare leptons, ℓ_{bare}, are the final state objects present after QED radiation. (b) illustrates the dressing algorithm which starts from the bare leptons and adds the four-vectors of photons radiated off of leptons falling into a cone around ℓ_{bare} to obtain the four-vector of ℓ_{dressed}

12.2. Iterations and convergence

The aforementioned convergence (Section 12.1) does not necessarily improve as the number of iterations rises. In fact, statistical fluctuations due to finite statistics in the smearing matrix will eventually lead to a worse agreement of the unfolded distribution with the true distribution as the unfolded distribution of the n-th iteration is used as prior of the (n+1)-th iteration, thus altering the unfolding matrix and therefore compounding statistical fluctuations in the process, requiring a criterion to limit the number of iterations, which is explained in the following.

12.2.1. Multiple priors

The prior dependence should vanish in an ideal scenario, i.e. unlimited statistics, meaning that the smearing matrix would only depend on the detector simulation and subsequent reconstruction. In reality, this is never achievable. In fact, some model-dependence is introduced as different simulation programs populate certain bins of distributions with different frequency.

`Imagiro` generally builds the initial unfolding matrix (first iteration) from smearing matrices obtained from reconstructed and true properties of simulation A. The prior is also taken from simulation A, i.e. the corresponding true distribution of an observable, T. The to be unfolded distribution, R, will then be unfolded using an unfolding matrix, $\mathbf{U}_A$, solely constructed from MC sample A.

If two MC simulations A and B are available[1] that used the same detector simulation and reconstruction, R can be unfolded with $\mathbf{U}_A$ and again with $\mathbf{U}_B$ (unfolding matrix solely relying on information from MC sample B). The results are two unfolded distributions C_A and C_B. The central values of the final unfolded distribution, C, is then simply taken as the mean of C_A and C_B. Any differences of $C_{A,B}$ with respect to C are considered as systematic model errors. (See Section 12.3).

In cases where multiple priors are available, `Imagiro` tries to estimate the most suitable number of iterations automatically. The procedure is again only based on MC information, even if the actual task is to unfold data. First, the reconstructed distribution of MC sample A, R_A, is unfolded using U_B. The result $C_B^{(n)}(R_A)$ is compared with the true distribution T_A after each iteration n. Then, the reconstructed distribution of MC

[1] In this analysis, two Monte-Carlo (MC) simulations are used, Sherpa and Pythia8

sample B, R_B, is unfolded using U_A and the result $C_A^{(n)}(R_B)$ is compared with T_B. The comparison of the $C_{B,A}^{(n)}(R_{A,B})$ with the $T_{A,B}$ is done using two statistical measures.

χ2 test: The χ^2 measure [124] is used in this test to estimate whether the two histograms in question are compatible. A hypothesis test is performed returning the corresponding p-value. `Imagiro` uses the implementation available for the basic histogram class in the `ROOT` framework [125].

KS test: A shape comparison is performed using the approach worked out by Kolmogorov and Smirnov [126] and implemented for the basic histogram class in the `ROOT` framework [125]. It allows to make a statement on whether a sample, S, comes from a distribution, D, by looking for the maximum distance between S and D. Although this test is strictly only valid for continuous distributions (unbinned data) it is used in `Imagiro` to compare histograms, since not the absolute values but the maxima (as function of the number of iterations) of the calculated probabilities are of interest.

A total of $n \in [1 \dots 10]$ iterations of the steps mentioned above are performed. The optimal number of iterations, $n_{A,B}^{KS,\chi}$, is based on the minimum in case of the χ2 test and the maximum in the KS test.

When looking only at the tests of unfolding with a single prior (U_x, $x \in [A, B]$), sometimes differences between n_x^{KS} and n_x^{χ} occur. If that happens, the smaller number of the two is used, yielding n_x ($x \in [A, B]$). Further, if the numbers n_A and n_B are different, the ceiling of the mean of the two is used:

$$c = \left\lceil \frac{\min[n_A^{KS}, n_A^{\chi}] + \min[n_B^{KS}, n_B^{\chi}]}{2} \right\rceil \tag{12.14}$$

In Figure 12.4 the test values obtained when unfolding two different observables are shown.

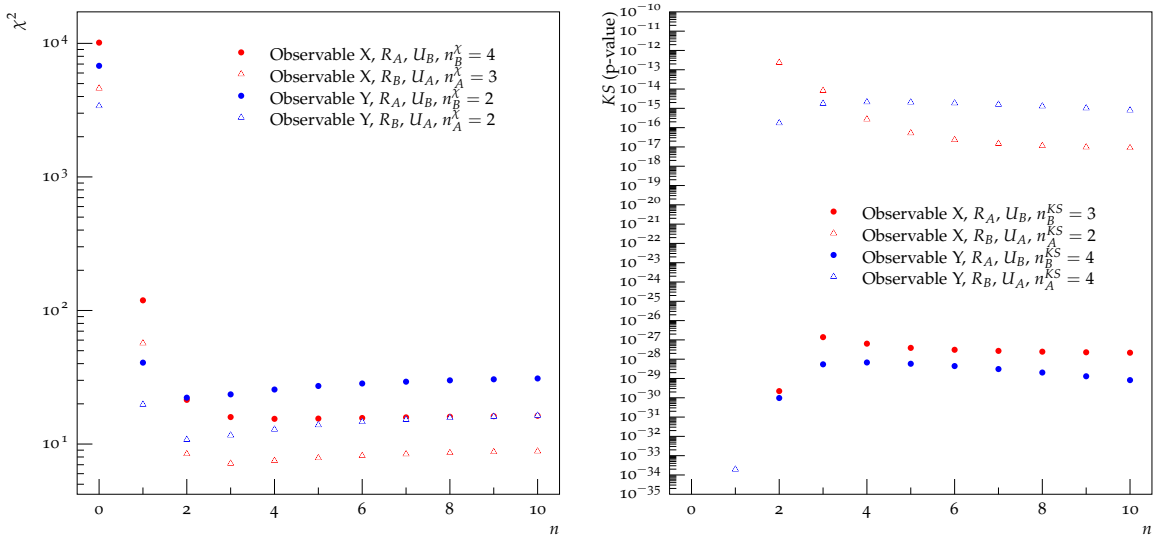

(a) χ^2 test **(b)** KS test

Figure 12.4.: Visualisation of the determination of the optimal number of iterations, c, in `Imagiro`. Both statistical measures are drawn as function of the number of iterations, n, for two different observables X and Y. The tests are performed unfolding R_A using U_B and unfolding R_B with U_A, yielding four numbers of potentially optimal numbers of iterations $n_{A,B}^{\chi,KS}$. Observable X will be unfolded using $c = 3$ iterations since in both unfoldings (U_A and U_B) the KS tests give the smaller numbers ($n_A^{KS} = 2$, $n_B^{KS} = 3$). The mean of n_A^{KS} and n_B^{KS} is not an integer which is why the ceiling, 3, will be used (equation (12.14)). Observable Y will be unfolded using $c = 2$ iterations as the χ^2 tests yield lower (and identical) numbers than the KS-tests.

12.3. Unfolding model error

Since two Monte-Carlo samples are available, `Imagiro` is able to estimate a model error systematic when unfolding with different priors. In that case, the central value, $f_c = (f_1 + f_2)/2$, of each bin of the unfolded distribution is simply the mean of all unfoldings performed. The systematic error corresponding to the unfolding with different priors is in the case of this analysis (two priors) is taken as the (asymmetric) differences of f_c and $f_{1,2}$ (Section 12.2).

12.4. Statistical uncertainties

The statistical uncertainties estimated with `Imagiro` contain two improvements of D'Agostini's original prescription. Both deal with the effect that the unfolding matrix is changed if more than one iteration is performed. First, the propagation of measurement uncertainties will be explained, and secondly the effect of finite statistics and the corresponding error propagation.

Let y correspond to the unfolded distributions and x to the reconstructed distributions. Then the Jacobian, $\mathbf{J}(x)$, is defined as:

$$J_{ij}(x) = \frac{\partial y_i}{\partial x_j}(x) \tag{12.15}$$

In both cases, the generalised error propagation law [127] is used for the determination of the statistical uncertainties of the unfolded distributions.

$$\mathbf{V}_y = \mathbf{J}(x) \cdot \mathbf{V}_x \cdot \mathbf{J}^\top(x) \tag{12.16}$$

where $\mathbf{V}_x$ and $\mathbf{V}_y$ are the covariance matrices of vectors x and y.

12.4.1. Propagation of measurement uncertainties

In the following, the error propagation will be explained using the example of equation (12.8).

The covariance matrix of the reconstructed distribution is taken in `Imagiro` as a diagonal matrix, i.e.

$$\mathbf{V}_x \widehat{=} V(N_{\text{trk}}(i), N_{\text{trk}}(j)) = \delta_{ij} N_{\text{trk}}(i) \tag{12.17}$$

The Jacobian corresponding to equation (12.8) can be written as

$$\frac{\partial N_{\text{ch}}(i)}{\partial N_{\text{trk}}(j)} = U_{ij} \tag{12.18}$$

which assumes that the unfolding matrix U_{ij} is independent from $N_{\text{trk}}(j)$[2]. However, this is only true for the first iteration, yielding , since according to equation (12.7) the unfolding matrix is changed in subsequent iterations in the sense that the new prior is taken as the result of the previous iteration:

$$N_{\text{ch}}(i)^{(0)} = \sum_{j}^{N} U_{\text{ij}} \cdot N_{\text{trk}}(j) \tag{12.19}$$

becomes

$$\tilde{N}_{\text{ch}}(i) \underset{(12.7)}{=} \sum_{j}^{N} \underbrace{\frac{P(N_{\text{trk}}(j)|N_{\text{ch}}(i)) \cdot N_{\text{ch}}(i)^{(0)}}{\sum_{l}^{N}[P(N_{\text{trk}}(j)|N_{\text{ch}}(l)) \cdot N_{\text{ch}}(l)^{(0)}]}}_{\tilde{U}_{ij}} \cdot N_{\text{trk}}(j) \tag{12.20}$$

[2]This resembles the original D'Agostini approach

Where $N_{\mathrm{ch}}(i)^{(0)}$ denotes the unfolded distribution of the previous iteration and $\tilde{U}_{ij}$ is the altered unfolding matrix. Since $N_{\mathrm{ch}}(i)^{(0)}$ depends on $N_{\mathrm{trk}}(j)^{(0)}$ (equation (12.19)), so does $\tilde{U}_{ij}$.

Hence the error propagation needs to be rewritten to take this effect into consideration. The full result (calculation by Adye, [122]) is the following:

$$\frac{\partial \tilde{N}_{\mathrm{ch}}(i)}{\partial N_{\mathrm{trk}}(j)} = U_{ij} + \underbrace{\frac{\tilde{N}_{\mathrm{ch}}(i)}{N_{\mathrm{ch}}(i)^{(0)}} \frac{\partial N_{\mathrm{ch}}(i)^{(0)}}{\partial N_{\mathrm{trk}}(j)} - \sum_{k=1}^{N}\sum_{l=1}^{N} \frac{N_{\mathrm{trk}}(k)\varepsilon_l}{N_{\mathrm{ch}}(l)^{(0)}} U_{ik}U_{lk} \frac{\partial N_{\mathrm{ch}}(l)^{(0)}}{\partial N_{\mathrm{trk}}(j)}}_{=0 \text{ if c=1 (equation (12.14))}} \tag{12.21}$$

The two additional terms were not present in the original D'Agostini treatment of errors. Both depend on the Jacobian $\frac{\partial N_{\mathrm{ch}}(l)^{(0)}}{\partial N_{\mathrm{trk}}(j)}$ which vanishes if only one iteration is performed. In subsequent iterations, $\frac{\partial N_{\mathrm{ch}}(i)^{(0)}}{\partial N_{\mathrm{trk}}(j)}$ is replaced with the matrix from the previous iteration, $\frac{\partial \tilde{N}_{\mathrm{ch}}(i)}{\partial N_{\mathrm{trk}}(j)}$.

This error propagation matrix is used to calculate the covariance matrix for the measurement errors, $V_{\mathrm{meas}}(\tilde{N}_{\mathrm{ch}}(k), \tilde{N}_{\mathrm{ch}}(l))$ as such (equation (12.16), (12.17)):

$$V_{\mathrm{meas}}(\tilde{N}_{\mathrm{ch}}(k), \tilde{N}_{\mathrm{ch}}(l)) = \sum_{i,j=1}^{N} \frac{\partial \tilde{N}_{\mathrm{ch}}(k)}{\partial N_{\mathrm{trk}}(i)} \cdot V_{\mathrm{meas}}(N_{\mathrm{trk}}(i), N_{\mathrm{trk}}(j)) \cdot \frac{\partial \tilde{N}_{\mathrm{ch}}(l)}{\partial N_{\mathrm{trk}}(j)} \tag{12.22}$$

12.4.2. Propagation of statistical uncertainties in the smearing matrix

Since the Monte-Carlo samples used to populate the smearing matrix in equation (12.7) always have limited statistics, the result of the unfolding is also subject to statistical uncertainties coming from the precision of $P(N_{\mathrm{trk}}(j)|N_{\mathrm{ch}}(i))$. D'Agostini presented the calculation of the corresponding uncertainties but omitted the effect that after the first iteration, the prior, $\tilde{N}_{\mathrm{ch}}(i)$, also depends on $P(N_{\mathrm{trk}}(j)|N_{\mathrm{ch}}(i))$.

ADYE calculated the error propagation matrix [122] which considers this effect as follows:

$$\begin{aligned}\frac{\partial \tilde{N}_{\mathrm{ch}}(i))}{\partial P(N_{\mathrm{trk}}(j)|N_{\mathrm{ch}}(k))} &= \frac{1}{\epsilon_i}\left(\frac{N_{\mathrm{ch}}(i)^{(0)}\cdot N_{\mathrm{trk}}(j)}{f(j)} - \tilde{N}_{\mathrm{ch}}(i)\right)\delta_{ik} \\ &- \frac{N_{\mathrm{ch}}(k)^{(0)}\cdot N_{\mathrm{trk}}(j)}{f(j)} U_{ij} \\ &+ \frac{\tilde{N}_{\mathrm{ch}}(i)}{N_{\mathrm{ch}}(i)^{(0)}}\cdot\frac{\partial N_{\mathrm{ch}}(i)^{(0)}}{\partial P(N_{\mathrm{trk}}(j)|N_{\mathrm{ch}}(k))} \\ &- \frac{\epsilon_i}{N_{\mathrm{ch}}(i)^{(0)}}\sum_{l.r=1}^{N} N_{\mathrm{trk}}(l)\, U_{il}U_{rl}\cdot\frac{\partial N_{\mathrm{ch}}(r)^{(0)}}{\partial P(N_{\mathrm{trk}}(j)|N_{\mathrm{ch}}(k))} \quad (12.23)\end{aligned}$$

Again, the last two terms in equation (12.23) vanish in case that only one iteration is performed, thus obtaining the original expression derived by D'AGOSTINI. In subsequent iterations, $\frac{\partial N_{\mathrm{ch}}(i)^{(0)}}{\partial P(N_{\mathrm{trk}}(j)|N_{\mathrm{ch}}(k))}$ is replaced by the result of the then previous iteration, $\frac{\partial \tilde{N}_{\mathrm{ch}}(i))}{\partial P(N_{\mathrm{trk}}(j)|N_{\mathrm{ch}}(k))}$ meaning that the effect that the new prior is subject to statistical uncertainties in the smearing matrix is accounted for.

The corresponding covariance matrix is then calculated according to equation (12.16):

$$V_{\mathrm{smear}}(\tilde{N}_{\mathrm{ch}}(k),\tilde{N}_{\mathrm{ch}}(l)) = \sum_{j,s}^{N}\sum_{i,r}^{N}\frac{\partial \tilde{N}_{\mathrm{ch}}(k))}{\partial P(N_{\mathrm{trk}}(j)|N_{\mathrm{ch}}(i))}\cdot V_{\mathrm{smear}}(ijrs)\cdot\frac{\partial \tilde{N}_{\mathrm{ch}}(l))}{\partial P(N_{\mathrm{trk}}(s)|N_{\mathrm{ch}}(r))} \quad (12.24)$$

With $V_{\mathrm{smear}}(ijrs) = V_{\mathrm{smear}}\left(P(N_{\mathrm{trk}}(j)|N_{\mathrm{ch}}(i)), P(N_{\mathrm{trk}}(s)|N_{\mathrm{ch}}(r))\right)$ being the covariance matrix of statistical uncertainties of the smearing matrix which are estimated in `Imagiro` assuming POISSONian distributed entries in the smearing matrix. Again, $V_{\mathrm{smear}}(ijrs)$ is a diagonal matrix.

In the case that two MC samples are available as it is in this analysis, `Imagiro` propagates the statistical uncertainties in the smearing matrix for both samples separately and calculates the mean of those for each bin when a bin's final statistical error is constructed.

12.4.3. Total statistical uncertainty

The final covariance matrices of both sources of statistical uncertainties on the unfolded distributions are added:

$V_{\text{total}} = V_{\text{meas}} + V_{\text{smear}}$

For each bin i, the statistical error, σ_i is calculated as:

$$\sigma_i = \sqrt{V_{\text{total}}(i,i)} \tag{12.25}$$

Examples of the effect of the ADYE correction on the final statistical errors can be found in Figure 12.6 where the σ_i are plotted for an unfolding of the observable F-Parameter in a pure Monte-Carlo test. The blue line (one iteration) shows the result consistent with the original D'AGOSTINI error calculation. It is obvious that as soon as more than one iteration is performed, the additional terms in equation (12.21) and (12.23) yield significantly larger uncertainties. This, together with the study of the number of iterations necessary to obtain an optimal unfolded distribution (Figure 12.5) can also be seen as justification of using a non-flat prior distribution in equation (12.7) contrary to what D'AGOSTINI originally proposed.

V_{total} can also be used to calculate the correlation matrix:

$$\rho_{ij} = \frac{V_{\text{total}}(i,j)}{\sqrt{V_{\text{total}}(i,i)}\sqrt{V_{\text{total}}(j,j)}} \tag{12.26}$$

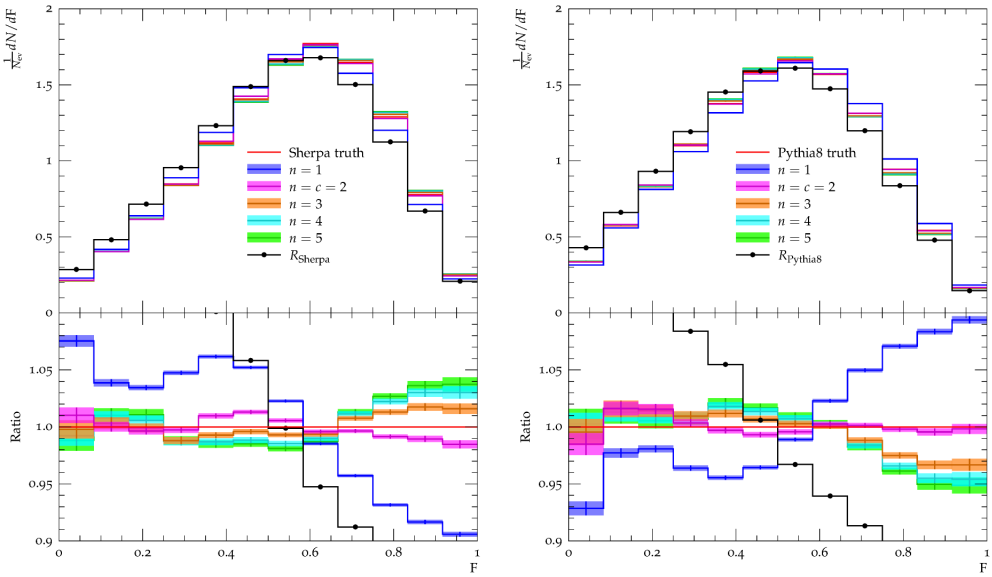

(a) $R_{\texttt{Sherpa}}$, $\mathbf{U}_{\texttt{Pythia8}}$, $p_\perp(Z) \in [0, \infty)$ GeV **(b)** $R_{\texttt{Pythia8}}$, $\mathbf{U}_{\texttt{Sherpa}}$, $p_\perp(Z) \in [0, \infty)$ GeV

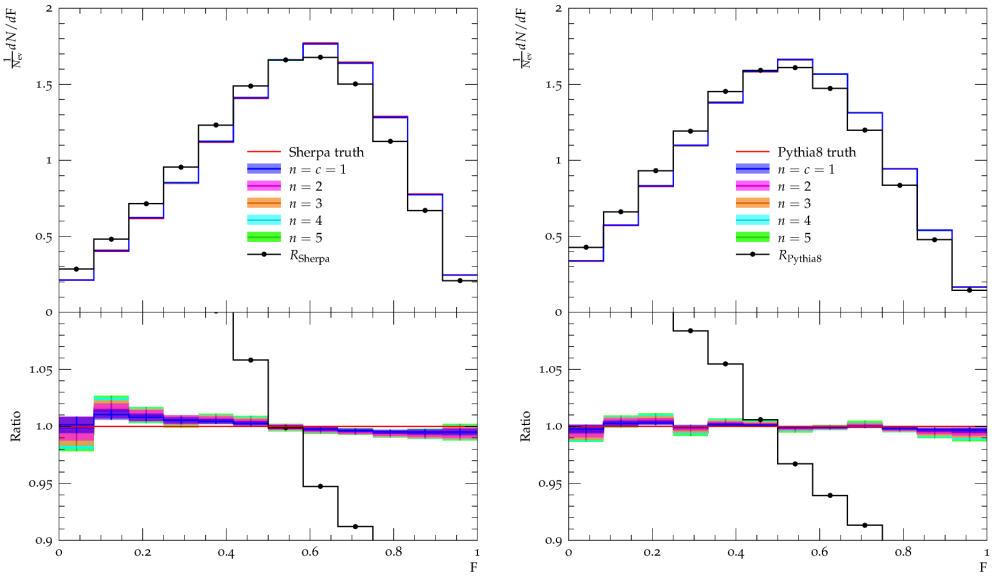

(c) $R_{\texttt{Sherpa}}$, $\mathbf{U}_{\texttt{Sherpa}}$, $p_\perp(Z) \in [0, \infty)$ GeV **(d)** $R_{\texttt{Pythia8}}$, $\mathbf{U}_{\texttt{Pythia8}}$, $p_\perp(Z) \in [0, \infty)$ GeV

Figure 12.5.: Monte-Carlo test of the evolution of unfolded distributions with the number of iterations applied using the example of the observable F-Parameter in the fully inclusive $p_\perp$(Z) phase-space region. Results of all possible combinations of unfolding the two samples Pythia8 and Sherpa are shown. The plots on top demonstrate nicely that the unfolding quickly converges with the true distribution and the effect of the build-up of statistical variations in subsequent iterations ($c = 2$). The convergence is even faster when unfolding Sherpa with Sherpa or Pythia8 with Pythia8 ($c = 1$). The evolution of the statistical uncertainties (Section 12.4) is presented in Figure 12.6 for the exact same plots shown here.

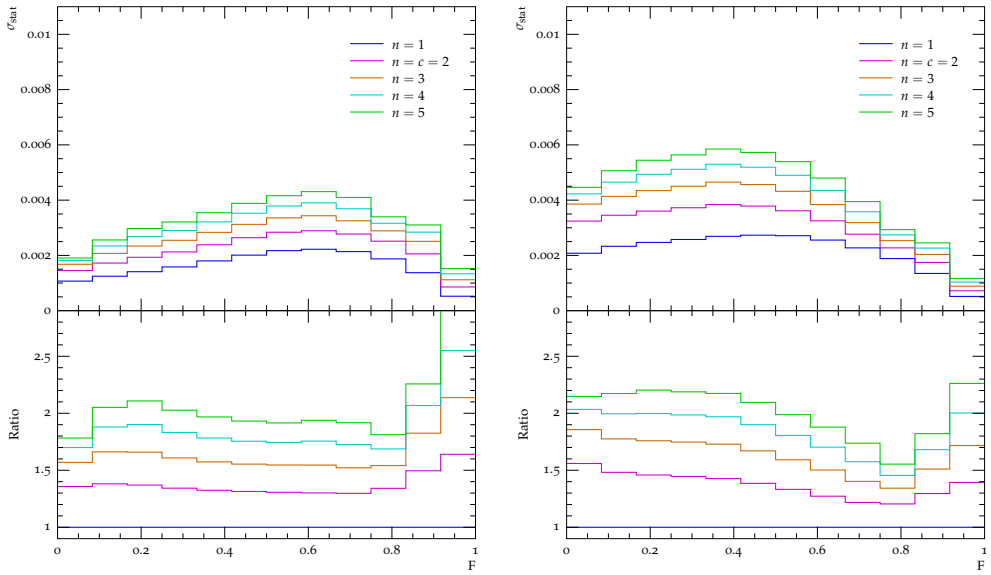

(a) $R_{\texttt{Sherpa}}$, $\mathbf{U}_{\texttt{Pythia8}}$, $p_\perp(Z) \in [0, \infty)$ GeV **(b)** $R_{\texttt{Pythia8}}$, $\mathbf{U}_{\texttt{Sherpa}}$, $p_\perp(Z) \in [0, \infty)$ GeV

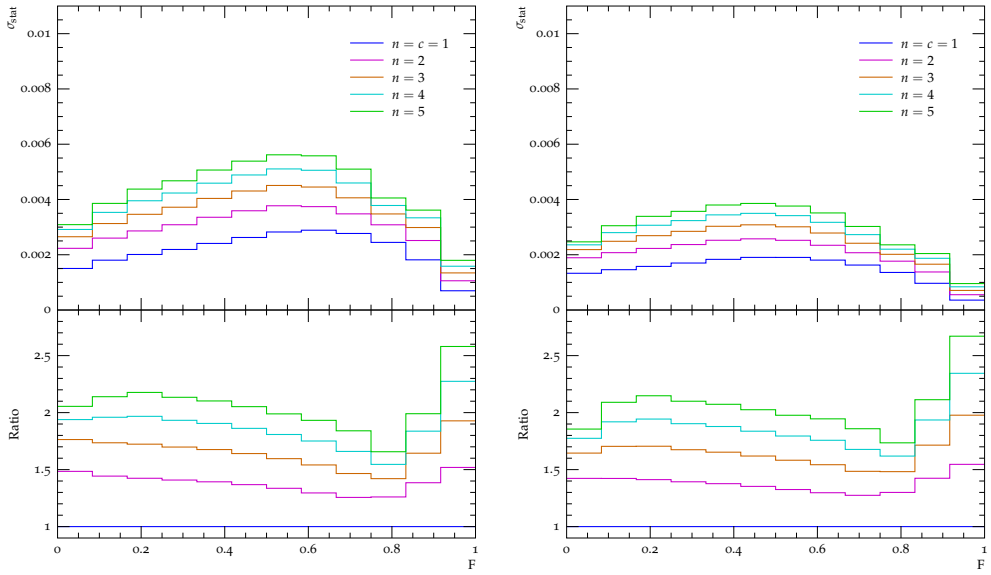

(c) $R_{\texttt{Sherpa}}$, $\mathbf{U}_{\texttt{Sherpa}}$, $p_\perp(Z) \in [0, \infty)$ GeV **(d)** $R_{\texttt{Pythia8}}$, $\mathbf{U}_{\texttt{Pythia8}}$, $p_\perp(Z) \in [0, \infty)$ GeV

Figure 12.6.: Evolution of the total statistical uncertainties with the number of iterations using the example of the observable F-Parameter in the fully inclusive $p_\perp$(Z) phase-space region. The blue line (one iteration) corresponds to the original D'Agostini errors that neglect the dependencies of the unfolding matrix on the measurement uncertainties and finite statistics in the smearing matrix. The ratio plots show that the Adye corrections to the original method can become important and that the original approach can severely underestimate the statistical uncertainties.

12.5. Propagation of systematic uncertainties

All sources of systematic uncertainties described so far need to be propagated through the unfolding as well in order to obtain systematic uncertainties on the final unfolded distributions. This includes the lepton systematics and tracking efficiencies outlined in Chapter 9 as well as the uncertainties related to the pile-up correction (Chapter 10) and QCD-background correction (Chapter 11).

The general procedure for the propagation of the systematic uncertainties mentioned above is to unfold the data again but with variations of either the reconstructed data, e.g. in case of the pile-up and QCD corrections, or the reconstructed Monte-Carlo properties as it is done in case of the tracking efficiency. Table 12.2 gives an overview on which part of equation (12.9) is affected when propagating the individual systematic uncertainties.

These unfoldings will yield slightly different results ,$\tilde{f}_{\text{syst}}$, with respect to the nominal or central unfolding, f_c. The systematic uncertainty of a particular effect is then taken as the difference between $\tilde{f}_{\text{syst}}$ and f_c.

Further, the unfolding model error (Section 12.3) needs to be accounted for when calculating the total systematic uncertainties.

12.5.1. Tracking efficiency

The tracking efficiency systematic has been described in 9.1. In order to obtain an estimate of the tracking efficiency systematic uncertainty onto unfolded data, the data distributions are once again unfolded - but with modified smearing matrices. Instead of using reconstructed properties corresponding to the nominal tracking efficiency, the ones

Systematic uncertainty	affects $\vec{R}$	affects $\mathbf{U}$ (reco part)
Pile-up correction	•	
QCD background correction	•	
Tracking efficiency		•
Lepton systematics		•

Table 12.2.: Overview of which part of the unfolding equation (equation (12.9)) is affected by the propagation of the individual systematics.

obtained using the systematic variation explained in 9.1 is used, resulting in $\tilde{R}_{\text{trkeff}}$ as input for the smearing matrices and a slightly different unfolded distribution, $\tilde{f}_{\text{trkeff}}$.

The difference of the central values of a particular bin of this result and the nominal unfolding result is taken as a (symmetric) systematic uncertainty of that bin.

Results can be found for all observables on the right-hand side plots in the figures in Section 12.7. The systematic uncertainty on the track reconstruction efficiency is generally found to be the dominant systematic uncertainty for observables where the number of charged particles does not cancel in the definition (N_{ch}, $\sum p_{\perp}$, Beamthrust) and reaches up to 10%. For all other observables it is typically found to be of the order of 1 to 3%. The contribution is of the same order when comparing unfolded distributions of the electron and the muon channel.

12.5.2. Lepton systematics

The propagation of systematic uncertainties related to the reconstruction of electrons and muons closely follows the procedure described above for the tracking efficiency. The only difference is that the number of systematics effects to be considered is much larger. The results can be found for all observables in the figures in Section 12.7.

Electron systematics

A total of 20 systematic variations with respect to the nominal reconstruction of electrons needs to be considered (Chapter 9), resulting in 20 different sets of reconstructed properties and thus 20 different smearing matrices and hence 20 different unfolded distributions per observable.

The resulting total lepton systematic, obtained when quadratically adding the individual contributions, can reach up to 10% in rare cases, it is mostly found to be of the order of 1 to 3% for most bins of most observables. However, the size of the electron systematics is dependent on the $p_{\perp}(\text{Z})$ phase-space region as could be expected since the electron systematics affect only the reconstructed properties of the electrons and thus $p_{\perp}(\text{Z})$ of an event. The event-shape distributions are affected due to the reconstructed $p_{\perp}(\text{Z})$ being used to sub-divide the data into different phase-space regions, leading to some fluctuations. A small effect is also expected due to the electron-track removal based on a cone approach (Chapter 5.1.3).

Muon systematics

The total number of systematic variations (Section 9.2.2) that are propagated through the unfolding in the muon channel is 9. The total muon systematic uncertainty is very dependent on the observable and $p_\perp$(Z) phase-space region. It is of the order of 1% for Thrust, Minor, F-Parameter and Spherocity but becomes more important for all other observables. For example, it reaches up to 20% in the last bin of Beamthrust when looking at the low $p_\perp$(Z) phase-space region and becomes almost negligible for the high $p_\perp$(Z) phase-space region (Figure C.5b and C.8b). Further, when comparing electron and muon systematics, it is found that the muon systematics for N_{ch}, $\sum p_\perp$and Beamthrust are generally larger than the electron systematics — with the exception of the high $p_\perp$(Z) phase-space region.

12.5.3. Pile-up correction systematics

The systematic uncertainty of the pile-up correction (Chapter 10) propagated through the unfolding is typically of the order of 1 to 3% with the exception of some low-statistics bins, such as the first few bins of Minor (Figure C.10-C.14). The dependence on the $p_\perp$(Z) phase-space region is not strong. When comparing the amount of the pile-up correction systematic of a specific bin of an observable for all $p_\perp$(Z) phase-space regions it becomes evident that the uncertainty is anti-correlated with the statistics of that bin. Results of the electron and muon channel are of comparable magnitude.

12.5.4. QCD background correction systematics

The systematic uncertainty of the background correction is negligible in almost all bins of all observables. Similar to the pile-up correction systematic, significant contributions arise in cases where the statistics of the bin in question is low.

12.5.5. Unfolding model error

For most observables, the unfolding model error is of the order of 1% or below. In cases of bins with low statistics it amounts up to 15% (Figure C.13). The magnitude observed in the electron and the muon channel are in agreement.

12.5.6. Total systematics

The total systematic uncertainties are constructed by adding the above systematic uncertainties in quadrature. The results are shown in the left hand side plots of the figures in Section 12.7. The systematic uncertainties in the electron channel are typically 1% larger than the ones obtained in the muon channel. They are are found to be of the order of 5 to 10% for those observables where the track reconstruction systematic is large (N_{ch}, $\sum p_{\perp}$, Beamthrust). For all other observables the systematic uncertainties rarely exceed 5% and are typically of the order of 2%.

12.6. Closure tests

To convince oneself that the correction strategy is working properly, closure tests are performed by unfolding reconstructed distributions obtained from a Monte-Carlo sample with pile-up. The smearing matrix and the priors are constructed from Monte-Carlo samples that were produced using the same Monte-Carlo generator. The closure test is considered passed if the unfolded distribution and the prior are compatible within errors.

Two Monte-Carlo simulations are available, one generated with Pythia8 and one with Sherpa in both channels of this analysis. In addition, both were generated once with an inclusion of pile-up interactions and once without. The samples without additional pile-up interactions have significantly more statistics (1.6 million events) while the samples with pile-up only contain about 500 thousand events.

Two different kinds of such closure test are presented in the following. The first method is similar to the correction strategy when unfolding data. The second method is performed as cross-check:

1. Unfold pile-up corrected (Chapter 10) distributions, $c_i^{\mathrm{PU}} R_i$, constructed from MC sample A with pile-up and unfolding matrix, $\mathbf{U}$, calculated from the sample *without* pile-up corresponding to MC sample A.

2. To be unfolded distributions, $\vec{R}$ (see equation (12.9)), constructed from MC sample A with pile-up and unfolding matrix, $\mathbf{U}$, calculated from the same sample A with pile-up

It should be noted that the truth distributions obtained from MC sample A with and without pile-up are identical.

A note about the selection of plots: The number of available closure-test plots is huge, since this analysis probes seven observables in five phase-space regions of $p_{\perp}(\mathrm{Z})$ in two channels, having two Monte-Carlo samples available. It was chosen to show only results for two observables, the charged particle multiplicity and transverse thrust in two of the $p_{\perp}(\mathrm{Z})$ phase-space regions for the muon channel only. The results for the electron channel are very similar. By choosing transverse thrust and N_{ch} the two observables are chosen shown that give the best and the worst (N_{ch}) closure of all observables studied. The remaining plots are included in the supporting note of the corresponding ATLAS analysis [118].

12.6.1. Unfolding test for pile-up corrected distributions

The test described here is very close to the strategy used when unfolding data. The smearing matrices are constructed from Monte-Carlo samples without pile-up, since prior to unfolding the to be unfolded distributions are corrected for pile-up using correction factors estimated as explained in Chapter 10. Further, the systematic uncertainties of the pile-up correction are propagated (Section 12.5) through the unfolding and included in the plots shown (Figure 12.7 and 12.8).

The closure is generally found to be depending on the observable, with almost perfect closure (when taking uncertainties into consideration) for the observables transverse thrust, minor, Spherocity and F-Parameter, i.e. those observables where the number of charged particles (track) does not enter the definition. On the other hand, there are a few low-multiplicity bins in N_{ch} where the non-closure amounts to 5%.

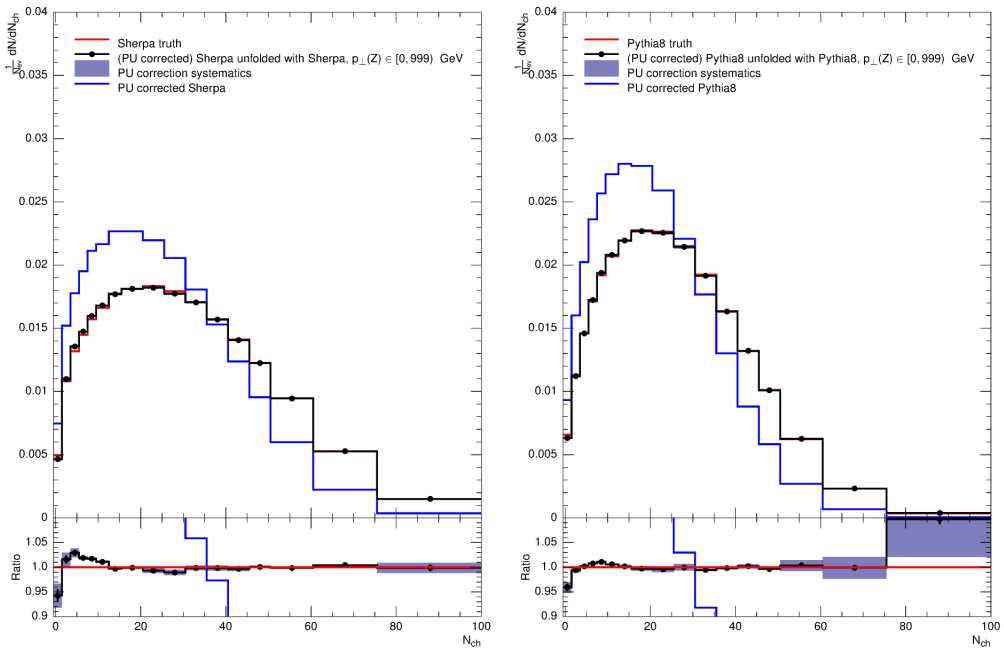

(a) Sherpa, $p_\perp(Z) \in [0, \infty)$ GeV **(b)** Pythia8, $p_\perp(Z) \in [0, \infty)$ GeV

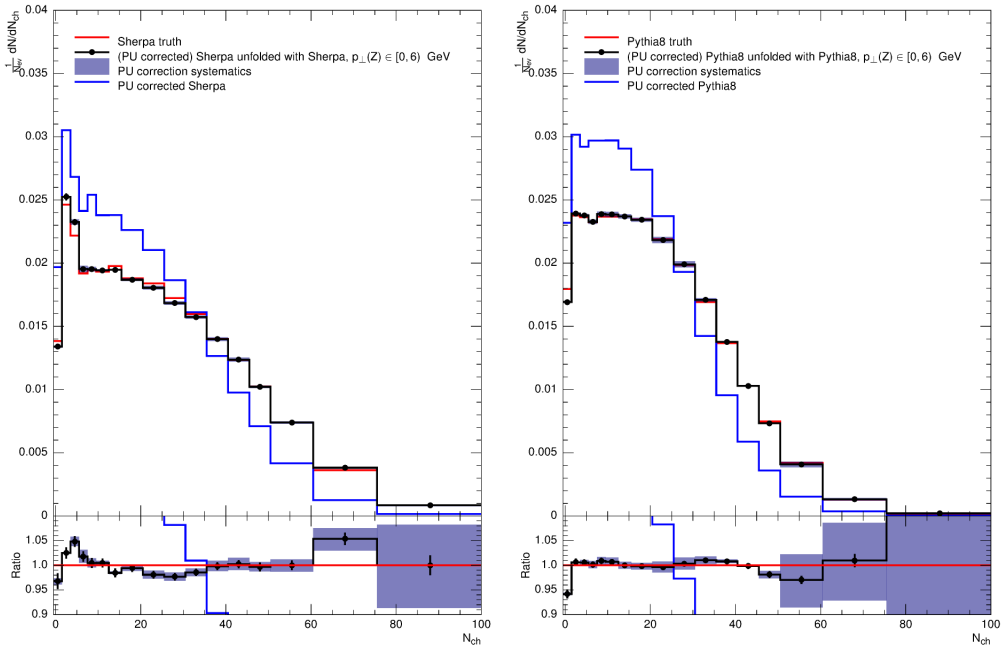

(c) Sherpa, $p_\perp(Z) \in [0, 6)$ GeV **(d)** Pythia8, $p_\perp(Z) \in [0, 6)$ GeV

Figure 12.7.: Unfolding closure tests with pile-up correction (Section 12.6.1) for transverse thrust. The smearing matrices are constructed from MC samples generated without pile-up. The to-be-unfolded distribution (blue) is obtained from the same MC generator but simulated with pile-up. Prior to unfolding, the latter is corrected for pile-up. The true distribution is shown in red, the unfolded distribution in black. Its error bars reflect the statistical uncertainty. The blue error bands show the propagated systematic uncertainty of the pile-up correction.

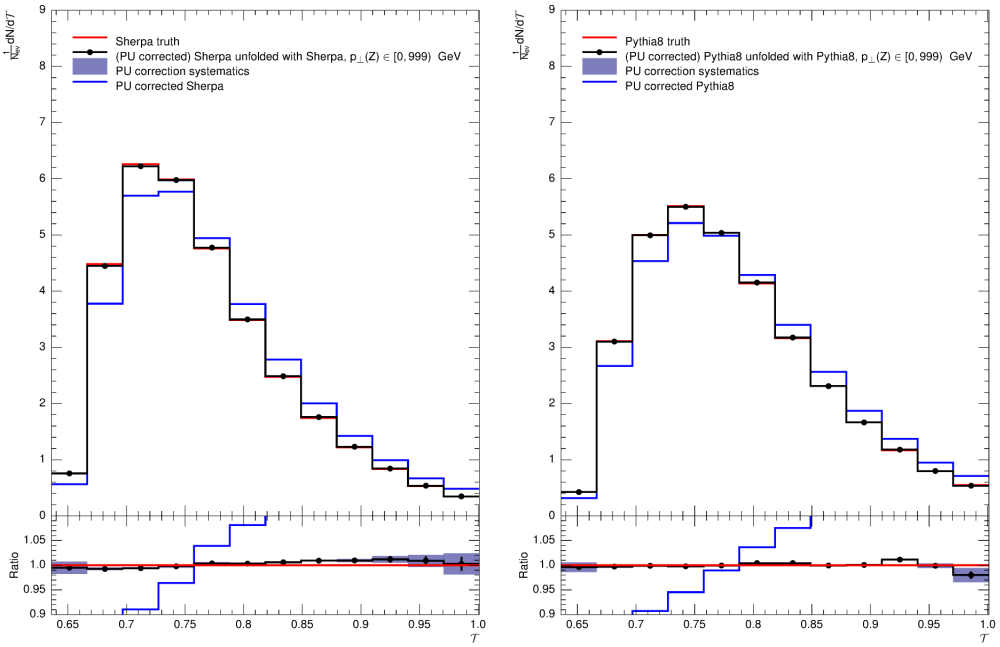

(a) Sherpa, $p_\perp(Z) \in [0, \infty)$ GeV

(b) Pythia8, $p_\perp(Z) \in [0, \infty)$ GeV

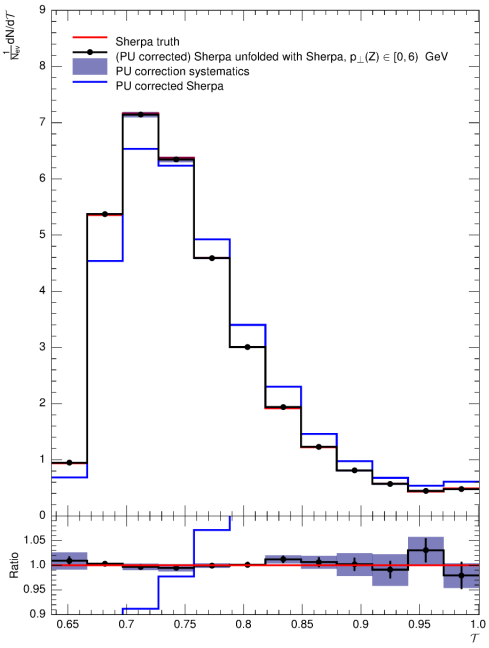

(c) Sherpa, $p_\perp(Z) \in [0, 6)$ GeV

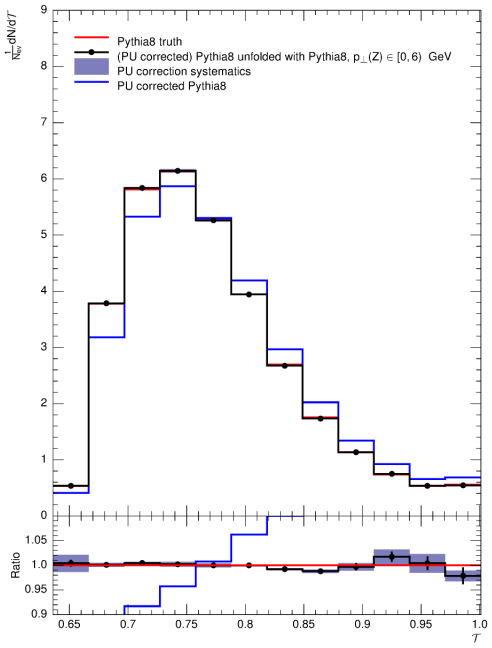

(d) Pythia8, $p_\perp(Z) \in [0, 6)$ GeV

Figure 12.8.: Unfolding closure tests with pile-up correction (Section 12.6.1) for transverse thrust. The smearing matrices are constructed from MC samples generated without pile-up. The to-be-unfolded distribution (blue) is obtained from the same MC generator but simulated with pile-up. Prior to unfolding, the latter is corrected for pile-up. The true distribution is shown in red, the unfolded distribution in black. Its error bars reflect the statistical uncertainty. The blue error bands show the propagated systematic uncertainty of the pile-up correction.

12.6.2. Unfolding test without pile-up correction

In this closure test, the smearing matrices are constructed from the Monte-Carlo samples that were generated with pile-up, such that a mapping exists of reconstructed, pile-up contaminated properties to hadron level (truth) information. Thus, pile-up is accounted for in the unfolding matrix. This test is meant as a cross-check to the Section 12.6.1.

Technically, the unfolding of distributions from pile-up sample A using an unfolding matrix from the same sample A further requires to split sample A into two independent samples of equal statistical power since otherwise a trivial cancellation in the unfolding matrix equation (12.7) occurs. A selection of such plots are shown in Figure 12.9 and Figure 12.10, demonstrating that the unfolding works as expected with the non-closure generally of the order of about 1% in the $p_{\perp}(\mathrm{Z})$ inclusive observables and up to 10% in the phase-space region $p_{\perp}(\mathrm{Z}) < 6$ GeV.

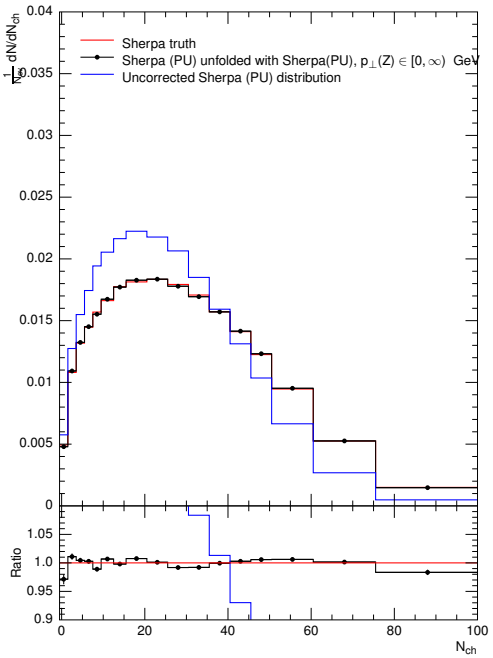

(a) Sherpa, $p_\perp(Z) \in [0, \infty)$ GeV

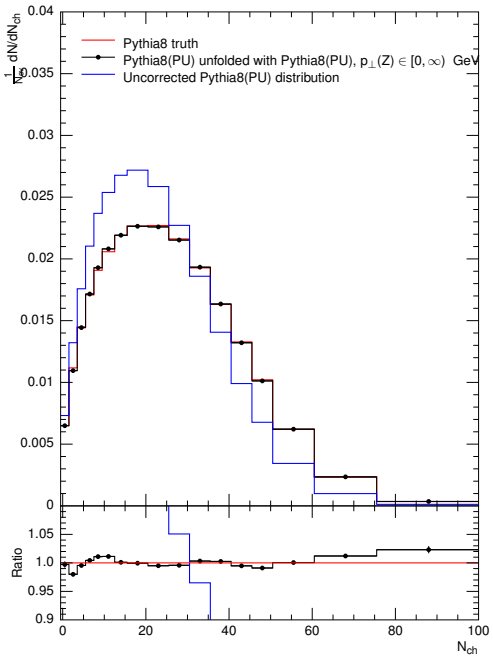

(b) Pythia8, $p_\perp(Z) \in [0, \infty)$ GeV

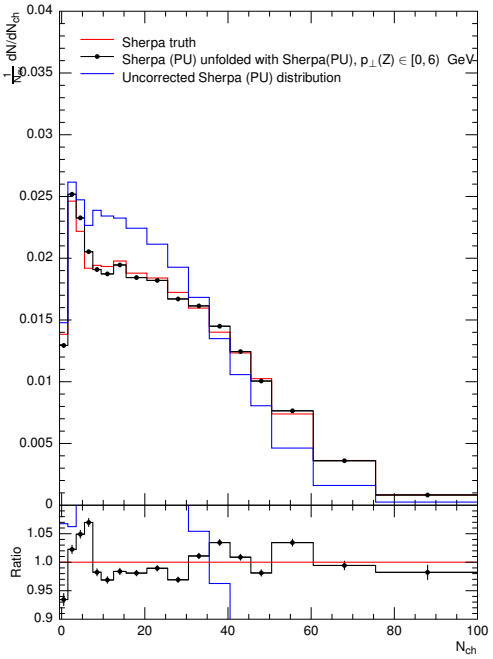

(c) Sherpa, $p_\perp(Z) \in [0, 6)$ GeV

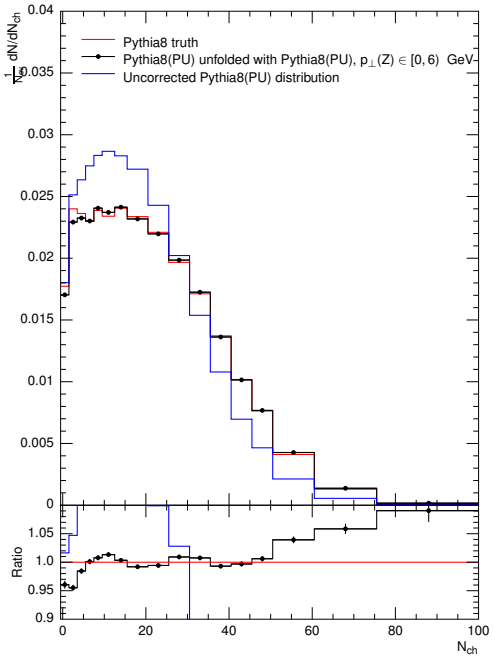

(d) Pythia8, $p_\perp(Z) \in [0, 6)$ GeV

Figure 12.9.: Unfolding closure tests (Section 12.6.2) without pile-up correction for the distribution of the number of charged particles. The uncorrected distribution is shown as blue line, the unfolded distribution is shown in black (errors are statistical) and the prior or true distribution is shown as red line.

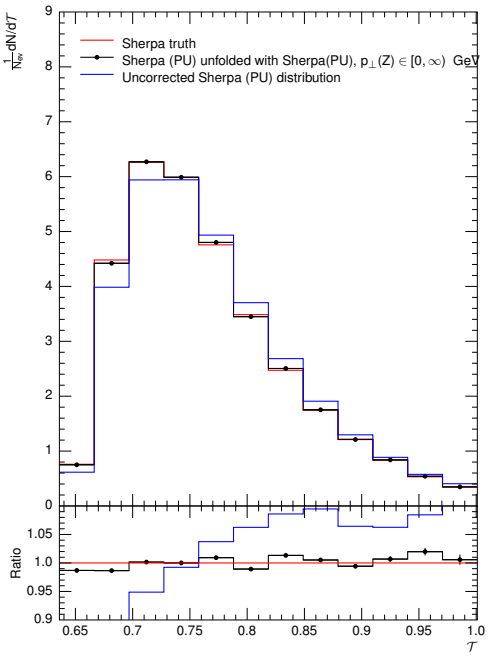

(a) Sherpa, $p_\perp(Z) \in [0, \infty)$ GeV

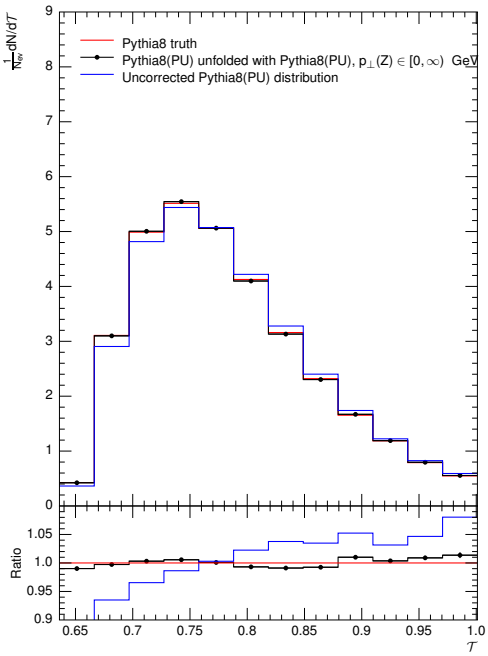

(b) Pythia8, $p_\perp(Z) \in [0, \infty)$ GeV

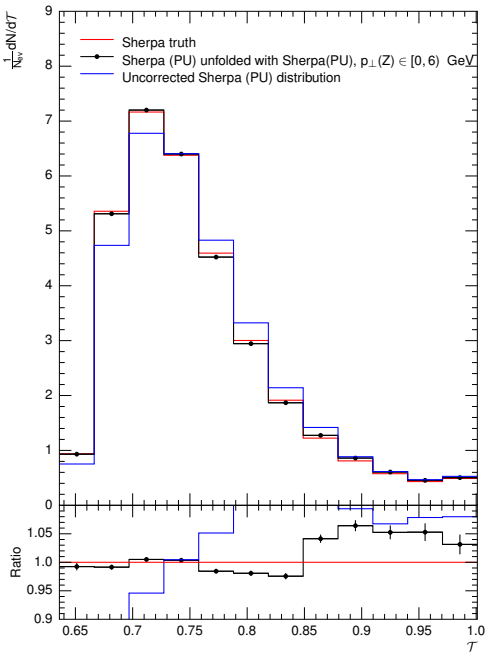

(c) Sherpa, $p_\perp(Z) \in [0, 6)$ GeV

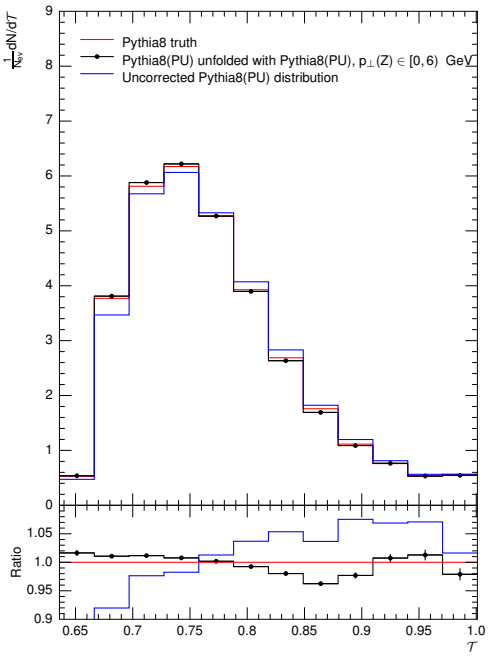

(d) Pythia8, $p_\perp(Z) \in [0, 6)$ GeV

Figure 12.10.: Unfolding closure tests (Section 12.6.2) without pile-up correction for transverse thrust. The uncorrected distribution is shown as blue line, the unfolded distribution is shown in black (errors are statistical) and the prior or true distribution is shown as red line.

12.6.3. Comparison of both methods to account for pile-up.

The correction method where pile-up is corrected and the one where pile-up is accounted for in the unfolding matrix can be considered successful for most bins of most observables. However, both appear to have a problem correcting the first bin of the distribution of charged particles ($N_{\mathrm{ch}} < 2$). However, the closure is generally better in the case of the unfolding using the MC samples without pile-up and pile-up correction of the to be unfolded distribution.

Figure 12.11 compares the result of both methods with the corresponding truth curve for N_{ch} and transverse thrust in the low $p_{\perp}(\mathrm{Z})$ phase-space region. For transverse thrust both MC samples yield almost perfect closure in the case of the pile-up correction when taking the uncertainties into consideration, while the other method yields bins with non-closure of up to 5%. A similar message can be read off the plots for N_{ch}, where the non-closure is smaller for the first method for the majority of bins.

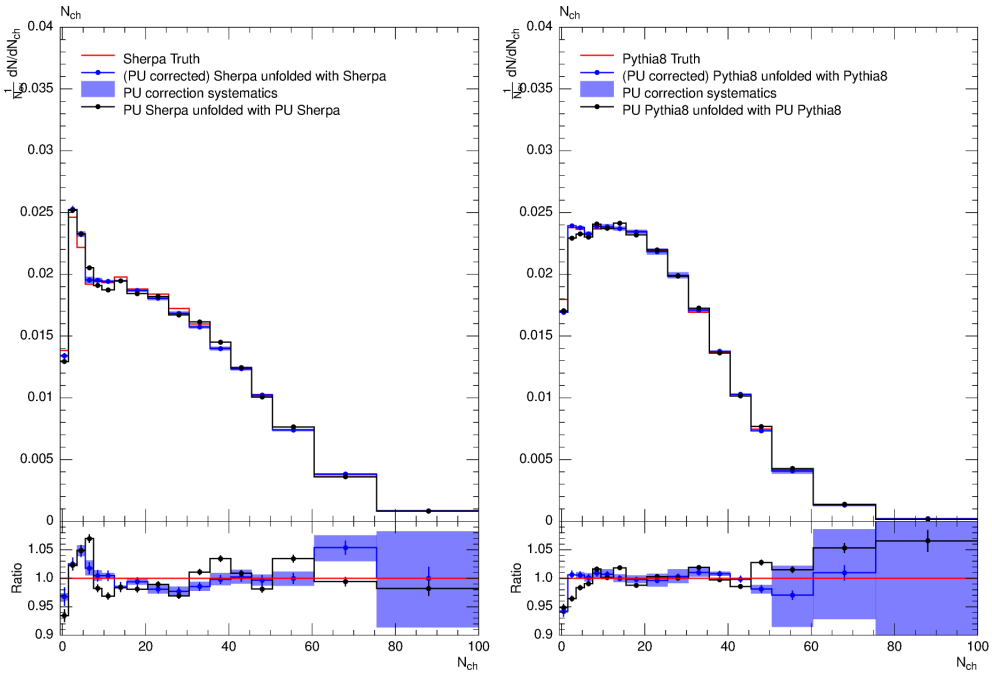

(a) N_{ch}

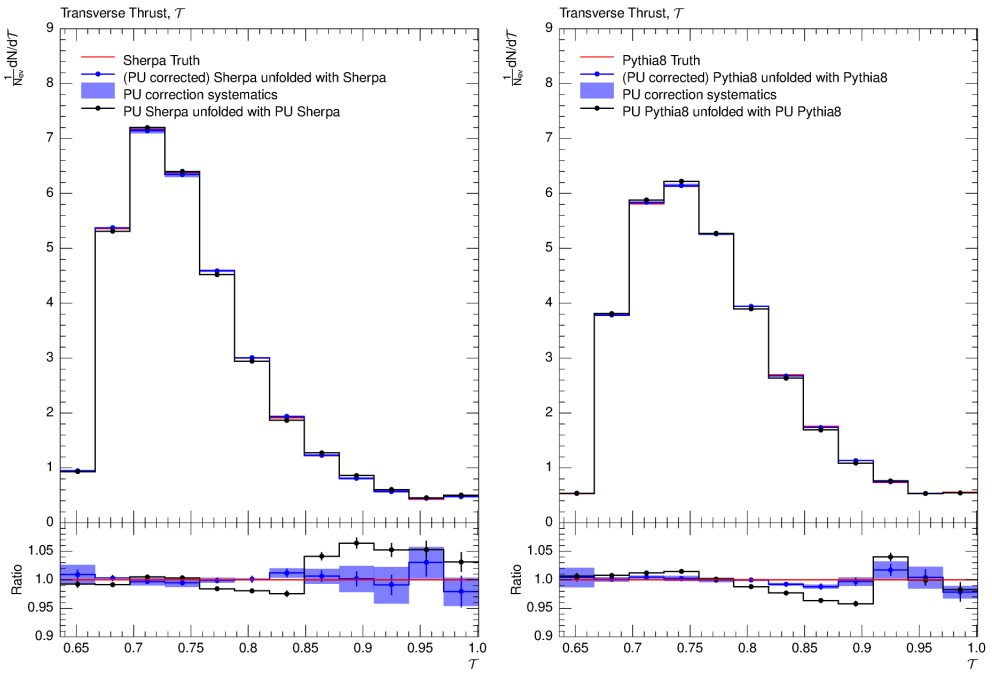

(b) Thrust

Figure 12.11.: Comparison of unfolding closure test methods. The result of the unfolding a pile-up corrected distribution is shown in blue (error bands show pile-up correction systematic) while the black line shows the result without pile-up correction. All error bars are statistical. Test using Sherpa samples are on the left hand side, the corresponding ones for Pythia8 on the right hand side. All plots are shown for $p_{\perp}(\mathrm{Z}) < 6$ GeV.

12.6.4. Unfolding closure tests using two Monte-Carlo samples

Since two Monte-Carlo samples are available, the closure tests when unfolding distributions corrected for pile-up with unfolding matrices built from samples without pile-up can be repeated, thus accounting also for any residual prior dependency and assignment of an unfolding model error which can be added in quadrature to the pile-up correction systematic (Section 12.2.1). By doing so, the remaining non-closure between the truth curve and the unfolded distribution and its uncertainties shrinks to less than 2% for most bins of most observables. Only the lowest multiplicity bin of N_{ch} when performing the closure test for Pythia8 retains a non-closure of 5% (Figure 12.12).

The closure of transverse thrust (Figure 12.13) can be considered perfect for all phase-space regions of $p_{\perp}(\mathrm{Z})$. Similarly good results are obtained for all other observables, i.e. Spherocity, F-Parameter, Beamthrust, $\sum p_{\perp}$ and Minor (not shown).

This strategy is later applied when unfolding data.

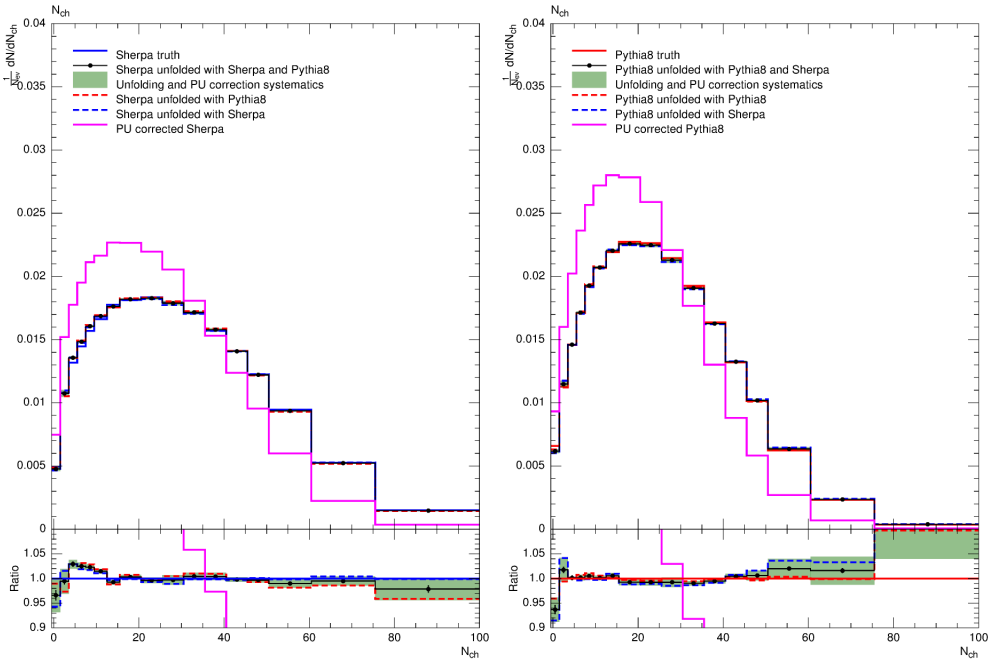

(a) N_{ch}, $p_{\perp}(Z) \in [0, \infty)$ GeV

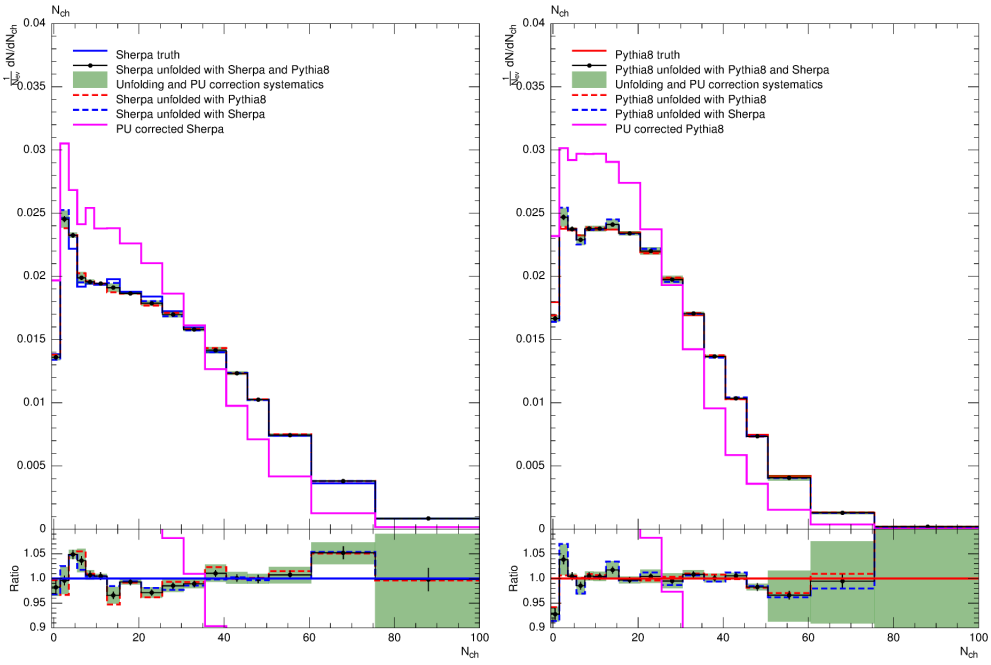

(b) N_{ch}, $p_{\perp}(Z) \in [0, 6)$ GeV

Figure 12.12.: Unfolding closure tests for the distribution of the number of tracks. The smearing matrices are constructed from MC samples generated without pile-up. The to-be-unfolded distribution (solid magenta line) is obtained from the same MC generator but simulated with pile-up. Prior to unfolding, the latter is corrected for pile-up. The central result of the unfolding is the mean obtained from the unfolded distributions using the two priors available (dashed lines). The spread of the two is identical to the asymmetric unfolding model error. The systematic uncertainty of the pile-up correction is added in quadrature to the latter (green band). The true distribution is shown as solid line (blue in case of Sherpa and red in case of Pythia8).

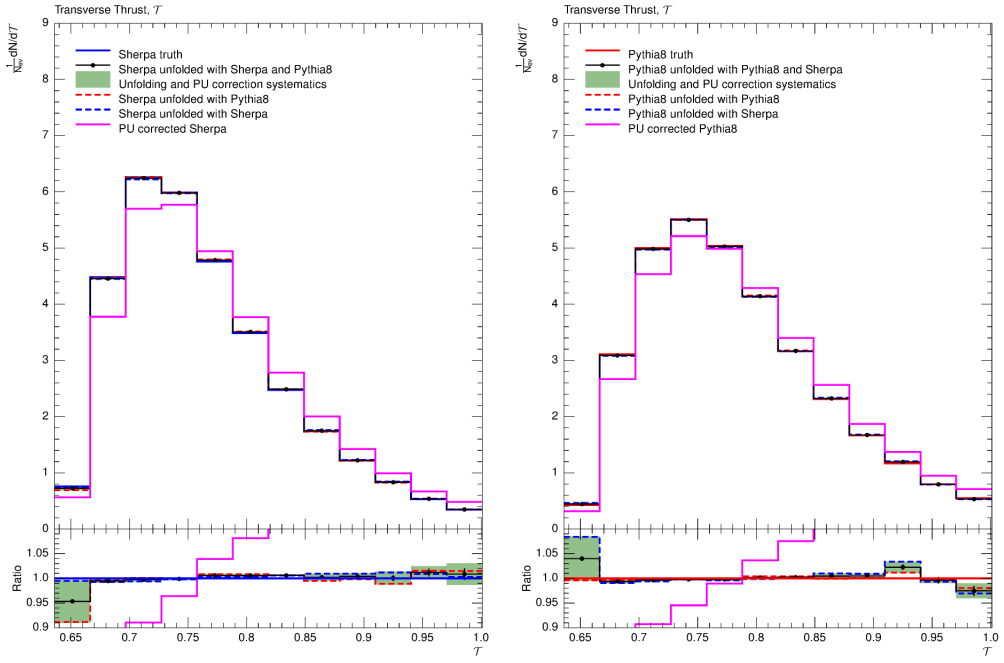

(a) Sherpa, $p_\perp(Z) \in [0, \infty)$ GeV

(b) Pythia8, $p_\perp(Z) \in [0, \infty)$ GeV

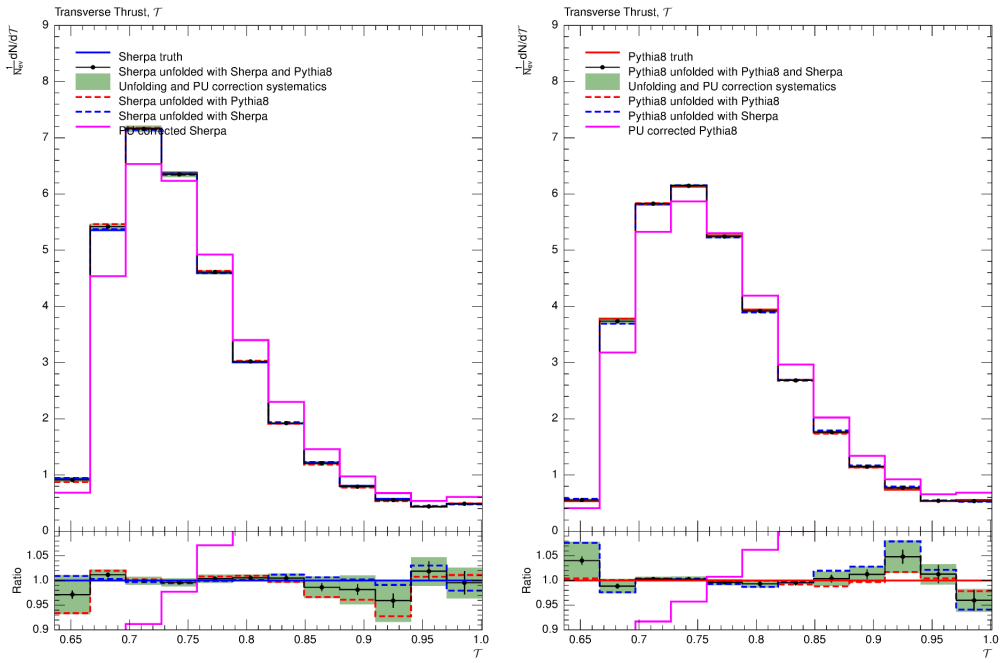

(c) Sherpa, $p_\perp(Z) \in [0, 6)$ GeV

(d) Pythia8, $p_\perp(Z) \in [0, 6)$ GeV

Figure 12.13.: Unfolding closure tests for Thrust distributions. The smearing matrices are constructed from MC samples generated without pile-up. The to-be-unfolded distribution (solid magenta line) is obtained from the same MC generator but simulated with pile-up. Prior to unfolding, the latter is corrected for pile-up. The central result of the unfolding is the mean obtained from the unfolded distributions using the two priors available (dashed lines). The spread of the two is identical to the asymmetric unfolding model error. The systematic uncertainty of the pile-up correction is added in quadrature to the latter (green band). The true distribution is shown as solid line (blue in case of Sherpa and red in case of Pythia8).

12.7. Unfolding data and results

This section contains the final unfolded results of N_{trk} and transverse thrust of both lepton channels in all $p_{\perp}(\text{Z})$ phase-space regions, including a break-down of the systematic uncertainties. All other observables can be found in the appendix (Section C.2) as are the data tables (Section D).

The reconstructed data distributions are corrected for pile-up (Chapter 10) and QCD background (Chapter 11) before they are unfolded.

The smearing matrices and initial priors are constructed from the Monte-Carlo samples without pile-up. All data distributions are unfolded using both Monte-Carlo samples. The number of iterations performed in the unfolding was determined by `Imagiro` automatically.

In Figure 12.14 the unfolded data distributions of all $p_{\perp}(\text{Z})$ phase-space regions of some of the event shapes measured in the electron-channel analysis are overlaid. These figures show that as $p_{\perp}(\text{Z})$ rises, i.e. as recoiling jets emerge, the number of particles increases as well, as do $\sum p_{\perp}$ and Beamthrust. The distributions of transverse thrust have been measured with the best precision (in terms of total uncertainties) and should therefore be well suited for the improvement of underlying event models.

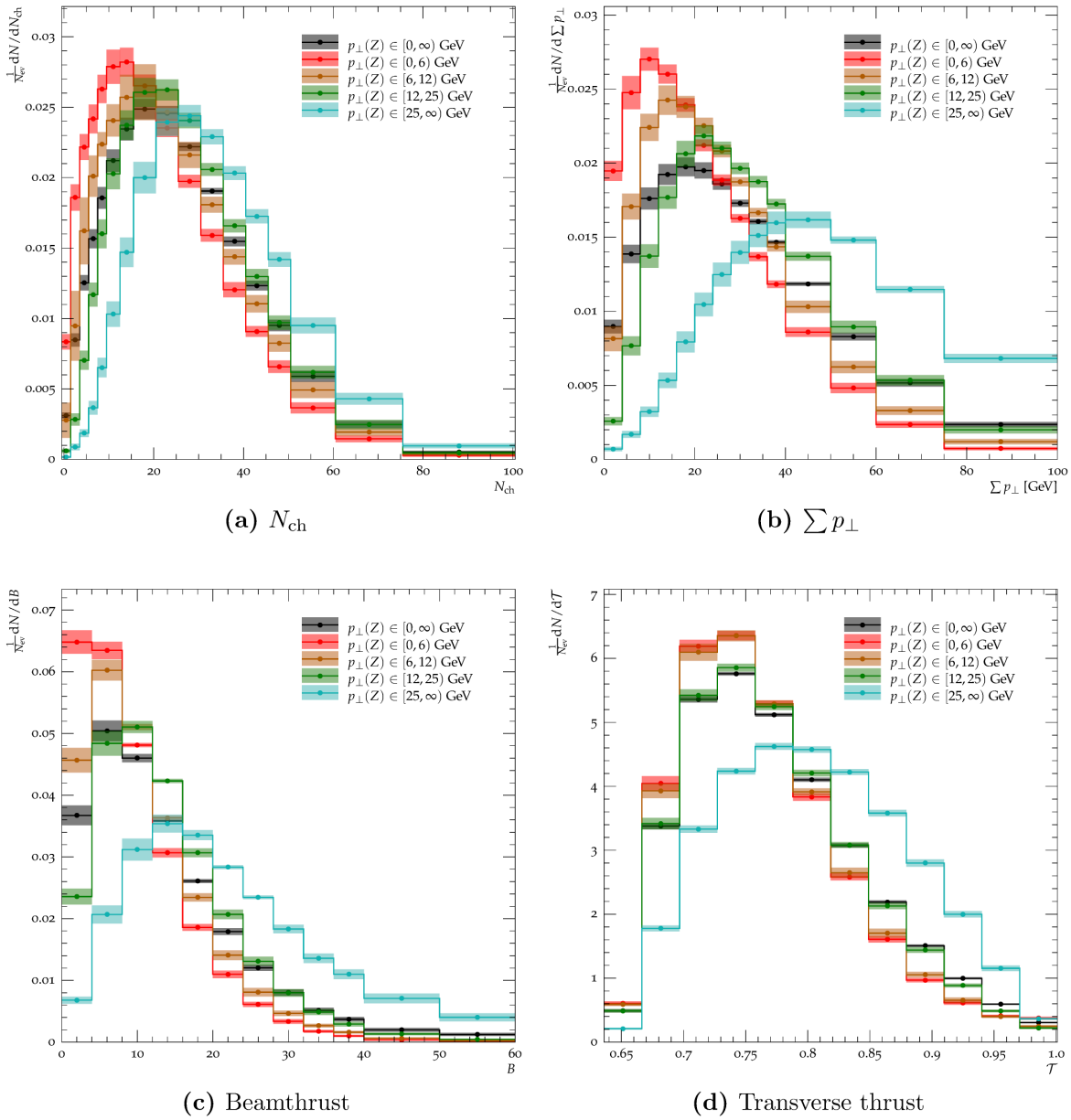

(a) N_{ch} **(b)** $\sum p_\perp$

(c) Beamthrust **(d)** Transverse thrust

Figure 12.14.: Comparison of unfolded electron channel data distributions for all analysed $p_\perp$(Z) phase-space regions showing the preference of higher values of transverse thrust in combination with more event activity in terms of the number of particles as well as their hardness being produced as a recoiling system evolves with increasing $p_\perp$(Z). The corresponding distributions of the muon channel are very similar. The bands show the quadratic sum of the total systematic and statistical errors.

12.8. Comparison of unfolded data with Monte-Carlo

The following figures, consecutively ordered by $p_\perp(\mathrm{Z})$, are arranged such that each figure contains four plots related to the same observable and $p_\perp(\mathrm{Z})$ phase-space region (see also Table 12.3):

- unfolded distribution, electron channel
- break-down of systematic uncertainties, electron channel
- unfolded distribution, muon channel
- break-down of systematic uncertainties, muon channel

The comparison of the unfolded data distributions with the predictions obtained with Sherpa and Pythia8 show poor agreement for most bins of most observables, independent on the $p_\perp(\mathrm{Z})$ phase-space region, except for $p_\perp(\mathrm{Z}) > 25$ GeV. This is the phase-space region where the event-activity is less likely to originate from MPI activity but from the system recoiling from the Z-boson, i.e. jets. Thus the MPI modelling is less important in that phase-space region. It can further be stated that the predictions obtained with Pythia8 are typically closer to the measured distributions than the predictions obtained with Sherpa.

The disagreement of the predictions from both simulations with the unfolded data is tried to be improved in Chapter 13.

Observable	Pages
N_{ch}	232 — 236
$\sum p_\perp$	264 — 268
Beamthrust	269 — 273
Thrust	237 — 241
Minor	274 — 278
F-Parameter	279 — 283
Spherocity	284 — 288

Table 12.3.: Guide to figures of unfolded distributions.

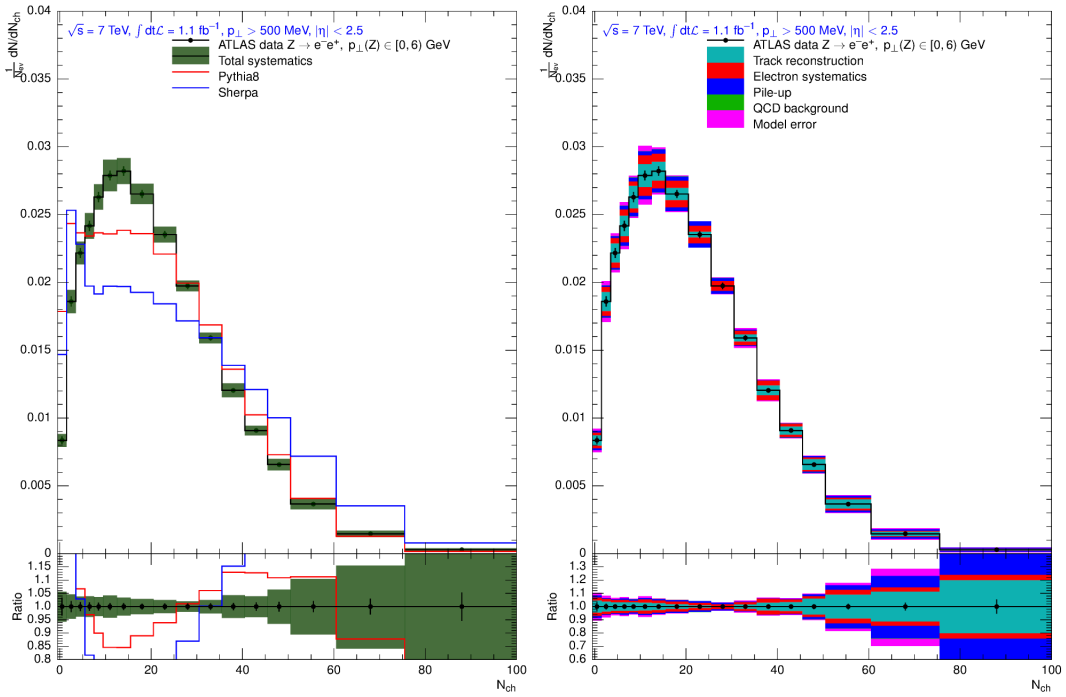

(a) N_{ch}, $p_\perp(\mathrm{Z}) < 6$ GeV, electron channel

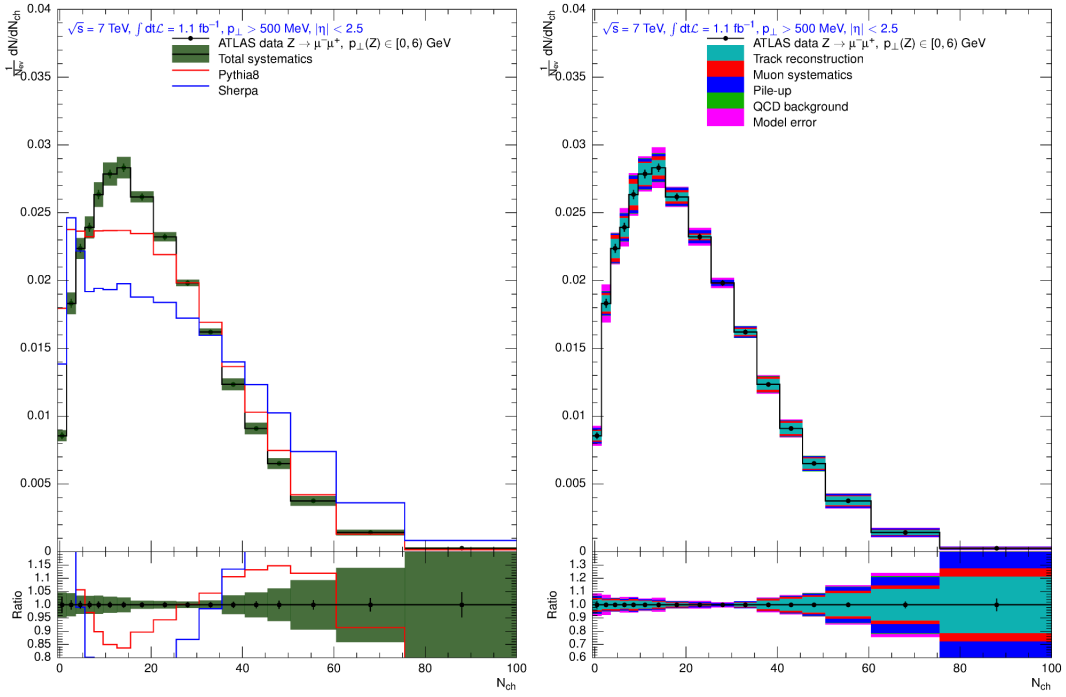

(b) N_{ch}, $p_\perp(\mathrm{Z}) < 6$ GeV, muon channel

Figure 12.15.: Left: Unfolded N_{ch} distribution with total systematic uncertainties (green band) and statistical uncertainties (black). Right: break-down of systematic uncertainties.

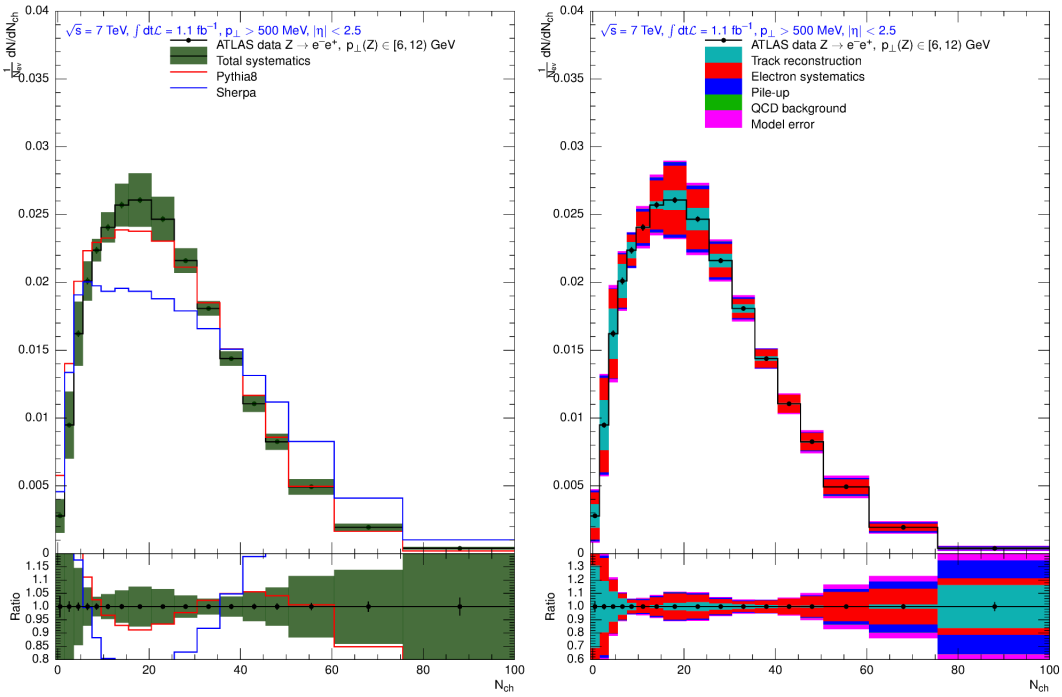

(a) N_{ch}, $p_\perp(\mathrm{Z}) \in [6, 12)$ GeV, electron channel

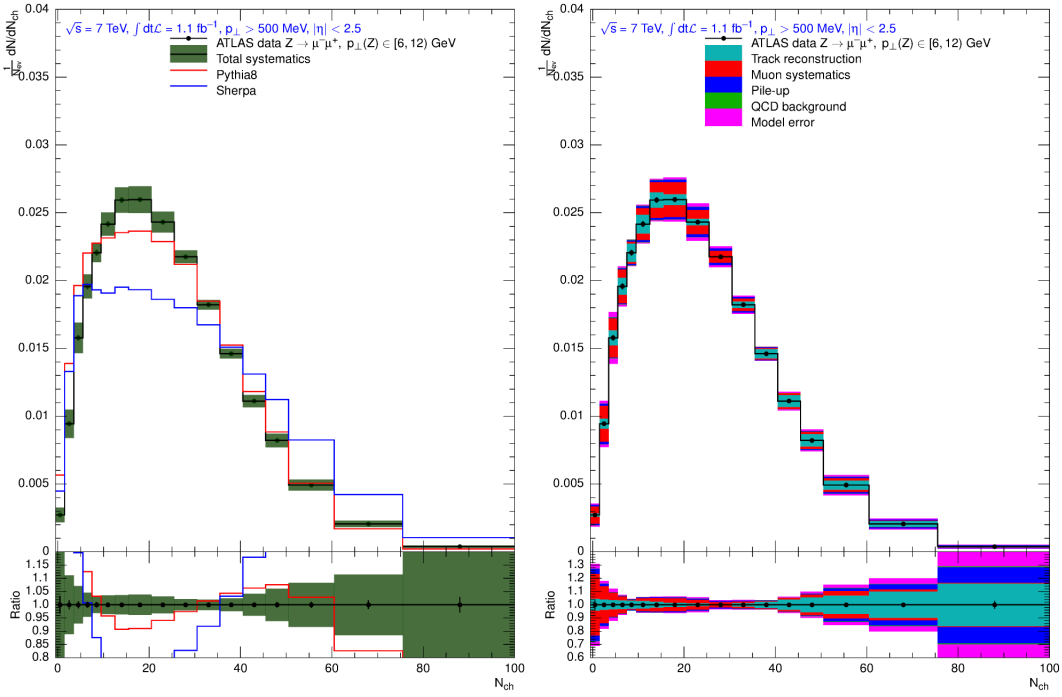

(b) N_{ch}, $p_\perp(\mathrm{Z}) \in [6, 12)$ GeV, muon channel

Figure 12.16.: Left: Unfolded N_{ch} distribution with total systematic uncertainties (green band) and statistical uncertainties (black). Right: break-down of systematic uncertainties.

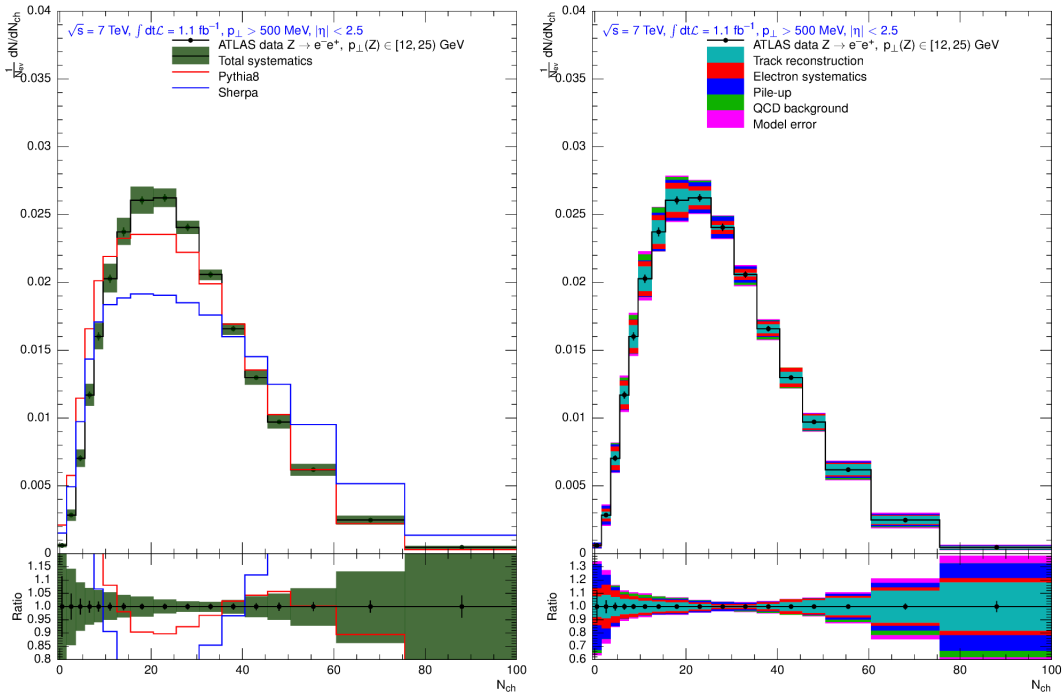

(a) N_{ch}, $p_{\perp}(\mathrm{Z}) \in [12, 25)$ GeV, electron channel

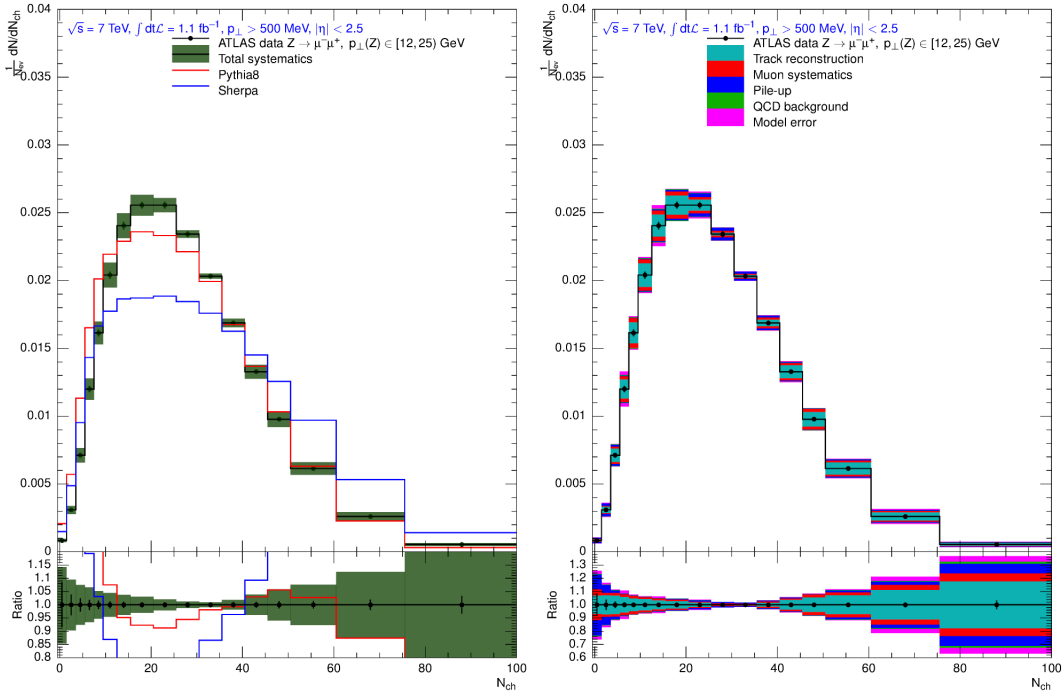

(b) N_{ch}, $p_{\perp}(\mathrm{Z}) \in [12, 25)$ GeV, muon channel

Figure 12.17.: Left: Unfolded N_{ch} distribution with total systematic uncertainties (green band) and statistical uncertainties (black). Right: break-down of systematic uncertainties.

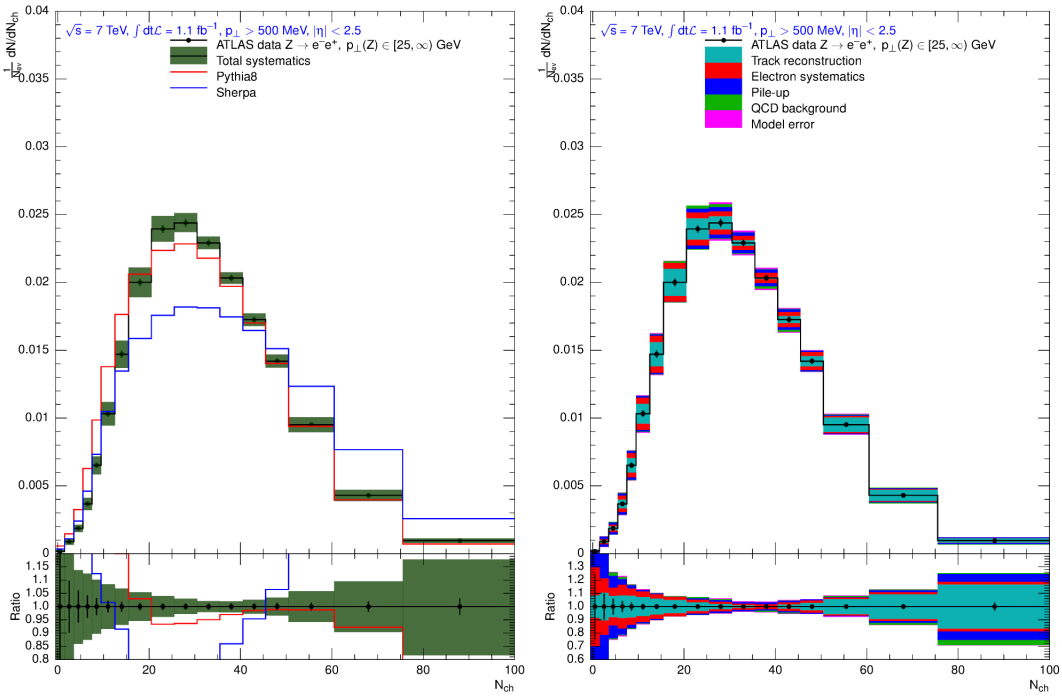

(a) N_{ch}, $p_\perp(\mathrm{Z}) > 25$ GeV, electron channel

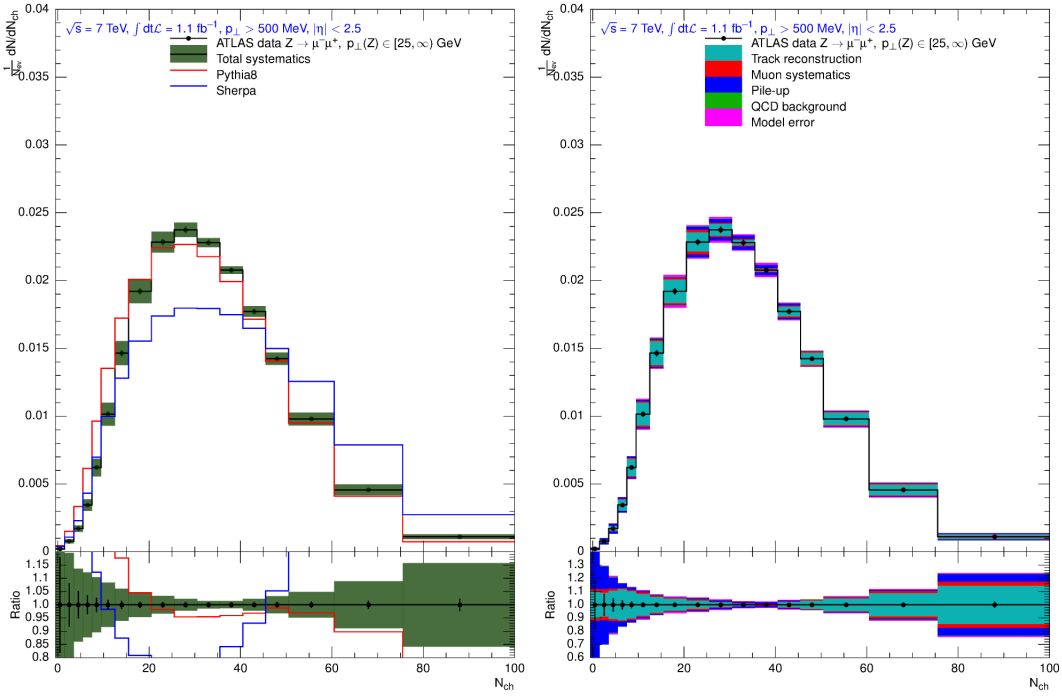

(b) N_{ch}, $p_\perp(\mathrm{Z}) > 25$ GeV, muon channel

Figure 12.18.: Left: Unfolded N_{ch} distribution with total systematic uncertainties (green band) and statistical uncertainties (black). Right: break-down of systematic uncertainties.

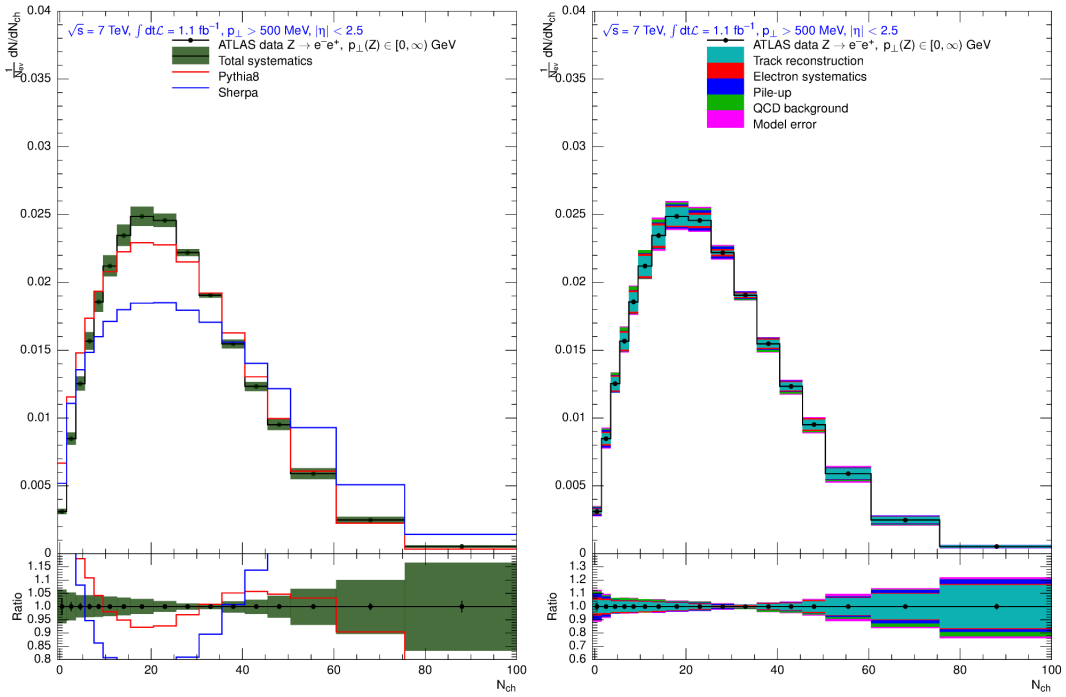

(a) N_{ch}, $p_{\perp}$(Z) inclusive electron channel

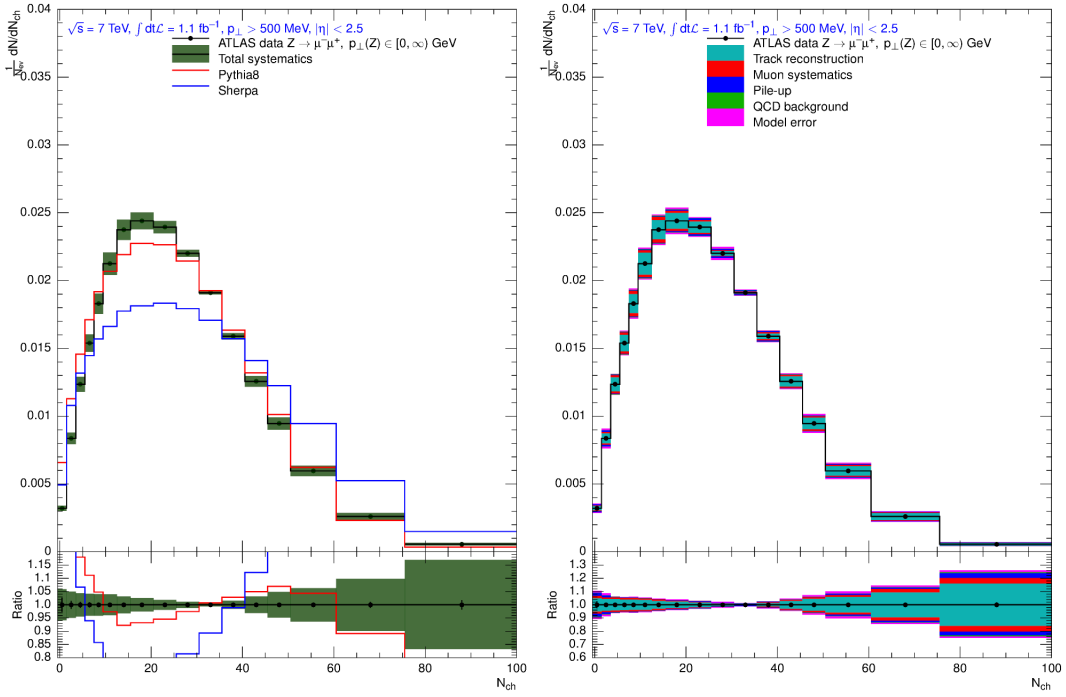

(b) N_{ch}, $p_{\perp}$(Z) inclusive, muon channel

Figure 12.19.: Left: Unfolded N_{ch} distribution with total systematic uncertainties (green band) and statistical uncertainties (black). Right: break-down of systematic uncertainties.

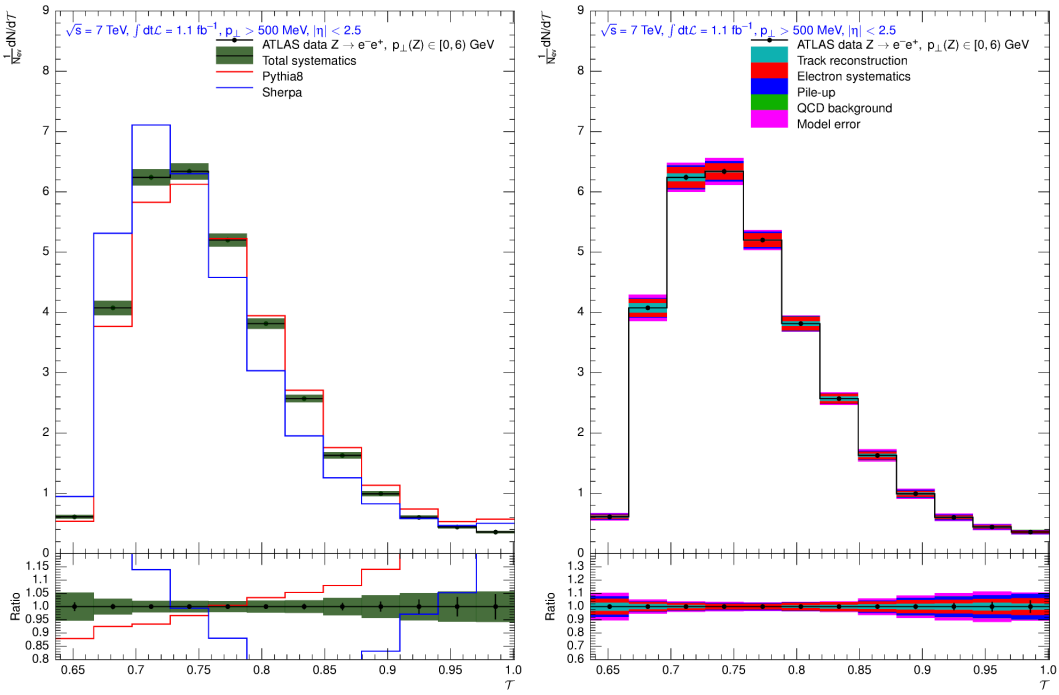

(a) Thrust, $p_\perp(\mathrm{Z}) < 6$ GeV, electron channel

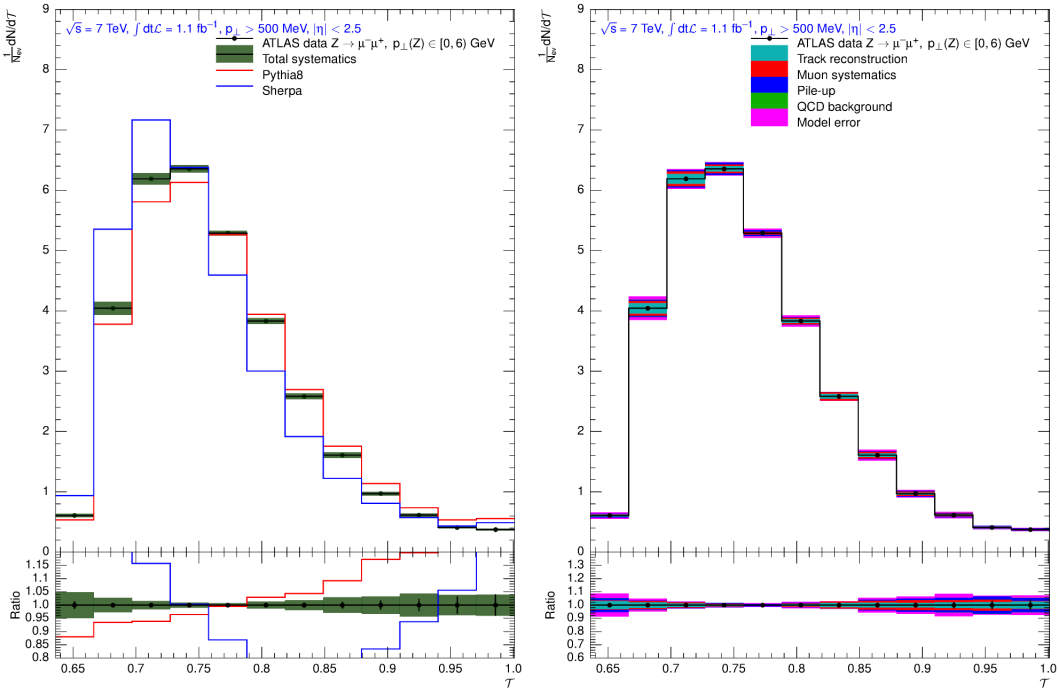

(b) Thrust, $p_\perp(\mathrm{Z}) < 6$ GeV, muon channel

Figure 12.20.: Left: Unfolded Thrust distribution with total systematic uncertainties (green band) and statistical uncertainties (black). Right: break-down of systematic uncertainties.

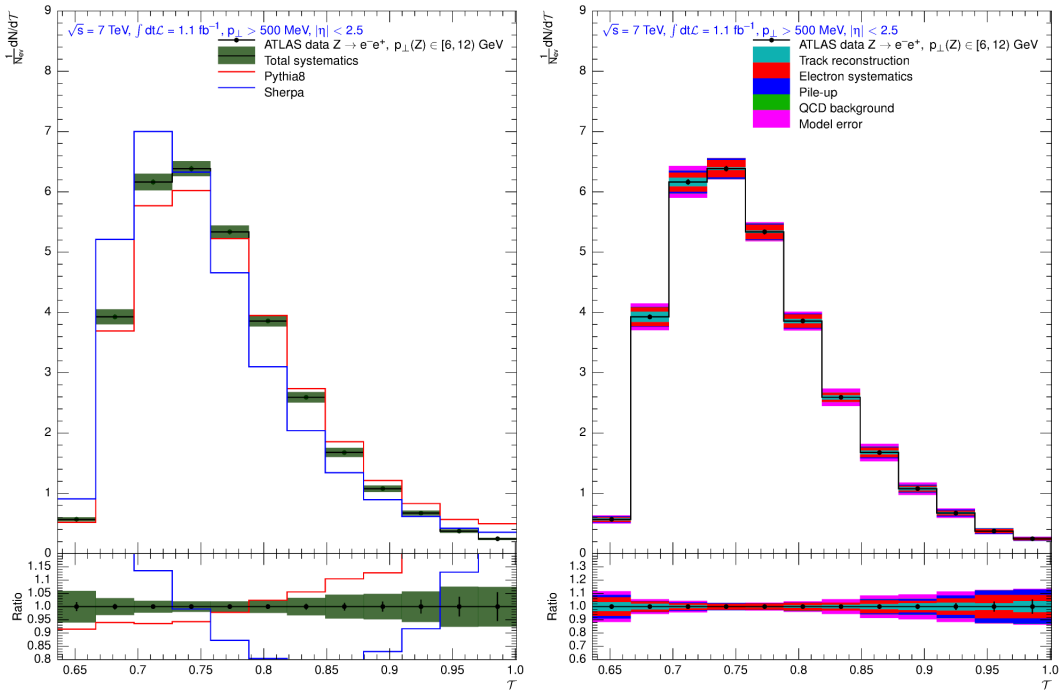

(a) Thrust, $p_\perp(\mathrm{Z}) \in [6, 12)$ GeV, electron channel

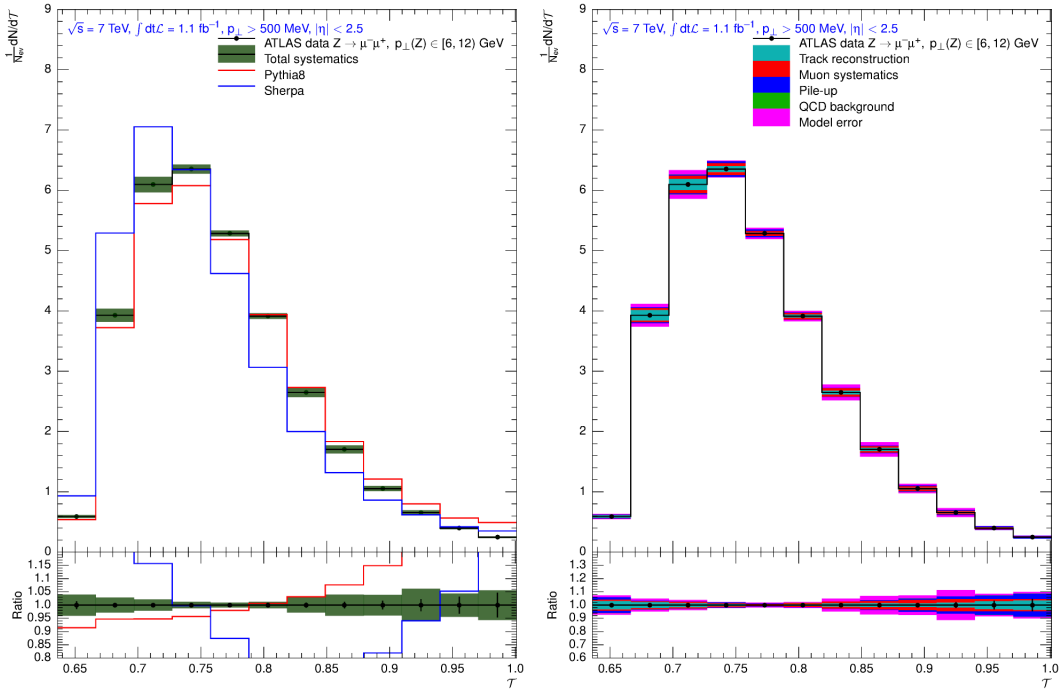

(b) Thrust, $p_\perp(\mathrm{Z}) \in [6, 12)$ GeV, muon channel

Figure 12.21.: Left: Unfolded Thrust distribution with total systematic uncertainties (green band) and statistical uncertainties (black). Right: break-down of systematic uncertainties.

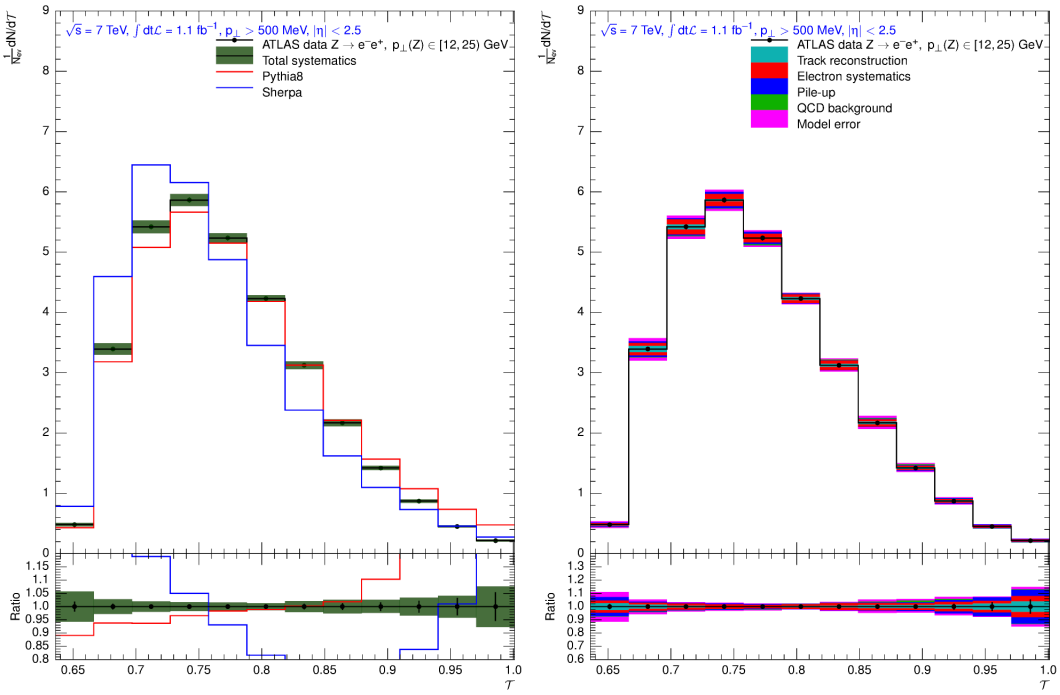

(a) Thrust, $p_\perp(\mathrm{Z}) \in [12, 25)$ GeV, electron channel

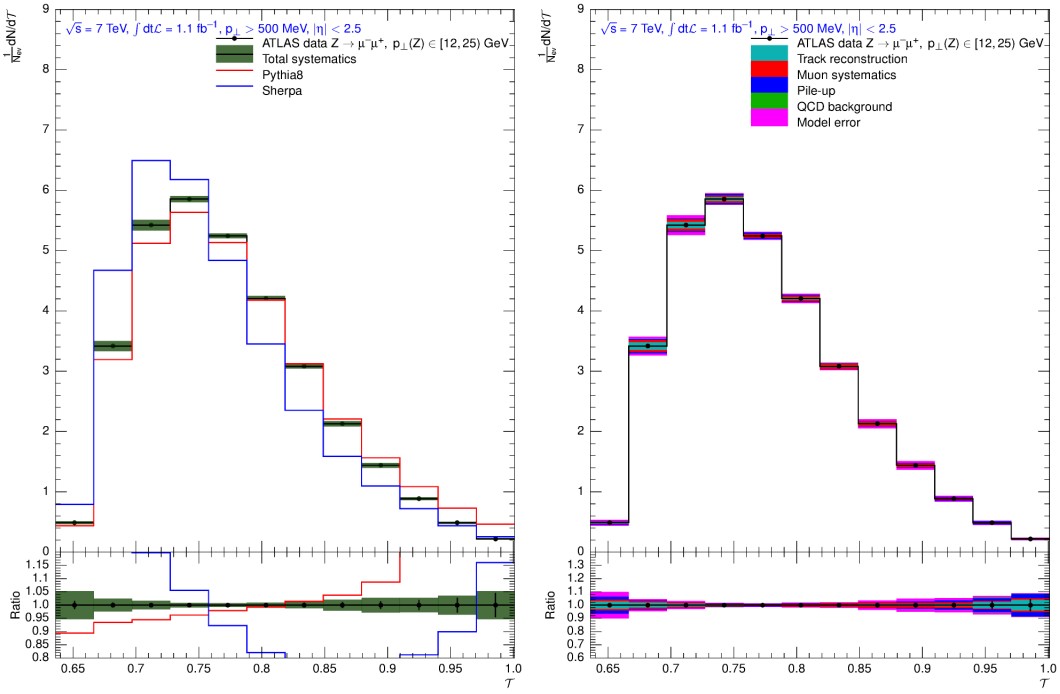

(b) Thrust, $p_\perp(\mathrm{Z}) \in [12, 25)$ GeV, muon channel

Figure 12.22.: Left: Unfolded Thrust distribution with total systematic uncertainties (green band) and statistical uncertainties (black). Right: break-down of systematic uncertainties.

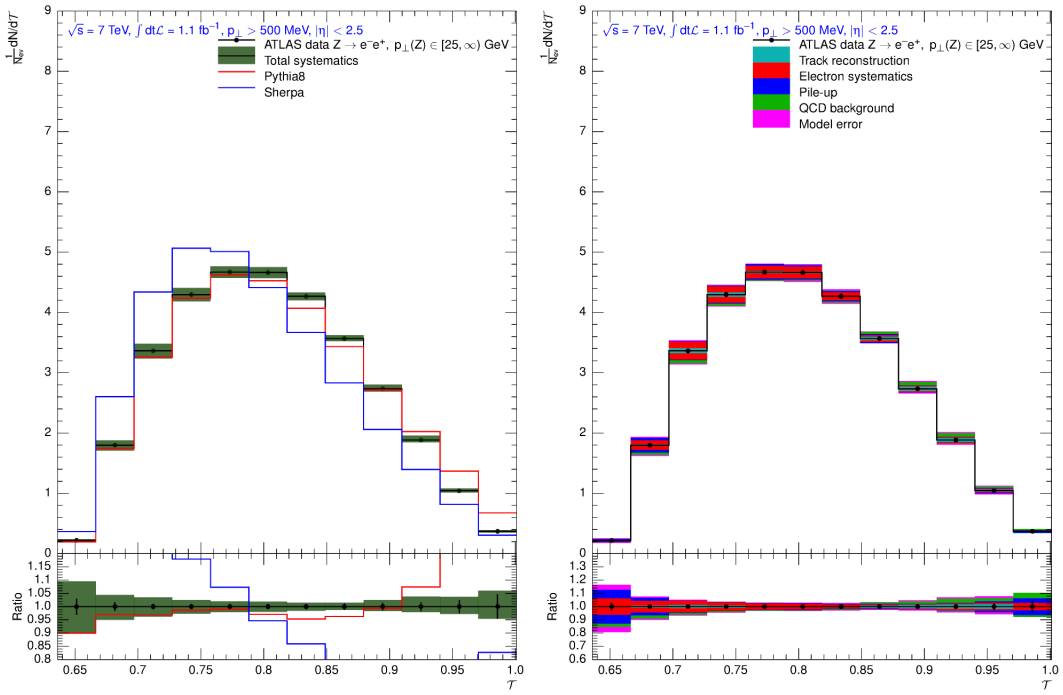

(a) Thrust, $p_\perp(\mathrm{Z}) > 25$ GeV, electron channel

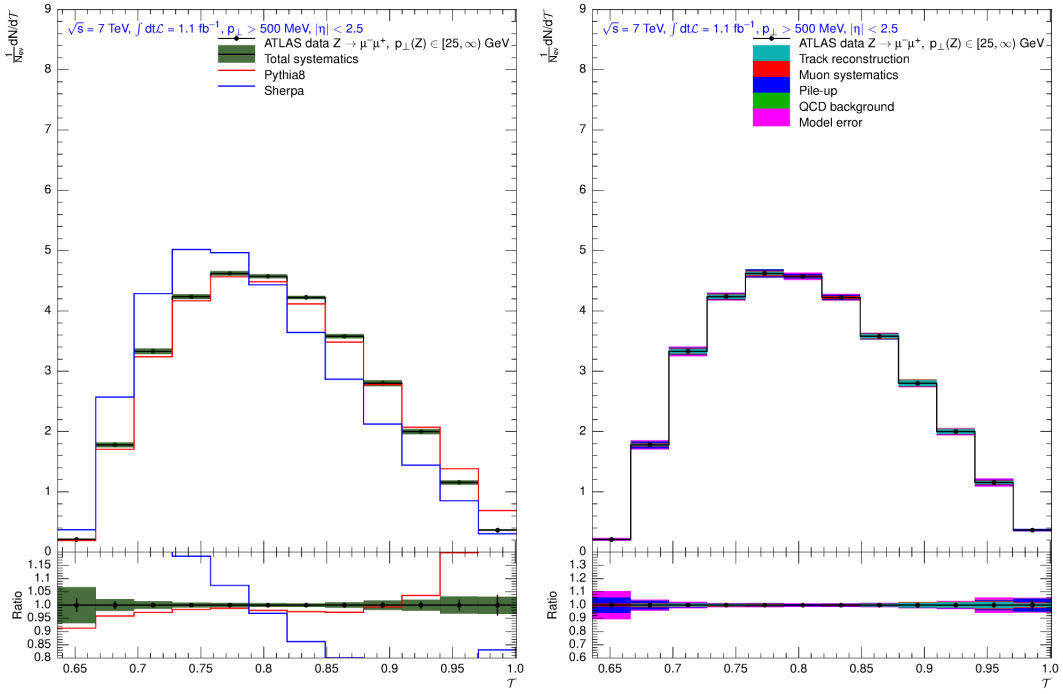

(b) Thrust, $p_\perp(\mathrm{Z}) > 25$ GeV, muon channel

Figure 12.23.: Left: Unfolded Thrust distribution with total systematic uncertainties (green band) and statistical uncertainties (black). Right: break-down of systematic uncertainties.

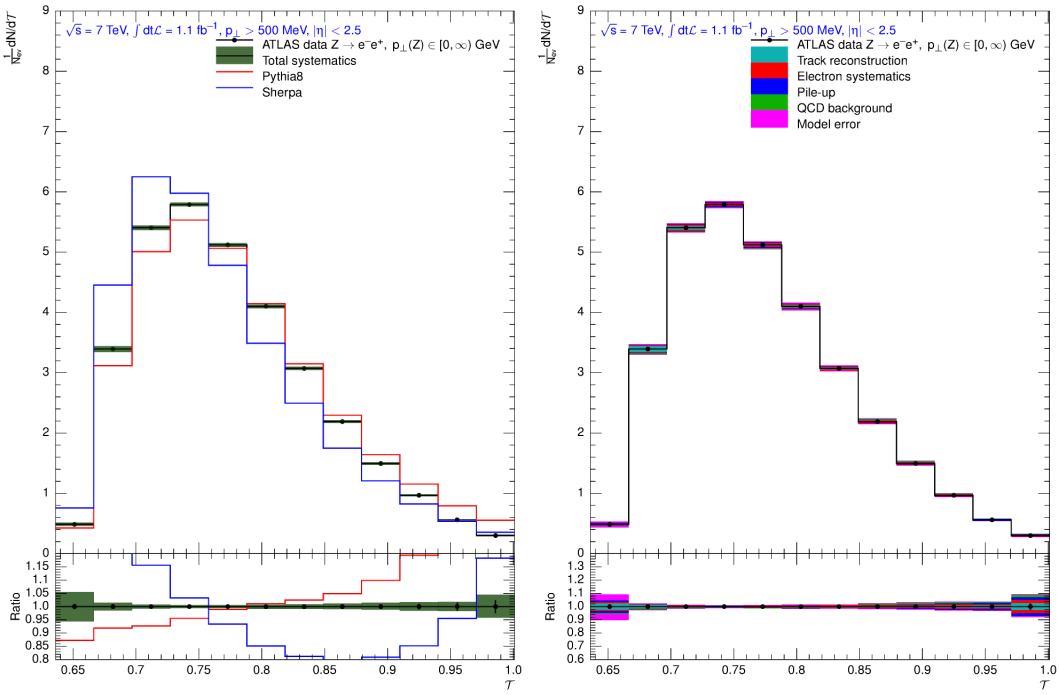

(a) Thrust, $p_\perp$(Z) inclusive electron channel

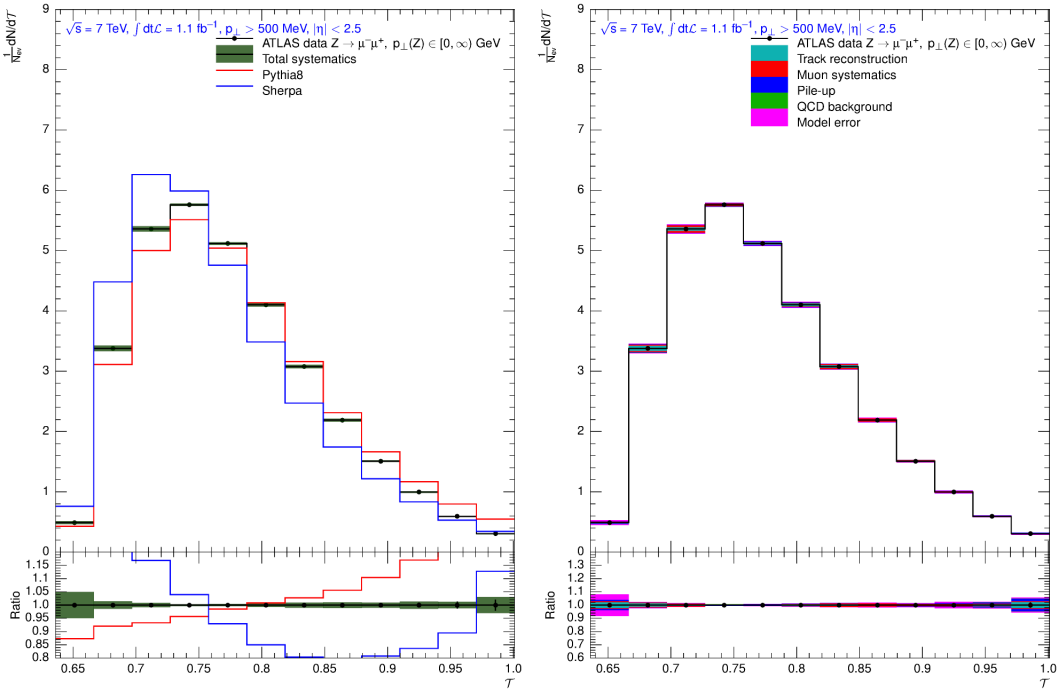

(b) Thrust, $p_\perp$(Z) inclusive, muon channel

Figure 12.24.: Left: Unfolded Thrust distribution with total systematic uncertainties (green band) and statistical uncertainties (black). Right: break-down of systematic uncertainties.

Chapter 13.

Tuning

In this chapter, it is attempted to use the unfolded data (Chapter 12) to improve the predictions obtained from the Monte-Carlo simulations of Sherpa and Pythia8 by adjusting the parameters of the underlying-event model. This technique is commonly referred to as "tuning".

Technically this is achieved by an implementation of this measurement as plug-in analysis in the framework `Rivet` [73] that analyses Monte-Carlo generator events in the common format `HepMC` [128]. The cuts on kinematic properties (η and $p_\perp$) for charged particles, leptons and Z-bosons in the `Rivet` implementation are identical to the truth-level cuts used in the unfolding of the data. Further, the same definition of leptons is used (i.e. dressed leptons). The binning of output histograms in the `Rivet` implementation is identical to that of the unfolded distributions, thus allowing for straight-forward comparison of data and Monte-Carlo predictions as well as the construction of a goodness-of-fit measure between data and MC.

The parameter space of the underlying-event model probed is four-dimensional in both Monte-Carlo programs. Instead of iteratively setting parameters, $\vec{p}$, and rerunning the generator to achieve improved agreement between data and MC, the Monte-Carlo generator response of each bin, b, of each observable is parametrised by means of cubic polynomials using the tool `Professor` [115], yielding a fast analytical pseudo-generator response $f_b(\vec{p})$. Let R_b be the value of a certain bin b and Δ_b the corresponding total uncertainty of an observable of the unfolded data, then a heuristic χ^2 measure can be constructed:

$$\chi^2(\vec{p}) = \sum_{b\in\mathcal{O}} w_b \frac{[f_b(\vec{p}) - R_b]^2}{\Delta_b^2} \tag{13.1}$$

where the sum runs over all bins of all observables one wishes to include in the tuning. The expression in equation (13.1) is numerically minimised yielding an optimal parameter point $\vec{p}_{\text{tune}}$ for the description of observables, $\mathcal{O}$. The factors w_b are user-steerable weights to bias this optimisation, which is needed to force the output to describe certain observables (or parts of it) better than others in case of imperfect models.

Common to both generators, Pythia8 and Sherpa, are implementations of the Sjöstrand-Zijl MPI model [86] with the differences already explained in Chapter 8. In the tunings described in the following, only parameters relevant to the MPI model are attempted to be optimised. Given the results shown in Chapter 12 it is tried to achieve a better description of observables measured in this analysis whilst trying to keep the description of recently published CMS data of a traditional underlying-event measurement intact [129], which was also performed in proton-proton collisions at $\sqrt{s} = 7$ TeV yielding Z-bosons decaying into a muon-antimuon-pair.

It should be stressed that the tuning attempts performed here only focus on the MPI part of the simulations. More thorough tunings are performed in a multi-step procedure, identifying consecutively tune-able parts of the generator. Typically, the first step is to tune the flavour and fragmentation sector of the simulations to hadron data measured with LEP. Afterwards, parameters related to the initial and final state radiation parton showers are tuned to jet-data. The last step, which is performed here, is to tune MPI parameters to underlying event data.

However, during the process of tuning it quickly became clear that trying to optimise MPI parameters only does not result in a set of parameter values able to consistently describe all data. It was hence tried to force the generator to agree with the measured event shapes in certain regions, using only the transverse thrust and charged multiplicity distributions at $p_\perp(\text{Z}) < 6$ GeV in the tuning attempts. Those tunings are labelled in the following way

- Force dijet: puts emphasis on high values of transverse thrust ($\mathcal{T} > 0.9$)
- Force spherical: puts emphasis on low values of transverse thrust ($\mathcal{T} < 0.7$)
- Force low N_{ch}: puts emphasis on low values of N_{ch} ($N_{\text{ch}} < 5$)

Observable $\mathcal{O}$	Bin-range	Weight w_b
Force dijet		
Transverse thrust, $p_\perp(\mathrm{Z}) < 6$ GeV	≤ 0.9	1
Transverse thrust, $p_\perp(\mathrm{Z}) < 6$ GeV	> 0.9	100
Force spherical		
Transverse thrust, $p_\perp(\mathrm{Z}) < 6$ GeV	≤ 0.7	100
Transverse thrust, $p_\perp(\mathrm{Z}) < 6$ GeV	> 0.7	1
Force low N_{ch}		
N_{ch}, $p_\perp(\mathrm{Z}) < 6$ GeV	≤ 5	500
N_{ch}, $p_\perp(\mathrm{Z}) < 6$ GeV	> 5	1
Force high N_{ch}		
N_{ch}, $p_\perp(\mathrm{Z}) < 6$ GeV	≤ 30	1
N_{ch}, $p_\perp(\mathrm{Z}) < 6$ GeV	> 30	100

Table 13.1.: Weights w_b of observables/bins used in the tuning attempts of Pythia8 and Sherpa. Both, the electron and the muon channel distributions were used in the tunings with the same weights applied to each.

- Force high N_{ch}: puts emphasis on high values of N_{ch} ($N_{\mathrm{ch}} > 30$)

A table with the weights, w_b (equation (13.1)), applied can be found in Table 13.1.

13.1. Tuning of Sherpa

Sherpa version 2.0 has been used for the production of input Monte-Carlo data. The MPI model is using a double-Gaussian matter distribution with parameters a_2 and β. Further, the cut-off parameter $p_{\perp,0}^{\mathrm{ref}}$ as well as the diffractive cross-section modifying parameter f_{ND} are tuned. A description of the parameters can be found in Section 8.5. The parameter-space sampled from is given in Table 13.2.

The tuning results are shown in Figure 13.1 and Table 13.2. As stated before, a common description of all observables deemed sensitive to the underlying event can not be reached. Moreover, a well-described charged multiplicity distribution comes with the price of

poorly described spherical and dijet-like events (extremal transverse thrust regions), as well as a severe undershot of the transverse momentum density (CMS data).

The transverse region $\sum p_\perp$ distribution is described reasonably well in the case of forcing a good description of dijet-like events (high transverse thrust) while breaking the agreement with N_{ch}. In the case of "Force dijet" the obtained best parameter value of β is very close to 1 meaning that the hadronic matter is almost completely inside the core region.

Forcing the spherical events to be described well (low values of transverse thrust) results in dramatically undershooting the dijet region (high transverse thrust). Further, the density of charged particles is well above the measurement performed by CMS. When looking at the corresponding tuned parameter values (Table 13.2) the extreme values of $p_{\perp,0}^{\text{ref}}$ and f_{ND} stand out. Taking equation (8.9) into consideration it is clear that the additional multiplicity density is indeed due to an largely increased number of MPI.

A good description of the onset of the charged multiplicity could not even closely be achieved with the parameters touched. This hints to a problem with the implementation, although it must be said that the phase-space for such events is an extremal one.

Putting it all together it can be stated that the Sjöstrand-Zijl model as it is implemented in Sherpa is unable to describe the measured event shapes. A mechanism that can shift the number of particles produced and their $p_\perp$ is likely to improve the situation at the cost of introducing yet another phenomenological model.

13.2. Tuning of Pythia8

It was tried to optimise the three parameters relevant for underlying event physics in the Pythia8 setup used for the author tune 4C [99] using the exponential matter overlap model discussed in Chapter 8 (Parameter P) as well as the colour-reconnection model (parameter CRC) and the cut-off parameter $p_{\perp,0}^{\text{ref}}$. The parameter sampling ranges as well as all tuning results can be found in Table 13.2.

It was found that in general the achieved agreement of data and Monte-Carlo prediction is of better quality with the implementation present in Pythia8 compared to the results obtained for Sherpa. It can generally be stated that the obtained values of the colour-

Parameter	min	max	Default (4C)	Force dijet	spherical	low N_{ch}	high N_{ch}
Sherpa— double Gaussian matter distribution							
a_2	0.25	1.0	0.76	0.71	0.79	0.57	0.84
β	0.25	1.0	0.58	0.98	0.29	0.22	0.66
$p_{\perp,0}^{\mathrm{ref}}$	2.0	4.0	2.44	2.26	3.79	2.11	2.07
f_{ND}	0.1	1.0	0.343	0.463	0.117	0.452	0.646
Pythia8— exponential matter overlap							
P	0.1	5.0	2.00	3.50	2.89	5.22	2.50
$p_{\perp,0}^{\mathrm{ref}}$	1.5	3.0	2.085	1.940	1.655	1.899	2.058
CRC	0.0	10.0	1.5	9.5	12.0	11.7	4.2

Table 13.2.: Parameter sampling boundaries, default parameters (in case of Pythia8, the values of the author tune 4C [99] are shown) and tuning results obtained with the weights shown in Table 13.1.

reconnection parameter are always significanlty higher than the value in the reference tune 4C, even exceeding the validity range quoted by the authors of Pythia8 ($CRC \in [0, 10]$).

The tuning results that yield a reasonable description of the event shapes and the CMS data (Figure 13.2) are "Force dijet" and "Force high N_{ch}". Interestingly, forcing a good description of dijet-like events (large values of transverse thrust) also yields in a good description of the spherical events (low transverse thrust values). It is likely that the colour-reconnection mechanism is responsible as it is designed as lever to shift the event properties of number and hardness of particles produced.

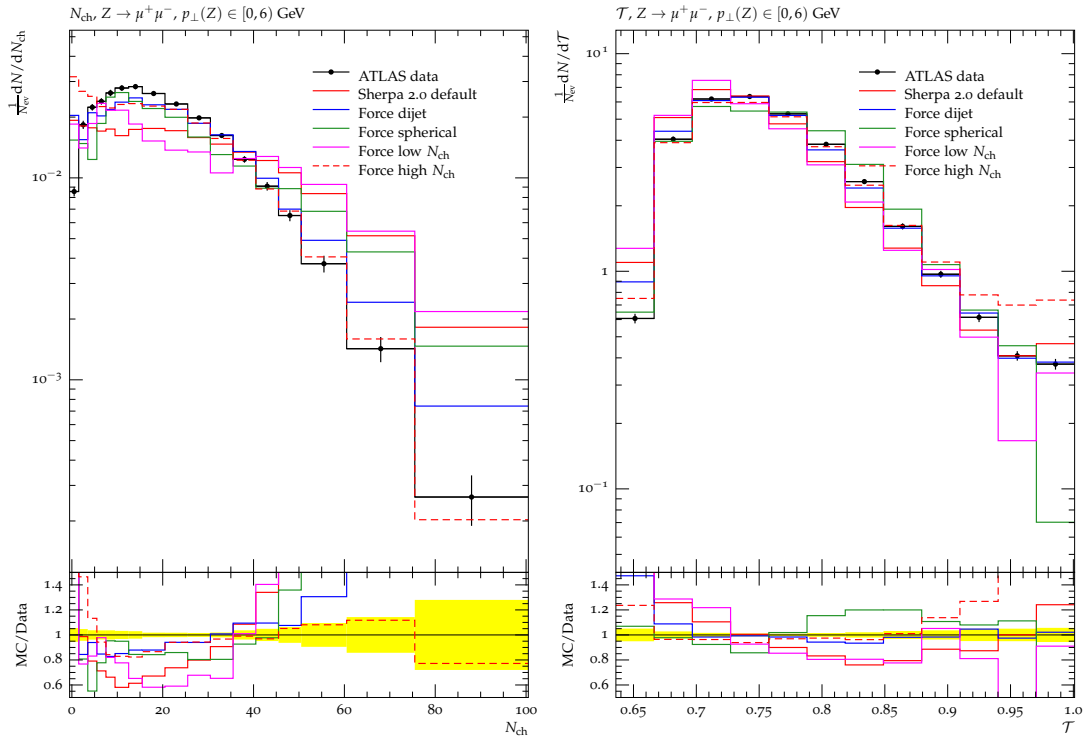

(a) Event shapes

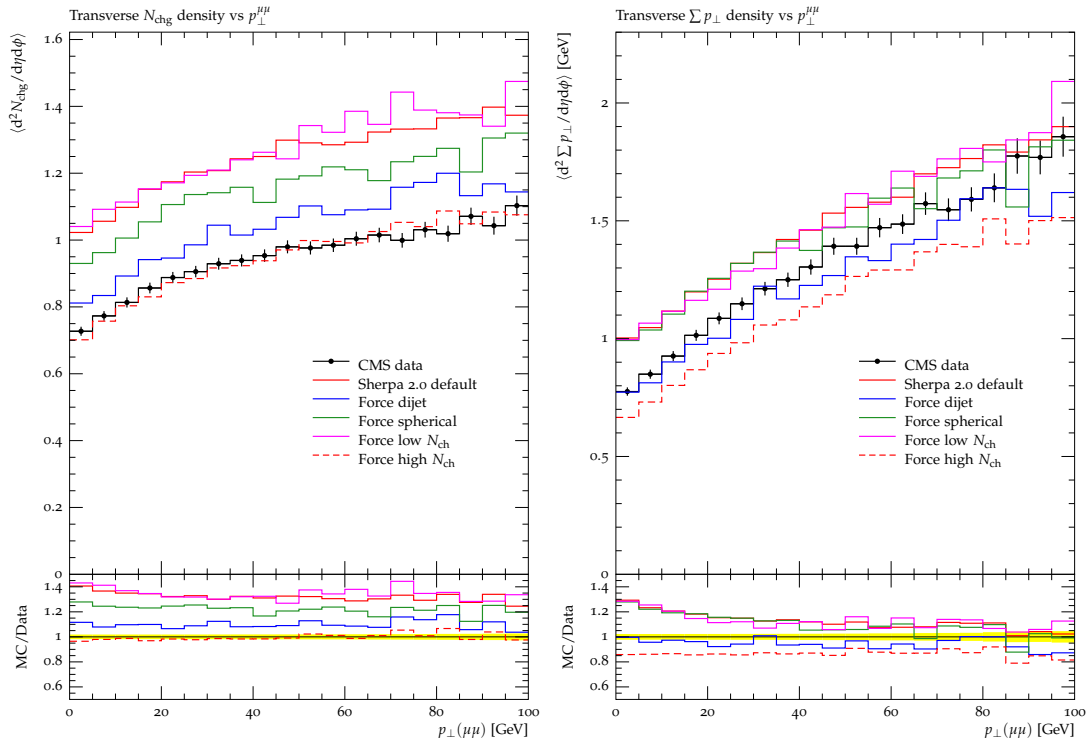

(b) CMS traditional UE

Figure 13.1.: Attempts of an optimisation of Sherpa parameters relevant to the underlying event trying to get an improved agreement of the event shapes measured in this analysis (Figure 13.1a) as well as recently published CMS data of a traditional underlying event (UE) analysis [129] (Figure 13.1b).

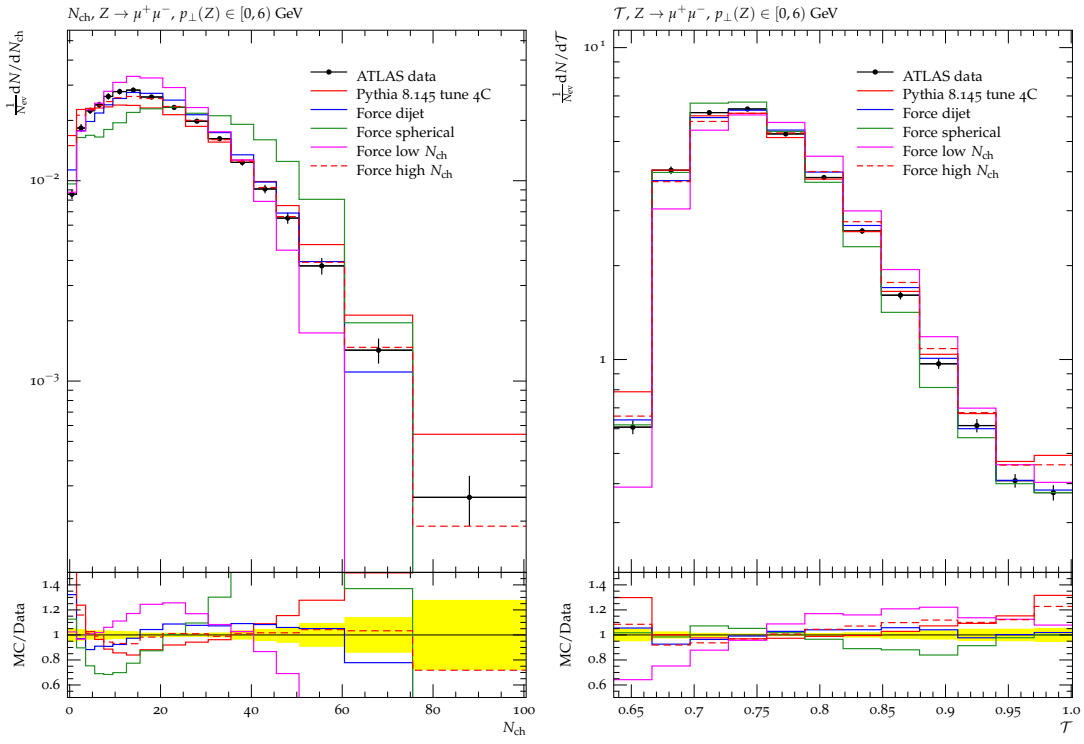

(a) Event shapes

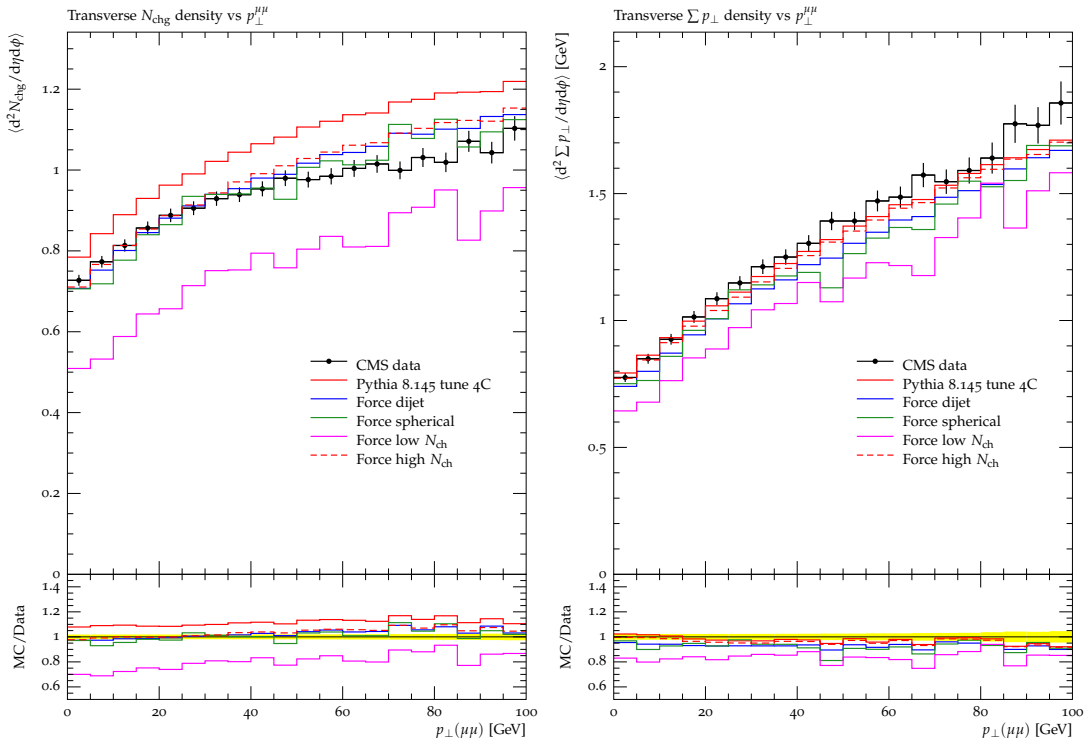

(b) CMS traditional UE

Figure 13.2.: Attempts of an optimisation of Pythia8 parameters relevant to the underlying event trying to get an improved agreement of the event shapes measured in this analysis (Figure 13.2a) as well as recently published CMS data of a traditional underlying event (UE) analysis [129] (Figure 13.2b).

Chapter 14.

Summary

In this thesis the first measurement of hadron-collider event shapes in proton-proton collisions at the LHC producing leptonically decaying Z-bosons was conducted. A total of $\mathcal{L} = 1.1$ fb^{-1} of data taken with the ATLAS experiment at $\sqrt{s} = 7$ TeV was analysed in an electron and a muon channel analysis chain. A selection of observables was made based on studies estimating the sensitivity to multiple parton interactions (MPI) models conducted by Daniel Weyh. The data was corrected for QCD background and pile-up using data driven methods. The latter was achieved using a novel technique based on the `HBOM` approach of recursively applying the detector-effect of pile-up to the data and subsequent extrapolation to the null-effect. The data was further corrected back to hadron level using a Bayesian iterative unfolding technique with the `Imagiro` program defining five phase-space regions in the transverse momentum of the Z-boson. This allows to study the change of the measured event shapes as more and more activity is present in the hard sub-process.

It was found that the Monte-Carlo predictions of Sherpa and Pythia8 significantly disagree with the unfolded data distributions thus prompting an attempt to improve the MPI models by means of tuning the corresponding paramaters to give an optimised description of the measured event shapes. Especially the phase-space region of $p_{\perp}(\mathrm{Z}) < 6$ GeV is deemed very sensitive to the effect of MPI as in the absence of a jet and after removal of the lepton tracks remaining event activity should stem from MPI activity. During the tuning attempts it became clear rather quickly that a unified description of more traditional underlying event measurements and the event shapes is not achievable in a satisfying way. Moreover it was found that certain regions of the event shapes can not be described with the models currently at hand. The optimised predictions obtained with the Pythia8 generator yield a qualitatively better description than those obtained

for Sherpa. This might very well be due to a phenomenological mechanism present in Pythia8 but absent in Sherpa, namely the mechanism of colour-reconnection which allows to balance the number and hardness of particles produced but goes beyond the original Sjöstrand-Zijl model for MPI.

The measured observables should therefore provide valuable insight into the phenomenon of MPI and especially the development of more involved MPI models than currently available which is important especially in view of the high-precision measurements currently performed at the LHC that are increasingly limited by uncertainties related to Monte-Carlo simulations.

Appendix A.

Datasets used

A.1. Data

Period	Dataset
	$Z \to e^+e^-$
D	data11_7TeV.periodD.physics_Egamma.PhysCont.AOD.repro10_v01
E	data11_7TeV.periodE.physics_Egamma.PhysCont.AOD.repro10_v01
F	data11_7TeV.periodF.physics_Egamma.PhysCont.AOD.repro10_v01
G	data11_7TeV.periodG.physics_Egamma.PhysCont.AOD.repro10_v01
H	data11_7TeV.periodH.physics_Egamma.PhysCont.AOD.repro10_v01
	$Z \to \mu^+\mu^-$
D	data11_7TeV.periodD.physics_Muons.PhysCont.AOD.pro10_v01
E	data11_7TeV.periodE.physics_Muons.PhysCont.AOD.pro10_v01
F	data11_7TeV.periodF.physics_Muons.PhysCont.AOD.pro10_v01
G	data11_7TeV.periodG.physics_Muons.PhysCont.AOD.pro10_v01
H	data11_7TeV.periodH.physics_Muons.PhysCont.AOD.pro10_v01

Table A.1.: Datasets recorded with ATLAS in 2011 used in this analysis.

A.2. Signal Monte-Carlos

Generator	Dataset
	$Z \to e^+e^-$ with pile-up
Sherpa 1.3.1	mc11_7TeV.114609.SherpaZ5jetstoee30GeV.merge.AOD.e931_a131_s1353_a139_r2900
Pythia8 8.1.50	mc11_7TeV.126184.Pythia8Zee.merge.AOD.e984_a131_s1353_a139_r2900
	$Z \to e^+e^-$ without pile-up
Sherpa 1.3.1	mc11_7TeV.114609.SherpaZ5jetstoee30GeV.merge.AOD.e931_a131_s1353_a141_r2900
Pythia8 8.1.50	mc11_7TeV.126184.Pythia8Zee.merge.AOD.e984_a131_s1353_a141_r2900
	$Z \to \mu^+\mu^-$ with pile-up
Sherpa 1.3.1	mc11_7TeV.114610.SherpaZ5jetstomumu30GeV.merge.AOD.e931_a131_s1353_a139_r2900
Pythia8 8.1.50	mc11_7TeV.126185.Pythia8Zmumu.merge.AOD.e984_a131_s1353_a139_r2900
	$Z \to \mu^+\mu^-$ without pile-up
Sherpa 1.3.1	mc11_7TeV.114610.SherpaZ5jetstomumu30GeV.merge.AOD.e931_a131_s1353_a141_r2900
Pythia8 8.1.50	mc11_7TeV.126185.Pythia8Zmumu.merge.AOD.e984_a131_s1353_a141_r2900

Table A.2.: Signal Monte-Carlo datasets used in this analysis.

A.3. Background Monte-Carlos

Generator	Dataset
	$Z \to t\bar{t}$ with pile-up
Sherpa 1.4.1	`mc11_7TeV.117800.SherpaTtbarLeptLept.merge.AOD.e995_a131_s1353_a139_r2900`
	Diboson (W, Z) with pile-up
Sherpa 1.4.1	`mc11_7TeV.126893.Sherpa_CT10_lllnu_WZ.evgen.EVNT.e1228_a131_s1353_a139_r2900`
	Diboson (Z, Z) with pile-up
Sherpa 1.4.1	`mc11_7TeV.126895.Sherpa_CT10_llnunu_ZZ.evgen.EVNT.e1228_a131_s1353_a139_r2900`
Sherpa 1.4.1	`mc11_7TeV.126894.Sherpa_CT10_llll_ZZ.evgen.EVNT.e1228_a131_s1353_a139_r2900`
	$Z \to \tau^+\tau^-$ with pile-up
Sherpa 1.4.1	`mc11_7TeV.147772.Sherpa_CT10_Ztautau.evgen.EVNT.e1516_a131_s1353_a139_r2900`

Table A.3.: Background Monte-Carlo datasets used in this analysis.

Appendix B.

Further explanations

B.1. Tag and probe method

Tag and probe methods are standard ways in ATLAS to determine efficiencies. In this analysis, various electron and muon efficiencies are determined this way. In both cases, reconstructed Z-boson samples are used that contain exactly two opposite-sign leptons, thus a high purity of lepton events is achieved.

Two slightly different reconstruction methods are used trying to reconstruct the same lepton. One of these reconstructions is called the tag lepton which is reconstructed using the method the efficiency is to be determined for (reconstruction method 1). Further is the tag muon required to have fired the trigger. The same lepton is reconstructed again using less tight requirements (reconstruction method 2). It is then tried to match the probe lepton to a tag lepton in the event. The match is considered successful, if the tag and the probe lepton have the same sign and depending on the specific efficiency other requirements such as the distance in $\eta - \Phi$ space are not too far apart.

The corresponding efficiency is calculated as the ratio of the number of matched leptons and the number of all leptons.

B.2. K-factor

A K-factor is typically a number a fixed order cross-section calculation is to be multiplied with in order to obtain corresponding cross-section of the next leading order. The concept has its limitations as e.g. next-to-leading order (NLO) distribution at times

have different shapes compared to their leading oder (LO) counterparts. Further, since K-factors are typically calculated for inclusive processes, there is no gurantee that they are also valid when e.g. explicitly asking for events with a certain jet mulitplicity or, as it is done in this analysis, for a certain window of $p_{\perp}$(Z).

Appendix C.

Additional plots

In this part of the appendix, additional plots to figures shown in the main document can be found.

C.1. Pile-up correction factors

The following figure supplement the figures shown Chapter 10.

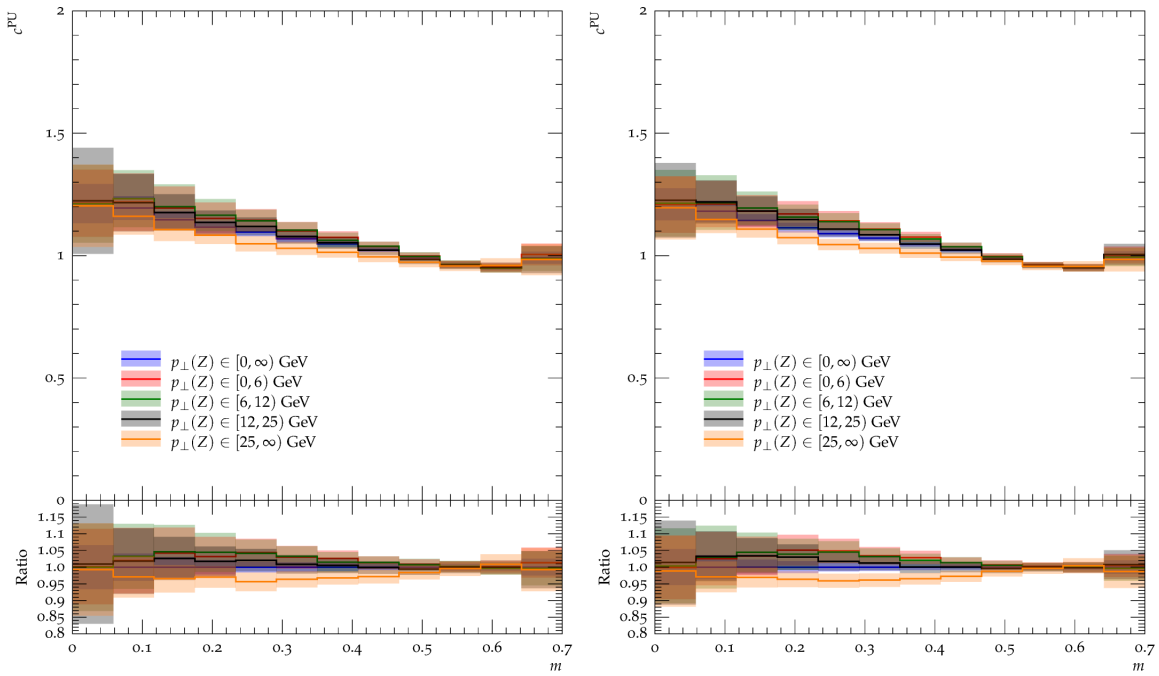

(a) Transverse minor

Figure C.1.: Pile-up correction factors obtained using the HBOM technique from the data samples to be corrected for pile-up. Plots on the left hand side show results for the electron channel, plots on the right hand side those of the muon channel. The error-bands show the total systematic uncertainty of the pile-up correction.

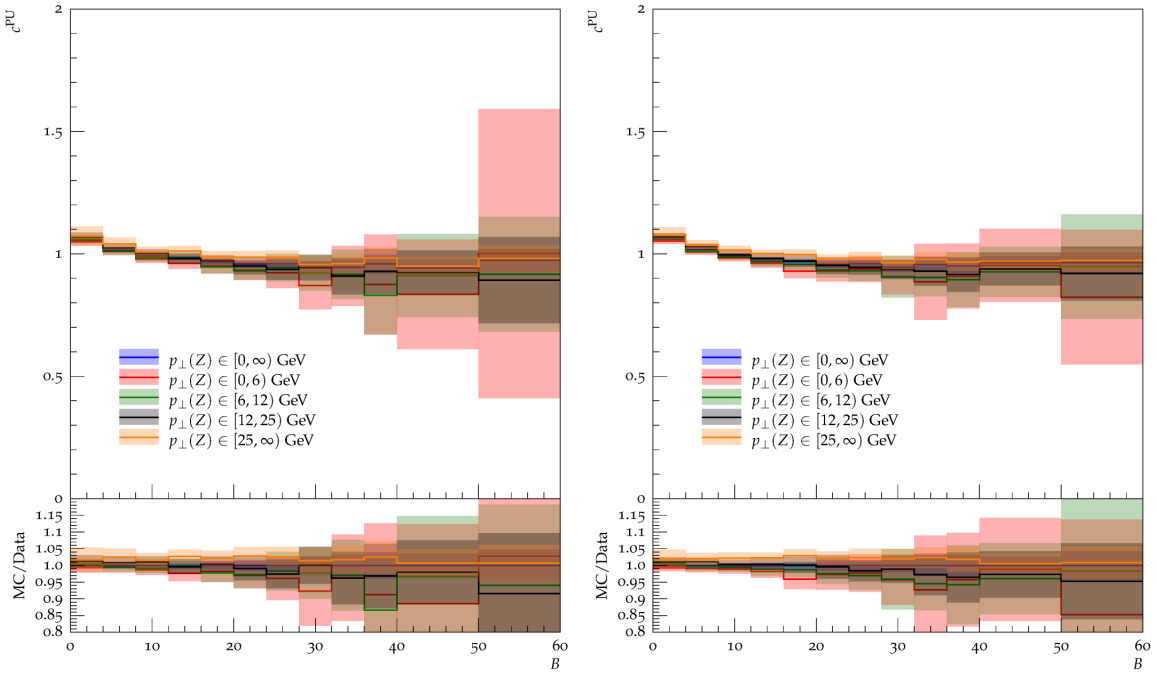

(b) Beamthrust

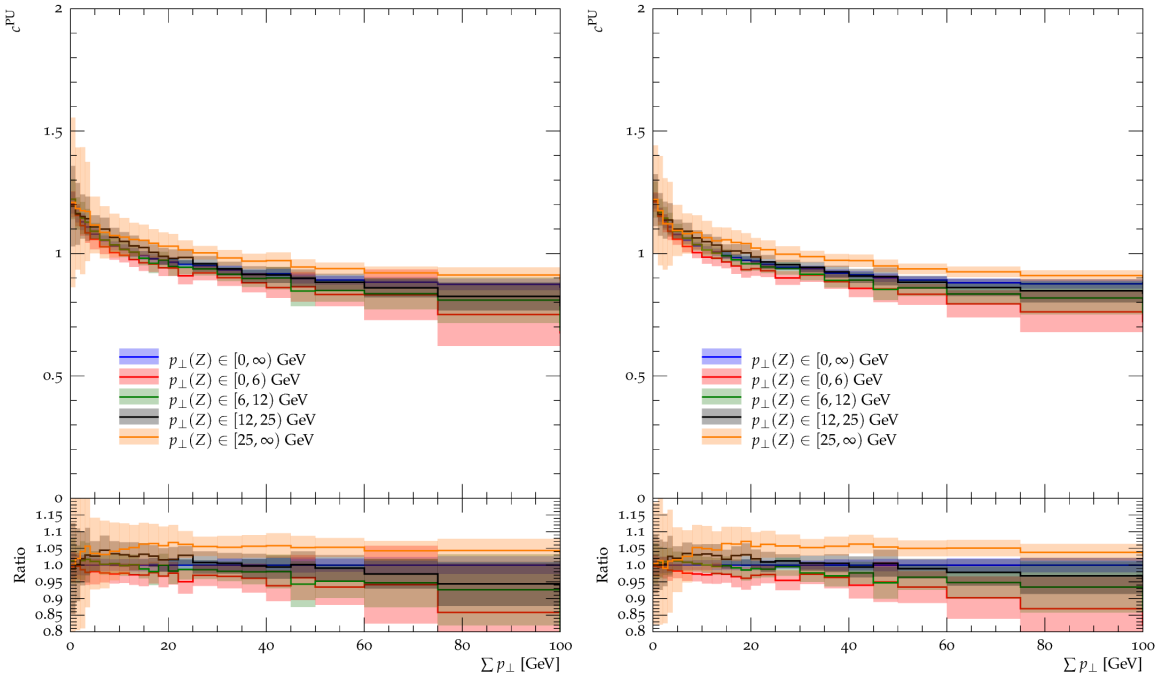

(c) $\sum p_\perp$

Figure C.0.: Pile-up correction factors obtained using the HBOM technique from the data samples to be corrected for pile-up. Plots on the left hand side show results for the electron channel, plots on the right hand side those of the muon channel. The error-bands show the total systematic uncertainty of the pile-up correction.

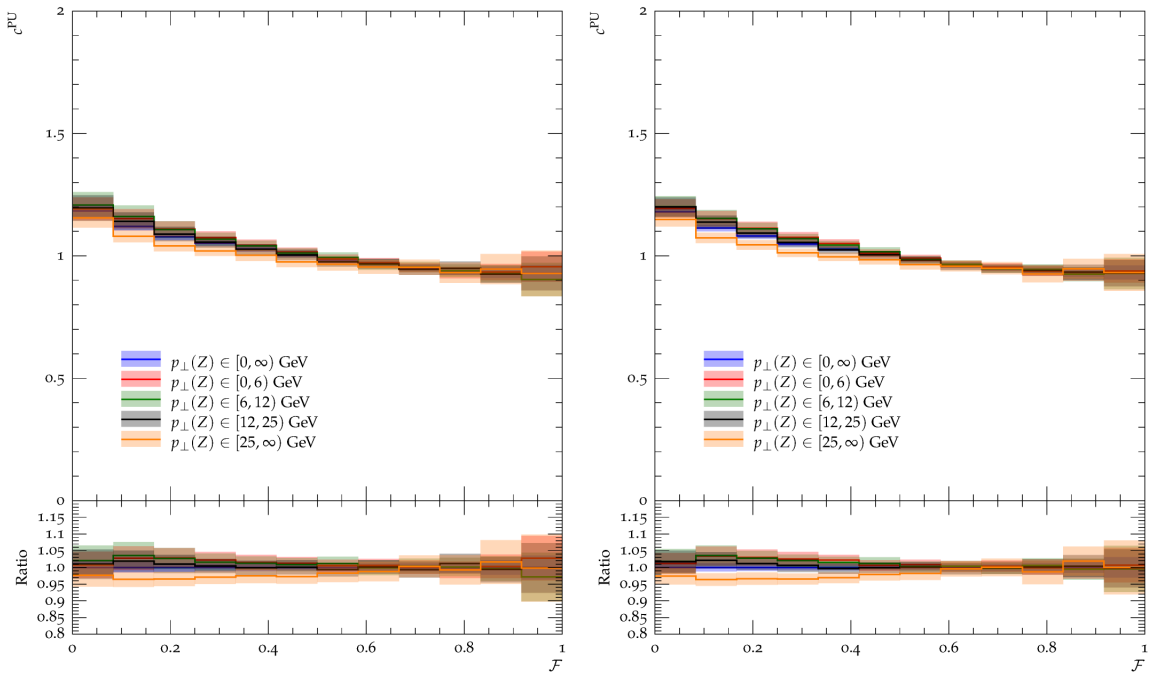

(d) F-Parameter

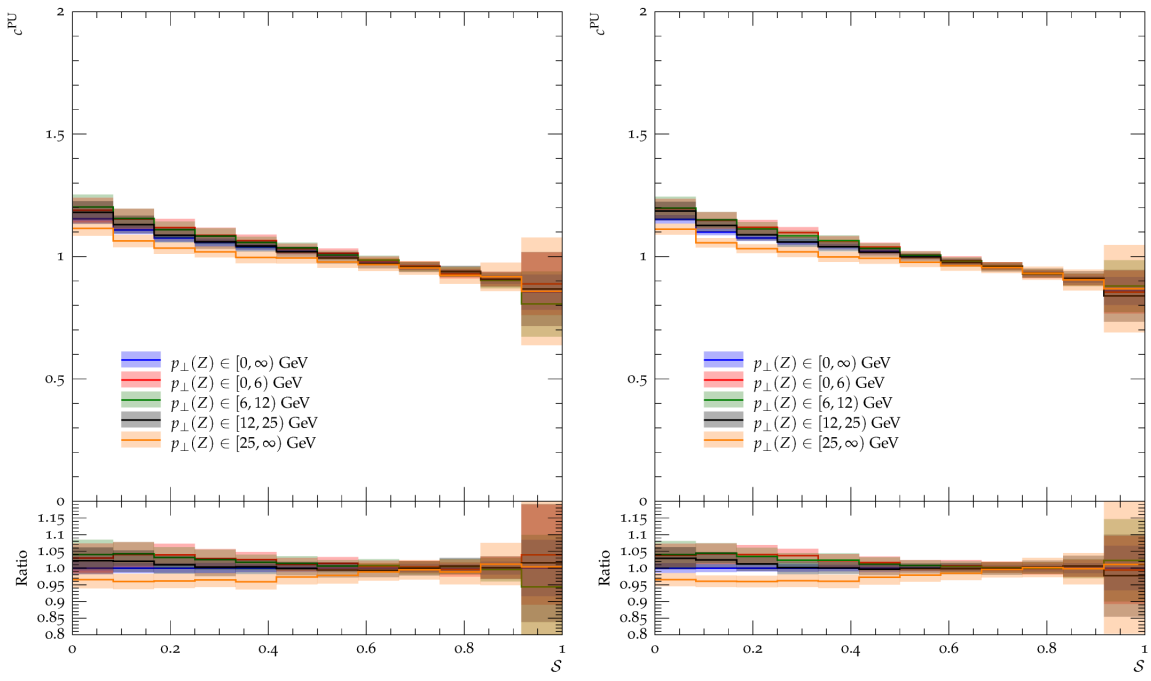

(e) Spherocity

Figure C.-1.: Pile-up correction factors obtained using the HBOM technique from the data samples to be corrected for pile-up. Plots on the left hand side show results for the electron channel, plots on the right hand side those of the muon channel. The error-bands show the total systematic uncertainty of the pile-up correction.

C.2. Unfolded distributions

The following figure supplement the figures shown Chapter 12.

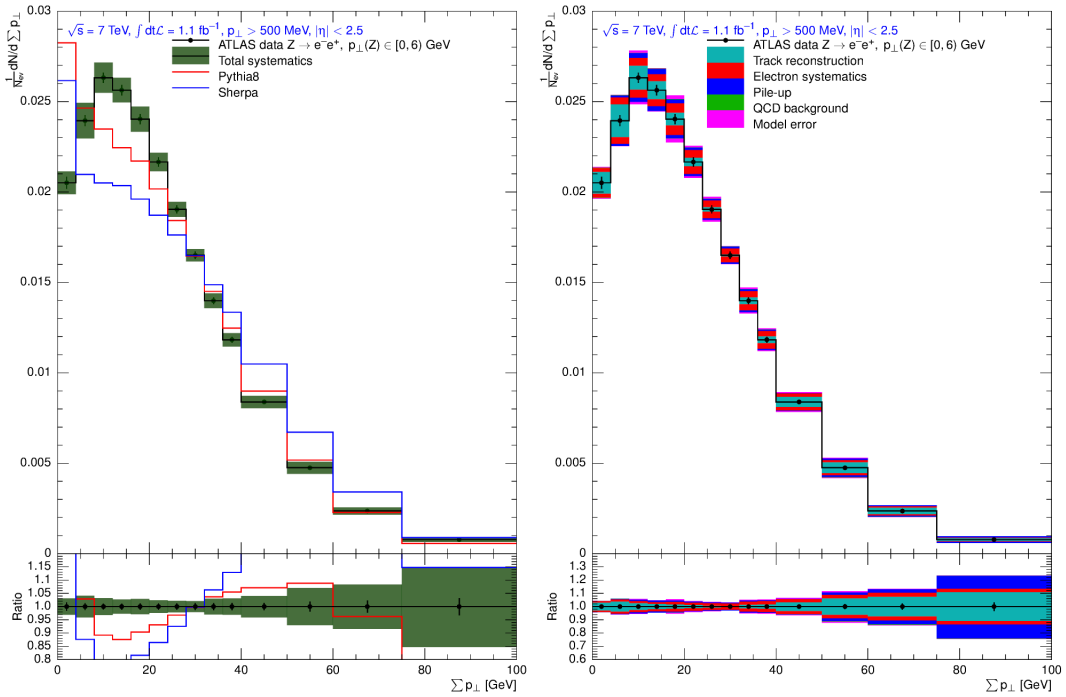

(a) $\sum p_\perp$, $p_\perp(\mathrm{Z}) < 6$ GeV, electron channel

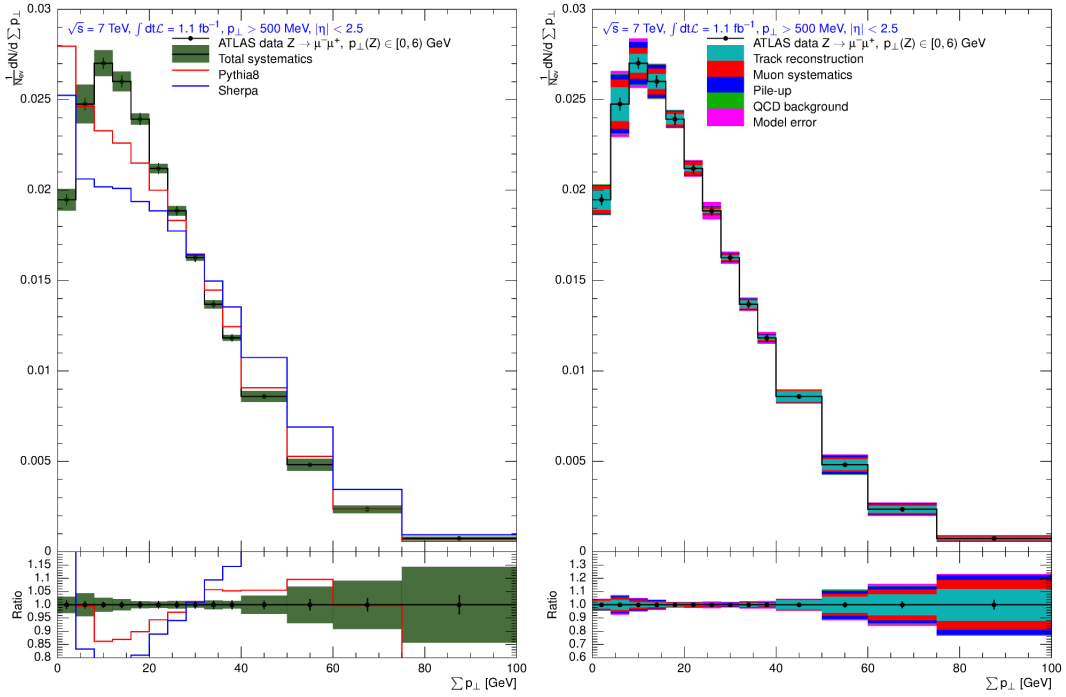

(b) $\sum p_\perp$, $p_\perp(\mathrm{Z}) < 6$ GeV, muon channel

Figure C.0.: Left: Unfolded $\sum p_\perp$ distribution with total systematic uncertainties (green band) and statistical uncertainties (black). Right: break-down of systematic uncertainties.

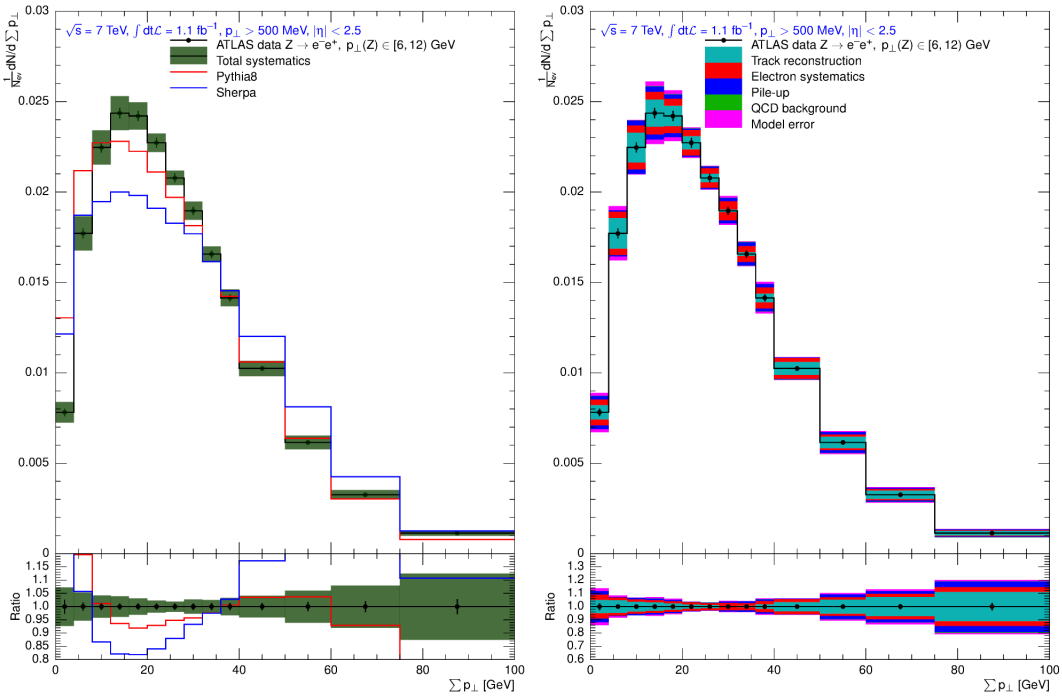

(a) $\sum p_\perp$, $p_\perp(\mathrm{Z}) \in [6, 12)$ GeV, electron channel

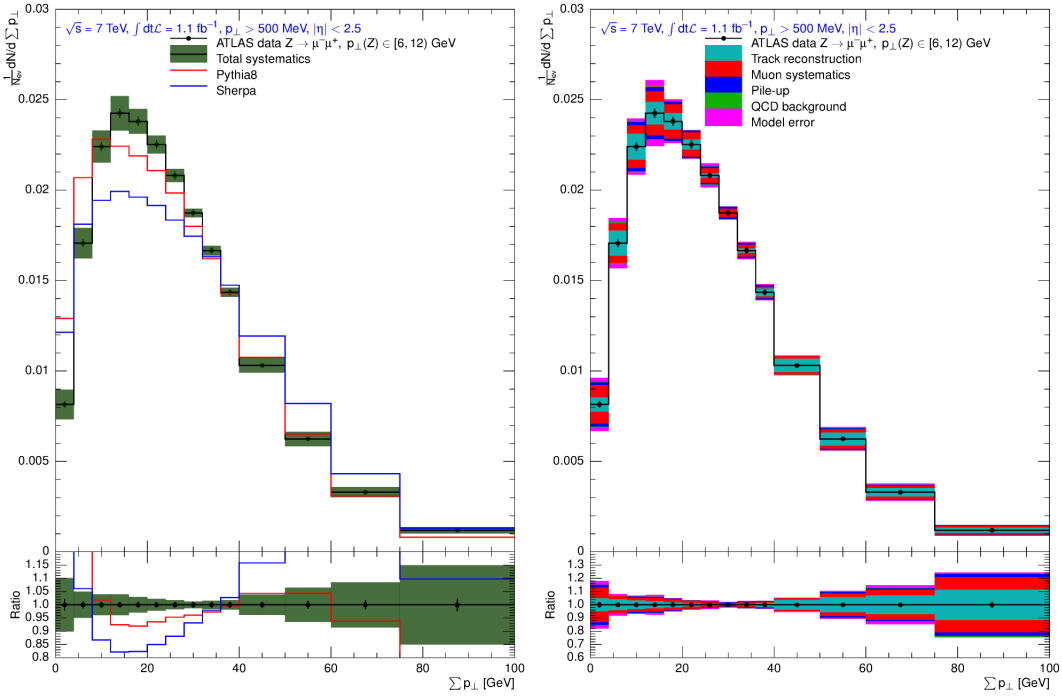

(b) $\sum p_\perp$, $p_\perp(\mathrm{Z}) \in [6, 12)$ GeV, muon channel

Figure C.1.: Left: Unfolded $\sum p_\perp$ distribution with total systematic uncertainties (green band) and statistical uncertainties (black). Right: break-down of systematic uncertainties.

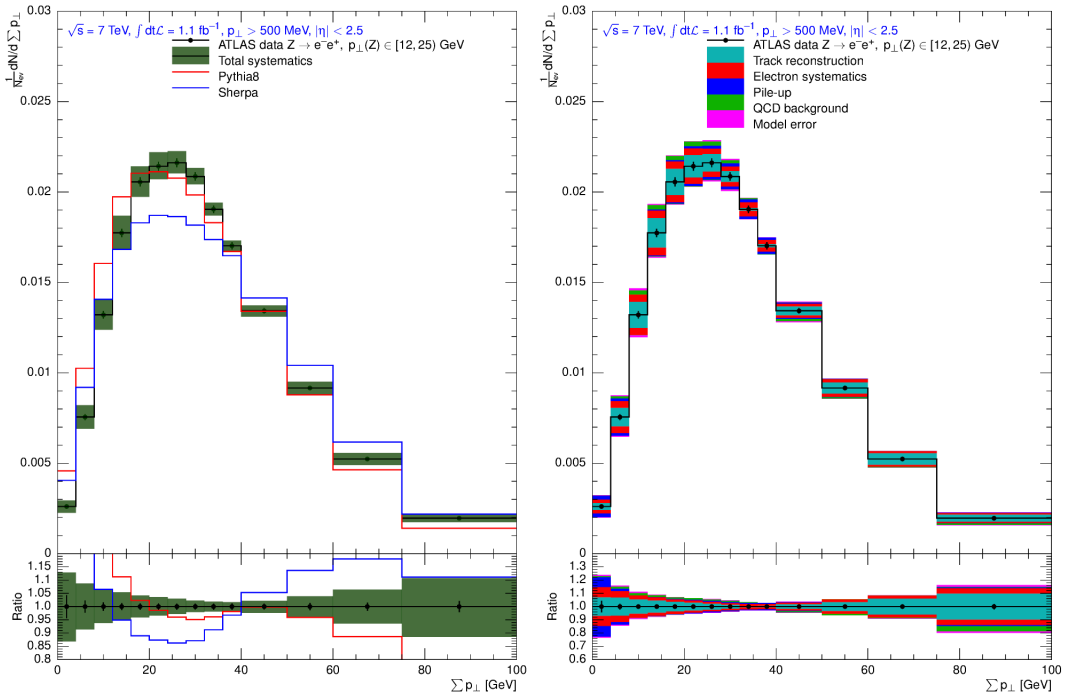

(a) $\sum p_\perp$, $p_\perp(\mathrm{Z}) \in [12, 25)$ GeV, electron channel

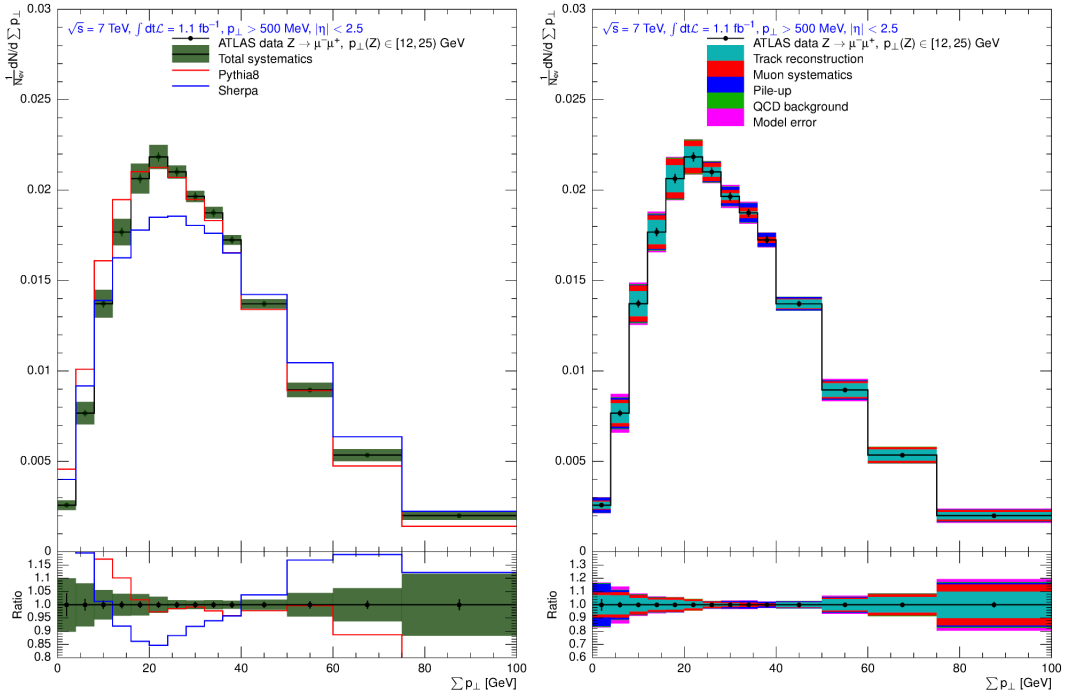

(b) $\sum p_\perp$, $p_\perp(\mathrm{Z}) \in [12, 25)$ GeV, muon channel

Figure C.2.: Left: Unfolded $\sum p_\perp$ distribution with total systematic uncertainties (green band) and statistical uncertainties (black). Right: break-down of systematic uncertainties.

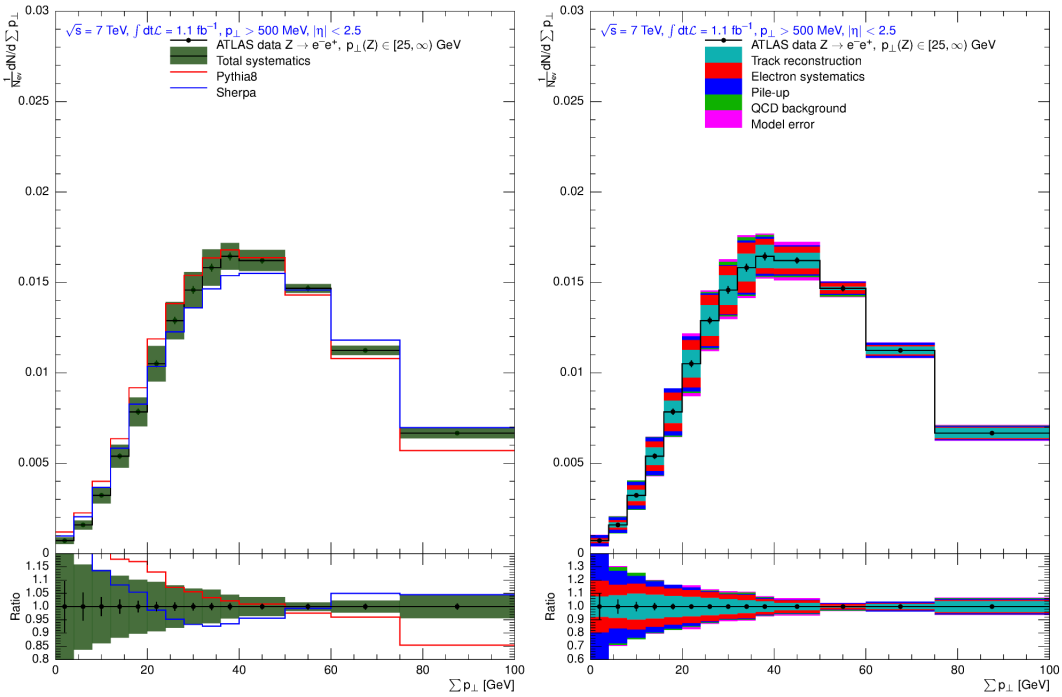

(a) $\sum p_\perp$, $p_\perp(\mathrm{Z}) > 25$ GeV, electron channel

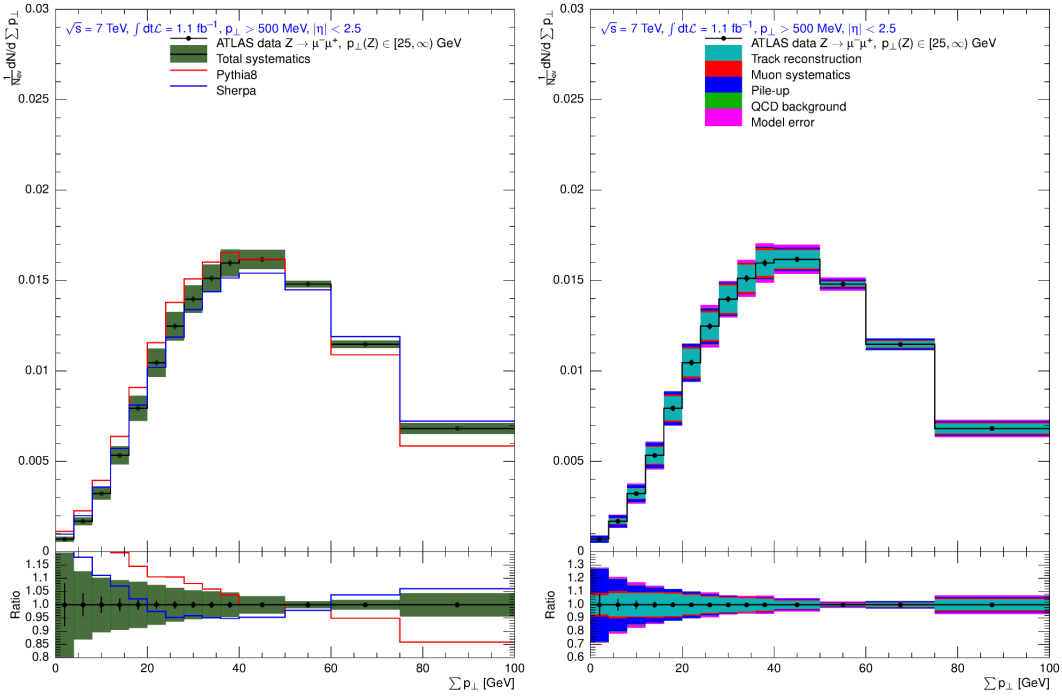

(b) $\sum p_\perp$, $p_\perp(\mathrm{Z}) > 25$ GeV, muon channel

Figure C.3.: Left: Unfolded $\sum p_\perp$ distribution with total systematic uncertainties (green band) and statistical uncertainties (black). Right: break-down of systematic uncertainties.

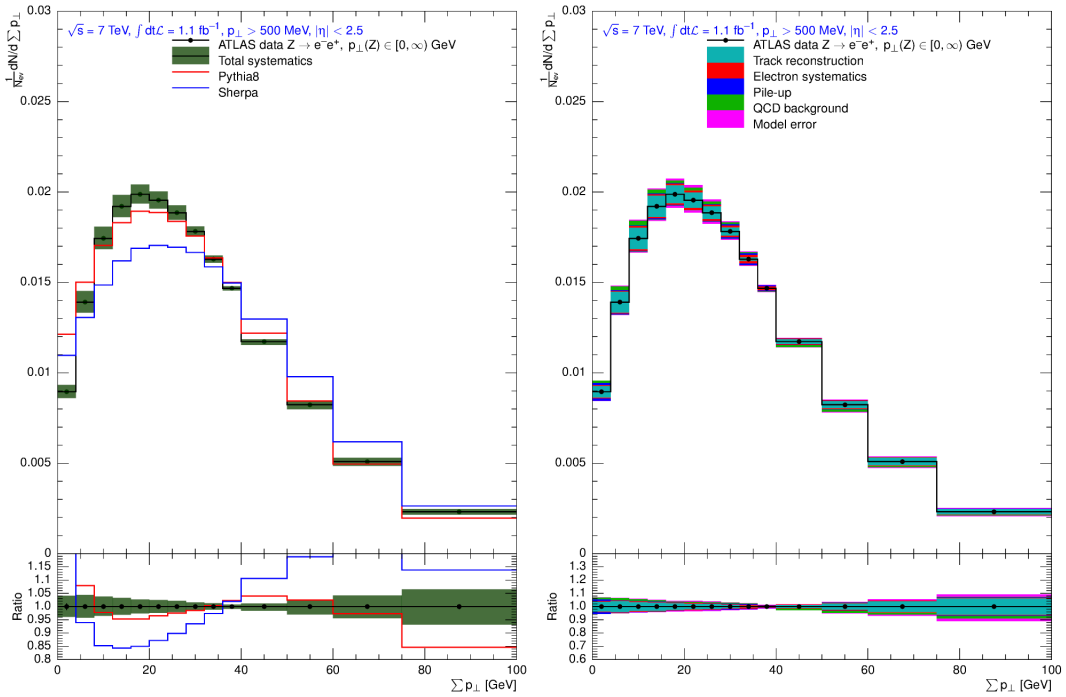

(a) $\sum p_\perp$, $p_\perp$(Z) inclusive electron channel

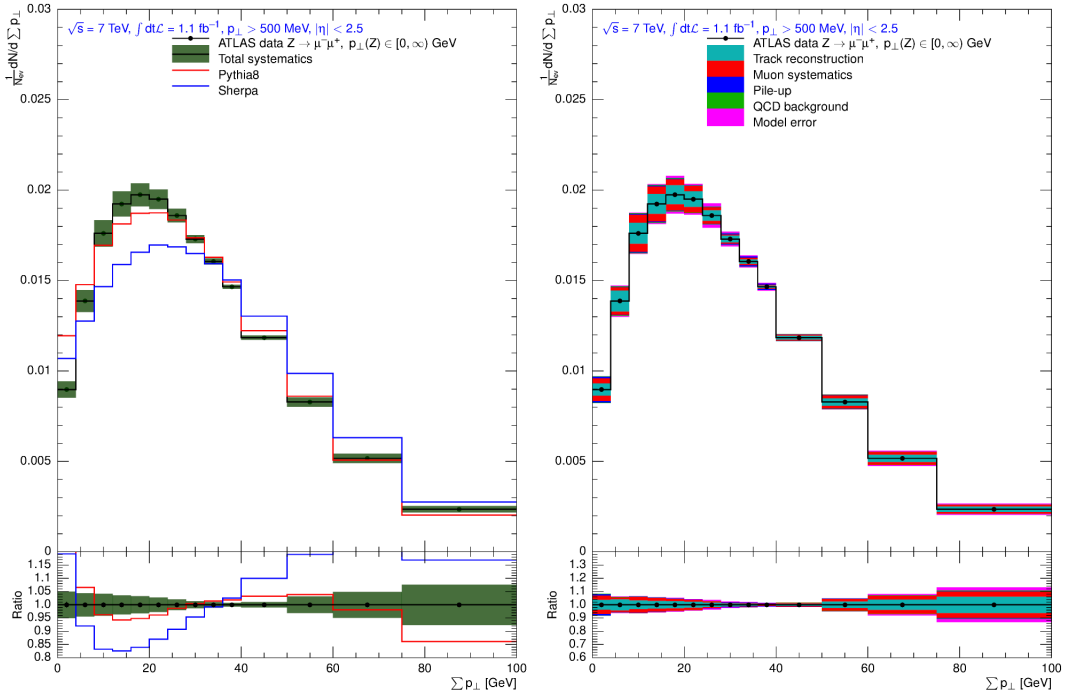

(b) $\sum p_\perp$, $p_\perp$(Z) inclusive, muon channel

Figure C.4.: Left: Unfolded $\sum p_\perp$ distribution with total systematic uncertainties (green band) and statistical uncertainties (black). Right: break-down of systematic uncertainties.

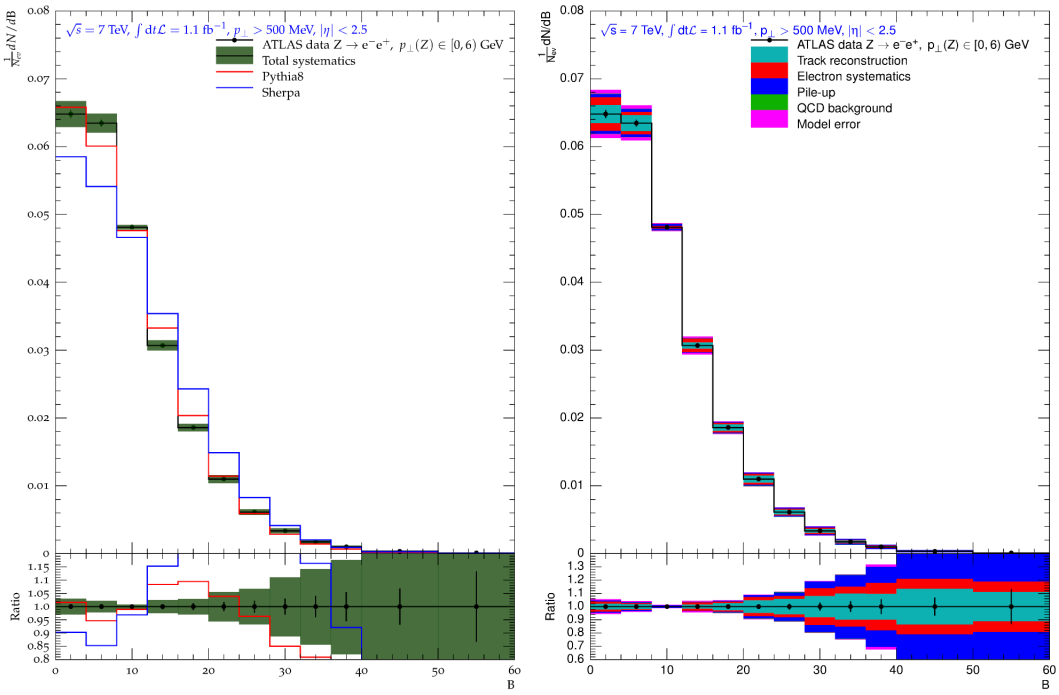

(a) Beamthrust, $p_\perp(\mathrm{Z}) < 6$ GeV, electron channel

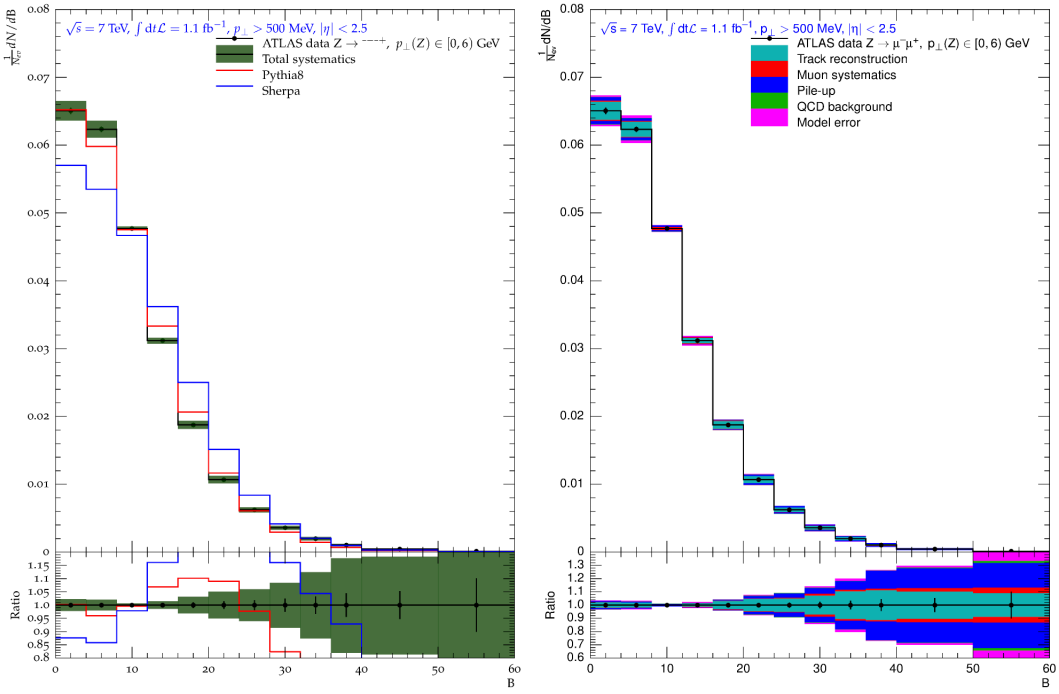

(b) Beamthrust, $p_\perp(\mathrm{Z}) < 6$ GeV, muon channel

Figure C.5.: Left: Unfolded Beamthrust distribution with total systematic uncertainties (green band) and statistical uncertainties (black). Right: break-down of systematic uncertainties.

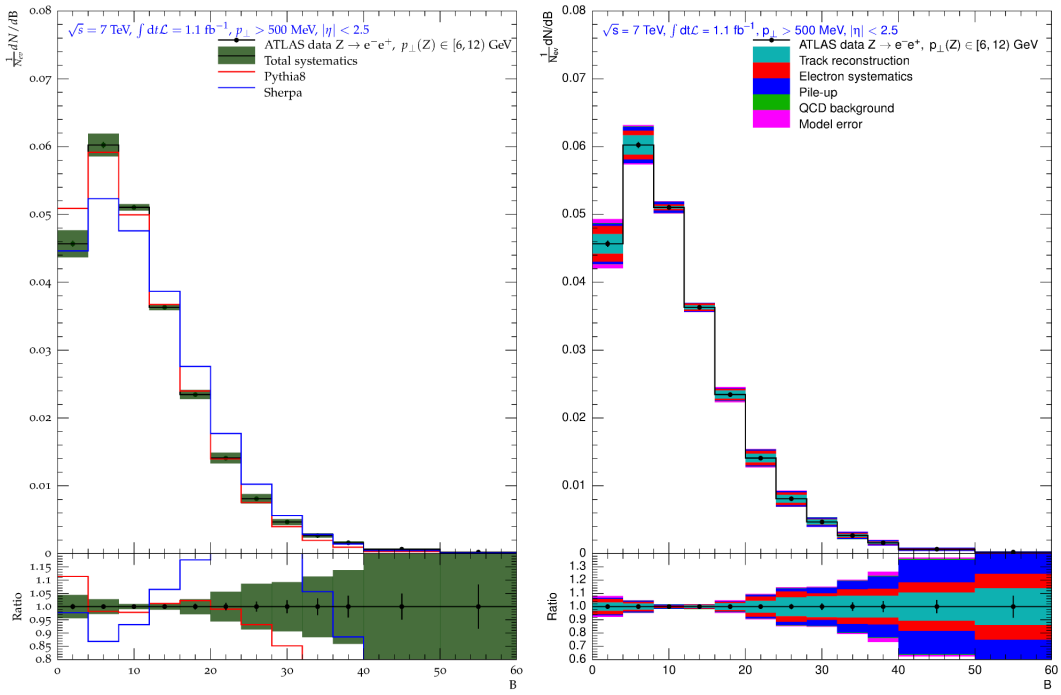

(a) Beamthrust, $p_\perp(\mathrm{Z}) \in [6, 12)$ GeV, electron channel

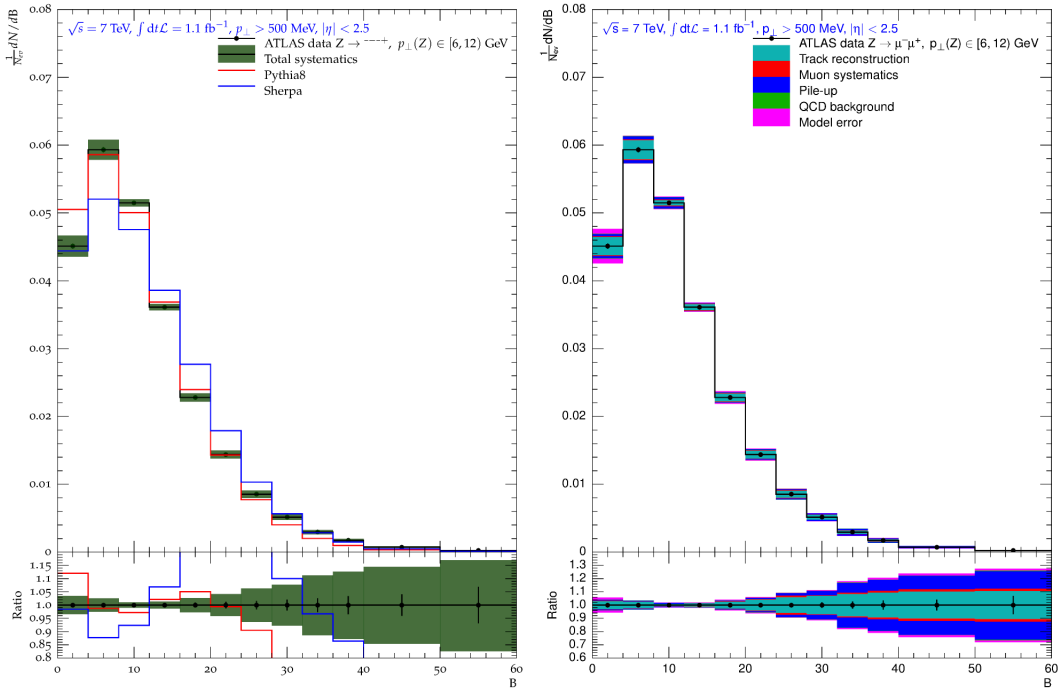

(b) Beamthrust, $p_\perp(\mathrm{Z}) \in [6, 12)$ GeV, muon channel

Figure C.6.: Left: Unfolded Beamthrust distribution with total systematic uncertainties (green band) and statistical uncertainties (black). Right: break-down of systematic uncertainties.

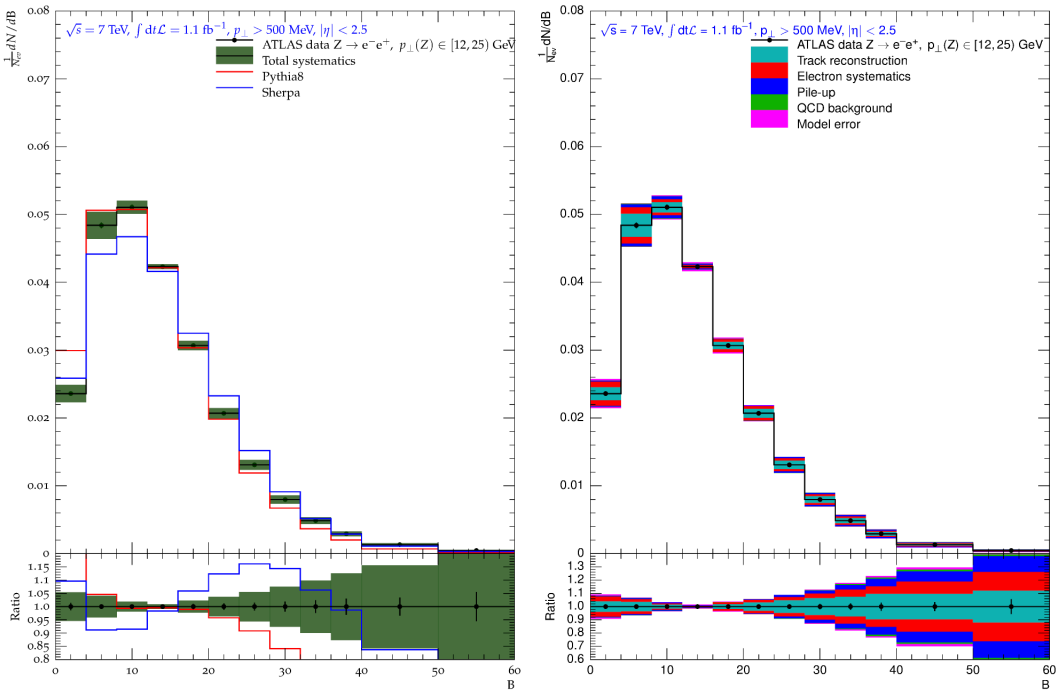

(a) Beamthrust, $p_\perp(\mathrm{Z}) \in [12, 25)$ GeV, electron channel

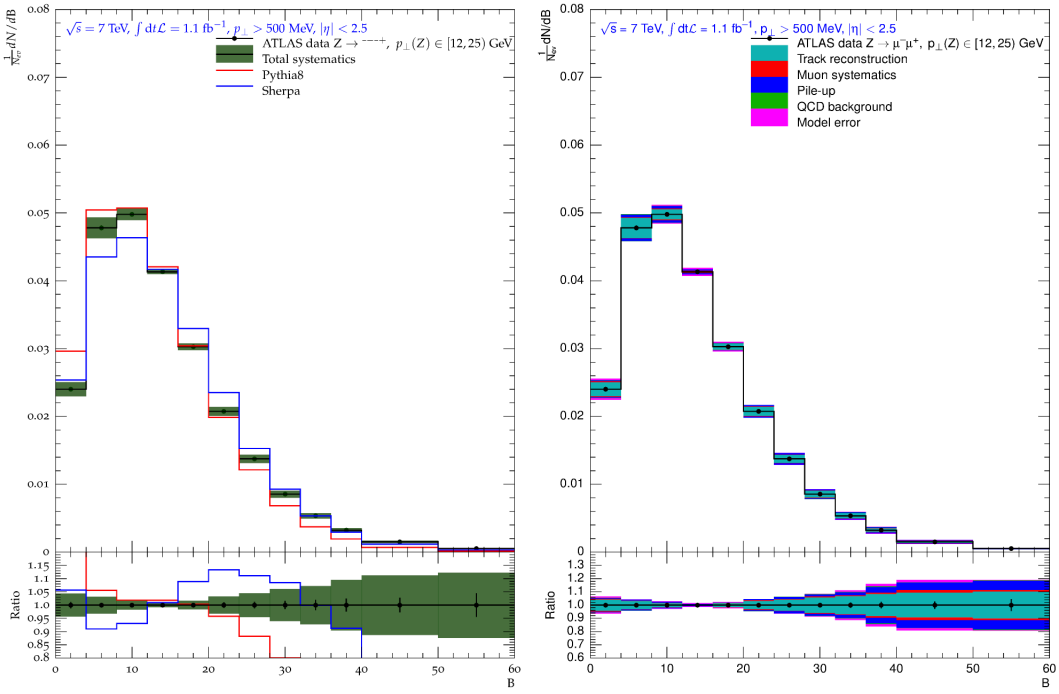

(b) Beamthrust, $p_\perp(\mathrm{Z}) \in [12, 25)$ GeV, muon channel

Figure C.7.: Left: Unfolded Beamthrust distribution with total systematic uncertainties (green band) and statistical uncertainties (black). Right: break-down of systematic uncertainties.

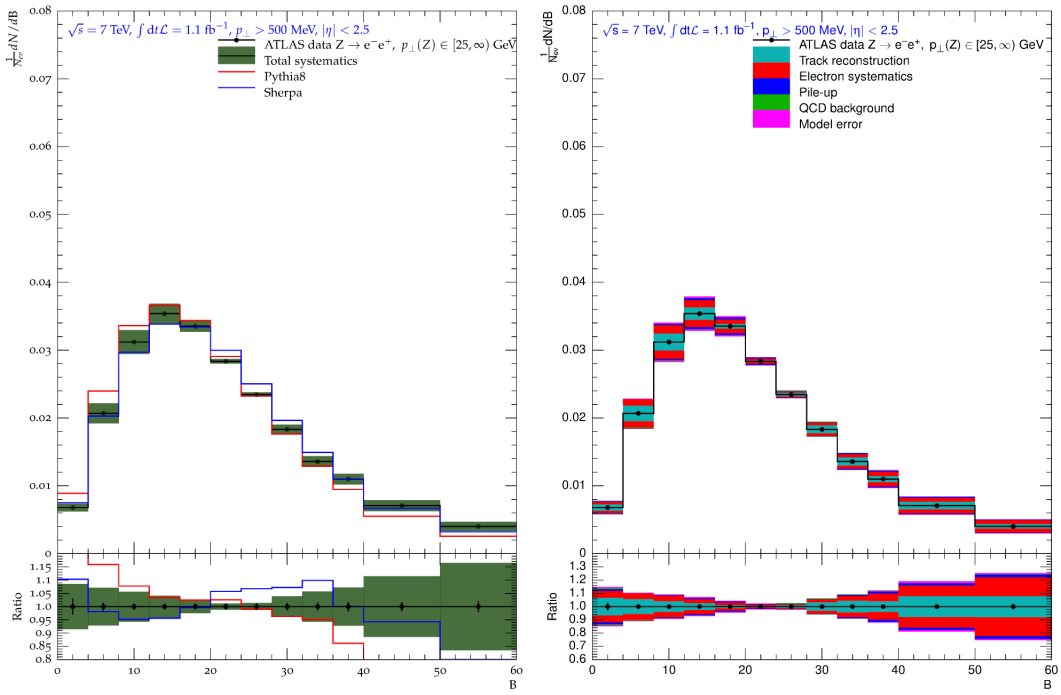

(a) Beamthrust, $p_\perp(\mathrm{Z}) > 25$ GeV, electron channel

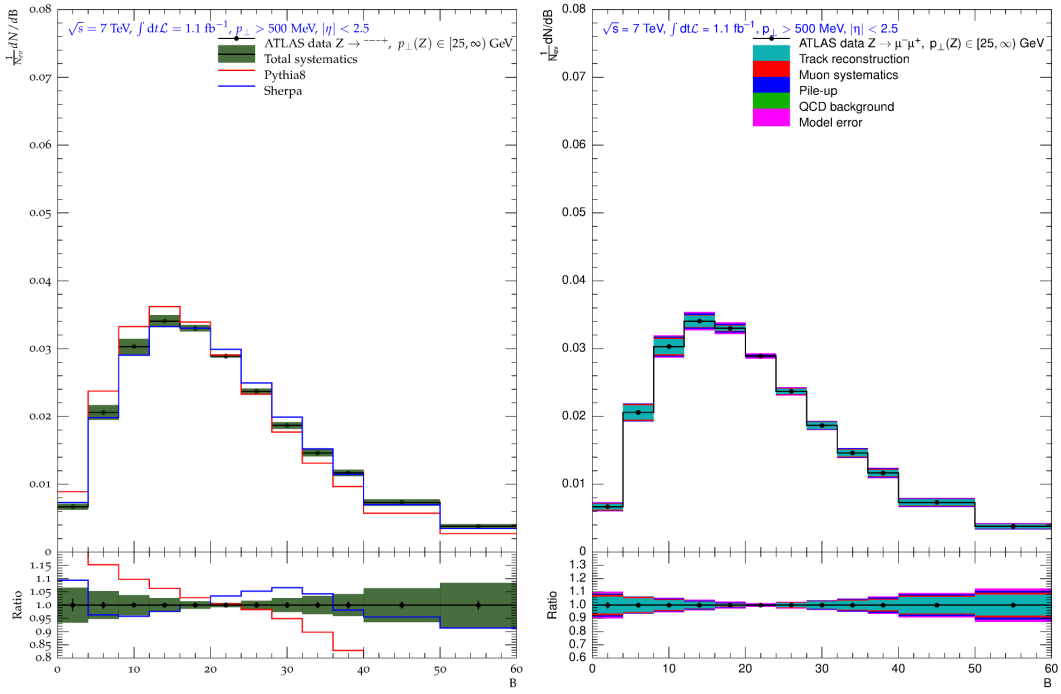

(b) Beamthrust, $p_\perp(\mathrm{Z}) > 25$ GeV, muon channel

Figure C.8.: Left: Unfolded Beamthrust distribution with total systematic uncertainties (green band) and statistical uncertainties (black). Right: break-down of systematic uncertainties.

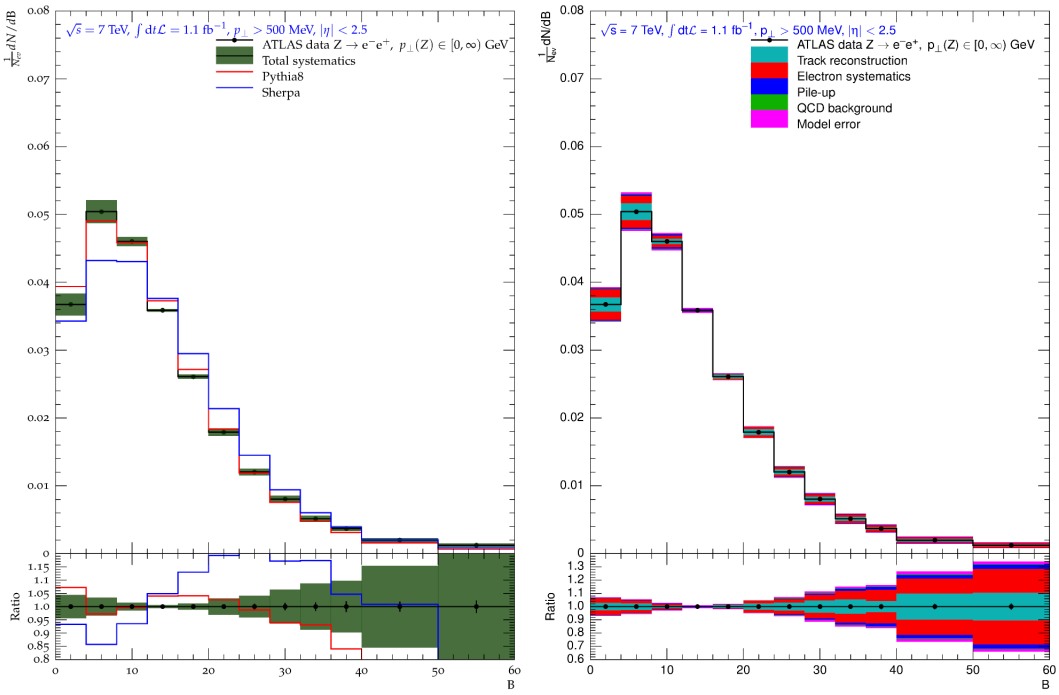

(a) Beamthrust, $p_\perp$(Z) inclusive electron channel

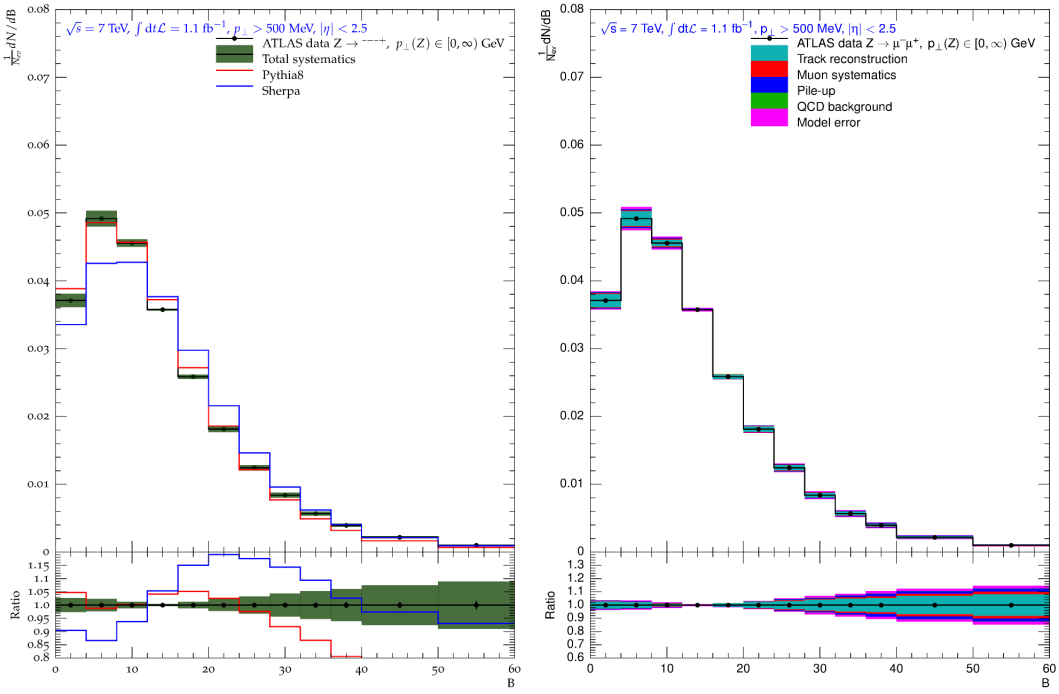

(b) Beamthrust, $p_\perp$(Z) inclusive, muon channel

Figure C.9.: Left: Unfolded Beamthrust distribution with total systematic uncertainties (green band) and statistical uncertainties (black). Right: break-down of systematic uncertainties.

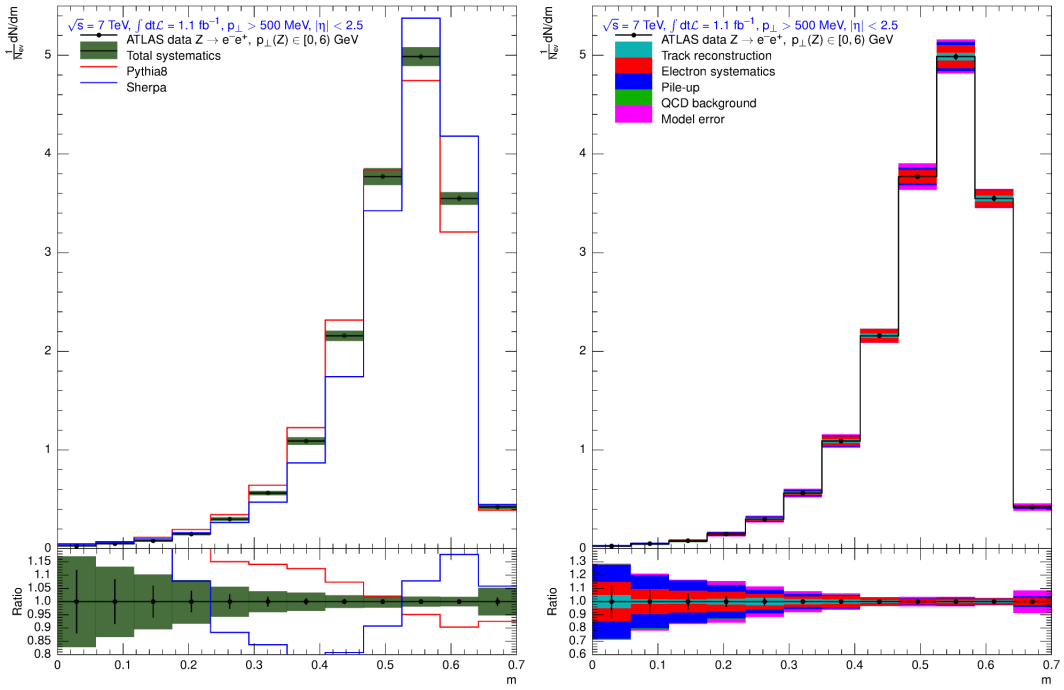

(a) Minor, $p_\perp(\mathrm{Z}) < 6$ GeV, electron channel

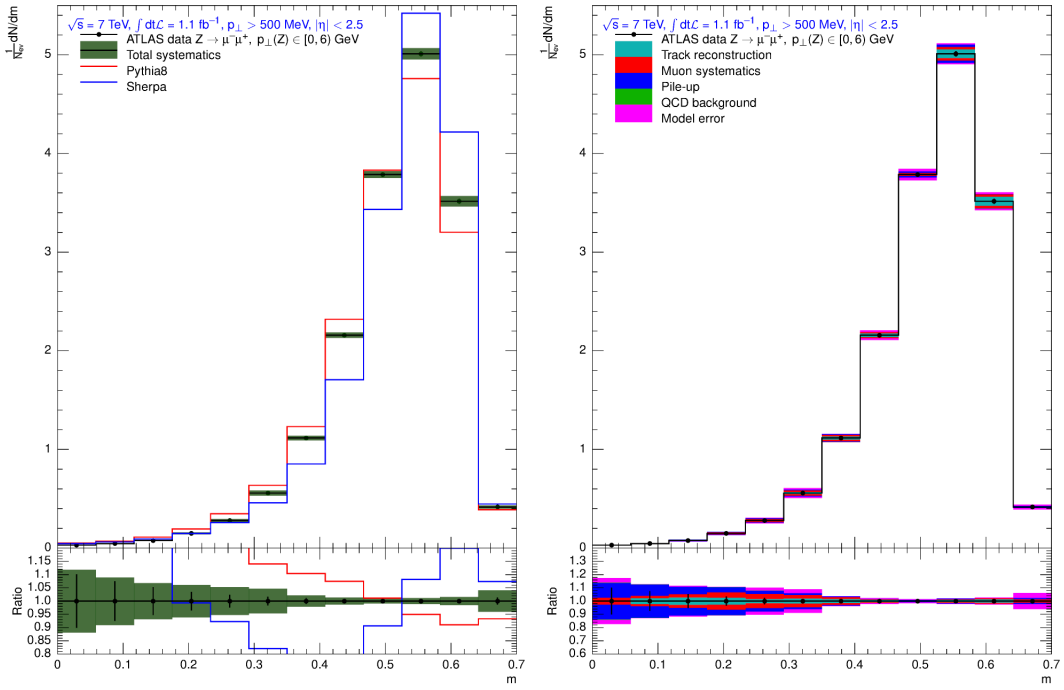

(b) Minor, $p_\perp(\mathrm{Z}) < 6$ GeV, muon channel

Figure C.10.: Left: Unfolded Minor distribution with total systematic uncertainties (green band) and statistical uncertainties (black). Right: break-down of systematic uncertainties.

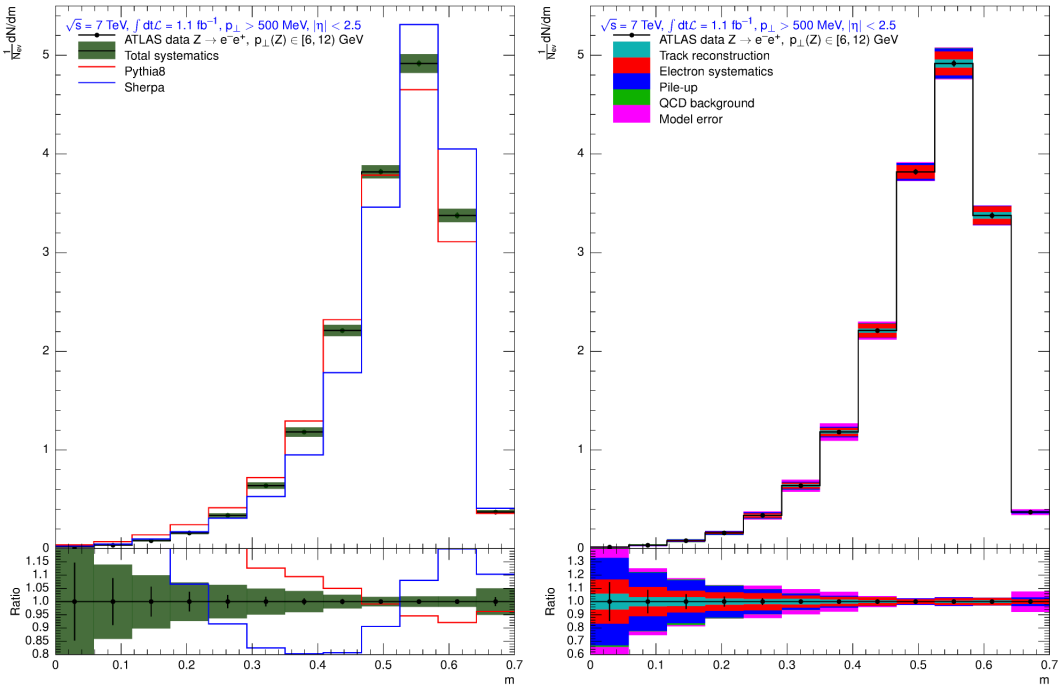

(a) Minor, $p_{\perp}(\mathrm{Z}) \in [6, 12)$ GeV, electron channel

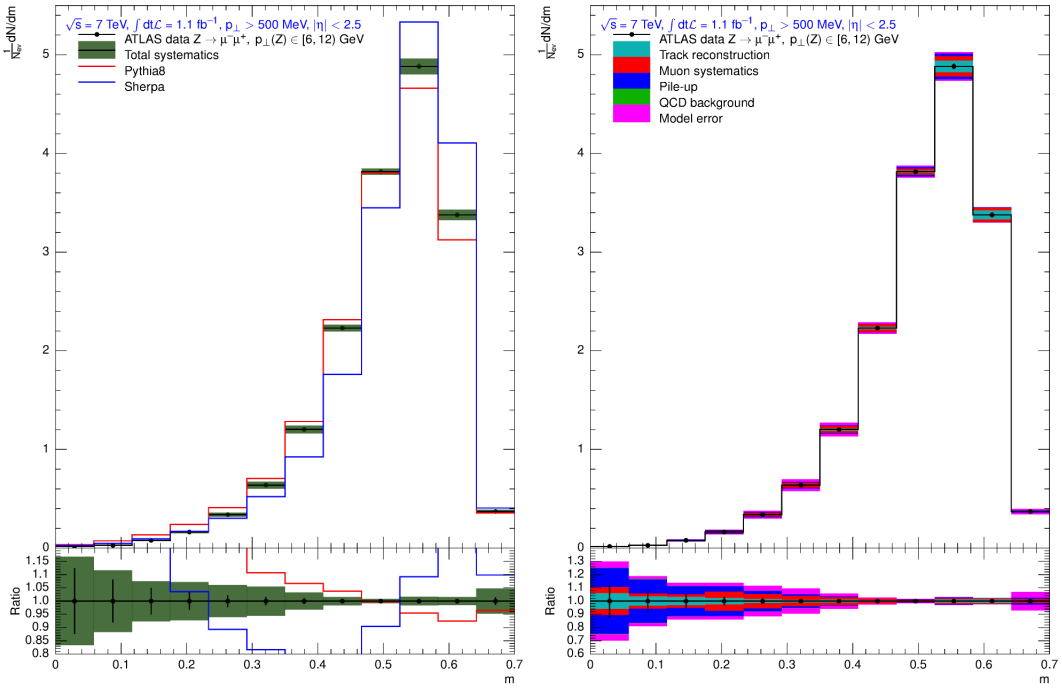

(b) Minor, $p_{\perp}(\mathrm{Z}) \in [6, 12)$ GeV, muon channel

Figure C.11.: Left: Unfolded Minor distribution with total systematic uncertainties (green band) and statistical uncertainties (black). Right: break-down of systematic uncertainties.

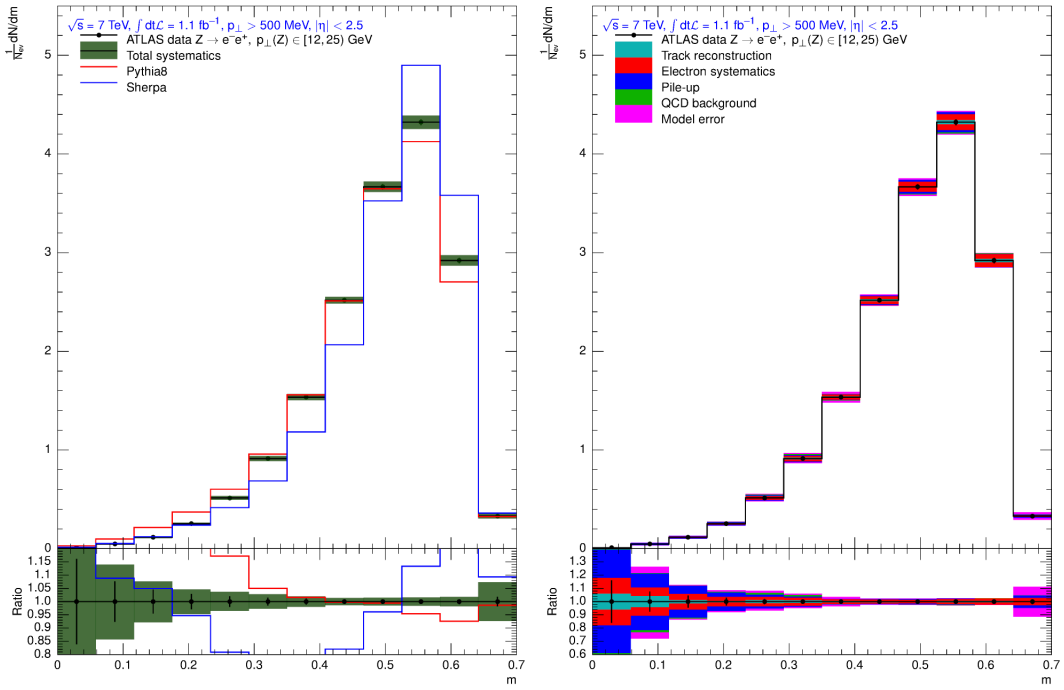

(a) Minor, $p_{\perp}(\mathrm{Z}) \in [12, 25)$ GeV, electron channel

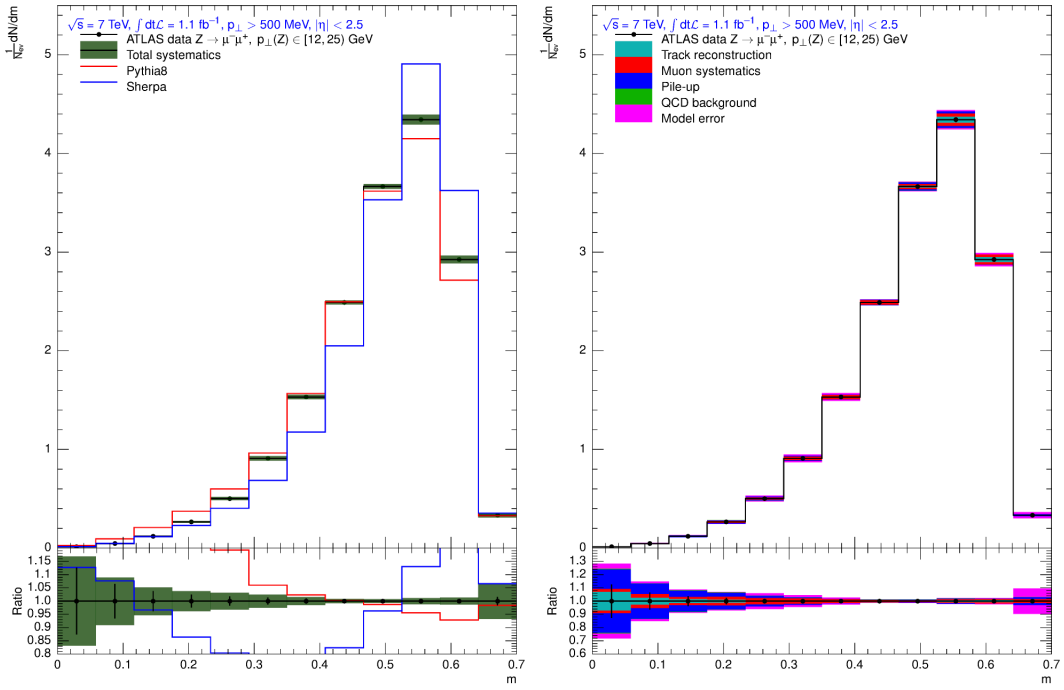

(b) Minor, $p_{\perp}(\mathrm{Z}) \in [12, 25)$ GeV, muon channel

Figure C.12.: Left: Unfolded Minor distribution with total systematic uncertainties (green band) and statistical uncertainties (black). Right: break-down of systematic uncertainties.

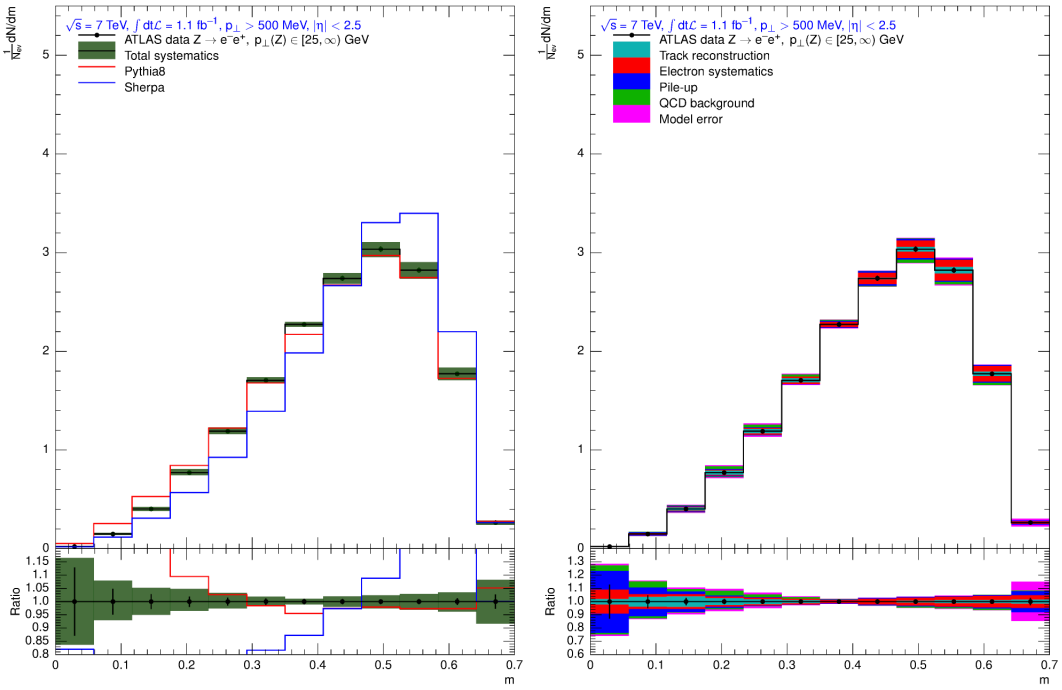

(a) Minor, $p_\perp(\mathrm{Z}) > 25$ GeV, electron channel

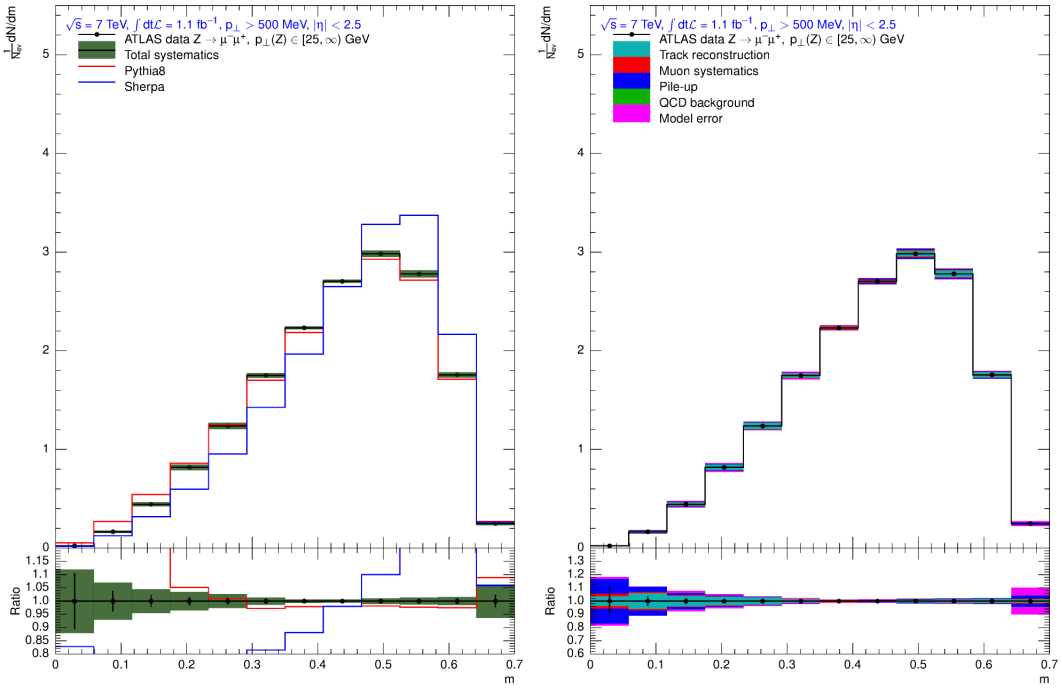

(b) Minor, $p_\perp(\mathrm{Z}) > 25$ GeV, muon channel

Figure C.13.: Left: Unfolded Minor distribution with total systematic uncertainties (green band) and statistical uncertainties (black). Right: break-down of systematic uncertainties.

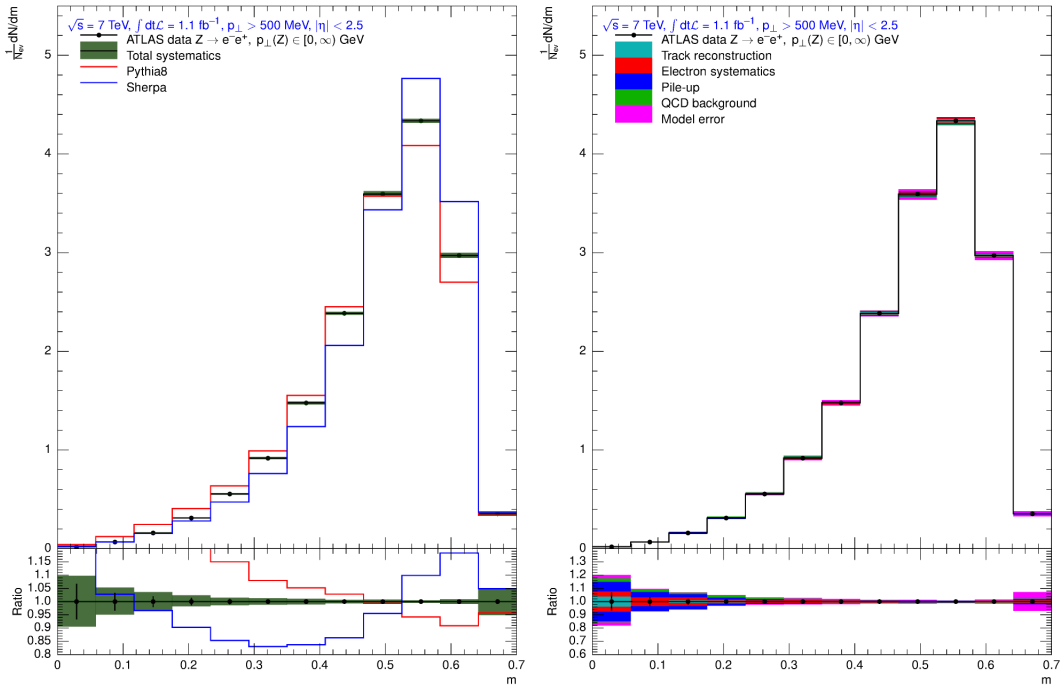

(a) Minor, $p_\perp$(Z) inclusive electron channel

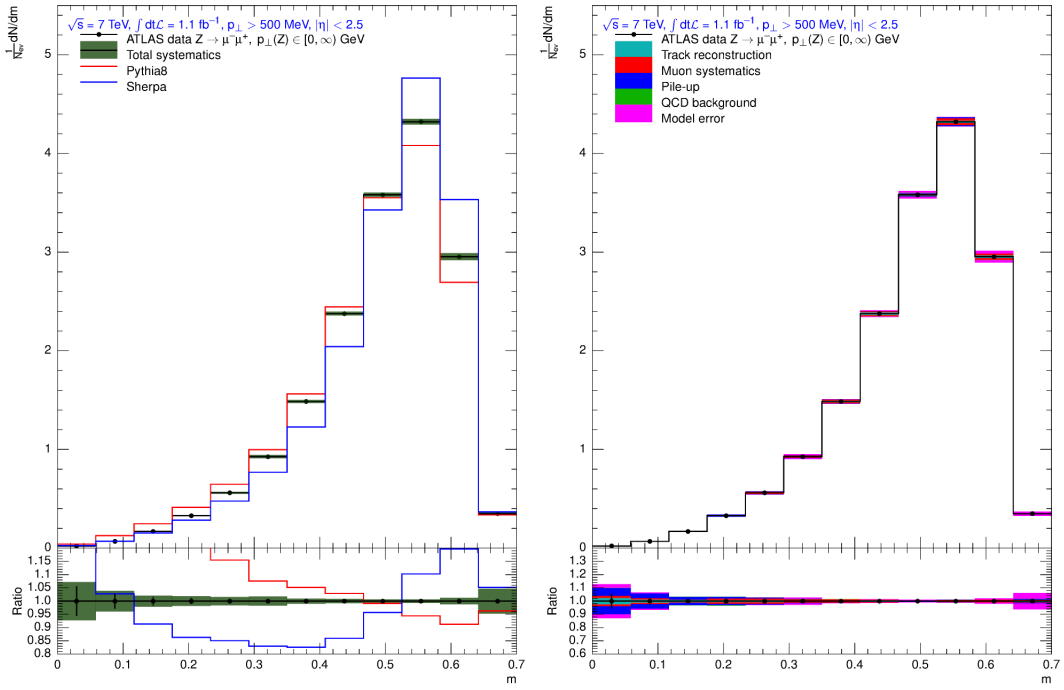

(b) Minor, $p_\perp$(Z) inclusive, muon channel

Figure C.14.: Left: Unfolded Minor distribution with total systematic uncertainties (green band) and statistical uncertainties (black). Right: break-down of systematic uncertainties.

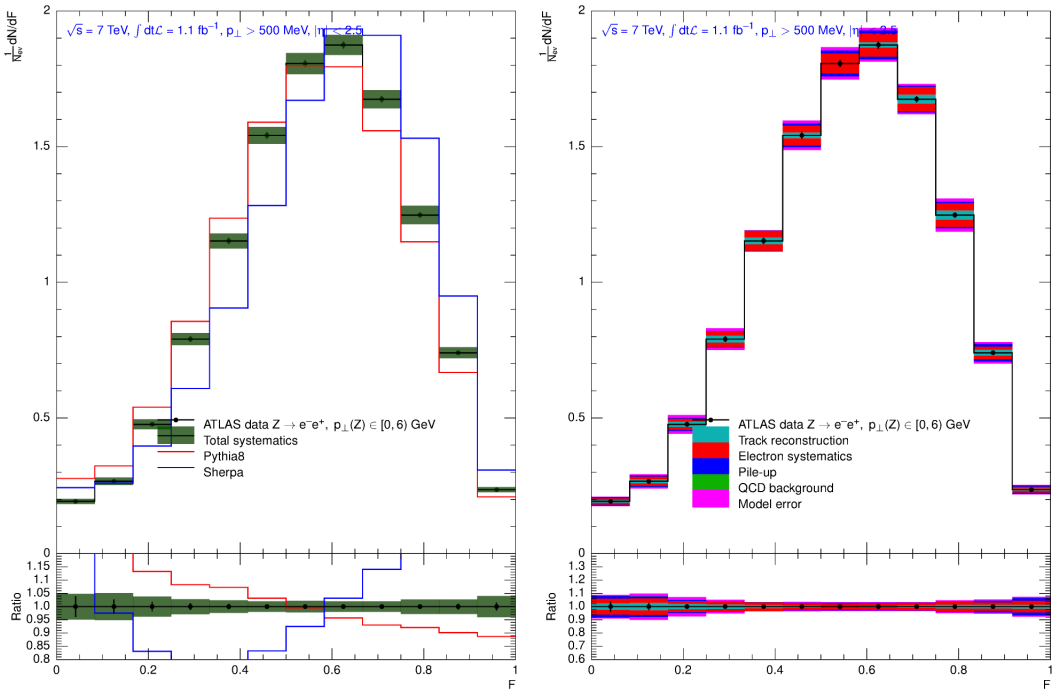

(a) F-Parameter, $p_\perp(\mathrm{Z}) < 6$ GeV, electron channel

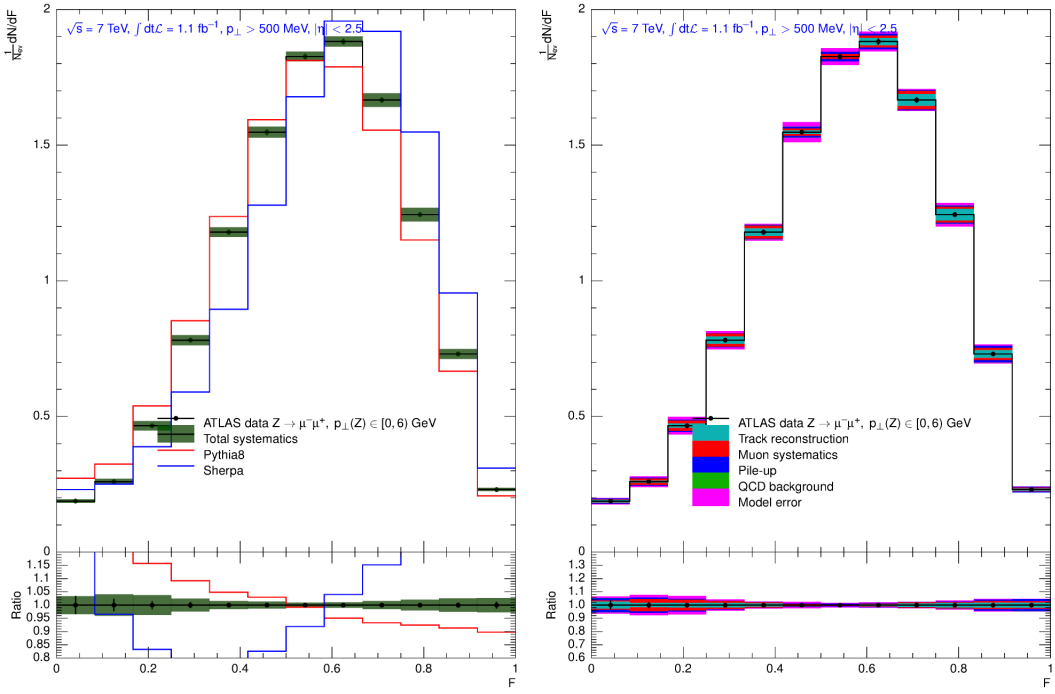

(b) F-Parameter, $p_\perp(\mathrm{Z}) < 6$ GeV, muon channel

Figure C.15.: Left: Unfolded F-Parameter distribution with total systematic uncertainties (green band) and statistical uncertainties (black). Right: break-down of systematic uncertainties.

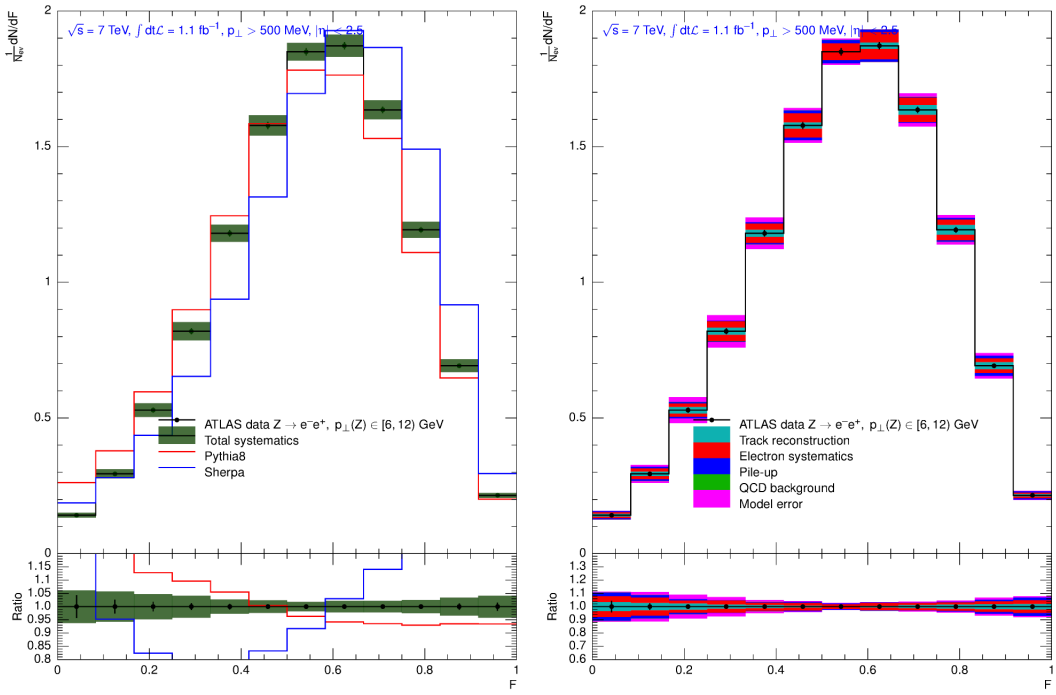

(a) F-Parameter, $p_{\perp}(\mathrm{Z}) \in [6, 12)$ GeV, electron channel

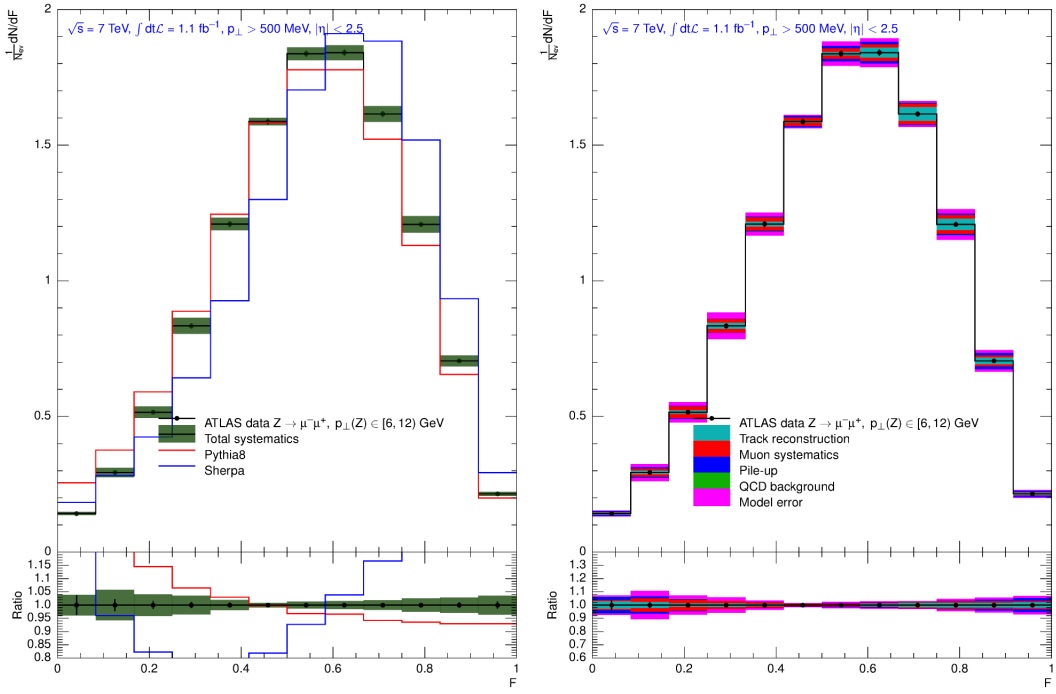

(b) F-Parameter, $p_{\perp}(\mathrm{Z}) \in [6, 12)$ GeV, muon channel

Figure C.16.: Left: Unfolded F-Parameter distribution with total systematic uncertainties (green band) and statistical uncertainties (black). Right: break-down of systematic uncertainties.

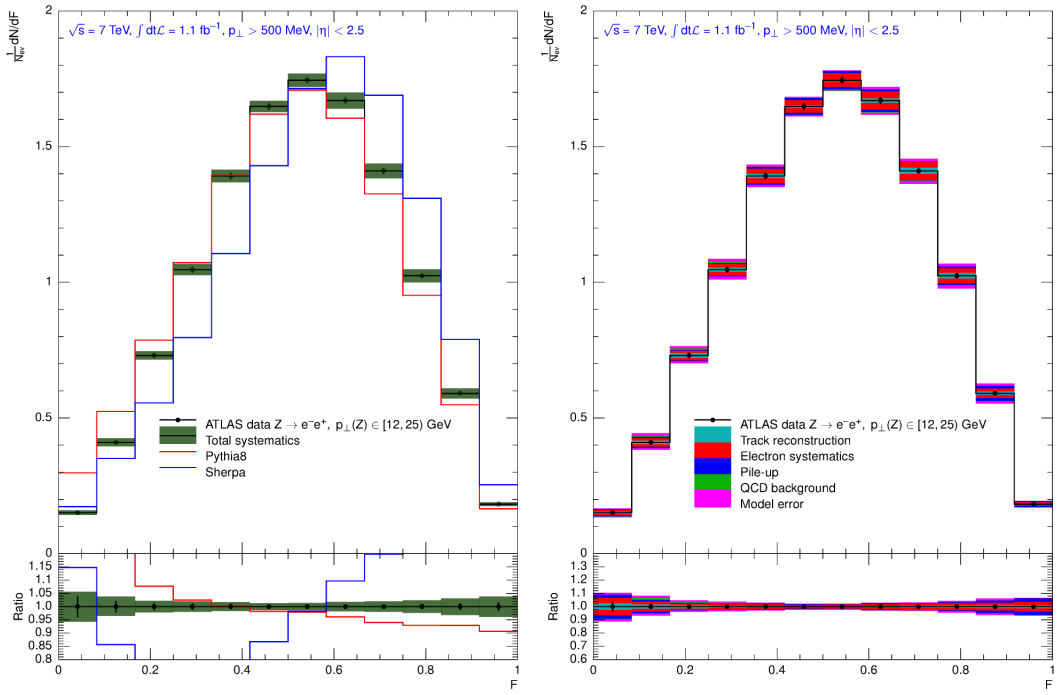

(a) F-Parameter, $p_\perp(\mathrm{Z}) \in [12, 25)$ GeV, electron channel

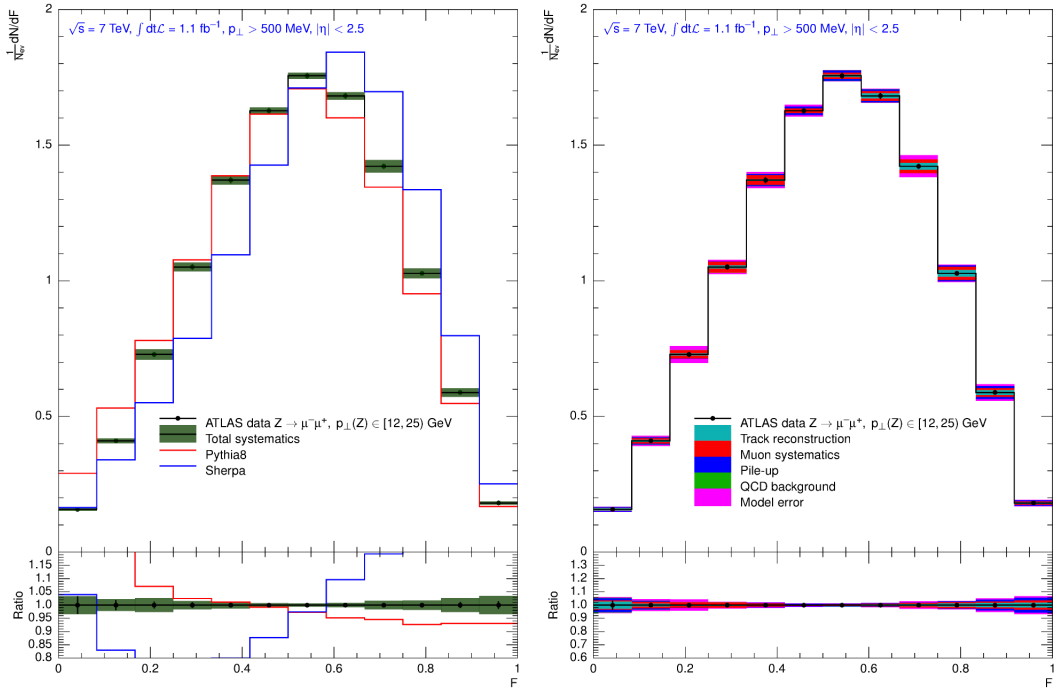

(b) F-Parameter, $p_\perp(\mathrm{Z}) \in [12, 25)$ GeV, muon channel

Figure C.17.: Left: Unfolded F-Parameter distribution with total systematic uncertainties (green band) and statistical uncertainties (black). Right: break-down of systematic uncertainties.

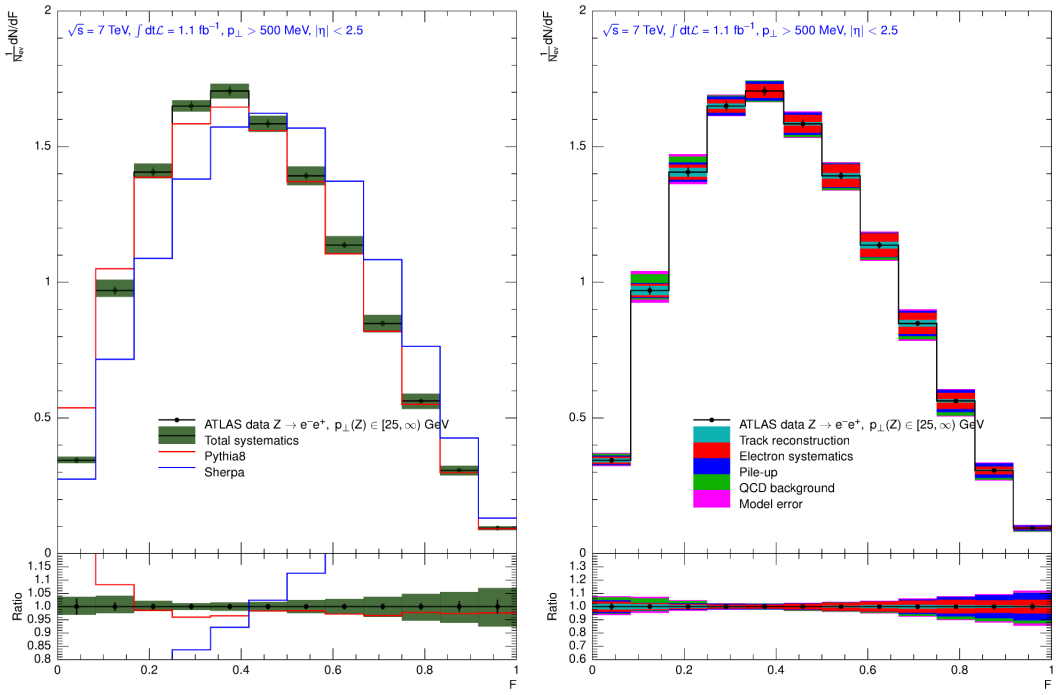

(a) F-Parameter, $p_\perp(\mathrm{Z}) > 25$ GeV, electron channel

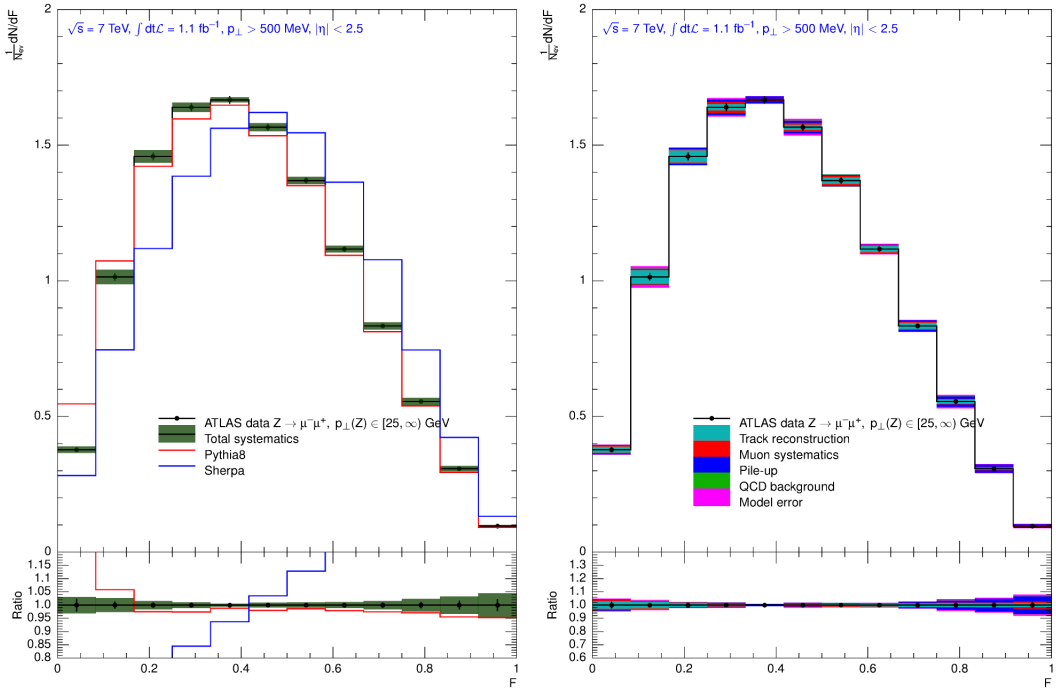

(b) F-Parameter, $p_\perp(\mathrm{Z}) > 25$ GeV, muon channel

Figure C.18.: Left: Unfolded F-Parameter distribution with total systematic uncertainties (green band) and statistical uncertainties (black). Right: break-down of systematic uncertainties.

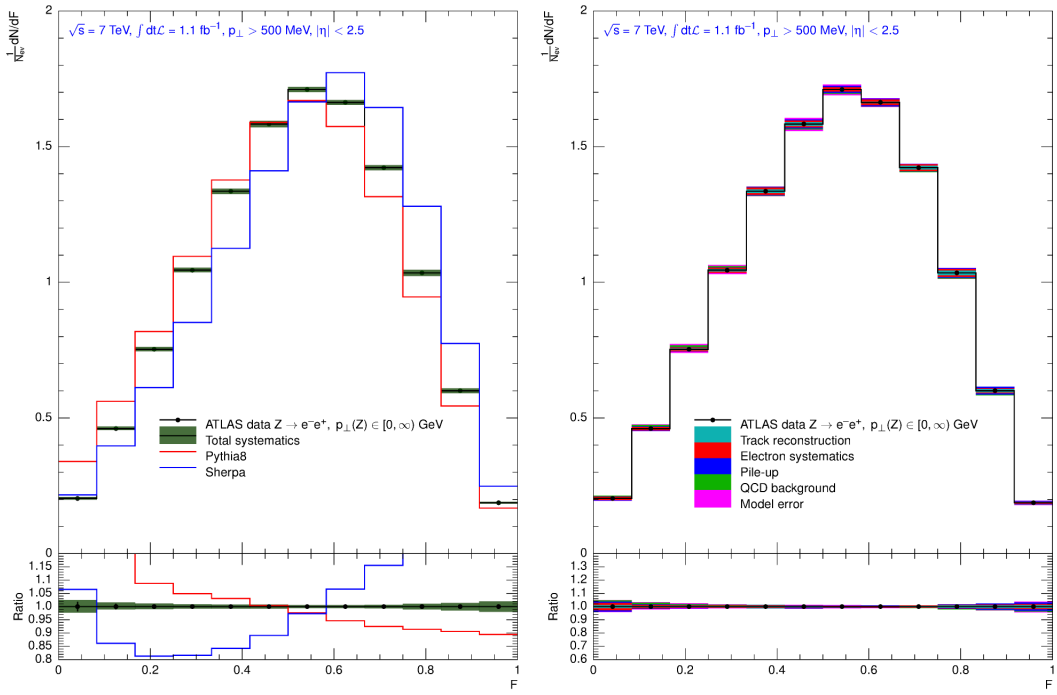

(a) F-Parameter, $p_\perp$(Z) inclusive electron channel

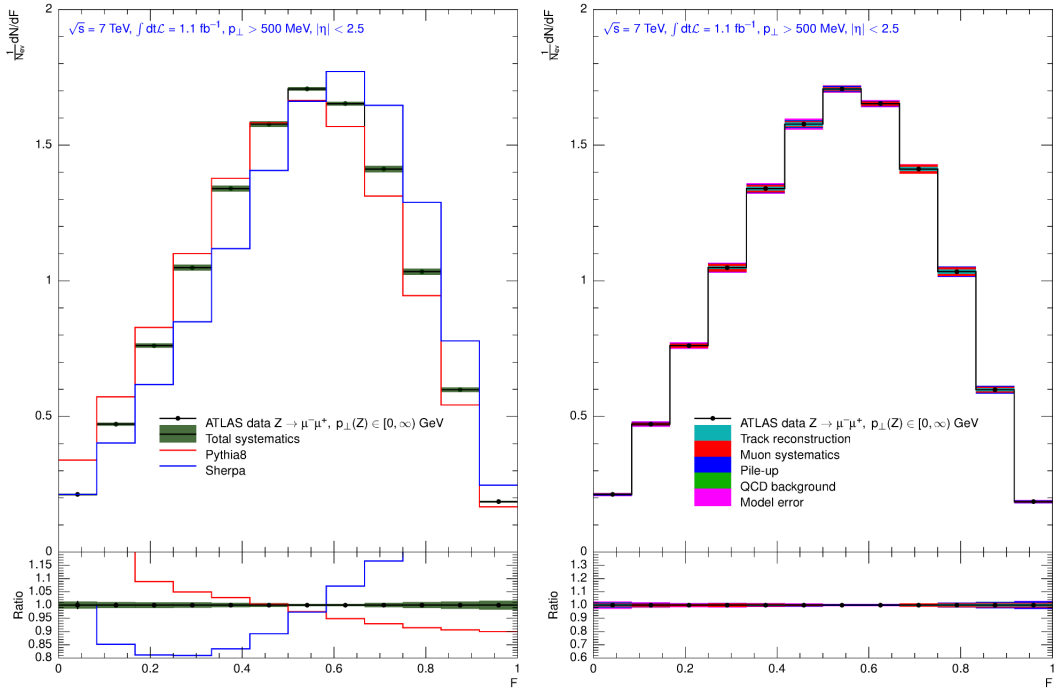

(b) F-Parameter, $p_\perp$(Z) inclusive, muon channel

Figure C.19.: Left: Unfolded F-Parameter distribution with total systematic uncertainties (green band) and statistical uncertainties (black). Right: break-down of systematic uncertainties.

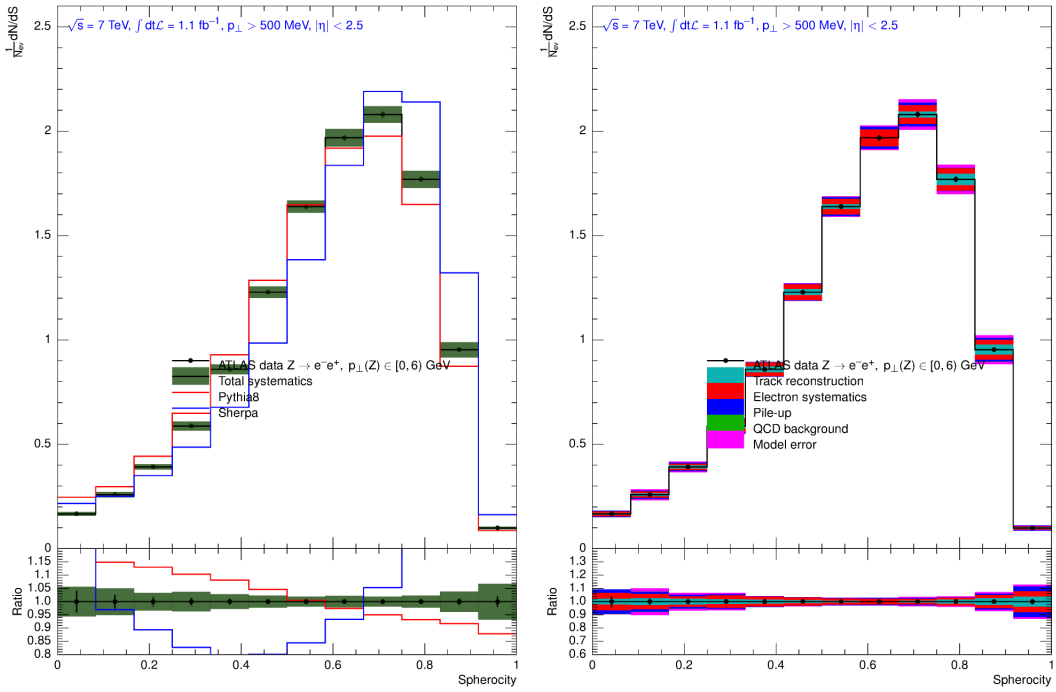

(a) Spherocity, $p_\perp(\mathrm{Z}) < 6$ GeV, electron channel

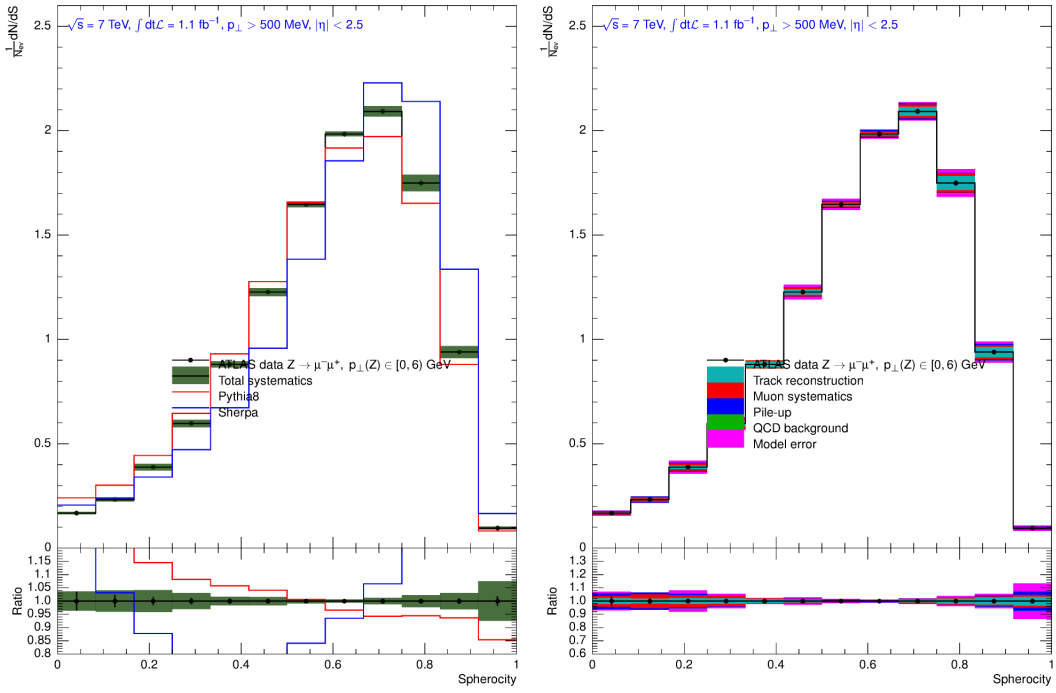

(b) Spherocity, $p_\perp(\mathrm{Z}) < 6$ GeV, muon channel

Figure C.20.: Left: Unfolded Spherocity distribution with total systematic uncertainties (green band) and statistical uncertainties (black). Right: break-down of systematic uncertainties.

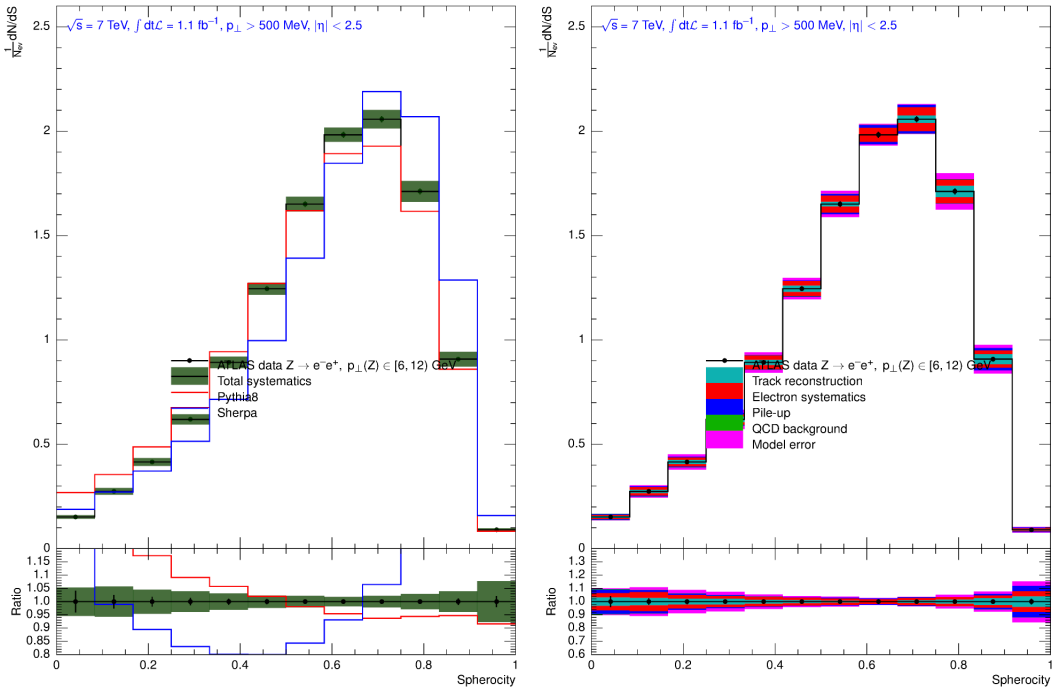

(a) Spherocity, $p_{\perp}(\mathrm{Z}) \in [6, 12)$ GeV, electron channel

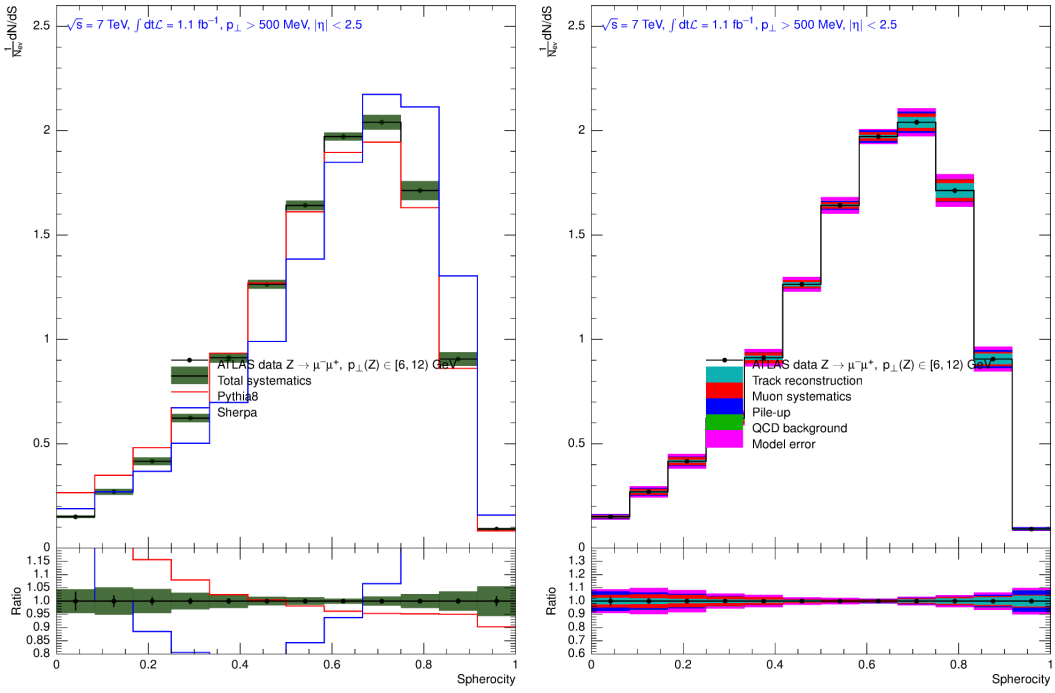

(b) Spherocity, $p_{\perp}(\mathrm{Z}) \in [6, 12)$ GeV, muon channel

Figure C.21.: Left: Unfolded Spherocity distribution with total systematic uncertainties (green band) and statistical uncertainties (black). Right: break-down of systematic uncertainties.

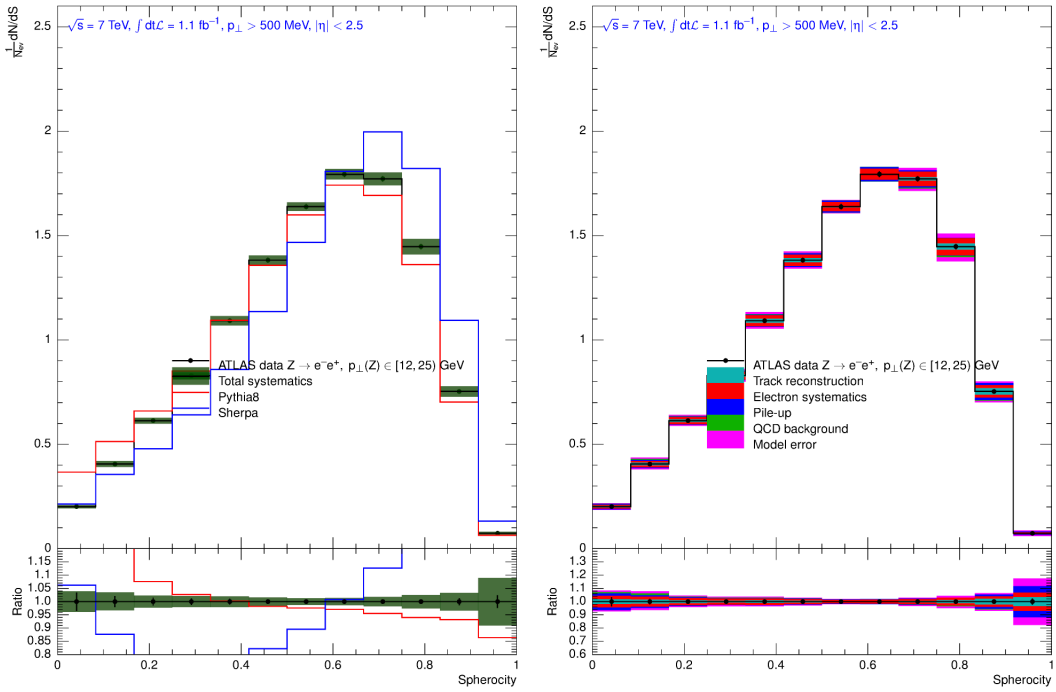

(a) Spherocity, $p_\perp(\mathrm{Z}) \in [12, 25)$ GeV, electron channel

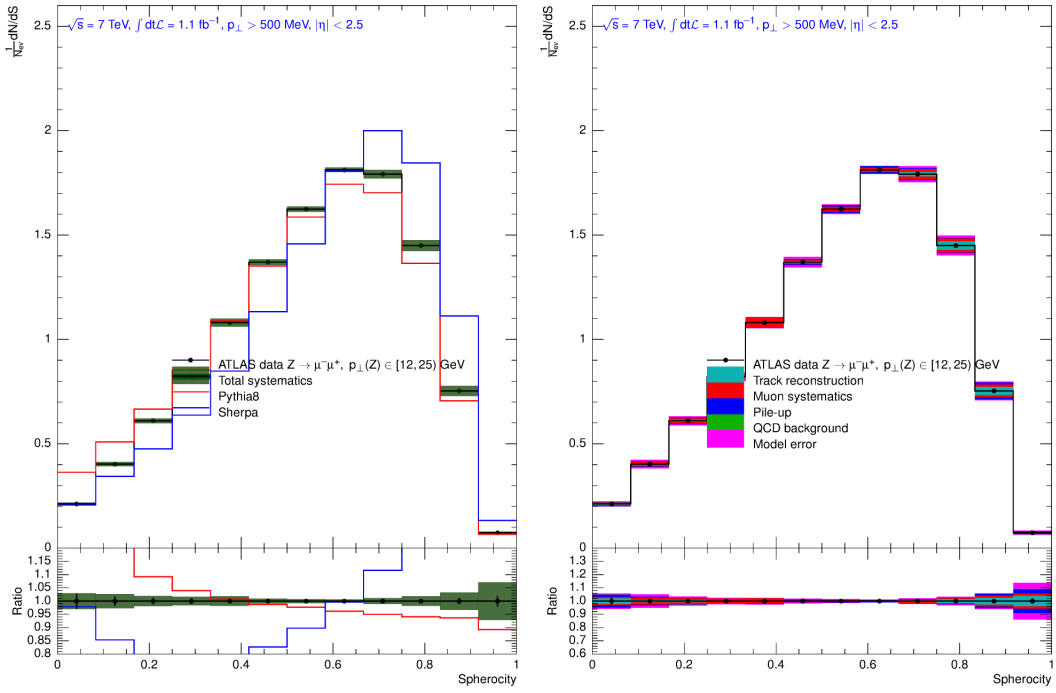

(b) Spherocity, $p_\perp(\mathrm{Z}) \in [12, 25)$ GeV, muon channel

Figure C.22.: Left: Unfolded Spherocity distribution with total systematic uncertainties (green band) and statistical uncertainties (black). Right: break-down of systematic uncertainties.

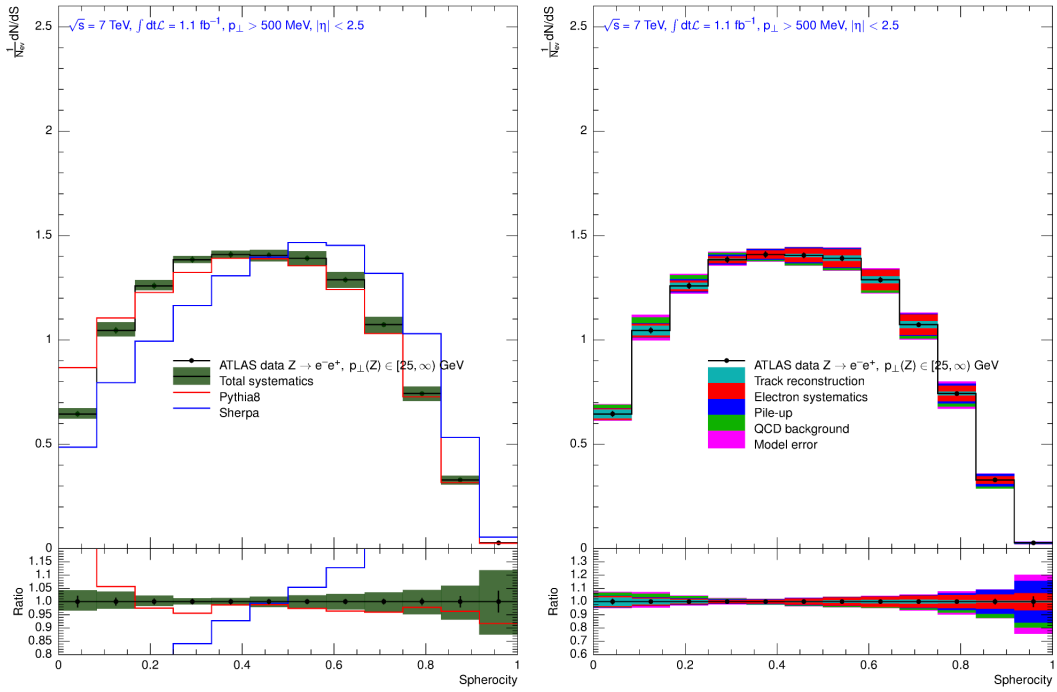

(a) Spherocity, $p_{\perp}(\mathrm{Z}) > 25$ GeV, electron channel

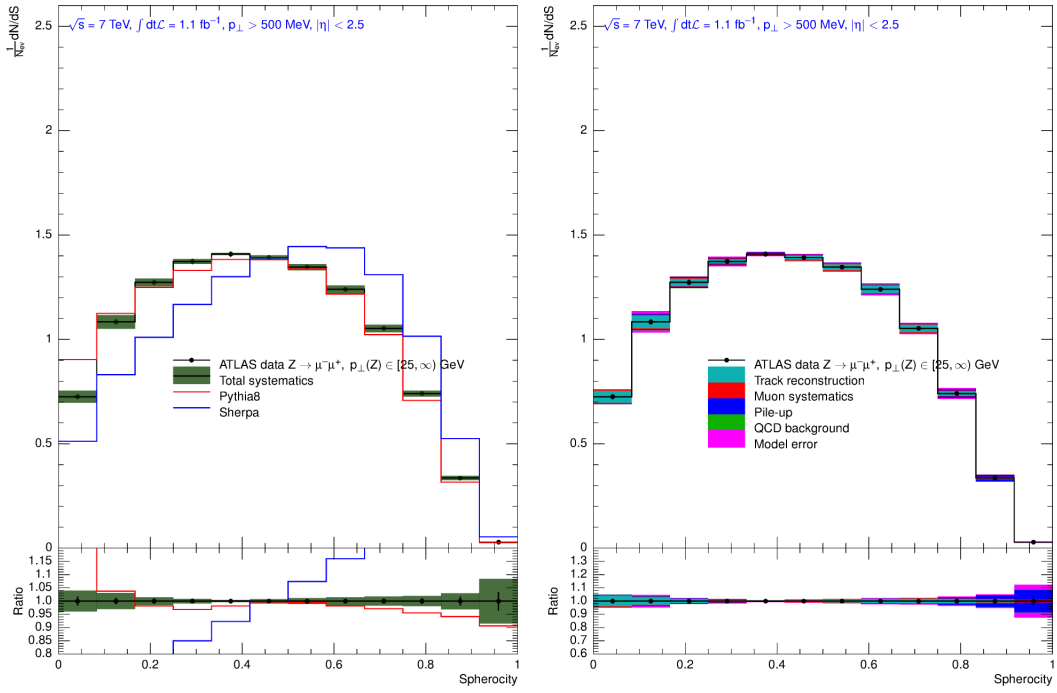

(b) Spherocity, $p_{\perp}(\mathrm{Z}) > 25$ GeV, muon channel

Figure C.23.: Left: Unfolded Spherocity distribution with total systematic uncertainties (green band) and statistical uncertainties (black). Right: break-down of systematic uncertainties.

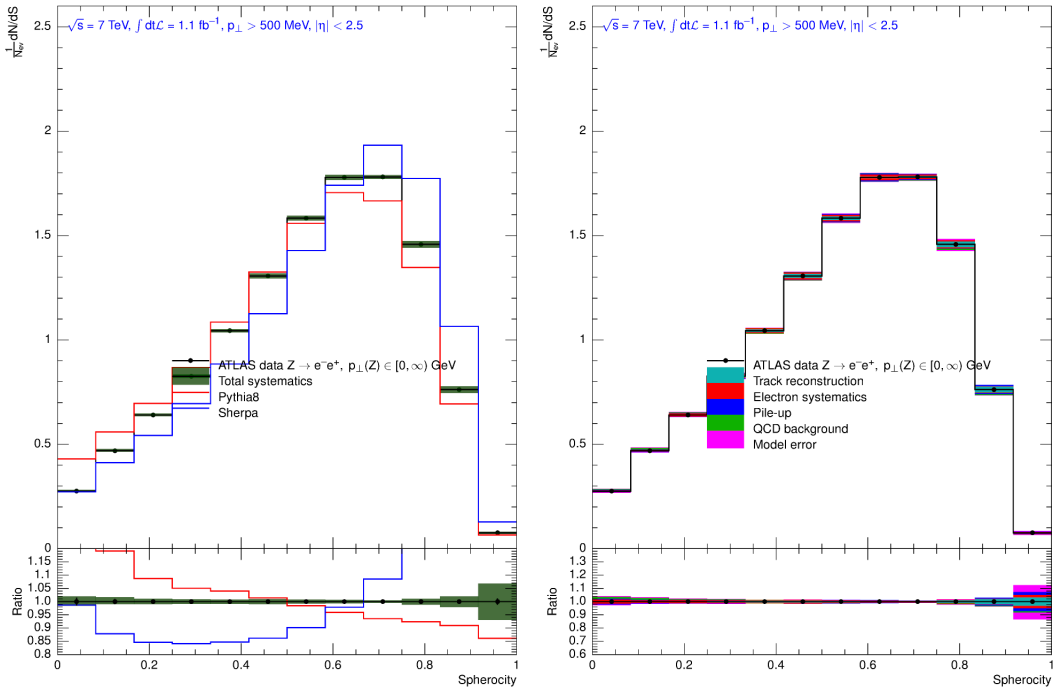

(a) Spherocity, $p_{\perp}$(Z) inclusive electron channel

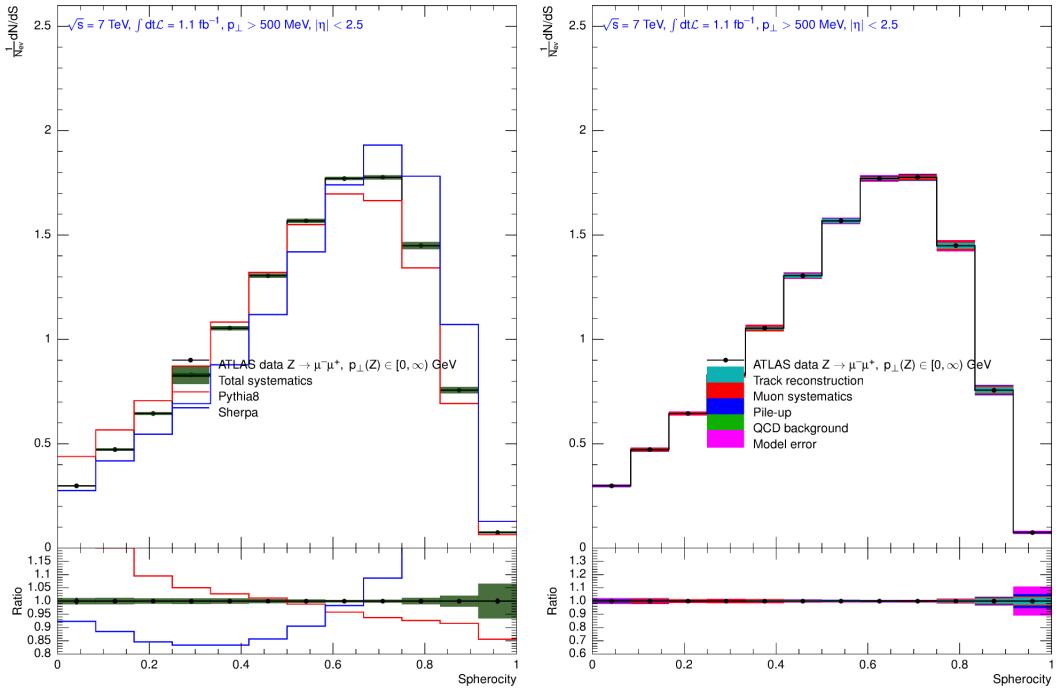

(b) Spherocity, $p_{\perp}$(Z) inclusive, muon channel

Figure C.24.: Left: Unfolded Spherocity distribution with total systematic uncertainties (green band) and statistical uncertainties (black). Right: break-down of systematic uncertainties.

Appendix D.

Data tables

The following tables give the unfolded data for all observables. First and second column define the binning. The third column contains the central values of each bin. The fourth column contains the corresponding statistical uncertainties (Chapter 12.4) and the fifth column contains the total assymetrical systematic uncertainty (Chapter 12.5) of each bin. The observable is always given in the caption of each table as are the lepton channel and the $p_\perp(\mathrm{Z})$ phase-space region.

$\mathcal{O}_{\mathrm{min}}$	$\mathcal{O}_{\mathrm{max}}$	$\frac{1}{N_{\mathrm{ev}}}\frac{\mathrm{d}N}{\mathrm{d}\mathcal{O}}$	δ_{stat}	δ_{syst}
0.000	0.083	0.203	± 0.0036	$^{+0.0050}_{-0.0045}$
0.083	0.167	0.459	± 0.0047	$^{+0.0071}_{-0.0050}$
0.167	0.250	0.750	± 0.0054	$^{+0.0087}_{-0.0070}$
0.250	0.333	1.040	± 0.0059	$^{+0.0088}_{-0.0080}$
0.333	0.417	1.330	± 0.0063	$^{+0.0097}_{-0.0098}$
0.417	0.500	1.576	± 0.0066	$^{+0.0114}_{-0.0119}$
0.500	0.583	1.703	± 0.0065	$^{+0.0095}_{-0.0098}$
0.583	0.667	1.656	± 0.0062	$^{+0.0086}_{-0.0086}$
0.667	0.750	1.416	± 0.0055	$^{+0.0090}_{-0.0092}$
0.750	0.833	1.030	± 0.0047	$^{+0.0107}_{-0.0111}$
0.833	0.917	0.598	± 0.0037	$^{+0.0084}_{-0.0087}$
0.917	1.000	0.187	± 0.0015	$^{+0.0036}_{-0.0038}$

Table D.1.: Unfolded data, $\mathcal{O}$ = F-Parameter, electron channel, $p_\perp(\mathrm{Z}) \in [0, \infty)$

$\mathcal{O}_{\text{min}}$	$\mathcal{O}_{\text{max}}$	$\frac{1}{N_{\text{ev}}}\frac{\mathrm{d}N}{\mathrm{d}\mathcal{O}}$	δ_{stat}	δ_{syst}
0.636	0.666	0.484	± 0.0044	$^{+0.0265}_{-0.0269}$
0.666	0.697	3.379	± 0.0179	$^{+0.0486}_{-0.0506}$
0.697	0.727	5.381	± 0.0203	$^{+0.0387}_{-0.0390}$
0.727	0.758	5.765	± 0.0209	$^{+0.0312}_{-0.0312}$
0.758	0.788	5.098	± 0.0198	$^{+0.0307}_{-0.0334}$
0.788	0.819	4.083	± 0.0179	$^{+0.0319}_{-0.0327}$
0.819	0.849	3.059	± 0.0158	$^{+0.0268}_{-0.0267}$
0.849	0.879	2.180	± 0.0137	$^{+0.0250}_{-0.0207}$
0.879	0.910	1.487	± 0.0118	$^{+0.0221}_{-0.0165}$
0.910	0.940	0.962	± 0.0102	$^{+0.0164}_{-0.0147}$
0.940	0.971	0.557	± 0.0085	$^{+0.0099}_{-0.0094}$
0.971	1.001	0.300	± 0.0072	$^{+0.0134}_{-0.0124}$

Table D.2.: Unfolded data, $\mathcal{O}$ = transverse thrust, electron channel, $p_\perp(\mathrm{Z}) \in [0, \infty)$

$\mathcal{O}_{\text{min}}$	$\mathcal{O}_{\text{max}}$	$\frac{1}{N_{\text{ev}}}\frac{\mathrm{d}N}{\mathrm{d}\mathcal{O}}$ [GeV]	δ_{stat}	δ_{syst}
−0.001	4.000	0.009	± 0.0001	$^{+0.0004}_{-0.0003}$
4.000	8.000	0.013	± 0.0001	$^{+0.0006}_{-0.0006}$
8.000	12.000	0.017	± 0.0001	$^{+0.0006}_{-0.0006}$
12.000	16.000	0.019	± 0.0001	$^{+0.0006}_{-0.0006}$
16.000	20.000	0.019	± 0.0001	$^{+0.0005}_{-0.0005}$
20.000	24.000	0.019	± 0.0001	$^{+0.0005}_{-0.0004}$
24.000	28.000	0.018	± 0.0001	$^{+0.0004}_{-0.0004}$
28.000	32.000	0.017	± 0.0001	$^{+0.0003}_{-0.0003}$
32.000	36.000	0.016	± 0.0001	$^{+0.0002}_{-0.0002}$
36.000	40.000	0.014	± 0.0001	$^{+0.0001}_{-0.0001}$
40.000	50.000	0.011	± 0.0001	$^{+0.0001}_{-0.0002}$
50.000	60.000	0.008	± 0.0001	$^{+0.0002}_{-0.0002}$
60.000	75.000	0.005	± 0.0000	$^{+0.0002}_{-0.0002}$
75.000	100.000	0.002	± 0.0000	$^{+0.0001}_{-0.0002}$

Table D.3.: Unfolded data, $\mathcal{O} = \sum p_\perp$, electron channel, $p_\perp(\mathrm{Z}) \in [0, \infty)$

$\mathcal{O}_{\text{min}}$	$\mathcal{O}_{\text{max}}$	$\frac{1}{N_{\text{ev}}}\frac{\text{d}N}{\text{d}\mathcal{O}}$	δ_{stat}	δ_{syst}
0.000	0.058	0.019	± 0.0013	$^{+0.0018}_{-0.0018}$
0.058	0.117	0.067	± 0.0022	$^{+0.0036}_{-0.0033}$
0.117	0.175	0.158	± 0.0032	$^{+0.0057}_{-0.0055}$
0.175	0.233	0.309	± 0.0042	$^{+0.0073}_{-0.0055}$
0.233	0.292	0.551	± 0.0053	$^{+0.0083}_{-0.0074}$
0.292	0.350	0.913	± 0.0067	$^{+0.0114}_{-0.0104}$
0.350	0.408	1.471	± 0.0084	$^{+0.0152}_{-0.0151}$
0.408	0.467	2.375	± 0.0108	$^{+0.0155}_{-0.0155}$
0.467	0.525	3.579	± 0.0133	$^{+0.0282}_{-0.0291}$
0.525	0.583	4.317	± 0.0147	$^{+0.0200}_{-0.0212}$
0.583	0.642	2.959	± 0.0132	$^{+0.0258}_{-0.0260}$
0.642	0.700	0.352	± 0.0031	$^{+0.0179}_{-0.0178}$

Table D.4.: Unfolded data, $\mathcal{O}$ = transverse minor, electron channel, $p_{\perp}(\text{Z}) \in [0, \infty)$

$\mathcal{O}_{\text{min}}$	$\mathcal{O}_{\text{max}}$	$\frac{1}{N_{\text{ev}}}\frac{\text{d}N}{\text{d}\mathcal{O}}$	δ_{stat}	δ_{syst}
0.000	0.083	0.274	± 0.0041	$^{+0.0055}_{-0.0042}$
0.083	0.167	0.467	± 0.0045	$^{+0.0079}_{-0.0046}$
0.167	0.250	0.637	± 0.0047	$^{+0.0067}_{-0.0057}$
0.250	0.333	0.823	± 0.0050	$^{+0.0074}_{-0.0072}$
0.333	0.417	1.039	± 0.0054	$^{+0.0082}_{-0.0083}$
0.417	0.500	1.301	± 0.0058	$^{+0.0120}_{-0.0122}$
0.500	0.583	1.576	± 0.0063	$^{+0.0117}_{-0.0117}$
0.583	0.667	1.771	± 0.0066	$^{+0.0118}_{-0.0117}$
0.667	0.750	1.773	± 0.0066	$^{+0.0084}_{-0.0087}$
0.750	0.833	1.452	± 0.0062	$^{+0.0154}_{-0.0164}$
0.833	0.917	0.759	± 0.0049	$^{+0.0152}_{-0.0159}$
0.917	1.000	0.075	± 0.0009	$^{+0.0051}_{-0.0052}$

Table D.5.: Unfolded data, $\mathcal{O}$ = Spherocity, electron channel, $p_{\perp}(\text{Z}) \in [0, \infty)$

$\mathcal{O}_{\text{min}}$	$\mathcal{O}_{\text{max}}$	$\frac{1}{N_{\text{ev}}}\frac{\mathrm{d}N}{\mathrm{d}\mathcal{O}}$	δ_{stat}	δ_{syst}
−0.500	1.500	0.003	$\pm$ 0.0001	$^{+0.0002}_{-0.0002}$
1.500	3.500	0.008	$\pm$ 0.0001	$^{+0.0004}_{-0.0004}$
3.500	5.500	0.012	$\pm$ 0.0002	$^{+0.0005}_{-0.0005}$
5.500	7.500	0.016	$\pm$ 0.0002	$^{+0.0007}_{-0.0006}$
7.500	9.500	0.018	$\pm$ 0.0002	$^{+0.0008}_{-0.0007}$
9.500	12.500	0.021	$\pm$ 0.0002	$^{+0.0008}_{-0.0008}$
12.500	15.500	0.023	$\pm$ 0.0002	$^{+0.0008}_{-0.0008}$
15.500	20.500	0.025	$\pm$ 0.0002	$^{+0.0007}_{-0.0007}$
20.500	25.500	0.024	$\pm$ 0.0002	$^{+0.0005}_{-0.0005}$
25.500	30.500	0.022	$\pm$ 0.0001	$^{+0.0003}_{-0.0003}$
30.500	35.500	0.019	$\pm$ 0.0001	$^{+0.0002}_{-0.0002}$
35.500	40.500	0.015	$\pm$ 0.0001	$^{+0.0003}_{-0.0003}$
40.500	45.500	0.012	$\pm$ 0.0001	$^{+0.0003}_{-0.0003}$
45.500	50.500	0.009	$\pm$ 0.0001	$^{+0.0004}_{-0.0004}$
50.500	60.500	0.006	$\pm$ 0.0001	$^{+0.0004}_{-0.0004}$
60.500	75.500	0.002	$\pm$ 0.0000	$^{+0.0002}_{-0.0003}$
75.500	100.500	0.001	$\pm$ 0.0000	$^{+0.0001}_{-0.0001}$

Table D.6.: Unfolded data, $\mathcal{O} = N_{\text{ch}}$, electron channel, $p_{\perp}(\text{Z}) \in [0, \infty)$

$\mathcal{O}_{\text{min}}$	$\mathcal{O}_{\text{max}}$	$\frac{1}{N_{\text{ev}}}\frac{\mathrm{d}N}{\mathrm{d}\mathcal{O}}$	δ_{stat}	δ_{syst}
−0.001	4.000	0.037	$\pm$ 0.0002	$^{+0.0016}_{-0.0016}$
4.000	8.000	0.050	$\pm$ 0.0003	$^{+0.0017}_{-0.0017}$
8.000	12.000	0.046	$\pm$ 0.0002	$^{+0.0007}_{-0.0007}$
12.000	16.000	0.036	$\pm$ 0.0002	$^{+0.0002}_{-0.0002}$
16.000	20.000	0.026	$\pm$ 0.0002	$^{+0.0003}_{-0.0003}$
20.000	24.000	0.018	$\pm$ 0.0002	$^{+0.0005}_{-0.0005}$
24.000	28.000	0.012	$\pm$ 0.0001	$^{+0.0005}_{-0.0005}$
28.000	32.000	0.008	$\pm$ 0.0001	$^{+0.0005}_{-0.0005}$
32.000	36.000	0.005	$\pm$ 0.0001	$^{+0.0004}_{-0.0004}$
36.000	40.000	0.004	$\pm$ 0.0001	$^{+0.0004}_{-0.0004}$
40.000	50.000	0.002	$\pm$ 0.0000	$^{+0.0003}_{-0.0003}$
50.000	60.000	0.001	$\pm$ 0.0000	$^{+0.0003}_{-0.0003}$

Table D.7.: Unfolded data, $\mathcal{O}$ = Beamthrust, electron channel, $p_\perp(\mathrm{Z}) \in [0, \infty)$

$\mathcal{O}_{\text{min}}$	$\mathcal{O}_{\text{max}}$	$\frac{1}{N_{\text{ev}}}\frac{\text{d}N}{\text{d}\mathcal{O}}$	δ_{stat}	δ_{syst}
0.000	0.083	0.175	± 0.0068	$^{+0.0084}_{-0.0085}$
0.083	0.167	0.242	± 0.0065	$^{+0.0122}_{-0.0123}$
0.167	0.250	0.433	± 0.0075	$^{+0.0164}_{-0.0165}$
0.250	0.333	0.719	± 0.0091	$^{+0.0203}_{-0.0203}$
0.333	0.417	1.048	± 0.0102	$^{+0.0251}_{-0.0251}$
0.417	0.500	1.401	± 0.0114	$^{+0.0281}_{-0.0280}$
0.500	0.583	1.642	± 0.0117	$^{+0.0354}_{-0.0352}$
0.583	0.667	1.705	± 0.0115	$^{+0.0335}_{-0.0334}$
0.667	0.750	1.523	± 0.0106	$^{+0.0304}_{-0.0304}$
0.750	0.833	1.135	± 0.0093	$^{+0.0309}_{-0.0309}$
0.833	0.917	0.673	± 0.0074	$^{+0.0181}_{-0.0183}$
0.917	1.000	0.214	± 0.0031	$^{+0.0085}_{-0.0086}$

Table D.8.: Unfolded data, $\mathcal{O}$ = F-Parameter, electron channel, $p_\perp(\text{Z}) \in [0, 6)$

$\mathcal{O}_{\text{min}}$	$\mathcal{O}_{\text{max}}$	$\frac{1}{N_{\text{ev}}}\frac{\text{d}N}{\text{d}\mathcal{O}}$	δ_{stat}	δ_{syst}
0.636	0.666	0.556	± 0.0090	$^{+0.0293}_{-0.0295}$
0.666	0.697	3.706	± 0.0353	$^{+0.1089}_{-0.1090}$
0.697	0.727	5.674	± 0.0388	$^{+0.1230}_{-0.1228}$
0.727	0.758	5.764	± 0.0382	$^{+0.1232}_{-0.1228}$
0.758	0.788	4.729	± 0.0348	$^{+0.0991}_{-0.0989}$
0.788	0.819	3.469	± 0.0302	$^{+0.0775}_{-0.0774}$
0.819	0.849	2.338	± 0.0252	$^{+0.0563}_{-0.0563}$
0.849	0.879	1.482	± 0.0208	$^{+0.0489}_{-0.0490}$
0.879	0.910	0.904	± 0.0170	$^{+0.0387}_{-0.0389}$
0.910	0.940	0.547	± 0.0145	$^{+0.0278}_{-0.0281}$
0.940	0.971	0.403	± 0.0146	$^{+0.0228}_{-0.0230}$
0.971	1.001	0.326	± 0.0154	$^{+0.0185}_{-0.0188}$

Table D.9.: Unfolded data, $\mathcal{O}$ = transverse thrust, electron channel, $p_\perp(\text{Z}) \in [0, 6)$

$\mathcal{O}_{\text{min}}$	$\mathcal{O}_{\text{max}}$	$\frac{1}{N_{\text{ev}}}\frac{\mathrm{d}N}{\mathrm{d}\mathcal{O}}$ [GeV]	δ_{stat}	δ_{syst}
−0.001	4.000	0.019	± 0.0003	$^{+0.0006}_{-0.0006}$
4.000	8.000	0.022	± 0.0003	$^{+0.0009}_{-0.0009}$
8.000	12.000	0.024	± 0.0003	$^{+0.0008}_{-0.0008}$
12.000	16.000	0.023	± 0.0003	$^{+0.0006}_{-0.0006}$
16.000	20.000	0.022	± 0.0003	$^{+0.0006}_{-0.0006}$
20.000	24.000	0.020	± 0.0002	$^{+0.0005}_{-0.0005}$
24.000	28.000	0.017	± 0.0002	$^{+0.0004}_{-0.0004}$
28.000	32.000	0.015	± 0.0002	$^{+0.0003}_{-0.0003}$
32.000	36.000	0.013	± 0.0002	$^{+0.0004}_{-0.0004}$
36.000	40.000	0.011	± 0.0002	$^{+0.0003}_{-0.0003}$
40.000	50.000	0.008	± 0.0001	$^{+0.0003}_{-0.0003}$
50.000	60.000	0.004	± 0.0001	$^{+0.0003}_{-0.0003}$
60.000	75.000	0.002	± 0.0000	$^{+0.0002}_{-0.0002}$
75.000	100.000	0.001	± 0.0000	$^{+0.0001}_{-0.0001}$

Table D.10.: Unfolded data, $\mathcal{O} = \sum p_\perp$, electron channel, $p_\perp(\mathrm{Z}) \in [0, 6)$

$\mathcal{O}_{\text{min}}$	$\mathcal{O}_{\text{max}}$	$\frac{1}{N_{\text{ev}}}\frac{\mathrm{d}N}{\mathrm{d}\mathcal{O}}$	δ_{stat}	δ_{syst}
0.000	0.058	0.025	± 0.0030	$^{+0.0042}_{-0.0043}$
0.058	0.117	0.045	± 0.0038	$^{+0.0060}_{-0.0060}$
0.117	0.175	0.072	± 0.0043	$^{+0.0074}_{-0.0075}$
0.175	0.233	0.136	± 0.0054	$^{+0.0111}_{-0.0112}$
0.233	0.292	0.272	± 0.0073	$^{+0.0154}_{-0.0155}$
0.292	0.350	0.512	± 0.0093	$^{+0.0200}_{-0.0202}$
0.350	0.408	0.991	± 0.0128	$^{+0.0340}_{-0.0341}$
0.408	0.467	1.961	± 0.0181	$^{+0.0467}_{-0.0467}$
0.467	0.525	3.428	± 0.0242	$^{+0.0774}_{-0.0772}$
0.525	0.583	4.533	± 0.0278	$^{+0.0867}_{-0.0864}$
0.583	0.642	3.227	± 0.0259	$^{+0.0568}_{-0.0568}$
0.642	0.700	0.383	± 0.0059	$^{+0.0200}_{-0.0200}$

Table D.11.: Unfolded data, $\mathcal{O}$ = transverse minor, electron channel, $p_\perp(\mathrm{Z}) \in [0, 6)$

$\mathcal{O}_{\text{min}}$	$\mathcal{O}_{\text{max}}$	$\frac{1}{N_{\text{ev}}} \frac{\text{d}N}{\text{d}\mathcal{O}}$	δ_{stat}	δ_{syst}
0.000	0.083	0.152	$\pm$ 0.0061	$^{+0.0084}_{-0.0085}$
0.083	0.167	0.235	$\pm$ 0.0061	$^{+0.0119}_{-0.0119}$
0.167	0.250	0.356	$\pm$ 0.0065	$^{+0.0119}_{-0.0119}$
0.250	0.333	0.534	$\pm$ 0.0073	$^{+0.0195}_{-0.0196}$
0.333	0.417	0.781	$\pm$ 0.0085	$^{+0.0213}_{-0.0214}$
0.417	0.500	1.118	$\pm$ 0.0100	$^{+0.0252}_{-0.0252}$
0.500	0.583	1.490	$\pm$ 0.0113	$^{+0.0272}_{-0.0271}$
0.583	0.667	1.790	$\pm$ 0.0122	$^{+0.0387}_{-0.0385}$
0.667	0.750	1.892	$\pm$ 0.0126	$^{+0.0359}_{-0.0357}$
0.750	0.833	1.609	$\pm$ 0.0122	$^{+0.0369}_{-0.0369}$
0.833	0.917	0.867	$\pm$ 0.0098	$^{+0.0331}_{-0.0332}$
0.917	1.000	0.090	$\pm$ 0.0018	$^{+0.0060}_{-0.0061}$

Table D.12.: Unfolded data, $\mathcal{O}$ = Spherocity, electron channel, $p_{\perp}(\text{Z}) \in [0, 6)$

$\mathcal{O}_{\text{min}}$	$\mathcal{O}_{\text{max}}$	$\frac{1}{N_{\text{ev}}}\frac{\mathrm{d}N}{\mathrm{d}\mathcal{O}}$	δ_{stat}	δ_{syst}
−0.500	1.500	0.008	± 0.0003	$^{+0.0004}_{-0.0004}$
1.500	3.500	0.017	± 0.0003	$^{+0.0008}_{-0.0008}$
3.500	5.500	0.020	± 0.0003	$^{+0.0008}_{-0.0008}$
5.500	7.500	0.022	± 0.0003	$^{+0.0009}_{-0.0009}$
7.500	9.500	0.024	± 0.0003	$^{+0.0009}_{-0.0008}$
9.500	12.500	0.025	± 0.0003	$^{+0.0011}_{-0.0011}$
12.500	15.500	0.026	± 0.0003	$^{+0.0009}_{-0.0009}$
15.500	20.500	0.024	± 0.0003	$^{+0.0007}_{-0.0007}$
20.500	25.500	0.021	± 0.0002	$^{+0.0005}_{-0.0005}$
25.500	30.500	0.018	± 0.0002	$^{+0.0004}_{-0.0004}$
30.500	35.500	0.014	± 0.0002	$^{+0.0004}_{-0.0004}$
35.500	40.500	0.011	± 0.0001	$^{+0.0005}_{-0.0005}$
40.500	45.500	0.008	± 0.0001	$^{+0.0003}_{-0.0003}$
45.500	50.500	0.006	± 0.0001	$^{+0.0004}_{-0.0004}$
50.500	60.500	0.003	± 0.0001	$^{+0.0003}_{-0.0004}$
60.500	75.500	0.001	± 0.0000	$^{+0.0002}_{-0.0002}$
75.500	100.500	0.000	± 0.0000	$^{+0.0001}_{-0.0001}$

Table D.13.: Unfolded data, $\mathcal{O} = N_{\text{ch}}$, electron channel, $p_{\perp}(\text{Z}) \in [0, 6)$

$\mathcal{O}_{\text{min}}$	$\mathcal{O}_{\text{max}}$	$\frac{1}{N_{\text{ev}}}\frac{\mathrm{d}N}{\mathrm{d}\mathcal{O}}$	δ_{stat}	δ_{syst}
−0.001	4.000	0.065	$\pm$ 0.0006	$^{+0.0019}_{-0.0019}$
4.000	8.000	0.063	$\pm$ 0.0005	$^{+0.0014}_{-0.0014}$
8.000	12.000	0.048	$\pm$ 0.0004	$^{+0.0003}_{-0.0003}$
12.000	16.000	0.031	$\pm$ 0.0003	$^{+0.0007}_{-0.0007}$
16.000	20.000	0.019	$\pm$ 0.0002	$^{+0.0005}_{-0.0005}$
20.000	24.000	0.011	$\pm$ 0.0002	$^{+0.0006}_{-0.0006}$
24.000	28.000	0.006	$\pm$ 0.0001	$^{+0.0004}_{-0.0004}$
28.000	32.000	0.003	$\pm$ 0.0001	$^{+0.0004}_{-0.0004}$
32.000	36.000	0.002	$\pm$ 0.0001	$^{+0.0002}_{-0.0003}$
36.000	40.000	0.001	$\pm$ 0.0001	$^{+0.0002}_{-0.0002}$
40.000	50.000	0.000	$\pm$ 0.0000	$^{+0.0001}_{-0.0001}$
50.000	60.000	0.000	$\pm$ 0.0000	$^{+0.0000}_{-0.0000}$

Table D.14.: Unfolded data, $\mathcal{O}$ = Beamthrust, electron channel, $p_\perp(\mathrm{Z}) \in [0, 6)$

$\mathcal{O}_{\text{min}}$	$\mathcal{O}_{\text{max}}$	$\frac{1}{N_{\text{ev}}}\frac{\mathrm{d}N}{\mathrm{d}\mathcal{O}}$	δ_{stat}	δ_{syst}
0.000	0.083	0.118	± 0.0050	$^{+0.0072}_{-0.0073}$
0.083	0.167	0.244	± 0.0063	$^{+0.0139}_{-0.0140}$
0.167	0.250	0.439	± 0.0076	$^{+0.0208}_{-0.0209}$
0.250	0.333	0.680	± 0.0087	$^{+0.0281}_{-0.0281}$
0.333	0.417	0.980	± 0.0099	$^{+0.0262}_{-0.0262}$
0.417	0.500	1.310	± 0.0109	$^{+0.0314}_{-0.0312}$
0.500	0.583	1.535	± 0.0113	$^{+0.0267}_{-0.0265}$
0.583	0.667	1.553	± 0.0109	$^{+0.0340}_{-0.0339}$
0.667	0.750	1.357	± 0.0100	$^{+0.0291}_{-0.0291}$
0.750	0.833	0.991	± 0.0086	$^{+0.0243}_{-0.0243}$
0.833	0.917	0.575	± 0.0068	$^{+0.0195}_{-0.0196}$
0.917	1.000	0.178	± 0.0027	$^{+0.0073}_{-0.0074}$

Table D.15.: Unfolded data, $\mathcal{O}$ = F-Parameter, electron channel, $p_\perp(\mathrm{Z}) \in [6, 12)$

$\mathcal{O}_{\text{min}}$	$\mathcal{O}_{\text{max}}$	$\frac{1}{N_{\text{ev}}}\frac{\mathrm{d}N}{\mathrm{d}\mathcal{O}}$	δ_{stat}	δ_{syst}
0.636	0.666	0.472	± 0.0080	$^{+0.0279}_{-0.0280}$
0.666	0.697	3.260	± 0.0330	$^{+0.1028}_{-0.1028}$
0.697	0.727	5.115	± 0.0366	$^{+0.1135}_{-0.1132}$
0.727	0.758	5.299	± 0.0364	$^{+0.1044}_{-0.1041}$
0.758	0.788	4.430	± 0.0335	$^{+0.0866}_{-0.0865}$
0.788	0.819	3.202	± 0.0287	$^{+0.0745}_{-0.0745}$
0.819	0.849	2.152	± 0.0239	$^{+0.0710}_{-0.0710}$
0.849	0.879	1.393	± 0.0197	$^{+0.0626}_{-0.0627}$
0.879	0.910	0.894	± 0.0167	$^{+0.0427}_{-0.0429}$
0.910	0.940	0.559	± 0.0144	$^{+0.0319}_{-0.0321}$
0.940	0.971	0.310	± 0.0115	$^{+0.0233}_{-0.0234}$
0.971	1.001	0.204	± 0.0109	$^{+0.0151}_{-0.0152}$

Table D.16.: Unfolded data, $\mathcal{O}$ = transverse thrust, electron channel, $p_\perp(\mathrm{Z}) \in [6, 12)$

$\mathcal{O}_{\text{min}}$	$\mathcal{O}_{\text{max}}$	$\frac{1}{N_{\text{ev}}}\frac{\mathrm{d}N}{\mathrm{d}\mathcal{O}}$ [GeV]	δ_{stat}	δ_{syst}
−0.001	4.000	0.006	± 0.0002	$^{+0.0005}_{-0.0005}$
4.000	8.000	0.015	± 0.0002	$^{+0.0008}_{-0.0008}$
8.000	12.000	0.018	± 0.0002	$^{+0.0008}_{-0.0008}$
12.000	16.000	0.020	± 0.0002	$^{+0.0008}_{-0.0008}$
16.000	20.000	0.020	± 0.0002	$^{+0.0006}_{-0.0006}$
20.000	24.000	0.019	± 0.0002	$^{+0.0004}_{-0.0004}$
24.000	28.000	0.017	± 0.0002	$^{+0.0003}_{-0.0003}$
28.000	32.000	0.016	± 0.0002	$^{+0.0004}_{-0.0004}$
32.000	36.000	0.014	± 0.0002	$^{+0.0003}_{-0.0003}$
36.000	40.000	0.012	± 0.0002	$^{+0.0004}_{-0.0004}$
40.000	50.000	0.008	± 0.0001	$^{+0.0003}_{-0.0003}$
50.000	60.000	0.005	± 0.0001	$^{+0.0003}_{-0.0003}$
60.000	75.000	0.003	± 0.0001	$^{+0.0002}_{-0.0002}$
75.000	100.000	0.001	± 0.0000	$^{+0.0001}_{-0.0001}$

Table D.17.: Unfolded data, $\mathcal{O} = \sum p_\perp$, electron channel, $p_\perp(\mathrm{Z}) \in [6, 12)$

$\mathcal{O}_{\text{min}}$	$\mathcal{O}_{\text{max}}$	$\frac{1}{N_{\text{ev}}}\frac{\mathrm{d}N}{\mathrm{d}\mathcal{O}}$	δ_{stat}	δ_{syst}
0.000	0.058	0.013	± 0.0020	$^{+0.0029}_{-0.0029}$
0.058	0.117	0.029	± 0.0025	$^{+0.0040}_{-0.0041}$
0.117	0.175	0.067	± 0.0038	$^{+0.0066}_{-0.0068}$
0.175	0.233	0.132	± 0.0049	$^{+0.0095}_{-0.0097}$
0.233	0.292	0.280	± 0.0070	$^{+0.0176}_{-0.0177}$
0.292	0.350	0.530	± 0.0094	$^{+0.0259}_{-0.0260}$
0.350	0.408	0.981	± 0.0126	$^{+0.0391}_{-0.0392}$
0.408	0.467	1.834	± 0.0173	$^{+0.0466}_{-0.0466}$
0.467	0.525	3.169	± 0.0229	$^{+0.0550}_{-0.0548}$
0.525	0.583	4.080	± 0.0261	$^{+0.0791}_{-0.0788}$
0.583	0.642	2.802	± 0.0240	$^{+0.0557}_{-0.0556}$
0.642	0.700	0.308	± 0.0050	$^{+0.0152}_{-0.0153}$

Table D.18.: Unfolded data, $\mathcal{O}$ = transverse minor, electron channel, $p_\perp(\mathrm{Z}) \in [6, 12)$

$\mathcal{O}_{\text{min}}$	$\mathcal{O}_{\text{max}}$	$\frac{1}{N_{\text{ev}}}\frac{\text{d}N}{\text{d}\mathcal{O}}$	δ_{stat}	δ_{syst}
0.000	0.083	0.126	± 0.0052	$^{+0.0067}_{-0.0067}$
0.083	0.167	0.228	± 0.0057	$^{+0.0130}_{-0.0131}$
0.167	0.250	0.345	± 0.0062	$^{+0.0156}_{-0.0157}$
0.250	0.333	0.514	± 0.0071	$^{+0.0200}_{-0.0200}$
0.333	0.417	0.741	± 0.0083	$^{+0.0226}_{-0.0226}$
0.417	0.500	1.034	± 0.0095	$^{+0.0239}_{-0.0239}$
0.500	0.583	1.370	± 0.0108	$^{+0.0292}_{-0.0291}$
0.583	0.667	1.646	± 0.0117	$^{+0.0284}_{-0.0282}$
0.667	0.750	1.708	± 0.0119	$^{+0.0370}_{-0.0369}$
0.750	0.833	1.420	± 0.0114	$^{+0.0410}_{-0.0410}$
0.833	0.917	0.754	± 0.0091	$^{+0.0292}_{-0.0293}$
0.917	1.000	0.075	± 0.0016	$^{+0.0058}_{-0.0058}$

Table D.19.: Unfolded data, $\mathcal{O}$ = Spherocity, electron channel, $p_{\perp}(\text{Z}) \in [6, 12)$

$\mathcal{O}_{\mathrm{min}}$	$\mathcal{O}_{\mathrm{max}}$	$\frac{1}{N_{\mathrm{ev}}}\frac{\mathrm{d}N}{\mathrm{d}\mathcal{O}}$	δ_{stat}	δ_{syst}
−0.500	1.500	0.002	$\pm$ 0.0001	$^{+0.0010}_{-0.0010}$
1.500	3.500	0.008	$\pm$ 0.0002	$^{+0.0020}_{-0.0020}$
3.500	5.500	0.013	$\pm$ 0.0002	$^{+0.0020}_{-0.0020}$
5.500	7.500	0.017	$\pm$ 0.0002	$^{+0.0012}_{-0.0012}$
7.500	9.500	0.019	$\pm$ 0.0002	$^{+0.0007}_{-0.0007}$
9.500	12.500	0.020	$\pm$ 0.0002	$^{+0.0009}_{-0.0009}$
12.500	15.500	0.021	$\pm$ 0.0002	$^{+0.0013}_{-0.0013}$
15.500	20.500	0.022	$\pm$ 0.0002	$^{+0.0016}_{-0.0016}$
20.500	25.500	0.020	$\pm$ 0.0002	$^{+0.0014}_{-0.0014}$
25.500	30.500	0.018	$\pm$ 0.0001	$^{+0.0008}_{-0.0008}$
30.500	35.500	0.015	$\pm$ 0.0001	$^{+0.0004}_{-0.0004}$
35.500	40.500	0.012	$\pm$ 0.0001	$^{+0.0004}_{-0.0004}$
40.500	45.500	0.009	$\pm$ 0.0001	$^{+0.0005}_{-0.0005}$
45.500	50.500	0.007	$\pm$ 0.0001	$^{+0.0005}_{-0.0005}$
50.500	60.500	0.004	$\pm$ 0.0001	$^{+0.0005}_{-0.0005}$
60.500	75.500	0.002	$\pm$ 0.0000	$^{+0.0002}_{-0.0002}$
75.500	100.500	0.000	$\pm$ 0.0000	$^{+0.0001}_{-0.0001}$

Table D.20.: Unfolded data, $\mathcal{O} = N_{\mathrm{ch}}$, electron channel, $p_{\perp}(\mathrm{Z}) \in [6, 12)$

$\mathcal{O}_{\text{min}}$	$\mathcal{O}_{\text{max}}$	$\frac{1}{N_{\text{ev}}}\frac{\mathrm{d}N}{\mathrm{d}\mathcal{O}}$	δ_{stat}	δ_{syst}
−0.001	4.000	0.046	$\pm$ 0.0004	$^{+0.0020}_{-0.0020}$
4.000	8.000	0.060	$\pm$ 0.0004	$^{+0.0017}_{-0.0017}$
8.000	12.000	0.051	$\pm$ 0.0004	$^{+0.0005}_{-0.0005}$
12.000	16.000	0.036	$\pm$ 0.0003	$^{+0.0004}_{-0.0004}$
16.000	20.000	0.023	$\pm$ 0.0002	$^{+0.0007}_{-0.0007}$
20.000	24.000	0.014	$\pm$ 0.0002	$^{+0.0008}_{-0.0008}$
24.000	28.000	0.008	$\pm$ 0.0001	$^{+0.0007}_{-0.0007}$
28.000	32.000	0.005	$\pm$ 0.0001	$^{+0.0004}_{-0.0004}$
32.000	36.000	0.003	$\pm$ 0.0001	$^{+0.0003}_{-0.0003}$
36.000	40.000	0.002	$\pm$ 0.0001	$^{+0.0002}_{-0.0002}$
40.000	50.000	0.001	$\pm$ 0.0000	$^{+0.0001}_{-0.0001}$
50.000	60.000	0.000	$\pm$ 0.0000	$^{+0.0001}_{-0.0001}$

Table D.21.: Unfolded data, $\mathcal{O}$ = Beamthrust, electron channel, $p_\perp(\mathrm{Z}) \in [6, 12)$

$\mathcal{O}_{\text{min}}$	$\mathcal{O}_{\text{max}}$	$\frac{1}{N_{\text{ev}}}\frac{\text{d}N}{\text{d}\mathcal{O}}$	δ_{stat}	δ_{syst}
0.000	0.083	0.136	$\pm\,0.0054$	$^{+0.0076}_{-0.0077}$
0.083	0.167	0.368	$\pm\,0.0079$	$^{+0.0138}_{-0.0127}$
0.167	0.250	0.655	$\pm\,0.0096$	$^{+0.0143}_{-0.0139}$
0.250	0.333	0.939	$\pm\,0.0106$	$^{+0.0185}_{-0.0183}$
0.333	0.417	1.248	$\pm\,0.0117$	$^{+0.0205}_{-0.0204}$
0.417	0.500	1.478	$\pm\,0.0122$	$^{+0.0184}_{-0.0183}$
0.500	0.583	1.565	$\pm\,0.0120$	$^{+0.0218}_{-0.0218}$
0.583	0.667	1.498	$\pm\,0.0112$	$^{+0.0264}_{-0.0264}$
0.667	0.750	1.265	$\pm\,0.0100$	$^{+0.0246}_{-0.0247}$
0.750	0.833	0.919	$\pm\,0.0086$	$^{+0.0215}_{-0.0216}$
0.833	0.917	0.530	$\pm\,0.0068$	$^{+0.0166}_{-0.0168}$
0.917	1.000	0.164	$\pm\,0.0028$	$^{+0.0063}_{-0.0064}$

Table D.22.: Unfolded data, $\mathcal{O}$ = F-Parameter, electron channel, $p_\perp(\text{Z}) \in [12, 25)$

$\mathcal{O}_{\text{min}}$	$\mathcal{O}_{\text{max}}$	$\frac{1}{N_{\text{ev}}}\frac{\text{d}N}{\text{d}\mathcal{O}}$	δ_{stat}	δ_{syst}
0.636	0.666	0.432	$\pm\,0.0080$	$^{+0.0245}_{-0.0247}$
0.666	0.697	3.043	$\pm\,0.0328$	$^{+0.0849}_{-0.0855}$
0.697	0.727	4.862	$\pm\,0.0372$	$^{+0.0938}_{-0.0942}$
0.727	0.758	5.260	$\pm\,0.0381$	$^{+0.0881}_{-0.0876}$
0.758	0.788	4.695	$\pm\,0.0362$	$^{+0.0725}_{-0.0745}$
0.788	0.819	3.794	$\pm\,0.0330$	$^{+0.0499}_{-0.0498}$
0.819	0.849	2.802	$\pm\,0.0287$	$^{+0.0575}_{-0.0569}$
0.849	0.879	1.946	$\pm\,0.0246$	$^{+0.0507}_{-0.0497}$
0.879	0.910	1.274	$\pm\,0.0206$	$^{+0.0329}_{-0.0298}$
0.910	0.940	0.782	$\pm\,0.0173$	$^{+0.0264}_{-0.0261}$
0.940	0.971	0.405	$\pm\,0.0133$	$^{+0.0166}_{-0.0169}$
0.971	1.001	0.195	$\pm\,0.0106$	$^{+0.0148}_{-0.0150}$

Table D.23.: Unfolded data, $\mathcal{O}$ = transverse thrust, electron channel, $p_\perp(\text{Z}) \in [12, 25)$

$\mathcal{O}_{\text{min}}$	$\mathcal{O}_{\text{max}}$	$\frac{1}{N_{\text{ev}}}\frac{\mathrm{d}N}{\mathrm{d}\mathcal{O}}$ [GeV]	δ_{stat}	δ_{syst}
−0.001	4.000	0.002	± 0.0001	$^{+0.0003}_{-0.0003}$
4.000	8.000	0.007	± 0.0001	$^{+0.0006}_{-0.0006}$
8.000	12.000	0.012	± 0.0002	$^{+0.0008}_{-0.0007}$
12.000	16.000	0.016	± 0.0002	$^{+0.0008}_{-0.0008}$
16.000	20.000	0.018	± 0.0002	$^{+0.0008}_{-0.0007}$
20.000	24.000	0.019	± 0.0002	$^{+0.0007}_{-0.0006}$
24.000	28.000	0.019	± 0.0002	$^{+0.0006}_{-0.0005}$
28.000	32.000	0.018	± 0.0002	$^{+0.0004}_{-0.0004}$
32.000	36.000	0.017	± 0.0002	$^{+0.0003}_{-0.0003}$
36.000	40.000	0.015	± 0.0002	$^{+0.0003}_{-0.0002}$
40.000	50.000	0.012	± 0.0001	$^{+0.0003}_{-0.0003}$
50.000	60.000	0.008	± 0.0001	$^{+0.0003}_{-0.0003}$
60.000	75.000	0.005	± 0.0001	$^{+0.0003}_{-0.0003}$
75.000	100.000	0.002	± 0.0000	$^{+0.0002}_{-0.0002}$

Table D.24.: Unfolded data, $\mathcal{O} = \sum p_\perp$, electron channel, $p_\perp(\mathrm{Z}) \in [12, 25)$

$\mathcal{O}_{\text{min}}$	$\mathcal{O}_{\text{max}}$	$\frac{1}{N_{\text{ev}}}\frac{\mathrm{d}N}{\mathrm{d}\mathcal{O}}$	δ_{stat}	δ_{syst}
0.000	0.058	0.008	± 0.0013	$^{+0.0020}_{-0.0020}$
0.058	0.117	0.042	± 0.0032	$^{+0.0059}_{-0.0060}$
0.117	0.175	0.103	± 0.0046	$^{+0.0079}_{-0.0081}$
0.175	0.233	0.226	± 0.0065	$^{+0.0104}_{-0.0106}$
0.233	0.292	0.461	± 0.0092	$^{+0.0170}_{-0.0159}$
0.292	0.350	0.819	± 0.0120	$^{+0.0231}_{-0.0219}$
0.350	0.408	1.377	± 0.0155	$^{+0.0272}_{-0.0273}$
0.408	0.467	2.258	± 0.0201	$^{+0.0303}_{-0.0303}$
0.467	0.525	3.289	± 0.0242	$^{+0.0478}_{-0.0478}$
0.525	0.583	3.876	± 0.0265	$^{+0.0604}_{-0.0610}$
0.583	0.642	2.619	± 0.0239	$^{+0.0474}_{-0.0472}$
0.642	0.700	0.296	± 0.0053	$^{+0.0216}_{-0.0216}$

Table D.25.: Unfolded data, $\mathcal{O}$ = transverse minor, electron channel, $p_\perp(\mathrm{Z}) \in [12, 25)$

$\mathcal{O}_{\text{min}}$	$\mathcal{O}_{\text{max}}$	$\frac{1}{N_{\text{ev}}} \frac{\text{d}N}{\text{d}\mathcal{O}}$	δ_{stat}	δ_{syst}
0.000	0.083	0.180	$\pm$ 0.0062	$^{+0.0070}_{-0.0070}$
0.083	0.167	0.364	$\pm$ 0.0074	$^{+0.0127}_{-0.0119}$
0.167	0.250	0.550	$\pm$ 0.0083	$^{+0.0125}_{-0.0124}$
0.250	0.333	0.744	$\pm$ 0.0090	$^{+0.0155}_{-0.0154}$
0.333	0.417	0.979	$\pm$ 0.0100	$^{+0.0198}_{-0.0197}$
0.417	0.500	1.240	$\pm$ 0.0110	$^{+0.0199}_{-0.0198}$
0.500	0.583	1.469	$\pm$ 0.0117	$^{+0.0182}_{-0.0181}$
0.583	0.667	1.609	$\pm$ 0.0121	$^{+0.0226}_{-0.0225}$
0.667	0.750	1.589	$\pm$ 0.0119	$^{+0.0278}_{-0.0280}$
0.750	0.833	1.298	$\pm$ 0.0113	$^{+0.0324}_{-0.0331}$
0.833	0.917	0.676	$\pm$ 0.0088	$^{+0.0220}_{-0.0224}$
0.917	1.000	0.066	$\pm$ 0.0016	$^{+0.0059}_{-0.0060}$

Table D.26.: Unfolded data, $\mathcal{O}$ = Spherocity, electron channel, $p_{\perp}(\text{Z}) \in [12, 25)$

$\mathcal{O}_{\text{min}}$	$\mathcal{O}_{\text{max}}$	$\frac{1}{N_{\text{ev}}}\frac{\mathrm{d}N}{\mathrm{d}\mathcal{O}}$	δ_{stat}	δ_{syst}
−0.500	1.500	0.001	± 0.0001	$^{+0.0001}_{-0.0001}$
1.500	3.500	0.003	± 0.0001	$^{+0.0004}_{-0.0004}$
3.500	5.500	0.006	± 0.0002	$^{+0.0006}_{-0.0006}$
5.500	7.500	0.010	± 0.0002	$^{+0.0007}_{-0.0007}$
7.500	9.500	0.014	± 0.0003	$^{+0.0009}_{-0.0008}$
9.500	12.500	0.018	± 0.0003	$^{+0.0010}_{-0.0009}$
12.500	15.500	0.021	± 0.0003	$^{+0.0009}_{-0.0009}$
15.500	20.500	0.023	± 0.0003	$^{+0.0009}_{-0.0009}$
20.500	25.500	0.024	± 0.0003	$^{+0.0006}_{-0.0006}$
25.500	30.500	0.022	± 0.0002	$^{+0.0004}_{-0.0004}$
30.500	35.500	0.018	± 0.0002	$^{+0.0003}_{-0.0004}$
35.500	40.500	0.015	± 0.0002	$^{+0.0004}_{-0.0004}$
40.500	45.500	0.012	± 0.0002	$^{+0.0005}_{-0.0005}$
45.500	50.500	0.009	± 0.0001	$^{+0.0004}_{-0.0004}$
50.500	60.500	0.006	± 0.0001	$^{+0.0004}_{-0.0004}$
60.500	75.500	0.002	± 0.0001	$^{+0.0003}_{-0.0003}$
75.500	100.500	0.000	± 0.0000	$^{+0.0001}_{-0.0001}$

Table D.27.: Unfolded data, $\mathcal{O} = N_{\text{ch}}$, electron channel, $p_{\perp}(\text{Z}) \in [12, 25)$

$\mathcal{O}_{\text{min}}$	$\mathcal{O}_{\text{max}}$	$\frac{1}{N_{\text{ev}}}\frac{\mathrm{d}N}{\mathrm{d}\mathcal{O}}$	δ_{stat}	δ_{syst}
−0.001	4.000	0.024	$\pm$ 0.0003	$^{+0.0013}_{-0.0013}$
4.000	8.000	0.048	$\pm$ 0.0004	$^{+0.0020}_{-0.0020}$
8.000	12.000	0.051	$\pm$ 0.0004	$^{+0.0010}_{-0.0010}$
12.000	16.000	0.042	$\pm$ 0.0003	$^{+0.0003}_{-0.0003}$
16.000	20.000	0.031	$\pm$ 0.0003	$^{+0.0007}_{-0.0007}$
20.000	24.000	0.021	$\pm$ 0.0002	$^{+0.0008}_{-0.0008}$
24.000	28.000	0.013	$\pm$ 0.0002	$^{+0.0007}_{-0.0007}$
28.000	32.000	0.008	$\pm$ 0.0001	$^{+0.0006}_{-0.0006}$
32.000	36.000	0.005	$\pm$ 0.0001	$^{+0.0005}_{-0.0005}$
36.000	40.000	0.003	$\pm$ 0.0001	$^{+0.0004}_{-0.0004}$
40.000	50.000	0.001	$\pm$ 0.0000	$^{+0.0002}_{-0.0002}$
50.000	60.000	0.000	$\pm$ 0.0000	$^{+0.0001}_{-0.0001}$

Table D.28.: Unfolded data, $\mathcal{O}$ = Beamthrust, electron channel, $p_\perp(\mathrm{Z}) \in [12, 25)$

$\mathcal{O}_{\text{min}}$	$\mathcal{O}_{\text{max}}$	$\frac{1}{N_{\text{ev}}}\frac{\mathrm{d}N}{\mathrm{d}\mathcal{O}}$	δ_{stat}	δ_{syst}
0.000	0.083	0.333	± 0.0098	$^{+0.0124}_{-0.0103}$
0.083	0.167	0.937	± 0.0150	$^{+0.0384}_{-0.0227}$
0.167	0.250	1.359	± 0.0164	$^{+0.0302}_{-0.0221}$
0.250	0.333	1.594	± 0.0165	$^{+0.0203}_{-0.0197}$
0.333	0.417	1.648	± 0.0159	$^{+0.0260}_{-0.0261}$
0.417	0.500	1.531	± 0.0146	$^{+0.0278}_{-0.0290}$
0.500	0.583	1.346	± 0.0131	$^{+0.0328}_{-0.0334}$
0.583	0.667	1.099	± 0.0113	$^{+0.0318}_{-0.0328}$
0.667	0.750	0.820	± 0.0095	$^{+0.0299}_{-0.0319}$
0.750	0.833	0.544	± 0.0075	$^{+0.0259}_{-0.0285}$
0.833	0.917	0.296	± 0.0058	$^{+0.0163}_{-0.0180}$
0.917	1.000	0.091	± 0.0024	$^{+0.0064}_{-0.0068}$

Table D.29.: Unfolded data, $\mathcal{O}$ = F-Parameter, electron channel, $p_\perp(\mathrm{Z}) \in [25, \infty)$

$\mathcal{O}_{\text{min}}$	$\mathcal{O}_{\text{max}}$	$\frac{1}{N_{\text{ev}}}\frac{\mathrm{d}N}{\mathrm{d}\mathcal{O}}$	δ_{stat}	δ_{syst}
0.636	0.666	0.211	± 0.0064	$^{+0.0201}_{-0.0210}$
0.666	0.697	1.739	± 0.0284	$^{+0.0765}_{-0.0869}$
0.697	0.727	3.252	± 0.0358	$^{+0.1131}_{-0.1220}$
0.727	0.758	4.153	± 0.0400	$^{+0.1038}_{-0.1088}$
0.758	0.788	4.513	± 0.0421	$^{+0.0900}_{-0.0907}$
0.788	0.819	4.506	± 0.0428	$^{+0.0863}_{-0.0878}$
0.819	0.849	4.126	± 0.0417	$^{+0.0617}_{-0.0640}$
0.849	0.879	3.448	± 0.0391	$^{+0.0522}_{-0.0420}$
0.879	0.910	2.642	± 0.0356	$^{+0.0657}_{-0.0434}$
0.910	0.940	1.822	± 0.0312	$^{+0.0688}_{-0.0382}$
0.940	0.971	1.010	± 0.0250	$^{+0.0370}_{-0.0282}$
0.971	1.001	0.357	± 0.0164	$^{+0.0215}_{-0.0165}$

Table D.30.: Unfolded data, $\mathcal{O}$ = transverse thrust, electron channel, $p_\perp(\mathrm{Z}) \in [25, \infty)$

$\mathcal{O}_{\text{min}}$	$\mathcal{O}_{\text{max}}$	$\frac{1}{N_{\text{ev}}}\frac{\mathrm{d}N}{\mathrm{d}\mathcal{O}}$ [GeV]	δ_{stat}	δ_{syst}
−0.001	4.000	0.001	± 0.0001	$^{+0.0002}_{-0.0002}$
4.000	8.000	0.001	± 0.0001	$^{+0.0002}_{-0.0002}$
8.000	12.000	0.003	± 0.0001	$^{+0.0004}_{-0.0004}$
12.000	16.000	0.005	± 0.0001	$^{+0.0005}_{-0.0005}$
16.000	20.000	0.007	± 0.0001	$^{+0.0007}_{-0.0007}$
20.000	24.000	0.009	± 0.0002	$^{+0.0008}_{-0.0008}$
24.000	28.000	0.011	± 0.0002	$^{+0.0009}_{-0.0009}$
28.000	32.000	0.013	± 0.0002	$^{+0.0009}_{-0.0008}$
32.000	36.000	0.014	± 0.0002	$^{+0.0009}_{-0.0009}$
36.000	40.000	0.014	± 0.0002	$^{+0.0006}_{-0.0006}$
40.000	50.000	0.014	± 0.0001	$^{+0.0005}_{-0.0005}$
50.000	60.000	0.013	± 0.0001	$^{+0.0002}_{-0.0002}$
60.000	75.000	0.010	± 0.0001	$^{+0.0002}_{-0.0002}$
75.000	100.000	0.006	± 0.0001	$^{+0.0003}_{-0.0003}$

Table D.31.: Unfolded data, $\mathcal{O} = \sum p_\perp$, electron channel, $p_\perp(\mathrm{Z}) \in [25, \infty)$

$\mathcal{O}_{\text{min}}$	$\mathcal{O}_{\text{max}}$	$\frac{1}{N_{\text{ev}}}\frac{\mathrm{d}N}{\mathrm{d}\mathcal{O}}$	δ_{stat}	δ_{syst}
0.000	0.058	0.021	± 0.0027	$^{+0.0035}_{-0.0034}$
0.058	0.117	0.144	± 0.0069	$^{+0.0114}_{-0.0100}$
0.117	0.175	0.388	± 0.0108	$^{+0.0201}_{-0.0193}$
0.175	0.233	0.744	± 0.0142	$^{+0.0359}_{-0.0256}$
0.233	0.292	1.151	± 0.0169	$^{+0.0376}_{-0.0289}$
0.292	0.350	1.648	± 0.0200	$^{+0.0313}_{-0.0268}$
0.350	0.408	2.196	± 0.0229	$^{+0.0236}_{-0.0222}$
0.408	0.467	2.647	± 0.0251	$^{+0.0514}_{-0.0517}$
0.467	0.525	2.932	± 0.0265	$^{+0.0696}_{-0.0759}$
0.525	0.583	2.727	± 0.0258	$^{+0.0787}_{-0.0825}$
0.583	0.642	1.713	± 0.0219	$^{+0.0598}_{-0.0638}$
0.642	0.700	0.255	± 0.0069	$^{+0.0210}_{-0.0211}$

Table D.32.: Unfolded data, $\mathcal{O}$ = transverse minor, electron channel, $p_\perp(\mathrm{Z}) \in [25, \infty)$

$\mathcal{O}_{\text{min}}$	$\mathcal{O}_{\text{max}}$	$\frac{1}{N_{\text{ev}}}\frac{\mathrm{d}N}{\mathrm{d}\mathcal{O}}$	δ_{stat}	δ_{syst}
0.000	0.083	0.624	± 0.0133	$^{+0.0267}_{-0.0213}$
0.083	0.167	1.011	± 0.0145	$^{+0.0383}_{-0.0272}$
0.167	0.250	1.217	± 0.0143	$^{+0.0271}_{-0.0197}$
0.250	0.333	1.338	± 0.0143	$^{+0.0172}_{-0.0147}$
0.333	0.417	1.362	± 0.0138	$^{+0.0182}_{-0.0190}$
0.417	0.500	1.358	± 0.0134	$^{+0.0257}_{-0.0273}$
0.500	0.583	1.345	± 0.0130	$^{+0.0323}_{-0.0335}$
0.583	0.667	1.245	± 0.0123	$^{+0.0357}_{-0.0370}$
0.667	0.750	1.037	± 0.0112	$^{+0.0361}_{-0.0380}$
0.750	0.833	0.719	± 0.0096	$^{+0.0317}_{-0.0344}$
0.833	0.917	0.318	± 0.0068	$^{+0.0191}_{-0.0215}$
0.917	1.000	0.027	± 0.0011	$^{+0.0032}_{-0.0034}$

Table D.33.: Unfolded data, $\mathcal{O}$ = Spherocity, electron channel, $p_{\perp}(\mathrm{Z}) \in [25, \infty)$

$\mathcal{O}_{\text{min}}$	$\mathcal{O}_{\text{max}}$	$\frac{1}{N_{\text{ev}}}\frac{\mathrm{d}N}{\mathrm{d}\mathcal{O}}$	δ_{stat}	δ_{syst}
−0.500	1.500	0.000	$\pm$ 0.0000	$^{+0.0001}_{-0.0001}$
1.500	3.500	0.001	$\pm$ 0.0001	$^{+0.0002}_{-0.0002}$
3.500	5.500	0.002	$\pm$ 0.0001	$^{+0.0002}_{-0.0003}$
5.500	7.500	0.004	$\pm$ 0.0001	$^{+0.0004}_{-0.0004}$
7.500	9.500	0.006	$\pm$ 0.0002	$^{+0.0006}_{-0.0006}$
9.500	12.500	0.010	$\pm$ 0.0002	$^{+0.0008}_{-0.0008}$
12.500	15.500	0.014	$\pm$ 0.0003	$^{+0.0010}_{-0.0010}$
15.500	20.500	0.019	$\pm$ 0.0003	$^{+0.0010}_{-0.0010}$
20.500	25.500	0.023	$\pm$ 0.0003	$^{+0.0009}_{-0.0009}$
25.500	30.500	0.023	$\pm$ 0.0003	$^{+0.0007}_{-0.0007}$
30.500	35.500	0.022	$\pm$ 0.0003	$^{+0.0005}_{-0.0004}$
35.500	40.500	0.020	$\pm$ 0.0002	$^{+0.0004}_{-0.0004}$
40.500	45.500	0.017	$\pm$ 0.0002	$^{+0.0004}_{-0.0004}$
45.500	50.500	0.014	$\pm$ 0.0002	$^{+0.0005}_{-0.0005}$
50.500	60.500	0.009	$\pm$ 0.0001	$^{+0.0005}_{-0.0005}$
60.500	75.500	0.004	$\pm$ 0.0001	$^{+0.0004}_{-0.0004}$
75.500	100.500	0.001	$\pm$ 0.0000	$^{+0.0002}_{-0.0002}$

Table D.34.: Unfolded data, $\mathcal{O} = N_{\text{ch}}$, electron channel, $p_{\perp}(\text{Z}) \in [25, \infty)$

$\mathcal{O}_{\text{min}}$	$\mathcal{O}_{\text{max}}$	$\frac{1}{N_{\text{ev}}}\frac{\mathrm{d}N}{\mathrm{d}\mathcal{O}}$	δ_{stat}	δ_{syst}
−0.001	4.000	0.007	$\pm$ 0.0002	$^{+0.0006}_{-0.0006}$
4.000	8.000	0.021	$\pm$ 0.0003	$^{+0.0015}_{-0.0015}$
8.000	12.000	0.031	$\pm$ 0.0003	$^{+0.0018}_{-0.0018}$
12.000	16.000	0.035	$\pm$ 0.0004	$^{+0.0014}_{-0.0014}$
16.000	20.000	0.034	$\pm$ 0.0003	$^{+0.0008}_{-0.0008}$
20.000	24.000	0.028	$\pm$ 0.0003	$^{+0.0003}_{-0.0003}$
24.000	28.000	0.023	$\pm$ 0.0003	$^{+0.0003}_{-0.0003}$
28.000	32.000	0.018	$\pm$ 0.0002	$^{+0.0007}_{-0.0007}$
32.000	36.000	0.014	$\pm$ 0.0002	$^{+0.0008}_{-0.0008}$
36.000	40.000	0.011	$\pm$ 0.0002	$^{+0.0008}_{-0.0008}$
40.000	50.000	0.007	$\pm$ 0.0001	$^{+0.0008}_{-0.0008}$
50.000	60.000	0.004	$\pm$ 0.0001	$^{+0.0007}_{-0.0007}$

Table D.35.: Unfolded data, $\mathcal{O}$ = Beamthrust, electron channel, $p_\perp(\mathrm{Z}) \in [25, \infty)$

$\mathcal{O}_{\text{min}}$	$\mathcal{O}_{\text{max}}$	$\frac{1}{N_{\text{ev}}}\frac{\text{d}N}{\text{d}\mathcal{O}}$	δ_{stat}	δ_{syst}
0.000	0.083	0.211	± 0.0032	$^{+0.0028}_{-0.0028}$
0.083	0.167	0.470	± 0.0042	$^{+0.0053}_{-0.0054}$
0.167	0.250	0.757	± 0.0047	$^{+0.0080}_{-0.0080}$
0.250	0.333	1.043	± 0.0052	$^{+0.0108}_{-0.0108}$
0.333	0.417	1.333	± 0.0055	$^{+0.0104}_{-0.0104}$
0.417	0.500	1.569	± 0.0057	$^{+0.0107}_{-0.0106}$
0.500	0.583	1.698	± 0.0057	$^{+0.0067}_{-0.0066}$
0.583	0.667	1.644	± 0.0053	$^{+0.0069}_{-0.0068}$
0.667	0.750	1.405	± 0.0047	$^{+0.0118}_{-0.0118}$
0.750	0.833	1.028	± 0.0040	$^{+0.0113}_{-0.0113}$
0.833	0.917	0.595	± 0.0032	$^{+0.0082}_{-0.0082}$
0.917	1.000	0.185	± 0.0013	$^{+0.0030}_{-0.0031}$

Table D.36.: Unfolded data, $\mathcal{O}$ = F-Parameter, muon channel, $p_\perp(\text{Z}) \in [0, \infty)$

$\mathcal{O}_{\text{min}}$	$\mathcal{O}_{\text{max}}$	$\frac{1}{N_{\text{ev}}}\frac{\text{d}N}{\text{d}\mathcal{O}}$	δ_{stat}	δ_{syst}
0.636	0.666	0.487	± 0.0038	$^{+0.0241}_{-0.0241}$
0.666	0.697	3.361	± 0.0154	$^{+0.0470}_{-0.0470}$
0.697	0.727	5.332	± 0.0174	$^{+0.0444}_{-0.0444}$
0.727	0.758	5.730	± 0.0180	$^{+0.0193}_{-0.0192}$
0.758	0.788	5.092	± 0.0172	$^{+0.0216}_{-0.0215}$
0.788	0.819	4.081	± 0.0156	$^{+0.0286}_{-0.0286}$
0.819	0.849	3.061	± 0.0138	$^{+0.0290}_{-0.0290}$
0.849	0.879	2.178	± 0.0119	$^{+0.0230}_{-0.0230}$
0.879	0.910	1.500	± 0.0104	$^{+0.0142}_{-0.0142}$
0.910	0.940	0.992	± 0.0091	$^{+0.0136}_{-0.0137}$
0.940	0.971	0.590	± 0.0077	$^{+0.0073}_{-0.0073}$
0.971	1.001	0.305	± 0.0063	$^{+0.0093}_{-0.0093}$

Table D.37.: Unfolded data, $\mathcal{O}$ = transverse thrust, muon channel, $p_\perp(\text{Z}) \in [0, \infty)$

$\mathcal{O}_{\text{min}}$	$\mathcal{O}_{\text{max}}$	$\frac{1}{N_{\text{ev}}}\frac{\mathrm{d}N}{\mathrm{d}\mathcal{O}}$ [GeV]	δ_{stat}	δ_{syst}
−0.001	4.000	0.009	± 0.0001	$^{+0.0004}_{-0.0004}$
4.000	8.000	0.013	± 0.0001	$^{+0.0006}_{-0.0006}$
8.000	12.000	0.017	± 0.0001	$^{+0.0007}_{-0.0007}$
12.000	16.000	0.018	± 0.0001	$^{+0.0007}_{-0.0007}$
16.000	20.000	0.019	± 0.0001	$^{+0.0006}_{-0.0006}$
20.000	24.000	0.019	± 0.0001	$^{+0.0005}_{-0.0005}$
24.000	28.000	0.018	± 0.0001	$^{+0.0004}_{-0.0004}$
28.000	32.000	0.017	± 0.0001	$^{+0.0002}_{-0.0002}$
32.000	36.000	0.015	± 0.0001	$^{+0.0002}_{-0.0002}$
36.000	40.000	0.014	± 0.0001	$^{+0.0001}_{-0.0001}$
40.000	50.000	0.011	± 0.0001	$^{+0.0001}_{-0.0001}$
50.000	60.000	0.008	± 0.0000	$^{+0.0002}_{-0.0002}$
60.000	75.000	0.005	± 0.0000	$^{+0.0002}_{-0.0002}$
75.000	100.000	0.002	± 0.0000	$^{+0.0002}_{-0.0002}$

Table D.38.: Unfolded data, $\mathcal{O} = \sum p_\perp$, muon channel, $p_\perp(\mathrm{Z}) \in [0, \infty)$

$\mathcal{O}_{\text{min}}$	$\mathcal{O}_{\text{max}}$	$\frac{1}{N_{\text{ev}}}\frac{\mathrm{d}N}{\mathrm{d}\mathcal{O}}$	δ_{stat}	δ_{syst}
0.000	0.058	0.021	± 0.0012	$^{+0.0015}_{-0.0015}$
0.058	0.117	0.068	± 0.0019	$^{+0.0026}_{-0.0027}$
0.117	0.175	0.168	± 0.0028	$^{+0.0034}_{-0.0035}$
0.175	0.233	0.328	± 0.0037	$^{+0.0060}_{-0.0060}$
0.233	0.292	0.558	± 0.0046	$^{+0.0088}_{-0.0088}$
0.292	0.350	0.923	± 0.0059	$^{+0.0155}_{-0.0155}$
0.350	0.408	1.478	± 0.0073	$^{+0.0141}_{-0.0141}$
0.408	0.467	2.364	± 0.0093	$^{+0.0189}_{-0.0189}$
0.467	0.525	3.563	± 0.0115	$^{+0.0227}_{-0.0226}$
0.525	0.583	4.299	± 0.0126	$^{+0.0276}_{-0.0275}$
0.583	0.642	2.938	± 0.0114	$^{+0.0352}_{-0.0352}$
0.642	0.700	0.348	± 0.0027	$^{+0.0163}_{-0.0163}$

Table D.39.: Unfolded data, $\mathcal{O}$ = transverse minor, muon channel, $p_\perp(\mathrm{Z}) \in [0, \infty)$

$\mathcal{O}_{\text{min}}$	$\mathcal{O}_{\text{max}}$	$\frac{1}{N_{\text{ev}}}\frac{\text{d}N}{\text{d}\mathcal{O}}$	δ_{stat}	δ_{syst}
0.000	0.083	0.297	$\pm$ 0.0037	$^{+0.0034}_{-0.0034}$
0.083	0.167	0.469	$\pm$ 0.0039	$^{+0.0058}_{-0.0058}$
0.167	0.250	0.642	$\pm$ 0.0041	$^{+0.0065}_{-0.0065}$
0.250	0.333	0.826	$\pm$ 0.0043	$^{+0.0088}_{-0.0088}$
0.333	0.417	1.048	$\pm$ 0.0047	$^{+0.0103}_{-0.0103}$
0.417	0.500	1.298	$\pm$ 0.0051	$^{+0.0103}_{-0.0103}$
0.500	0.583	1.560	$\pm$ 0.0055	$^{+0.0104}_{-0.0104}$
0.583	0.667	1.762	$\pm$ 0.0057	$^{+0.0079}_{-0.0079}$
0.667	0.750	1.767	$\pm$ 0.0057	$^{+0.0101}_{-0.0101}$
0.750	0.833	1.442	$\pm$ 0.0053	$^{+0.0171}_{-0.0171}$
0.833	0.917	0.753	$\pm$ 0.0042	$^{+0.0154}_{-0.0154}$
0.917	1.000	0.075	$\pm$ 0.0007	$^{+0.0049}_{-0.0049}$

Table D.40.: Unfolded data, $\mathcal{O}$ = Spherocity, muon channel, $p_{\perp}(\text{Z}) \in [0, \infty)$

$\mathcal{O}_{\text{min}}$	$\mathcal{O}_{\text{max}}$	$\frac{1}{N_{\text{ev}}}\frac{\mathrm{d}N}{\mathrm{d}\mathcal{O}}$	δ_{stat}	δ_{syst}
−0.500	1.500	0.003	± 0.0001	$^{+0.0002}_{-0.0002}$
1.500	3.500	0.008	± 0.0001	$^{+0.0004}_{-0.0004}$
3.500	5.500	0.012	± 0.0001	$^{+0.0005}_{-0.0005}$
5.500	7.500	0.015	± 0.0001	$^{+0.0006}_{-0.0006}$
7.500	9.500	0.018	± 0.0002	$^{+0.0007}_{-0.0007}$
9.500	12.500	0.021	± 0.0001	$^{+0.0008}_{-0.0008}$
12.500	15.500	0.024	± 0.0002	$^{+0.0007}_{-0.0007}$
15.500	20.500	0.024	± 0.0001	$^{+0.0006}_{-0.0006}$
20.500	25.500	0.024	± 0.0001	$^{+0.0004}_{-0.0004}$
25.500	30.500	0.022	± 0.0001	$^{+0.0003}_{-0.0003}$
30.500	35.500	0.019	± 0.0001	$^{+0.0001}_{-0.0001}$
35.500	40.500	0.016	± 0.0001	$^{+0.0002}_{-0.0002}$
40.500	45.500	0.012	± 0.0001	$^{+0.0004}_{-0.0004}$
45.500	50.500	0.009	± 0.0001	$^{+0.0005}_{-0.0005}$
50.500	60.500	0.006	± 0.0000	$^{+0.0004}_{-0.0004}$
60.500	75.500	0.003	± 0.0000	$^{+0.0003}_{-0.0003}$
75.500	100.500	0.001	± 0.0000	$^{+0.0001}_{-0.0001}$

Table D.41.: Unfolded data, $\mathcal{O} = N_{\text{ch}}$, muon channel, $p_{\perp}(\text{Z}) \in [0, \infty)$

$\mathcal{O}_{\text{min}}$	$\mathcal{O}_{\text{max}}$	$\frac{1}{N_{\text{ev}}}\frac{\mathrm{d}N}{\mathrm{d}\mathcal{O}}$	δ_{stat}	δ_{syst}
−0.001	4.000	0.037	± 0.0002	$^{+0.0010}_{-0.0010}$
4.000	8.000	0.049	± 0.0002	$^{+0.0011}_{-0.0011}$
8.000	12.000	0.046	± 0.0002	$^{+0.0005}_{-0.0005}$
12.000	16.000	0.036	± 0.0001	$^{+0.0002}_{-0.0001}$
16.000	20.000	0.026	± 0.0001	$^{+0.0003}_{-0.0003}$
20.000	24.000	0.018	± 0.0001	$^{+0.0004}_{-0.0004}$
24.000	28.000	0.012	± 0.0001	$^{+0.0004}_{-0.0004}$
28.000	32.000	0.008	± 0.0001	$^{+0.0004}_{-0.0004}$
32.000	36.000	0.006	± 0.0001	$^{+0.0003}_{-0.0003}$
36.000	40.000	0.004	± 0.0000	$^{+0.0002}_{-0.0002}$
40.000	50.000	0.002	± 0.0000	$^{+0.0002}_{-0.0002}$
50.000	60.000	0.001	± 0.0000	$^{+0.0001}_{-0.0001}$

Table D.42.: Unfolded data, $\mathcal{O}$ = Beamthrust, muon channel, $p_\perp(\mathrm{Z}) \in [0, \infty)$

$\mathcal{O}_{\text{min}}$	$\mathcal{O}_{\text{max}}$	$\frac{1}{N_{\text{ev}}}\frac{\mathrm{d}N}{\mathrm{d}\mathcal{O}}$	δ_{stat}	δ_{syst}
0.000	0.083	0.174	± 0.0059	$^{+0.0059}_{-0.0059}$
0.083	0.167	0.240	± 0.0056	$^{+0.0097}_{-0.0097}$
0.167	0.250	0.431	± 0.0067	$^{+0.0160}_{-0.0160}$
0.250	0.333	0.722	± 0.0080	$^{+0.0173}_{-0.0173}$
0.333	0.417	1.091	± 0.0094	$^{+0.0163}_{-0.0163}$
0.417	0.500	1.431	± 0.0102	$^{+0.0187}_{-0.0186}$
0.500	0.583	1.689	± 0.0106	$^{+0.0164}_{-0.0163}$
0.583	0.667	1.740	± 0.0104	$^{+0.0176}_{-0.0175}$
0.667	0.750	1.541	± 0.0094	$^{+0.0234}_{-0.0234}$
0.750	0.833	1.150	± 0.0082	$^{+0.0232}_{-0.0232}$
0.833	0.917	0.675	± 0.0065	$^{+0.0170}_{-0.0171}$
0.917	1.000	0.214	± 0.0027	$^{+0.0057}_{-0.0057}$

Table D.43.: Unfolded data, $\mathcal{O}$ = F-Parameter, muon channel, $p_\perp(\mathrm{Z}) \in [0, 6)$

$\mathcal{O}_{\text{min}}$	$\mathcal{O}_{\text{max}}$	$\frac{1}{N_{\text{ev}}}\frac{\mathrm{d}N}{\mathrm{d}\mathcal{O}}$	δ_{stat}	δ_{syst}
0.636	0.666	0.561	± 0.0078	$^{+0.0273}_{-0.0274}$
0.666	0.697	3.740	± 0.0311	$^{+0.1007}_{-0.1008}$
0.697	0.727	5.725	± 0.0343	$^{+0.0886}_{-0.0885}$
0.727	0.758	5.879	± 0.0343	$^{+0.0569}_{-0.0563}$
0.758	0.788	4.892	± 0.0316	$^{+0.0361}_{-0.0356}$
0.788	0.819	3.545	± 0.0270	$^{+0.0463}_{-0.0463}$
0.819	0.849	2.389	± 0.0227	$^{+0.0450}_{-0.0450}$
0.849	0.879	1.487	± 0.0185	$^{+0.0434}_{-0.0435}$
0.879	0.910	0.896	± 0.0151	$^{+0.0294}_{-0.0295}$
0.910	0.940	0.568	± 0.0133	$^{+0.0245}_{-0.0246}$
0.940	0.971	0.378	± 0.0122	$^{+0.0144}_{-0.0146}$
0.971	1.001	0.346	± 0.0140	$^{+0.0136}_{-0.0138}$

Table D.44.: Unfolded data, $\mathcal{O}$ = transverse thrust, muon channel, $p_\perp(\mathrm{Z}) \in [0, 6)$

$\mathcal{O}_{\text{min}}$	$\mathcal{O}_{\text{max}}$	$\frac{1}{N_{\text{ev}}}\frac{\mathrm{d}N}{\mathrm{d}\mathcal{O}}$ [GeV]	δ_{stat}	δ_{syst}
−0.001	4.000	0.018	± 0.0003	$^{+0.0005}_{-0.0005}$
4.000	8.000	0.023	± 0.0003	$^{+0.0010}_{-0.0010}$
8.000	12.000	0.025	± 0.0003	$^{+0.0007}_{-0.0007}$
12.000	16.000	0.024	± 0.0003	$^{+0.0005}_{-0.0005}$
16.000	20.000	0.022	± 0.0003	$^{+0.0003}_{-0.0003}$
20.000	24.000	0.020	± 0.0003	$^{+0.0002}_{-0.0002}$
24.000	28.000	0.017	± 0.0002	$^{+0.0002}_{-0.0002}$
28.000	32.000	0.015	± 0.0002	$^{+0.0002}_{-0.0002}$
32.000	36.000	0.013	± 0.0002	$^{+0.0002}_{-0.0002}$
36.000	40.000	0.011	± 0.0002	$^{+0.0002}_{-0.0002}$
40.000	50.000	0.008	± 0.0001	$^{+0.0003}_{-0.0003}$
50.000	60.000	0.004	± 0.0001	$^{+0.0003}_{-0.0003}$
60.000	75.000	0.002	± 0.0001	$^{+0.0002}_{-0.0002}$
75.000	100.000	0.001	± 0.0000	$^{+0.0001}_{-0.0001}$

Table D.45.: Unfolded data, $\mathcal{O} = \sum p_\perp$, muon channel, $p_\perp(\mathrm{Z}) \in [0, 6)$

$\mathcal{O}_{\text{min}}$	$\mathcal{O}_{\text{max}}$	$\frac{1}{N_{\text{ev}}}\frac{\mathrm{d}N}{\mathrm{d}\mathcal{O}}$	δ_{stat}	δ_{syst}
0.000	0.058	0.028	± 0.0028	$^{+0.0033}_{-0.0033}$
0.058	0.117	0.042	± 0.0032	$^{+0.0038}_{-0.0038}$
0.117	0.175	0.071	± 0.0038	$^{+0.0048}_{-0.0049}$
0.175	0.233	0.138	± 0.0048	$^{+0.0083}_{-0.0084}$
0.233	0.292	0.259	± 0.0061	$^{+0.0135}_{-0.0136}$
0.292	0.350	0.516	± 0.0083	$^{+0.0238}_{-0.0239}$
0.350	0.408	1.032	± 0.0117	$^{+0.0218}_{-0.0218}$
0.408	0.467	1.996	± 0.0162	$^{+0.0260}_{-0.0260}$
0.467	0.525	3.502	± 0.0216	$^{+0.0317}_{-0.0315}$
0.525	0.583	4.633	± 0.0249	$^{+0.0526}_{-0.0523}$
0.583	0.642	3.251	± 0.0229	$^{+0.0498}_{-0.0498}$
0.642	0.700	0.385	± 0.0051	$^{+0.0155}_{-0.0156}$

Table D.46.: Unfolded data, $\mathcal{O}$ = transverse minor, muon channel, $p_\perp(\mathrm{Z}) \in [0, 6)$

$\mathcal{O}_{\text{min}}$	$\mathcal{O}_{\text{max}}$	$\frac{1}{N_{\text{ev}}}\frac{\mathrm{d}N}{\mathrm{d}\mathcal{O}}$	δ_{stat}	δ_{syst}
0.000	0.083	0.155	± 0.0055	$^{+0.0056}_{-0.0056}$
0.083	0.167	0.215	± 0.0050	$^{+0.0086}_{-0.0087}$
0.167	0.250	0.359	± 0.0058	$^{+0.0149}_{-0.0149}$
0.250	0.333	0.552	± 0.0067	$^{+0.0166}_{-0.0166}$
0.333	0.417	0.814	± 0.0078	$^{+0.0133}_{-0.0133}$
0.417	0.500	1.135	± 0.0089	$^{+0.0177}_{-0.0177}$
0.500	0.583	1.523	± 0.0102	$^{+0.0129}_{-0.0129}$
0.583	0.667	1.835	± 0.0110	$^{+0.0107}_{-0.0105}$
0.667	0.750	1.935	± 0.0113	$^{+0.0233}_{-0.0233}$
0.750	0.833	1.618	± 0.0108	$^{+0.0369}_{-0.0369}$
0.833	0.917	0.869	± 0.0086	$^{+0.0266}_{-0.0266}$
0.917	1.000	0.089	± 0.0016	$^{+0.0066}_{-0.0067}$

Table D.47.: Unfolded data, $\mathcal{O}$ = Spherocity, muon channel, $p_{\perp}(\mathrm{Z}) \in [0, 6)$

$\mathcal{O}_{\text{min}}$	$\mathcal{O}_{\text{max}}$	$\frac{1}{N_{\text{ev}}}\frac{\mathrm{d}N}{\mathrm{d}\mathcal{O}}$	δ_{stat}	δ_{syst}
−0.500	1.500	0.008	$\pm$ 0.0002	$^{+0.0004}_{-0.0004}$
1.500	3.500	0.017	$\pm$ 0.0003	$^{+0.0007}_{-0.0007}$
3.500	5.500	0.021	$\pm$ 0.0003	$^{+0.0007}_{-0.0007}$
5.500	7.500	0.022	$\pm$ 0.0003	$^{+0.0008}_{-0.0007}$
7.500	9.500	0.024	$\pm$ 0.0003	$^{+0.0008}_{-0.0008}$
9.500	12.500	0.026	$\pm$ 0.0003	$^{+0.0008}_{-0.0008}$
12.500	15.500	0.026	$\pm$ 0.0003	$^{+0.0007}_{-0.0007}$
15.500	20.500	0.024	$\pm$ 0.0002	$^{+0.0004}_{-0.0004}$
20.500	25.500	0.022	$\pm$ 0.0002	$^{+0.0003}_{-0.0003}$
25.500	30.500	0.018	$\pm$ 0.0002	$^{+0.0002}_{-0.0002}$
30.500	35.500	0.015	$\pm$ 0.0002	$^{+0.0002}_{-0.0002}$
35.500	40.500	0.011	$\pm$ 0.0001	$^{+0.0004}_{-0.0004}$
40.500	45.500	0.008	$\pm$ 0.0001	$^{+0.0004}_{-0.0004}$
45.500	50.500	0.006	$\pm$ 0.0001	$^{+0.0004}_{-0.0004}$
50.500	60.500	0.003	$\pm$ 0.0001	$^{+0.0003}_{-0.0003}$
60.500	75.500	0.001	$\pm$ 0.0000	$^{+0.0002}_{-0.0002}$
75.500	100.500	0.000	$\pm$ 0.0000	$^{+0.0001}_{-0.0001}$

Table D.48.: Unfolded data, $\mathcal{O} = N_{\text{ch}}$, muon channel, $p_{\perp}(\text{Z}) \in [0, 6)$

$\mathcal{O}_{\text{min}}$	$\mathcal{O}_{\text{max}}$	$\frac{1}{N_{\text{ev}}}\frac{\mathrm{d}N}{\mathrm{d}\mathcal{O}}$	δ_{stat}	δ_{syst}
−0.001	4.000	0.065	$\pm$ 0.0005	$^{+0.0014}_{-0.0014}$
4.000	8.000	0.062	$\pm$ 0.0004	$^{+0.0012}_{-0.0012}$
8.000	12.000	0.048	$\pm$ 0.0003	$^{+0.0003}_{-0.0003}$
12.000	16.000	0.031	$\pm$ 0.0002	$^{+0.0004}_{-0.0004}$
16.000	20.000	0.019	$\pm$ 0.0002	$^{+0.0006}_{-0.0006}$
20.000	24.000	0.011	$\pm$ 0.0002	$^{+0.0005}_{-0.0005}$
24.000	28.000	0.006	$\pm$ 0.0001	$^{+0.0004}_{-0.0004}$
28.000	32.000	0.004	$\pm$ 0.0001	$^{+0.0003}_{-0.0003}$
32.000	36.000	0.002	$\pm$ 0.0001	$^{+0.0002}_{-0.0002}$
36.000	40.000	0.001	$\pm$ 0.0000	$^{+0.0002}_{-0.0002}$
40.000	50.000	0.000	$\pm$ 0.0000	$^{+0.0001}_{-0.0001}$
50.000	60.000	0.000	$\pm$ 0.0000	$^{+0.0000}_{-0.0000}$

Table D.49.: Unfolded data, $\mathcal{O}$ = Beamthrust, muon channel, $p_\perp(\mathrm{Z}) \in [0, 6)$

$\mathcal{O}_{\text{min}}$	$\mathcal{O}_{\text{max}}$	$\frac{1}{N_{\text{ev}}}\frac{\text{d}N}{\text{d}\mathcal{O}}$	δ_{stat}	δ_{syst}
0.000	0.083	0.122	$\pm\,0.0045$	$^{+0.0047}_{-0.0048}$
0.083	0.167	0.251	$\pm\,0.0056$	$^{+0.0144}_{-0.0145}$
0.167	0.250	0.441	$\pm\,0.0067$	$^{+0.0180}_{-0.0180}$
0.250	0.333	0.713	$\pm\,0.0079$	$^{+0.0254}_{-0.0254}$
0.333	0.417	1.034	$\pm\,0.0091$	$^{+0.0199}_{-0.0199}$
0.417	0.500	1.357	$\pm\,0.0099$	$^{+0.0119}_{-0.0118}$
0.500	0.583	1.571	$\pm\,0.0102$	$^{+0.0202}_{-0.0201}$
0.583	0.667	1.574	$\pm\,0.0097$	$^{+0.0235}_{-0.0234}$
0.667	0.750	1.381	$\pm\,0.0088$	$^{+0.0249}_{-0.0248}$
0.750	0.833	1.033	$\pm\,0.0077$	$^{+0.0260}_{-0.0260}$
0.833	0.917	0.603	$\pm\,0.0061$	$^{+0.0172}_{-0.0174}$
0.917	1.000	0.184	$\pm\,0.0024$	$^{+0.0065}_{-0.0066}$

Table D.50.: Unfolded data, $\mathcal{O}$ = F-Parameter, muon channel, $p_\perp(\text{Z}) \in [6, 12)$

$\mathcal{O}_{\text{min}}$	$\mathcal{O}_{\text{max}}$	$\frac{1}{N_{\text{ev}}}\frac{\text{d}N}{\text{d}\mathcal{O}}$	δ_{stat}	δ_{syst}
0.636	0.666	0.505	$\pm\,0.0074$	$^{+0.0199}_{-0.0200}$
0.666	0.697	3.360	$\pm\,0.0292$	$^{+0.0942}_{-0.0943}$
0.697	0.727	5.214	$\pm\,0.0324$	$^{+0.1101}_{-0.1100}$
0.727	0.758	5.433	$\pm\,0.0327$	$^{+0.0652}_{-0.0648}$
0.758	0.788	4.520	$\pm\,0.0300$	$^{+0.0414}_{-0.0410}$
0.788	0.819	3.347	$\pm\,0.0262$	$^{+0.0397}_{-0.0396}$
0.819	0.849	2.265	$\pm\,0.0219$	$^{+0.0642}_{-0.0642}$
0.849	0.879	1.457	$\pm\,0.0180$	$^{+0.0579}_{-0.0579}$
0.879	0.910	0.901	$\pm\,0.0148$	$^{+0.0348}_{-0.0349}$
0.910	0.940	0.561	$\pm\,0.0126$	$^{+0.0343}_{-0.0344}$
0.940	0.971	0.341	$\pm\,0.0108$	$^{+0.0149}_{-0.0151}$
0.971	1.001	0.212	$\pm\,0.0098$	$^{+0.0118}_{-0.0120}$

Table D.51.: Unfolded data, $\mathcal{O}$ = transverse thrust, muon channel, $p_\perp(\text{Z}) \in [6, 12)$

$\mathcal{O}_{\text{min}}$	$\mathcal{O}_{\text{max}}$	$\frac{1}{N_{\text{ev}}}\frac{\mathrm{d}N}{\mathrm{d}\mathcal{O}}$ [GeV]	δ_{stat}	δ_{syst}
−0.001	4.000	0.007	± 0.0002	$^{+0.0007}_{-0.0007}$
4.000	8.000	0.014	± 0.0002	$^{+0.0007}_{-0.0007}$
8.000	12.000	0.019	± 0.0002	$^{+0.0007}_{-0.0007}$
12.000	16.000	0.021	± 0.0002	$^{+0.0008}_{-0.0008}$
16.000	20.000	0.020	± 0.0002	$^{+0.0006}_{-0.0006}$
20.000	24.000	0.019	± 0.0002	$^{+0.0004}_{-0.0004}$
24.000	28.000	0.018	± 0.0002	$^{+0.0003}_{-0.0003}$
28.000	32.000	0.016	± 0.0002	$^{+0.0002}_{-0.0002}$
32.000	36.000	0.014	± 0.0002	$^{+0.0002}_{-0.0002}$
36.000	40.000	0.012	± 0.0001	$^{+0.0002}_{-0.0002}$
40.000	50.000	0.009	± 0.0001	$^{+0.0003}_{-0.0003}$
50.000	60.000	0.005	± 0.0001	$^{+0.0003}_{-0.0003}$
60.000	75.000	0.003	± 0.0000	$^{+0.0002}_{-0.0002}$
75.000	100.000	0.001	± 0.0000	$^{+0.0002}_{-0.0002}$

Table D.52.: Unfolded data, $\mathcal{O} = \sum p_\perp$, muon channel, $p_\perp(\mathrm{Z}) \in [6, 12)$

$\mathcal{O}_{\text{min}}$	$\mathcal{O}_{\text{max}}$	$\frac{1}{N_{\text{ev}}}\frac{\mathrm{d}N}{\mathrm{d}\mathcal{O}}$	δ_{stat}	δ_{syst}
0.000	0.058	0.014	± 0.0018	$^{+0.0024}_{-0.0024}$
0.058	0.117	0.025	± 0.0020	$^{+0.0029}_{-0.0029}$
0.117	0.175	0.067	± 0.0033	$^{+0.0050}_{-0.0051}$
0.175	0.233	0.140	± 0.0045	$^{+0.0101}_{-0.0101}$
0.233	0.292	0.290	± 0.0063	$^{+0.0175}_{-0.0176}$
0.292	0.350	0.545	± 0.0084	$^{+0.0298}_{-0.0299}$
0.350	0.408	1.028	± 0.0115	$^{+0.0330}_{-0.0330}$
0.408	0.467	1.907	± 0.0157	$^{+0.0297}_{-0.0297}$
0.467	0.525	3.262	± 0.0207	$^{+0.0271}_{-0.0269}$
0.525	0.583	4.173	± 0.0232	$^{+0.0678}_{-0.0676}$
0.583	0.642	2.887	± 0.0213	$^{+0.0443}_{-0.0443}$
0.642	0.700	0.317	± 0.0044	$^{+0.0150}_{-0.0150}$

Table D.53.: Unfolded data, $\mathcal{O}$ = transverse minor, muon channel, $p_\perp(\mathrm{Z}) \in [6, 12)$

$\mathcal{O}_{\text{min}}$	$\mathcal{O}_{\text{max}}$	$\frac{1}{N_{\text{ev}}} \frac{\text{d}N}{\text{d}\mathcal{O}}$	δ_{stat}	δ_{syst}
0.000	0.083	0.129	$\pm$ 0.0046	$^{+0.0057}_{-0.0058}$
0.083	0.167	0.231	$\pm$ 0.0050	$^{+0.0118}_{-0.0118}$
0.167	0.250	0.356	$\pm$ 0.0056	$^{+0.0162}_{-0.0162}$
0.250	0.333	0.533	$\pm$ 0.0064	$^{+0.0167}_{-0.0167}$
0.333	0.417	0.780	$\pm$ 0.0076	$^{+0.0205}_{-0.0205}$
0.417	0.500	1.081	$\pm$ 0.0087	$^{+0.0177}_{-0.0177}$
0.500	0.583	1.404	$\pm$ 0.0097	$^{+0.0195}_{-0.0194}$
0.583	0.667	1.686	$\pm$ 0.0105	$^{+0.0161}_{-0.0160}$
0.667	0.750	1.745	$\pm$ 0.0106	$^{+0.0302}_{-0.0301}$
0.750	0.833	1.465	$\pm$ 0.0102	$^{+0.0388}_{-0.0388}$
0.833	0.917	0.775	$\pm$ 0.0080	$^{+0.0279}_{-0.0280}$
0.917	1.000	0.078	$\pm$ 0.0014	$^{+0.0044}_{-0.0044}$

Table D.54.: Unfolded data, $\mathcal{O}$ = Spherocity, muon channel, $p_{\perp}(\text{Z}) \in [6, 12)$

$\mathcal{O}_{\text{min}}$	$\mathcal{O}_{\text{max}}$	$\frac{1}{N_{\text{ev}}}\frac{\mathrm{d}N}{\mathrm{d}\mathcal{O}}$	δ_{stat}	δ_{syst}
−0.500	1.500	0.002	± 0.0001	$^{+0.0005}_{-0.0005}$
1.500	3.500	0.008	± 0.0001	$^{+0.0009}_{-0.0009}$
3.500	5.500	0.013	± 0.0002	$^{+0.0010}_{-0.0010}$
5.500	7.500	0.017	± 0.0002	$^{+0.0008}_{-0.0008}$
7.500	9.500	0.019	± 0.0002	$^{+0.0006}_{-0.0006}$
9.500	12.500	0.021	± 0.0002	$^{+0.0007}_{-0.0007}$
12.500	15.500	0.022	± 0.0002	$^{+0.0008}_{-0.0008}$
15.500	20.500	0.022	± 0.0002	$^{+0.0008}_{-0.0008}$
20.500	25.500	0.021	± 0.0001	$^{+0.0007}_{-0.0007}$
25.500	30.500	0.019	± 0.0001	$^{+0.0004}_{-0.0004}$
30.500	35.500	0.016	± 0.0001	$^{+0.0003}_{-0.0003}$
35.500	40.500	0.012	± 0.0001	$^{+0.0003}_{-0.0003}$
40.500	45.500	0.009	± 0.0001	$^{+0.0004}_{-0.0004}$
45.500	50.500	0.007	± 0.0001	$^{+0.0004}_{-0.0004}$
50.500	60.500	0.004	± 0.0000	$^{+0.0003}_{-0.0003}$
60.500	75.500	0.002	± 0.0000	$^{+0.0002}_{-0.0002}$
75.500	100.500	0.000	± 0.0000	$^{+0.0001}_{-0.0001}$

Table D.55.: Unfolded data, $\mathcal{O} = N_{\text{ch}}$, muon channel, $p_{\perp}(\text{Z}) \in [6, 12)$

$\mathcal{O}_{\text{min}}$	$\mathcal{O}_{\text{max}}$	$\frac{1}{N_{\text{ev}}}\frac{\mathrm{d}N}{\mathrm{d}\mathcal{O}}$	δ_{stat}	δ_{syst}
−0.001	4.000	0.045	± 0.0004	$^{+0.0016}_{-0.0016}$
4.000	8.000	0.059	± 0.0004	$^{+0.0015}_{-0.0015}$
8.000	12.000	0.051	± 0.0003	$^{+0.0005}_{-0.0005}$
12.000	16.000	0.036	± 0.0003	$^{+0.0005}_{-0.0005}$
16.000	20.000	0.023	± 0.0002	$^{+0.0006}_{-0.0006}$
20.000	24.000	0.014	± 0.0002	$^{+0.0006}_{-0.0006}$
24.000	28.000	0.009	± 0.0001	$^{+0.0005}_{-0.0005}$
28.000	32.000	0.005	± 0.0001	$^{+0.0004}_{-0.0004}$
32.000	36.000	0.003	± 0.0001	$^{+0.0003}_{-0.0003}$
36.000	40.000	0.002	± 0.0001	$^{+0.0002}_{-0.0002}$
40.000	50.000	0.001	± 0.0000	$^{+0.0001}_{-0.0001}$
50.000	60.000	0.000	± 0.0000	$^{+0.0000}_{-0.0000}$

Table D.56.: Unfolded data, $\mathcal{O}$ = Beamthrust, muon channel, $p_\perp(\mathrm{Z}) \in [6, 12)$

$\mathcal{O}_{\text{min}}$	$\mathcal{O}_{\text{max}}$	$\frac{1}{N_{\text{ev}}}\frac{\mathrm{d}N}{\mathrm{d}\mathcal{O}}$	δ_{stat}	δ_{syst}
0.000	0.083	0.143	± 0.0048	$^{+0.0048}_{-0.0048}$
0.083	0.167	0.371	± 0.0069	$^{+0.0082}_{-0.0083}$
0.167	0.250	0.658	± 0.0084	$^{+0.0172}_{-0.0172}$
0.250	0.333	0.950	± 0.0094	$^{+0.0148}_{-0.0148}$
0.333	0.417	1.239	± 0.0102	$^{+0.0154}_{-0.0154}$
0.417	0.500	1.470	± 0.0105	$^{+0.0113}_{-0.0111}$
0.500	0.583	1.587	± 0.0105	$^{+0.0102}_{-0.0100}$
0.583	0.667	1.520	± 0.0097	$^{+0.0126}_{-0.0125}$
0.667	0.750	1.285	± 0.0087	$^{+0.0209}_{-0.0209}$
0.750	0.833	0.929	± 0.0074	$^{+0.0162}_{-0.0163}$
0.833	0.917	0.532	± 0.0058	$^{+0.0138}_{-0.0140}$
0.917	1.000	0.164	± 0.0023	$^{+0.0056}_{-0.0056}$

Table D.57.: Unfolded data, $\mathcal{O}$ = F-Parameter, muon channel, $p_{\perp}(\mathrm{Z}) \in [12, 25)$

$\mathcal{O}_{\text{min}}$	$\mathcal{O}_{\text{max}}$	$\frac{1}{N_{\text{ev}}}\frac{\mathrm{d}N}{\mathrm{d}\mathcal{O}}$	δ_{stat}	δ_{syst}
0.636	0.666	0.441	± 0.0068	$^{+0.0232}_{-0.0234}$
0.666	0.697	3.089	± 0.0285	$^{+0.0752}_{-0.0754}$
0.697	0.727	4.902	± 0.0320	$^{+0.0787}_{-0.0786}$
0.727	0.758	5.293	± 0.0330	$^{+0.0458}_{-0.0453}$
0.758	0.788	4.741	± 0.0316	$^{+0.0348}_{-0.0345}$
0.788	0.819	3.803	± 0.0287	$^{+0.0363}_{-0.0362}$
0.819	0.849	2.785	± 0.0250	$^{+0.0326}_{-0.0326}$
0.849	0.879	1.925	± 0.0213	$^{+0.0400}_{-0.0400}$
0.879	0.910	1.301	± 0.0184	$^{+0.0358}_{-0.0359}$
0.910	0.940	0.800	± 0.0153	$^{+0.0217}_{-0.0219}$
0.940	0.971	0.440	± 0.0121	$^{+0.0155}_{-0.0157}$
0.971	1.001	0.199	± 0.0091	$^{+0.0105}_{-0.0106}$

Table D.58.: Unfolded data, $\mathcal{O}$ = transverse thrust, muon channel, $p_{\perp}(\mathrm{Z}) \in [12, 25)$

$\mathcal{O}_{\text{min}}$	$\mathcal{O}_{\text{max}}$	$\frac{1}{N_{\text{ev}}}\frac{\mathrm{d}N}{\mathrm{d}\mathcal{O}}$ [GeV]	δ_{stat}	δ_{syst}
−0.001	4.000	0.002	± 0.0001	$^{+0.0002}_{-0.0002}$
4.000	8.000	0.007	± 0.0002	$^{+0.0005}_{-0.0005}$
8.000	12.000	0.012	± 0.0002	$^{+0.0007}_{-0.0007}$
12.000	16.000	0.016	± 0.0002	$^{+0.0006}_{-0.0006}$
16.000	20.000	0.018	± 0.0002	$^{+0.0007}_{-0.0007}$
20.000	24.000	0.019	± 0.0002	$^{+0.0006}_{-0.0006}$
24.000	28.000	0.019	± 0.0002	$^{+0.0003}_{-0.0003}$
28.000	32.000	0.017	± 0.0002	$^{+0.0003}_{-0.0003}$
32.000	36.000	0.017	± 0.0002	$^{+0.0003}_{-0.0003}$
36.000	40.000	0.015	± 0.0002	$^{+0.0002}_{-0.0002}$
40.000	50.000	0.012	± 0.0001	$^{+0.0002}_{-0.0002}$
50.000	60.000	0.008	± 0.0001	$^{+0.0004}_{-0.0004}$
60.000	75.000	0.005	± 0.0001	$^{+0.0003}_{-0.0003}$
75.000	100.000	0.002	± 0.0000	$^{+0.0002}_{-0.0002}$

Table D.59.: Unfolded data, $\mathcal{O} = \sum p_\perp$, muon channel, $p_\perp(\mathrm{Z}) \in [12, 25)$

$\mathcal{O}_{\text{min}}$	$\mathcal{O}_{\text{max}}$	$\frac{1}{N_{\text{ev}}}\frac{\mathrm{d}N}{\mathrm{d}\mathcal{O}}$	δ_{stat}	δ_{syst}
0.000	0.058	0.012	± 0.0015	$^{+0.0020}_{-0.0020}$
0.058	0.117	0.041	± 0.0027	$^{+0.0036}_{-0.0037}$
0.117	0.175	0.109	± 0.0041	$^{+0.0056}_{-0.0058}$
0.175	0.233	0.240	± 0.0059	$^{+0.0090}_{-0.0092}$
0.233	0.292	0.454	± 0.0079	$^{+0.0145}_{-0.0146}$
0.292	0.350	0.822	± 0.0106	$^{+0.0203}_{-0.0204}$
0.350	0.408	1.384	± 0.0136	$^{+0.0213}_{-0.0213}$
0.408	0.467	2.250	± 0.0175	$^{+0.0185}_{-0.0185}$
0.467	0.525	3.312	± 0.0211	$^{+0.0230}_{-0.0226}$
0.525	0.583	3.924	± 0.0230	$^{+0.0457}_{-0.0454}$
0.583	0.642	2.643	± 0.0206	$^{+0.0350}_{-0.0350}$
0.642	0.700	0.301	± 0.0047	$^{+0.0204}_{-0.0204}$

Table D.60.: Unfolded data, $\mathcal{O}$ = transverse minor, muon channel, $p_\perp(\mathrm{Z}) \in [12, 25)$

$\mathcal{O}_{\text{min}}$	$\mathcal{O}_{\text{max}}$	$\frac{1}{N_{\text{ev}}}\frac{\mathrm{d}N}{\mathrm{d}\mathcal{O}}$	δ_{stat}	δ_{syst}
0.000	0.083	0.191	± 0.0055	$^{+0.0056}_{-0.0057}$
0.083	0.167	0.364	± 0.0064	$^{+0.0097}_{-0.0097}$
0.167	0.250	0.551	± 0.0072	$^{+0.0104}_{-0.0104}$
0.250	0.333	0.742	± 0.0079	$^{+0.0120}_{-0.0120}$
0.333	0.417	0.977	± 0.0087	$^{+0.0174}_{-0.0174}$
0.417	0.500	1.238	± 0.0096	$^{+0.0119}_{-0.0119}$
0.500	0.583	1.468	± 0.0101	$^{+0.0113}_{-0.0112}$
0.583	0.667	1.638	± 0.0105	$^{+0.0099}_{-0.0098}$
0.667	0.750	1.619	± 0.0104	$^{+0.0184}_{-0.0184}$
0.750	0.833	1.310	± 0.0097	$^{+0.0238}_{-0.0238}$
0.833	0.917	0.681	± 0.0076	$^{+0.0221}_{-0.0222}$
0.917	1.000	0.067	± 0.0013	$^{+0.0047}_{-0.0048}$

Table D.61.: Unfolded data, $\mathcal{O}$ = Spherocity, muon channel, $p_{\perp}(\mathrm{Z}) \in [12, 25)$

$\mathcal{O}_{\text{min}}$	$\mathcal{O}_{\text{max}}$	$\frac{1}{N_{\text{ev}}}\frac{\mathrm{d}N}{\mathrm{d}\mathcal{O}}$	δ_{stat}	δ_{syst}
−0.500	1.500	0.001	$\pm$ 0.0001	$^{+0.0001}_{-0.0001}$
1.500	3.500	0.003	$\pm$ 0.0001	$^{+0.0003}_{-0.0003}$
3.500	5.500	0.006	$\pm$ 0.0002	$^{+0.0005}_{-0.0005}$
5.500	7.500	0.011	$\pm$ 0.0002	$^{+0.0007}_{-0.0007}$
7.500	9.500	0.015	$\pm$ 0.0002	$^{+0.0008}_{-0.0008}$
9.500	12.500	0.018	$\pm$ 0.0002	$^{+0.0008}_{-0.0008}$
12.500	15.500	0.022	$\pm$ 0.0003	$^{+0.0008}_{-0.0008}$
15.500	20.500	0.023	$\pm$ 0.0002	$^{+0.0007}_{-0.0007}$
20.500	25.500	0.023	$\pm$ 0.0002	$^{+0.0005}_{-0.0005}$
25.500	30.500	0.021	$\pm$ 0.0002	$^{+0.0003}_{-0.0002}$
30.500	35.500	0.018	$\pm$ 0.0002	$^{+0.0002}_{-0.0002}$
35.500	40.500	0.015	$\pm$ 0.0002	$^{+0.0003}_{-0.0003}$
40.500	45.500	0.012	$\pm$ 0.0001	$^{+0.0005}_{-0.0005}$
45.500	50.500	0.009	$\pm$ 0.0001	$^{+0.0005}_{-0.0005}$
50.500	60.500	0.006	$\pm$ 0.0001	$^{+0.0004}_{-0.0004}$
60.500	75.500	0.002	$\pm$ 0.0000	$^{+0.0003}_{-0.0003}$
75.500	100.500	0.000	$\pm$ 0.0000	$^{+0.0001}_{-0.0001}$

Table D.62.: Unfolded data, $\mathcal{O} = N_{\text{ch}}$, muon channel, $p_{\perp}(\text{Z}) \in [12, 25)$

$\mathcal{O}_{\text{min}}$	$\mathcal{O}_{\text{max}}$	$\frac{1}{N_{\text{ev}}}\frac{\mathrm{d}N}{\mathrm{d}\mathcal{O}}$	δ_{stat}	δ_{syst}
−0.001	4.000	0.024	$\pm$ 0.0003	$^{+0.0010}_{-0.0010}$
4.000	8.000	0.048	$\pm$ 0.0003	$^{+0.0015}_{-0.0015}$
8.000	12.000	0.050	$\pm$ 0.0003	$^{+0.0008}_{-0.0008}$
12.000	16.000	0.041	$\pm$ 0.0003	$^{+0.0003}_{-0.0003}$
16.000	20.000	0.030	$\pm$ 0.0002	$^{+0.0005}_{-0.0005}$
20.000	24.000	0.021	$\pm$ 0.0002	$^{+0.0007}_{-0.0007}$
24.000	28.000	0.014	$\pm$ 0.0002	$^{+0.0006}_{-0.0006}$
28.000	32.000	0.009	$\pm$ 0.0001	$^{+0.0005}_{-0.0005}$
32.000	36.000	0.005	$\pm$ 0.0001	$^{+0.0004}_{-0.0004}$
36.000	40.000	0.003	$\pm$ 0.0001	$^{+0.0003}_{-0.0003}$
40.000	50.000	0.002	$\pm$ 0.0000	$^{+0.0002}_{-0.0002}$
50.000	60.000	0.001	$\pm$ 0.0000	$^{+0.0001}_{-0.0001}$

Table D.63.: Unfolded data, $\mathcal{O}$ = Beamthrust, muon channel, $p_\perp(\mathrm{Z}) \in [12, 25)$

$\mathcal{O}_{\text{min}}$	$\mathcal{O}_{\text{max}}$	$\frac{1}{N_{\text{ev}}}\frac{\mathrm{d}N}{\mathrm{d}\mathcal{O}}$	δ_{stat}	δ_{syst}
0.000	0.083	0.364	± 0.0087	$^{+0.0111}_{-0.0112}$
0.083	0.167	0.977	± 0.0130	$^{+0.0256}_{-0.0256}$
0.167	0.250	1.405	± 0.0142	$^{+0.0222}_{-0.0222}$
0.250	0.333	1.579	± 0.0139	$^{+0.0168}_{-0.0166}$
0.333	0.417	1.605	± 0.0132	$^{+0.0090}_{-0.0087}$
0.417	0.500	1.508	± 0.0122	$^{+0.0141}_{-0.0140}$
0.500	0.583	1.319	± 0.0108	$^{+0.0130}_{-0.0130}$
0.583	0.667	1.076	± 0.0094	$^{+0.0120}_{-0.0120}$
0.667	0.750	0.803	± 0.0077	$^{+0.0124}_{-0.0125}$
0.750	0.833	0.535	± 0.0063	$^{+0.0126}_{-0.0129}$
0.833	0.917	0.296	± 0.0048	$^{+0.0095}_{-0.0098}$
0.917	1.000	0.093	± 0.0021	$^{+0.0041}_{-0.0042}$

Table D.64.: Unfolded data, $\mathcal{O}$ = F-Parameter, muon channel, $p_\perp(\mathrm{Z}) \in [25, \infty)$

$\mathcal{O}_{\text{min}}$	$\mathcal{O}_{\text{max}}$	$\frac{1}{N_{\text{ev}}}\frac{\mathrm{d}N}{\mathrm{d}\mathcal{O}}$	δ_{stat}	δ_{syst}
0.636	0.666	0.202	± 0.0051	$^{+0.0137}_{-0.0139}$
0.666	0.697	1.714	± 0.0235	$^{+0.0376}_{-0.0385}$
0.697	0.727	3.209	± 0.0297	$^{+0.0448}_{-0.0449}$
0.727	0.758	4.082	± 0.0333	$^{+0.0382}_{-0.0381}$
0.758	0.788	4.453	± 0.0352	$^{+0.0372}_{-0.0368}$
0.788	0.819	4.407	± 0.0356	$^{+0.0320}_{-0.0315}$
0.819	0.849	4.069	± 0.0350	$^{+0.0268}_{-0.0265}$
0.849	0.879	3.449	± 0.0331	$^{+0.0350}_{-0.0350}$
0.879	0.910	2.698	± 0.0305	$^{+0.0475}_{-0.0475}$
0.910	0.940	1.926	± 0.0273	$^{+0.0397}_{-0.0397}$
0.940	0.971	1.112	± 0.0226	$^{+0.0359}_{-0.0360}$
0.971	1.001	0.353	± 0.0137	$^{+0.0112}_{-0.0116}$

Table D.65.: Unfolded data, $\mathcal{O}$ = transverse thrust, muon channel, $p_\perp(\mathrm{Z}) \in [25, \infty)$

$\mathcal{O}_{\text{min}}$	$\mathcal{O}_{\text{max}}$	$\frac{1}{N_{\text{ev}}}\frac{\mathrm{d}N}{\mathrm{d}\mathcal{O}}$ [GeV]	δ_{stat}	δ_{syst}
−0.001	4.000	0.001	± 0.0000	$^{+0.0001}_{-0.0001}$
4.000	8.000	0.001	± 0.0001	$^{+0.0002}_{-0.0002}$
8.000	12.000	0.003	± 0.0001	$^{+0.0003}_{-0.0003}$
12.000	16.000	0.004	± 0.0001	$^{+0.0004}_{-0.0004}$
16.000	20.000	0.007	± 0.0001	$^{+0.0006}_{-0.0006}$
20.000	24.000	0.009	± 0.0001	$^{+0.0006}_{-0.0006}$
24.000	28.000	0.010	± 0.0001	$^{+0.0006}_{-0.0006}$
28.000	32.000	0.011	± 0.0001	$^{+0.0006}_{-0.0006}$
32.000	36.000	0.012	± 0.0001	$^{+0.0006}_{-0.0006}$
36.000	40.000	0.013	± 0.0001	$^{+0.0006}_{-0.0006}$
40.000	50.000	0.013	± 0.0001	$^{+0.0004}_{-0.0004}$
50.000	60.000	0.012	± 0.0001	$^{+0.0002}_{-0.0002}$
60.000	75.000	0.009	± 0.0001	$^{+0.0002}_{-0.0002}$
75.000	100.000	0.006	± 0.0001	$^{+0.0002}_{-0.0002}$

Table D.66.: Unfolded data, $\mathcal{O} = \sum p_\perp$, muon channel, $p_\perp(\mathrm{Z}) \in [25, \infty)$

$\mathcal{O}_{\text{min}}$	$\mathcal{O}_{\text{max}}$	$\frac{1}{N_{\text{ev}}}\frac{\mathrm{d}N}{\mathrm{d}\mathcal{O}}$	δ_{stat}	δ_{syst}
0.000	0.058	0.022	± 0.0024	$^{+0.0027}_{-0.0027}$
0.058	0.117	0.159	± 0.0062	$^{+0.0111}_{-0.0113}$
0.117	0.175	0.428	± 0.0095	$^{+0.0191}_{-0.0192}$
0.175	0.233	0.788	± 0.0123	$^{+0.0275}_{-0.0275}$
0.233	0.292	1.193	± 0.0146	$^{+0.0312}_{-0.0312}$
0.292	0.350	1.685	± 0.0171	$^{+0.0232}_{-0.0232}$
0.350	0.408	2.150	± 0.0190	$^{+0.0141}_{-0.0141}$
0.408	0.467	2.605	± 0.0209	$^{+0.0157}_{-0.0154}$
0.467	0.525	2.873	± 0.0220	$^{+0.0308}_{-0.0306}$
0.525	0.583	2.677	± 0.0213	$^{+0.0352}_{-0.0352}$
0.583	0.642	1.691	± 0.0183	$^{+0.0260}_{-0.0261}$
0.642	0.700	0.239	± 0.0055	$^{+0.0151}_{-0.0152}$

Table D.67.: Unfolded data, $\mathcal{O}$ = transverse minor, muon channel, $p_\perp(\mathrm{Z}) \in [25, \infty)$

$\mathcal{O}_{\text{min}}$	$\mathcal{O}_{\text{max}}$	$\frac{1}{N_{\text{ev}}} \frac{\mathrm{d}N}{\mathrm{d}\mathcal{O}}$	δ_{stat}	δ_{syst}
0.000	0.083	0.699	± 0.0120	$^{+0.0275}_{-0.0275}$
0.083	0.167	1.044	± 0.0124	$^{+0.0315}_{-0.0315}$
0.167	0.250	1.227	± 0.0122	$^{+0.0180}_{-0.0179}$
0.250	0.333	1.323	± 0.0120	$^{+0.0114}_{-0.0113}$
0.333	0.417	1.358	± 0.0117	$^{+0.0054}_{-0.0054}$
0.417	0.500	1.341	± 0.0112	$^{+0.0098}_{-0.0098}$
0.500	0.583	1.297	± 0.0107	$^{+0.0142}_{-0.0142}$
0.583	0.667	1.195	± 0.0101	$^{+0.0176}_{-0.0176}$
0.667	0.750	1.014	± 0.0092	$^{+0.0175}_{-0.0175}$
0.750	0.833	0.714	± 0.0080	$^{+0.0136}_{-0.0137}$
0.833	0.917	0.324	± 0.0056	$^{+0.0096}_{-0.0099}$
0.917	1.000	0.027	± 0.0010	$^{+0.0023}_{-0.0023}$

Table D.68.: Unfolded data, $\mathcal{O}$ = Spherocity, muon channel, $p_{\perp}(\mathrm{Z}) \in [25, \infty)$

$\mathcal{O}_{\text{min}}$	$\mathcal{O}_{\text{max}}$	$\frac{1}{N_{\text{ev}}}\frac{\mathrm{d}N}{\mathrm{d}\mathcal{O}}$	δ_{stat}	δ_{syst}
−0.500	1.500	0.000	± 0.0000	$^{+0.0001}_{-0.0001}$
1.500	3.500	0.001	± 0.0001	$^{+0.0001}_{-0.0002}$
3.500	5.500	0.002	± 0.0001	$^{+0.0002}_{-0.0002}$
5.500	7.500	0.003	± 0.0001	$^{+0.0004}_{-0.0004}$
7.500	9.500	0.006	± 0.0002	$^{+0.0006}_{-0.0006}$
9.500	12.500	0.010	± 0.0002	$^{+0.0008}_{-0.0008}$
12.500	15.500	0.014	± 0.0002	$^{+0.0009}_{-0.0009}$
15.500	20.500	0.018	± 0.0002	$^{+0.0008}_{-0.0008}$
20.500	25.500	0.022	± 0.0002	$^{+0.0007}_{-0.0007}$
25.500	30.500	0.023	± 0.0002	$^{+0.0005}_{-0.0005}$
30.500	35.500	0.022	± 0.0002	$^{+0.0003}_{-0.0003}$
35.500	40.500	0.020	± 0.0002	$^{+0.0003}_{-0.0003}$
40.500	45.500	0.017	± 0.0002	$^{+0.0004}_{-0.0004}$
45.500	50.500	0.014	± 0.0002	$^{+0.0004}_{-0.0004}$
50.500	60.500	0.009	± 0.0001	$^{+0.0005}_{-0.0005}$
60.500	75.500	0.004	± 0.0001	$^{+0.0004}_{-0.0004}$
75.500	100.500	0.001	± 0.0000	$^{+0.0002}_{-0.0002}$

Table D.69.: Unfolded data, $\mathcal{O} = N_{\text{ch}}$, muon channel, $p_{\perp}(\text{Z}) \in [25, \infty)$

$\mathcal{O}_{\text{min}}$	$\mathcal{O}_{\text{max}}$	$\frac{1}{N_{\text{ev}}}\frac{\mathrm{d}N}{\mathrm{d}\mathcal{O}}$	δ_{stat}	δ_{syst}
−0.001	4.000	0.007	± 0.0002	$^{+0.0004}_{-0.0004}$
4.000	8.000	0.021	± 0.0002	$^{+0.0011}_{-0.0011}$
8.000	12.000	0.030	± 0.0003	$^{+0.0011}_{-0.0011}$
12.000	16.000	0.034	± 0.0003	$^{+0.0009}_{-0.0009}$
16.000	20.000	0.033	± 0.0003	$^{+0.0005}_{-0.0005}$
20.000	24.000	0.029	± 0.0003	$^{+0.0002}_{-0.0002}$
24.000	28.000	0.024	± 0.0002	$^{+0.0004}_{-0.0004}$
28.000	32.000	0.019	± 0.0002	$^{+0.0005}_{-0.0005}$
32.000	36.000	0.015	± 0.0002	$^{+0.0005}_{-0.0005}$
36.000	40.000	0.012	± 0.0002	$^{+0.0005}_{-0.0005}$
40.000	50.000	0.007	± 0.0001	$^{+0.0005}_{-0.0005}$
50.000	60.000	0.004	± 0.0001	$^{+0.0003}_{-0.0003}$

Table D.70.: Unfolded data, $\mathcal{O}$ = Beamthrust, muon channel, $p_\perp(\mathrm{Z}) \in [25, \infty)$

Bibliography

[1] E. Noether, Invariant variation problems, *Transport Theory and Statistical Physics*, 1:186–207, 1971, doi:10.1080/00411457108231446.

[2] S. Weinberg, A Model of Leptons, *Phys.Rev.Lett.*, 19:1264–1266, 1967, doi:10.1103/PhysRevLett.19.1264, URL http://link.aps.org/doi/10.1103/PhysRevLett.19.1264.

[3] C. N. Yang and R. L. Mills, Conservation of Isotopic Spin and Isotopic Gauge Invariance, *Phys.Rev.*, 96:191–195, 1954, doi:10.1103/PhysRev.96.191, URL http://link.aps.org/doi/10.1103/PhysRev.96.191.

[4] G. 'tHooft, Renormalization of massless Yang-Mills fields, *Nuclear Physics B*, 33(1):173 – 199, 1971, ISSN 0550-3213, doi:http://dx.doi.org/10.1016/0550-3213(71)90395-6, URL http://www.sciencedirect.com/science/article/pii/0550321371903956.

[5] F. Englert and R. Brout, Broken Symmetry and the Mass of Gauge Vector Mesons, *Phys.Rev.Lett.*, 13:321–323, 1964, doi:10.1103/PhysRevLett.13.321, URL http://link.aps.org/doi/10.1103/PhysRevLett.13.321.

[6] P. W. Higgs, Broken Symmetries and the Masses of Gauge Bosons, *Phys.Rev.Lett.*, 13:508–509, 1964, doi:10.1103/PhysRevLett.13.508, URL http://link.aps.org/doi/10.1103/PhysRevLett.13.508.

[7] G. S. Guralnik, C. R. Hagen, and T. W. B. Kibble, Global Conservation Laws and Massless Particles, *Phys.Rev.Lett.*, 13:585–587, 1964, doi:10.1103/PhysRevLett.13.585, URL http://link.aps.org/doi/10.1103/PhysRevLett.13.585.

[8] ATLAS collaboration, A Particle Consistent with the Higgs Boson Observed with the ATLAS Detector at the Large Hadron Collider, *Science*, 338(6114):1576–1582, 2012, doi:10.1126/science.1232005, URL http://www.sciencemag.org/content/

338/6114/1576.abstract.

[9] CMS collaboration, Observation of a new boson at a mass of 125 GeV with the CMS experiment at the LHC, *Phys.Lett.*, B716:30–61, 2012, doi:10.1016/j.physletb.2012.08.021.

[10] Wikimedia Commons, Standard Model of Elementary Particles, February 2014, URL http://commons.wikimedia.org/wiki/File:Standard_Model_of_Elementary_Particles.svg.

[11] Particle Data Group, Review of Particle Physics, *Phys.Rev.*, D86:010001, 2012, doi:10.1103/PhysRevD.86.010001, URL http://link.aps.org/doi/10.1103/PhysRevD.86.010001.

[12] UA1 collaboration, Experimental observation of isolated large transverse energy electrons with associated missing energy at $\sqrt{s} = 540$ GeV , *Phys.Lett.*, B122(1):103 – 116, 1983, ISSN 0370-2693, doi:http://dx.doi.org/10.1016/0370-2693(83)91177-2, URL http://www.sciencedirect.com/science/article/pii/0370269383911772.

[13] CMS collaboration, Observation of single isolated electrons of high transverse momentum in events with missing transverse energy at the cern pp collider, *Phys.Lett.*, B122(56):476 – 485, 1983, ISSN 0370-2693, doi:http://dx.doi.org/10.1016/0370-2693(83)91605-2, URL http://www.sciencedirect.com/science/article/pii/0370269383916052.

[14] F. Halzen and A. D. Martin, Quarks and leptons: An introductory course in modern particle physics, *Wiley*, 1984.

[15] ATLAS collaboration, Measurement of the inclusive cross sections in the μ decay channels in pp-collisions at $\sqrt{s} = 7$ TeV with the ATLAS detector, *Phys.Rev.*, D85: 072004, 2012, doi:10.1103/PhysRevD.85.072004, URL http://link.aps.org/doi/10.1103/PhysRevD.85.072004.

[16] TOTEM collaboration, First measurement of the total proton-proton cross section at the LHC energy of $\sqrt{s}$ =7 TeV, *Europhys.Lett.*, 96:21002, 2011, doi:10.1209/0295-5075/96/21002.

[17] S. Bethke, The 2009 World Average of α_s, *Eur.Phys.J.*, C64:689–703, 2009, doi:10.1140/epjc/s10052-009-1173-1.

[18] B. Pontecorvo, Neutrino Experiments and the Problem of Conservation of Leptonic Charge, *Soviet Journal of Experimental and Theoretical Physics*, 26:984, 1968.

[19] V. Trimble, Existence and Nature of Dark Matter in the Universe, *Annual Review of Astronomy and Astrophysics*, 25(1):425–472, 1987, doi:10.1146/annurev.aa.25.090187.002233, URL http://www.annualreviews.org/doi/abs/10.1146/annurev.aa.25.090187.002233.

[20] W. R. Leo, Techniques for Nuclear and Particle Physics Experiments, *Springer*, 1987, doi:10.1007/978-3-642-00829-0.

[21] N. Craig, The State of Supersymmetry after Run I of the LHC, 2013, URL http://arxiv.org/abs/1309.0528.

[22] ATLAS collaboration, ATLAS Technical Proposal - for a General-Purpose pp Experiment at the Large Hadron Collider at CERN, *LHC Tech. Proposal*, 1994, CERN/LHCC/94-43, LHCC/P2, ISBN 92-9083-067-0.

[23] ATLAS collaboration, ATLAS detector and physics performance: Technical Design Report, 2, *CERN, ATLAS Design Report*, 1999, URL http://cds.cern.ch/record/391177.

[24] ATLAS collaboration, Charged-particle multiplicities in pp interactions at $\sqrt{s} = 900$ GeV measured with the ATLAS detector at the LHC, *Phys.Lett.*, B688:21–42, 2010, doi:10.1016/j.physletb.2010.03.064.

[25] ATLAS collaboration, The ATLAS Experiment at the CERN Large Hadron Collider, *JINST*, 3(08):S08003, 2008, URL http://stacks.iop.org/1748-0221/3/i=08/a=S08003.

[26] The ATLAS TRT collaboration, The ATLAS Transition Radiation Tracker (TRT) proportional drift tube: design and performance, *JINST*, 3(02):P02013, 2008, URL http://stacks.iop.org/1748-0221/3/i=02/a=P02013.

[27] ATLAS collaboration, Expected electron performance in the ATLAS experiment, *ATLAS note*, ATL-PHYS-PUB-2011-006, 2011.

[28] M. Aharrouche, J. Colas, L. D. Ciaccio, et al., Energy linearity and resolution of the ATLAS electromagnetic barrel calorimeter in an electron testbeam, *Nucl. Instr. Meth. Phys. Res.*, A568(2):601 – 623, 2006, ISSN 0168-9002, doi:10.1016/j.nima.2006.07.053, URL http://www.sciencedirect.com/

science/article/pii/S0168900206013222.

[29] ATLAS collaboration, The ATLAS Inner Detector commissioning and calibration, *Eur.Phys.J.*, C70:787–821, 2010, doi:10.1140/epjc/s10052-010-1366-7.

[30] ATLAS collaboration, Construction, assembly and tests of the ATLAS electromagnetic end-cap calorimeters, *JINST*, 3:P06002, 2008.

[31] ATLAS collaboration, Construction, assembly and tests of the ATLAS electromagnetic barrel calorimeter, *Nucl. Instr. Meth. Phys. Res.*, A558(2):388–418, 2006, QC 20100525.

[32] D. E. Groom, N. V. Mokhov, and S. I. Striganov, Muon stopping power and range tables 10 MeV - 100 TeV, *Atomic Data and Nuclear Data Tables*, 78(2):183 – 356, 2001, ISSN 0092-640X, doi:http://dx.doi.org/10.1006/adnd.2001.0861, URL http://www.sciencedirect.com/science/article/pii/S0092640X01908617.

[33] M. Berger, J. Coursey, M. Zucker, and J. Chang, ESTAR, PSTAR, and ASTAR: Computer Programs for Calculating Stopping-Power and Range Tables for Electrons, Protons, and Helium Ions, *National Institute of Standards and Technology, Gaithersburg, MD*, 2005, URL http://www.nist.gov/pml/data/star/.

[34] J. Snuverink, The ATLAS Muon Spectrometer: Commissioning and Tracking, 2009, PhD thesis, doi:10.3990/1.9789036529129.

[35] ATLAS collaboration, Calibration and Performance of the ATLAS Muon Spectrometer, *ATLAS note*, ATL-COM-MUON-2011-019, 2011.

[36] K. Nagai, Thin gap chambers in ATLAS, *Nucl. Instr. Meth. Phys. Res.*, A384 (1):219 – 221, 1996, ISSN 0168-9002, doi:http://dx.doi.org/10.1016/S0168-9002(96)01065-0, URL http://www.sciencedirect.com/science/article/pii/S0168900296010650, BEAUTY '96.

[37] ATLAS collaboration, Measurement of muon momentum resolution of the ATLAS detector, *Eur.Phys.J.*, 28:12039, 2012, doi:10.1051/epjconf/20122812039.

[38] ATLAS collaboration, The ATLAS Experiment at the CERN Large Hadron Collider, *JINST*, 3:S08003, 2008, doi:10.1088/1748-0221/3/08/S08003.

[39] ATLAS collaboration, Concepts, Design and Implementation of the ATLAS New Tracking (NEWT), *ATLAS note*, ATL-SOFT-PUB-2007-007. ATL-COM-SOFT-2007-002, 2007.

[40] S. Montesano and F. Ragusa, Commissioning of the tracking system in the ATLAS detector, PhD thesis, CERN-THESIS-2010-018.

[41] G. Welch and G. Bishop, An Introduction to the Kalman Filter, *University of North Carolina at Chapel Hill*, 1995.

[42] ATLAS collaboration, Performance of primary vertex reconstruction in proton-proton collisions at $\sqrt{s}$ =7 TeV in the ATLAS experiment, *ATLAS note*, ATLAS-CONF-2010-069, 2010.

[43] R. Fruhwirth, W. Waltenberger, and P. Vanlaer, Adaptive vertex fitting, *J.Phys.*, G34:N343, 2007, doi:10.1088/0954-3899/34/12/N01.

[44] ATLAS collaboration, Charged-particle multiplicities in pp interactions measured with the ATLAS detector at the LHC, *New J.Phys.*, 13:053033, 2011, doi:10.1088/1367-2630/13/5/053033.

[45] ATLAS collaboration, Track Reconstruction Efficiency in $\sqrt{s}$ = 7 TeV Data for Tracks with $p_\perp > 100$ MeV, *ATLAS note*, ATL-PHYS-INT-2011-001, 2011.

[46] ATLAS collaboration, Electron performance measurements with the ATLAS detector using the 2010 LHC proton-proton collision data, *Eur.Phys.J.*, C72 (3):1–46, 2012, ISSN 1434-6044, doi:10.1140/epjc/s10052-012-1909-1, URL http://dx.doi.org/10.1140/epjc/s10052-012-1909-1.

[47] ATLAS collaboration, Electron performance measurements with the ATLAS detector using the 2010 LHC proton-proton collision data, *Eur.Phys.J.*, C72:1909, 2012, doi:10.1140/epjc/s10052-012-1909-1.

[48] ATLAS collaboration, EnergyRescalerTool from egammaAnalysisUtils version 00-04-17.

[49] J. Alison, The road to discovery: Detector alignment, electron identification, particle misidentification, WW physics, and the discovery of the Higgs Boson, *ProQuest Dissertations and Theses*, 2012, URL http://search.proquest.com/docview/1287097601, PhD thesis.

[50] ATLAS collaboration, Measurement of the electron reconstruction and identification efficiencies in ATLAS, (ATL-PHYS-PROC-2014-035), 2014, URL https://atlas.web.cern.ch/Atlas/GROUPS/PHYSICS/EGAMMA/PublicPlots/20130926/ATL-COM-PHYS-2013-1287/index.html.

[51] ATLAS collaboration, Determination of the muon reconstruction efficiency in ATLAS at the Z resonance in proton-proton collisons at $\sqrt{s} = 7$ TeV, *ATLAS note*, ATLAS-CONF-2011-008, 2011.

[52] R. O. Duda and P. E. Hart, Use of the Hough Transformation to Detect Lines and Curves in Pictures, *Commun. ACM*, 15(1):11–15, 1972, ISSN 0001-0782, doi:10.1145/361237.361242, URL http://doi.acm.org/10.1145/361237.361242.

[53] ATLAS collaboration, Measurement of observables sensitive to the underlying event in inclusive Z-boson production at 7 TeV, *ATLAS note*, ATL-COM-PHYS-2013-071, 2013.

[54] ATLAS collaboration, Performance of the Electron and Photon Trigger in p-p Collisions at $\sqrt{s} = 7$ TeV with the ATLAS Detector at the LHC in 2011, *ATLAS note*, ATL-COM-DAQ-2012-008, 2012.

[55] ATLAS collaboration, Performance of the ATLAS muon trigger in 2011, *ATLAS note*, ATLAS-CONF-2012-099, 2012.

[56] G. Hanson, G. S. Abrams, A. M. Boyarski, et al., Evidence for Jet Structure in Hadron Production by e^+e^- Annihilation, *Phys.Rev.Lett.*, 35:1609–1612, 1975, doi:10.1103/PhysRevLett.35.1609, URL http://link.aps.org/doi/10.1103/PhysRevLett.35.1609.

[57] TASSO collaboration, Global jet properties at 14 - 44 GeV center of mass energy in e+e- annihilation, *Z.Phys.*, C47(2):187–198, 1990, ISSN 0170-9739, doi:10.1007/BF01552339, URL http://dx.doi.org/10.1007/BF01552339.

[58] JADE collaboration, Movilla Fernandez, P.A., Biebel, O., Bethke, S., Kluth, S., Pfeifenschneider, P., A Study of event shapes and determinations of α_s using data of e^+e^- annihilations at $\sqrt{s} = 22$-GeV to 44-GeV, *Eur.Phys.J.*, C1:461–478, 1998, doi:10.1007/s100520050096.

[59] MARK-2 collaboration, Studies of Jet Production Rates in e^+e^- Annihilation at $\sqrt{s} = 29$ GeV, *Z.Phys.*, C43:325, 1989, doi:10.1007/BF01506527.

[60] TOPAZ collaboration, Measurements of alpha-s in e+ e- annihilation at TRISTAN, *Phys.Lett.*, B313:475–482, 1993, doi:10.1016/0370-2693(93)90022-A.

[61] AMY collaboration, A Determination of alpha-s in e+ e- annihilation at $\sqrt{s} = 57.3$ GeV, *Phys.Lett.*, B355:394–400, 1995, doi:10.1016/0370-2693(95)00689-I.

[62] VENUS collaboration, Determination of the QCD scale parameter Lambda (ms) with QCD cascade on the basis of the next-to-leading logarithmic approximation, *Phys.Lett.*, B240:232–236, 1990, doi:10.1016/0370-2693(90)90440-H.

[63] SLD collaboration, Measurement of $\alpha_s(M_Z^2)$ from hadronic event observables at the Z0 resonance, *Phys.Rev.*, D51:962–984, 1995, doi:10.1103/PhysRevD.51.962.

[64] DELPHI collaboration, Tuning and test of fragmentation models based on identified particles and precision event shape data, *Z.Phys.*, C73:11–60, 1996, doi:10.1007/s002880050295.

[65] ALEPH collaboration, Studies of quantum chromodynamics with the ALEPH detector, *Phys.Rept.*, 294:1–165, 1998, doi:10.1016/S0370-1573(97)00045-8.

[66] ALEPH collaboration, Studies of QCD at e+ e- centre-of-mass energies between 91-GeV and 209-GeV, *Eur.Phys.J.*, C35:457–486, 2004, doi:10.1140/epjc/s2004-01891-4.

[67] S. Bethke, A. H. Hoang, S. Kluth, et al., Workshop on Precision Measurements of α_s, 2011.

[68] A. Banfi, G. P. Salam, and G. Zanderighi, Phenomenology of event shapes at hadron colliders, *JHEP*, 1006:038, 2010, doi:10.1007/JHEP06(2010)038.

[69] D. Weyh, About the measurement of hadronic event shapes for underlying event model tuning with the ATLAS detector at $\sqrt{s} = 7$ TeV, 2011, Master thesis at Mathematisch-Naturwissenschaftliche Fakultät I, HU Berlin.

[70] I. W. Stewart, F. J. Tackmann, and W. J. Waalewijn, The Beam Thrust Cross Section for Drell-Yan at NNLL Order, *Phys.Rev.Lett.*, 106:032001, 2011, doi:10.1103/PhysRevLett.106.032001.

[71] T. Sjostrand, S. Mrenna, and P. Z. Skands, PYTHIA 6.4 Physics and Manual, *JHEP*, 0605:026, 2006, doi:10.1088/1126-6708/2006/05/026.

[72] E. Cuautle, R. Jimenez, I. Maldonado, et al., Disentangling the soft and hard components of the pp collisions using the sphero(i)city approach, 2014, URL http://arxiv.org/abs/1404.2372.

[73] A. Buckley, J. Butterworth, D. Grellscheid, et al., Rivet user manual, *Computer Physics Communications*, 184(12):2803 – 2819, 2013, ISSN 0010-4655, doi:http://dx.doi.org/10.1016/j.cpc.2013.05.021, URL http://www.sciencedirect.com/science/article/pii/S0010465513001914.

[74] ATLAS collaboration, Measurement of charged-particle event shape variables in $\sqrt{s} = 7$ TeV proton-proton interactions with the ATLAS detector, *Phys.Rev.*, D88:032004, 2013, doi:10.1103/PhysRevD.88.032004.

[75] CMS collaboration, Event shapes and azimuthal correlations in Z + jets events in pp collisions at $\sqrt{s} = 7$ TeV, *Phys.Lett.*, B722:238–261, 2013, doi:10.1016/j.physletb.2013.04.025.

[76] CMS collaboration, First Measurement of Hadronic Event Shapes in pp Collisions at $\sqrt(s) = 7$ TeV, *Phys.Lett.*, B699:48–67, 2011, doi:10.1016/j.physletb.2011.03.060.

[77] ATLAS collaboration, Measurement of event shapes at large momentum transfer with the ATLAS detector in pp collisions at $\sqrt{s} = 7$ TeV, *Eur.Phys.J.*, C72:2211, 2012, doi:10.1140/epjc/s10052-012-2211-y.

[78] J. C. Collins, D. E. Soper, and G. F. Sterman, Factorization of Hard Processes in QCD, *Adv.Ser.Direct.High Energy Phys.*, 5:1–91, 1988.

[79] A. Buckley, J. Butterworth, S. Gieseke, et al., General-purpose event generators for LHC physics, *Phys.Rept.*, 504:145–233, 2011, doi:10.1016/j.physrep.2011.03.005.

[80] ATLAS collaboration, Further ATLAS tunes of PYTHIA6 and Pythia 8, *ATLAS note*, ATL-PHYS-PUB-2011-014, 2011.

[81] J. Pumplin, D. Stump, J. Huston, et al., New generation of parton distributions with uncertainties from global QCD analysis, *JHEP*, 0207:012, 2002, doi:10.1088/1126-6708/2002/07/012.

[82] C. Duhr, S. Hoeche, and F. Maltoni, Color-dressed recursive relations for multi-parton amplitudes, *JHEP*, 0608:062, 2006, doi:10.1088/1126-6708/2006/08/062.

[83] S. Catani, F. Krauss, R. Kuhn, and B. Webber, QCD matrix elements + parton showers, *JHEP*, 0111:063, 2001.

[84] F. Krauss, Matrix elements and parton showers in hadronic interactions, *JHEP*, 0208:015, 2002.

[85] M. L. Mangano, M. Moretti, F. Piccinini, R. Pittau, and A. D. Polosa, ALPGEN, a generator for hard multiparton processes in hadronic collisions, *JHEP*, 0307:001, 2003.

[86] T. Sjostrand and M. van Zijl, A Multiple Interaction Model for the Event Structure in Hadron Collisions, *Phys.Rev.*, D36:2019, 1987, doi:10.1103/PhysRevD.36.2019.

[87] G. A. Schuler and T. Sjostrand, Hadronic diffractive cross-sections and the rise of the total cross-section, *Phys.Rev.*, D49:2257–2267, 1994, doi:10.1103/PhysRevD.49.2257.

[88] A. Donnachie and P. Landshoff, Total cross-sections, *Phys.Lett.*, B296:227–232, 1992, doi:10.1016/0370-2693(92)90832-O.

[89] A. Martin, W. Stirling, R. Thorne, and G. Watt, Parton distributions for the LHC, *Eur.Phys.J.*, C63:189–285, 2009, doi:10.1140/epjc/s10052-009-1072-5.

[90] S. Amendolia, G. Bellettini, P. Braccini, et al., Total cross-section measurement at the ISR, *Il Nuovo Cimento A*, 17(4):735–755, 1973, ISSN 0369-3546, doi:10.1007/BF02786846, URL http://dx.doi.org/10.1007/BF02786846.

[91] UA4 collaboration, Measurement of the proton-antiproton elastic and total cross section at a centre-of-mass energy of 540 GeV , *Phys.Lett.*, B117(12):126 – 130, 1982, ISSN 0370-2693, doi:http://dx.doi.org/10.1016/0370-2693(82)90888-7, URL http://www.sciencedirect.com/science/article/pii/0370269382908887.

[92] UA5 collaboration, Antiproton-proton cross sections at 200 and 900 GeV c.m. energy, *Z.Phys.*, D32(2):153–161, 1986, ISSN 0170-9739, doi:10.1007/BF01552491, URL http://dx.doi.org/10.1007/BF01552491.

[93] E710 collaboration, Measurement of the total cross section at $\sqrt{s}$=1.8 TeV, *Phys.Rev.Lett.*, 63:2784–2786, 1989, doi:10.1103/PhysRevLett.63.2784, URL http://link.aps.org/doi/10.1103/PhysRevLett.63.2784.

[94] E811 collaboration, A measurement of the proton-antiproton total cross section at $\sqrt{s}$ = 1.8 TeV , *Phys.Lett.*, B445(34):419 – 422, 1999, ISSN 0370-2693, doi:http://dx.doi.org/10.1016/S0370-2693(98)01421-X, URL http://www.sciencedirect.com/science/article/pii/S037026939801421X.

[95] CDF collaboration, Measurement of small angle antiproton-proton elastic scattering at $\sqrt{s}$ =546 and 1800 GeV, *Phys.Rev.*, D50:5518–5534,

1994, doi:10.1103/PhysRevD.50.5518, URL http://link.aps.org/doi/10.1103/PhysRevD.50.5518.

[96] TOTEM collaboration, Measurement of proton-proton elastic scattering and total cross-section at $\sqrt{s} = 7\,TeV$, *Europhys.Lett.*, 101(2):21002, 2013, URL http://stacks.iop.org/0295-5075/101/i=2/a=21002.

[97] ATLAS collaboration, Summary of ATLAS Pythia 8 tunes, *ATLAS note*, ATL-PHYS-PUB-2012-003, 2012.

[98] T. Sjostrand, S. Mrenna, and P. Z. Skands, A Brief Introduction to PYTHIA 8.1, *Comput.Phys.Commun.*, 178:852–867, 2008, doi:10.1016/j.cpc.2008.01.036.

[99] T. Sjostrand, S. Mrenna, and P. Z. Skands, Pythia8 online manual, http://home.thep.lu.se/ torbjorn/pythia81html.

[100] CDF collaboration, The transverse momentum and total cross section of e^+e^- pairs in the Z boson region from $p\bar{p}$ collisions at $\sqrt{s} = 1.8$ TeV, *Phys.Rev.Lett.*, 84:845–850, 2000, doi:10.1103/PhysRevLett.84.845.

[101] B. Povh, K. Rith, C. Scholz, F. Zetsche, and W. Rodejohann, Teilchen und Kerne: Eine Einführung in die physikalischen Konzepte, *Springer Berlin Heidelberg*, 2013, URL http://books.google.de/books?id=jCU_ngEACAAJ.

[102] B. Andersson, S. Mohanty, and F. Soderberg, Recent developments in the Lund model, 2002, LU-TP-02-45.

[103] R. D. Field and S. Wolfram, A QCD model for e^+e^- annihilation , *Nucl.Phys.*, B213(1):65 – 84, 1983, ISSN 0550-3213, doi:http://dx.doi.org/10.1016/0550-3213(83)90175-X, URL http://www.sciencedirect.com/science/article/pii/055032138390175X.

[104] D. Yennie, S. Frautschi, and H. Suura, The infrared divergence phenomena and high-energy processes, *Annals of Physics*, 13(3):379 – 452, 1961, ISSN 0003-4916, doi:http://dx.doi.org/10.1016/0003-4916(61)90151-8, URL http://www.sciencedirect.com/science/article/pii/0003491661901518.

[105] M. Schönherr and F. Krauss, Soft Photon Radiation in Particle Decays in SHERPA, *JHEP*, 0812:018, 2008, doi:10.1088/1126-6708/2008/12/018.

[106] J. Allison, K. Amako, J. Apostolakis, et al., Geant4 developments and applications, *Nuclear Science, IEEE Transactions on*, 53(1):270–278, 2006, ISSN 0018-9499,

doi:10.1109/TNS.2006.869826.

[107] ATLAS collaboration, Fast Simulation for ATLAS: Atlfast-II and ISF, *ATLAS note*, ATL-SOFT-PROC-2012-065, ATL-COM-SOFT-2012-137, 2012.

[108] ATLAS collaboration, Validation of the ATLFAST-II package for the simulation of supersymmetry events, *ATLAS note*, ATL-COM-PHYS-2011-1181, 2011.

[109] ATLAS collaboration, Track Reconstruction Efficiency in $\sqrt{s} = 7$ TeV Data for Tracks with $p_\perp > 100$ MeV, *ATLAS note*, ATL-COM-PHYS-2010-682, 2010, This is the track reconstruction efficiency supporting note for the MinBias 2 paper.

[110] ATLAS collaboration, Higgs mass measurements and uncertainties in 2011 and 2012 data, *ATLAS note*, ATL-COM-PHYS-2012-1774, 2012.

[111] ATLAS collaboration, Improved electron reconstruction in ATLAS using the Gaussian Sum Filter-based model for bremsstrahlung, *ATLAS note*, ATLAS-CONF-2012-047, 2012.

[112] ATLAS collaboration, Muon reconstruction efficiency in reprocessed 2010 LHC proton-proton collision data recorded with the ATLAS detector, *ATLAS note*, ATLAS-CONF-2011-063, 2011.

[113] ATLAS collaboration, Muon Momentum Resolution in First Pass Reconstruction of pp Collision Data Recorded by ATLAS in 2010, *ATLAS note*, ATLAS-CONF-2011-046, 2011.

[114] J. W. Monk and C. Oropeza-Barrera, The HBOM Method for Unfolding Detector Effects, *Nucl.Instrum.Meth.*, A701:17–24, 2013, doi:10.1016/j.nima.2012.09.045.

[115] A. Buckley, H. Hoeth, H. Lacker, H. Schulz, and J. E. von Seggern, Systematic event generator tuning for the LHC, *Eur.Phys.J.*, C65:331–357, 2010, doi:10.1140/epjc/s10052-009-1196-7.

[116] K. M. Brown, Computer Oriented Methods for Fitting Tabular Data in the Linear and Nonlinear Least Squares Sense, *Proceedings of the December 5-7, 1972, Fall Joint Computer Conference, Part II*, AFIPS72:1309–1315, 1972, doi:10.1145/1480083.1480176, URL http://doi.acm.org/10.1145/1480083.1480176.

[117] ATLAS collaboration, Measurement of the production cross section of jets in association with a Z boson in pp collisions at $\sqrt{s} = 7$ TeV with the ATLAS

detector, *JHEP*, 1307:032, 2013, doi:10.1007/JHEP07(2013)032.

[118] H. Schulz, H. Lacker, and M. Leyton, Measurement of hadron-collider event shapes in Drell-Yan events at $\sqrt{s} = 7$ TeV with ATLAS: Analysis support note, *ATLAS note*, ATL-COM-PHYS-2014-285, 2014.

[119] G. Cowan, Statistical Data Analysis, *Oxford University Press, Oxford*, 1998.

[120] G. D'Agostini, Improved iterative Bayesian unfolding, 2010, URL http://arxiv.org/abs/1010.0632.

[121] B. Wynne, Imagiro: an implementation of Bayesian iterative unfolding for high energy physics, 2012, URL http://arxiv.org/abs/1203.4981.

[122] T. Adye, Unfolding algorithms and tests using RooUnfold, 2011, URL http://arxiv.org/abs/1105.1160.

[123] ATLAS collaboration, Measurement of the production cross section for Z/gamma* in association with jets in *pp* collisions at $\sqrt{s} = 7$ TeV with the ATLAS detector, *Phys.Rev.*, D85:032009, 2012, doi:10.1103/PhysRevD.85.032009.

[124] N. D. Gagunashvili, Comparison of weighted and unweighted histograms, 2006, URL http://arxiv.org/abs/physics/0605123.

[125] R. Brun and F. Rademakers, ROOT, *Nucl. Instr. Meth. Phys. Res.*, A389, 1997.

[126] I. M. Chakravarti, R. G. Laha, and J. Roy, Handbook of Methods of Applied Statistics, *John Wiley and Sons*, 1967.

[127] R. R. J. Barlow, Statistics : a guide to the use of statistical methods in the physical sciences, *Wiley*, 1989, URL http://opac.inria.fr/record=b1087341.

[128] M. Dobbs and J. Hansen, HepMC C++ Monte Carlo event record for High Energy Physics, *Computer Physics Communications*, 134(1):41–46, 2001.

[129] CMS collaboration, Measurement of the underlying event in the Drell-Yan process in proton-proton collisions at $\sqrt{s} = 7$ TeV, *Eur.Phys.J.*, C72:2080, 2012, doi:10.1140/epjc/s10052-012-2080-4.

[130] A. Buckley, The hepthesis LaTeX class, URL http://www.ctan.org/pkg/hepthesis.

List of figures

List of tables

Colophon

This thesis was made in LaTeX 2_ε using the "hepthesis" class [130].

Acknowledgements

First and foremost I would like to thank my supervisor Prof. Dr. Heiko Lacker whose continuous support and scrutiny over a period of many years have tremendously helped to conduct the measurement described in this document. I would also like to thank Prof. Dr. Frank Krauss for proposing this analysis in the first place as well as for being helpful especially in all question related to Monte-Carlo event generators. In that context I would also like to thank Dr. Marek Schönherr, Dr. Frank Siegert, Jun.-Prof. Dr. Steffen Schumann and Dr. Stefan Hoeche, especially for answering countless questions so quickly and thorough.

A big thank you goes to Dr. Andy Buckley for encouraging me to work on data analysis in the first place, for cheering me up after several ATLAS-related setbacks and the opportunity to be involved in the development of Rivet.

The development and successful application of the pile-up correction method would have been impossible without numerous enlightening discussions with Dr. Simone Pagan Griso and Dr. Olrich Kepka. Further I would like to thank Dr. Benjamin Wynne for helping me to implement the pile-up correction method in the unfolding software.

Dr. Michael Leyton and Dr. Gerhard Brandt deserve thanks for setting up the analysis chain and for solving many conceptual problems. As does M.Sc. Daniel Weyh whom it was a privilege to work for.

A very warm thank you goes to all my former colleagues sharing office 2411. I would like to thank Rocco and Dennis for their support in all ATLAS-related struggles. My sanity would have significantly deteriorated without you. I would like to thank Geoff and Laura for providing me with tomatoes and cat videos to cheer me up especially during the finalisation of the analysis. I would also like to thank Christoph and Conrad for some much appreciated last-minute help.

Bedanken möchte ich mich zudem bei Josi und Luki, Ende guuut, alles guuut, Doktorhuuut.

Es sei noch erwähnt, dass Patrick Rieck mit seinen Weißheiten ganz entscheidend am Gelingen dieser Arbeit beteiligt war.

Ein herzliches Dankschön auch an Veronika Schneider für ihre grenzenlose Geduld mit mir und meiner Vergesslichkeit.

Zuletzt möchte ich all meinen Freunden und meiner Familie für ihre Unterstützung danken und mit der Bemerkung schließen, dass große Teile dieser Arbeit ohne übermäßigen Konsum koffeinhaltiger Getränke nie entstanden wären.

Erklärung

Ich versichere, dass ich die vorliegende Dissertation selbstständig und nur unter Verwendung der in der Promotionsordnung angegebenen Hilfen und Hilfsmittel angefertigt habe.

Berlin, 17. April, 2014 Holger Schulz